AD-A160 566 PLACES (POSITION LOCATION AND COMMUNICATION EFFECTS SIMULATIONS) BEACON EXPERIMENT TEST RESULTS(U) ESL INC SUNNYVALE CA J MARSHALL ET AL. 01 AUG 84 DNA-TR-84-376 1/5

UNCLASSIFIED DNA001-81-C-0149 F/G 20/14 NL

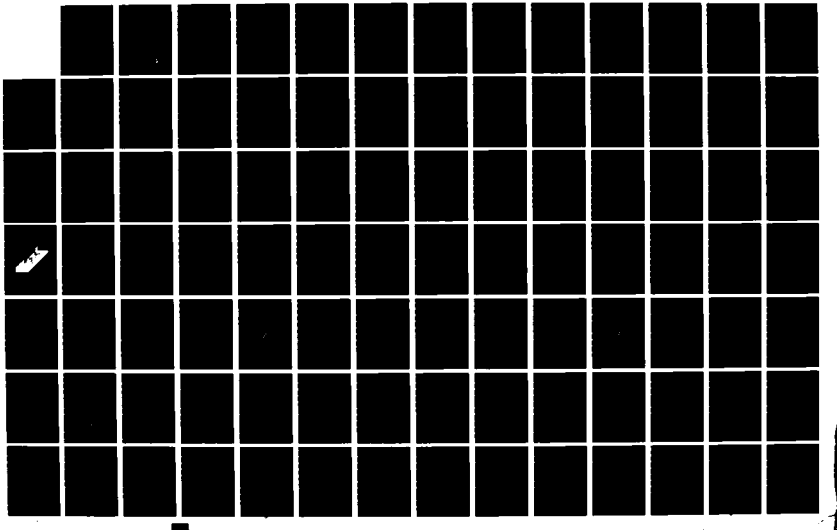

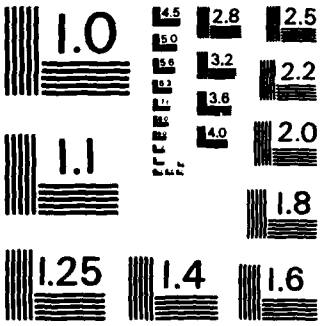

MICROCOPY RESOLUTION TEST CHART
NATIONAL BUREAU OF STANDARDS-1963-A

E3-1829

AD-A160 566

DNA-TR-84-376

PLACES BEACON EXPERIMENT TEST RESULTS

Dr. James Marshall
Gary W. Elston
Jeff W. Lehman
ESL Incorporated
P.O. Box 3510
Sunnyvale, CA 94088-3510

1 August 1984

Technical Report

CONTRACT No. DNA 001-81-C-0149

Approved for public release, distribution is unlimited.

THIS WORK WAS SPONSORED BY THE DEFENSE NUCLEAR AGENCY
UNDER RDT&E RMSS CODE B322082466 S99QAXHB00007 H2590D.

Prepared for
Director
DEFENSE NUCLEAR AGENCY
Washington, DC 20305-1000

Destroy this report when it is no longer needed. Do not return to sender.

PLEASE NOTIFY THE DEFENSE NUCLEAR AGENCY, ATTN: STTI, WASHINGTON, DC 20305-1000, IF YOUR ADDRESS IS INCORRECT, IF YOU WISH IT DELETED FROM THE DISTRIBUTION LIST, OR IF THE ADDRESSEE IS NO LONGER EMPLOYED BY YOUR ORGANIZATION.

UNCLASSIFIED

SECURITY CLASSIFICATION OF THIS PAGE AD-A160 566

REPORT DOCUMENTATION PAGE

1a REPORT SECURITY CLASSIFICATION UNCLASSIFIED	1b RESTRICTIVE MARKINGS
2a SECURITY CLASSIFICATION AUTHORITY	3 DISTRIBUTION/AVAILABILITY OF REPORT Approved for public release; distribution is unlimited.
2b DECLASSIFICATION/DOWNGRADING SCHEDULE N/A since UNCLASSIFIED	
4 PERFORMING ORGANIZATION REPORT NUMBER(S)	5 MONITORING ORGANIZATION REPORT NUMBER(S) DNA-TR-84-376
6a NAME OF PERFORMING ORGANIZATION ESL Incorporated 6b OFFICE SYMBOL (If applicable)	7a NAME OF MONITORING ORGANIZATION Director Defense Nuclear Agency
6c ADDRESS (City, State, and ZIP Code) P.O. Box 3510 Sunnyvale, CA 94088-3510	7b ADDRESS (City, State, and ZIP Code) Washington, DC 20305-1000
8a NAME OF FUNDING/SPONSORING ORGANIZATION 8b OFFICE SYMBOL (If applicable)	9 PROCUREMENT INSTRUMENT IDENTIFICATION NUMBER DNA 001-81-C-0149
8c ADDRESS (City, State, and ZIP Code)	10 SOURCE OF FUNDING NUMBERS

PROGRAM ELEMENT NO	PROJECT NO	TASK NO	WORK UNIT ACCESSION NO
62715H	S99QAXH	B	DH005440

11 TITLE (Include Security Classification)
PLACES BEACON EXPERIMENT TEST RESULTS

12 PERSONAL AUTHOR(S)
Dr James Marshall, Gary W. Elston, and Jeff W. Lehman

13a TYPE OF REPORT	13b TIME COVERED	14 DATE OF REPORT (Year Month Day)	15 PAGE COUNT
Technical	FROM 810501 TO 840801	1984, August 1	424

16 SUPPLEMENTARY NOTATION
This work was sponsored by the Defense Nuclear Agency under RDT&E RMSS Code B322082466 S99QAXHB00007 H2590D.

17 COSATI CODES			18 SUBJECT TERMS (Continue on reverse if necessary and identify by block number)	
FIELD	GROUP	SUB-GROUP	PLACES Experiment	Frequency Selective Fading
20	14		Barium Release	Satellite Communications
17	2		Ionospheric Scintillation	Navigation

19 ABSTRACT (Continue on reverse if necessary and identify by block number)

During December 1980, the Position Location and Communication Effects Simulations (PLACES) Experiment was conducted to investigate the effects of structured ionospheric plasmas on satellite communications and navigation systems. A series of four separate artificial inospheric plasma environments were created on separate evenings by 48-kg barium releases from rockets launched from Eglin AFB, FL. This report describes the measurements of the time-of-arrival spread of energy (channel impulse response) on a phase coded spread spectrum signal emanating from a rocket launched behind the barium cloud and received at specially constructed ground receiving site in northern Florida (Beacon Experiment). The data are shown to be in good agreement with the DNA propagation channel model and a geometric optics interpretation of the observed propagation effects.

20 DISTRIBUTION/AVAILABILITY OF ABSTRACT	21 ABSTRACT SECURITY CLASSIFICATION	
☐ UNCLASSIFIED/UNLIMITED ☒ SAME AS RPT ☐ DTIC USERS	UNCLASSIFIED	
22a NAME OF RESPONSIBLE INDIVIDUAL Betty L. Fox	22b TELEPHONE (Include Area Code) (202) 325-7042	22c OFFICE SYMBOL DNA/STTI

DD FORM 1473, 84 MAR 83 APR edition may be used until exhausted
All other editions are obsolete

SECURITY CLASSIFICATION OF THIS PAGE
UNCLASSIFIED

18. SUBJECT TERMS (Continued)

Striations
Propagation

PREFACE

The PLACES Beacon Experiment has provided a unique set of data, only a portion of which has been examined in detail. The goal of this report is to present a summary of those data that are believed to be of most interest to the DNA community and to provide an overview of the data availability.

The authors would like to single out the assistance of Dr. Clifford Prettie of Berkeley Research Associates for his continued participation and assistance throughout this data reduction effort.

TABLE OF CONTENTS

TABLE OF CONTENTS (Continued)

TABLE OF CONTENTS (Continued)

TABLE OF CONTENTS (Continued)

TABLE OF CONTENTS (Concluded)

LIST OF ILLUSTRATIONS

LIST OF ILLUSTRATIONS (Continued)

LIST OF ILLUSTRATIONS (Continued)

LIST OF ILLUSTRATIONS (Continued)

LIST OF ILLUSTRATIONS (Continued)

LIST OF ILLUSTRATIONS (Continued)

LIST OF ILLUSTRATIONS (Continued)

LIST OF ILLUSTRATIONS (Continued)

LIST OF ILLUSTRATIONS (Continued)

LIST OF ILLUSTRATIONS (Continued)

LIST OF ILLUSTRATIONS (Continued)

LIST OF ILLUSTRATIONS (Continued)

LIST OF ILLUSTRATIONS (Continued)

LIST OF ILLUSTRATIONS (Continued)

LIST OF ILLUSTRATIONS (Continued)

LIST OF ILLUSTRATIONS (Concluded)

LIST OF TABLES

SECTION I
INTRODUCTION

1.1 GENERAL

During December 1980, the Position Location and Communications Effects Simulations (PLACES) Experiment was conducted to investigate the effects of structured ionospheric plasmas on satellite communications and navigation systems. A structured plasma environment was created by a 48-kgm barium release from a rocket launched from Eglin AFB, Florida. Measurements of the time-of-arrival spread of energy were accomplished during what is referred to here as the Beacon Experiment on signals emanating from a rocket transiting behind the barium cloud as viewed from ground receiving sites in northern Florida (1,4,3). Additionally, during what is referred to as the Aircraft Experiment (1,2,4,5), measurements of propagation effects on signals from the LES-8 satellite over the Pacific Ocean to a KC 135 aircraft operating in the Florida area were conducted. This report is intended to provide a summary of the Beacon Experiment test results.

The PLACES Experiment was conceived to investigate the effects of the frequency selective fading environment associated with radio wave propagation through a strongly scattering striated ionospheric plasma on satellite communication and navigation systems. An experimental verification of the propagation relations that are used to specify the time-of-arrival spread and jitter of significance to wide bandwidth satellite communication and navigation systems was desired. The rocket Beacon Experiment provided a unique but approximate measurement of the channel impulse response, and a direct measurement of the time-of-arrival spread and jitter associated with pseudonoise phase-shift-keyed spread spectrum systems. Good agreement with the existing DNA channel model (13) has been demonstrated.

1.2 TEST EVENTS

A total of four 48 kgm barium releases were conducted. These releases were named GAIL (12/4/80), HOPE (12/6/80), IRIS (12/8/80), and JAN (12/12/80). The release altitudes were between 180 and 185 km. The ionizing action of the sun's ultraviolet rays on the barium generates the ionized plasma, which becomes elongated along the earth's magnetic field. Subsequent neutral wind cross-field drag causes the field aligned irregularities (striations) to be created. Two beacon rockets were flown during event IRIS and one probe rocket was flown during event JAN. The aircraft experiment was conducted following each release.

A Pulsed Plasma Probe Experiment (9,14) was also conducted during which a rocket was fired directly through the barium cloud to measure the in-situ structured plasma properties. Mass spectrometer measurements were taken simultaneously with the plasma probe measurements. Because of operational constraints, the plasma probe experiment measurements were obtained on a barium release subsequent to the beacon rocket occultation measurements.

1.3 BEACON EXPERIMENT TEST CONCEPT

The Beacon Experiment used two signals transmitted from the beacon rocket. A strongly scattering striated environment is created by the barium plasma at VHF. For this reason, a VHF link at 98 MHz was used. A 9.8 megachip per second pseudorandom (PN) digital wavetrain was used to biphase modulate the VHF signal. The beacon receiver stations, by virtue of the high rate PN modulation, performed high resolution in-phase and quadrature cross-correlation measurements of the received signal at 90 delay positions (1/3 chip delay spacing) spanning approximately 3 microseconds of delay. These measurements provide a direct measurement of the channel impulse response and the

signal time-of-arrival fluctuation and spread properties. A C-band CW signal at 4116 MHz (98 MHz x 42) was also transmitted by the rocket motion induced on the VHF signal, thus, leaving only the propagation channel effects.

1.4 BEACON EXPERIMENT RESULTS AND CONCLUSIONS

Two beacon rockets were launched during event IRIS of the PLACES Experiment. Successful data were recorded from each of these beacons at both ground receiving sites, Cape San Blas (D3A) and St. George Island (SGI). The ground receiving systems effectively measured the complex channel impulse response of the striated barium plasma. The technique used to recover the channel impulse response relies on the processing of the pseudorandom phase modulation of the rocket transmitted signal. The received signal in-phase and quadrature components are hardware cross-correlated with a replica of the modulating PN sequence in the ground station receiver. Provided the PN sequence autocorrelation is sufficiently narrow compared with the time delay extent of the channel impulse response, an accurate representation of the channel impulse response is realized. This approximation was presented in Appendix A of the quicklook report (1) along with a description of the hardware configuration.

The rocket trajectories flown on Beacon 1 (flight 1) and Beacon 2 (flight 2) are shown on Figures 1-1 and 1-2. The time since launch is indicated on these trajectories in seconds. Also shown is the indicated FPS-85 radar location of the maximum density portion of the ion cloud at the occultation time. The cloud projection to the aircraft operating altitude from LES-8 is also shown for reference.

Table 1-1 provides a summary of the occultation geometry. The beacon rocket on both these launches was targeted 40 km behind the TV optics cloud track point. On flight 1, the beacon rocket flew approximately 26.9 km behind the radar maximum density point.

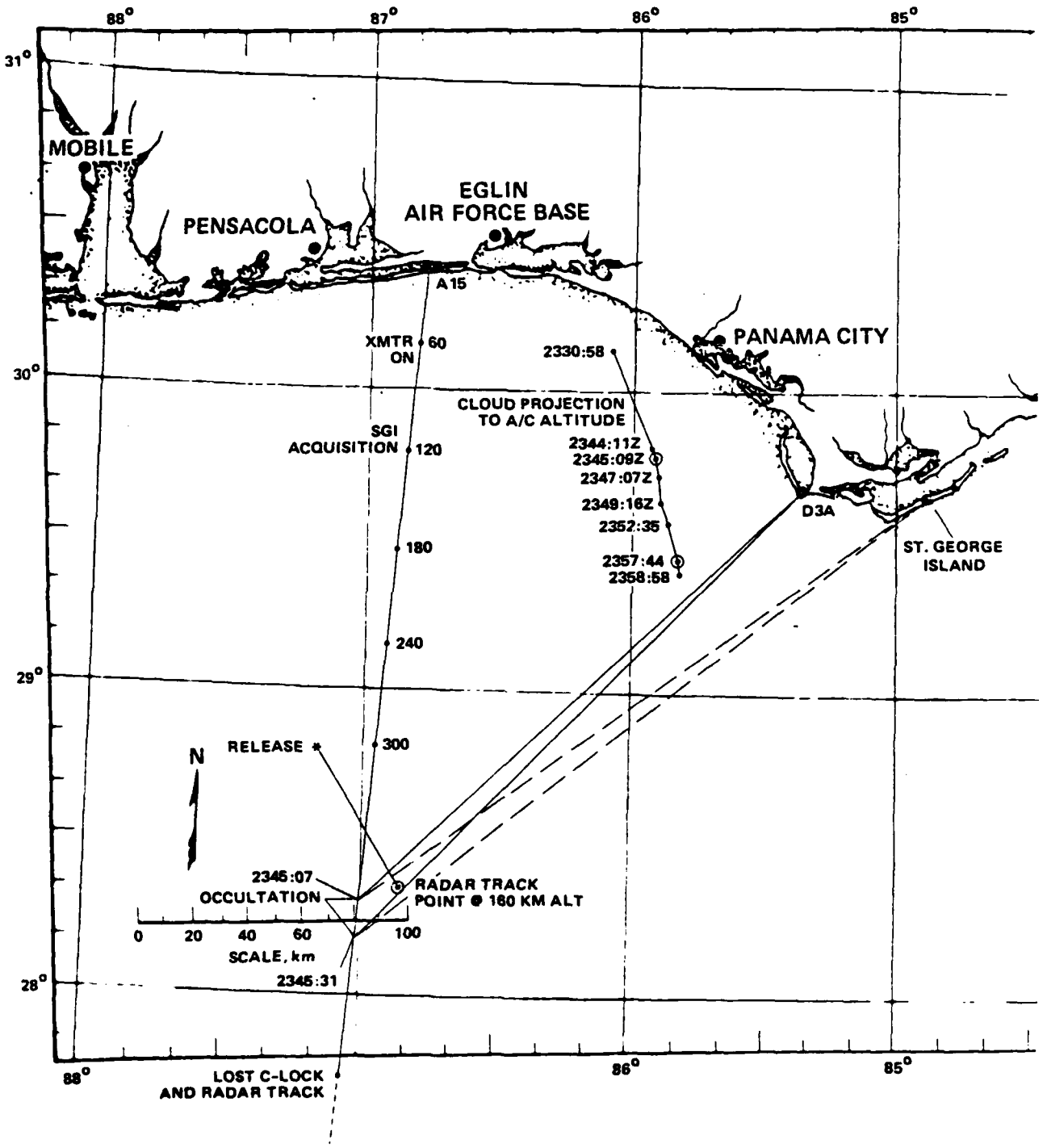

Figure 1-1. Beacon rocket trajectory, Beacon 1.

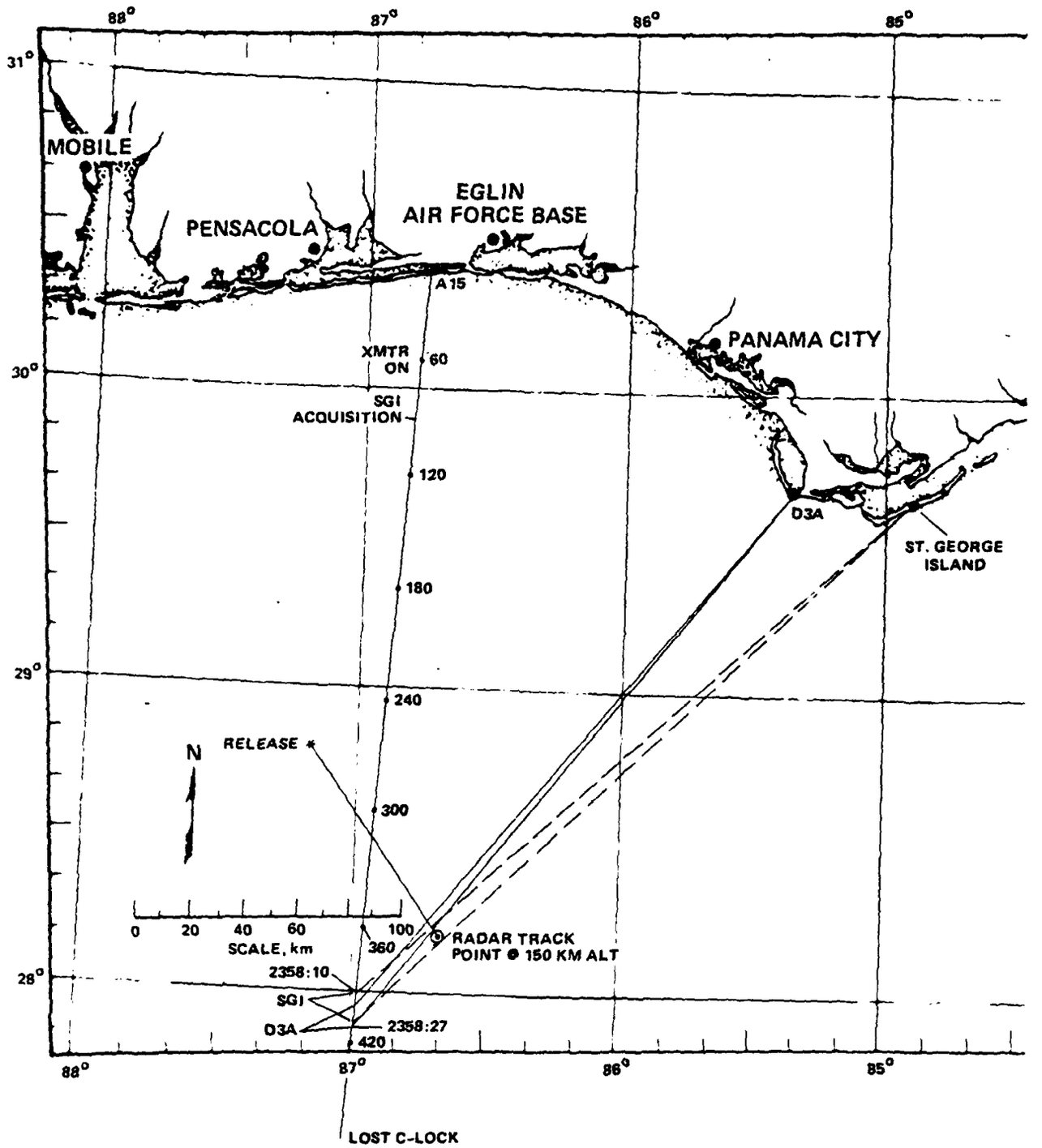

Figure 1-2. Beacon rocket trajectory, Beacon 2.

Table 1-1. Occultation summary.

IRIS RELEASE AT 2313:08Z, 182.2 km ALTITUDE

FLIGHT	SITE	OCCULTATION INTERVAL	CLOUD[1] LOCATION LAT, LON, ALT	N_e MAX (m^{-3})[2]	TO ROCKET FROM SITE			NOMINAL OCCULTATION DISTANCE TO N_e PEAK (km)	MAGNETIC ASPECT (deg)
					ELEVATION (deg)	AZIMUTH (deg)	SLANT RANGE (km)		
BEACON 1	ST. GEORGE ISLAND (29°38'36", 84°54'07")	2345:08.7 TO 2345:30.0	28.3488° 86.8488° 160 km @2345:24Z	3.7×10^{12} 28.3488° 86.8488°	36.1	236.2	321.1	28.9	~ 37.9
	CAPE SAN BLAS (D3A) (29°40'00", 85°21'18")	2345:10.1 TO 2345:30.7			38.2	230.1	303.3	-	~ 38
BEACON 2	ST. GEORGE ISLAND	2358:10 TO 2358:25	28.1609° 86.6906° 160 km @ 2358:20Z	3.5×10^{12} 28.1609° 86.6906°	32.6	228.4	331.1	42.4	~ 41
	CAPE SAN BLAS	2358:17 TO 2358:27			32.9	222.6	313.6	-	~ 36

[1] NEAR PEAK N_e POINT, PER RADAR TRACK

[2] PER RADAR (REF. 10)

The ray path to St. George Island missed slicing the cloud through this maximum density point by approximately 1.9 km. On flight 2, the beacon rocket flew approximately 42 km behind the indicated maximum density point. The line-of-sight to St. George Island sliced through the cloud approximately 4.8 km north of the maximum density point and exhibited considerably less angular scattering than the prior event. The corresponding path to Cape San Blas sliced through the cloud approximately 11 km to the north of the maximum density point. The path to Cape San Blas missed the structured plasma region and does not exhibit angular scattering effects. This is in agreement with the optical photography showing the structure just south of this slice. Additional details of the occultation geometries to each site are discussed in Sections 2,3,4, and 5.

Intense angular scattering of the 98-MHz beacon signal was produced as predicted and the complex channel impulse response was successfully measured. The effects observed have been used to rigorously test theory. The results are shown to be in good agreement with a geometric optics approach to the prediction of time-of-arrival jitter and delay spread through striated plasmas. These measurements of the complex channel impulse response support the current DNA channel impulse response model.

A geometrical approach based on angular spectrum arguments can be used to predict the signal energy delay power profile as well as the spectrum of the signal at each component of delay. The geometrical arguments indicate that the basic cause of signal time-of-arrival spread is the geometric increase in path length produced by the plasma angular scattering. The time-of-arrival is largely due to the dispersive plasma phase fluctuations. The angular scattering is closely given by the angular spectrum of the signal at frequencies near the center of the signal bandwidth. Thus, a direct mapping between the angular spectrum and the energy delay profile is expected

and demonstrated. The generalized power spectrum (13), $\Gamma(f,\tau)$ describes the power spectrum of the received signal at a fixed delay and spectral frequency. The generalized power spectrum was extracted from the PLACES data and the functional form is shown to be in excellent agreement with theory. Its functional dependence and the geometric knowns in the experiment are also shown to be in good quantitative agreement. As a result of this experimental verification, the DNA channel model for structured plasma and the associated propagation theory is believed to be well understood and adequately modeled.

The PLACES Experiment has also resulted in an improved understanding of the phenomenology of the late-time evolution of structured inospheric plasmas as reported elsewhere (3).

The PLACES code cross-correlation data graphically exhibit the potential for the loss of code lock and false lock in PN spread spectrum systems as well as the usual difficulties in operating through fading environments. It is not difficult to envision the intersymbol interference difficulties high data rate systems might encounter as well.

The PLACES Experiment has achieved its objectives.

SECTION 2
BEACON EXPERIMENT DATA FOR ST. GEORGE ISLAND, BEACON 1

2.1 GENERAL

Intense angular scattering effects were observed on the signal received from the beacon rocket on flight 1. This section discusses these data measurements. The data reduction effort has concentrated on the data received at St. George Island from the first beacon rocket. The occultation geometry achieved is presented first, followed by the measurements of the PN code cross-correlation measurements (channel impulse response). From these data the time-of-arrival (TOA) delay spread and jitter are represented. The differential Doppler for several situations is presented along with the derived channel transfer function representation. Back-propagation of the 98-MHz spectral component of the received signal is shown along with an average power of energy-of-arrival distribution and comparisons with the DNA channel model are presented.

2.2 OCCULTATION GEOMETRY

IRIS, the third barium release, occurred on 8 December 1980 at 2313:08. The release altitude was approximately 182.2 kilometers at a latitude and longitude of 28.7633°N and 87.1853°W. The first beacon rocket was launched at 2338:36Z and occulted the barium plasma as viewed from St. George Island during the interval 2345:07.7 to 2345:30.0Z.

2.2.1 Correlation to Radar Data

The occultation geometry relative to a radar mapping of the cloud ionization is provided in Figure 2-1. The radar ionization contours are those obtained approximately 2.5 minutes after occultation and translated to the peak electron density track point at 2345:20Z during the center of the occultation interval. These contours were chosen because they provided more complete definition than those available at the time of occultation (16,10). Note that the direct path slices the cloud through the maximum density region ($\sim 3 \times 10^6$ cm^{-3}), which is located at 160-km altitude at the time of occultation (release + 32 minutes). The rocket is following a downward trajectory making approximately a 65-degree angle with the horizontal at the time of occultation. As a further aid to visualizing the manner in which the line-of-sight path slices through the cloud, a line is shown indicating the 160-km altitude point along the magnetic field lines that pass through the ray path. The declination of the magnetic field is near zero.

The line-of-sight path is shown at several times of interest. The intersection of the path with the 160-km altitude plane is indicated by the transition from the solid to dotted line. The three paths show the time at which the first caustic ray is evident in the data, the time at which the maximum electron content (signal delay) is observed, and the time at which the signal exits the cloud. The rocket altitude at these times is also indicated. For instance, at the time the path entered the cloud, the rocket was at an altitude of 194.3 km and when the path exited the cloud, its altitude was 163.3 km. Various altitude points are shown along each ray path as well.

2.2.2 Correlation to Optical Data

Photographic coverage indicates that most of the striations appear to the northeast side on the ion cloud. Optical data available around 2345Z from six sites were analyzed in Reference 3 in order to estimate the striation region boundaries so that the geometrical aspects of the propagation data might be examined. The mapping of these data results in the approximate striation region boundaries shown in Figure 2-1. In the 160-km altitude plane the line-of-sight path slices the bulk of the striations. The propagation distance to the striation region boundaries can be determined to vary from approximately 20 to 50 km.

2.3 MEASURED CHANNEL IMPULSE RESPONSE

The beacon rocket transmitted a 98-MHz signal that was biphase modulated by a 9.8-MHz pseudonoise code. The effects of the plasma striations on this transmission can be represented by a time varying channel impulse response. As shown in Reference 1, the signal cross-correlation measurements made at the beacon receivers provide a good approximation to the actual channel impulse response. If we represent the equivalent complex baseband channel impulse response as

$$h(t,s) = h_I(t,s) + h_Q(t,s) \quad ,$$

then the received signal $y(t)$ may be expressed as

$$y(t) = c(t) * h_I(t,s) \cos (w_o t + \psi)$$

$$+ c(t) * h_Q(t,s) \sin (w_o t + \psi)$$

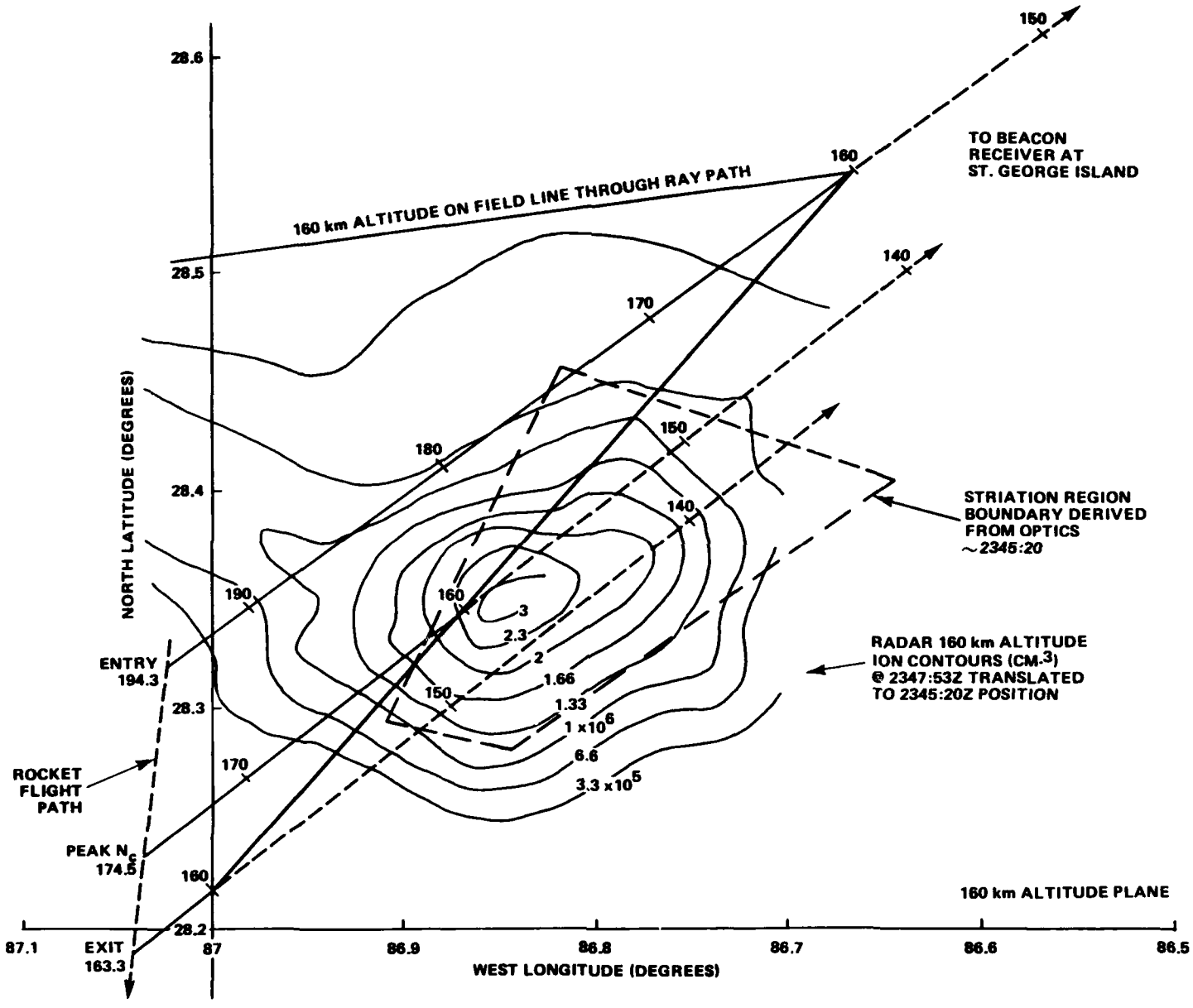

Figure 2-1. Occultation geometry for St. George Island, Beacon 1.

where

* denotes a convolution,
ψ is the gross plasma phase shift at 98 MHz, and
$c(t)$ is the PN code (± 1).

For simplicity the Doppler removed by the C-Band reference signal is not shown in the above equation. The in-phase and quadrature code cross-correlations performed at the beacon receivers provide a weighted average measurement of $h_I(t,s)$ and $h_Q(t,s)$, respectively, averaged over a narrow window (a code chip interval) about the code delay so that

$$I(t,\tau) \cong \cos(\psi)\ h_I(t,\tau)$$

and

$$Q(t,\tau) \cong \sin(\psi)\ h_Q(t,\tau)$$

where $I(\ )$ and $Q(\ )$ are the in-phase and quadrature cross-correlation measurements, respectively.

2.3.1 Composite Data

The magnitude of channel impulse response $|h(t,\tau)|$ measured at the St. George Island beacon receiver site is shown in Figure 2-2. Initially a phase windup can be noted along with an attendant delay in the signal TOA. Discrete refracted ray caustic contributions appearing at late time delays are evident as the rocket approaches the barium plasma cloud. As expected, the relative delay of these caustics decreases as the transmitter approaches the cloud. This is a result of the decreasing difference in distance to the receiver between the beacon rocket direct path and the caustic ray paths refracting from the cloud. During occultation, when the rocket is behind the barium plasma, many caustic paths appear to merge,

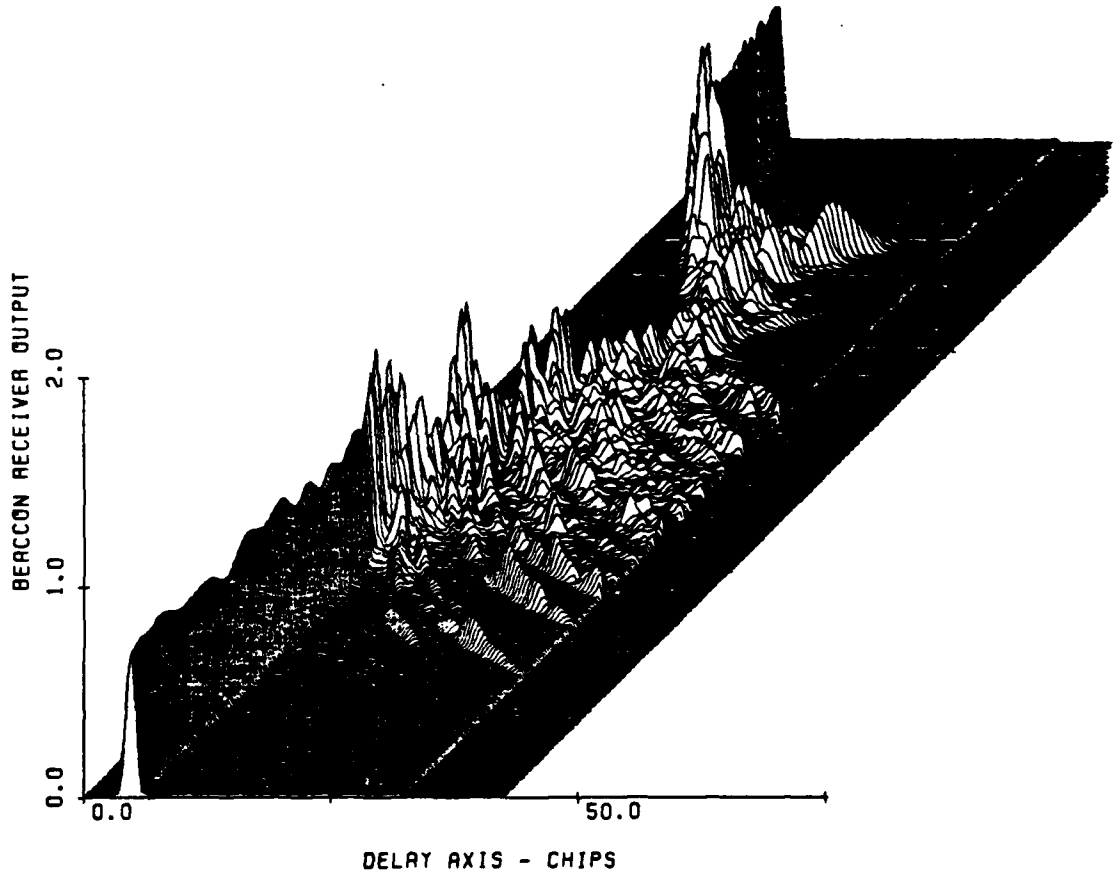

Figure 2-2. Magnitude of channel impulse response, St. George Island first beacon, time span from 2345:1.8 to 2345:34.2.

giving a more random appearance to the delay spread. The gross plasma also causes the TOA of the direct path energy to be delayed resulting in the large delay near the center of the occultation. The gross plasma also acts like a giant lens causing substantial defocusing to occur, reducing the signal amplitude near the center of the occultation. As the rocket flight continues, identifiable caustics again appear on emergence from occultation. On this figure, one chip delay is approximately 0.1 microsecond.

Figure 2-2 represents data collected over the time interval from 2345:01.8 to 2345:34.2, where time is shown as the third dimension. During this time interval, approximately 12,960 samples of the impulse response were taken by the receiving hardware. For plotting purposes, 32 of these responses were averaged to produce each of the 400 horizontal scans presented in the figure.

2.3.2 Energy Delay Profiles

Samples of the energy delay profile (magnitude of the channel impulse response) are shown in Figures 2-3 through 2-6 sampled approximately each 0.5 second. Near the time of maximum integrated electron content when the line-of-sight path to St. George Island passes through the center of the striations (~2345:23), the signal exhibits a significant defocusing and delay spread. Near this time a delay spread of greater than 10 chips (~1 microsecond) occurs. In comparing this response with the unperturbed signal prior to occultation, it is apparent that a net TOA delay of about 13 chips (~1.3 microseconds) has been added by the gross electron content of the barium ion cloud. Most strikingly apparent in these figures is the large spread that occurs and the potential implications to PN code tracking system design.

Figures 2-7 through 2-14 provide additional examples of the channel impulse response with 0.1 second averaging (40 records). These figures correspond to the computed frequency transfer functions and frequency correlation functions presented in Section 2-7.

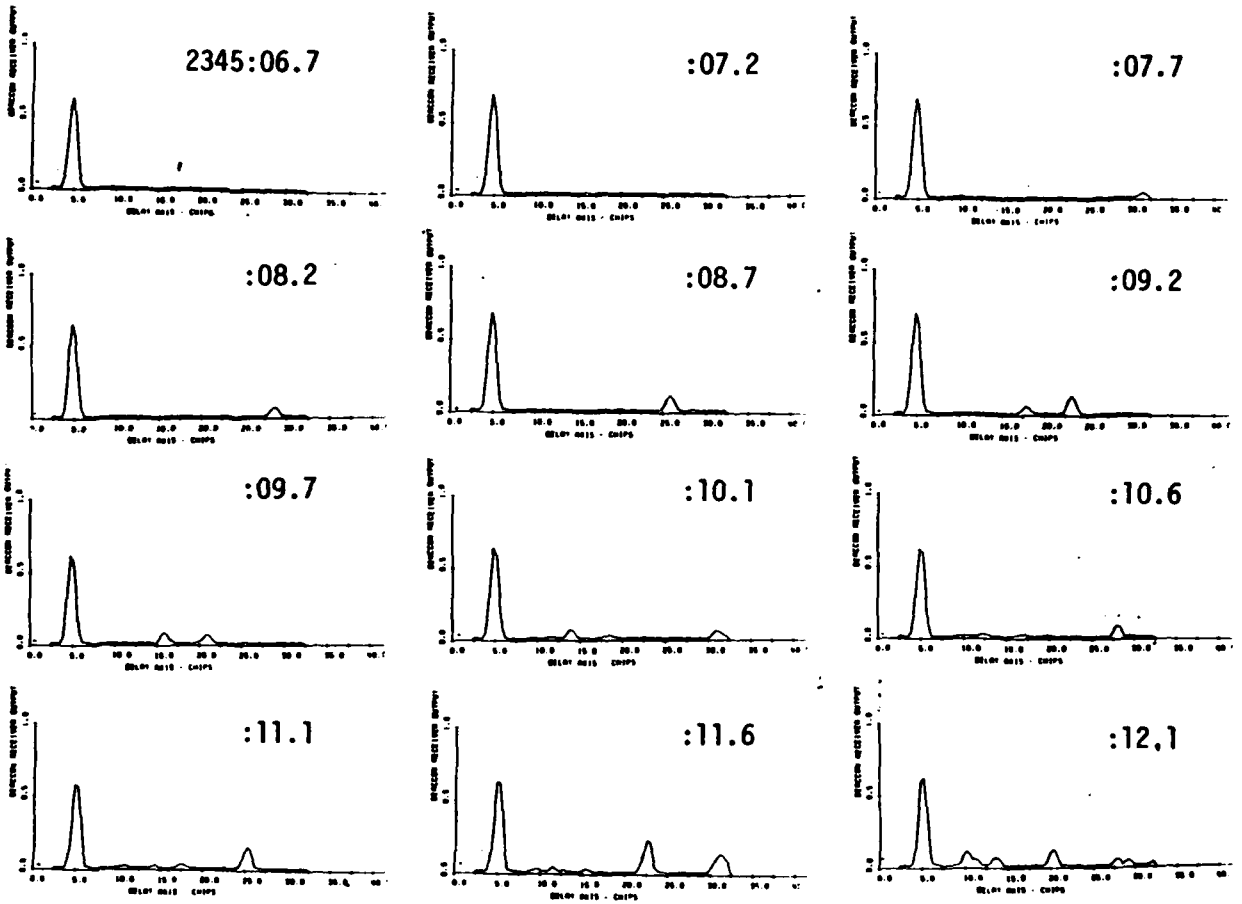

Figure 2-3. Energy delay profile between 2345:06.67 and 2345:12.1, St. George Island.

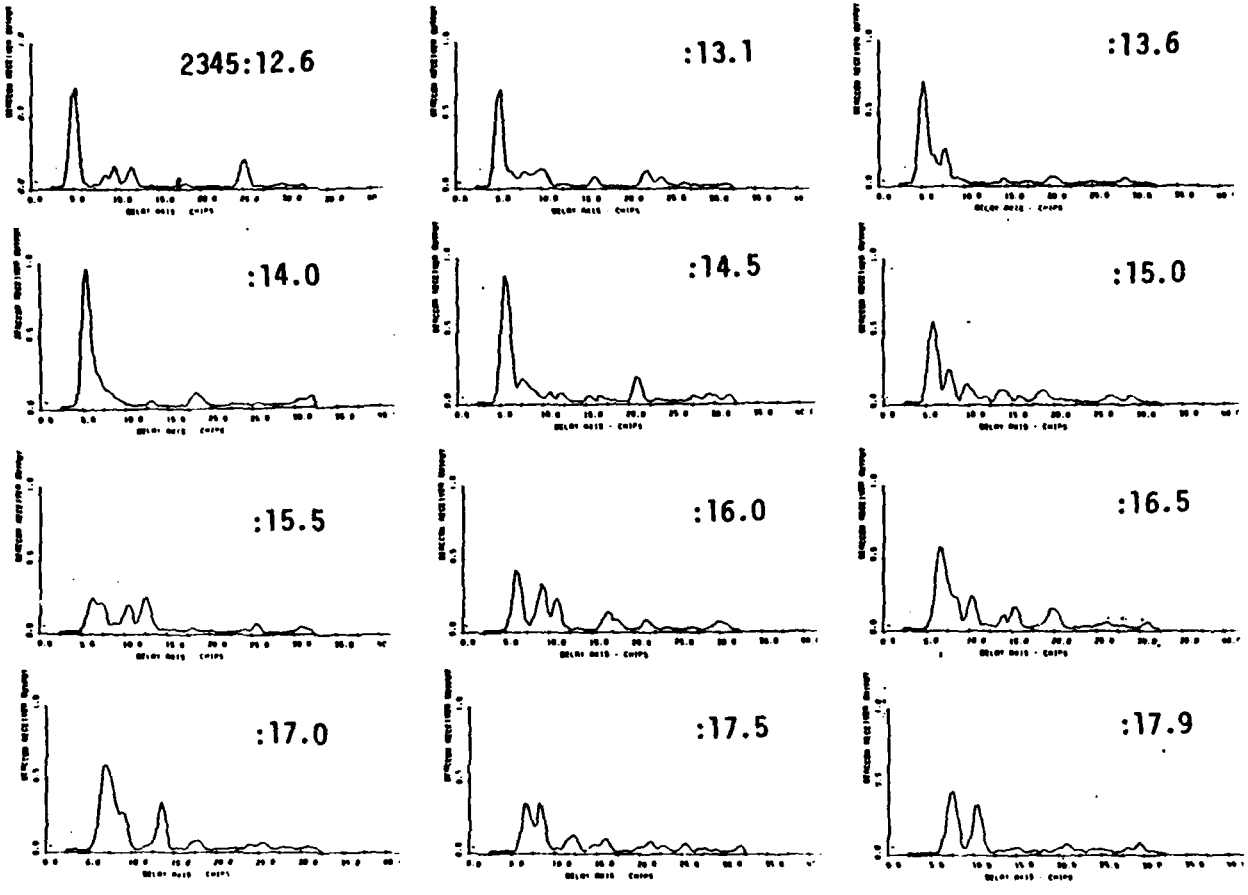

Figure 2-4. Energy delay profile between 2345:12.6 and 2345:17.9, St. George Island.

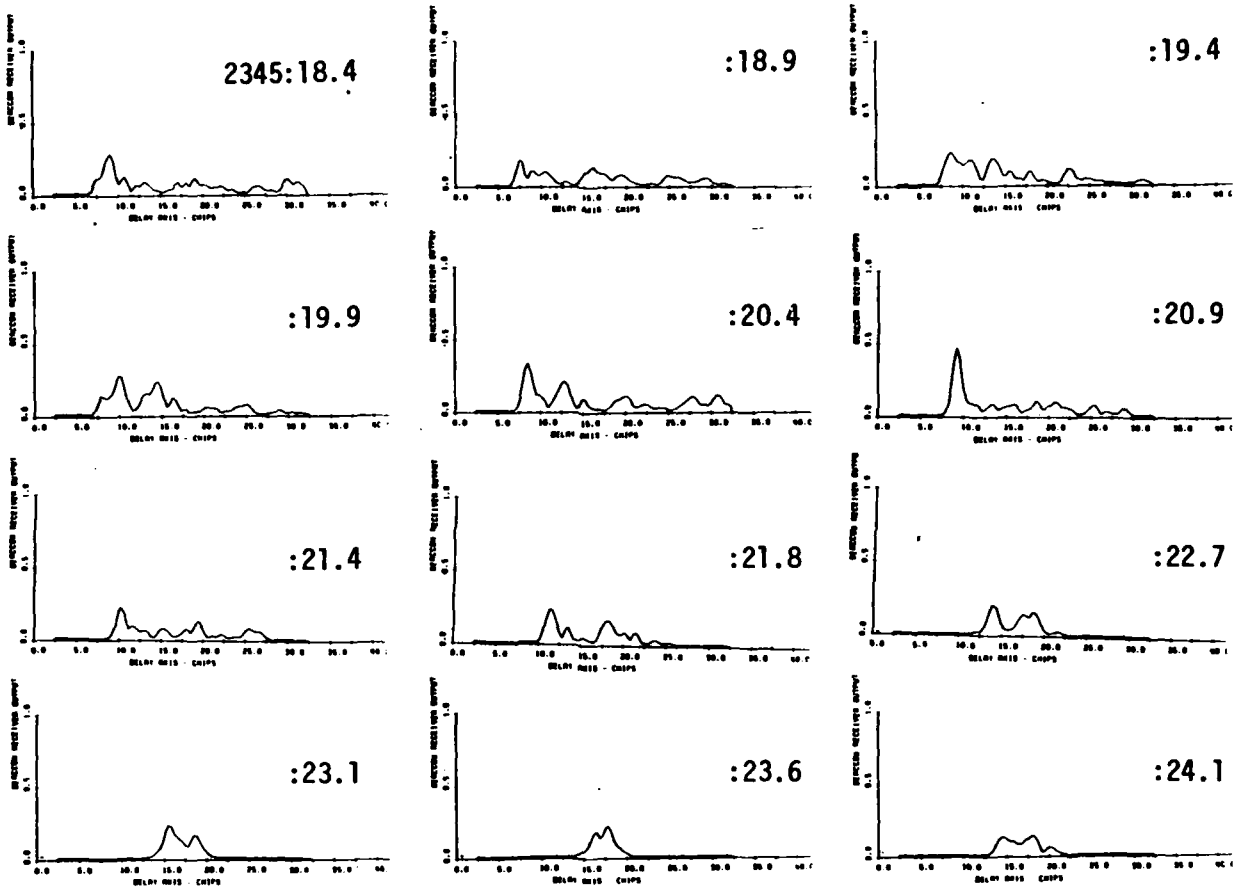

Figure 2-5. Energy delay profile between 2345:18.4 and 2345:24.1, St. George Island.

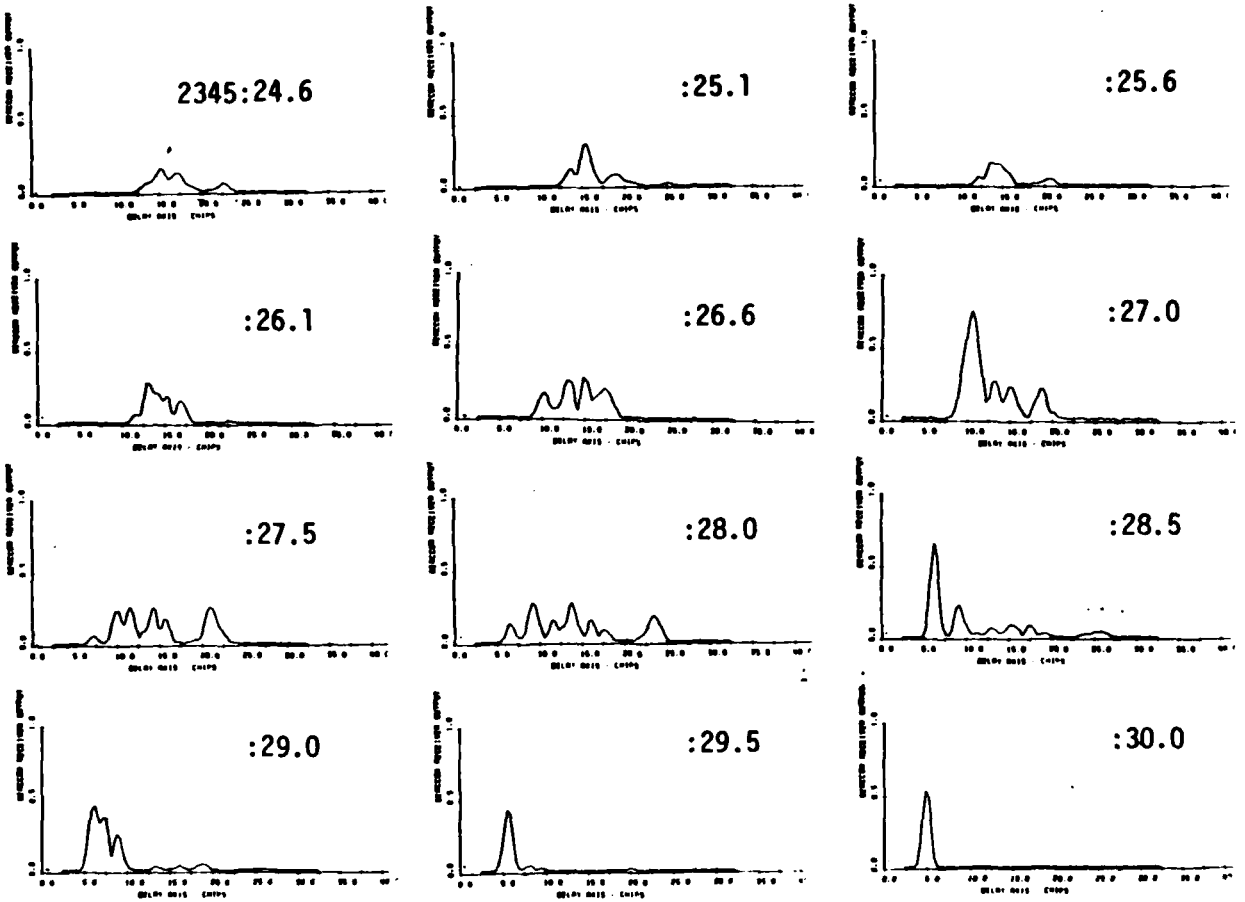

Figure 2-6. Energy delay profile between 2345:24.6 and 2345:30.0, St. George Island.

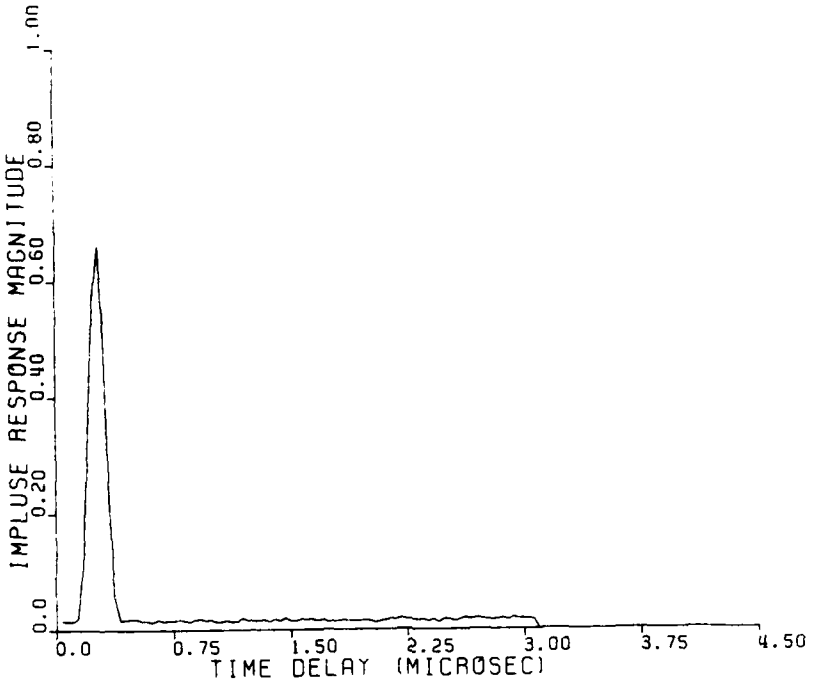

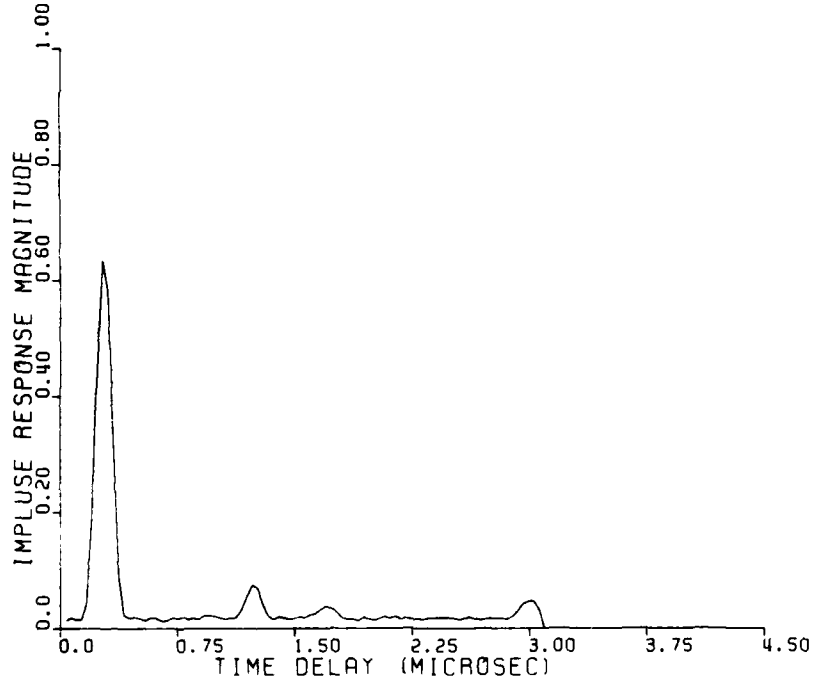

Figure 2-7. Impulse response magnitude at 2345:05.1 and 2345:10.2Z.

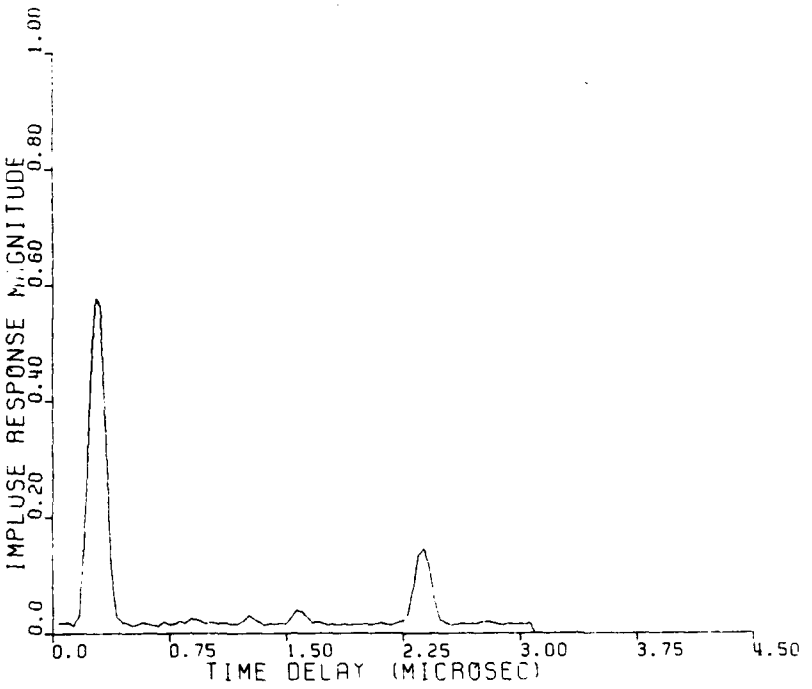

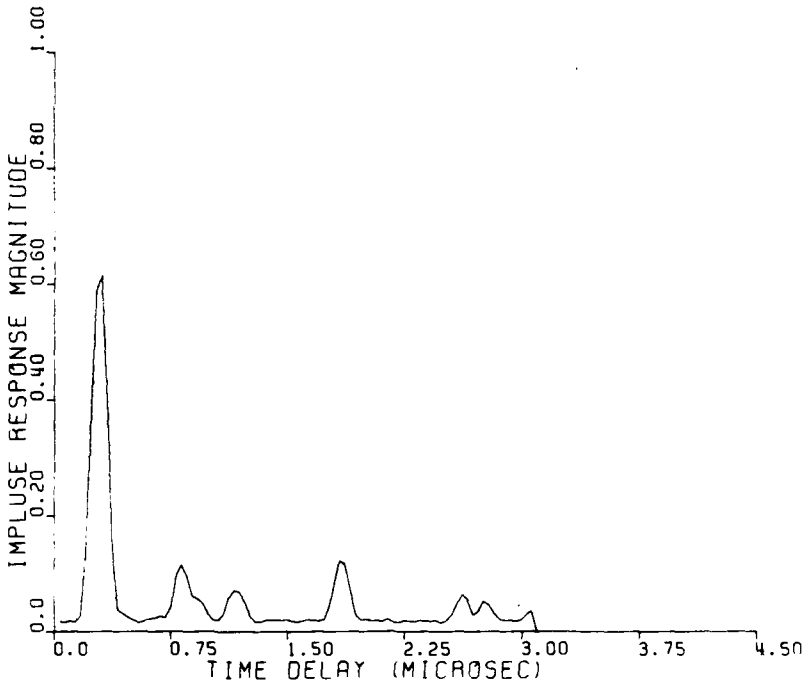

Figure 2-8. Impulse response magnitude at 2345:11.2 and 2345:12.2Z.

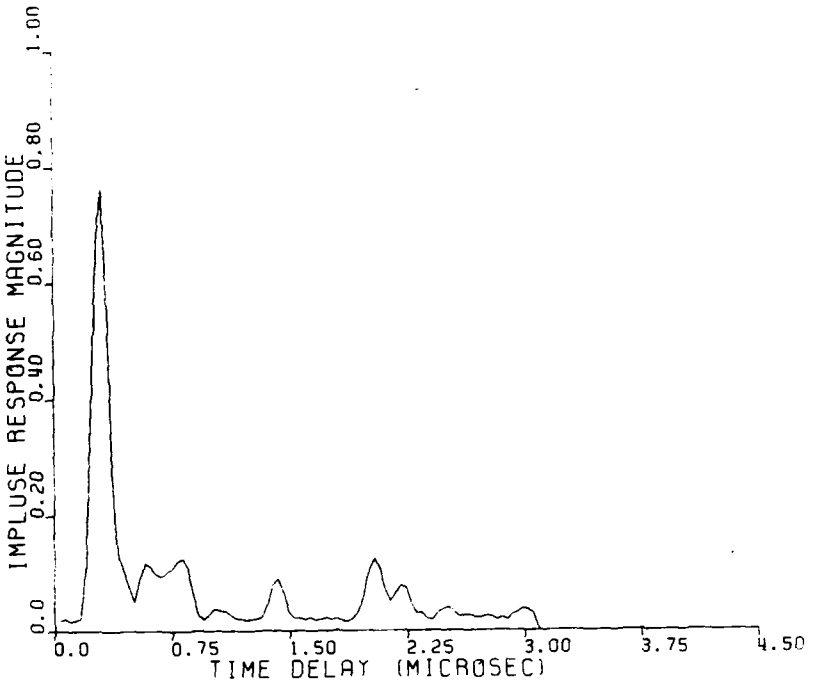

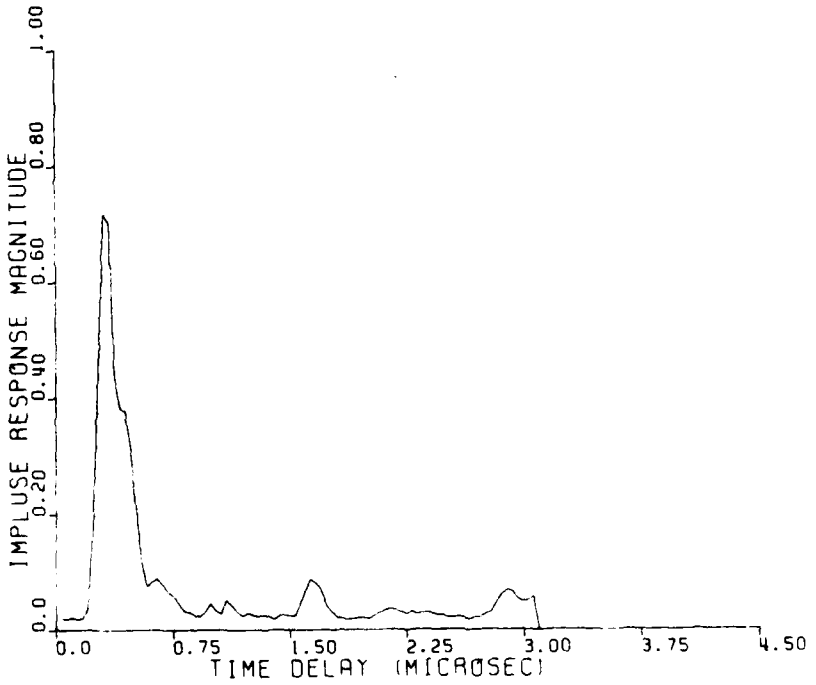

Figure 2-9. Impulse response magnitude at 2345:13.2 and 2345:14.2z.

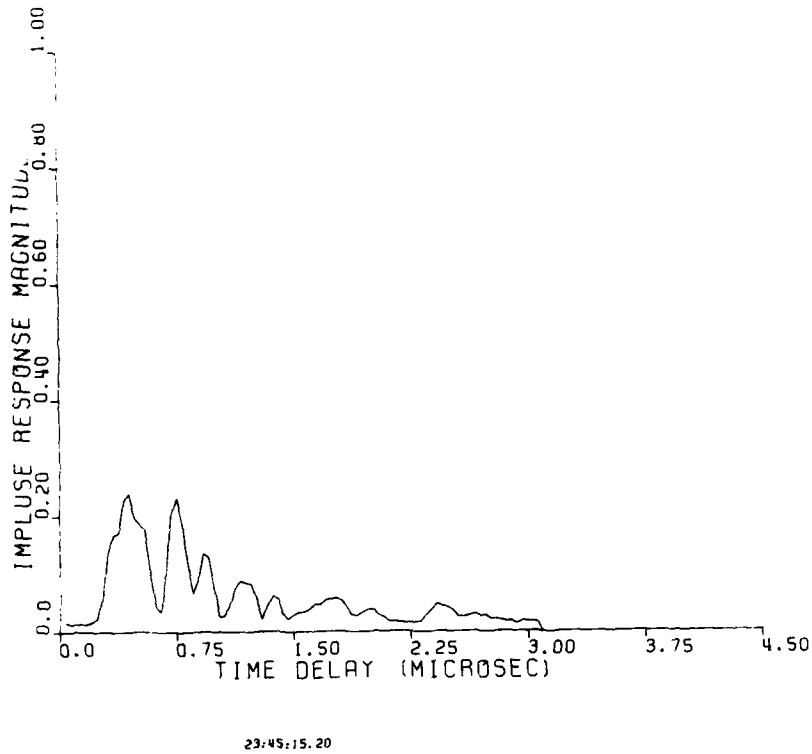

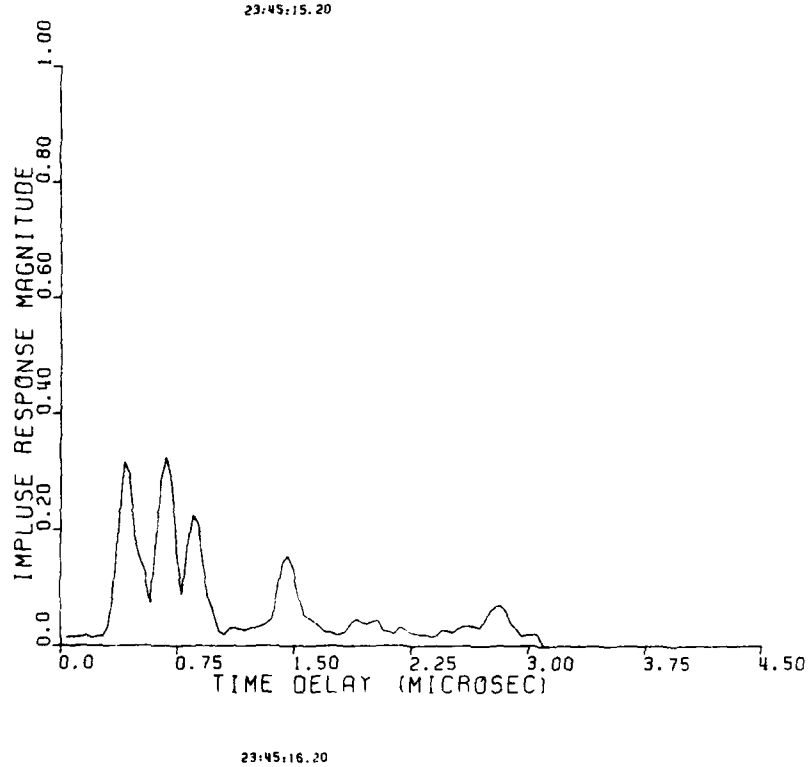

Figure 2-10. Impulse response magnitude at 2345:15.2 and 2345:16.2z.

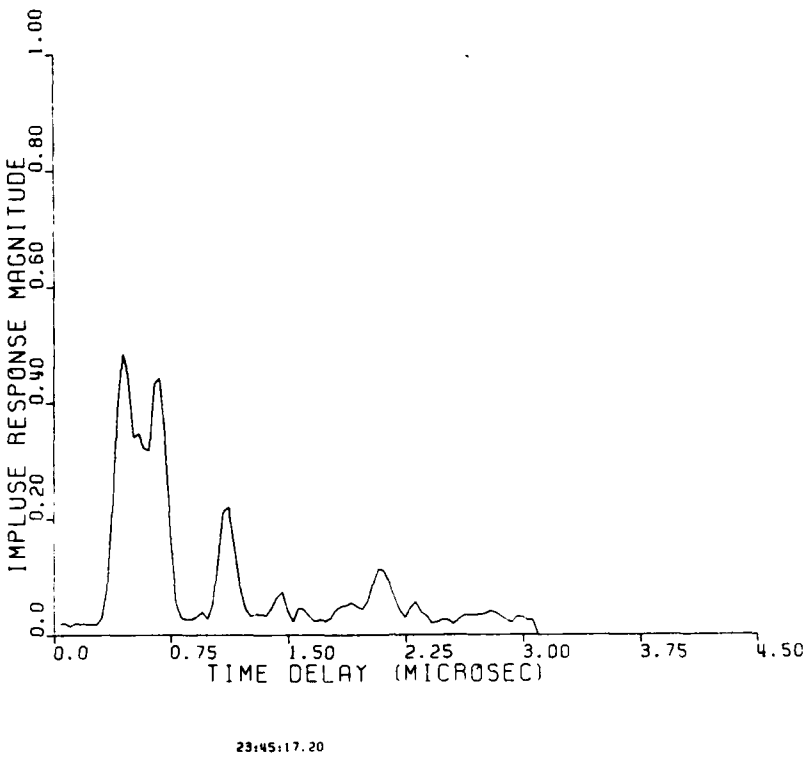

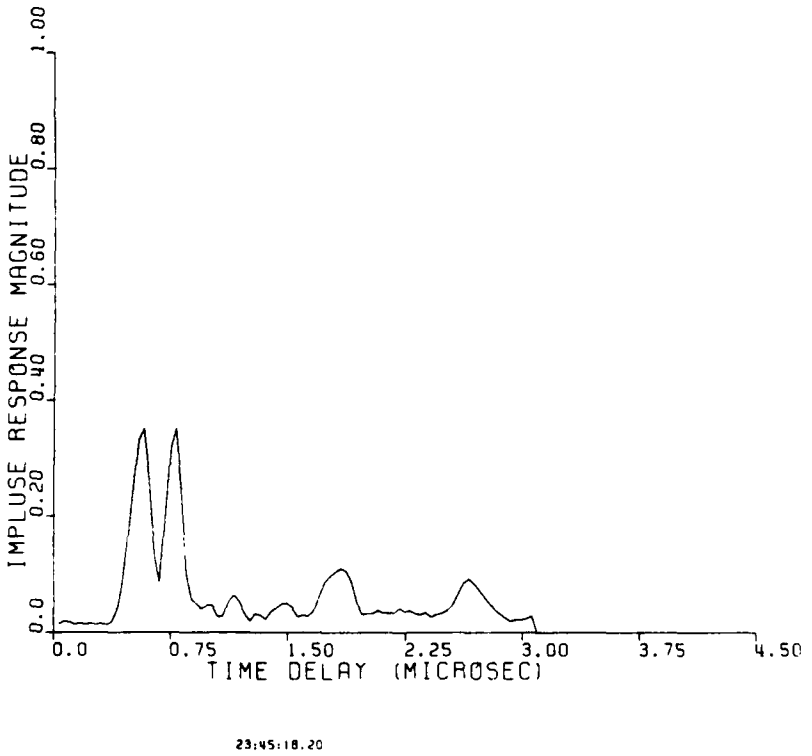

Figure 2-11. Impulse response magnitude at 2345:17.2 and 2345:18.2Z.

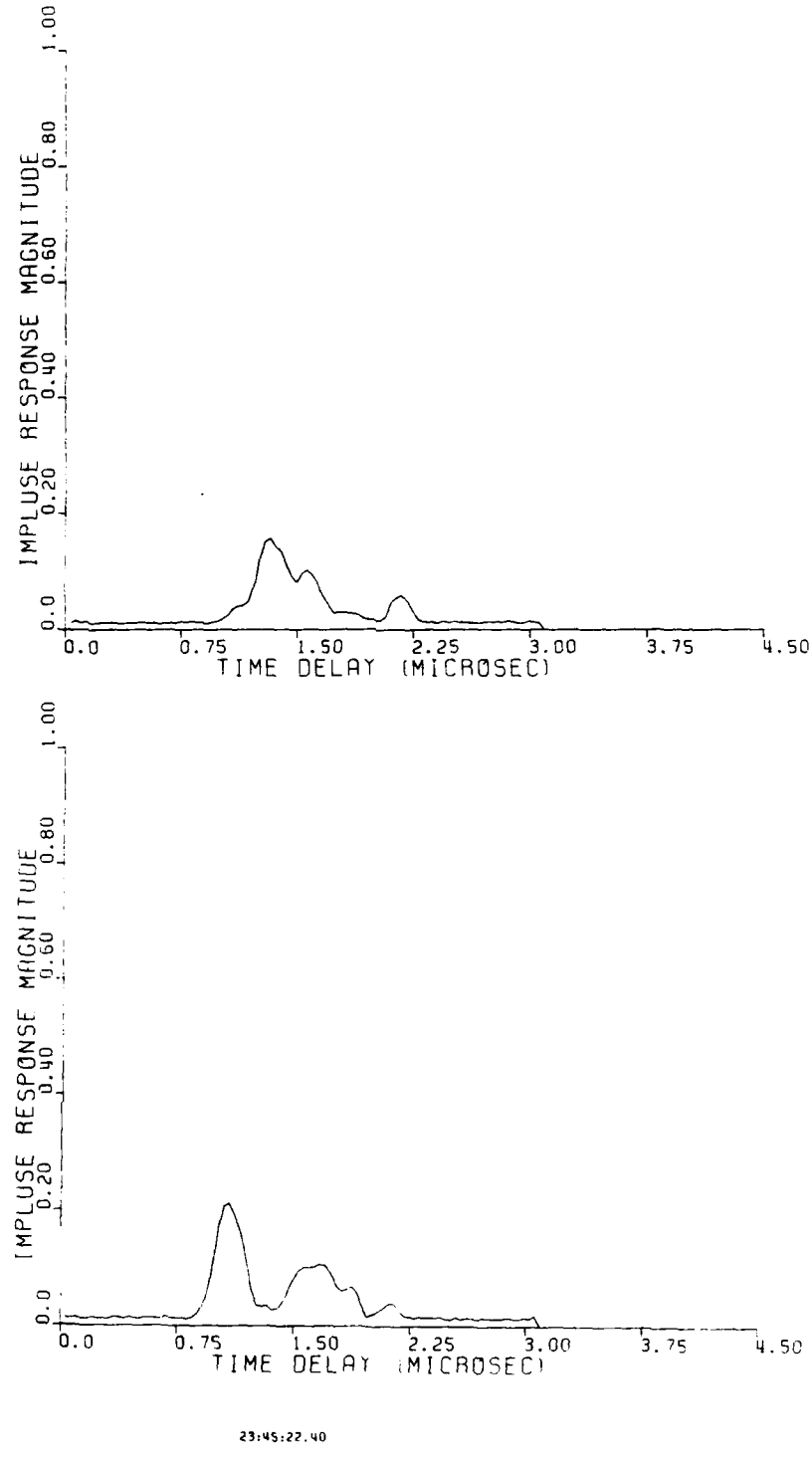

Figure 2-12. Impulse response magnitude at 2345:19.2 and 2345:22.4Z.

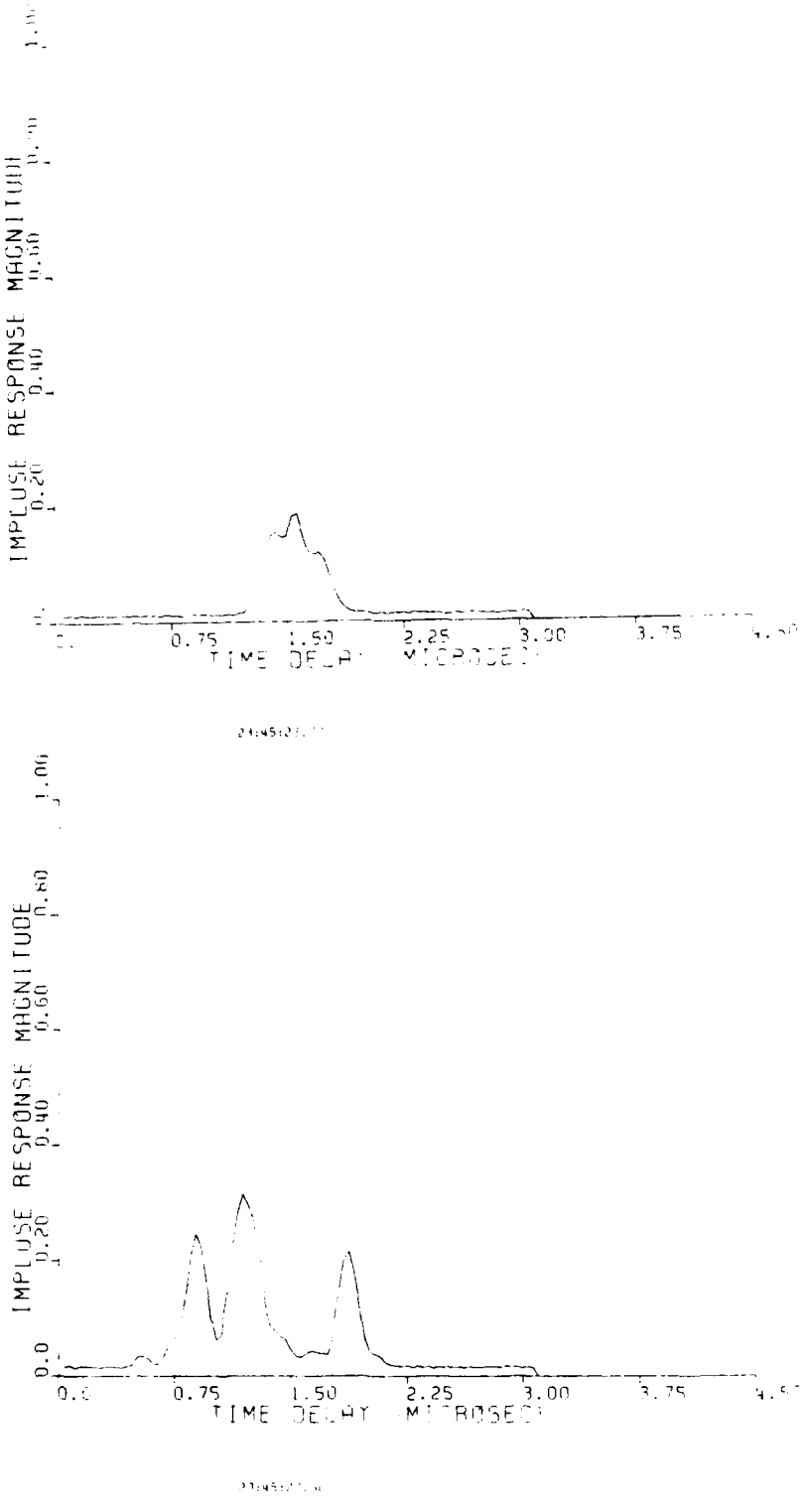

Figure 2-13. Impulse response magnitude at 2345:23.7 and 2345:27.5Z.

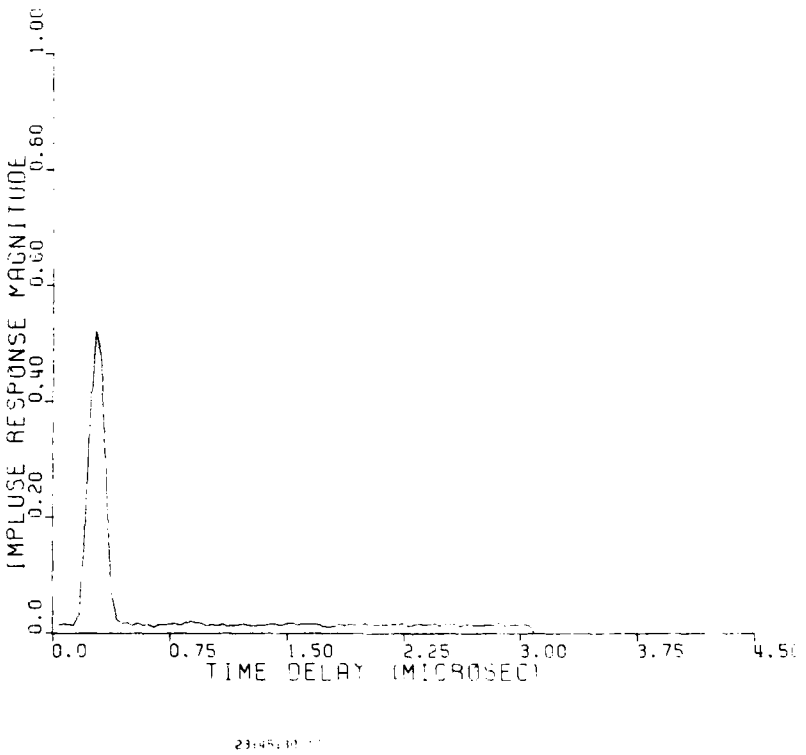

Figure 2-14. Impulse response magnitude at 2345:30.1Z.

Figure 2-15 provides an example of the data quality available without averaging. Because of the high occultation velocity of the beacon rocket, the impulse response varies rapidly as can be seen by comparing these figures and the averaged records shown in Figures 2-4 and 2-9. While the character of these records are all similar, the rapid fluctuation of the mainlobe is clearly evident in Figure 2-15.

2.4 TIME-OF-ARRIVAL DELAY

The preceding figures presented in Section 2.3 provide a snapshot in time of the magnitude of the channel impulse response and indicate the nature of the power delay profile. Here we provide a view of the relative delay of the multipath signal components and the integrated electron content associated with the direct path delay.

2.4.1 TOA Composite Data

In order to examine the fundamental relations associated with classical geometric optics, TOA of the signal energy was examined. A unique perspective of the TOA position of each energy peak (ray) is shown in Figure 2-16. This clearly shows the defocusing effects of the gross plasma forcing energy outward at certain preferential angles. Figure 2-16 is a plot of the location of the centroid of each peak in signal energy at each time point. The peak centroiding algorithm, described in Appendix A, was developed in order to circumvent the usual difficulties associated with peak detection in noise. Also evident in this figure is a TOA jitter of the direct path signal.

The data appear to support a geometric optics approach to the prediction of TOA jitter and delay spread through striated plasmas. A geometrical approach based on angular spectrum arguments

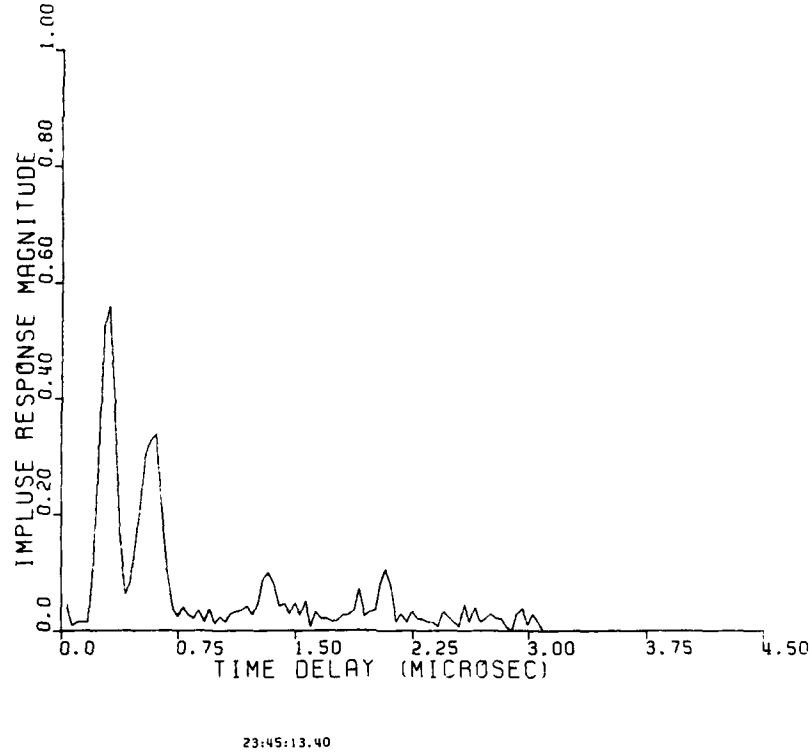

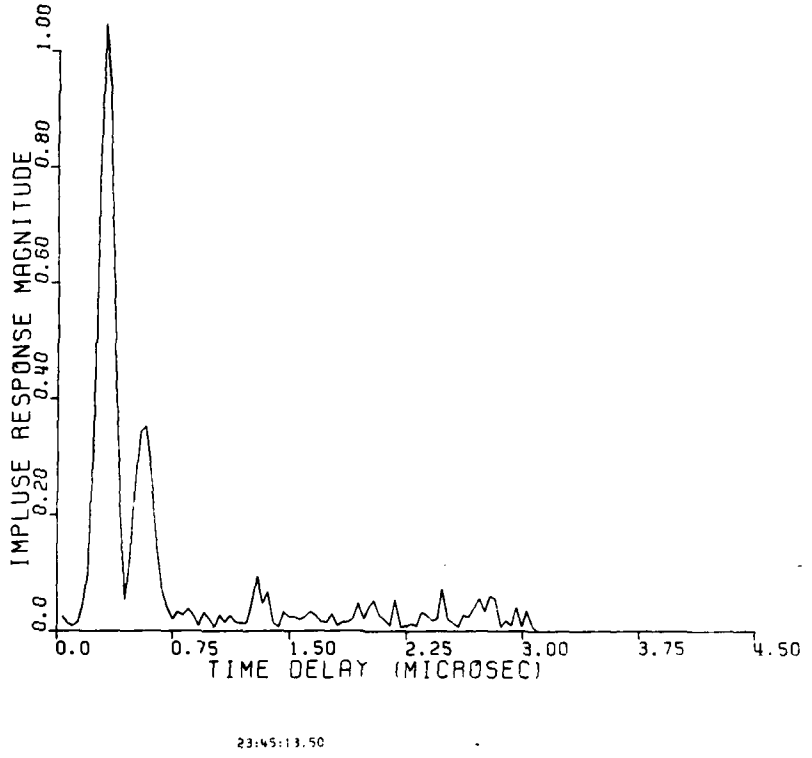

Figure 2-15. Impulse response magnitude without averaging at 2345:13.4 and 2345:13.5Z.

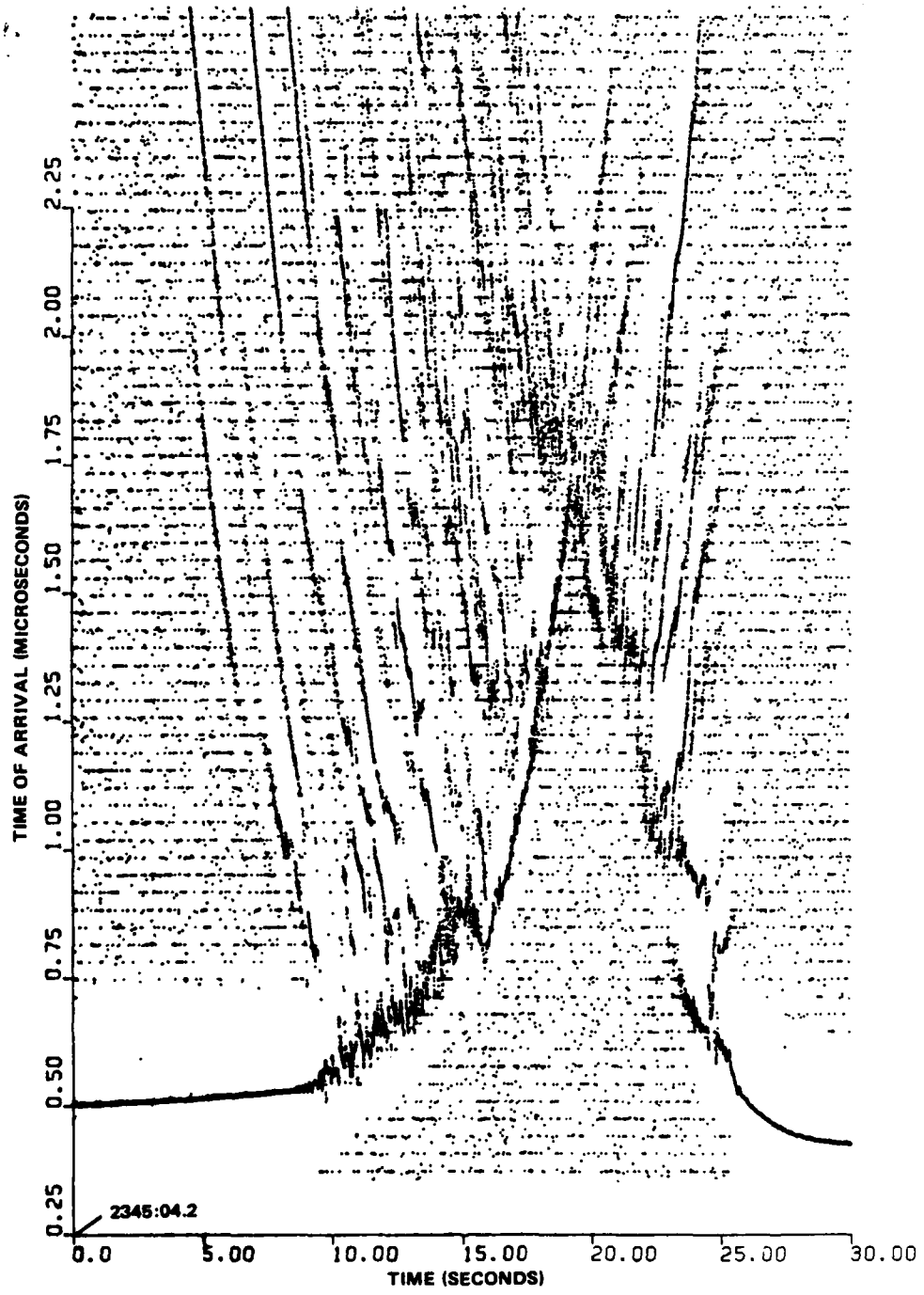

Figure 2-16. Energy peak time-of-arrival delay, all peaks.

can be used to predict the signal energy delay power profile as well as the spectrum of the signal at each component of delay. The geometrical arguments indicate that the basic cause of signal TOA spread is the geometric increase in path length produced by the plasma angular scattering. The TOA jitter is due to the dispersive plasma phase fluctuations. The angular scattering is closely given by the angular spectrum of the signal at frequencies near the center of the signal bandwidth. Thus, a direct mapping between the angular spectrum and the energy delay profile is expected. These intuitive relations are well supported by the data.

2.4.2 TOA Direct Path Data and Integrated Electron Content

The TOA of the direct path through the plasma can be extracted from Figure 2-16 and is plotted in Figure 2-17. The process of distinguishing the peaks corresponding to the first arrival of signal energy from the peaks resulting from random noise and multipath components required the development of a special algorithm as described in Appendix A. Ultimately, this task was accomplished by fitting a curve through those peaks that correspond to the first detected signals in Figure 2-16; a tracking algorithm was then employed that detected the earliest peak that arrived within a given window width around that curve. A window width of $\pm 2/3$ chip was used to construct Figure 2-17. The jitter evident during the first ten seconds can be associated with the dispersive jitter as described in Section 2.5.1.

The integrated electron content can be calculated based on the TOA shift in the received signal at each instant in time. From the usual Appelton-Hartree equation for the point refractive index, one RF cycle of phase shift is produced for each 7.29×10^{10} cm^{-2} of

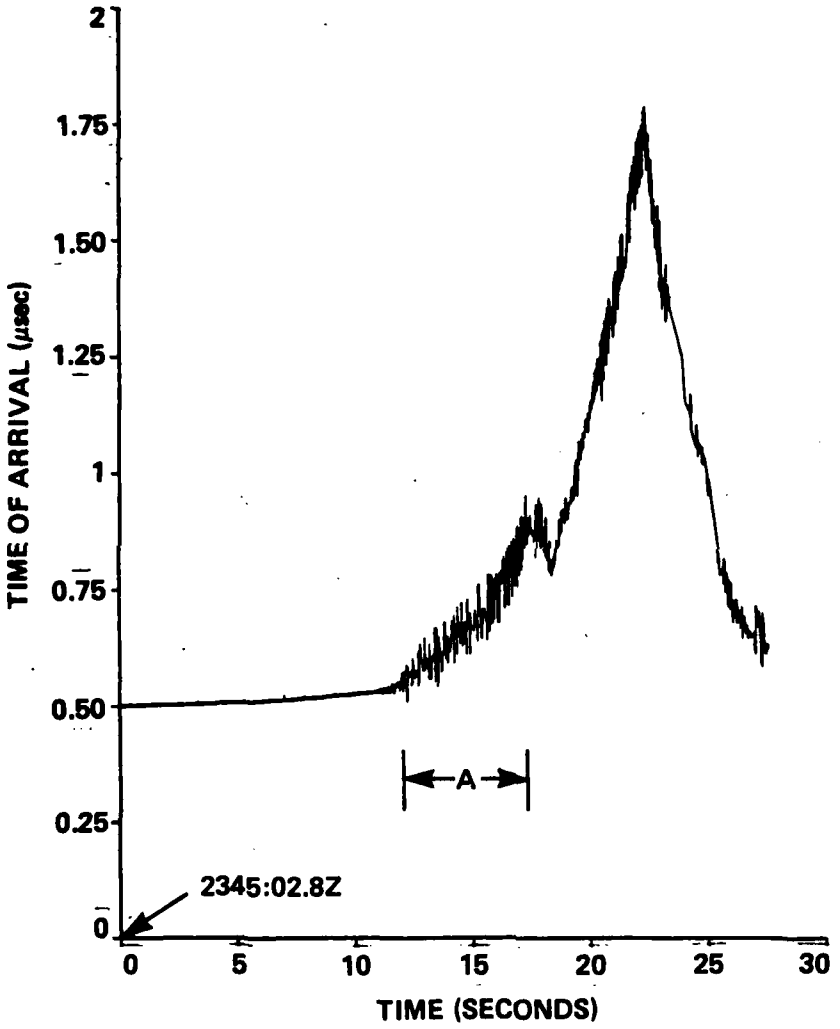

Figure 2-17. Direct path TOA delay.

electron content at 98 MHz. Likewise, 100 cycles of RF phase shift correspond to each microsecond of TOA delay at 98 MHz.

The measured electron content over the entire trajectory along the path to St. George Island for the first beacon is shown in Figure 2-18. The contribution of the background ionosphere is small as indicated. The peak electron content associated with the barium plasma is approximately 8.2×10^{12} cm^{-2}. The total peak integrated electron content including the background ionosphere is approximately 9.0×10^{12} cm^{-2}.

2.5 Time Delay Jitter

As mentioned earlier, the jitter in the direct path TOA evident during the first ten seconds of Figure 2-17 can be associated with dispersive phase effects. This relationship is described further here.

2.5.1 Direct Path TOA Jitter

A heuristic interpretation of TOA jitter can be associated with the dispersive time delay, t_d, as given by the simple relation

$$t_d = \phi/f$$

where f is the signal frequency in Hz, and

ϕ is the absolute phase shift in cycles produced by the plasma at the frequency f.

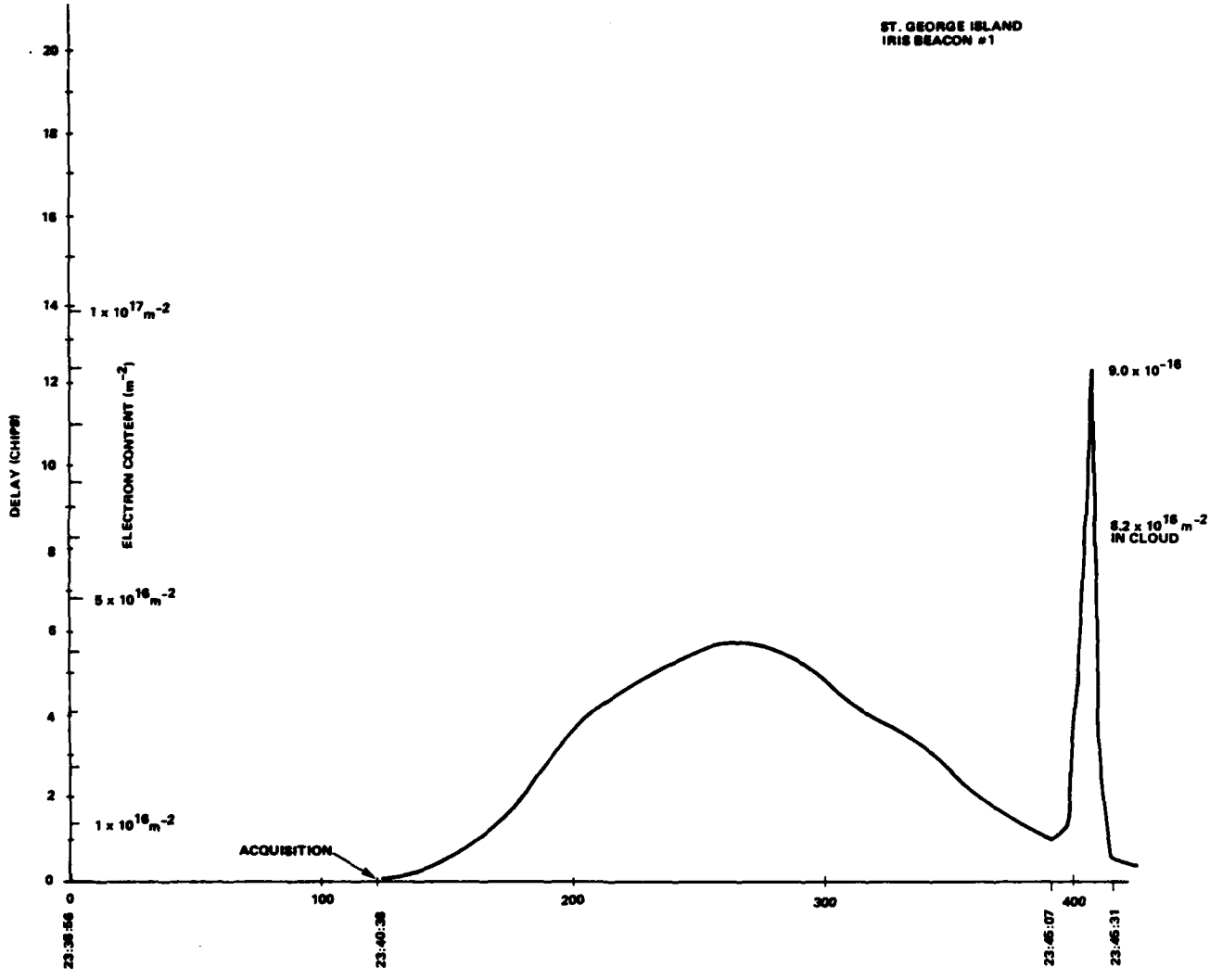

Figure 2-18. Measured electron content for St. George Island, Beacon 1.

The rms dispersive time delay jitter can therefore be expressed in terms of the rms phase (in cycles) associated with the rms integrated electron content fluctuations along the line of sight. The phase shift associated with the integrated electron content is given by the equation

$$\phi = r_e \lambda N_T \text{ (radians)},$$

where r_e is the classical electron radius (cm),
λ is the RF wavelength (cm), and
N_T is the integrated electron content (cm^{-2}).

2.5.2 TOA Jitter Spectrum

The interval labeled "A" (2345:13.4 to 2345:19.6) in Figure 2-17 was detrended to remove the deterministic slope and transformed to determine the time delay jitter power spectrum. This is shown in Figure 2-19. The TOA jitter spectrum break frequency can be estimated to be 4 Hz from this figure. This frequency can be converted to a spatial dimension by dividing by the effective transverse velocity of the beacon rocket across the striations (~980 m/sec; see Appendix D) to give a spatial frequency of 0.0041 cycles/m or a spatial size of approximately 245 meters. This corresponds to a Fresnel size given by

$$F = \sqrt{\lambda z (1-z/d)} = 288 \text{ meters}$$

for the test parameters:

λ = 3.06 m
z = 30 km
d = 320 km.

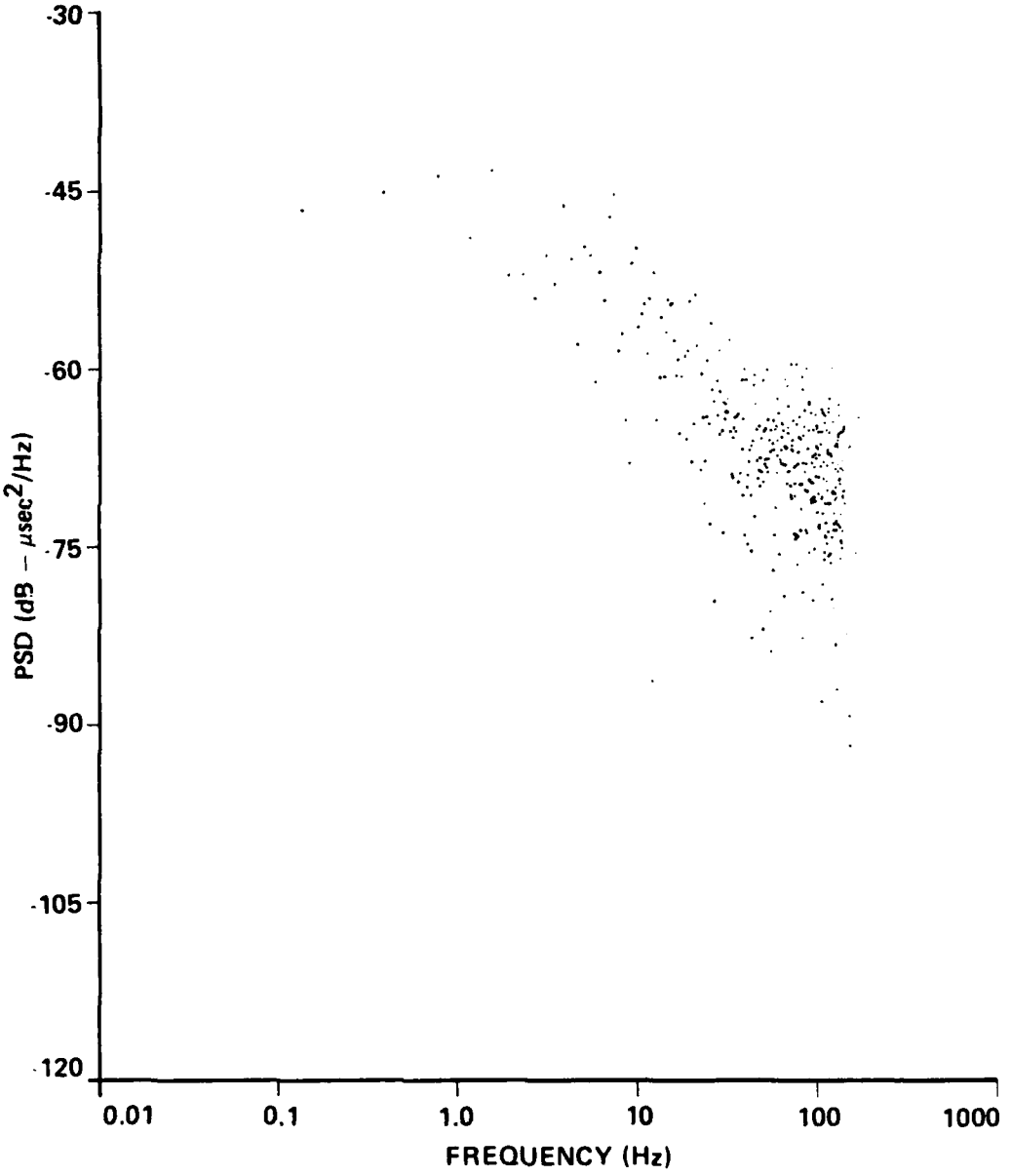

Figure 2-19. Time delay jitter spectrum for segment A.

This is intuitively appealing in that it implies the jitter measured indeed results from large scale structure variation in the TOA (dispersive jitter) and not small angle scatter.

The rms jitter can be estimated by integrating the area under the spectrum to give approximately 0.023 microseconds. From the equation for the dispersive jitter, the rms phase fluctuations for this portion of the cloud can be estimated to be approximately 14.1 radians.

In order to investigate the relationship between the measured generalized power spectrum and theory (Section 2.6.7), it is necessary to consider segments of the occultation data due to the changing dispersive phase and delay spread over the occultation interval. Accordingly, the rms TOA jitter was divided into the segments shown in Figure 2-20 in order to measure the rms dispersive phase. Each segment was detrended in order to remove the deterministic TOA delay and transformed to determine the rms time delay power spectrum. Figures 2-21 through 2-28 show the detrended data and the corresponding time delay jitter spectrum for those intervals noted on Figure 2-20. Table 2-1 provides a summary of the measured rms time delay jitter and the corresponding path integrated rms dispersive phase.

The algorithm described in Appendix A used to determine the direct path TOA was set such that the jitter window was ± 1 chip (0.1 microsecond) about the detrended value of TOA. It was noted that the TOA jitter spectrum break frequency did not vary significantly with the window set larger than $\pm 2/3$ chip. Likewise, the rms jitter measured does not vary significantly when the window is larger than ± 1 chip.

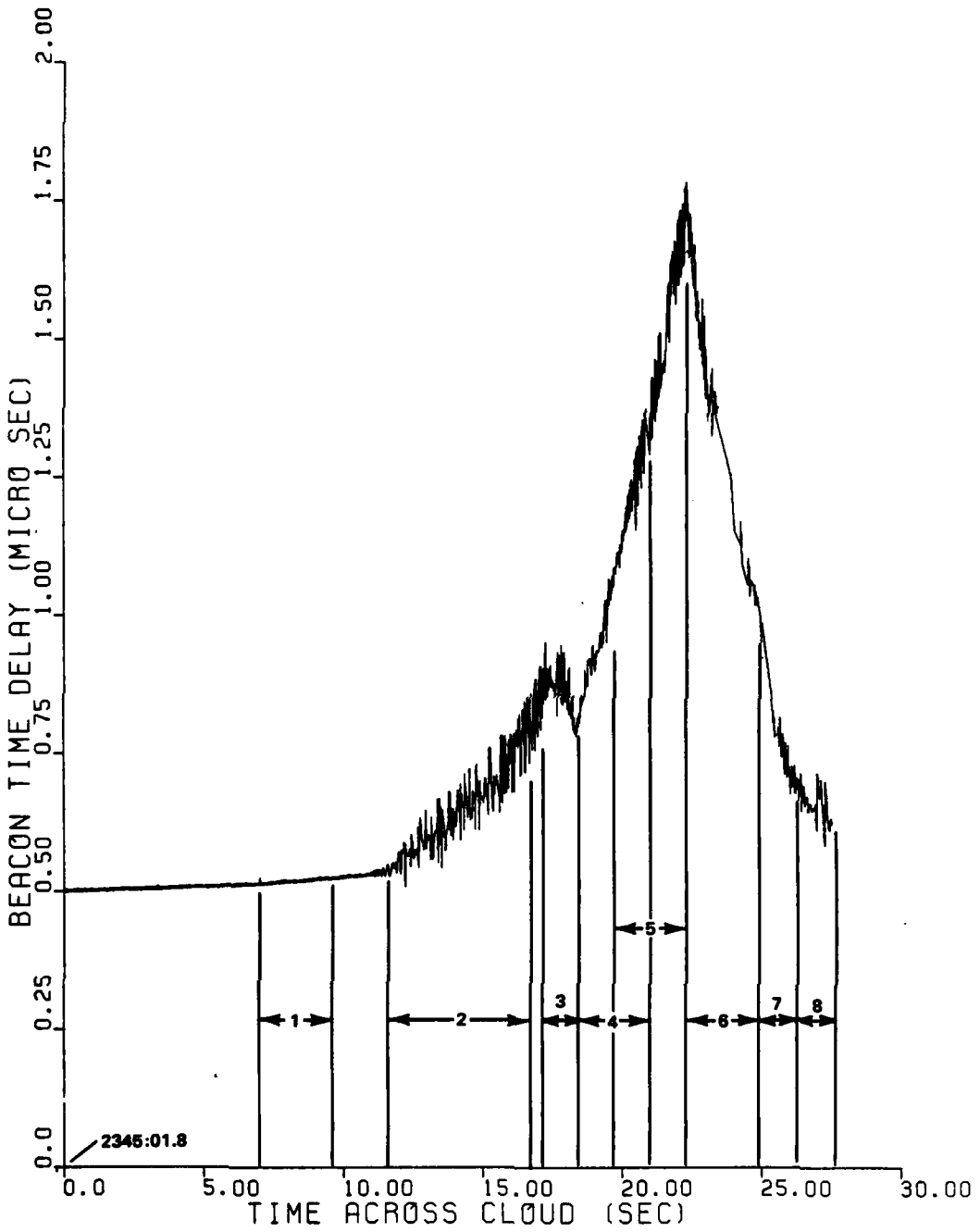

23 45 1.80

Figure 2-20. Direct path time-of-arrival delay segments.

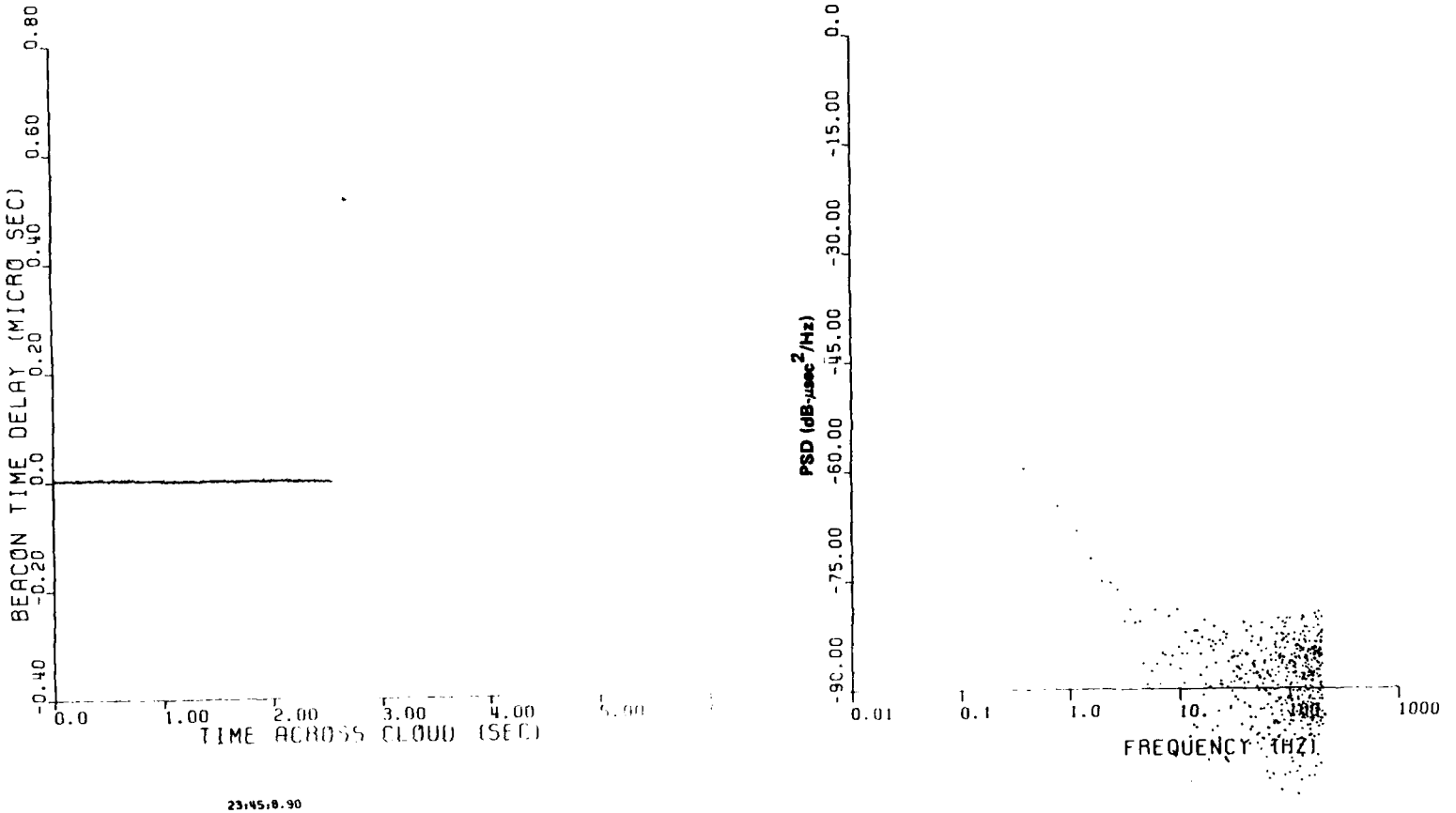

Figure 2-21. Detrended TOA jitter and jitter spectrum for segment 1, noise only.

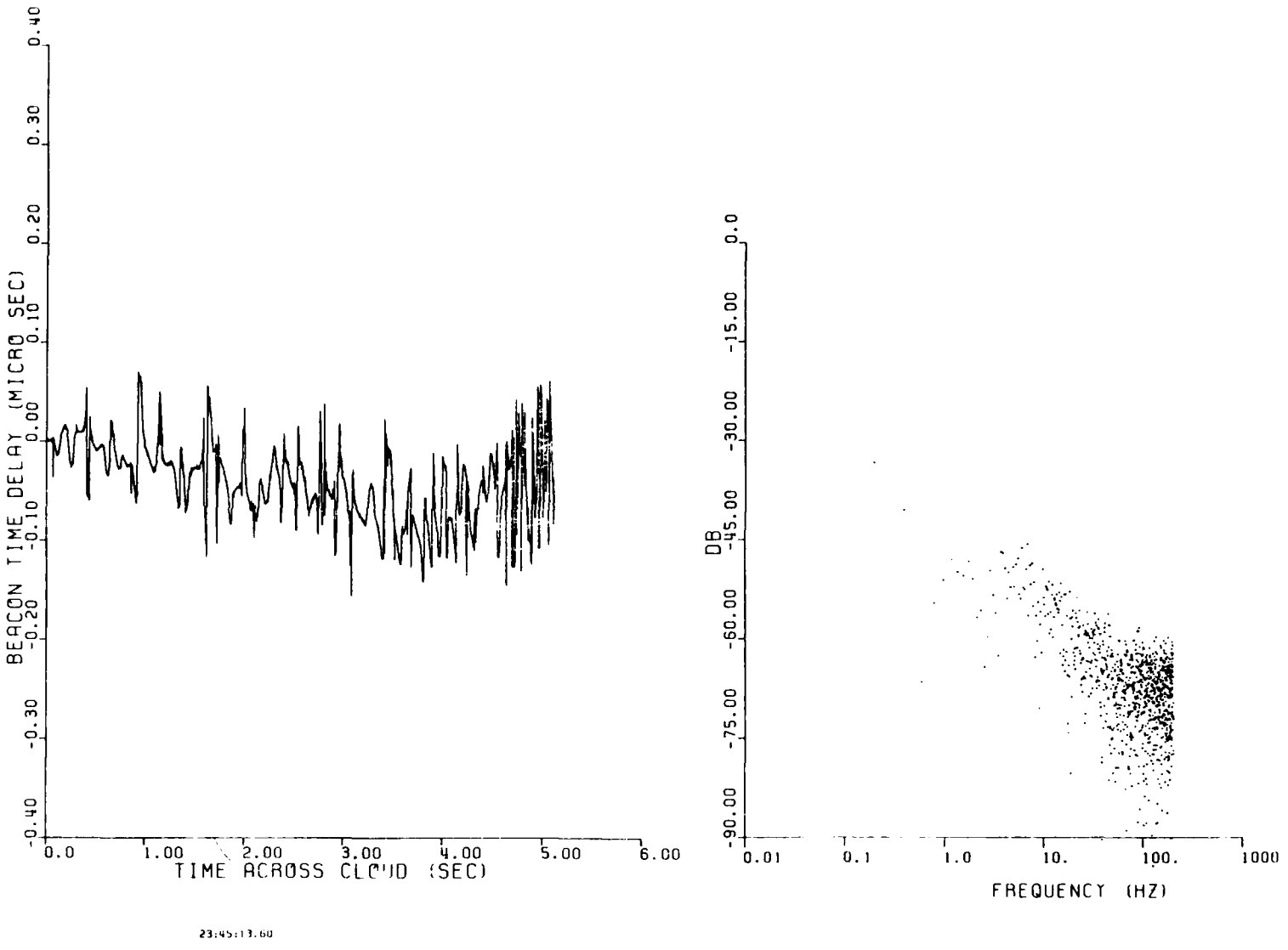

Figure 2-22. Detrended TOA jitter and jitter spectrum for Segment 2, beginning of TOA jitter.

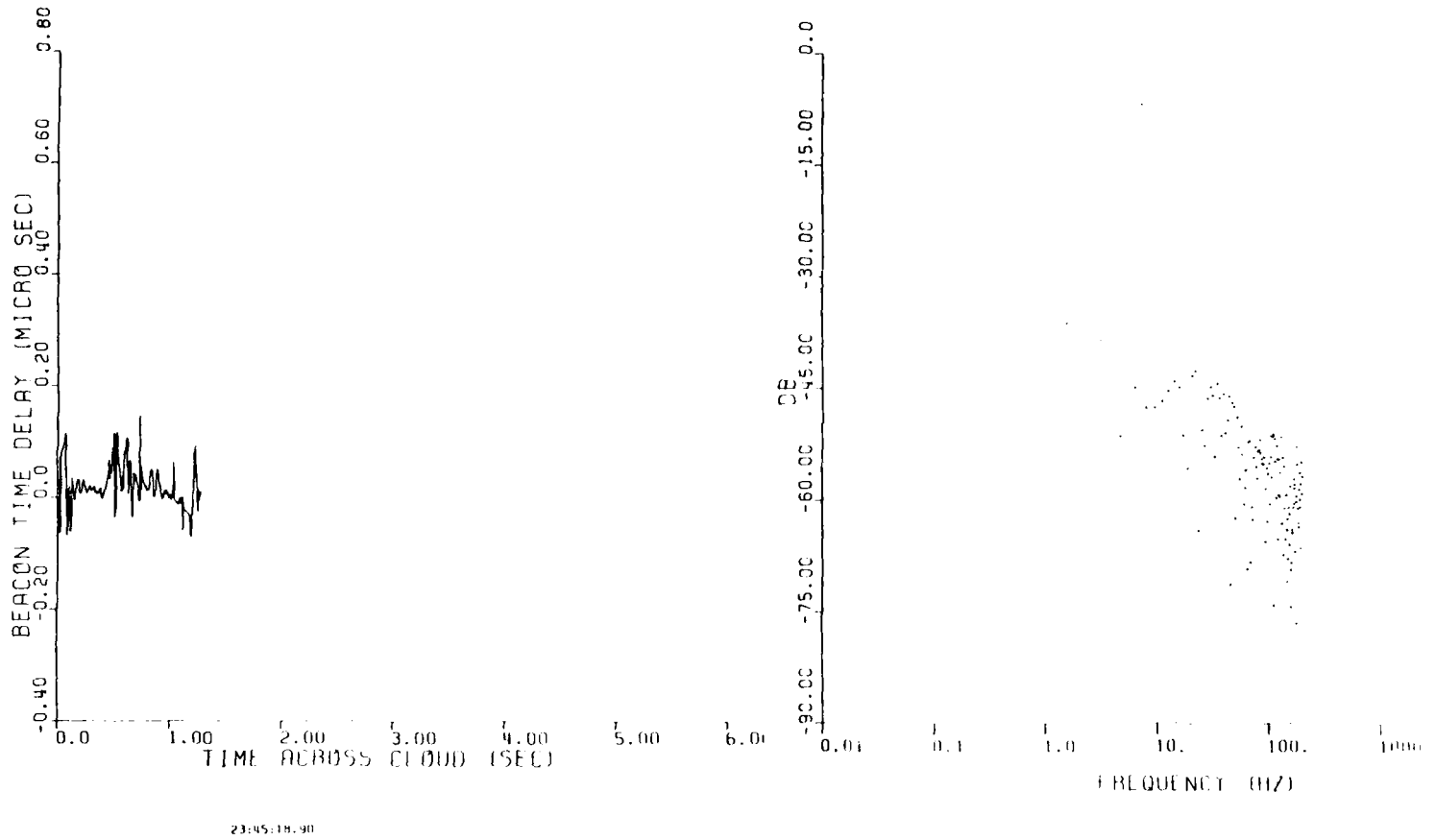

Figure 2-23. Detrended TOA jitter and jitter spectrum for Segment 3, decreasing TOA

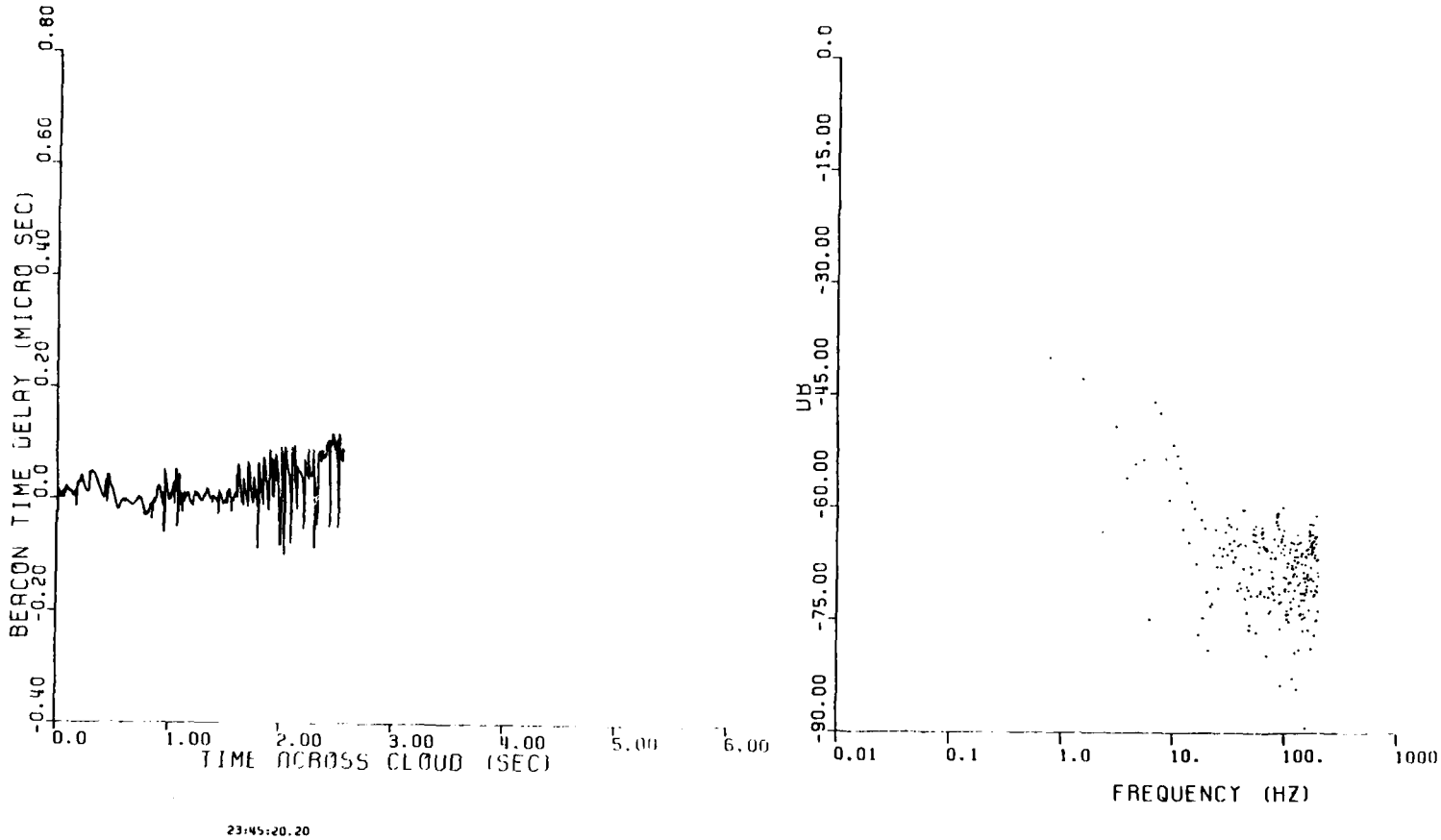

Figure 2-24. Detrended TOA jitter and jitter spectrum for Segment 4.

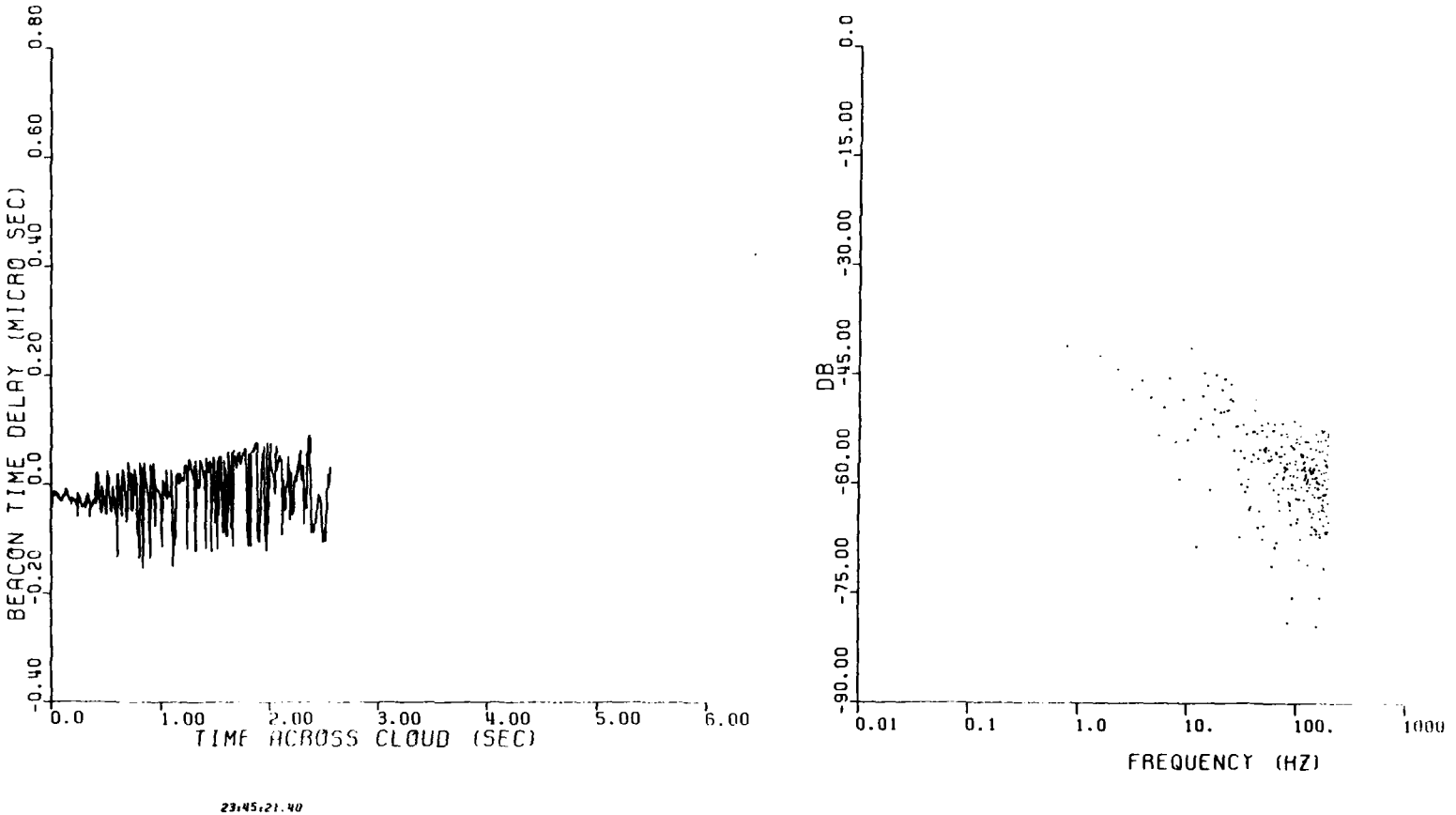

Figure 2-25. Detrended TOA jitter and jitter spectrum for Segment 5, prior to maximum TOA delay.

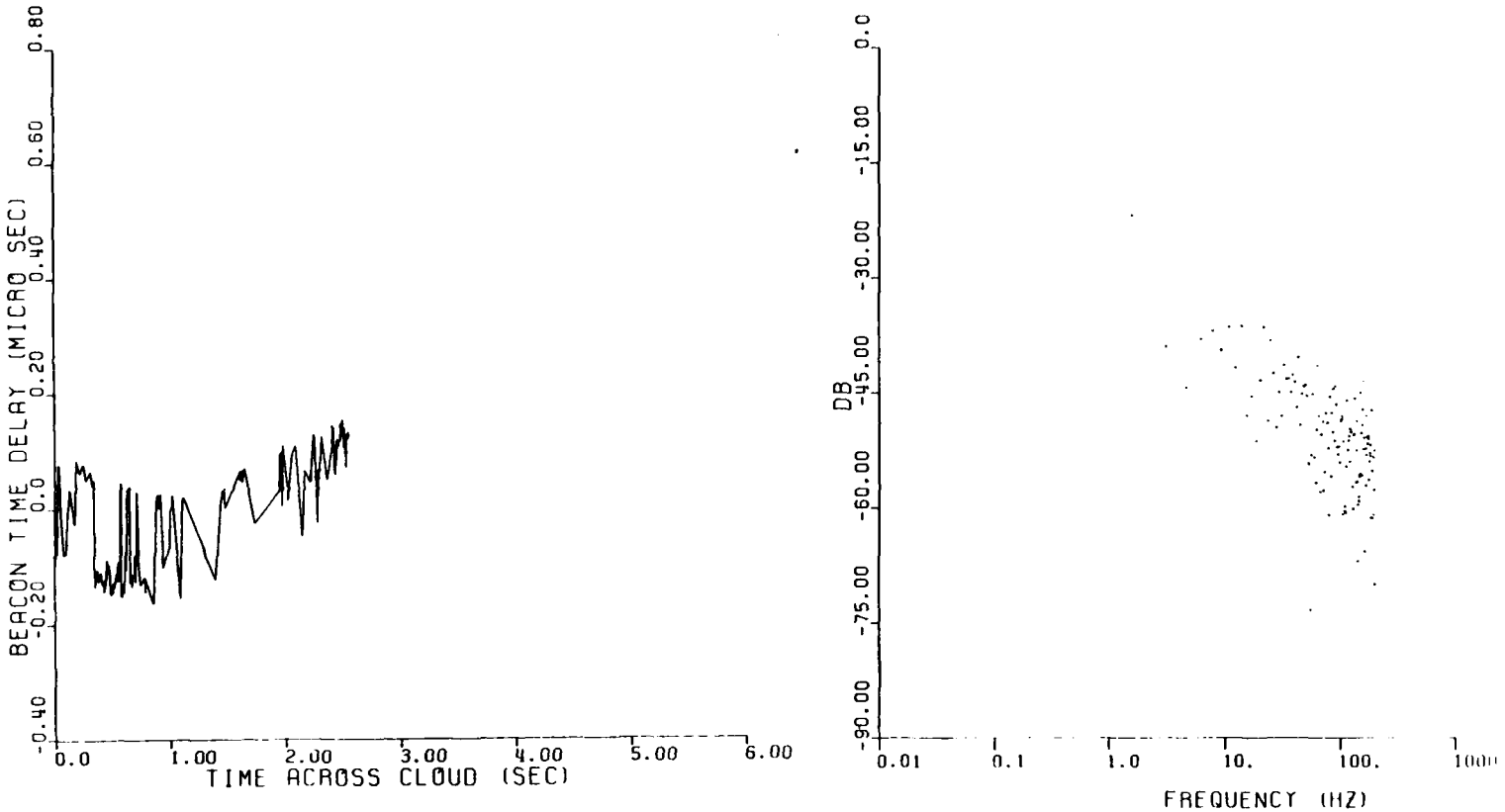

Figure 2-26. Detrended TOA jitter and jitter spectrum for Segment 6, following maximum TOA delay.

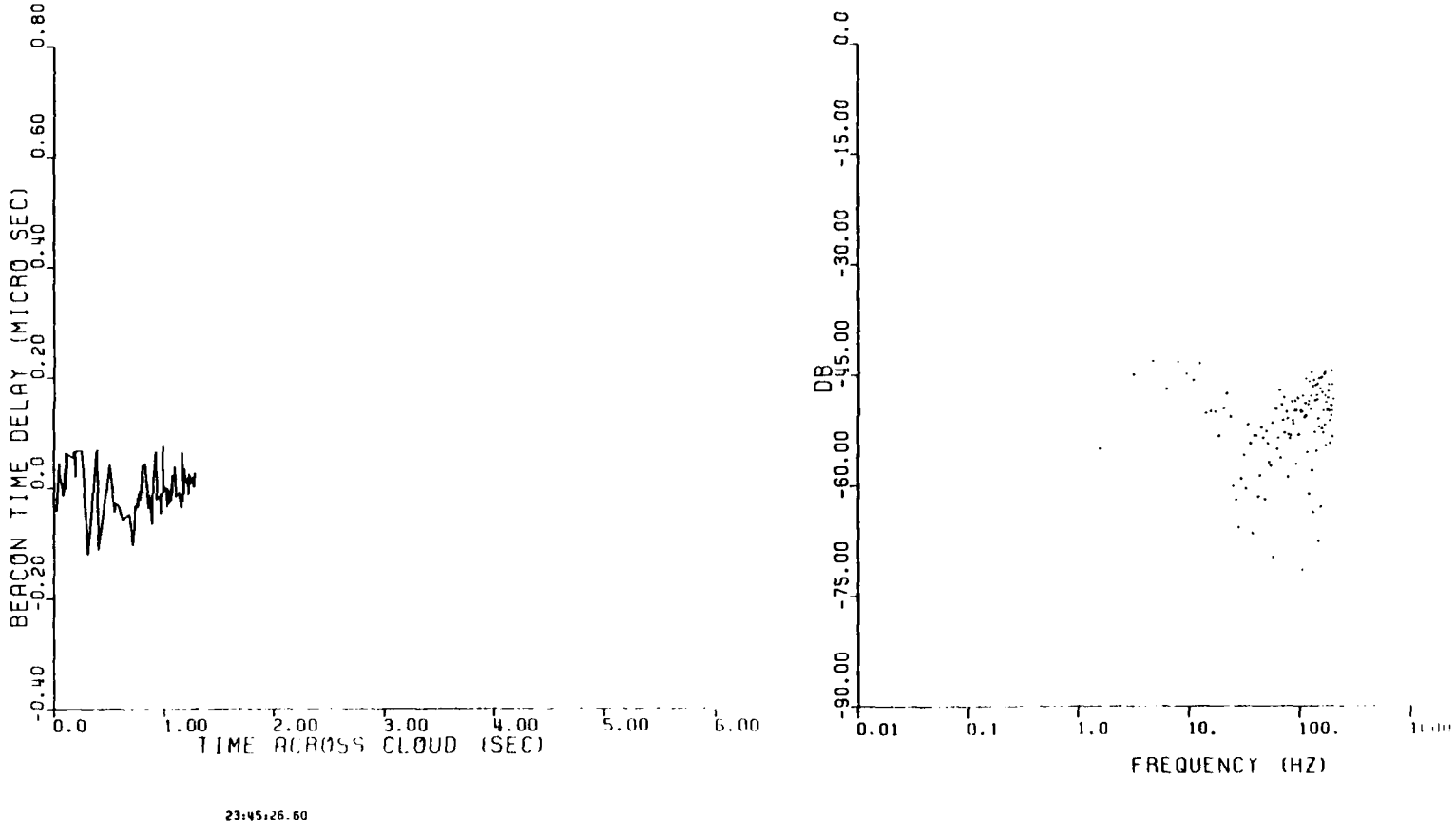

Figure 2-27. Detrended TOA jitter and jitter spectrum for Segment 7.

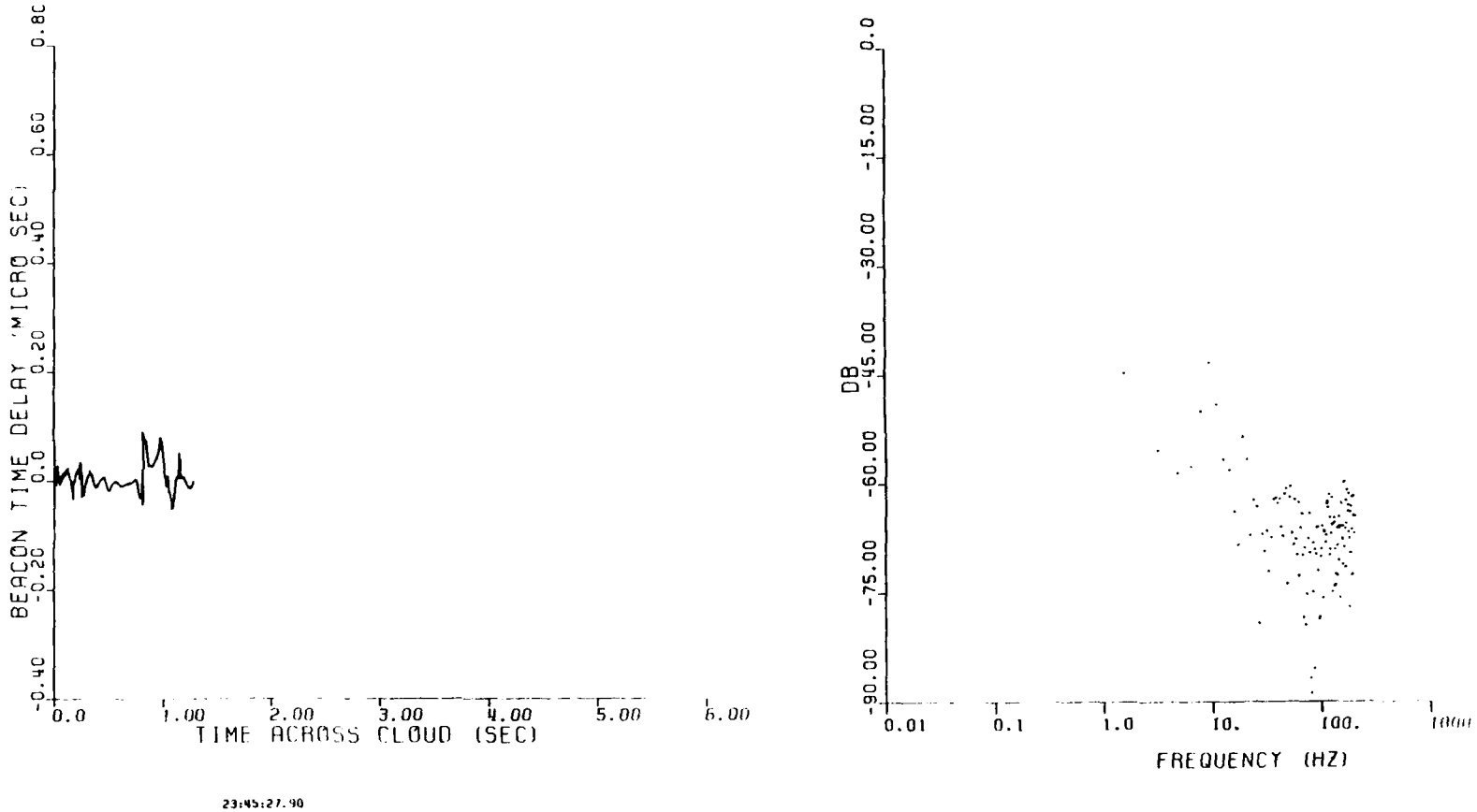

Figure 2-28. Detrended TOA jitter and jitter spectrum for Segment 8.

Table 2-1. Rms time delay jitter data segment summary.

Interval	Data Interval Start (UT)	End (UT)	RMS TOA Jitter (US)	RMS Phase (Radians)	Data Points	Jitter Points	Mean TOA (US)	Comment
1	2345:08.9	:11.5	0.0017	1.0	1024	1024	.00086	Prior To Noticeable Jitter
2	:13.6	:18.7	0.0229	14.1	2048			Segment A, Beginning of Jitter
3	:18.9	:20.2	0.0316	19.4	512	420	.0196	Decreasing TOA
4	:20.2	:22.8	0.0335	20.6	1024	949	.0196	
5	:21.4	:24.0	0.0435	26.8	1024	802	.0115	Prior to TOA Maximum Delay, Jitter may be underestimated
6	:24.0	:26.6	0.0988	60.8	1024	257	.00909	Following Max. TOA Delay
7	:26.6	:27.9	0.0371	22.8	512	127	.00397	
8	:27.9	:29.2	0.0227	14.0	512	469	.00574	

It should be noted that for some of the segments the detrending was imperfect and a residual trend remained. A significant trend value will result in an overestimate of the rms delay jitter. A low frequency component of the jitter spectrum can be noted for segments 2, 3, 4 and 5; this is evident in the first two or three spectral data points of Figures 2-22, 2-23, 2-24 and 2-26. The values of rms delay jitter given in Table 2-1 were computed directly from the detrended TOA jitter values with the exception of that for Segment 2, which was computed from the area under the jitter spectrum, ignoring the first few low frequency terms. Based on some data manipulations experiments, it is estimated that the rms jitter might be as much as 20 percent high for Segments 3, 4 and 6. Segment 5 in retrospect appears that it may not have been windowed properly, resulting in an asymmetric jitter (see Figure 2-25). This would have the effect of underestimating the rms jitter, which would offset the effect of imperfect detrending. Generally, the data show a consistent trend toward stronger jitter when the integrated electron content (TOA delay) was at a maximum as the rocket approached the center of the cloud, and diminished as the electron content decreased, as one would expect. The data from Segment 1, prior to significant TOA jitter, would indicate a TOA measurement accuracy of approximately 1 radian in rms phase.

It should be noted that the spectrum plots provided are only over the first 2^N points. In some cases, a TOA peak point could not be found within the ± 1 chip window of the trend line. Table 2-1 shows the number of sample points examined and the number of TOA jitter data points found within the jitter window. Only Segment 6 and 7 show a significant number of samples for which a TOA peak was not found within the jitter window. These two segments, as indicated on Figure 2-16, have very little energy in the direct path TOA signal, making it difficult to estimate the TOA (also see Figures 2-6 and 2-13). Though these signal drop out intervals, the trendline shown in Figure 2-20 was used.

2.6 DIFFERENTIAL DOPPLER DATA

2.6.1 Geometric Optics Interpretation of Places Differential Doppler Data

Geometrical arguments indicate that the basic cause of signal TOA spread is the geometric increase in path length produced by the plasma angular scattering. Likewise, because of the transit velocity of the beacon rocket, the scattered energy will have a slightly different Doppler component dependent on the angle scattered (and thus on delay). As shown in Appendix E, this differential Doppler may be expressed as:

$$f_d = \frac{V}{\lambda} \sqrt{\frac{2c\tau}{Z_f}} \qquad (2\text{-}1)$$

where

f_d is the differential Doppler relative to the direct path

V is the striation pattern velocity (velocity component orthogonal to striation axis in viewing plane)

λ is RV wavelength

τ is energy arrival time delay relative to direct path

Z_f is the (Fresnel) distance to striation screen as measured in the plane perpendicular to the geomagnetic field ($Z_f = Z \cdot CSC\alpha$ where Z is the slant distance to the striation screen)

c is velocity of light

α is the magnetic aspect angle (angle between propagation path and magnetic field at striations, 37.8° for SGI, Beacon 1).

This relationship can be tested using the beacon data. Conversely, this relationship can be used to determine discrete striation object locations.

2.6.2 First Refracted Ray

The first refracted ray provides an isolated ray that can be readily tracked as the beacon rocket moves behind the striation object giving rise to it. The differential Doppler can be determined from the phase at each delay tap position as the ray moves through that tap. Continuous phase plots can be used as well as angular spectrum plots as described in Appendix C. Figure 2-29 is a plot of the data for the first ray spanning 2345:07.7 when the ray first appears, to 2345:13.1 when the relative delay goes to zero as the rocket moves directly behind the striation object. Energy from the ray is generally in each tap approximately 0.5 second, allowing a good Doppler estimate.

From the angular spectrum data, the -10 dB Doppler spread of the ray energy has been measured and is shown at several delays. Each dot is the measured Doppler peak at each tap position (every 1/3 of a PN code chip). The direct path signal energy spread to the -10 dB points is also shown.

Also shown is the theoretical differential Doppler curve using the derived pattern velocity of 980 m/sec at 40 km distance. The pattern velocity derivation is given in Appendix D. A value of Z around 32 km gives a reasonable fit to the data.

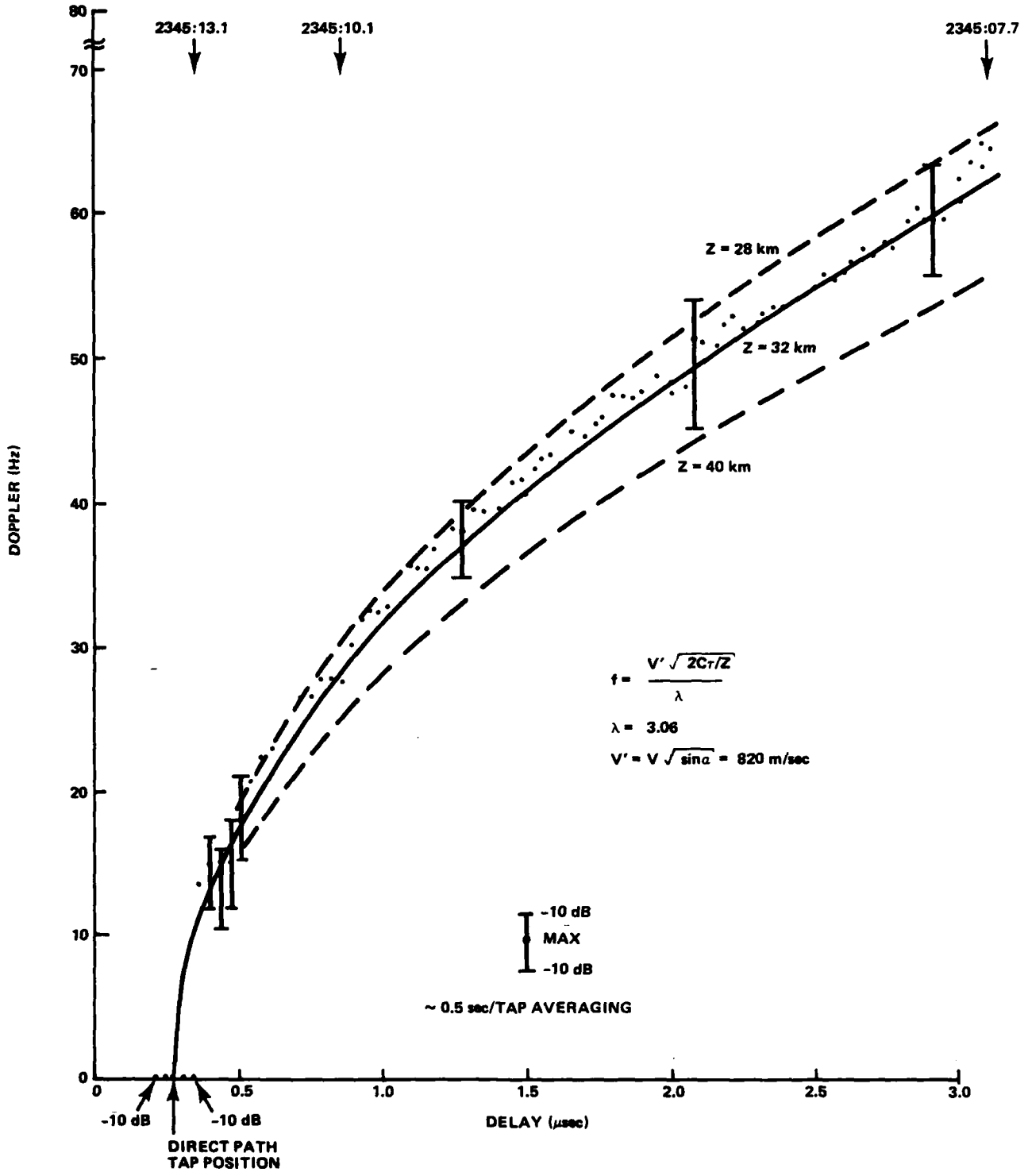

Figure 2-29. Differential Doppler delay history of first refracted ray, St. George Island, Beacon 1.

2.6.3 Multiple Ray Data

Figure 2-30 is a plot of the data measured in the interval 2345:15.0 to 2345:20.1 where there is a large number of rays apparent in the data. Thus, this figure no longer corresponds to a single ray, but rather between six and eight discrete rays can be observed. A 5-second observation interval was used to allow a ray to be present in all positions. This data too would imply a 32 km average occultation distance for a velocity of 980 m/sec.

During this interval, the dispersive jitter of the direct path is significant as indicated. Additionally, there is a slight increasing delay over this measurement period. The indicated direct path position corresponds to the maximum average power position over this 5-second interval.

It should be possible to trace each ray and provide a separate plot for each with more refined processing.

2.6.4 Correlation with Optical Data

2.6.4.1 First Object

Triangulation using optical photography and LLTV frames has permitted the visible striation locations to be determined as a general mass (as discussed in Section 2.2.2). This striation boundary is shown on Figure 2-31, which provides the occultation geometry for St. George Island along with the radar map of the ion cloud.[16] The ion cloud contour and the optical data striation boundaries are shown on a 160-km altitude plane. This corresponds to the maximum density altitude at the time of occultation as measured by the FPS-85 radar. The occultation intervals corresponding to Figures 2-29 and 2-30 are also indicated.

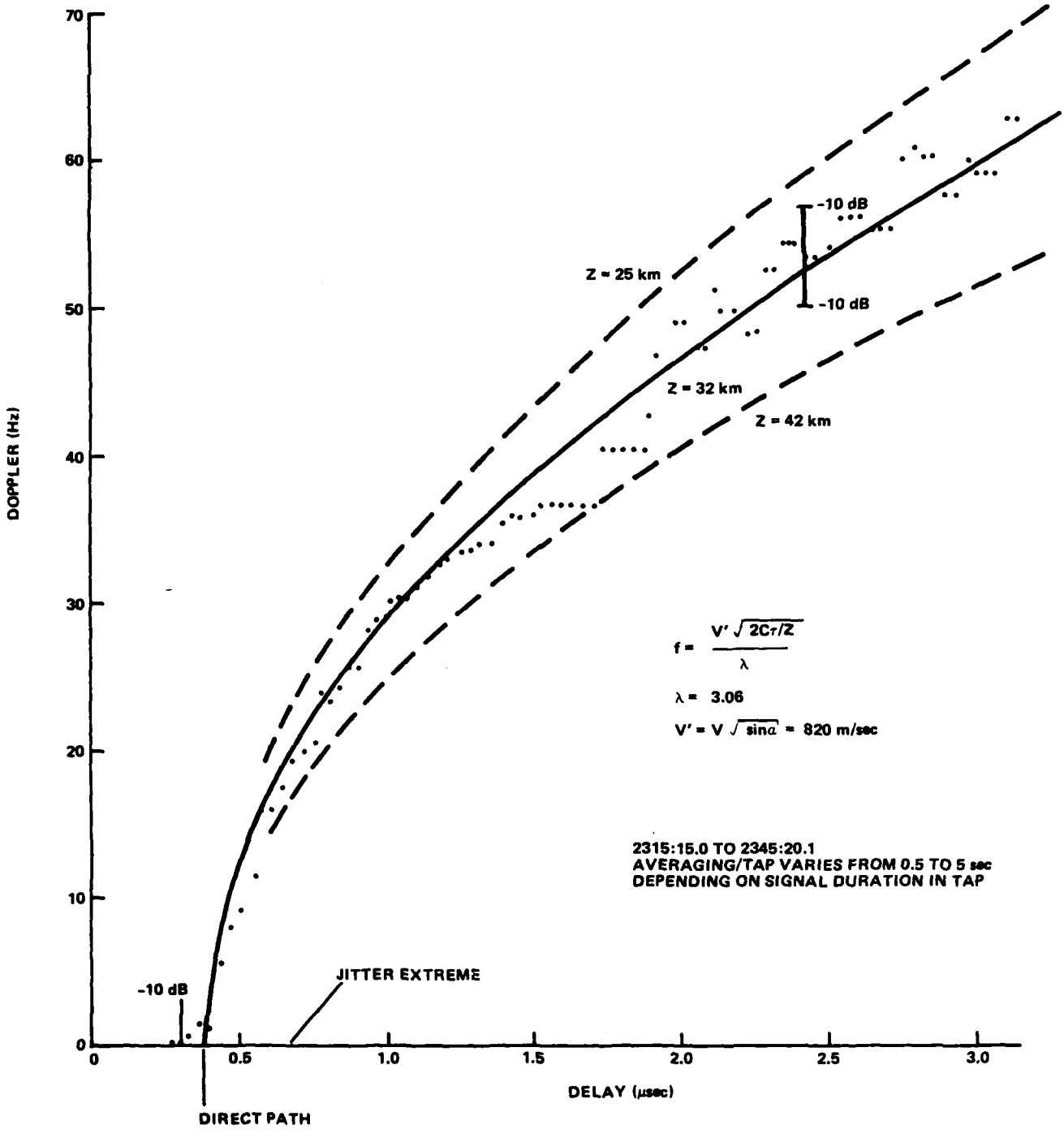

Figure 2-30. Differential Doppler versus delay, many refraction rays, St. George Island, Beacon 1.

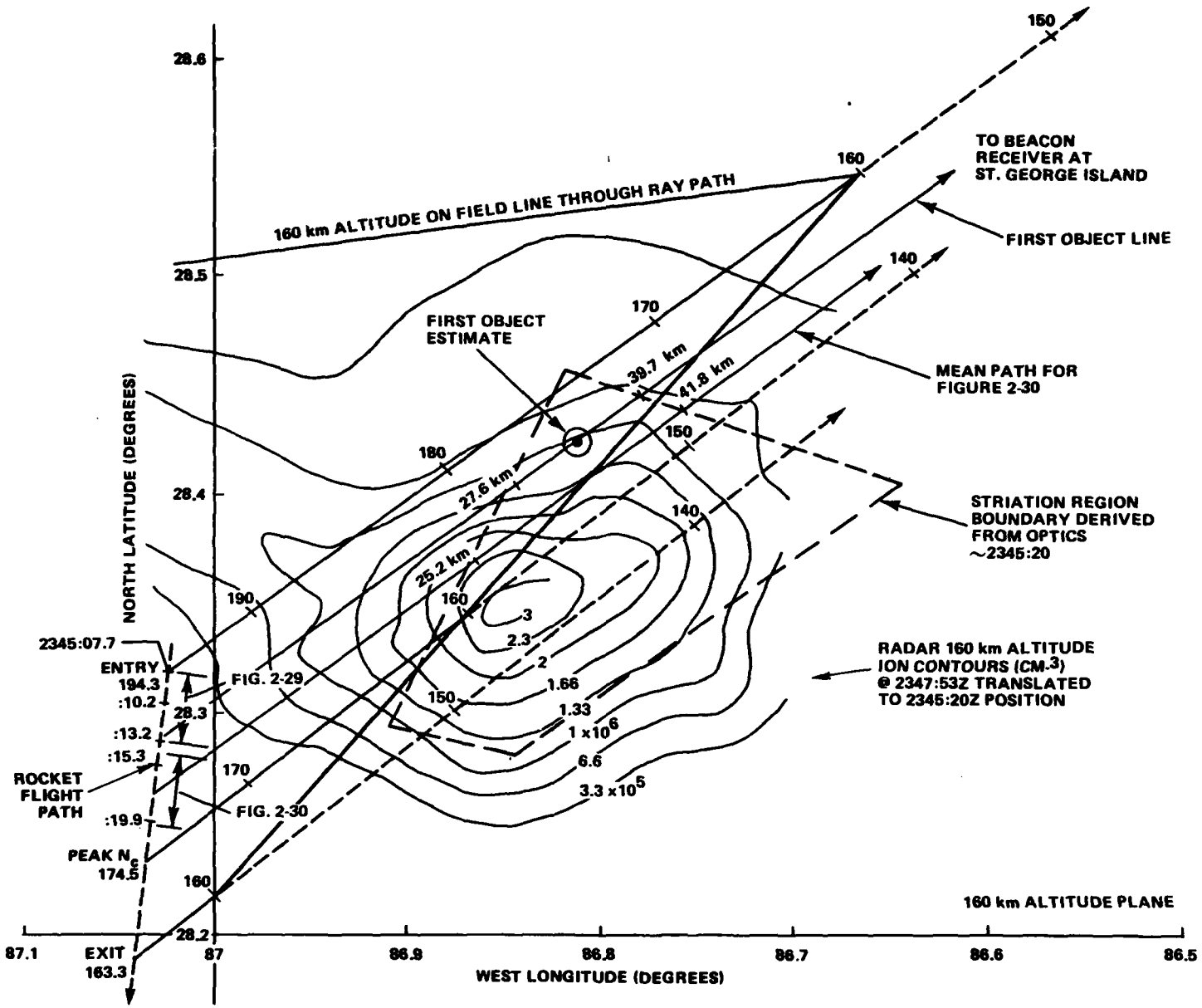

Figure 2-31. Occultation geometry for Figures 2-19 and 2-20 for St. George Island, Beacon 1.

The first object position as estimated from the differential Doppler data has been plotted at the indicated slant range of approximately 32 km. This location is in good agreement with the optically derived striation boundaries, which show the striations to be between 28 and 40 km along the line-of-sight at the first object occultation time.

2.6.4.2 Multiple Rays

As drawn on Figure 2-30, the curve that appears to give a reasonable fit to the data is given by the ratio of $V/\sqrt{Z} = 4.6188$, the same as for Figure 2-29. From the optical data, these rays should lie between approximately 25 and 42 km. Using the computed velocity of 980 m/sec, a mean striation distance around 32 km from the beacon rocket provides a good fit to the data as shown in Figure 2-30. Also as indicated on Figure 2-30, the data are well bounded by 25 and 42 km using a 980 m/sec velocity, in good agreement with the optics data.

2.6.5 Relationship to Generalized Power Spectrum

A geometrical approach based on angular spectra arguments can be used to predict the signal power delay profile as well as the spectrum of the signal at each component of delay as done in the preceding section. The relationship between the delay and the differential Doppler is also manifested in the relationships for the generalized power spectral density, $\Gamma_1(f,\tau)$, given in Equation 46 of Reference 13 (DNA 534D). Because of the cross-striation occultation geometry, the generalized power spectrum corresponding to the measured data should be that given by the one-dimensional generalized power spectrum. The generalized power spectrum is given below for reference

$$\Gamma_1(f_d,\tau) = 2^{1/2}\pi\tau_o f' \left[f_c/(f'\sigma_{\phi R})\right] \exp\left[-(\pi\tau_o f_d)^2\right] \qquad (2\text{-}2)$$

$$\exp[-1/2(\{\pi \tau_o f_d\}^2 - 2\pi f'\tau)^2 \ (f_c/\{f'\sigma_{\phi R}\})^2] \qquad (2\text{-}3)$$

where

τ_o is the signal decorrelation time,
f_d is the differential Doppler,
f' is a parameter = $1/(2\pi\sigma_s)$,
σ_s is the rms time delay spread,
$\sigma_{\phi R}$ is the Rayleigh phase variance,
τ is the delay, and
f_c is the carrier frequency.

The term $\sigma_{\phi R}/f_c$ is the dispersive phase term that describes the rms TOA jitter. Thus, the quantity $f_c/(f'\sigma_{\phi R})$ can also be thought of as the ratio of the rms delay spread to the rms delay jitter, σ_s/σ_j. When the ratio of the rms delay spread is much larger than the rms delay jitter, the dog-leg contributions strongly dominate the dispersive contributions giving rise to a sharply defined Doppler peak at each delay. The jitter term has the effect of smearing the delay power spectrum and, thus, smearing the Doppler spectrum at each delay.

From the above equation, the Doppler peaks can be seen to occur when the exponential term approaches zero, or when

$$(\pi\tau_o f_d)^2 = 2\pi f'\tau, \qquad (2\text{-}4)$$

or when

$\tau = A f_d^2$. This is the same functional form as derived in Appendix E from purely geometrical considerations.

The geometry is contained in the A term, which is given by

$$A = \frac{\pi}{2} \frac{\tau_o^2}{f'} \quad . \qquad (2\text{-}5)$$

The ratio of τ_o^2 to f' can be evaluated (Reference 18) for the δ-layer values given in Appendix C of DNA 5304D. Its value should agree very closely with the value of A if dispersive effects are ignored. Following the nomenclature of DNA 5304D,

$$\pi/(2\ f') \ = \ \sqrt{2}\ \pi^2\ \sigma_t$$

where

$$\sigma_t \ = \ \frac{\sqrt{2}\ \sigma_\phi^2\ B_n\ z_f}{k^2\ c} \ \frac{(L_x^4 + L_y^4 + 2L_{xy}^2)^{1/2}}{(L_x^2\ L_y^2 - L_{xy}^2)} \ , \qquad (2\text{-}6)$$

and thus

$$\frac{\pi}{2f'} \ = \ \frac{\sigma_\phi^2\ B_n\ z_f \lambda}{2\ f} \ \frac{(L_x^4 + L_y^4 + 2L_{xy}^2)^{1/2}}{(L_x^2\ L_y^2 - L_{xy}^2)}$$

The value of τ_o^2 from DNA 5304D Appendix C can be seen to be

$$\tau_o^2 \ = \ \tau_\perp^2 \ = \ \frac{L_x^2\ L_y^2 - L_{xy}^2}{B_n \sigma_\phi^2 \left(\frac{z_1}{z_t}\right)^2 (L_y^2\ V_x^2 + L_x^2\ V_y^2 - 2L_{xy}\ V_x\ V_y)}$$

where $B(n, \sigma_\phi^2) = 1$ and $m = 2$ have been used in the intermediate steps. Substituting this result into the expression for A yields

$$A \ = \ \frac{z_f \lambda}{2f\ V_a^2}$$

where

$$V_a^2 \ = \ \frac{L_y^2\ V_x^2 + L_x\ V_y^2 - 2L_{xy}\ V_x\ V_y}{(L_x^4 + L_y^4\ 2L_{xy}^2)\ 1/2} \qquad (2\text{-}7)$$

$$V_x \ = \ \hat{x} \cdot V$$
$$V_y \ = \ \hat{y} \cdot V$$

and

$$V = \frac{z_t - z_1}{z_t} V_{tr} + V_{st} - \frac{z_1}{z_t} V_{re} \quad .$$

For the beacon occultation geometry,

$$V \cong (z_t - z_1)/z_t \cdot V_{tr} \quad .$$

For highly elongated structures, L_x is small and L_y is big and thus the effective velocity, V_a, is approximately equal to V_x. Thus, we obtain for the desired relation for the differential Doppler,

$$f_d \cong \frac{V}{\lambda} \sqrt{\frac{2c\tau}{z_f}} \quad .$$

Thus, the geometric approach presented in Appendix E and disucssed in Section 2.6 is in agreement with the formalism developed in Reference 13.

2.6.6 Generalized Power Spectrum

The analytical expressions for the generalized power spectrum, $\Gamma_1(f_d,\tau)$, given in the preceding section describe the relationship between Doppler and delay as discussed. Fundamentally, the generalized power spectrum describes the power spectrum of the received signal at a fixed delay. The frequency of maximum intensity of the spectrum at any fixed delay was shown to be given by the differential Doppler relationship derived from geometrical considerations as well as from the generalized power spectrum relationship of Reference 13. The spectrum is concentrated about this peak frequency, which can thus be considered to be similar to a Doppler effect. Thus, it is natural to refer to a Doppler plane and a delay plane when describing the generalized power spectrum. Figure 2-32 is a plot of the generalized power spectrum with a normalized selective fading bandwidth, f_o

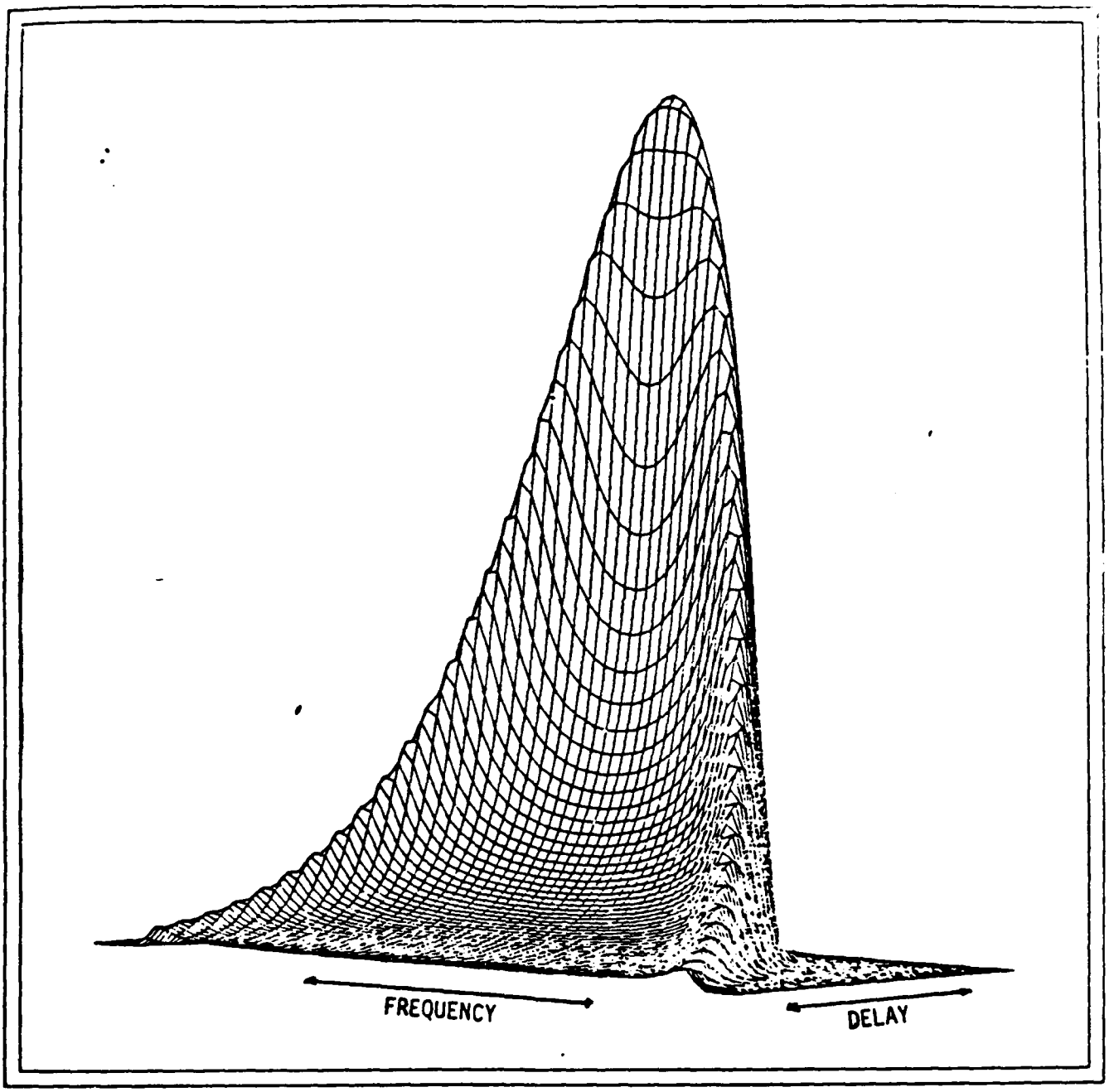

Figure 2-32. Generalized power spectrum for f_o = 1 Hz and τ_o = 1 second.

of 1 Hz and a normalized signal decorrelation time, τ_o, of 1 second. Each frequency step shown on Figure 2-32 is 0.023 Hz and the delay step is 0.01 second.

The two-dimensional Fourier transform of the generalized power spectrum is the mutual coherence function for the complex signal envelope defined as

$$G(z,x,y,k) = \overline{U^*(z,\vec{r}_1,k_1)\ U(z,\vec{r}_2 k_2)} \quad ,$$

where the propagating carrier signal is expressed as

$$E(z,\vec{r},k) = \frac{U(z,\vec{r},k)\ \exp\{ik(|\vec{r}|^2 + z^2)^{1/2}\}}{z} \quad .$$

Transforming the spatial dependence of time, the mutual coherence function corresponding to the generalized power spectrum given earlier is

$$G_1(z_t,\Delta t,\Delta f) = [1/\{(1-i\Delta f/f')^{1/2}\}] \quad .$$

$$\exp[-(\sigma_{\phi r}^2/2) \cdot (\Delta f/f_c)^2 - (\Delta t^2/\tau_o^2) \cdot \{1/(1-i\Delta f/f')\}].$$

Figure 2-33 is a plot of the mutual coherence function obtained in transforming Figure 2-32. The time axis increments on Figure 2-33 are 0.17 second and 0.391 Hz. The peak corresponds to $\Delta t=0$ and $\Delta f=0$.

The two-frequency mutual coherence function described in Section 2-11 is a "slice" along the frequency axis of the 2-D autocorrelation function or mutual coherence function described above. Likewise, the time autocorrelation function is a "slice" along the time axis.

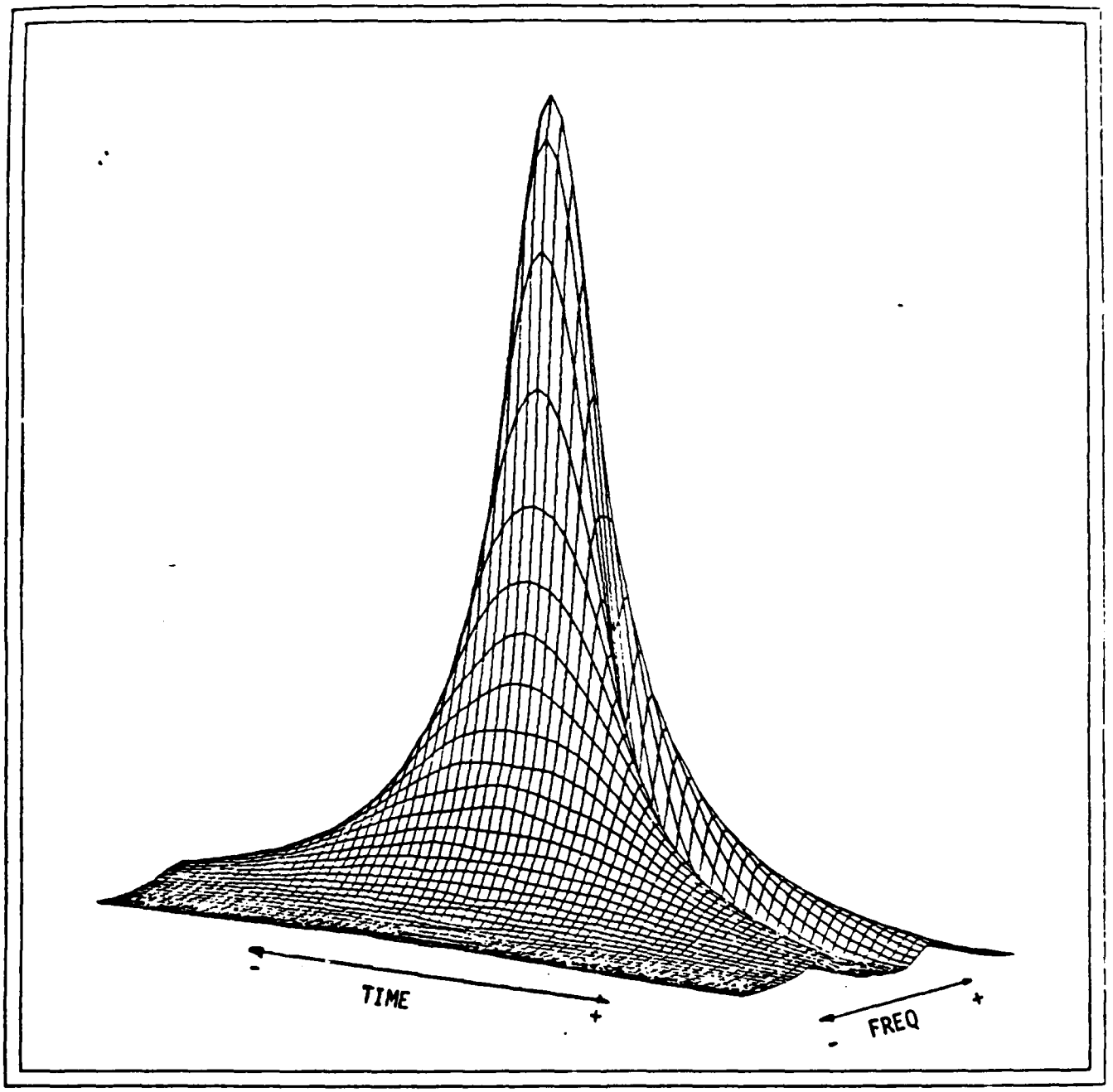

Figure 2-33. Mutual coherence function for f_o = 1 Hz and τ_o = 1 second.

The signal Doppler spectrum (angular spectrum) is given by integrating out the delay variable in the generalized power spectrum,

$$\Gamma_1(f_d) = \int \Gamma_1 (f_d,\tau)\, d\tau \quad .$$

The Doppler spectrum can be obtained from the data by computing the spectrum of each tap (delay) position and summing over all tap delays.

Likewise, signal delay power spectrum or energy arrival distribution is obtained by integrating out the Doppler frequency variable in the generalized power spectrum,

$$\Gamma_1(\tau) = \int \Gamma_1 (f_d,\tau)\, df_d \quad .$$

2.6.7 Delay Power Spectrum

It is relatively simple to compute the delay power spectrum by simply summing the squares of the channel impulse response magnitudes shown earlier at each tap delay and normalizing the result such that the integral equals unity to correspond with the DNA channel model definition,

$$\int_{-\infty}^{\infty} \Gamma_1(\tau)\, d\tau = 1.$$

The correspondence to the DNA channel model is made difficult, however, by the gross plasma TOA delay. The generalized power spectrum formulation describes the power distribution due to the random angular scattering effects and does not account for the strong lens like defocusing of the barium cloud. Accordingly, in constructing the delay power spectrum, it is necessary to remove the TOA shift before summing. Furthermore, there is some distortion that cannot be

removed that is a result of the gross plasma TOA delay. This has the effect of putting more energy in the longer delays than would occur otherwise if the angular defocusing were not present. That is, on Figure 2-16 it can be noted that those rays that first show up at the long delays have a greater gross plasma TOA delay associated with them as the rocket approaches the TOA peak delay. Because of this, we might expect better agreement with theory by averaging over smaller segments as opposed to averaging over the entire cloud. With this in mind, we anticipate only a first-order agreement with theory.

Figures 2-34 through 2-42 show the results of these calculations for those intervals summarized in Table 2-1. The TOA shown in Figure 2-17 was used to remove the TOA bias. In order not to remove the effects of the dispersive jitter, a mean TOA curve was obtained from Figure 2-17 and the power summed relative to the mean delay at each time sample. The mean TOA profile is believed to be accurate to within $\pm 1/4$ of a chip (± 0.025 microsecond). Figure 2-42 shows the delay power spectrum over the entire occulation interval.

Generally, the individual segments do not conform to the long-term statistical average of the theoretical delay power spectrum because of the discrete rays evident in each segment. To compensate for the energy at large delays, which should average to a much smaller value than the individual rays present during each segment, these segments were renormalized over that portion of the profile that appears to correspond to a smooth power profile. This was done to facilitate a comparison with theory. The results of these calculations are shown in Figures 2-43 through 2-49. The normalization interval used is indicated on each figure, referenced to the number of chips past zero delay. Segment 1 does not have significant energy beyond the direct-path signal and thus did not require renormalization. Figure 2-43 inadvertently covers only the first half of Segment 2.

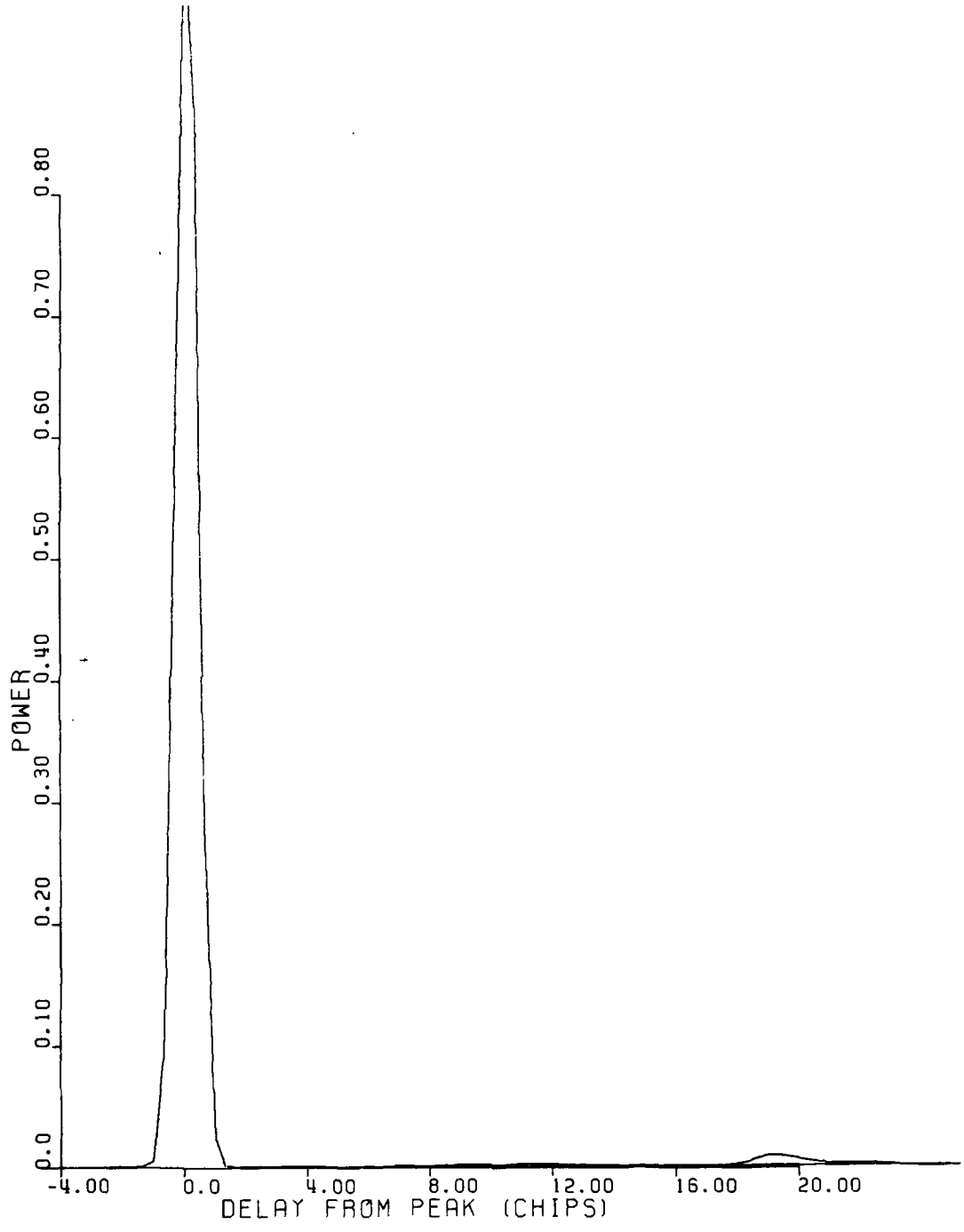

Figure 2-34. Delay power spectrum for Segment 1.

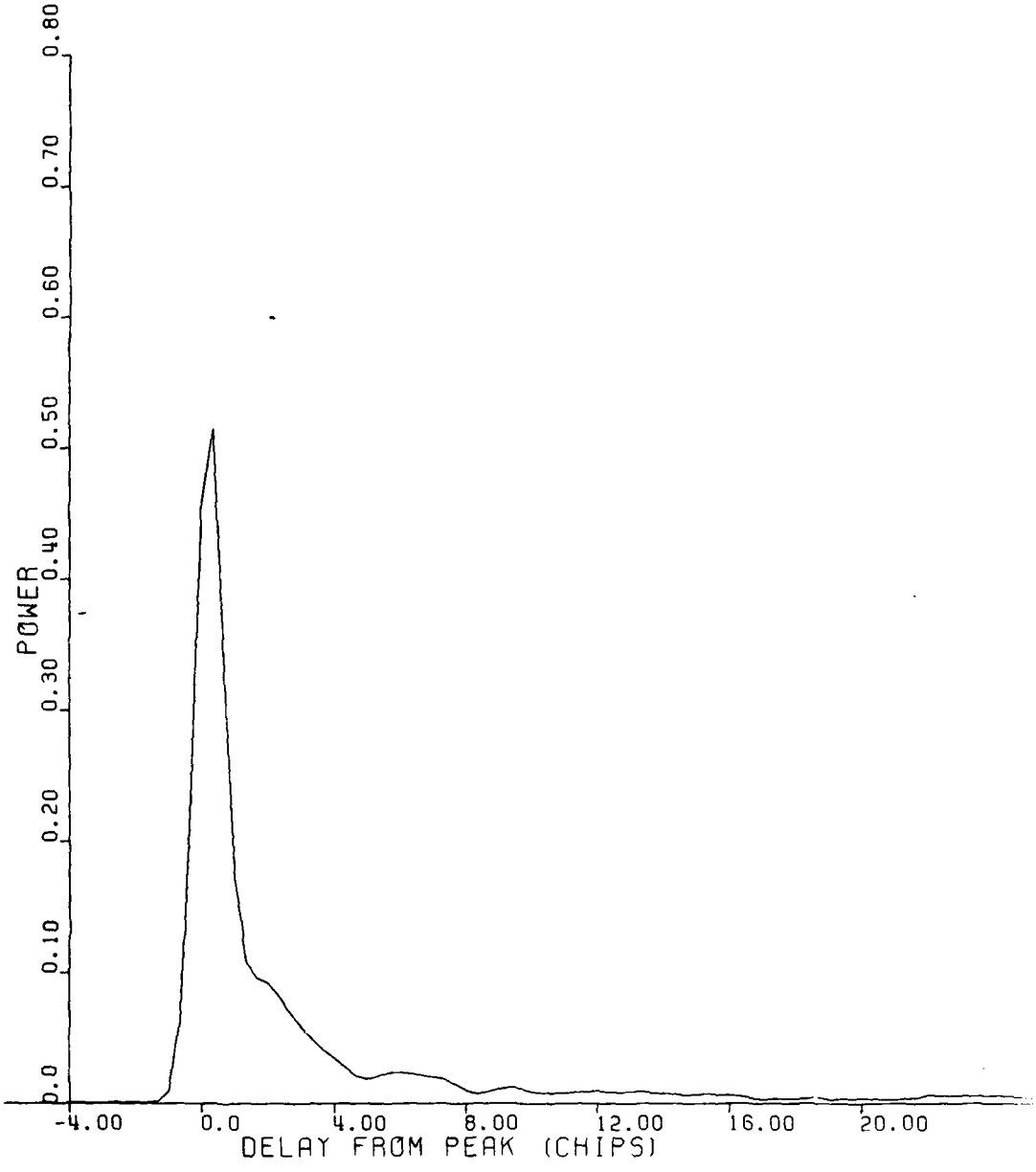

Figure 2-35. Delay power spectrum for Segment 2.

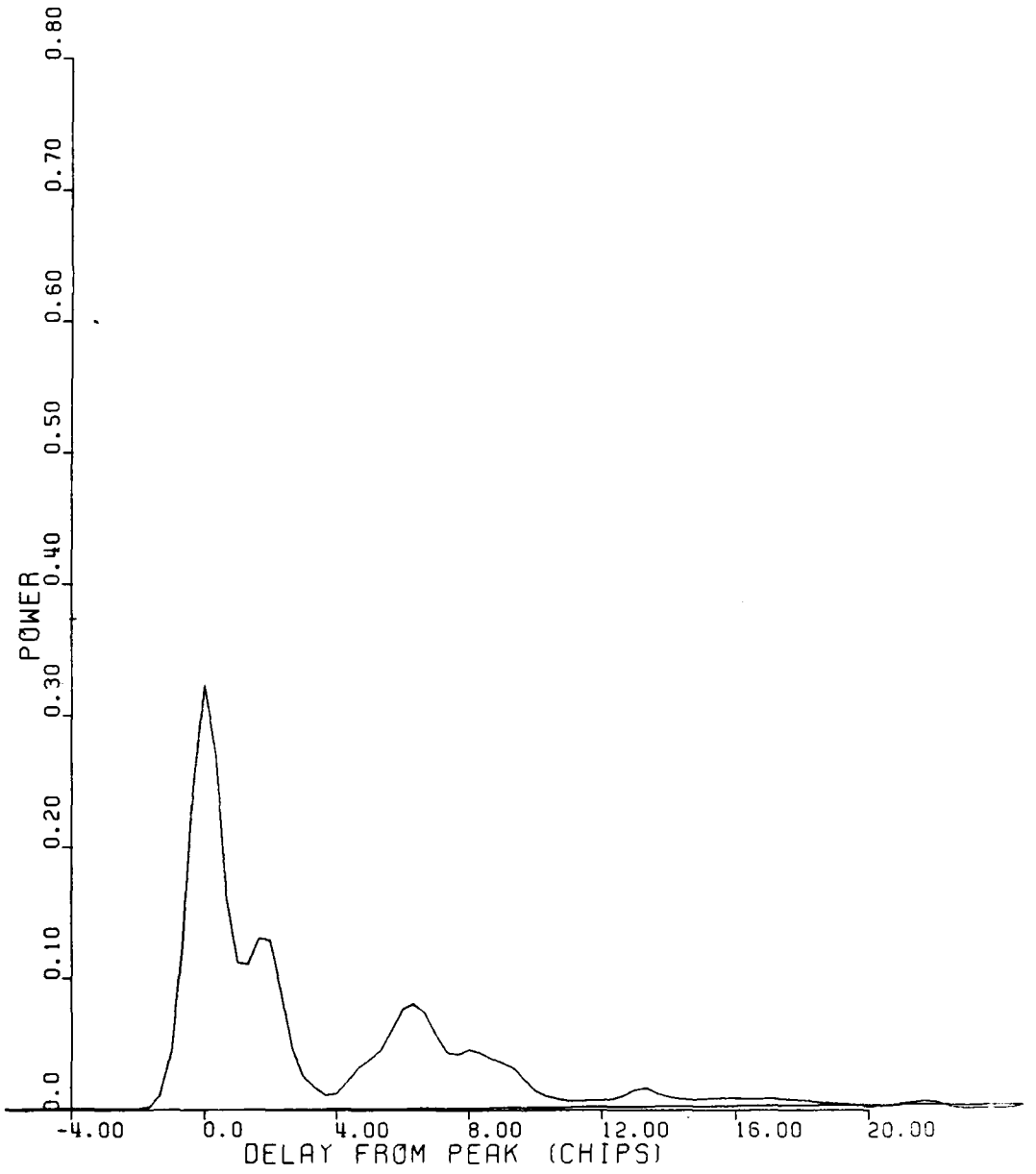

Figure 2-36. Delay power spectrum for Segment 3.

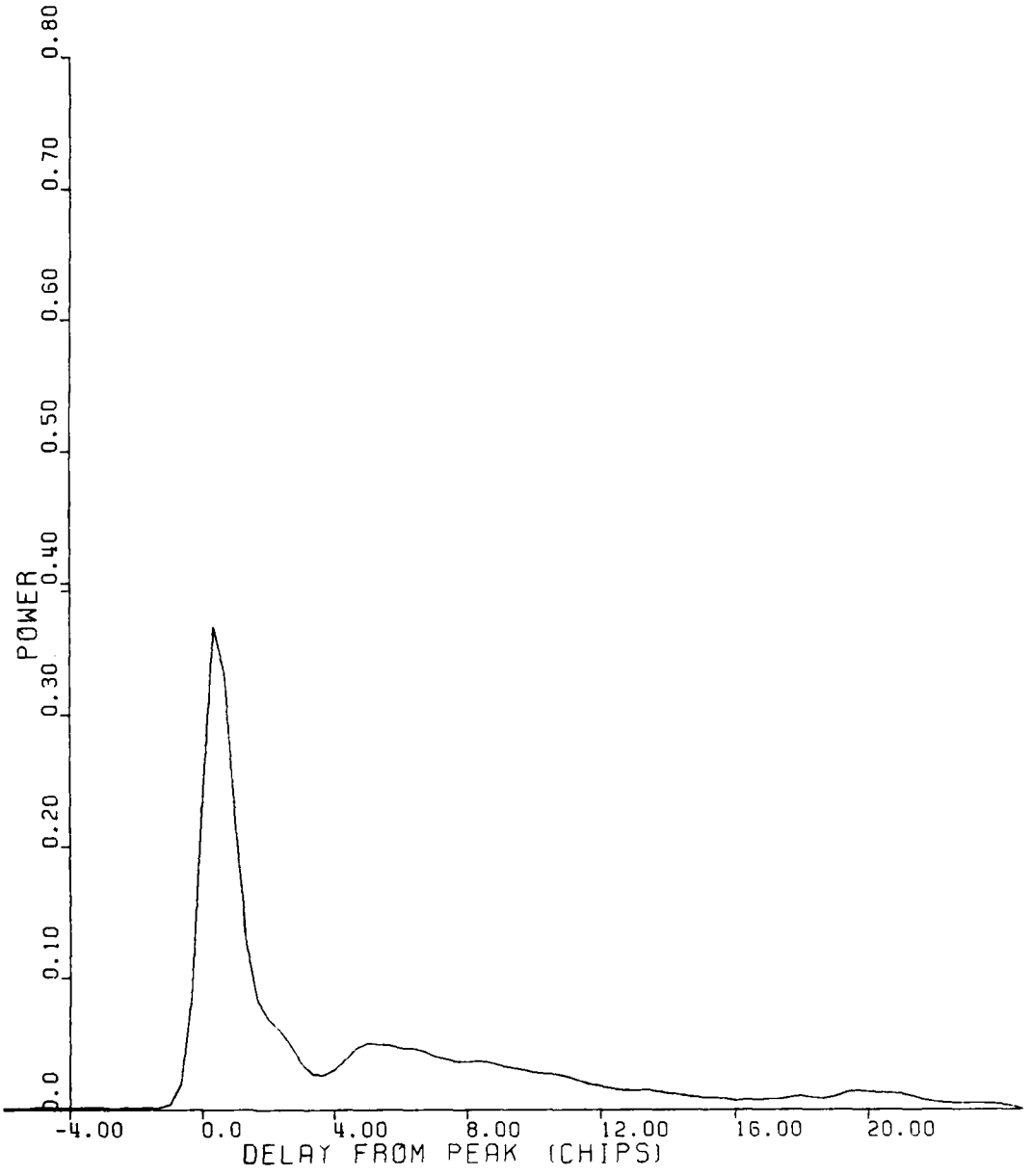

Figure 2-37. Delay power spectrum for Segment 4.

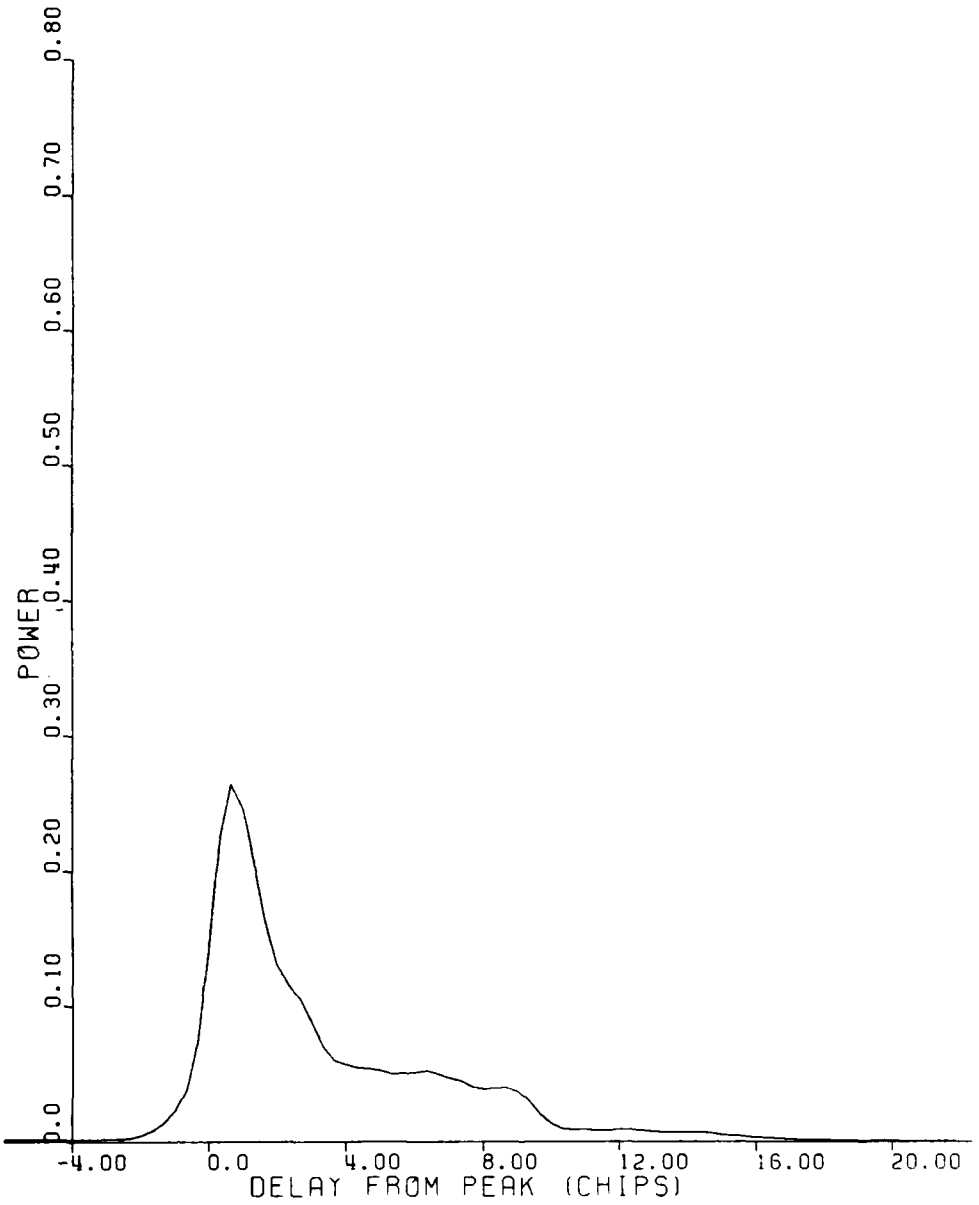

Figure 2-38. Delay power spectrum for Segment 5.

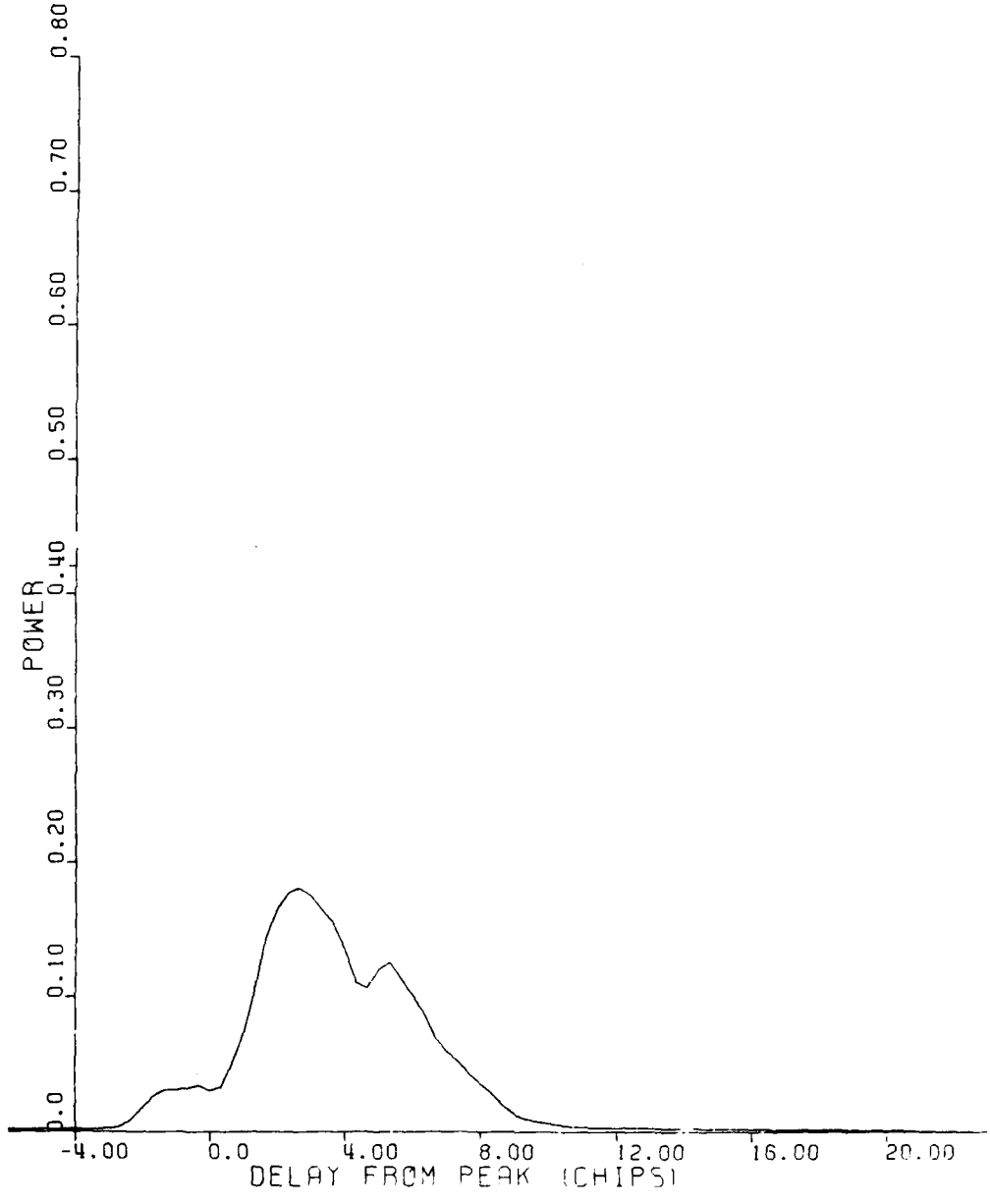

Figure 2-39. Delay power spectrum for Segment 6.

AD-A160 566 PLACES (POSITION LOCATION AND COMMUNICATION EFFECTS SIMULATIONS) BEACON EXPERIMENT TEST RESULTS(U) ESL INC SUNNYVALE CA J MARSHALL ET AL. 01 AUG 84 DNA-TR-84-376 2/3

UNCLASSIFIED DNA001-81-C-0149 F/G 20/14 NL

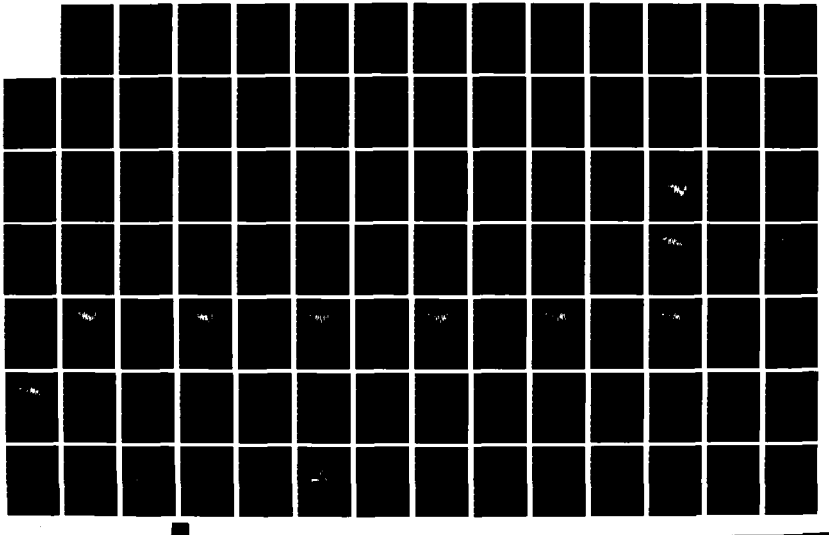

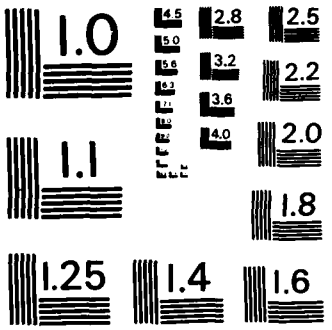

MICROCOPY RESOLUTION TEST CHART
NATIONAL BUREAU OF STANDARDS-1963-A

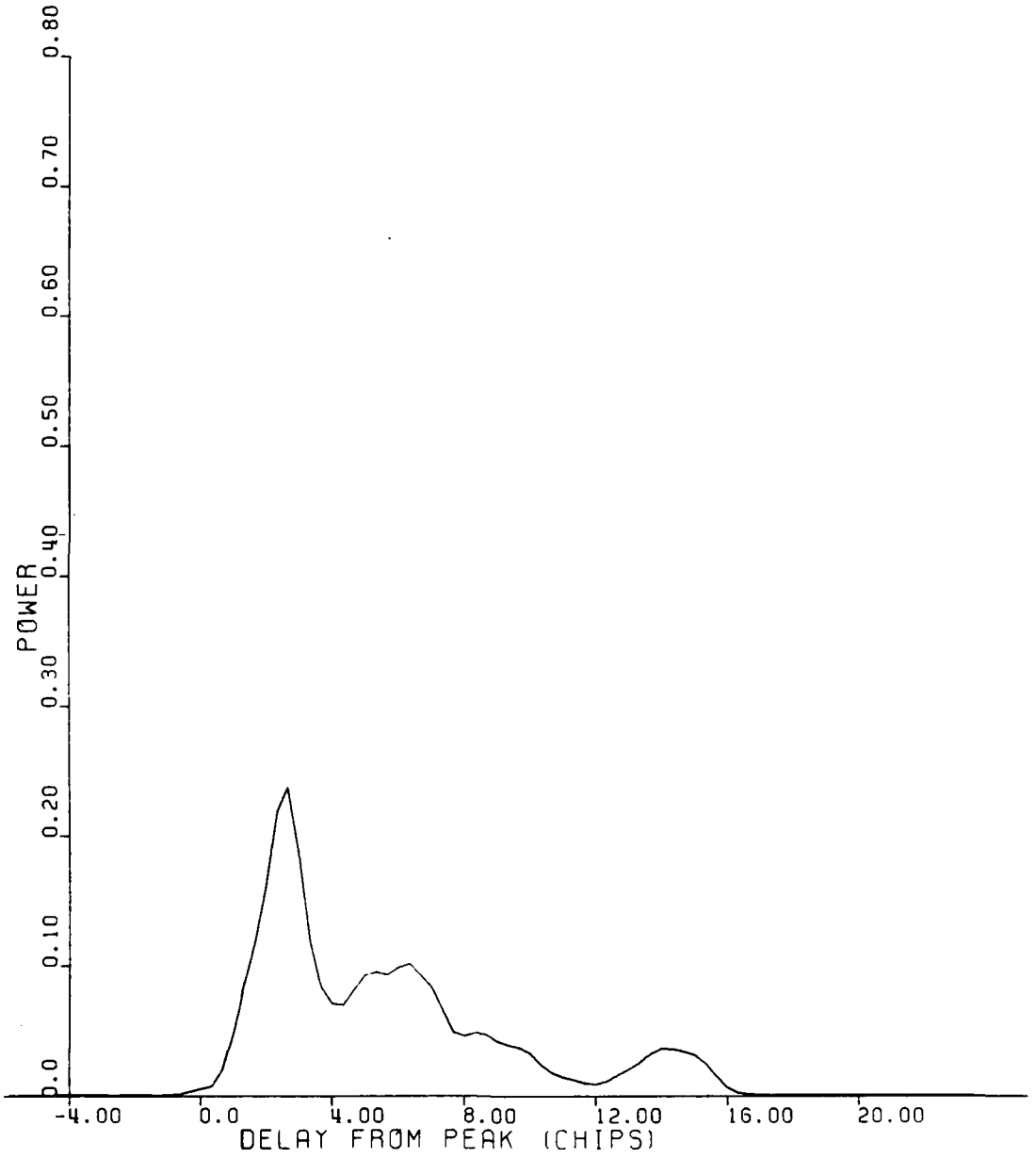

Figure 2-40. Delay power spectrum for Segment 7.

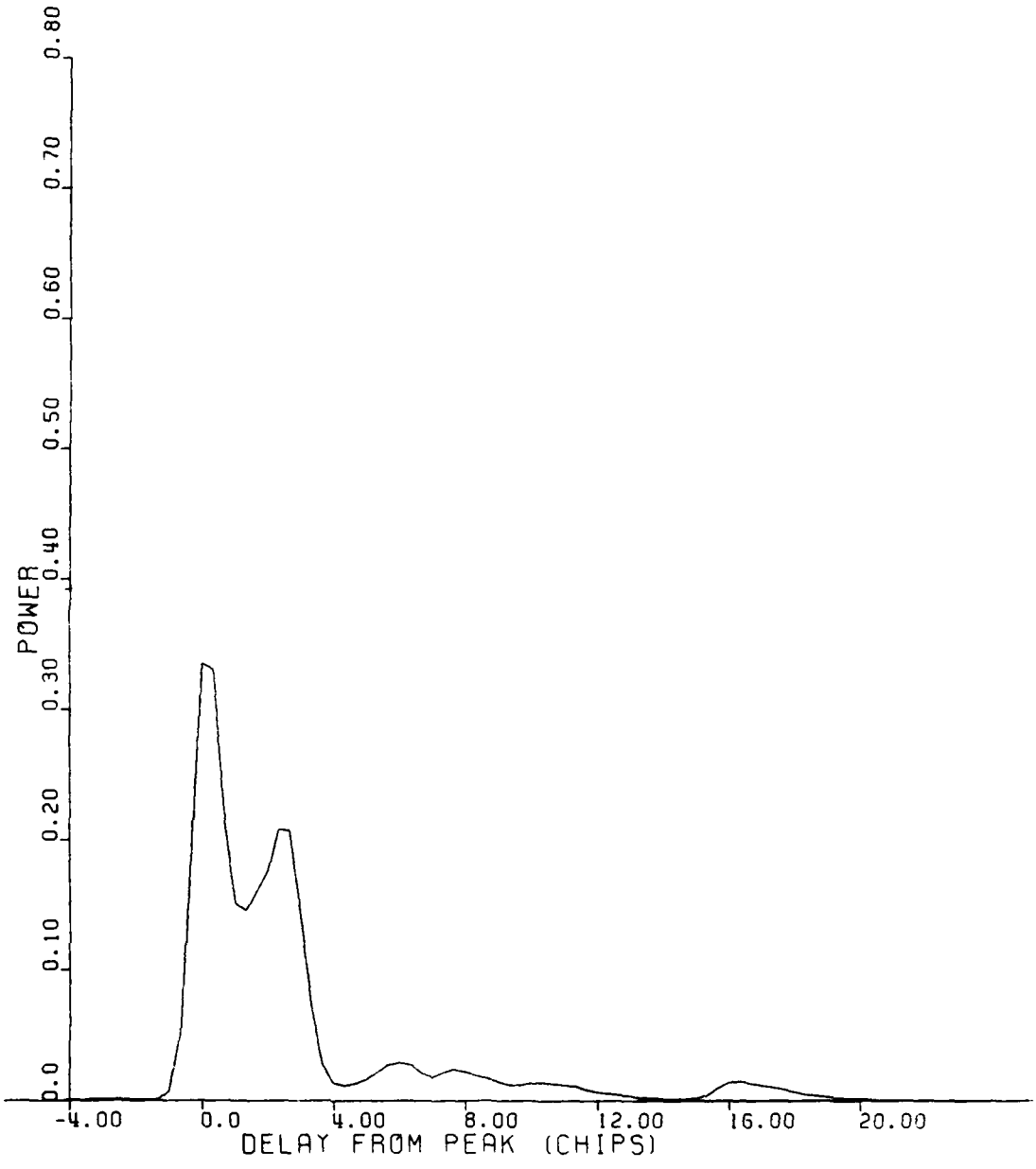

Figure 2-41. Delay power spectrum for Segment 8.

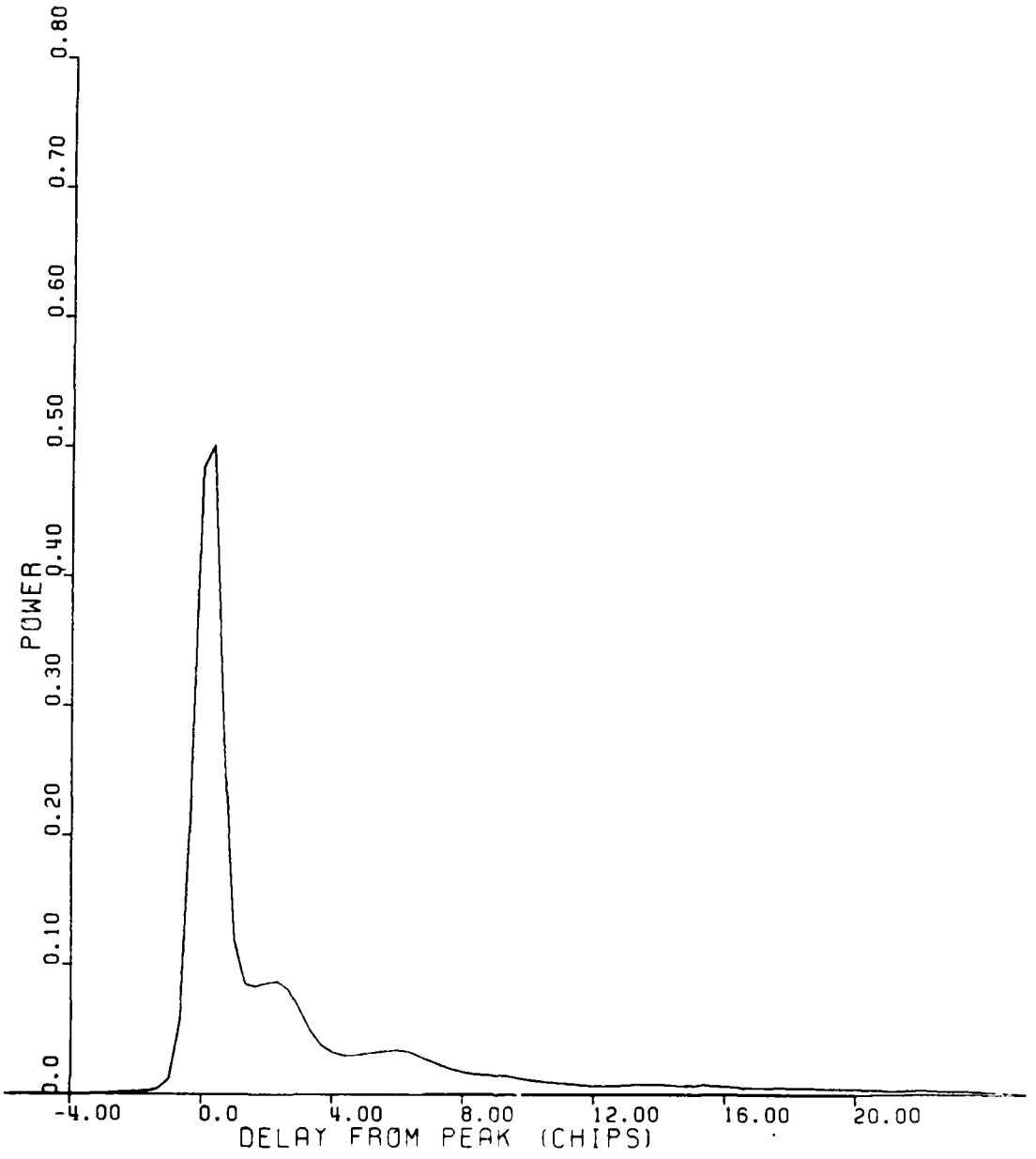

Figure 2-42. Delay power spectrum for entire occultation interval, 2345:08.9 to 2345:29.4.

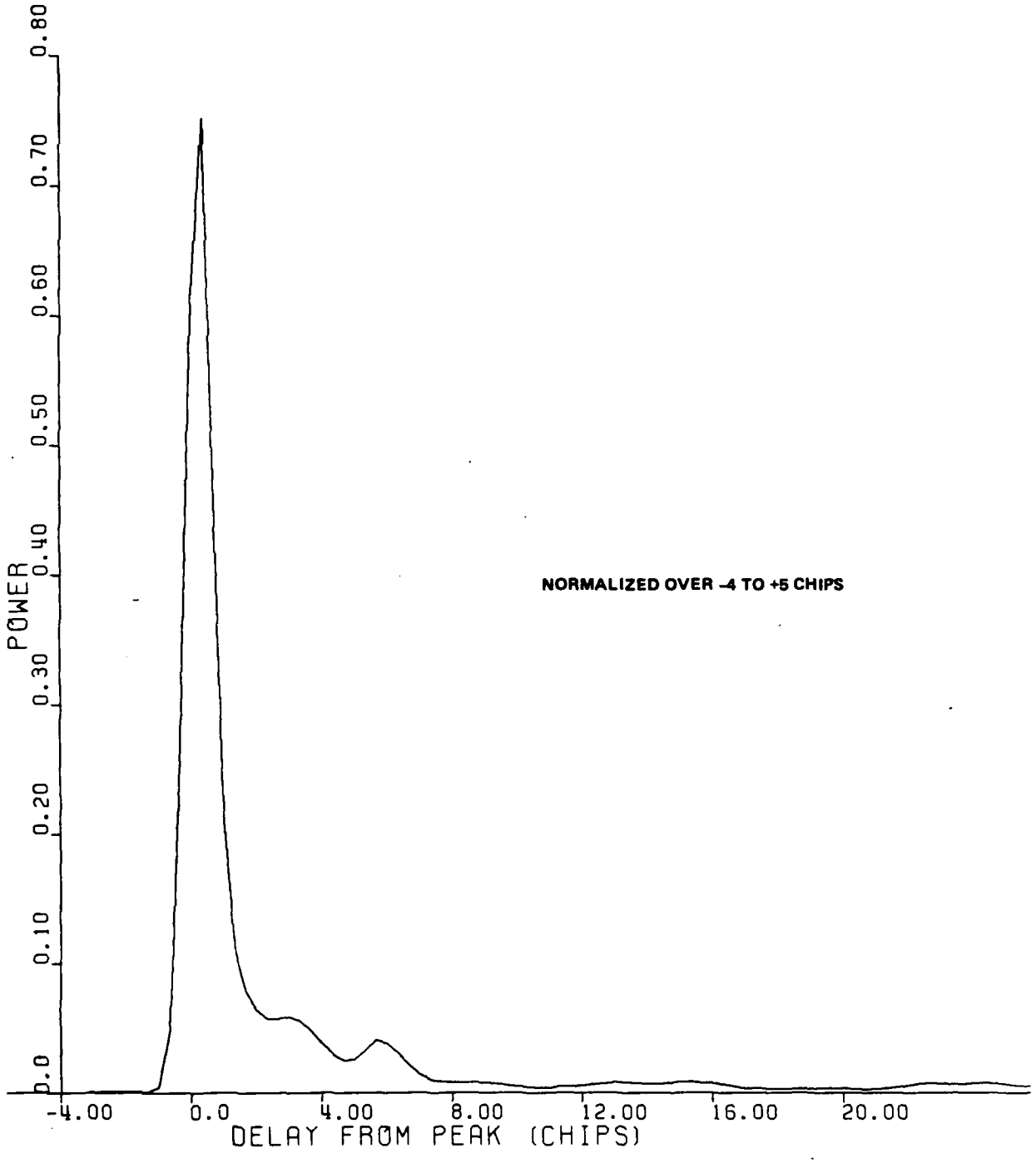

Figure 2-43. Renormalized delay power spectrum for first half of Segment 2 (2345:13.6 to 2345:16.2).

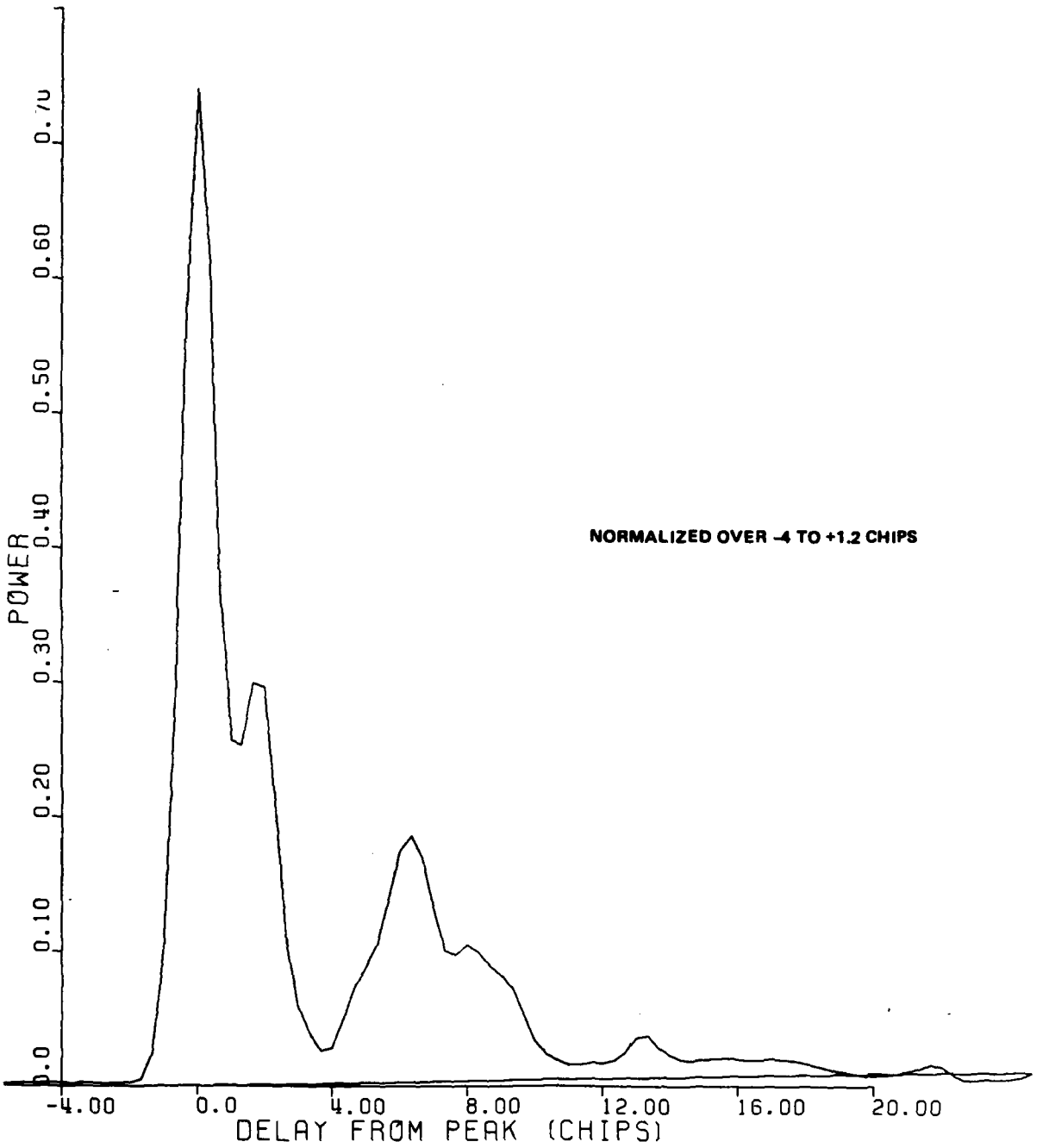

Figure 2-44. Renormalized delay power spectrum for Segment 3.

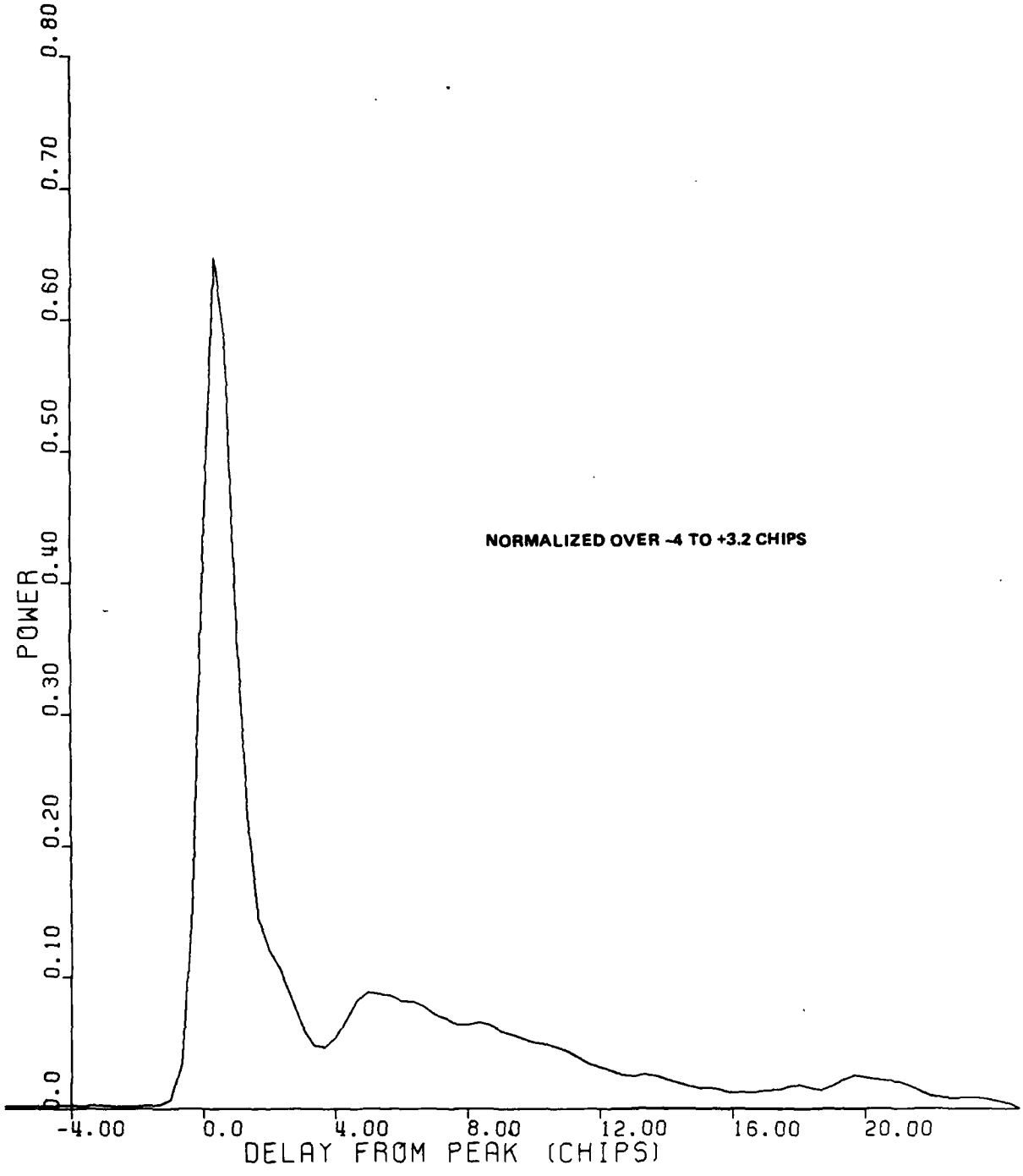

Figure 2-45. Renormalized delay power spectrum for Segment 4.

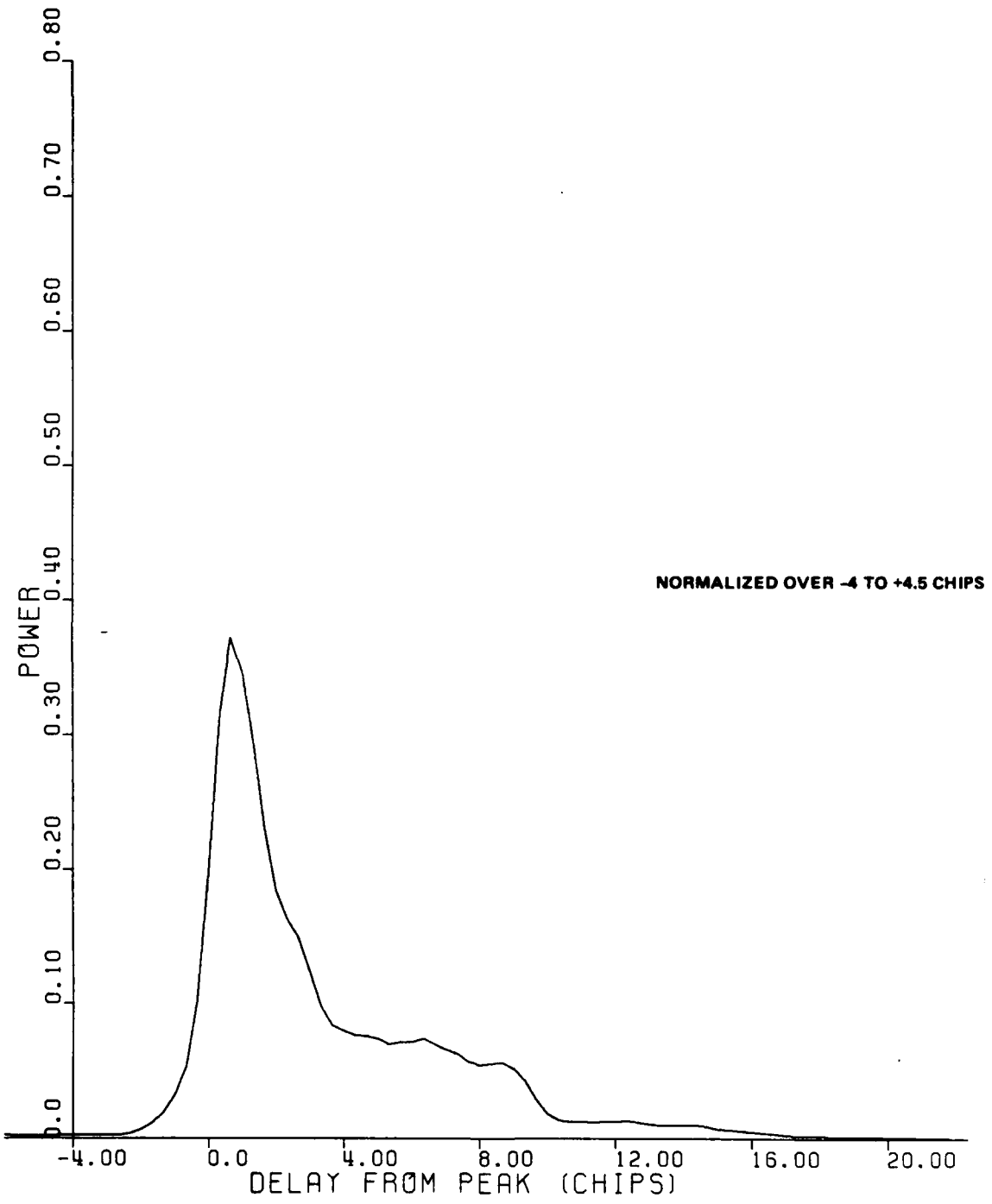

Figure 2-46. Renormalized delay power spectrum for Segment 5.

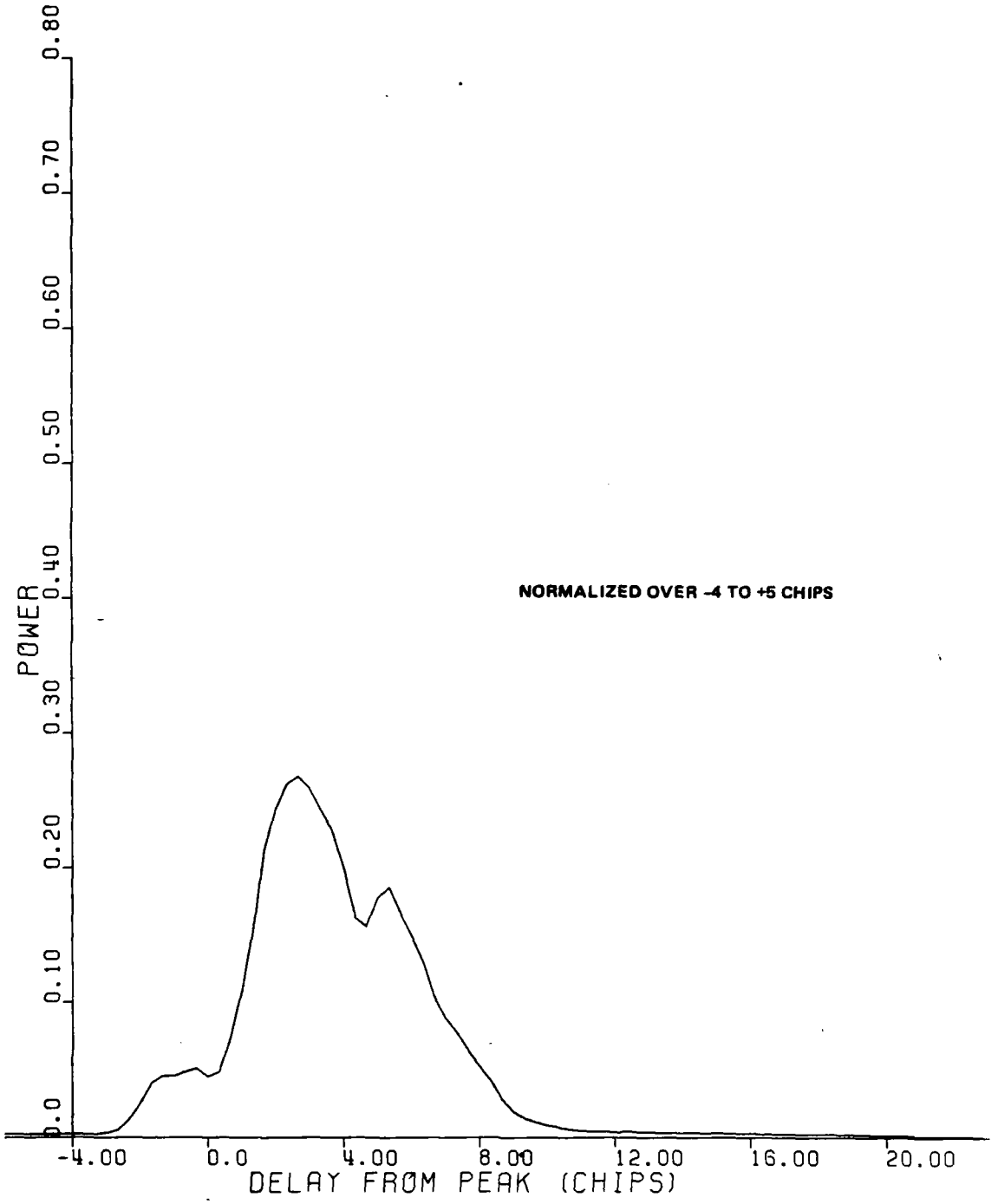

Figure 2-47. Renormalized delay power spectrum for Segment 6.

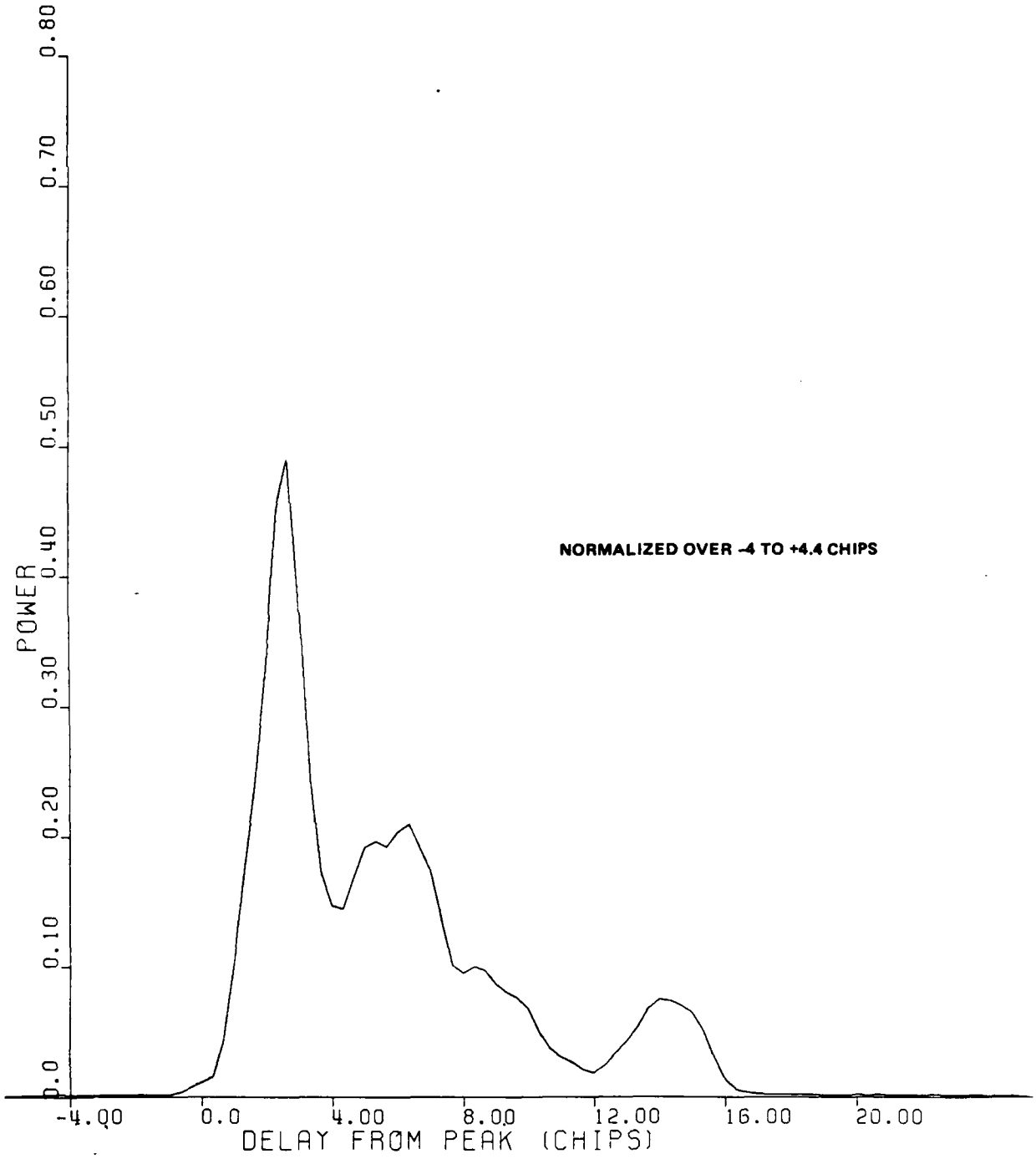

Figure 2-48. Renormalized delay power spectrum for Segment 7.

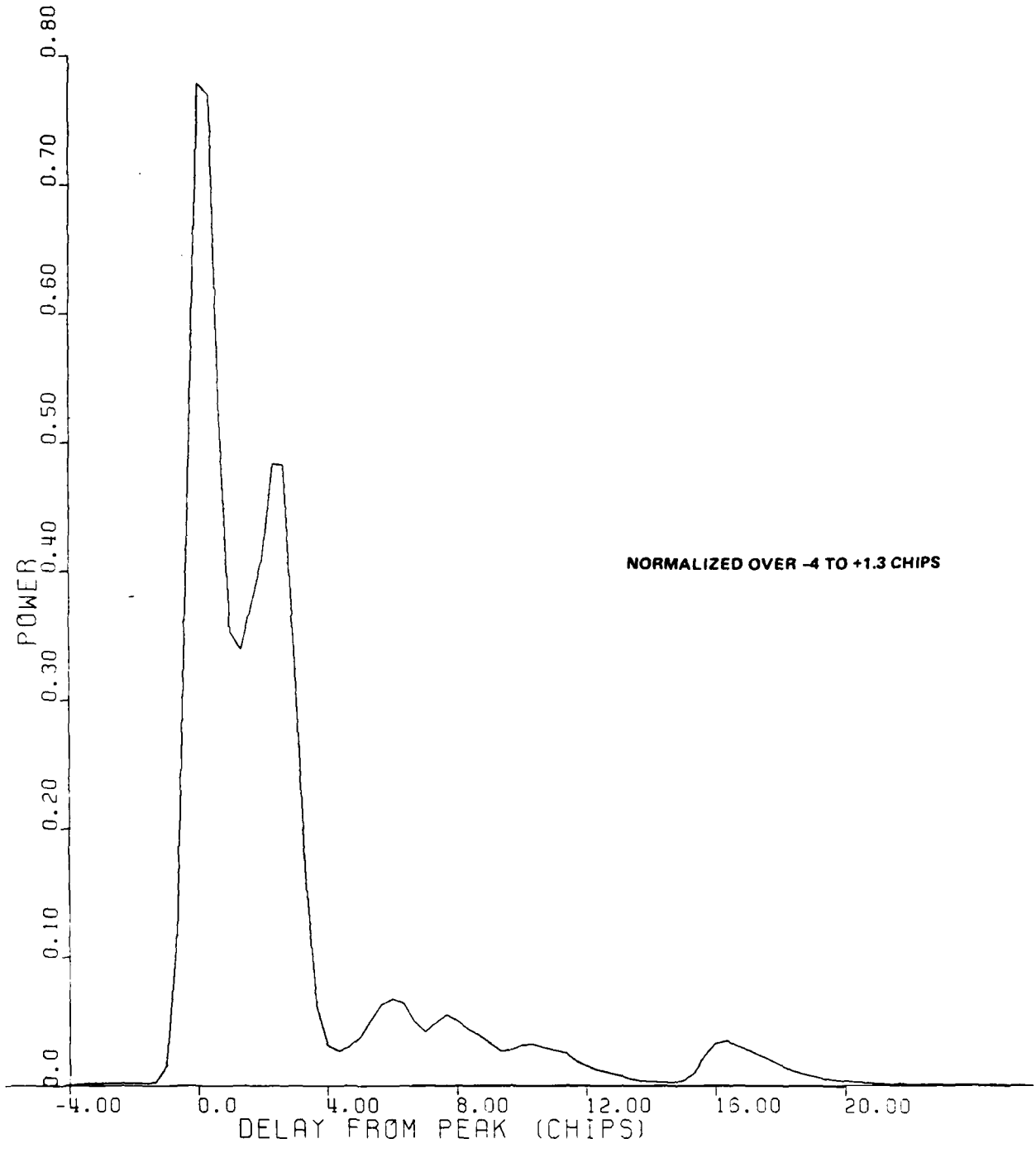

Figure 2-49. Renormalized delay power spectrum for Segment 8.

2.6.7.1 Comparison With Theory

Since the $\Gamma_1(\tau)$ does not depend strongly on the decorrelation time, τ_o, theory can be used to estimate the ratio of the rms delay spread to the rms delay jitter parameter and the coherence bandwidth, f_o, by matching theoretical curves against the measured data presented in Figures 2-34 through 2-49. The estimated values for these parameters can then be compared to other measurements presented later. Furthermore, since the ratio of the rms delay jitter to delay spread is small, the shape of the power delay spectrum depends primarily on the choice of f_o. Furthermore since the amplitude of the delay power spectrum is a strong function of f_o, a fairly sensitive measure of f_o is achieved. The ratio of the rms delay jitter to the delay spread primarily determines the smearing, or rounding of these curves.

Figures 2-50 through 2-53 illustrate the theoretical behavior. Table 2-2 summarizes the result of matching the measured curves to theory. For Segment 1, which is prior to any significant jitter or spread, an f_o in excess of 4 MHz is required, limited by the signal bandwidth, as expected. In fitting the theoretical curves to these data, the lower values at large delays were not emphasized. Rather, the peak amplitude and width of the main lobe were emphasized. The average over the entire occultation interval was renormalized (not shown) in obtaining the fit summarized in Table 2-2.

Since the frequency correlation bandwidth parameter is defined as

$$f_o = 1/2\pi\sigma_\tau = \frac{1}{2\pi\sqrt{\sigma_j^2 + \sigma_s^2}}$$

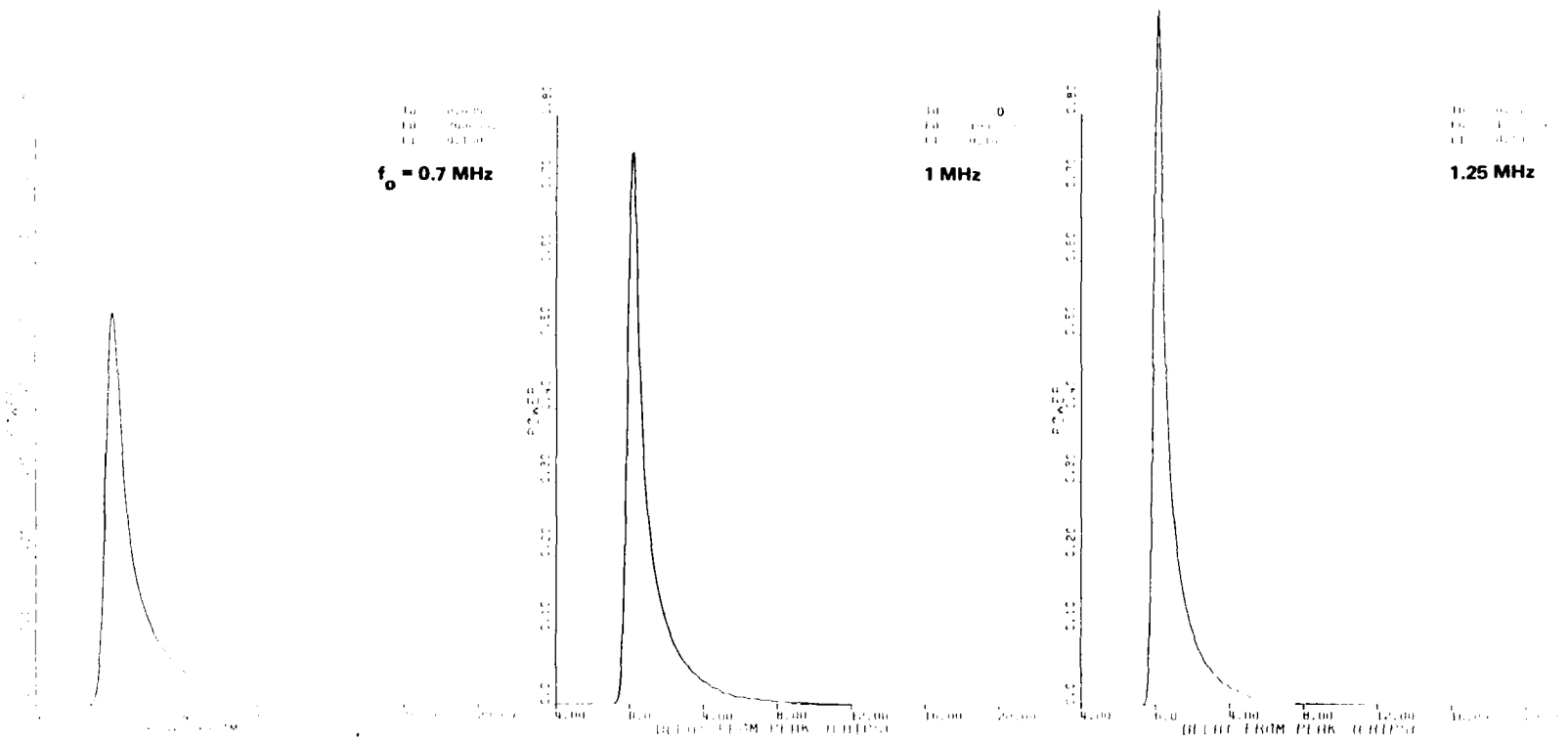

Figure 2-50. Theoretical delay power spectrum for σ_j/σ_s = 0.1.

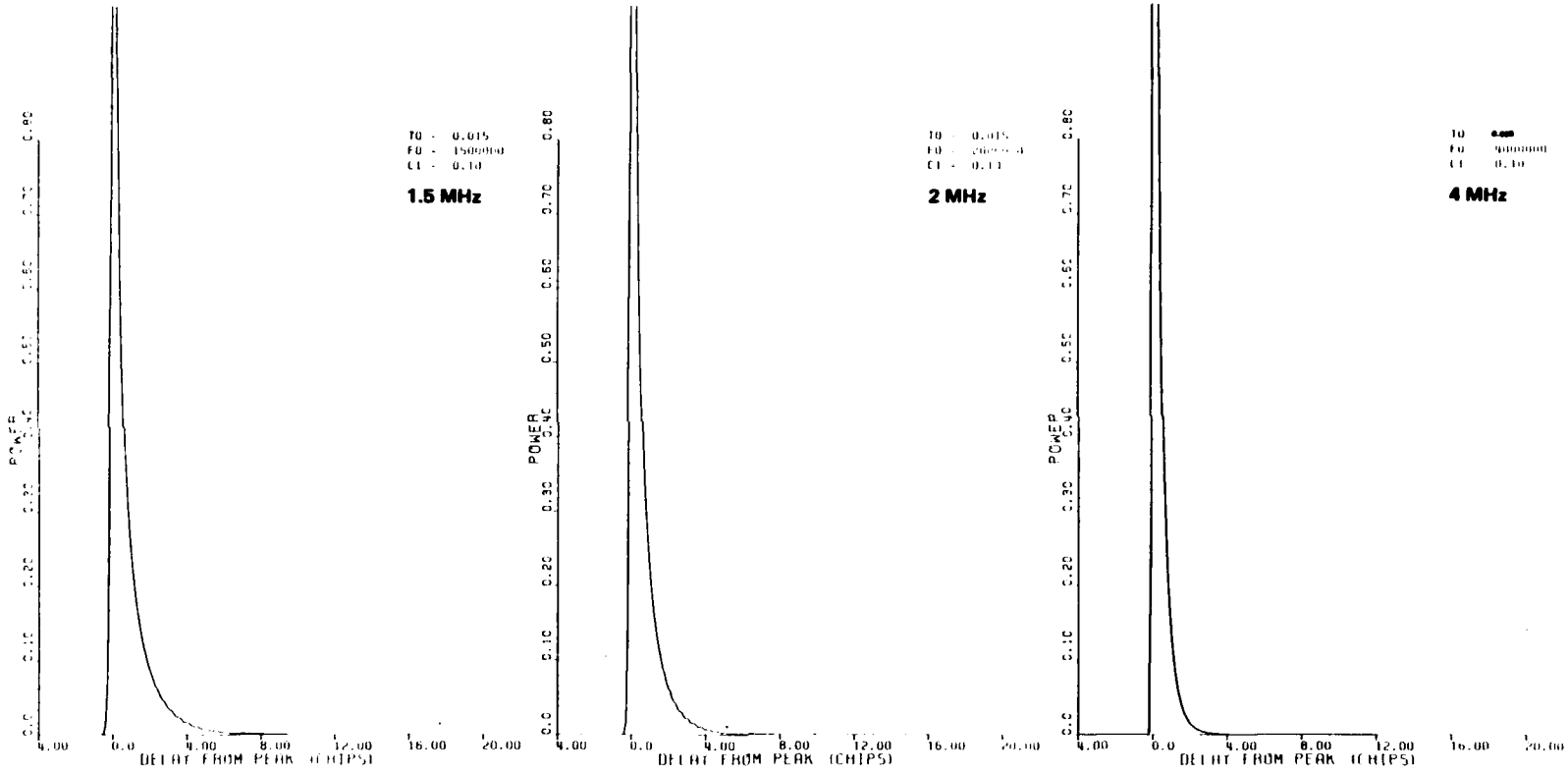

Figure 2-50. Theoretical delay power spectrum for σ_j/σ_s = 0.1 (Concluded).

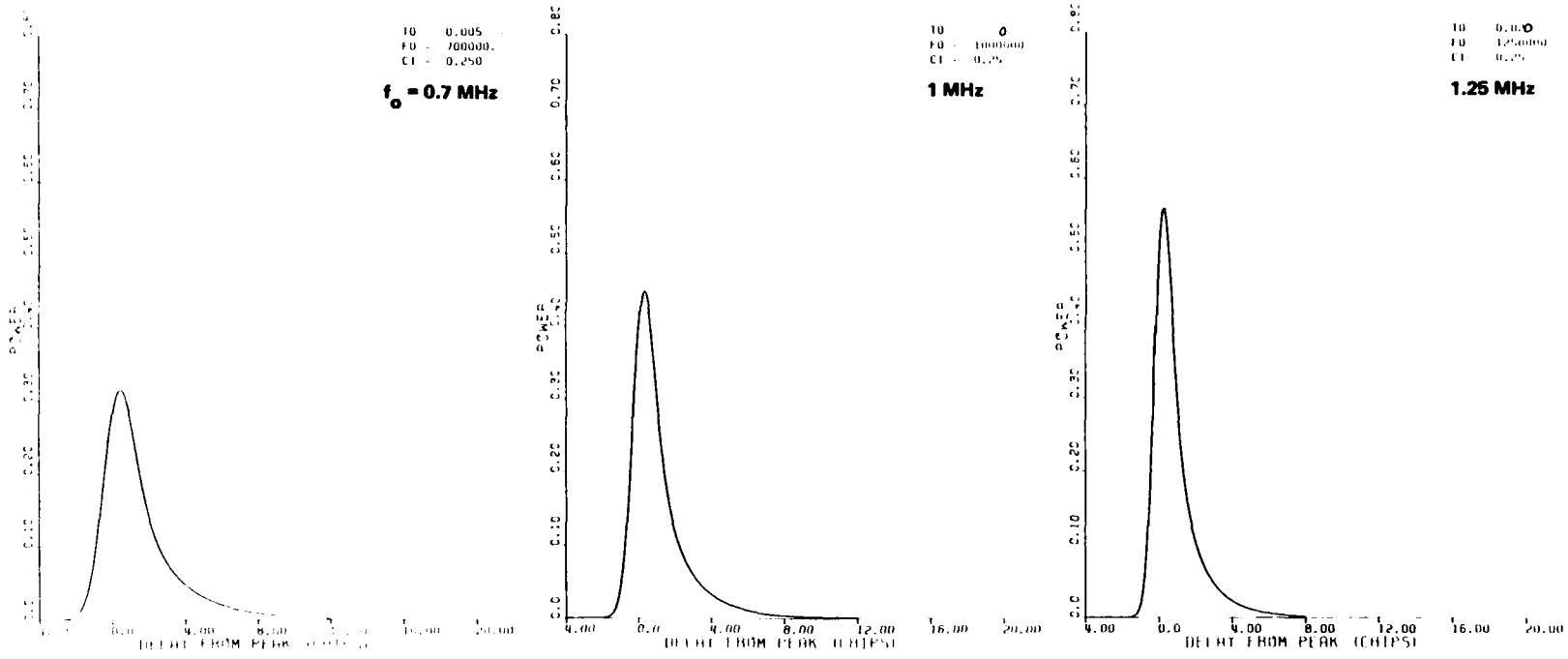

Figure 2-51. Theoretical delay power spectrum for σ_j/σ_s = 0.25.

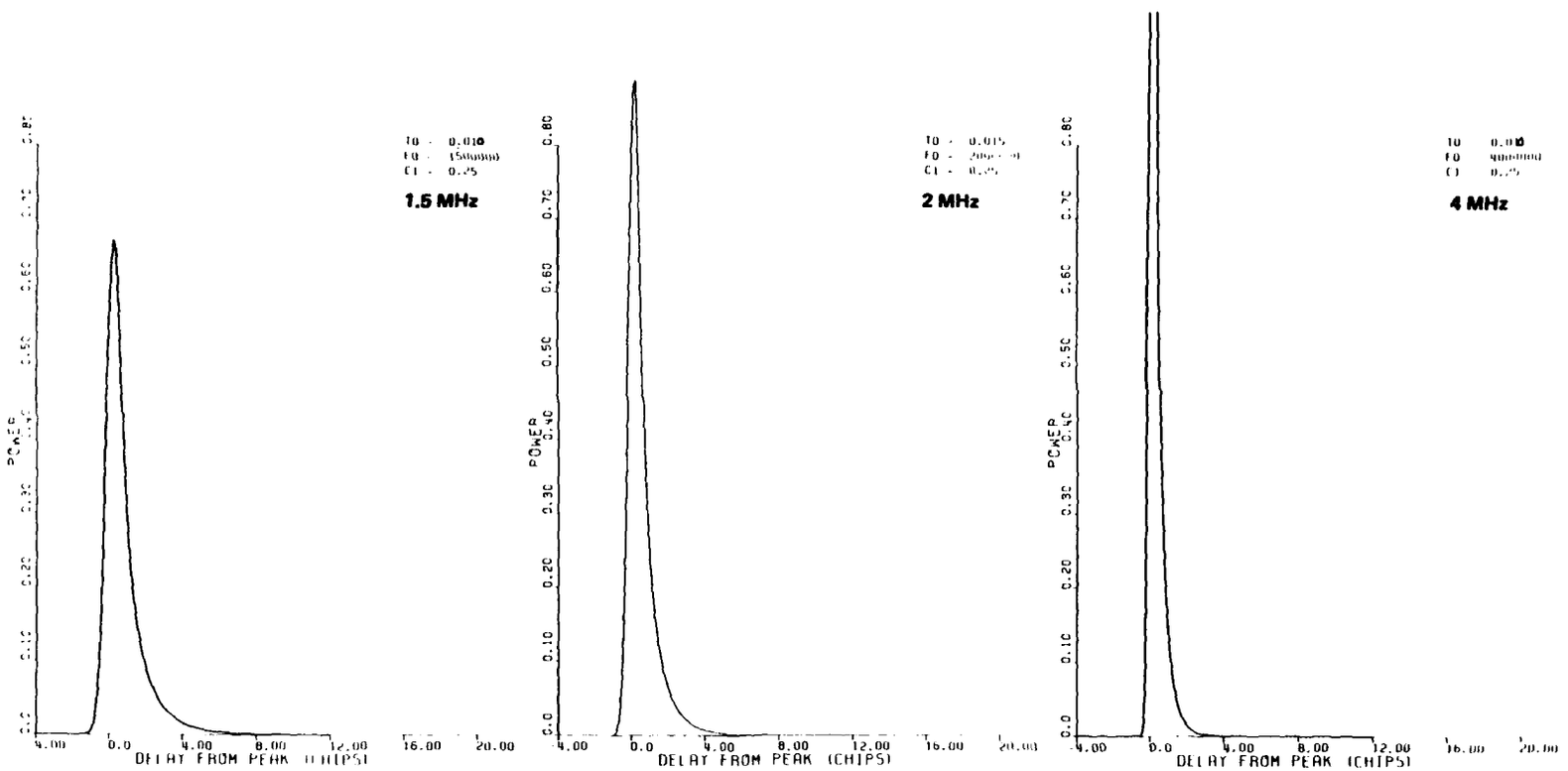

Figure 2-51. Theoretical delay power spectrum for $\sigma_j/\sigma_s = 0.25$ (Concluded).

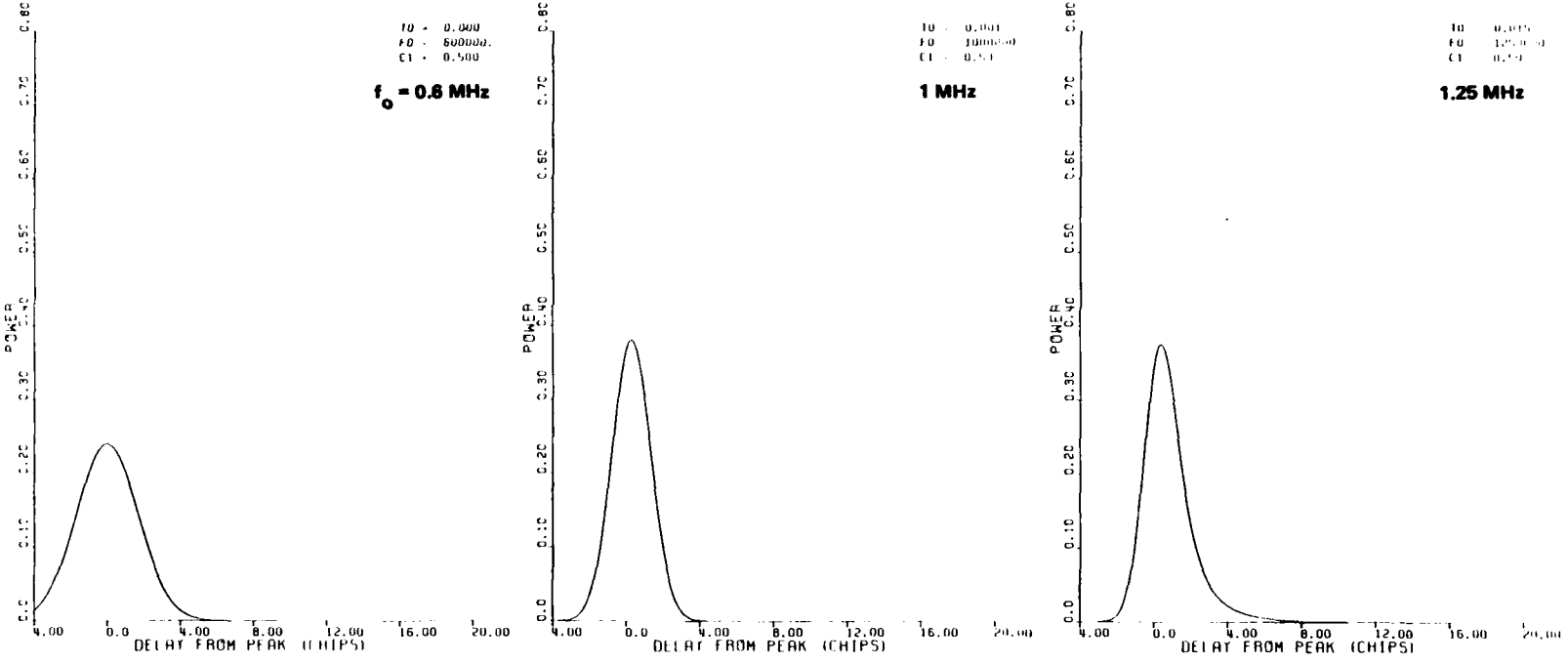

Figure 2-52. Theoretical delay power spectrum for σ_j/σ_s = 0.5.

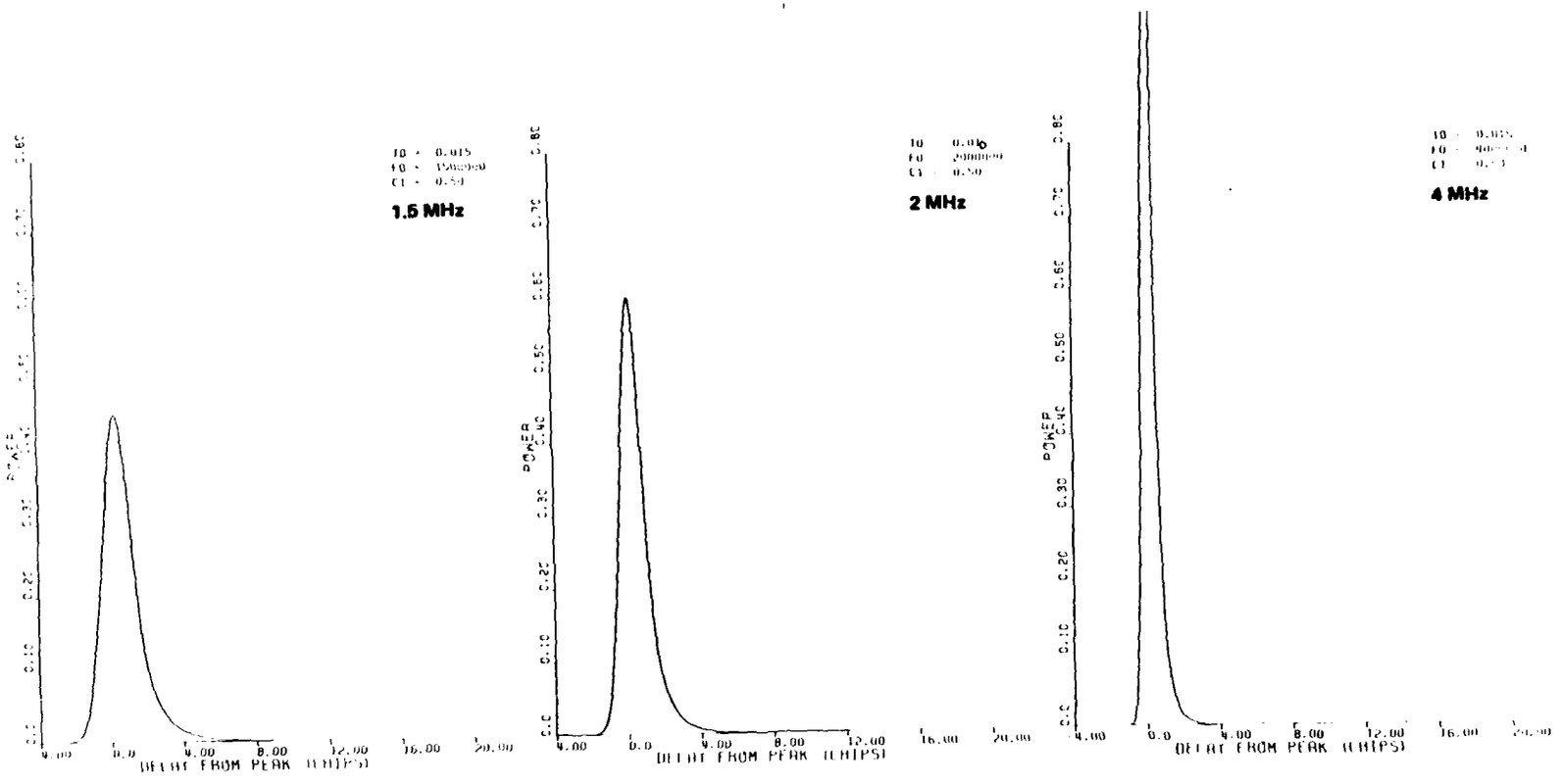

Figure 2-52. Theoretical delay power spectrum for σ_j/σ_s = 0.5 (Concluded).

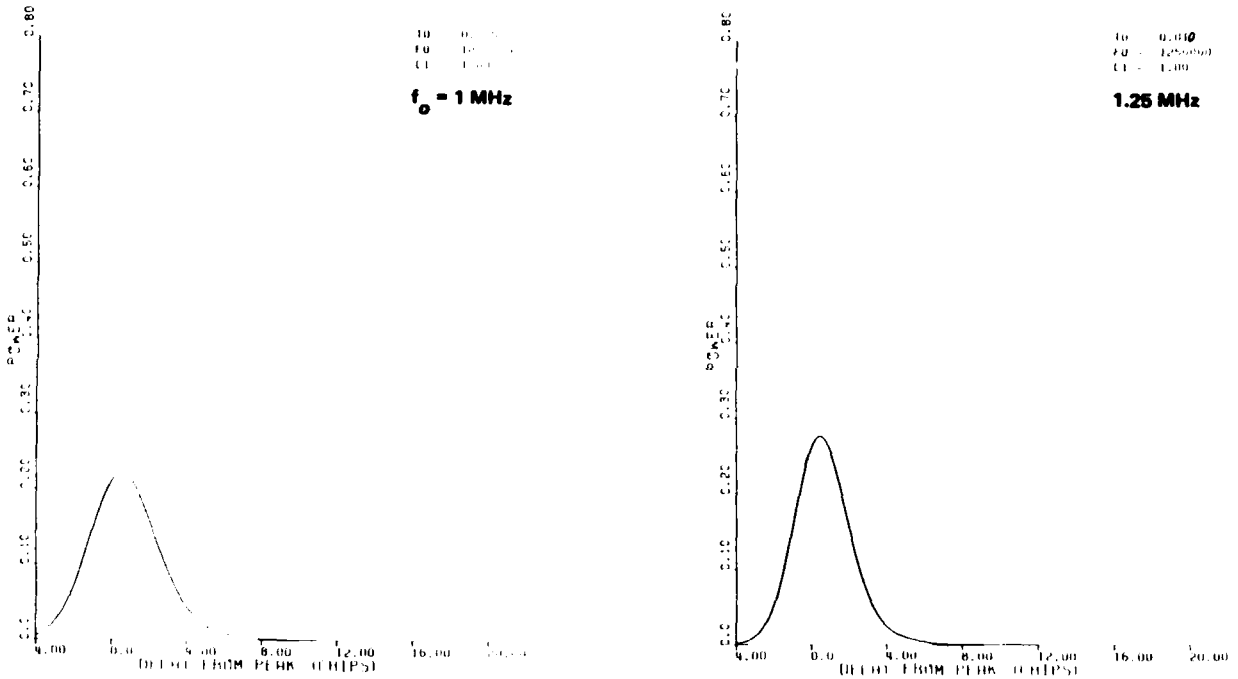

Figure 2-53. Theoretical delay power spectrum for σ_j/σ_s = 1.0.

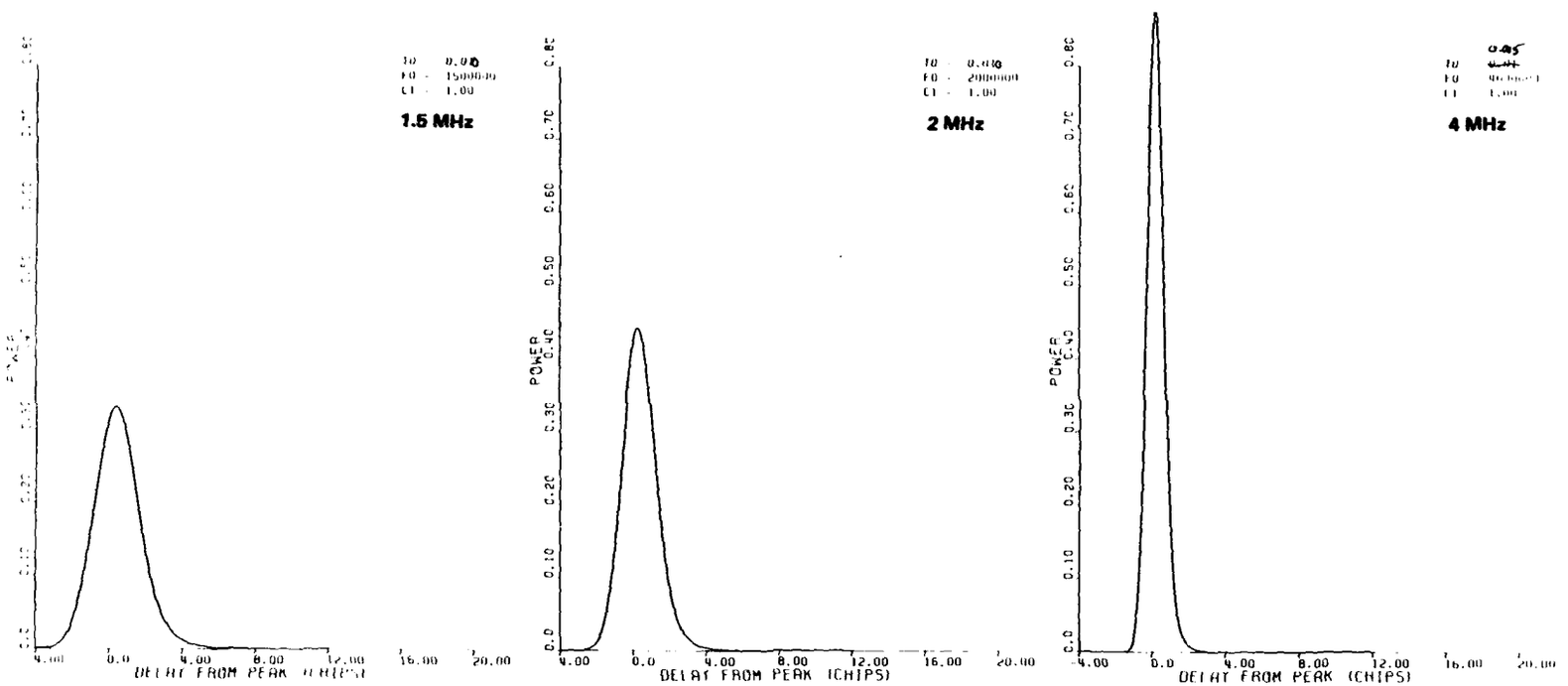

Figure 2-53. Theoretical delay power spectrum for σ_j/σ_s = 1.0 (Concluded).

Table 2-2. Parameter summary for best fit to measured normalized power delay profiles.

Segment	f_o	RMS Jitter to Spread Ratio	Comment
1	>4 MHz	~1	Jitter and Spread small
2	1.7	0.25	
3	1.7	0.25	
4	1.3	0.25	
5	0.9	0.25	
6	1.25	1.0	
7	1.7	0.5	
8	2.0	0.25	
Entire Occultation	2.1	0.5	

where

σ_j is the rms TOA jitter and
σ_s is the rms delay spread,

an estimate of the delay spread can be computed using the rms TOA jitter estimate from Table 2-1. The result of this calculation for each data segment is shown in Table 2-3. The time delay jitter estimate for the entire cloud has been taken as the weighted average of the preceding data segments. Note that in general good agreement is obtained between the derived values of the jitter-to-spread ratio obtained from Table 2-2 and the computed value.

2.7 Channel Transfer Function

The channel transfer function by definition is the Fourier transform of the channel impulse response. Since this is a familiar concept to communication engineers, samples of the transfer function are presented here along with the derived frequency correlation function. While direct comparison has not been made, the frequency correlation measurement provides another quality check on the frequency coherence parameter, f_o, estimates in Table 2-2.

2.7.1 Channel Transfer Function Magnitude

The complex channel impulse response measured and presented in Figures 2-7 through 2-14 can be transformed to obtain a channel transfer function representation. Figures 2-54 through 2-61 show the magnitude of the channel transfer function corresponding to the earlier channel impulse response figures. The impulse response data from which these are derived were averaged over 0.1 second (40 samples). The record at 2345:05.1 (Figure 2-54) is just prior to the occultation interval. The spectrum shown at 2345:05.1 is essentially

Table 2-3. Comparison with RMS jitter data.

SEGMENT	FROM TABLE 2-2		FROM TABLE 2-1	COMPUTED	
	f_o (MHz)	RMS JITTER TO SPREAD RATIO σ_j/σ_s	RMS TOA JITTER (μsec)	RMS DELAY SPREAD (μsec)	JITTER/ SPREAD σ_j/σ_s
1	> 4	~ 1	0.0017	0.0398	~ 0.43
2	1.7	0.25	0.0229	0.0908	0.25
3	1.7	0.25	0.0316	0.0882	0.36
4	1.3	0.25	0.0335	0.1178	0.28
5	0.9	0.25	0.0435	0.1715	0.25
6	1.25	1.0	0.0988	0.0804	1.23
7	1.7	0.5	0.0371	0.0860	0.43
8	2.0	0.25	0.0227	0.0763	0.30
ENTIRE CLOUD	2.1	0.5	0.0414	0.0635	0.65

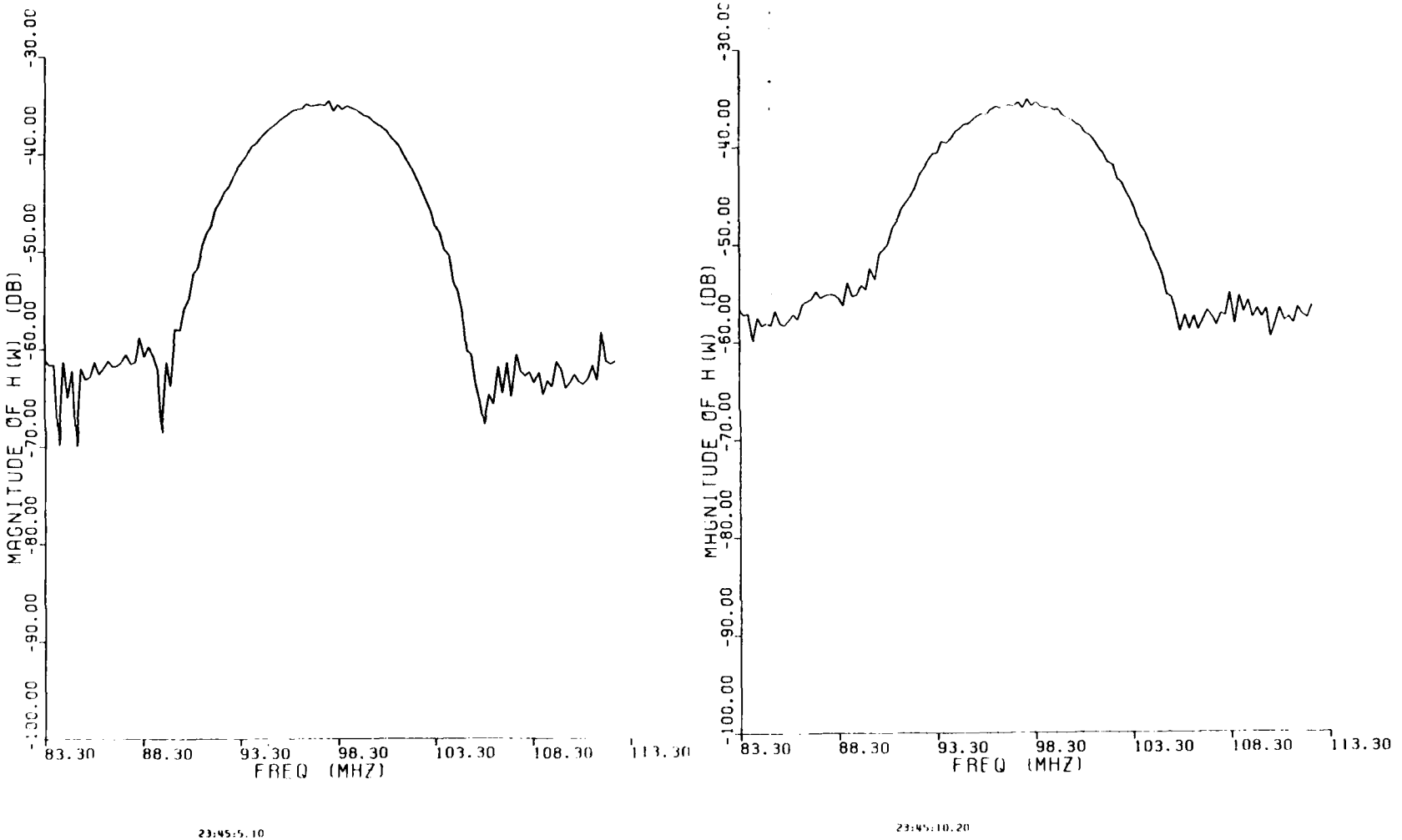

Figure 2-54. Channel transfer function magnitude at 2345:05.1 and 2345:10.2Z.

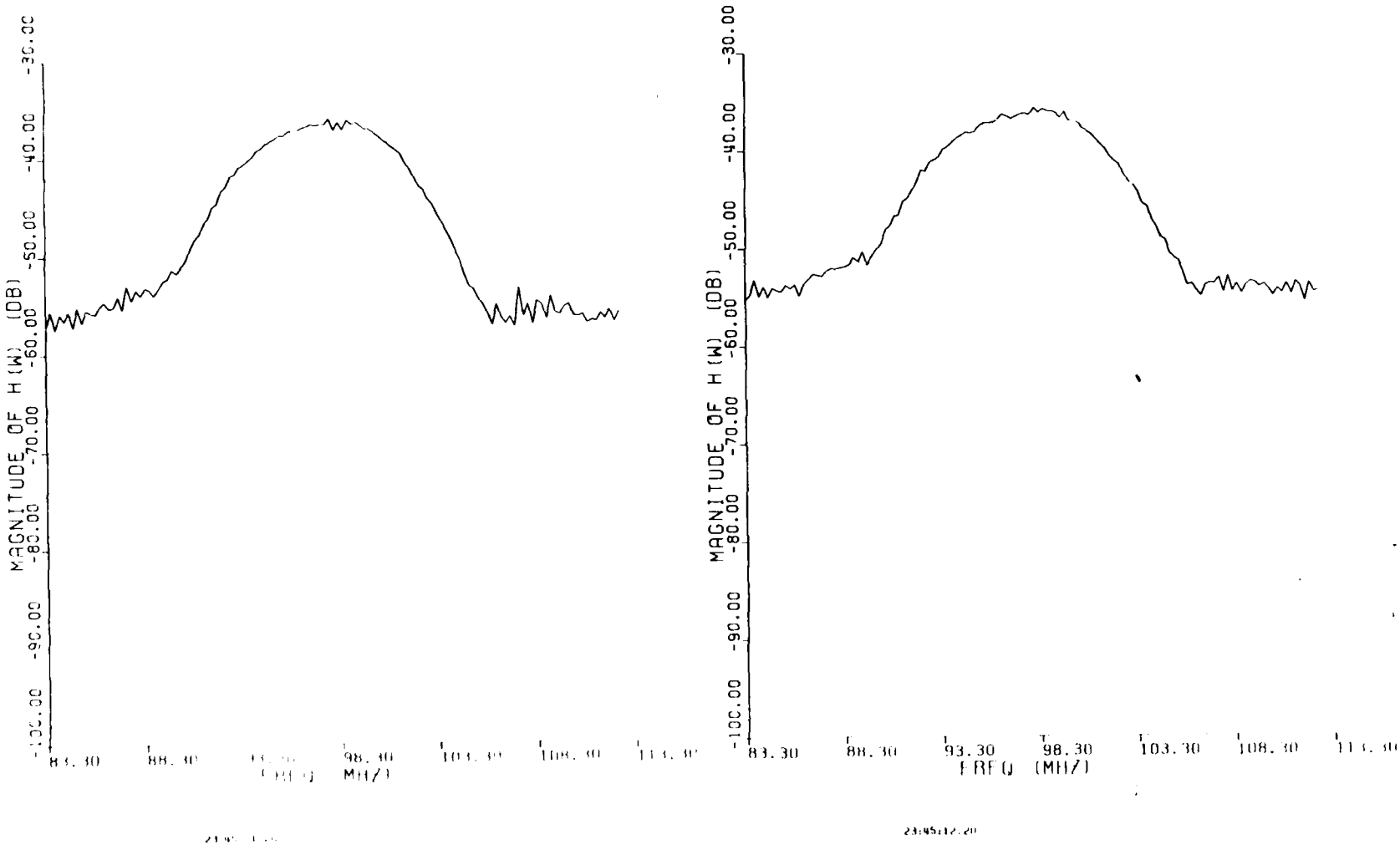

Figure 2-55. Channel transfer function magnitude at 2345:11.2 and 2345:12.22.

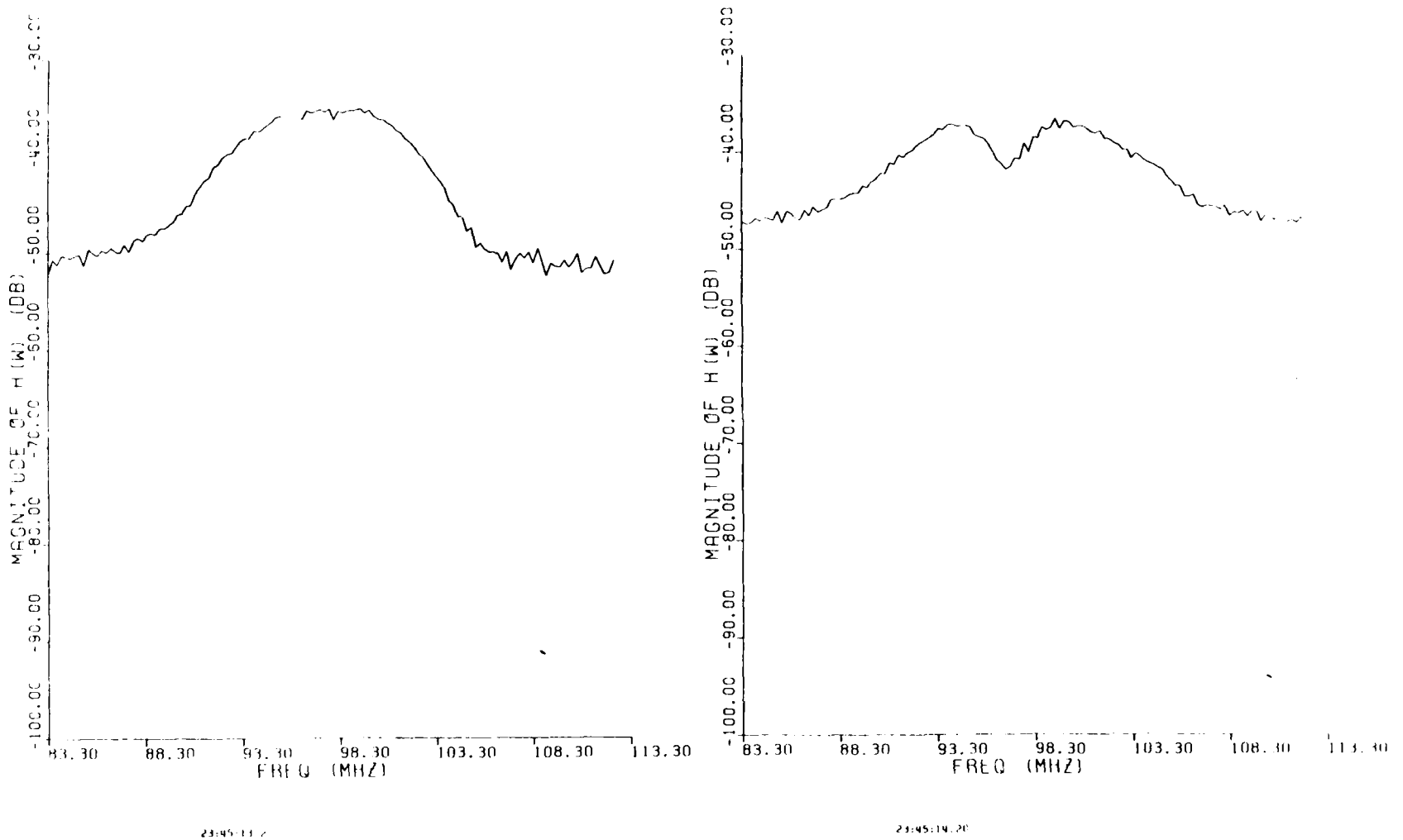

Figure 2-56. Transfer function magnitude at 2345:13.2 and 2345:14.2Z.

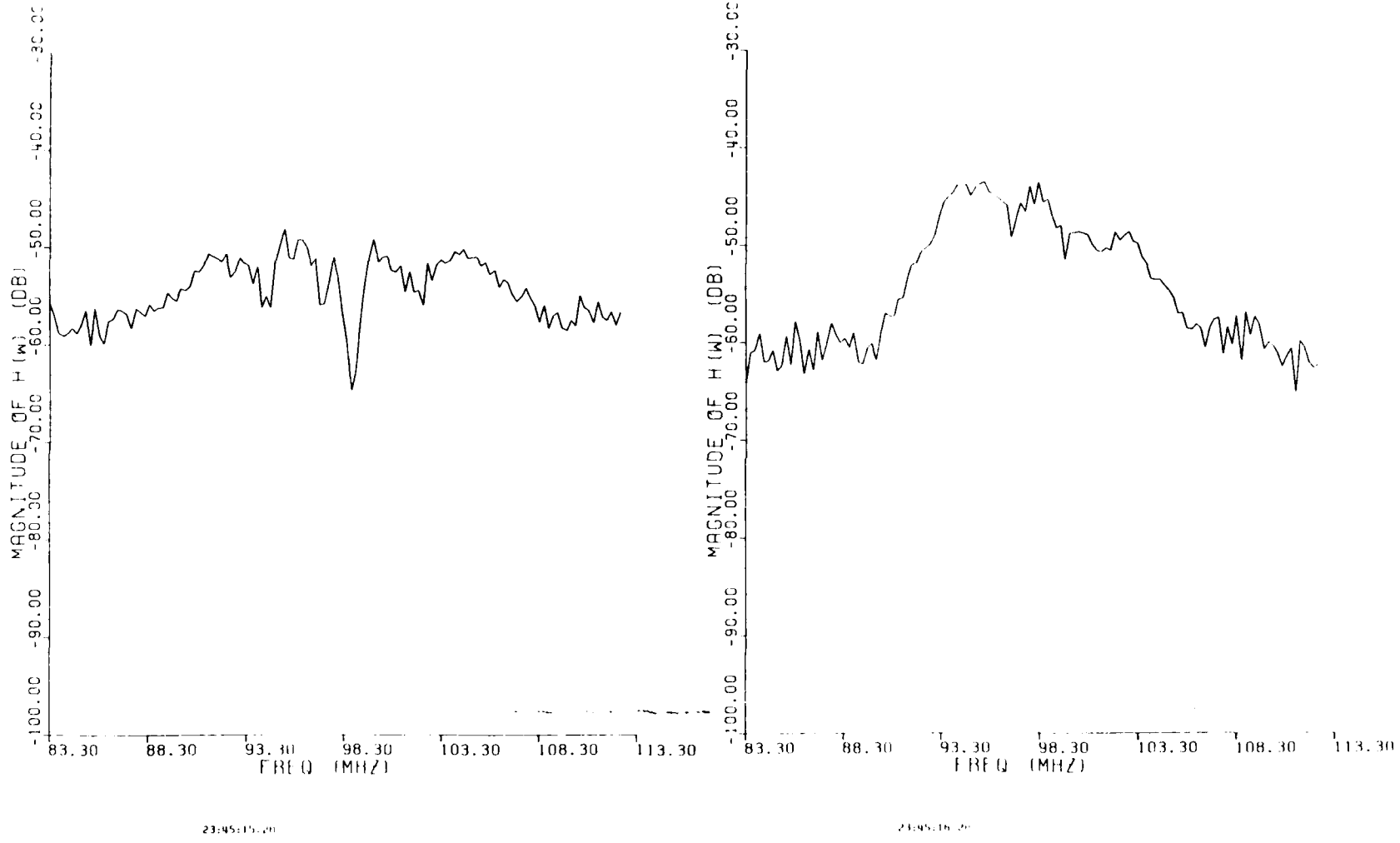

Figure 2-57. Channel transfer function magnitude at 2345:15.2 and 2345:16.2Z.

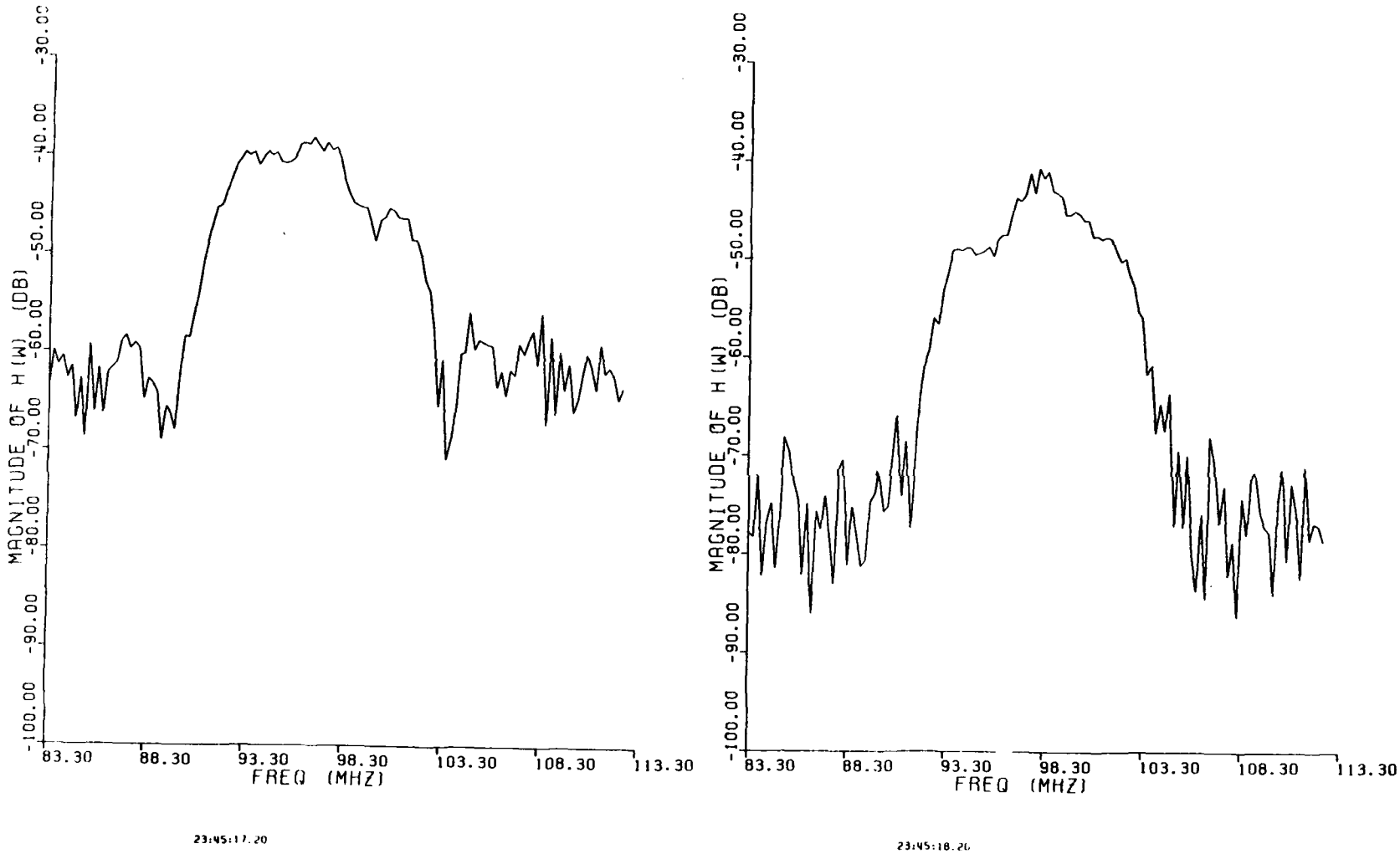

Figure 2-58. Channel transfer function magnitude at 2345:17.2 and 2345:18.22.

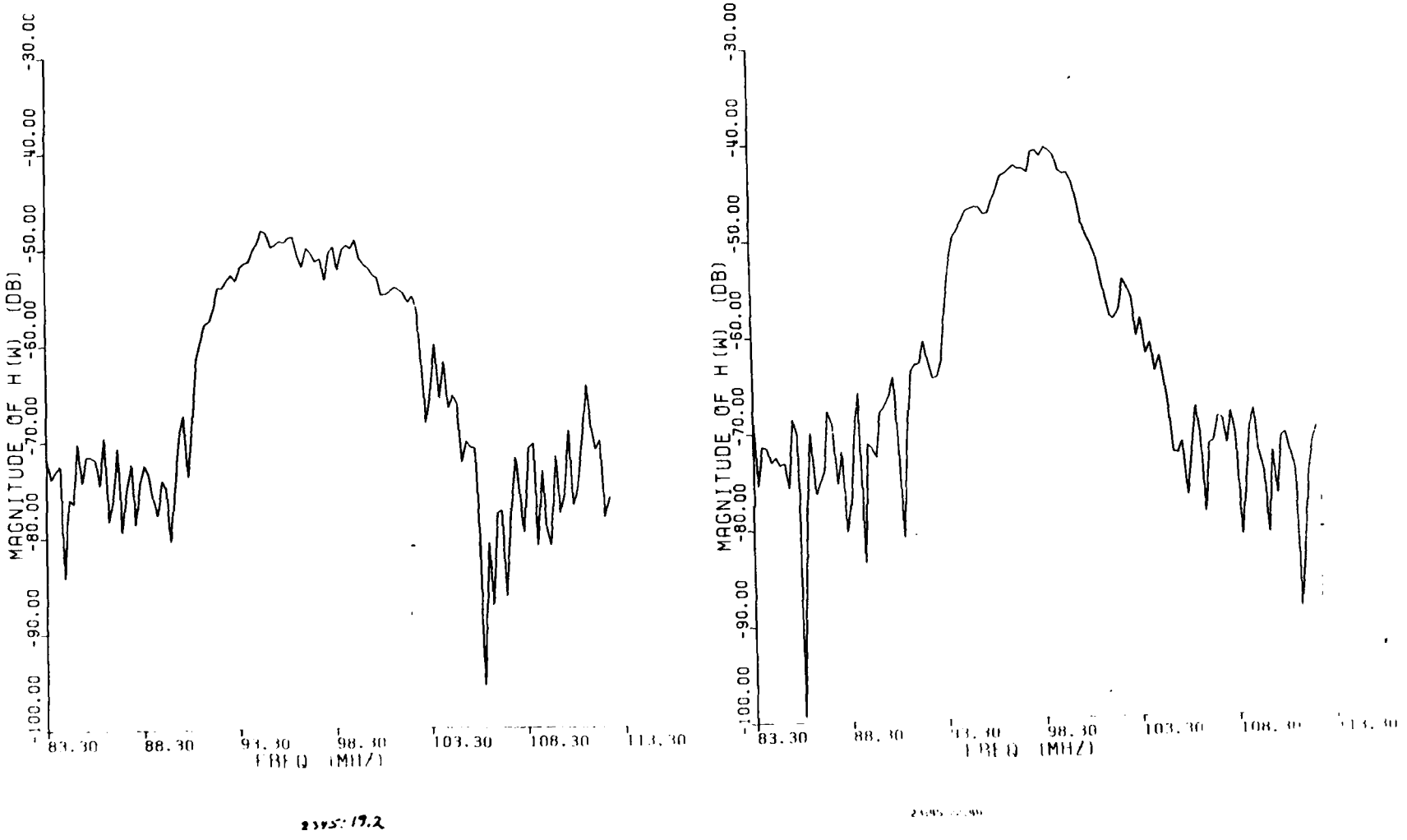

Figure 2-59. Channel transfer function magnitude at 2345:19.2 and 2345:22.4Z.

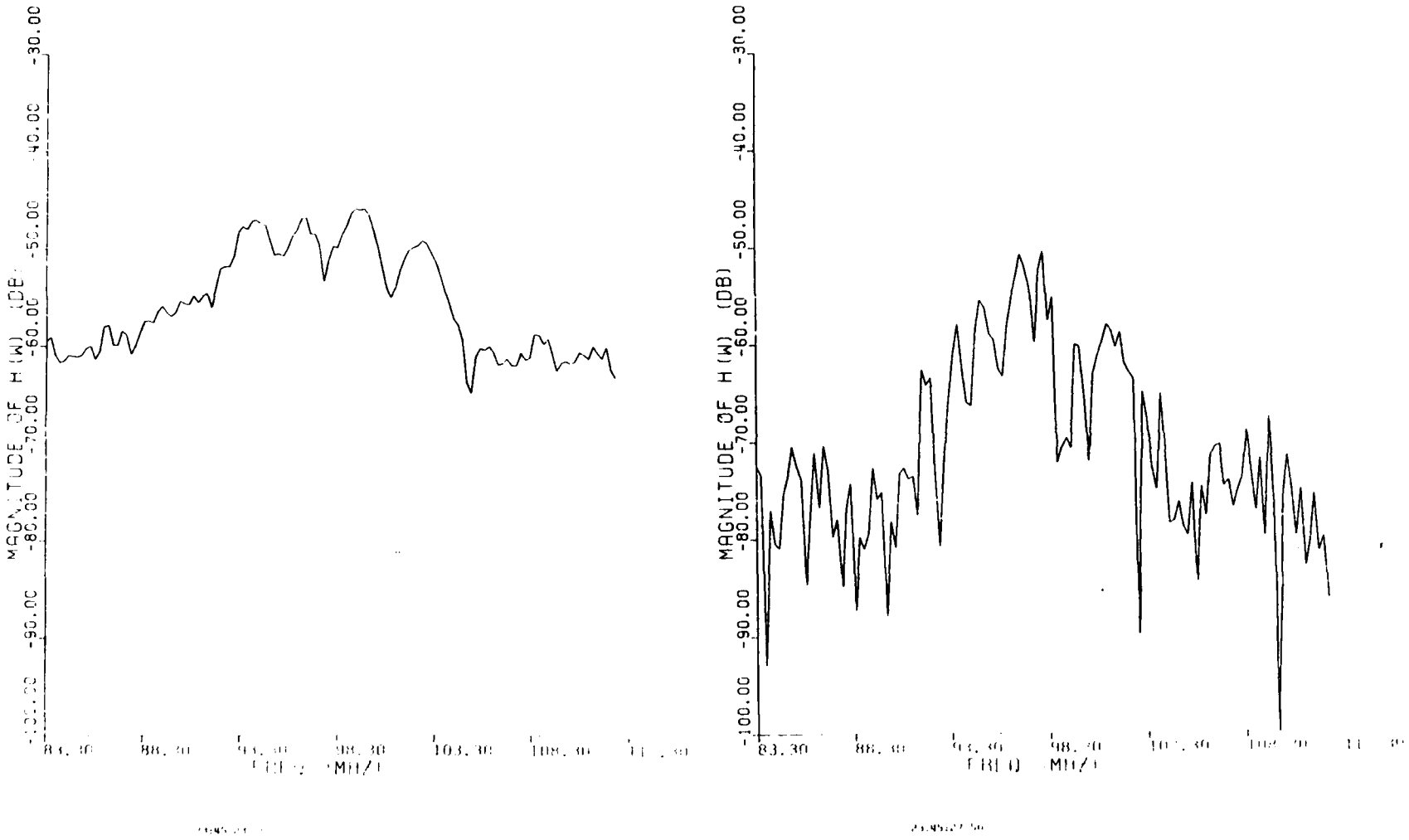

Figure 2-60. Channel transfer function magnitude at 2345:23.7 and 2345:27.5Z.

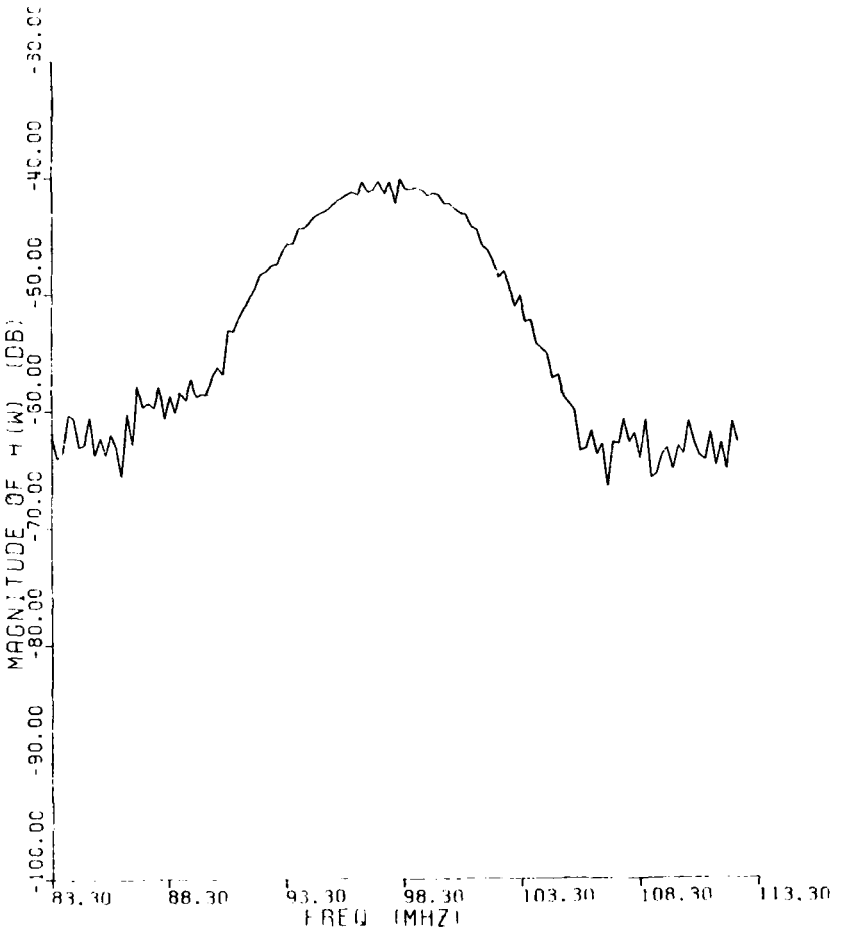

Figure 2-61. Channel transfer function magnitude at 2345:30.1z.

that of the transmitted signal and shows no effects of bandlimiting by the transmission medium. Since the signal presented in Figure 2-7 was in reality the convolution of the transmitted signal autocorrelation with the true channel impulse response, $s(t)*h(t)$, these figures actually represent the product of the signal autocorrelation transform and the channel transfer function, $S(f)\cdot H(f)$. These could be inverted using the sample at 2345:05.1 as the reference signal spectrum to obtain the true channel transfer function; however, this has not been done.

2.7.2 Frequency Correlation Function

The frequency correlation function may be computed directly from the channel transfer function. In performing the correlation, only that data corresponding to the central lobe from 88 to 108 MHz were used to avoid the noise evident beyond the central lobe. A cyclic correlation function was computed over the central lobe as follows

$$R_H(f) = \sum_i H^*(f_i)H(f_i + f) \text{ for } 88 < f_i < 108 \text{ MHz}$$

and for $(f_i + f) > 108$ the $(f_i + f) = 88 + [(f_i + f) - 108]$.

The resulting correlation function, which is real except for a small residual, was normalized using

$$R_H'(f) = R_H(f) \; / \; R_H(0).$$

In normalizing over this interval, a true measure of the transmission medium correlation function is obtained.

Figures 2-62 through 2-65 plot the frequency correlation function. As expected, the frequency correlation is flat prior to the occultation interval at 2345:05.1Z (Figure 2-62). Table 2-4 summarizes the estimated frequency correlation bandwidth taken as the e^{-1} point on the frequency correlation curve. The frequency correlation bandwidth measured at the e^{-1} point is approximately a factor of 2.5 larger than the corresponding value of the coherence bandwidth parameter, f_o. The correponding value for f_o is also shown in Table 2-4.

For the same corresponding time interval, these data show reasonable agreement with the value of f_o given in Table 2-2, which was derived from the parameter estimation of the delay power spectrum.

2.8 FADING WAVEFORM AT 98 MHZ

The fading waveform at 98 MHz can be systhesized from the channel transfer function data presented earlier. This permits a calculation of the received phase PSD and a calculation of the angular spectrum at 98 MHz. These data are presented here.

The fading waveform at 98 MHz can be obtained by transforming the channel impulse response of each data record collected during the occultation to obtain the channel transfer function, samples of which were shown in Section 2.7. From these transformed records, the 98-MHz component can be selected and plotted as shown in Figure 2-66. The phase has been plotted inverted from the true phase wind up in Figure 2-66. The peak phase advance associated with the barium plasma can be estimated to be 98.6 cycles from these data. As discussed in Section 2.4.3, each cycle of phase shift corresponds to 7.29×10^{10} cm^{-2} of electron content at 98 MHz. This provides an

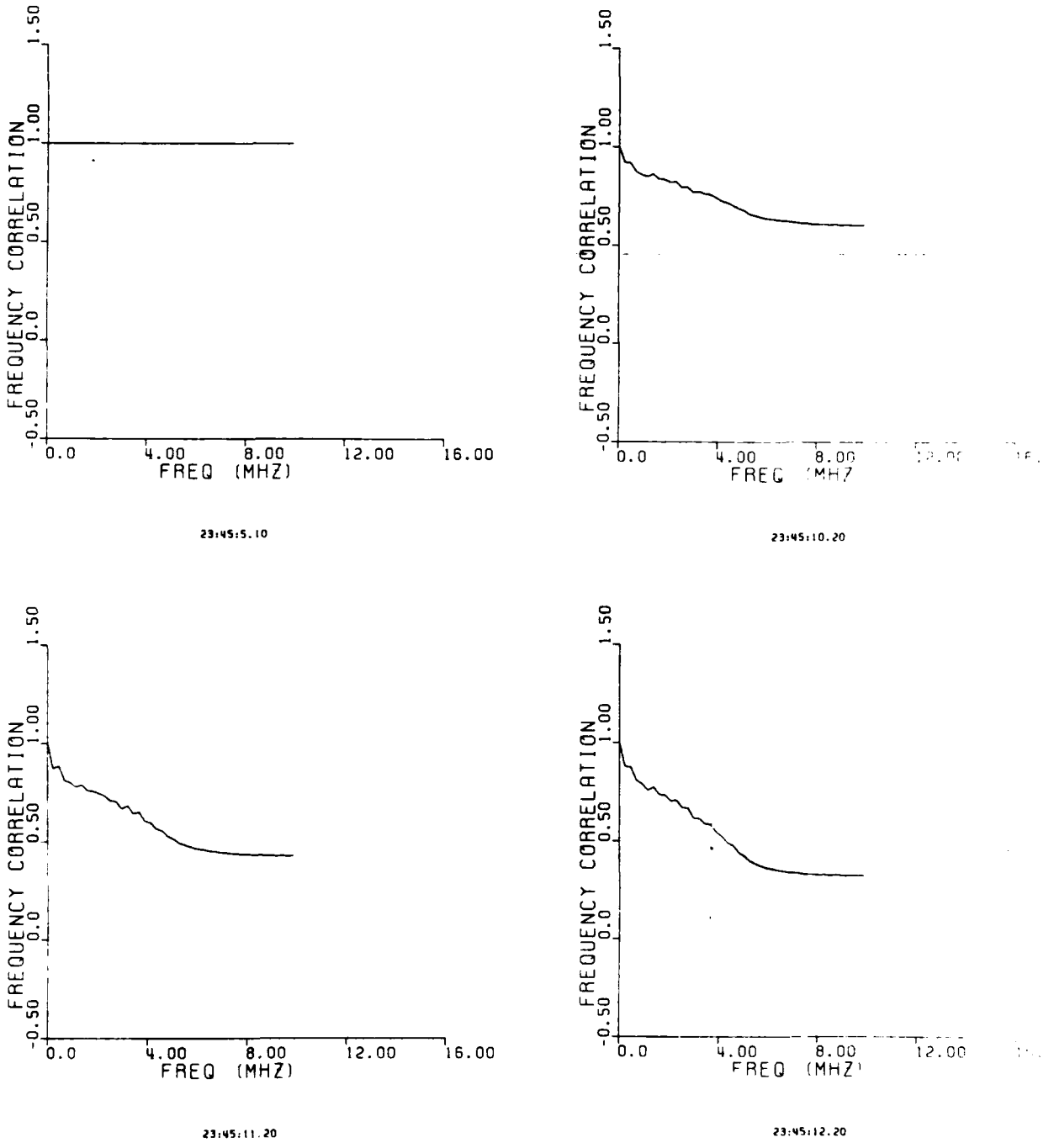

Figure 2-62. Frequency Correlation Function at 2345:05.1, :10.2, :11.2 and :12.22.

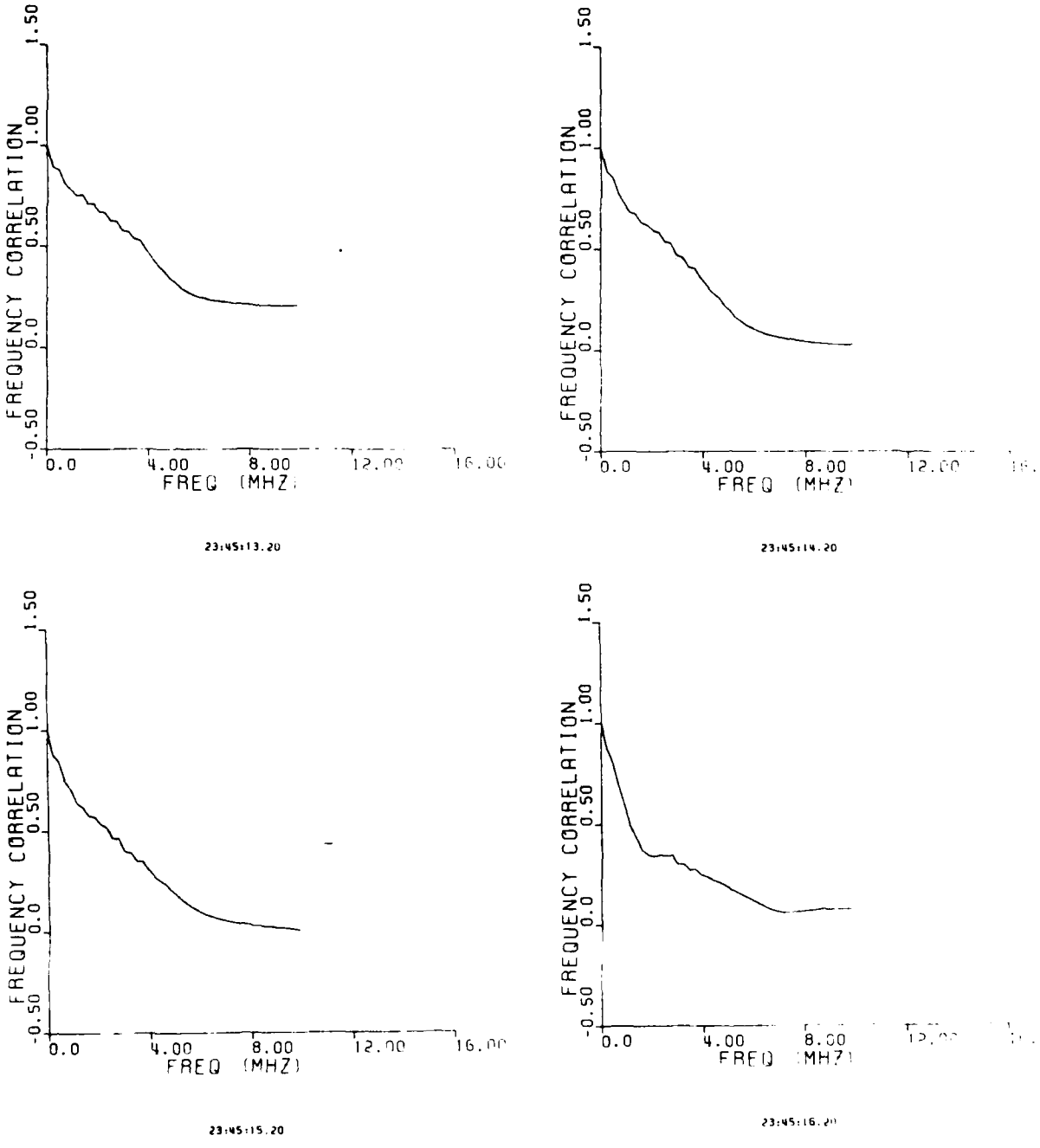

Figure 2-63. Frequency correlation function at 2345:13.2, :14.2, :15.2 and :16.2Z.

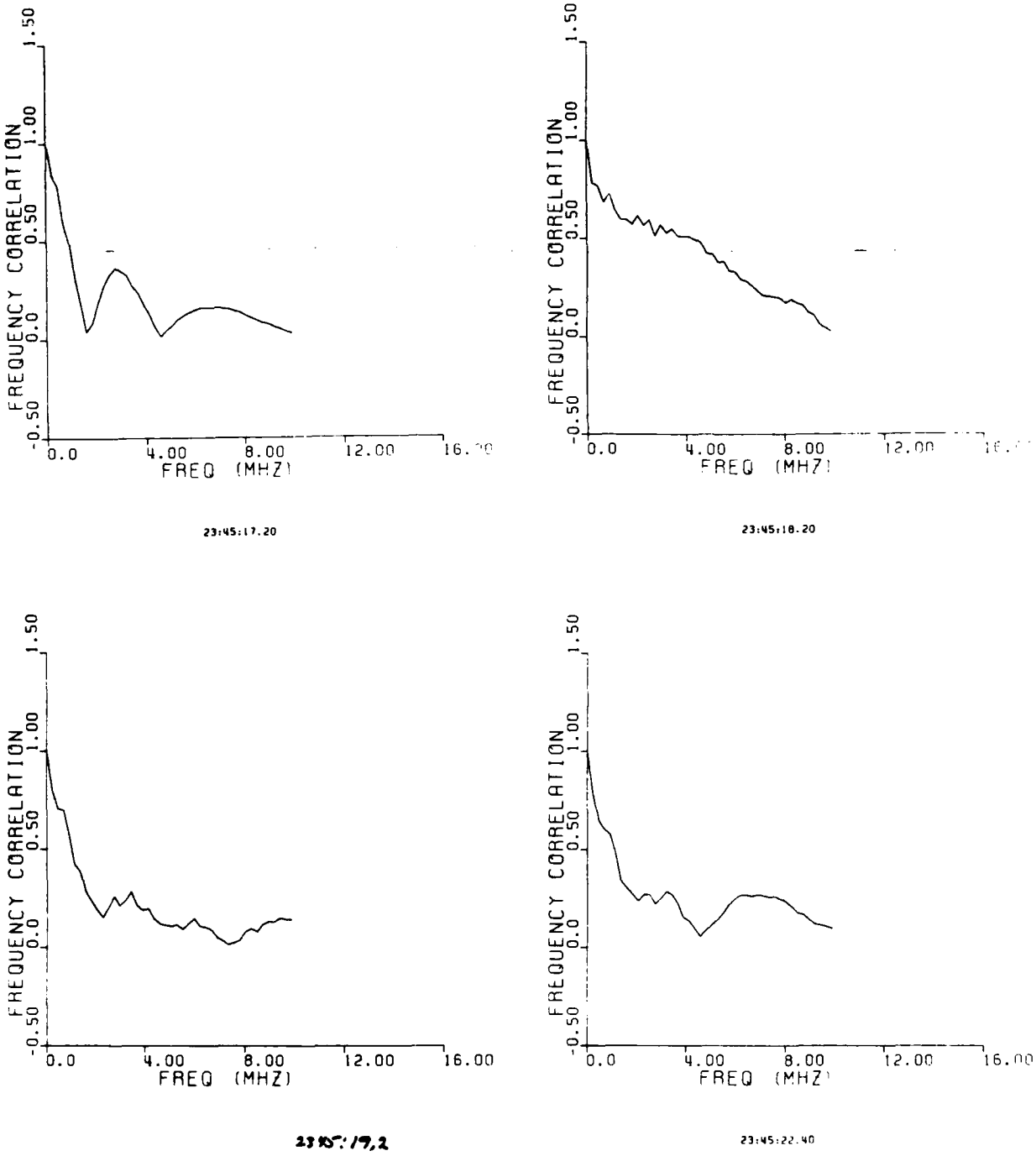

Figure 2-64. Frequency correlation function at 2345:17.2, :18.2, :19.2 and :22.4Z.

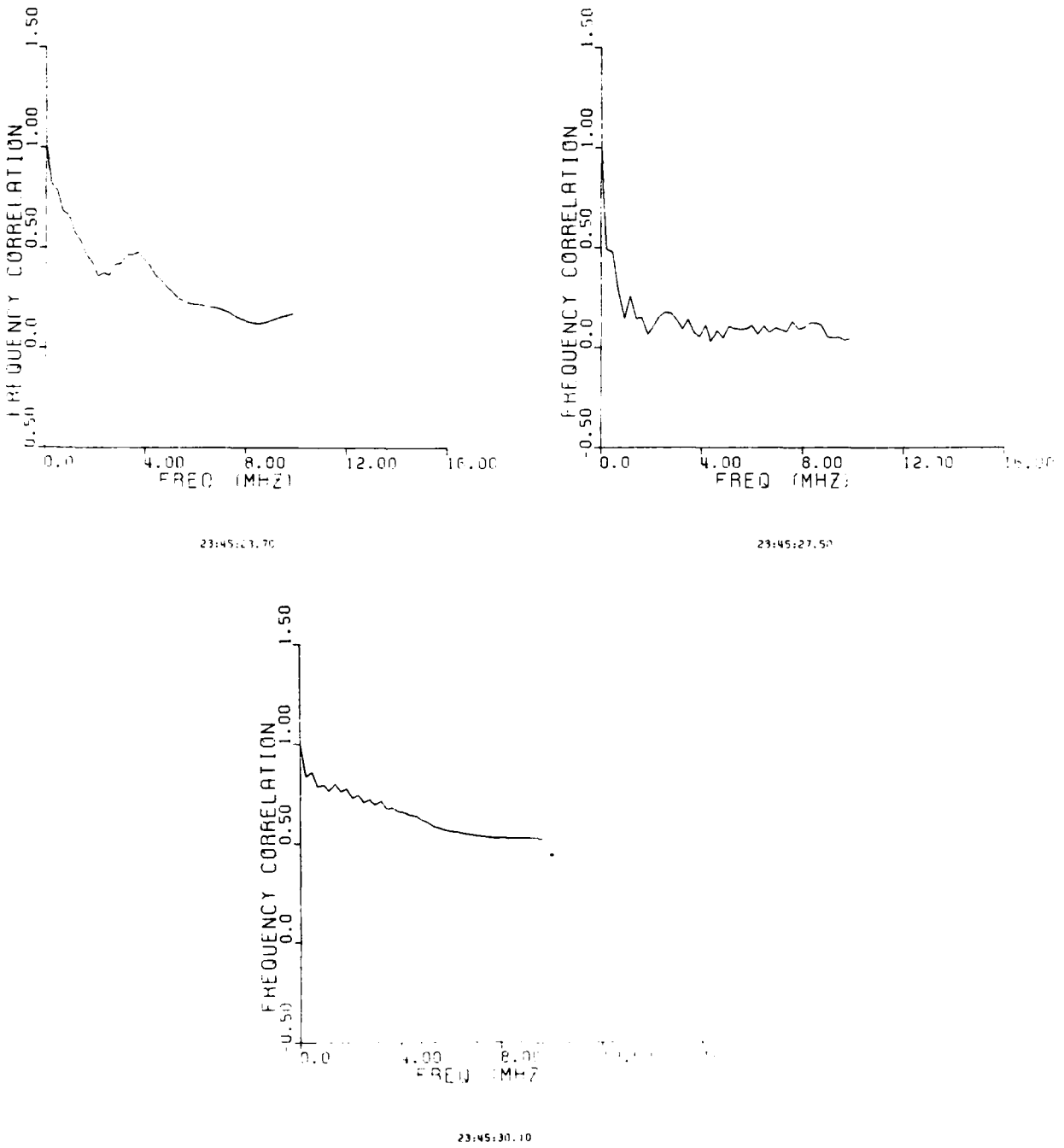

Figure 2-65. Frequency correlation function at 2345:23.7, :27.5, and :30.1Z.

Table 2-4. Frequency correlation bandwidth.

Sample Time	$f_{e^{-1}}$	f_o	Comment
2345:05.1	>10 MHz	>4 MHz	Prior to Occultation
:10.2	>10	>4	in Segment 1
:11.2	~12	~4.8	" " 1
:12.2	5.5	2.2	
:13.2	4.5	1.8	
:14.2	4.0	1.6	in Segment 2
:15.2	3.2	1.3	" " 2
:16.2	1.6	0.6	" " 2
:17.2	1.1	0.4	" " 2
:18.2	5.7	2.3	" " 2
:19.2	1.5	0.6	" " 3
:22.4	1.4	0.6	" " 4
:23.7	2.0	0.8	" " 5
:27.5	0.5	0.2	" " 7
:30.1	>12	>4.8	At end of Occultation

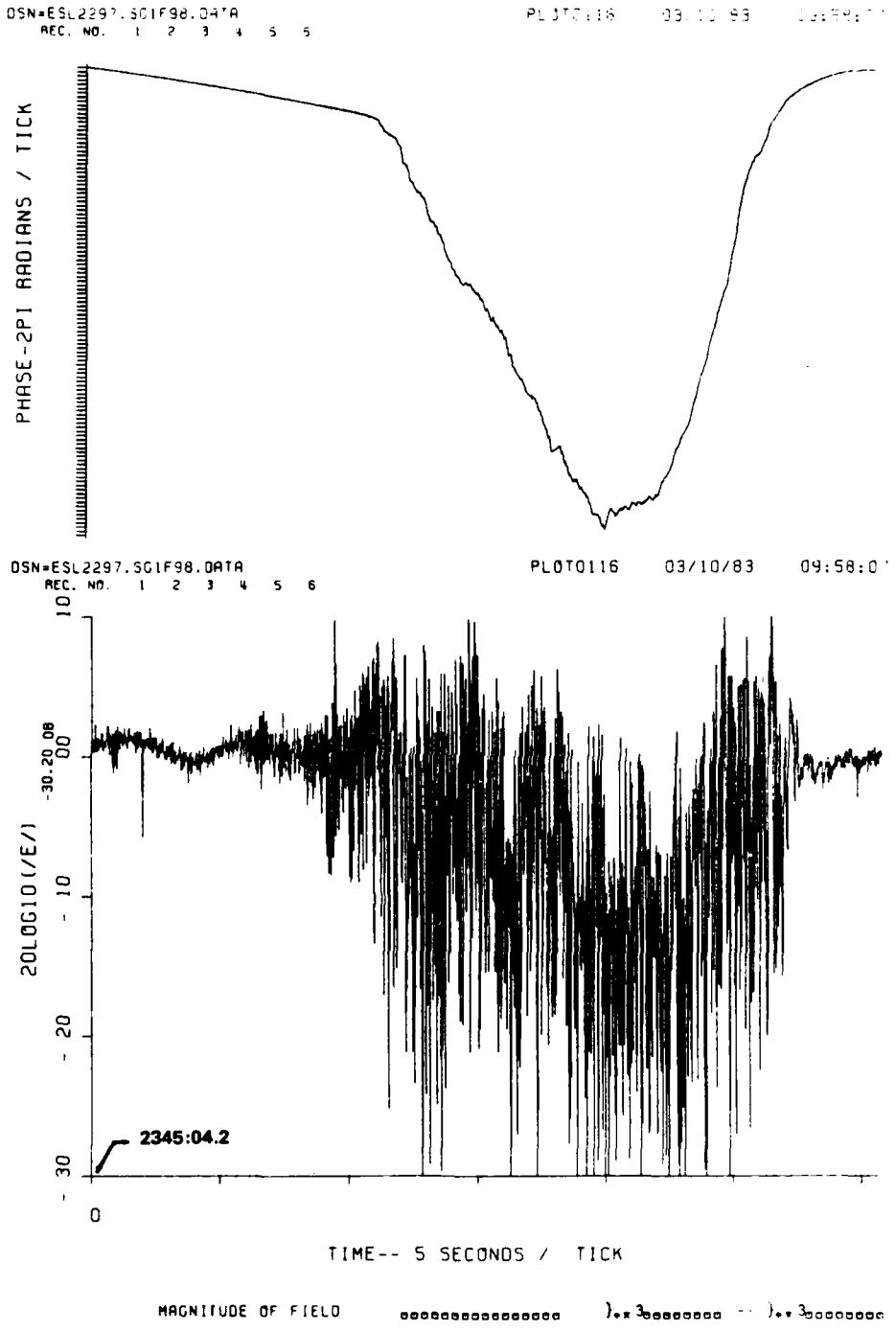

Figure 2-66. Received amplitude and phase at 98 MHz, St. George Island, Beacon 1.

estimate for the peak electron content associated with the barium plasma of approximately 7.2 x 10^{12} cm^{-2}. This is in excellent agreement with the estimate obtained earlier in Section 2.4.2 from the TOA shift, which was 8.2 x 10^{12} cm^{-2}.

2.8.1 Received Phase PSD at 98 MHz

The phase power spectral density (PSD) corresponding to the received signal phase is shown in Figure 2-67. The slope corresponds the approximately 22.9 dB/decade or $f^{-2.3}$. This is typical of the phase PSD expected in the far field of a diffraction screen[2].

2.8.2 Angular Spectrum at 98 MHz

The transform of the complex fading waveform at 98 MHz yields the angular spectrum of the received signal. This results, since time corresponds to spatial position, in the diffraction field. The angular spectrum is shown in Figure 2-68. The real frequency axis may be converted to angle through the transform

$$\theta = \sin^{-1} (f\lambda/V),$$

where

V is the rocket transverse transit velocity.

As shown in Appendix D, the transverse pattern velocity is approximately 980 m/sec. Thus, 10 Hz corresponds to approximately 1.8 degrees.

The abrupt decrease in the signal spectrum around 40 Hz (7.2 degrees) appears to correspond to the approximate maximum rate of change of the gross plasma phase delay and not the geometrical extent of the cloud that subtends a half width of approximately 18 degrees (~10 km at 30 km distance).

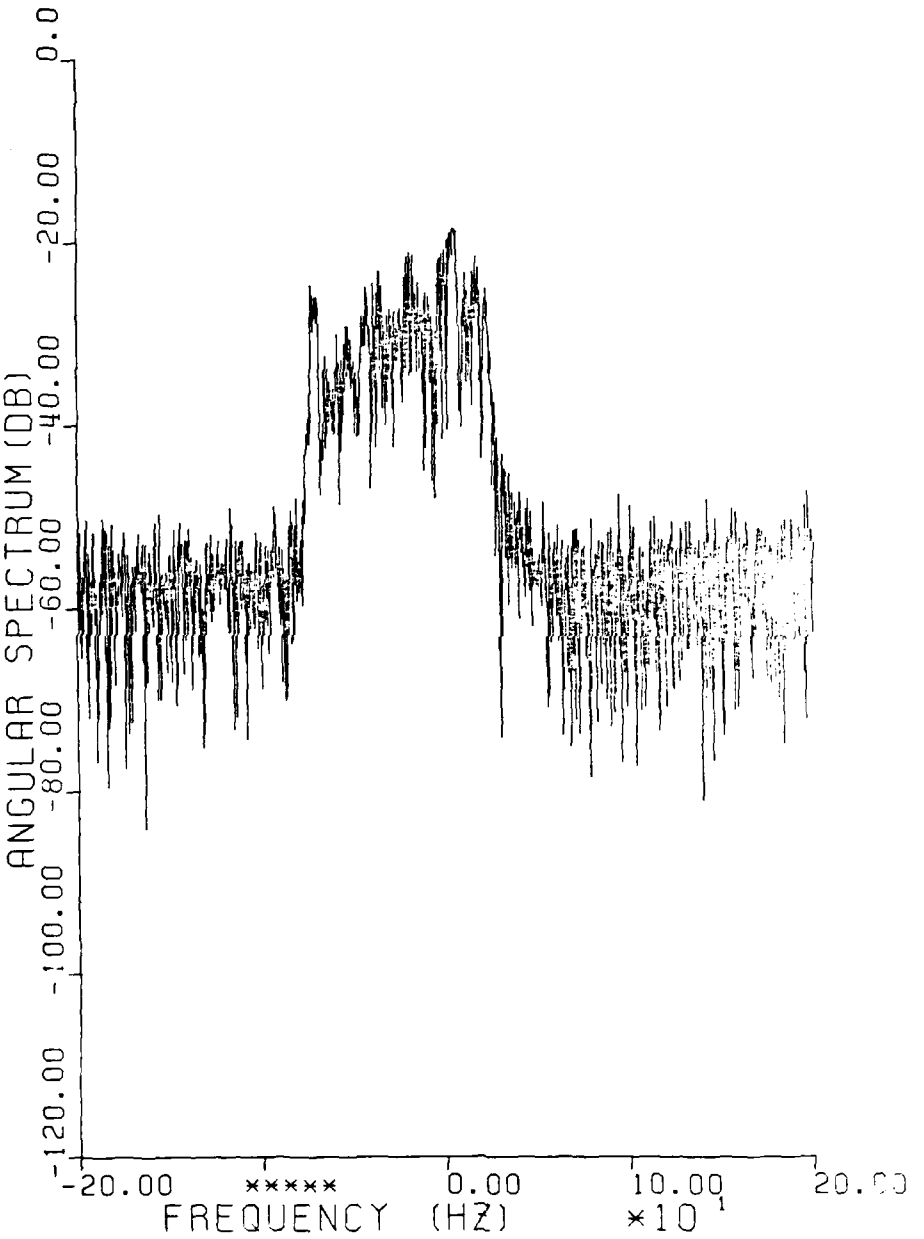

Figure 2-113. Two-sided angular Spectrum for Segment 6.

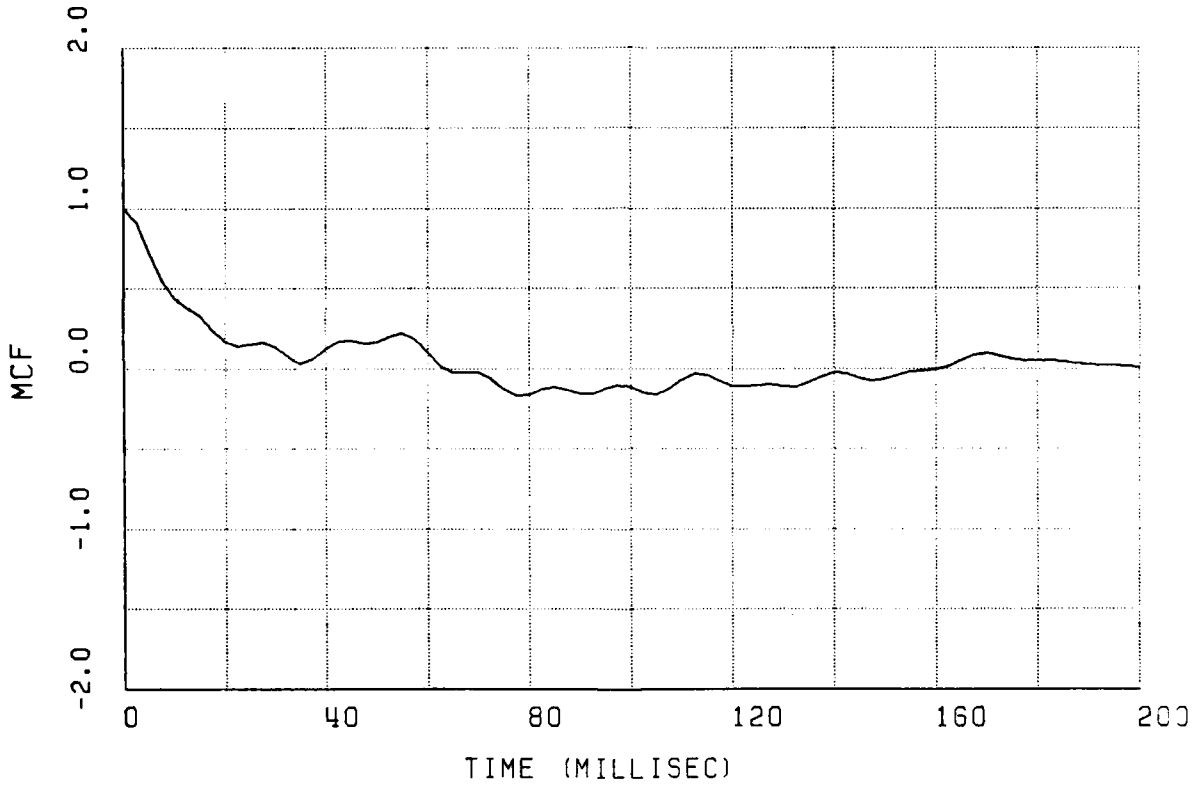

Figure 2-114. Mutual coherence function for Segment 6.

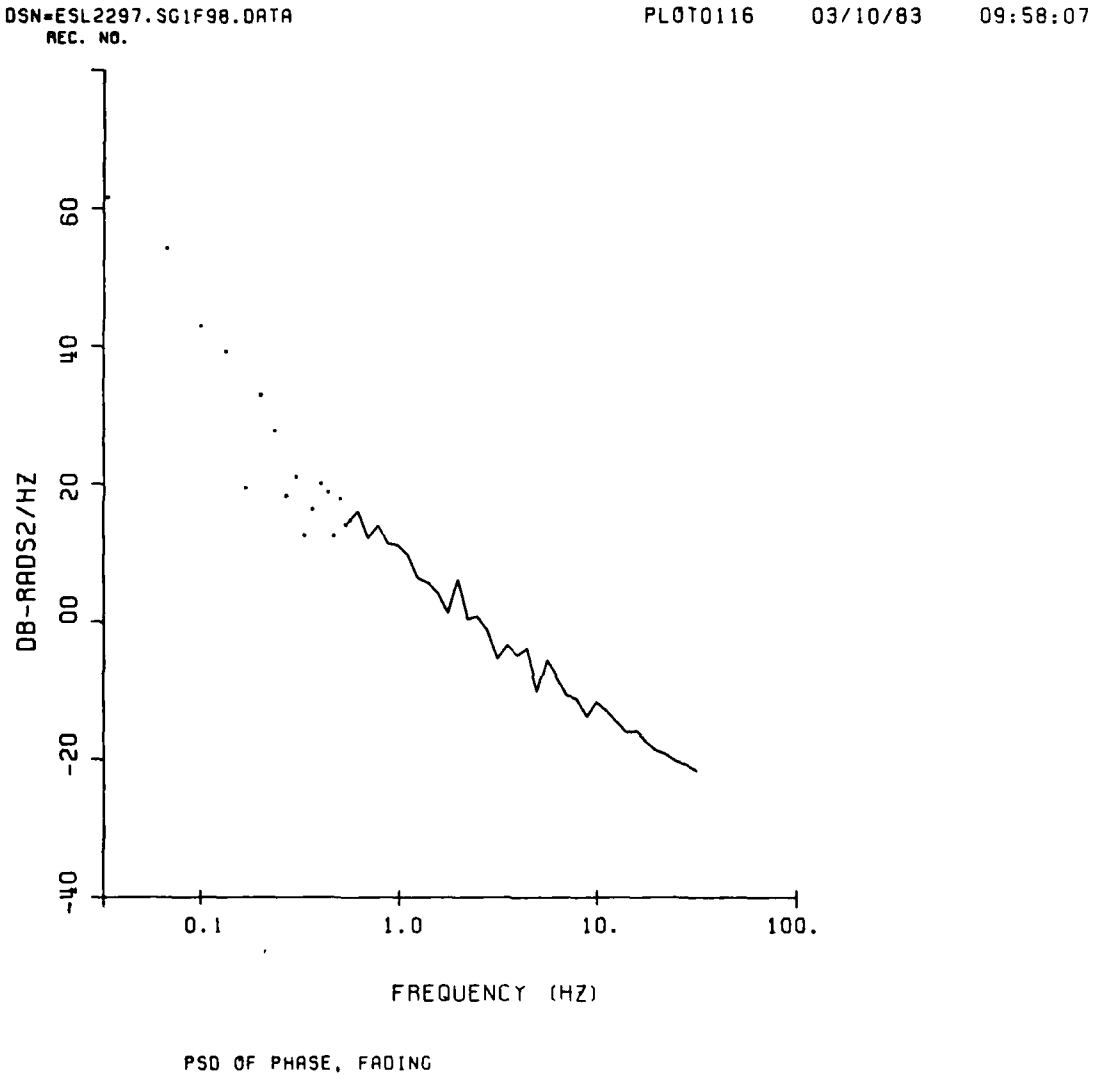

Figure 2-67. Phase power spectral density at 98 MHz.

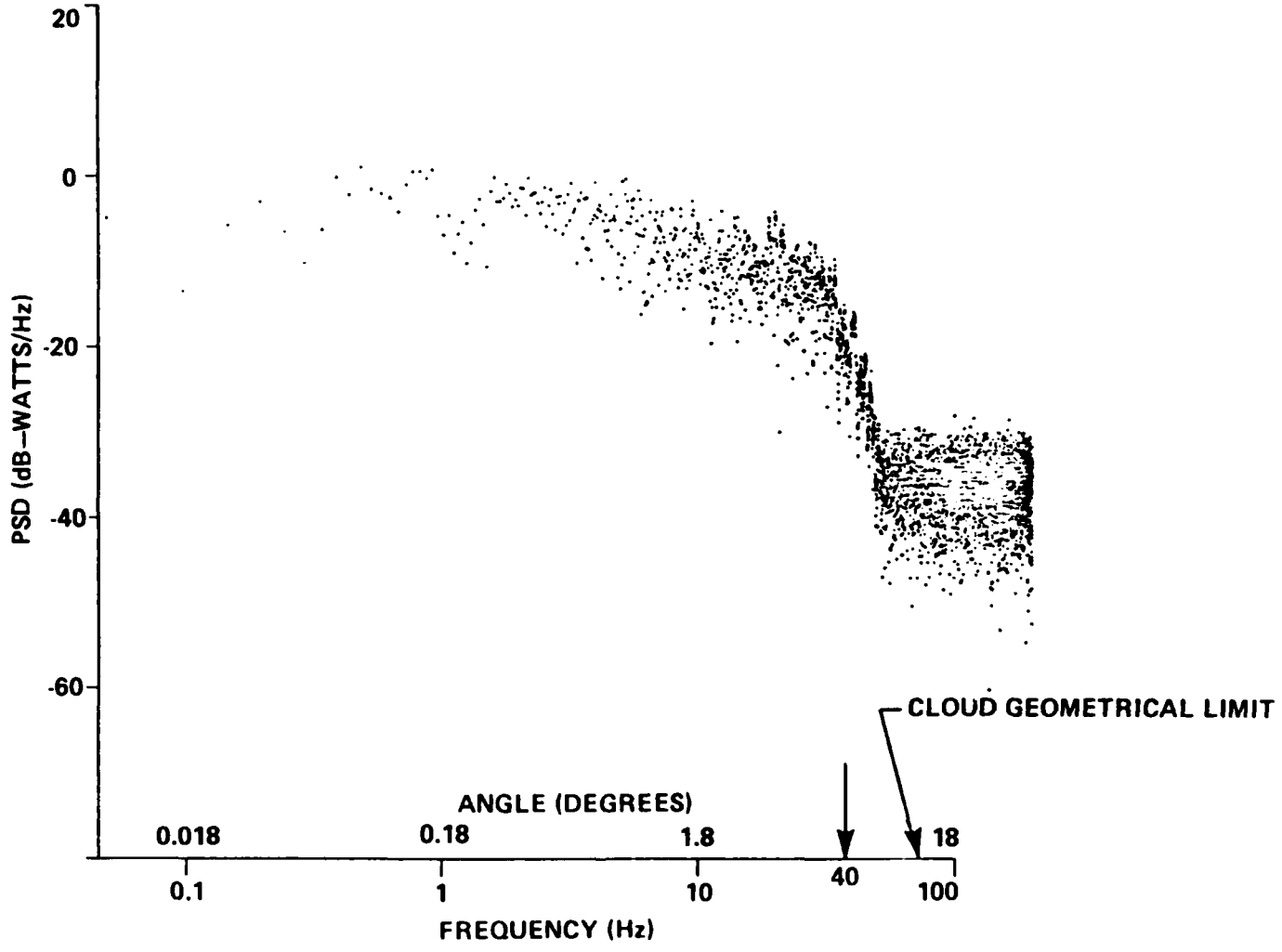

Figure 2-68. Angular spectrum at St. George Island, Beacon 1.

2.8.3 RMS Time Delay Spread and Angular Spectrum

As discussed, geometrical arguments indicate that the basic cause of signal TOA spread is the geometric increase in path length produced by the plasma angular scattering. The angular scattering is closely given by the angular spectrum of the signal at frequencies near the center of the signal bandwidth. Thus, a direct mapping between the angular spectrum and the energy delay profile (delay power spectrum) is expected. The rms angular bandwidth should correspond approximately to the -3 dB point on the angular spectrum shown in Figure 2-68. This rms angular extent is approximately 2.5 degrees.

From the geometric optics relation for time delay, the angular scatter time delay or time delay spread, τ_s, is dependent on the scattering angle, θ, and the propagation distance z as follows:

$$\tau_s \cong z\,\theta^2/(2c)$$

where c is the velocity of light. It follows that the delay spread should be simply related to the angular spectrum.

Strictly speaking, $\tau_{s_{rms}}$ does not equate to σ_s as the mean of θ^2 is not zero. If we assume θ is a zero mean Gaussian process, then

$$E\,\theta^4 = 3\,\sigma_\theta^4 ,$$

and $$E\,\theta^2 = \sigma_\theta^2 ,$$

so that

$$\sigma_{\theta^2}^2 = 2\,\sigma_\theta^4 .$$

Thus,

$$\sigma_s = z\ \sigma_\theta 2/(2c) = z\sqrt{2}\ \sigma_\theta^2/(2c)$$

and

$$\sigma_s = 0.14 \text{ microseconds}$$

for σ_θ = 2.5 degrees (0.044 radians) and a 32 km occultation distance.

The rms delay spread can be measured directly from the channel impulse response data presented earlier by tracking out the direct path TOA using Figure 2-17, which includes the jitter leaving only the spread contribution, and averaging the resulting power delay profiles over the occultation interval. When this was done, the rms time delay spread of power was computed to be approximately 0.09 microseconds, in good agreement with the geometric optics interpretation of the angular spectrum.

The angular spectrum also has an interpretation as the power spectrum of the complex envelope of the fading signal where the relationship between the signal power spectrum frequency and angle was expressed by the relation given previously. In the strong scatter limit, the signal energy can be considered to arrive over a spectrum of angles described by a Gaussian distribution (Reference 13, Equation 33). The angular spectrum may thus be described by

$$P(\theta) = \exp[-\theta^2/(2\sigma_\theta^2)]$$

where

σ_θ is the rms angle of arrival.

Likewise, from Reference 13, Equation 33, the signal power spectrum can be written as

$$P(f) = \sqrt{\pi}\ \tau_o \exp[-(\pi f\ \tau_o)^2] \ .$$

where

τ_o is the fading decorrelation time, and

$$\tau_o = 1/(\sqrt{2}\pi\sigma_f) \ .$$

This expression is shown in Figure 2-69 plotted on the 98-MHz signal power spectrum. This Gaussian form provides an excellent fit to the angular spectrum. The rms frequency, σ_f, of 18.5 Hz corresponds to an rms angular spread, $\sigma\theta$, of 2.3 degrees and the corresponding decorrelation time is approximately 12 milliseconds. The rms time delay spread can be computed to be approximately 0.086 microseconds in excellent agreement with the delay spread computed directly.

Also shown on Figure 2-69 is the expression given by Reference 13, Equation 34 for a power law spectral index of 2 for the in-situ plasma irregularity spectrum. This form is sometimes used to provide a conservative estimate of the power spectrum for systems sensitive to high frequency fluctuations. Clearly this form results in too high power in the high frequency portion of the signal power spectrum. The analytical expression is given by the form

$$P(f) = [1 + (f/f')^2]^{-3/2} \ ,$$

where

$$f' = 1.66/(2\pi\tau_o) \ .$$

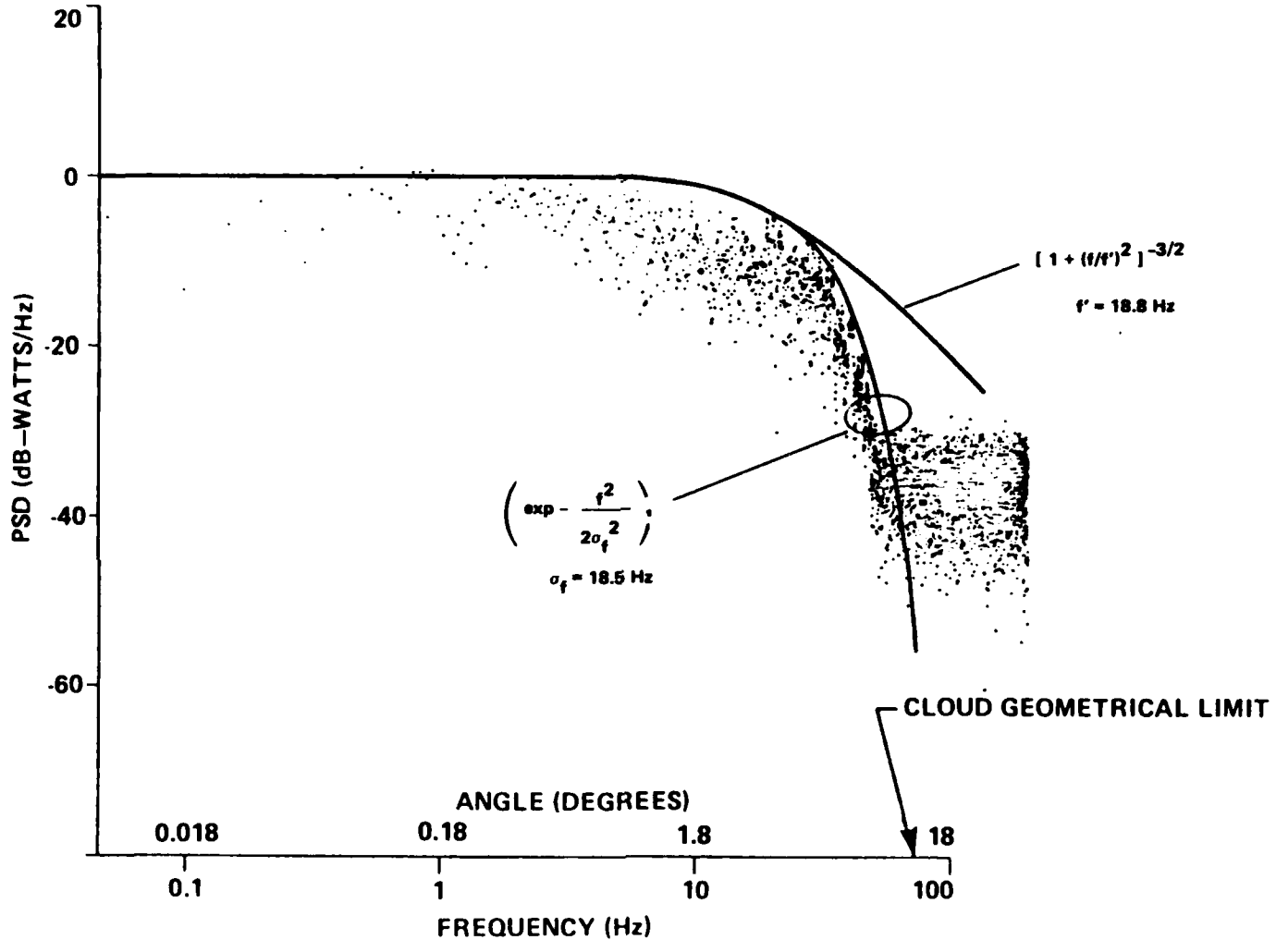

Figure 2-69. Angular spectrum comparison with theory.

The best match of this expression to the data yields f' = 18.8 Hz. The corresponding angle is 3.36 degrees, but the rms angular scattering is given by the 2.5 degrees estimated initially above for the -3 dB point. The decorrelation time computed using this spectral shape yields 14 milliseconds.

Thus, both spectral shapes give roughly the same estimates; however, the Gaussian shape clearly provides the best bit. Table 2-5 summarizes the angular spectrum data.

Table 2-5. Angular spectrum parameters at 98 MHz, St. George Island, Beacon 1.

Spectrum Shape	RMS Bandwidth	RMS Angular Spread	RMS Time Delay Spread	Decorrelation Time
Gaussian	18.5 Hz	2.3 Deg.	0.086 usec	12 milliseconds

2.9 BACK-PROPAGATION PROCESSING AT 98 MHZ

Backward propagation of the 98-MHz signal component of the received diffraction pattern swept out by the beacon rocket can be performed on a computer using thin phase screen angular spectrum techniques[2]. Conceptually the amplitude diffraction effects can, thus, effectively be removed leaving only the phase perturbations due to the integrated electron content plasma fluctuations along the propagation line of sight. The extent to which the amplitude fluctuations diminish is a function of the extent of the striated plasma along the line of sight and the amplitude and phase noise received during the measurement.

Because the rocket trajectory takes the beacon on a downward path that moves away from the striation mass over the occultation interval, no one back-propagation distance is uniquely correct. Furthermore, the striation mass extends over 30 km along the propagation line of sight as described in Section 2.2. For these reasons, it is not possible to determine the in-situ phase power spectral density from the beacon data. The scintillation index and the back-propagation results obtained are described in the following sections. The data are interesting only in that the S^4 index versus back-propagation distance and the 98-MHz signal amplitude behavior provide qualitative agreement with the optical data discussed in Section 2.2.

It can be noted in comparing Figure 2-71 with Figure 2-83 that the scintillation effects near the beginning of the occultation diminish in frequency and intensity near 30 km, consistent with the optical observations of the striation locations presented in Section 2.2.2. As noted, no single back-propagation distance is uniquely correct over the occultation interval; further, the relative thickness of the striation media prevents the removal of all significant diffraction effects with back-propagation. Accordingly, the behavior exhibited versus propagation distance is consistent with expectations.

2.9.1 S^4 Versus Distance

The scintillation index is used as a measure of the amplitude fluctuations of signals. The scintillation index, S^4, is defined by

$$S^4 = \left[\left(\langle E^4 \rangle - \langle E^2 \rangle^2 \right) / \langle E^2 \rangle^2 \right]^{1/2} ,$$

where

E is the received signal voltage, and
$\langle\ \rangle$ indicates a statistical average.

While S^4 is usually considered to provide a measure of the depth of signal fluctuation, it is also very sensitive to signal focusing effects.

The amount the S^4 index decreases with back-propagation and its value after back-propagation gives a good indication as to how well the data back-propagated in a thin phase screen sense. Figure 2-70 is a plot of the scintillation index versus back-propagation distance for St. George Island, Beacon 1. The back-propagation distance was originally computed for an estimated effective transverse velocity, V_e, of the rocket of 890 m/sec. The correct velocity is 980 m/sec (see Appendix D). The distance axis scales by the factor $(V_T/V_e)^2$, where V_T is the true transverse velocity. The corrected distance scale is also shown on this figure.

The S^4 index shows a rapid decrease over the first 10 km of back-propagation. This characteristic is also observed in the Cape San Blas data over the first 27 km. The S^4 index is very sensitive to signal focuses, which appear from the back-propagation data presented in the next section to diminish slightly over the initial 10 km. Thereafter, the scintillation index remains around unity. The San Blas data, however, reach a minimum of 0.8 at -27 km (see Section 3-7). This is consistent with the optical data that would indicate striations from around 18 km to over 50 km from the rocket over its occultation interval (see Section 2.2).

2.9.2 Back-Propagation Plots

The back-propagation processing was conducted using the same routines as developed for the STRESS Experiment and described in Reference 2. Plots of the back-propagated signal amplitude, phase, and phase power spectrum are presented in Figures 2-71 through 2-88 over the first 40 km. The distances noted are the uncorrected values corresponding to the 890 m/sec velocity noted on Figure 2-70.

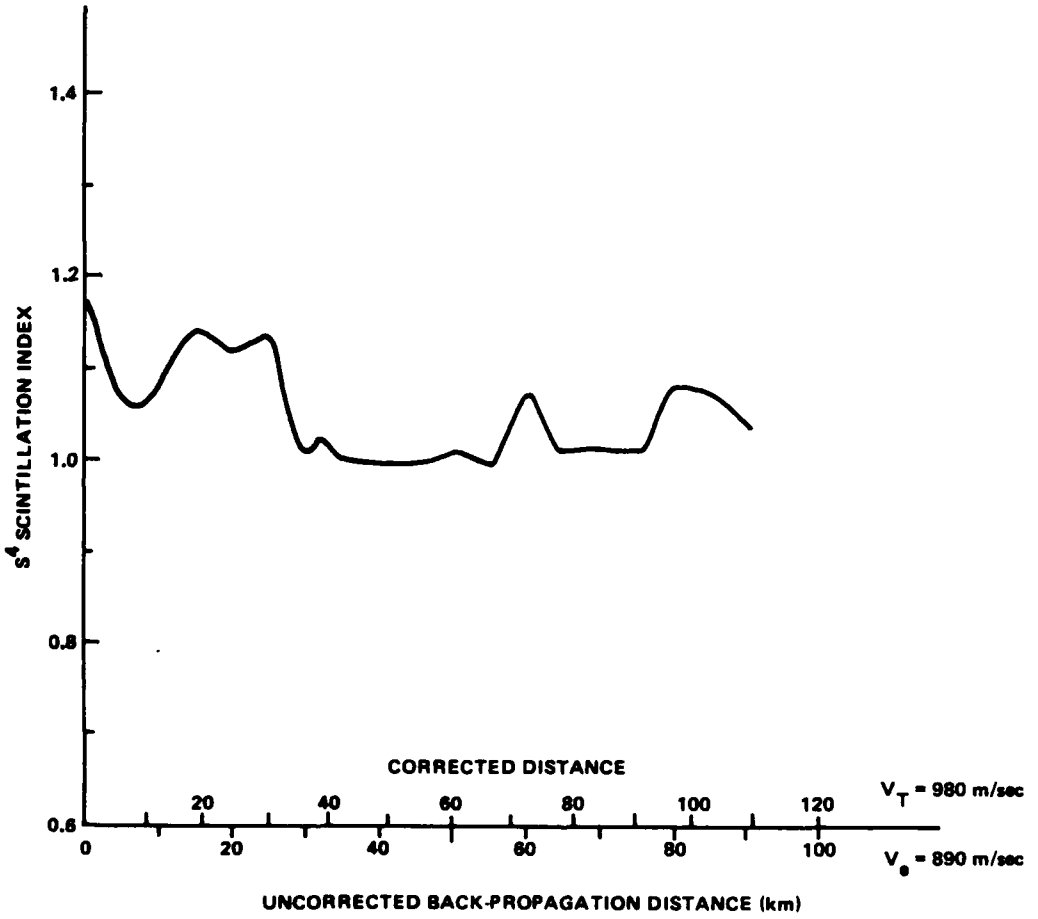

Figure 2-70. S^4 scintillation index versus back-propagation distance for St. George Island, Beacon 1.

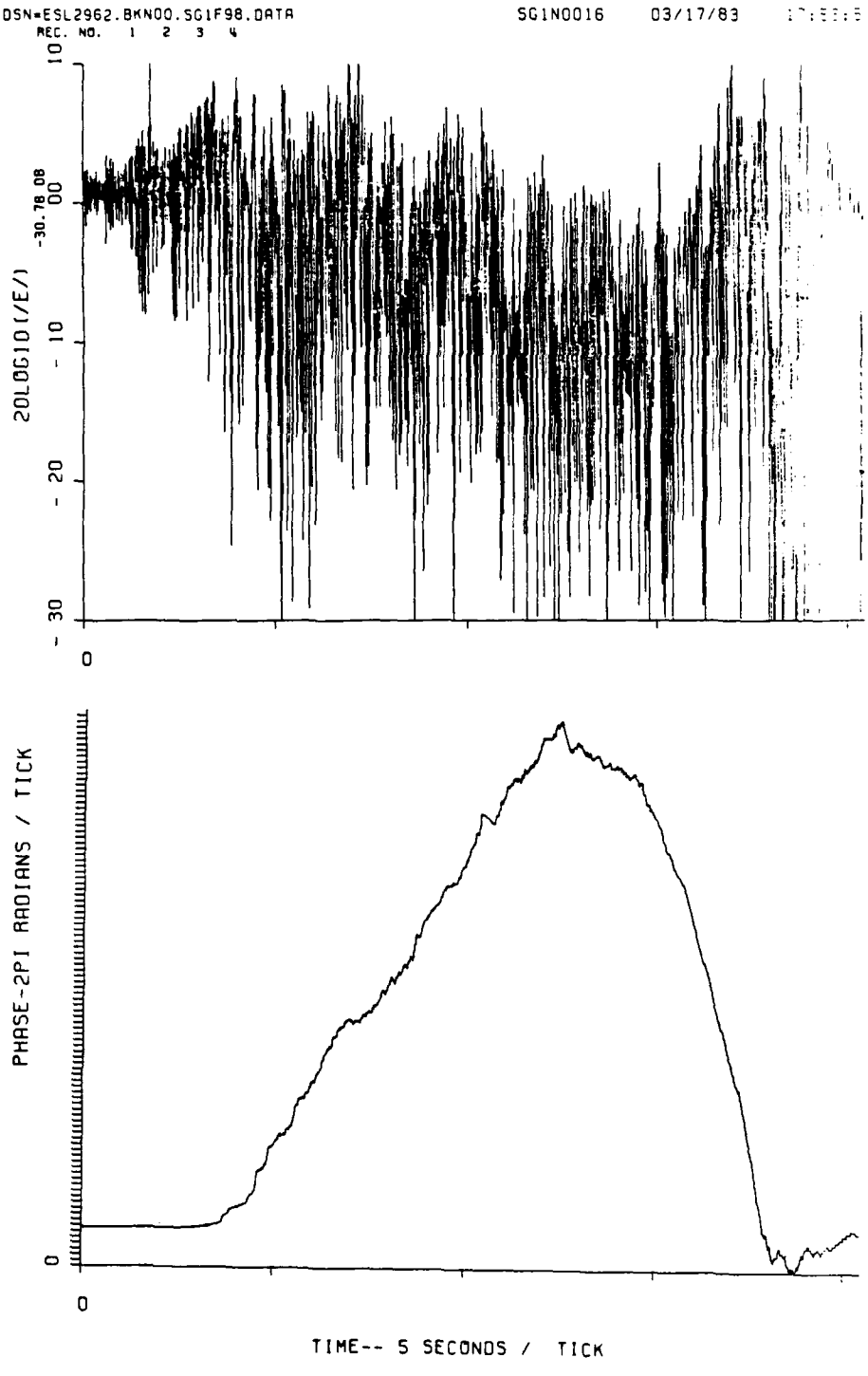

Figure 2-71. Amplitude and phase before back-propagation, St. George Island, Beacon 1.

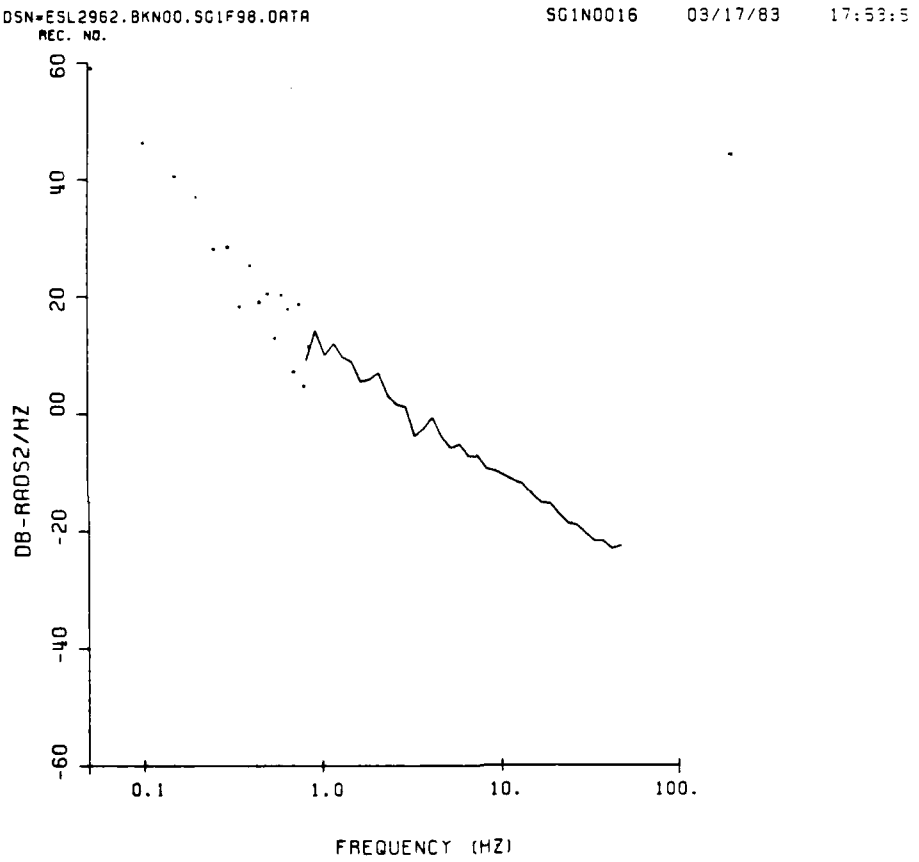

Figure 2-72. Phase power spectrum before back-propagation, St. George Island, Beacon 1.

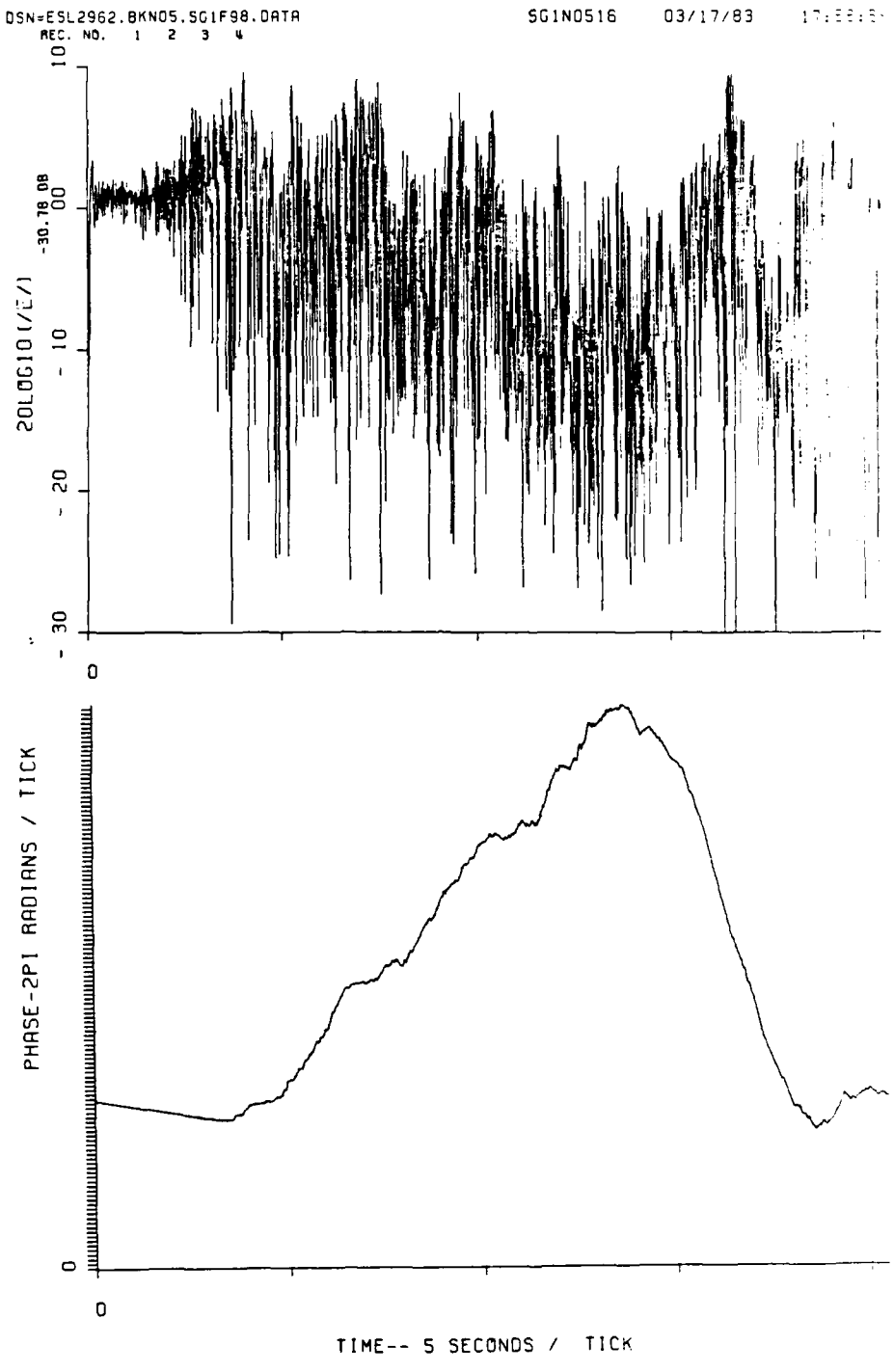

Figure 2-73. Back-propagated amplitude and phase, St. George Island, Beacon 1, 5 km.

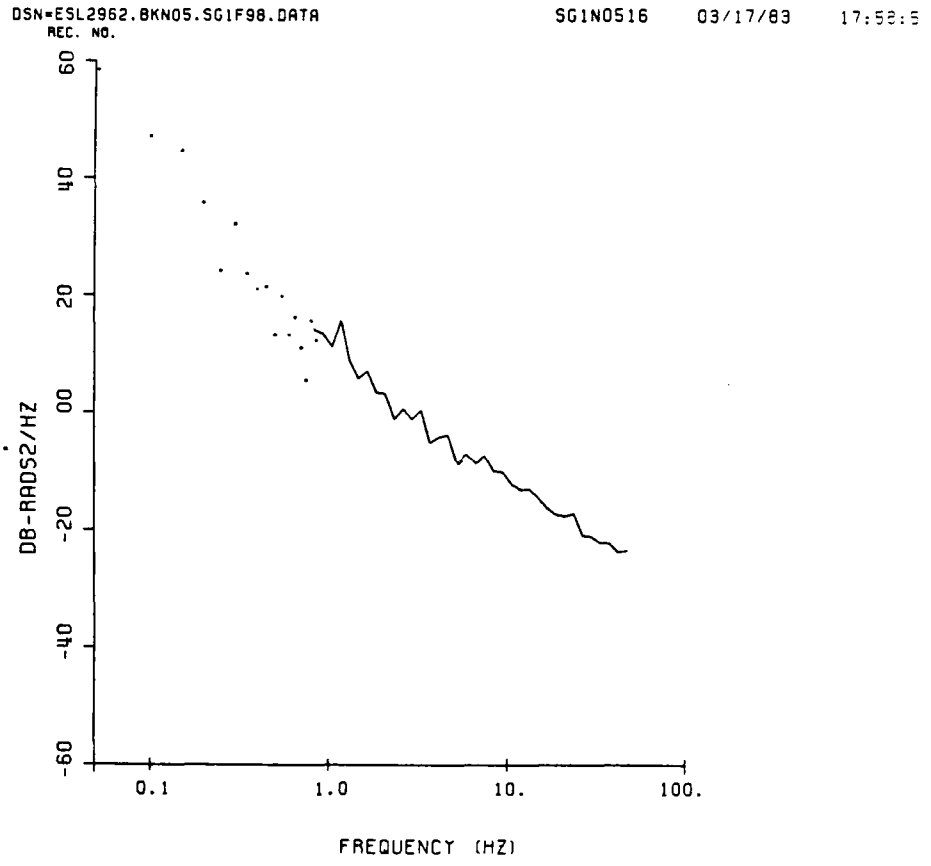

Figure 2-74. Back-propagated phase power spectrum, St. George Island, Beacon 1, 5 km.

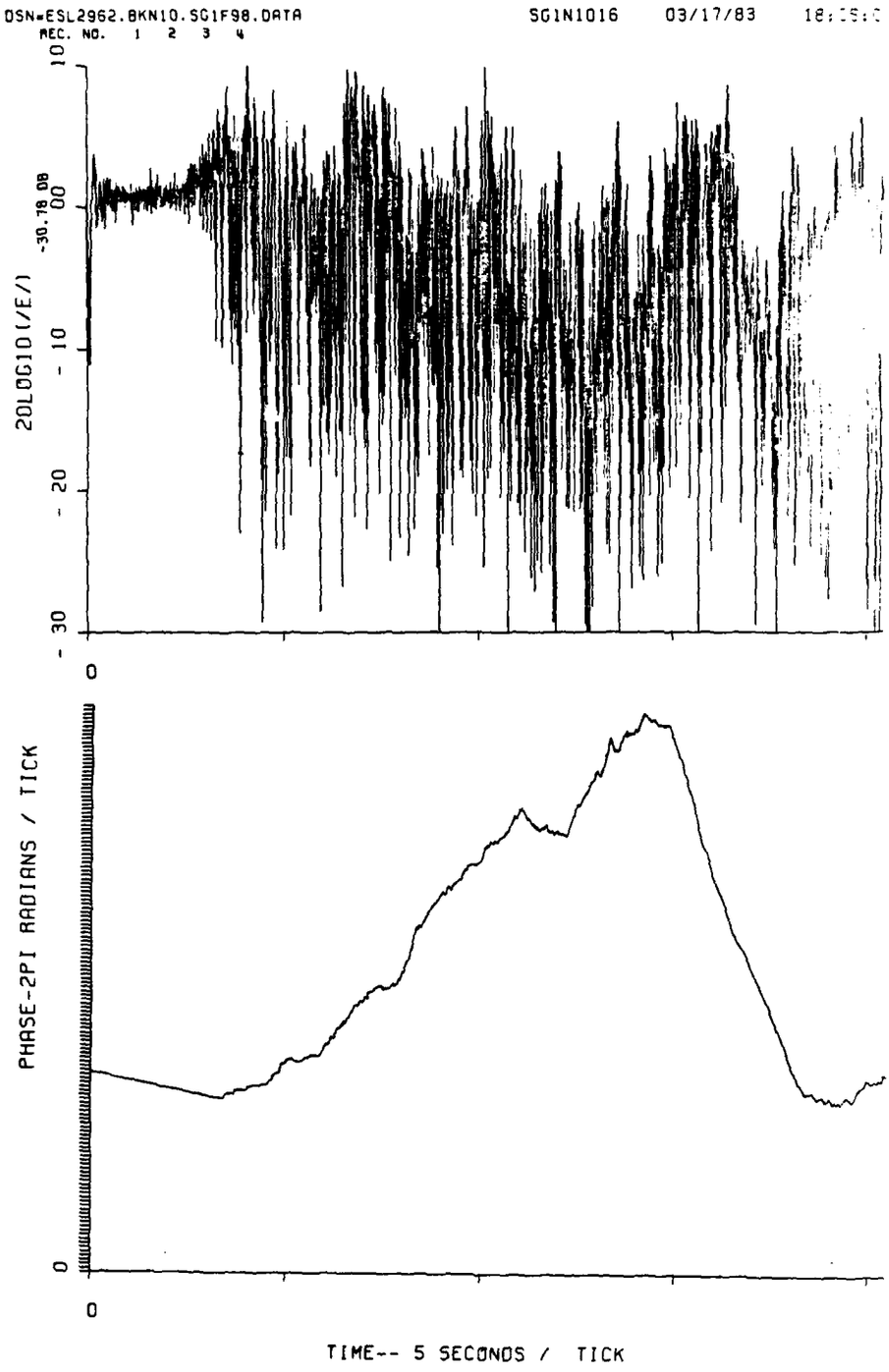

Figure 2-75. Back-propagated amplitude and phase, St. George Island, Beacon 1, 10 km.

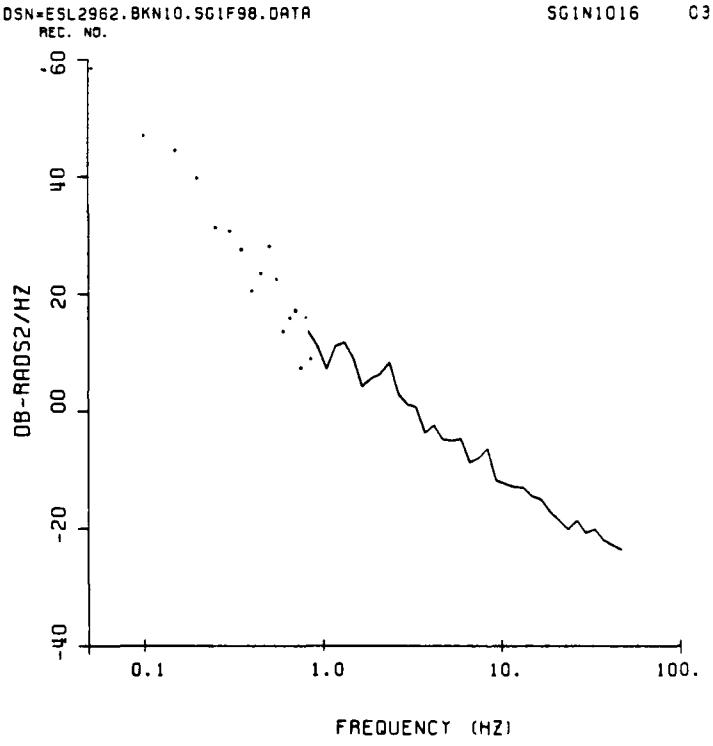

Figure 2-76. Back-propagated phase power spectrum, St. George Island, Beacon 1, 10 km.

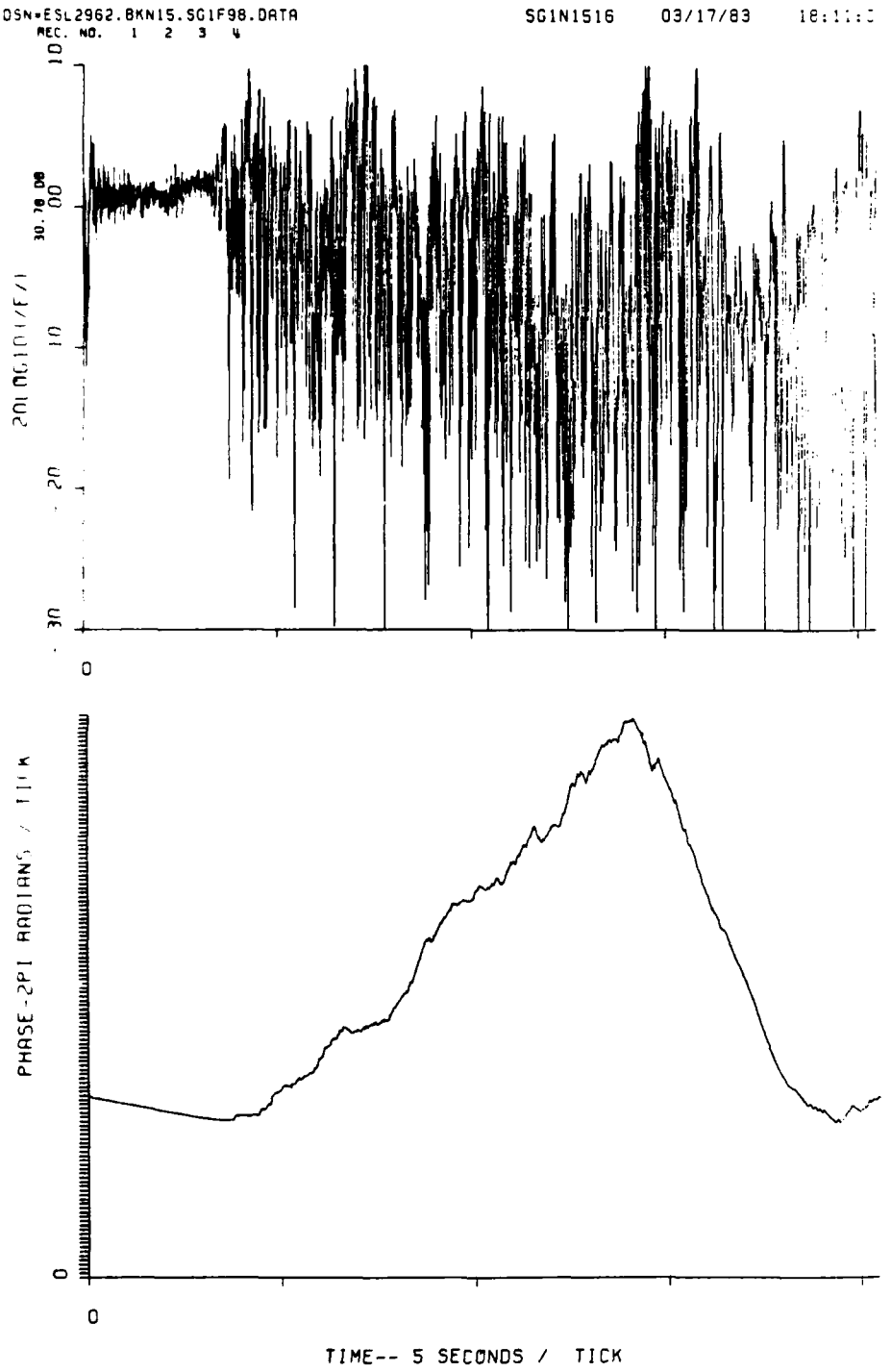

Figure 2-77. Back-propagated amplitude and phase, St. George Island, Beacon 1, 15 km.

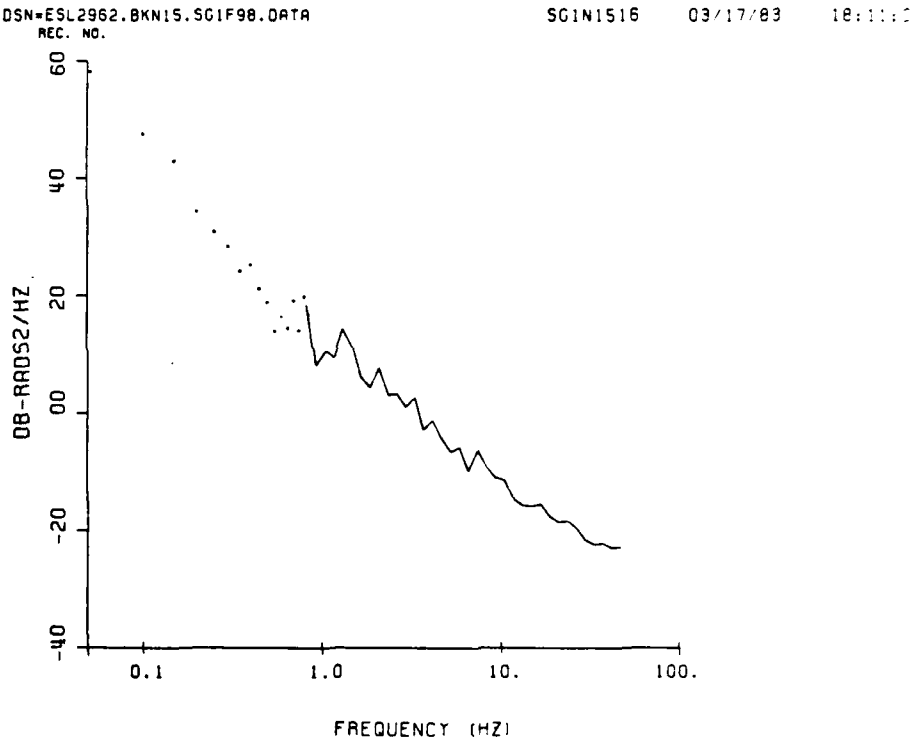

Figure 2-78. Back-propagated phase power spectrum, St. George Island, Beacon 1, 15 km.

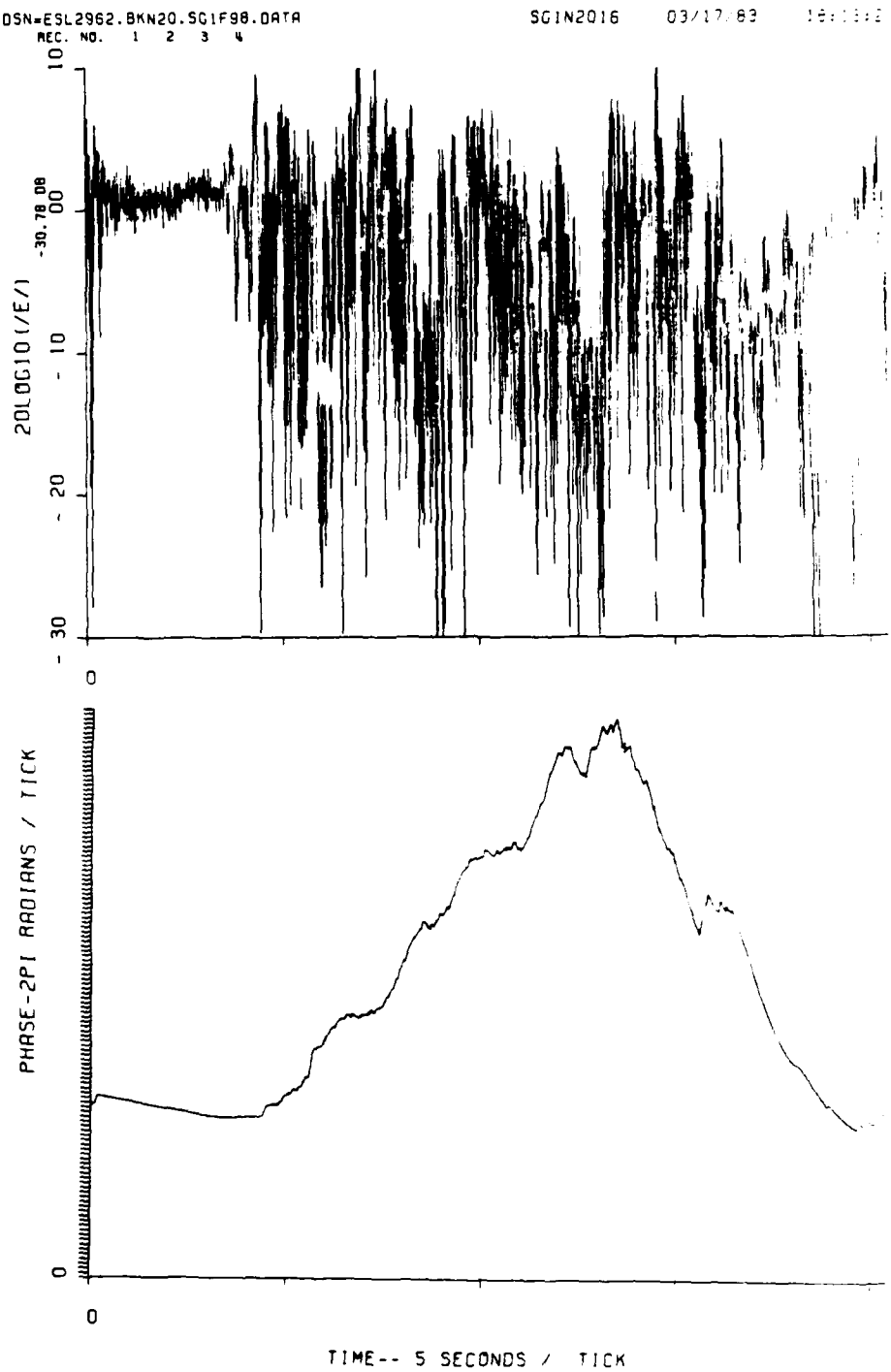

Figure 2-79. Back-propagated amplitude and phase, St. George Island, Beacon 1, 20 km.

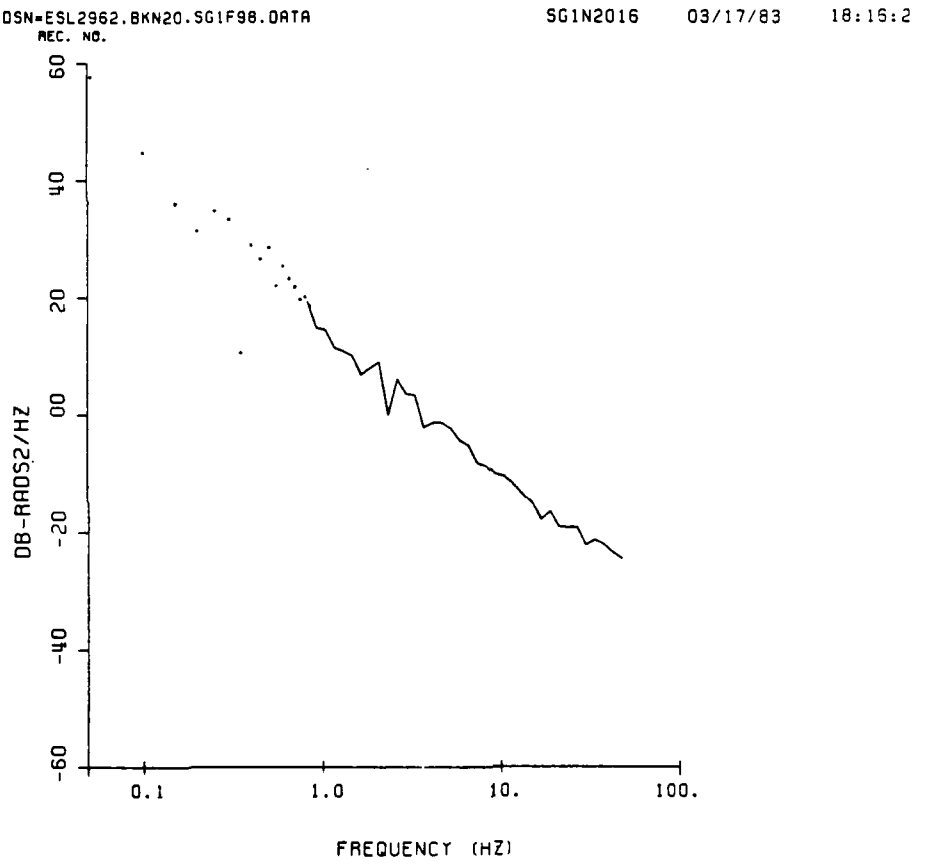

Figure 2-80. Back-propagated phase power spectrum, St. George Island, Beacon 1, 20 km.

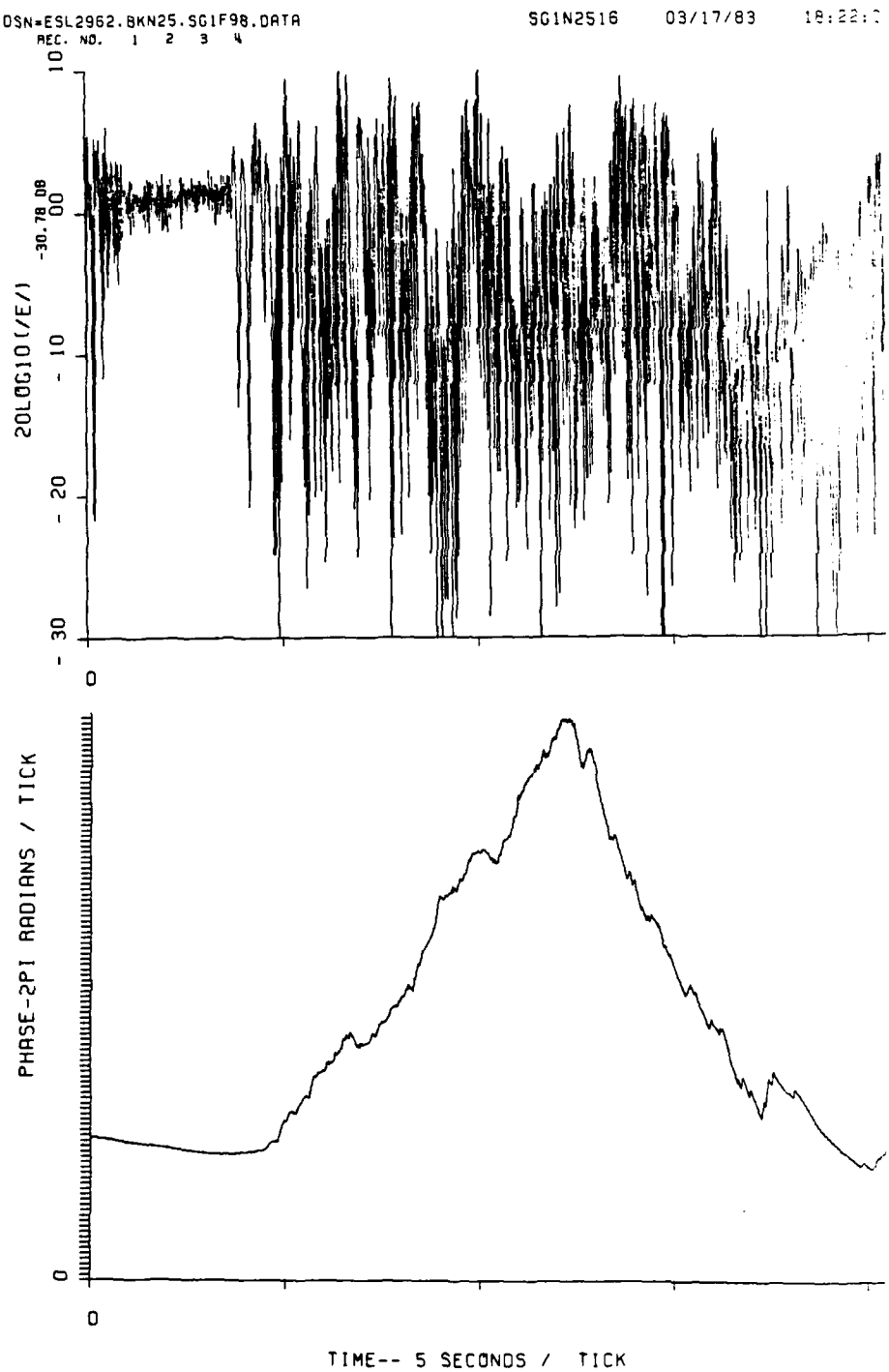

Figure 2-81. Back-propagated amplitude and phase, St. George Island, Beacon 1, 25 km.

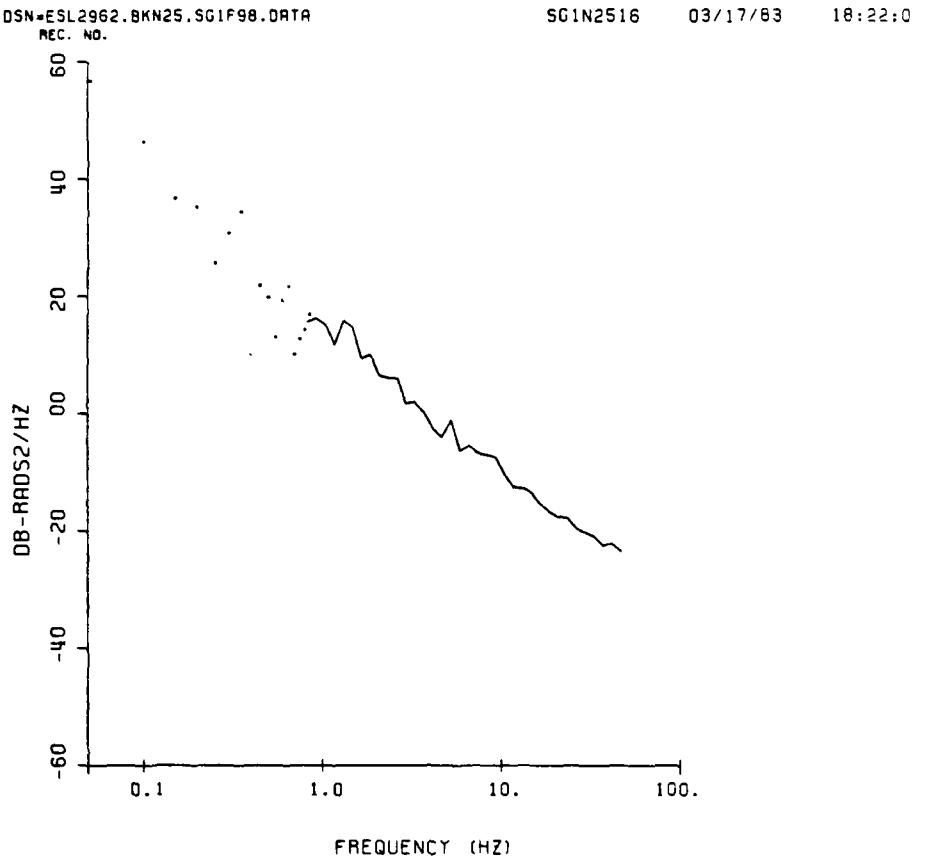

Figure 2-82. Back-propagated phase power spectrum, St. George Island, Beacon 1, 25 km.

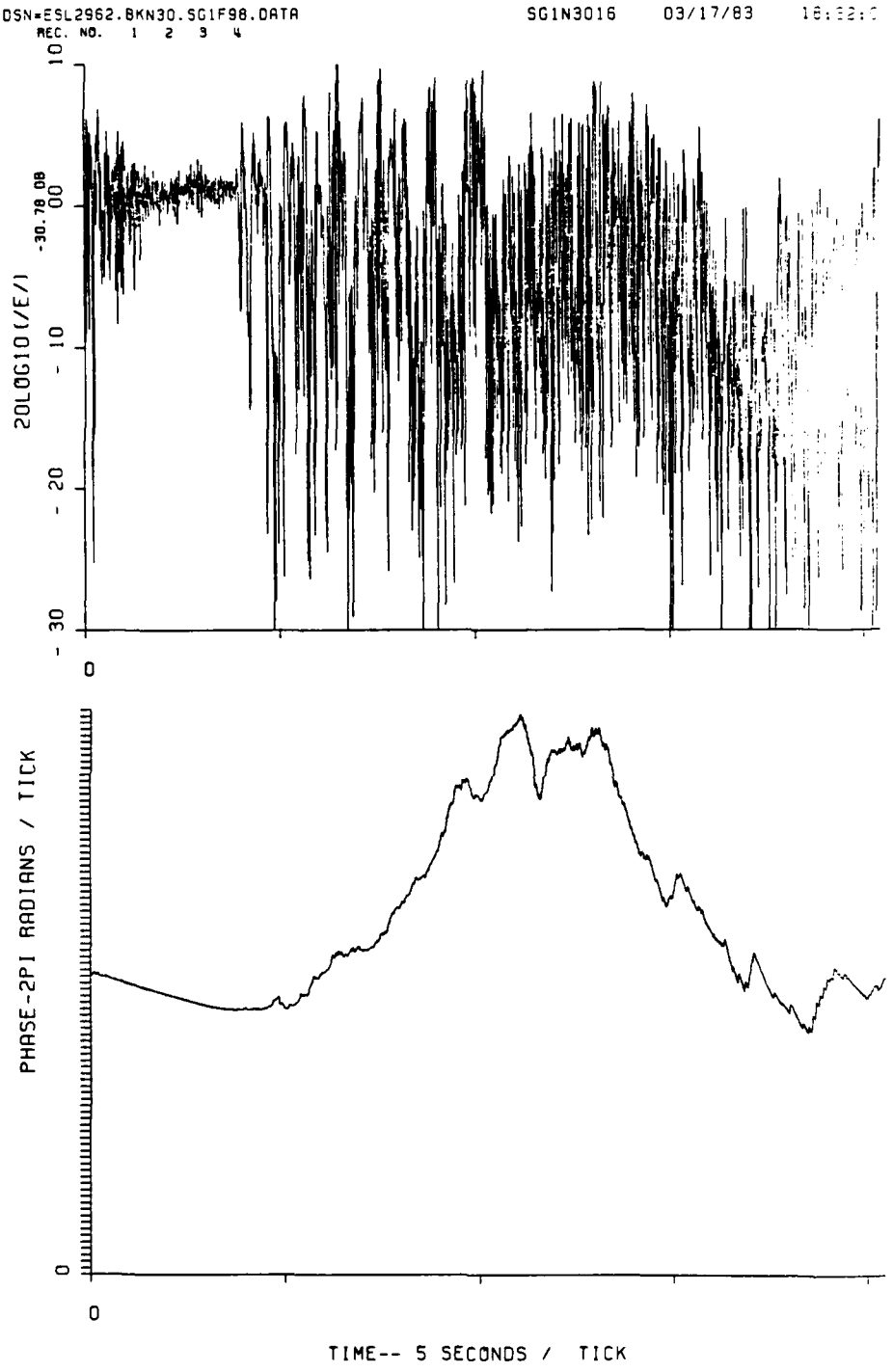

Figure 2-83. Back-propagated amplitude and phase, St. George Island, Beacon 1, 30 km.

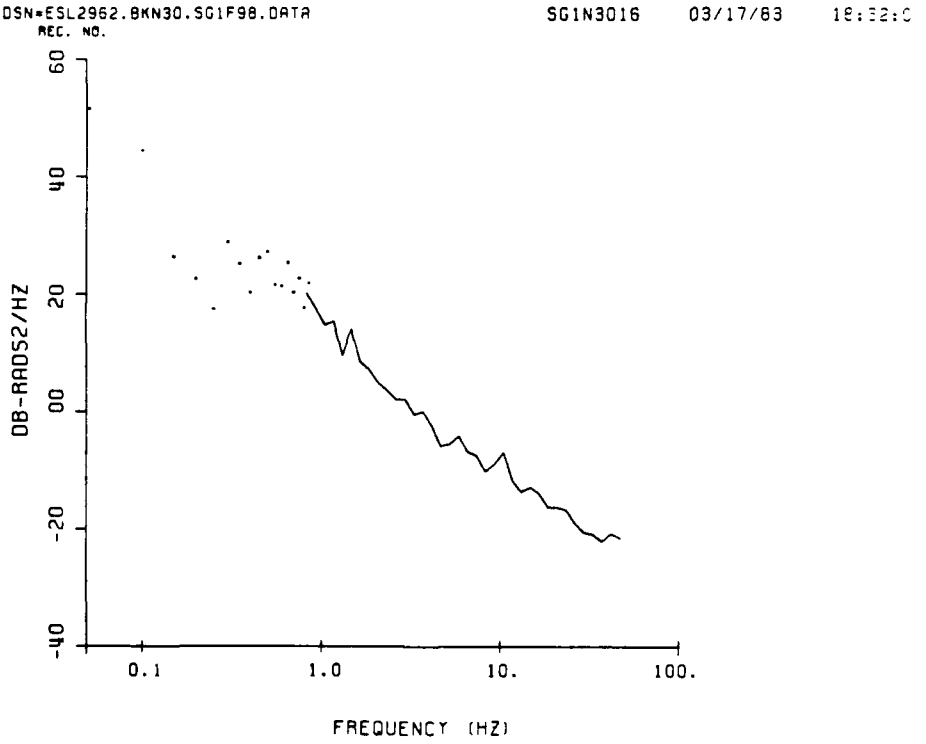

Figure 2-84. Back-propagated phase power spectrum, St. George Island, Beacon 1, 30 km.

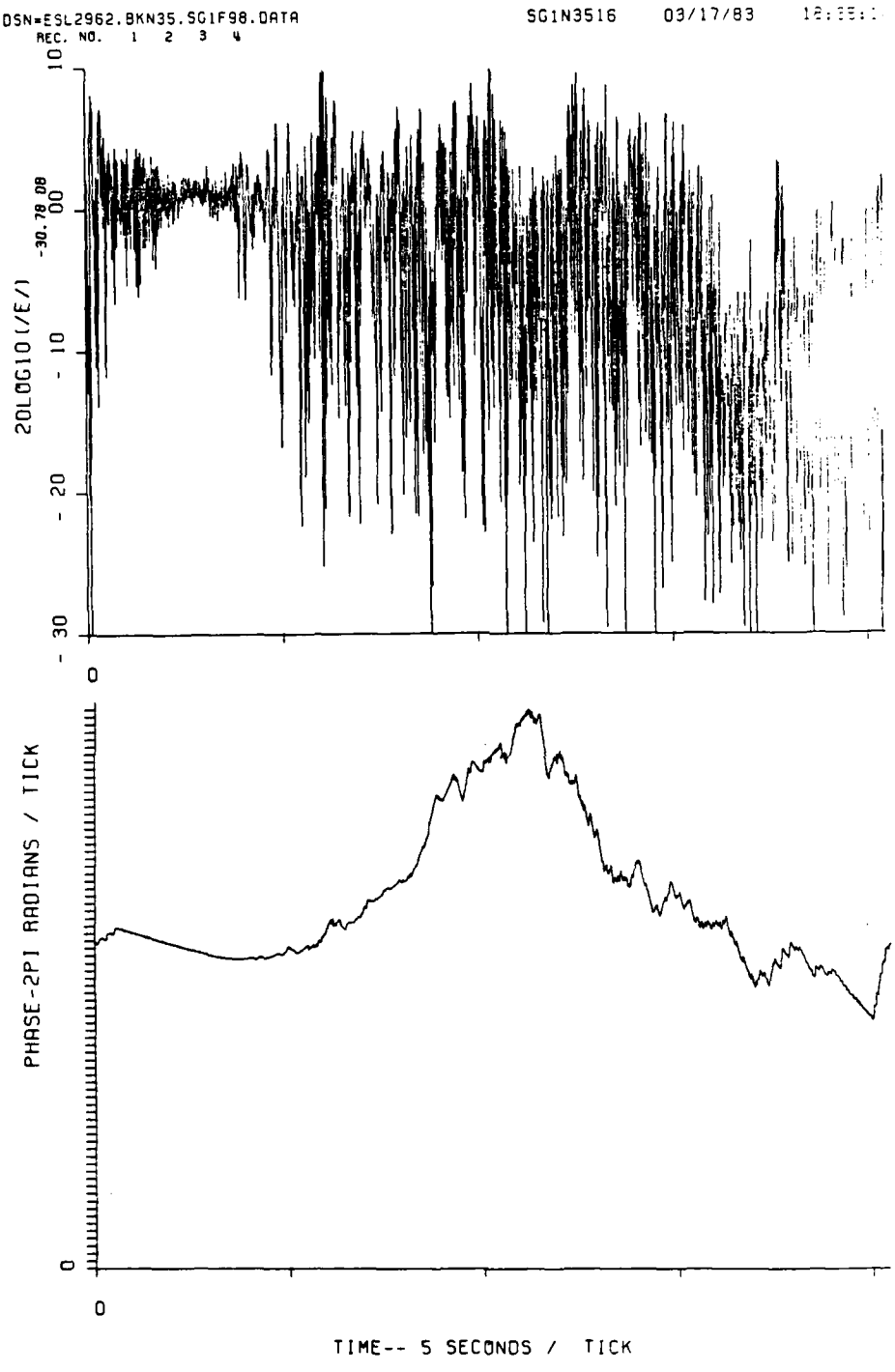

Figure 2-85. Back-propagated amplitude and phase, St. George Island, Beacon 1, 35 km.

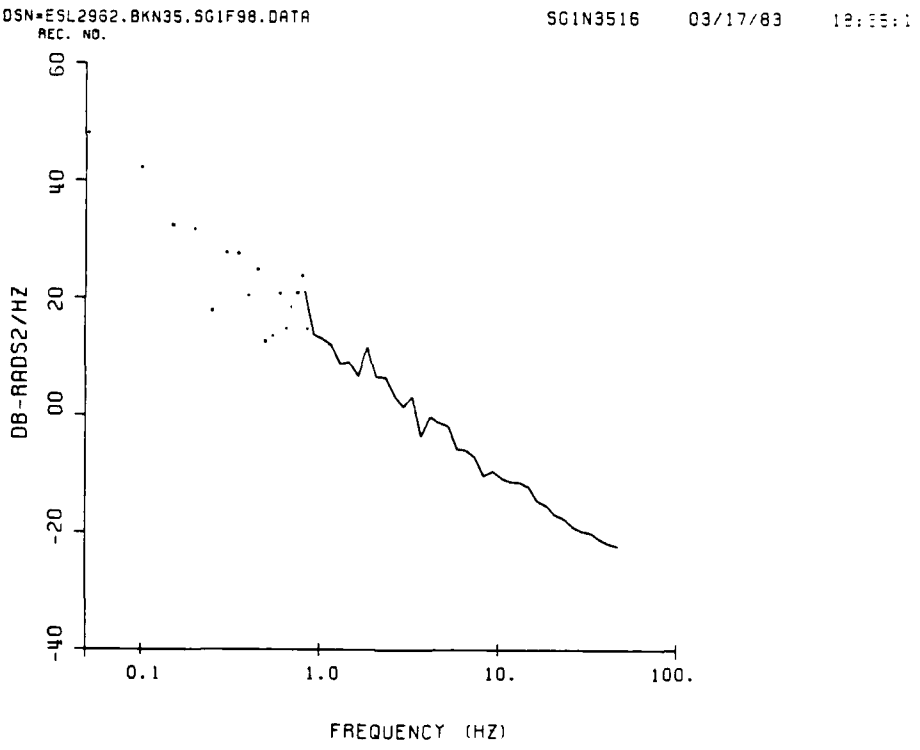

Figure 2-86. Back-propagated phase power spectrum, St. George Island, Beacon 1, 35 km.

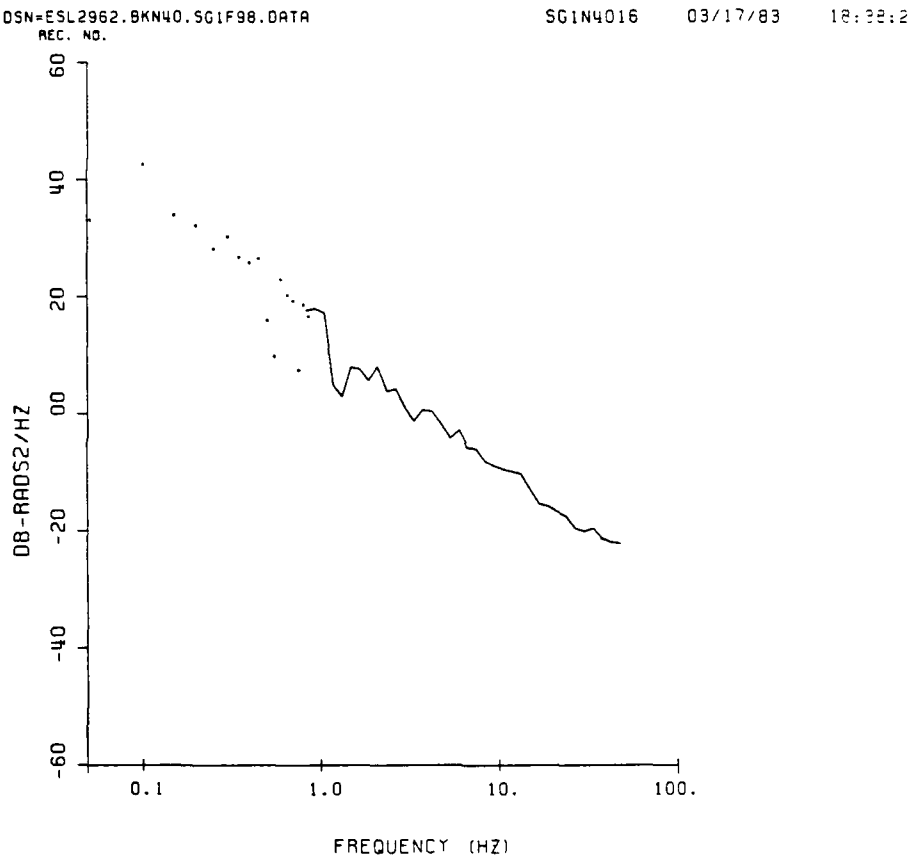

Figure 2-87. Back-propagated amplitude and phase, St. George Island, Beacon 1, 40 km.

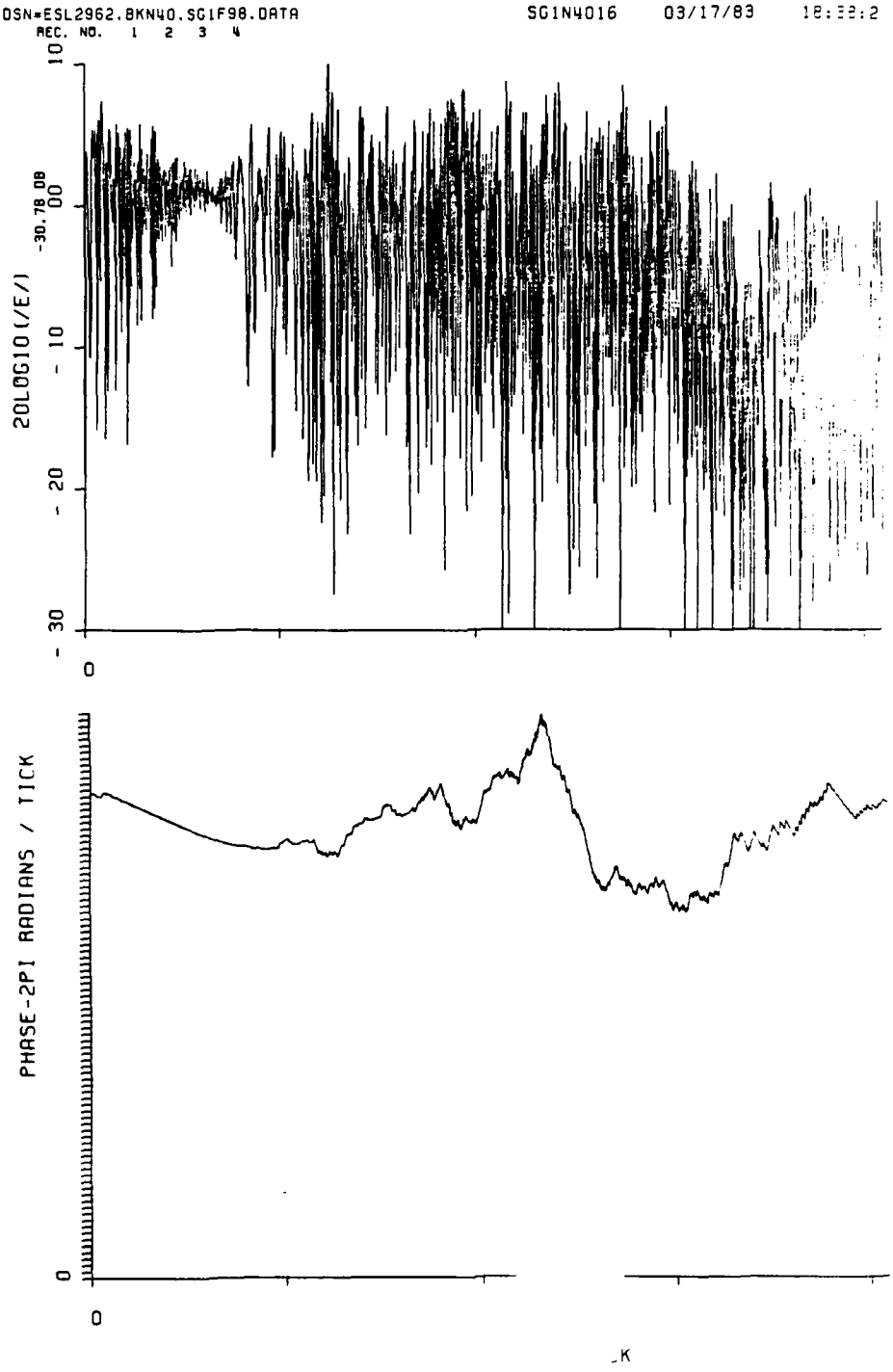

Figure 2-88. Back phase power spectrum, St. Ge and, Beacon 1, 40 km.

2.10 MUTUAL COHERENCE FUNCTION AND IN-SITU PHASE SPECTRAL DENSITY

The power spectral density (PSD) of the received signal phase does not correspond to the phase PSD of the in-situ striation structure because of diffraction effects. At a high enough frequency where diffraction effects can be neglected, the received phase is an integral measure of the in-situ structure along the propagation path. Phenomenology studies of striation development are aided by knowledge of the in-situ phase PSD. If the shape of the in-situ spectrum of electron irregularities does not vary along the propagation path, then the power-law index of the measured 1-D (path integrated) phase spectrum (without diffraction effects) is one less than the corresponding index of the 1-D in-situ electron density spectral index that would be measured by an in-situ rocket; i.e., a k^{-3} path integrated phase spectrum corresponds to a k^{-2} in-situ electron density spectrum.

The in-situ path integrated phase PSD can be derived from the received signal in spite of the diffraction effects, however. As pointed out in Reference 11, the single frequency mutual coherence function (or the autocorrelation function of the received signal complex envelope) is independent of the signal propagation diffraction effects. Appendix F provides a correspondence of the mutual coherence function (MCF) and a communications channel interpretation using the signal autocorrelation function.

2.10.1 The MCF Approach

The single frequency mutual coherence function is defined in terms of the temporal signal properties as

$$G_1(z,t,O) = R_u(t) = \langle U(t')\, U^*(t' + t) \rangle \quad .$$

where G_1 is the two frequency mutual coherence function presented in Section 2.6.6, and U is the complex envelope of the received signal. Thus, the mutual coherence function can be computed directly from the 98-MHz fading waveform data presented in Section 2.8.

Reference 11 shows that the form for the single frequency mutual coherence function is given by

$$R_u(t) = \exp[-1/2\ D(t)] \quad ,$$

where D(t) is the phase structure function and t is the temporal correlation variable. The structure function can be approximately expressed as

$$D(t) = C_{\delta\phi}^2\ V_e\ |t|^{\min(2v-1,\ 2)} \quad .$$

where v is the power law index for a three-dimensional spectral density function of the form $C_s q^{-(2v+1)}$, $C_{\delta\phi}^2$ is the phase structure constant, and V_e is the effective velocity. The corresponding form for the in-situ phase PSD should follow

$$S_\phi(f) \simeq T\ f^{-2v} \quad .$$

For the beacon data, we anticipate the structure function having the form

$$D(t) = C\ t^2 \quad ,$$

and the phase PSD roll-off of the form

$$S_\phi(f) \simeq T\ f^{-3} \quad .$$

We also note from Section 2.6.6 that the DNA model for satellite applications uses the following form for the MCF

$$G_1(z,t,0) = \exp[-\tau^2 \tau_o^2] = R_u(t),$$

which provides a correspondence with the decorrelation time τ_o.

As shown in Appendix F, the autocorrelation of the complex signal envelope can also be related to the in-situ phase autocorrelation function through the expression

$$R_u(t) = \exp[-\{R_\phi(0) - R_\phi(t)\}] \quad ,$$

where

$R_\phi(t)$ = the autocorrelation of the in-situ integrated path phase function, and

$R_\phi(0) = \sigma_{\phi R}^2$, the Rayleigh phase variance.

The form for the phase power spectral density function frequently used in thin phase screen simulations of barium plasmas is

$$S_\phi(v) = \sigma_{\phi R}^2 \frac{2}{\sqrt{\pi}} \frac{\Gamma\left(\frac{N}{2}\right)}{\Gamma\left(\frac{N-1}{2}\right)} \frac{\ell_o}{\left[1 + (\ell_o \ v^2)\right]^{N/2}}$$

where

V = spatial frequency in cycles per km,
ℓ_o = outer scale size (km),
$\sigma_\phi{}^2 R$ = Rayleigh phase variance (rad^2), and
10 N = asymptotic slope in dB per decade.

The corresponding form for the temporal phase autocorrelation function with N = 3 is given by

$$R_{\phi}(\tau) = \sigma_{\phi R}^{2} \, (\tau/\tau_o) \, K_1(\tau/\tau_o) \quad ,$$

where

K_1 is a modified Bessel Function of the second kind.

Thus, there are several nearly equivalent nominal forms that one might expect for the mutual coherence function.

The Fourier transform of the temporal MCF gives the Doppler spectrum or the received signal power spectrum. Reference 13 gives

$$\mathcal{F}[G_1(z,t,0)] = \Gamma_1(f_d) = \sqrt{\pi}\,\tau_o \exp[-(\pi f \tau_o)^2] \quad .$$

Moreover, the transform of the natural logarithm of R_u provides, by virtue of the earlier expression, the in-situ phase power spectrum, S_{ϕ} ,

$$\mathcal{F}[\ \ln\{R_u(t)\}] = -\sigma_{\phi}^{2}{}_R \, \delta(o) + S_{\phi}(f) \quad .$$

Thus, the phase power spectrum can be derived from the 98-MHz fading signal waveform as well as the decorrelation time, τ_o, and the rms path integrated phase, $\sigma_{\phi R}$.

2.10.2 MCF Data for St. George Island, Beacon 1, Direct Calculation

From the preceding relations, it is clear that any trend-like or systematic phase variations due to the gross background plasma will distort the mutual coherence function. Thus, in general, it is difficult to apply to the beacon data because of the strong

phase associated with the background barium ion cloud that is cut by the propagation path from the beacon rocket. The best method for doing this is to use detrended segments of the data, which restricts the observation of an outer scale. Nonetheless, as noted in Reference 11, under strong scatter conditions, the decorrelation of the phase occurs sufficiently rapidly that the nonstationary component can evidently be neglected.

The computation of the MCF begins with the extraction of the monochromatic fading data from the complex beacon signal delay measurements. This is accomplished through the transformation of the delay measurement (channel impulse response) over its 3-microsecond range to its frequency domain representation (channel transfer function) over the 30-MHz signal bandwidth as presented in Section 2.7. These transforms are performed over all the delay profiles (400 samples/second) recorded during the occultation period, a single spectral component at 98 MHz is taken from each transform, and these components strung together to represent the temporal fading behavior of the signal. The MCF can then be computed directly from its definition

$$R_u(t) = \langle U(t') \, U^*(t' + t) \rangle \quad .$$

As discussed, from a theoretical perspective, in the absence of any systematic or nonstationary component, we expect a purely real function to result. Figures 2-89 through 2-97 show the results of these calculations where only the real part of the MCF is plotted. The data intervals shown correspond to the segments presented in Table 2-1. It was noted that over the principal lobe that the imaginary component is significant at times, forcing a negative value to the MCF.

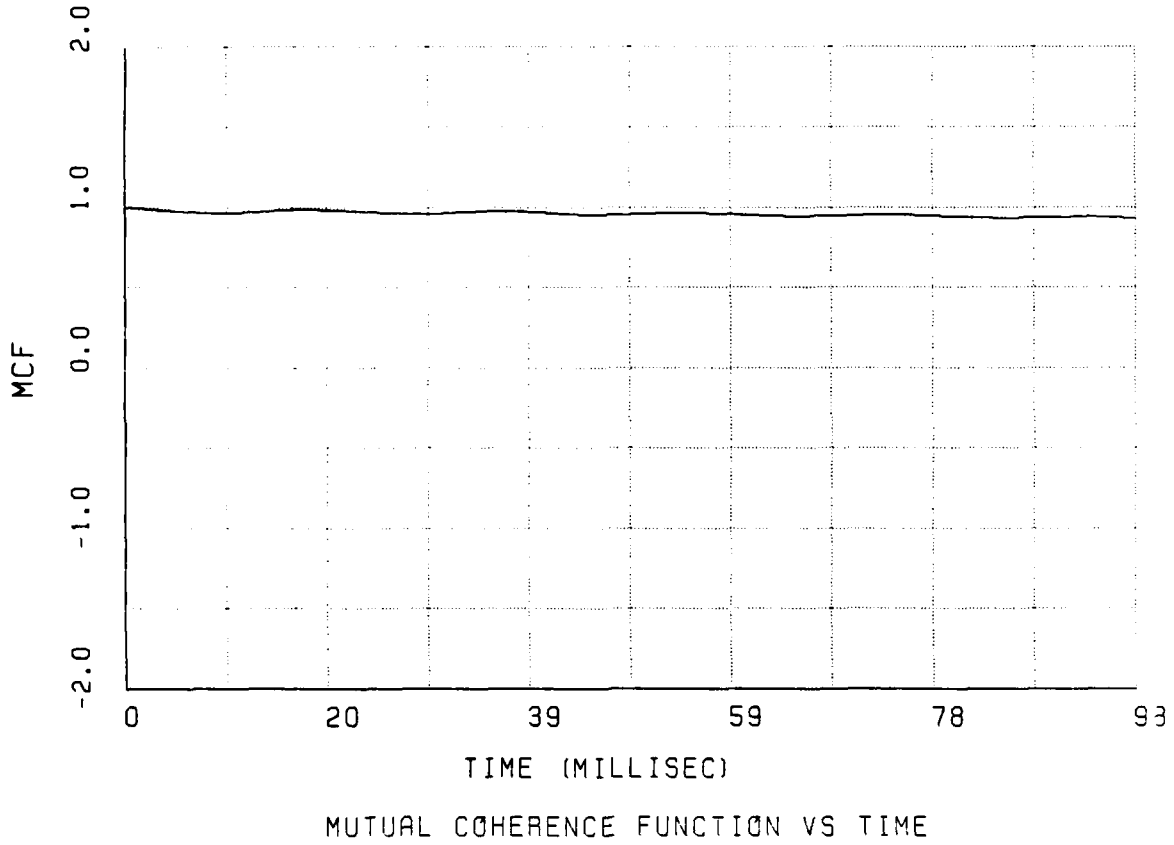

Figure 2-89. Real part of MCF for Segment 1.

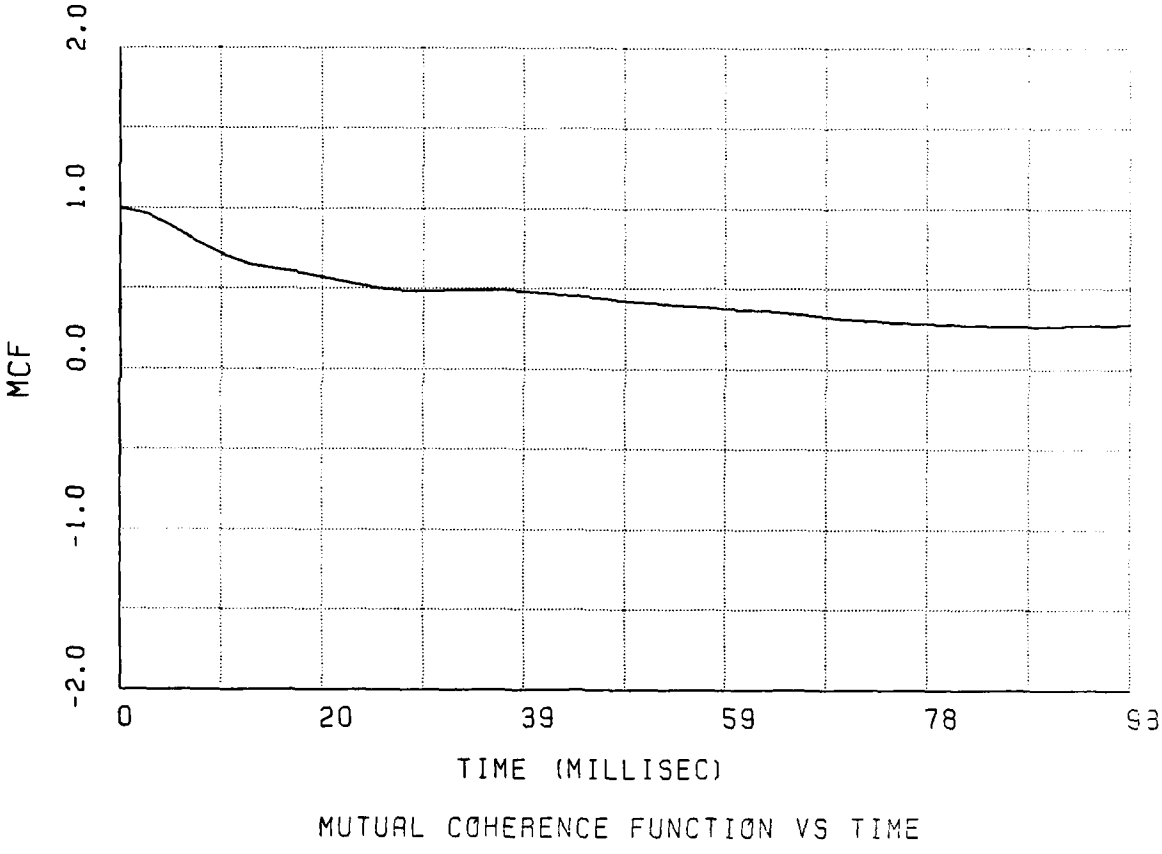

Figure 2-90. Real part of MCF for Segment 2.

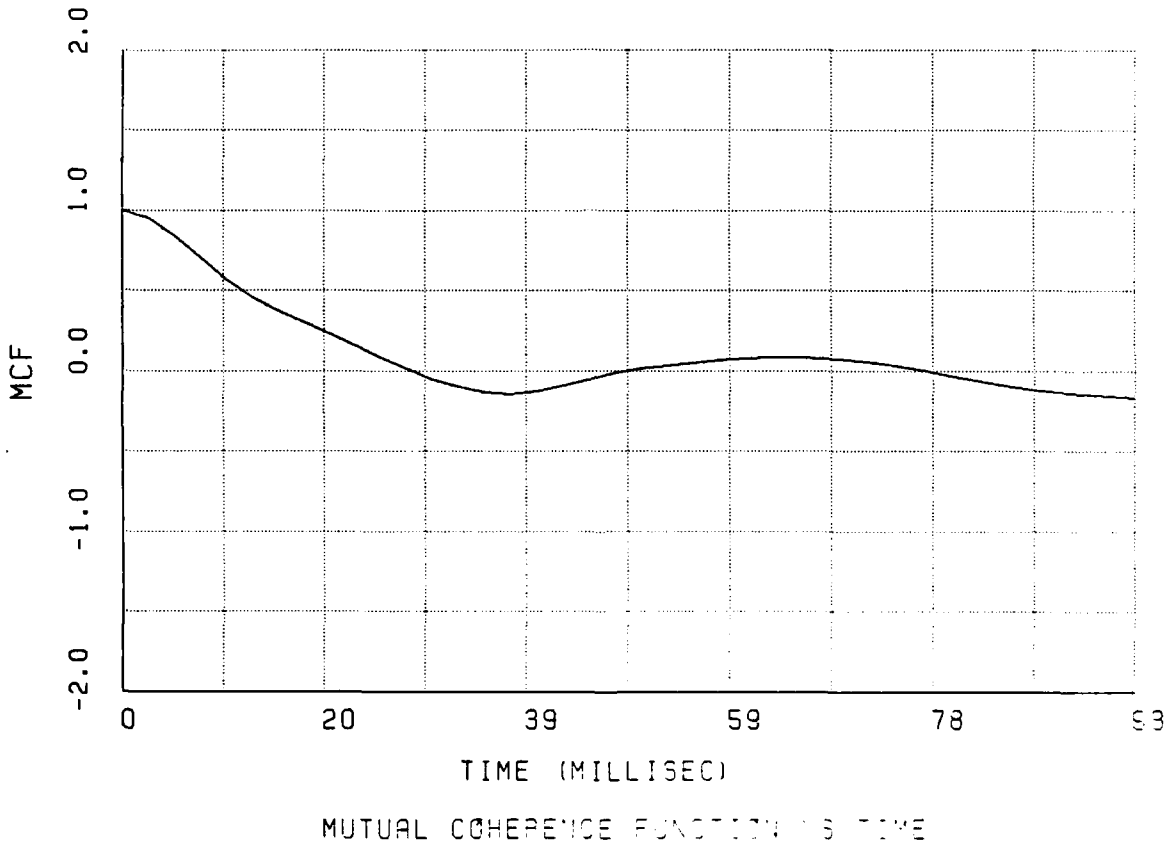

Figure 2-91. Real part of MCF for Segment 3.

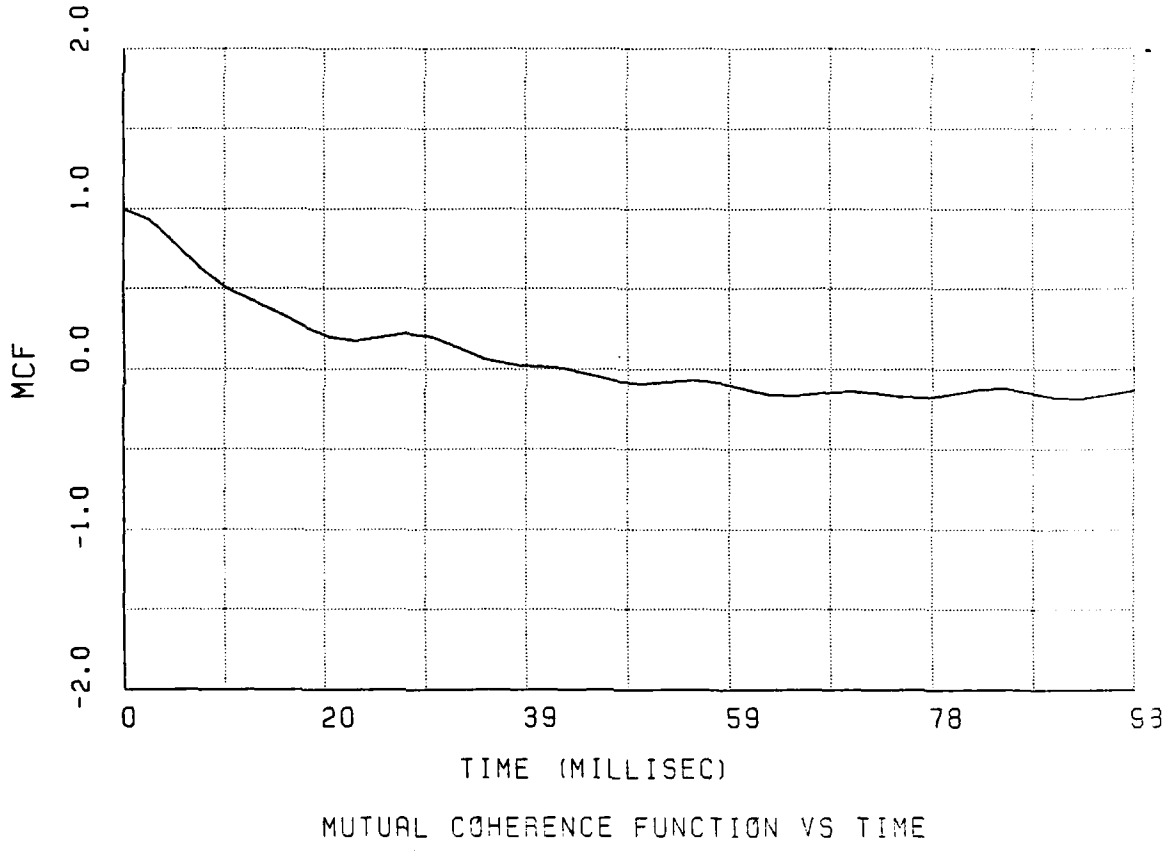

Figure 2-92. Real part of MCF for Segment 4.

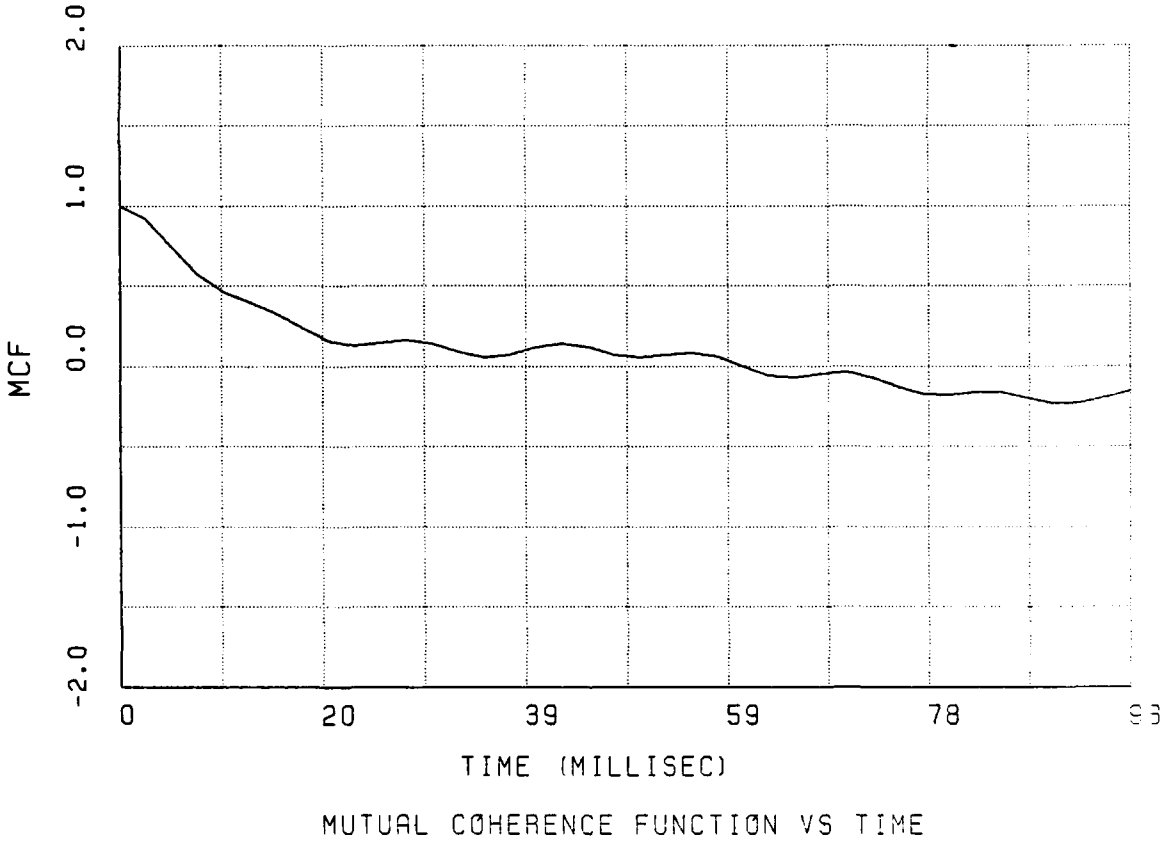

Figure 2-93. Real part of MCF for Segment 5.

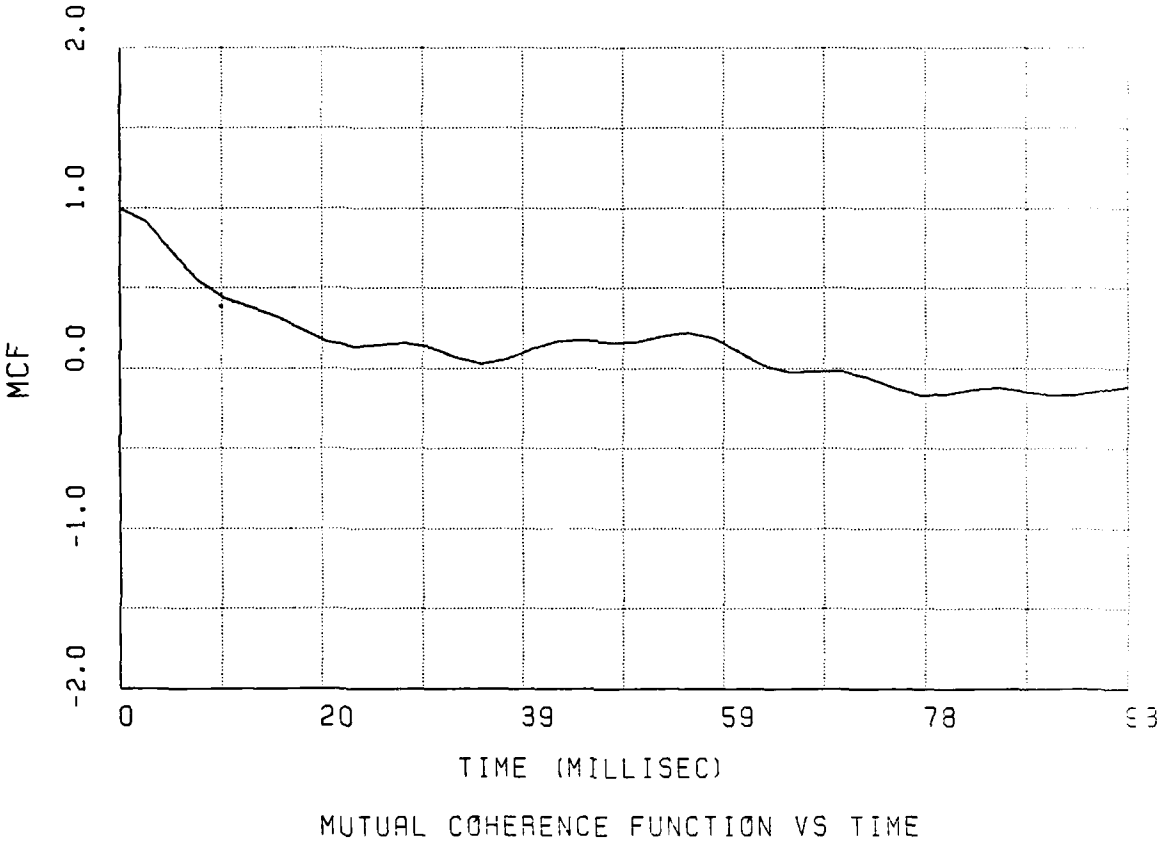

Figure 2-94. Real part of MCF for Segment 6.

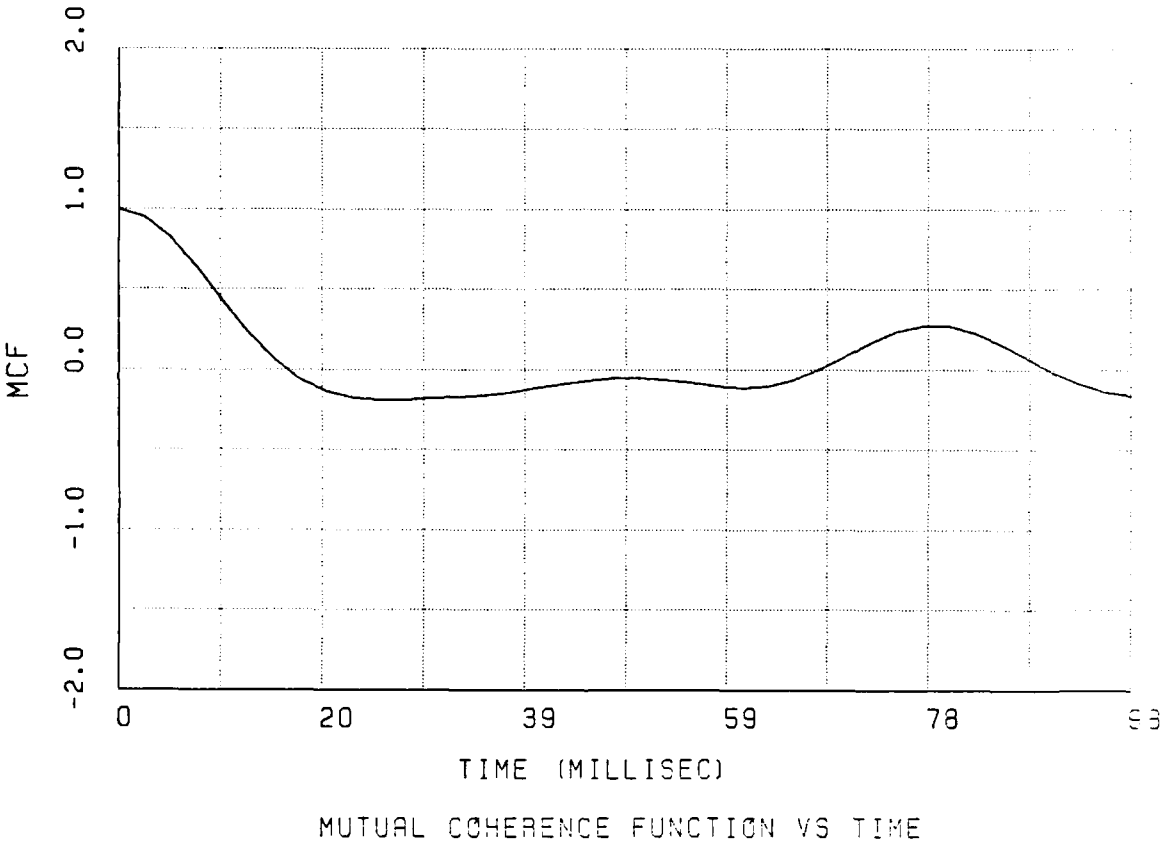

Figure 2-95. Real part of MCF for Segment 7.

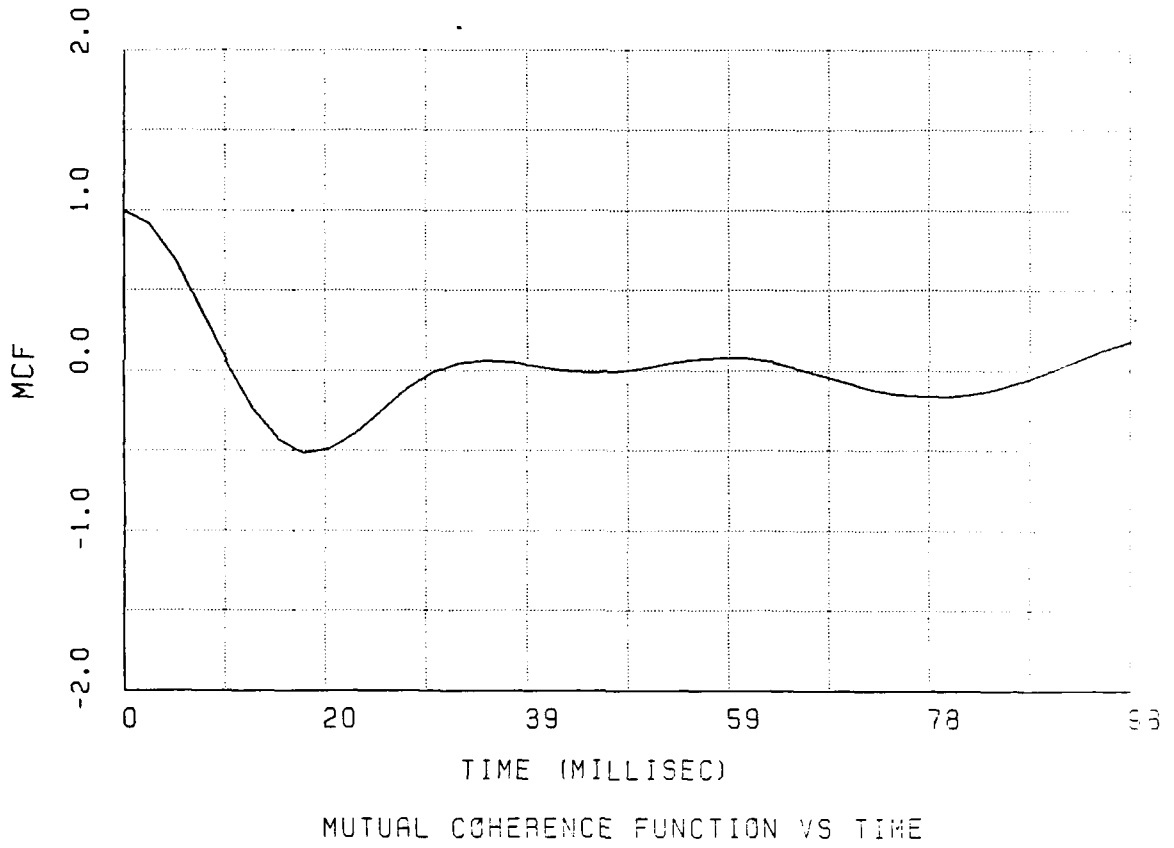

Figure 2-96. Real part of MCF for Segment 8.

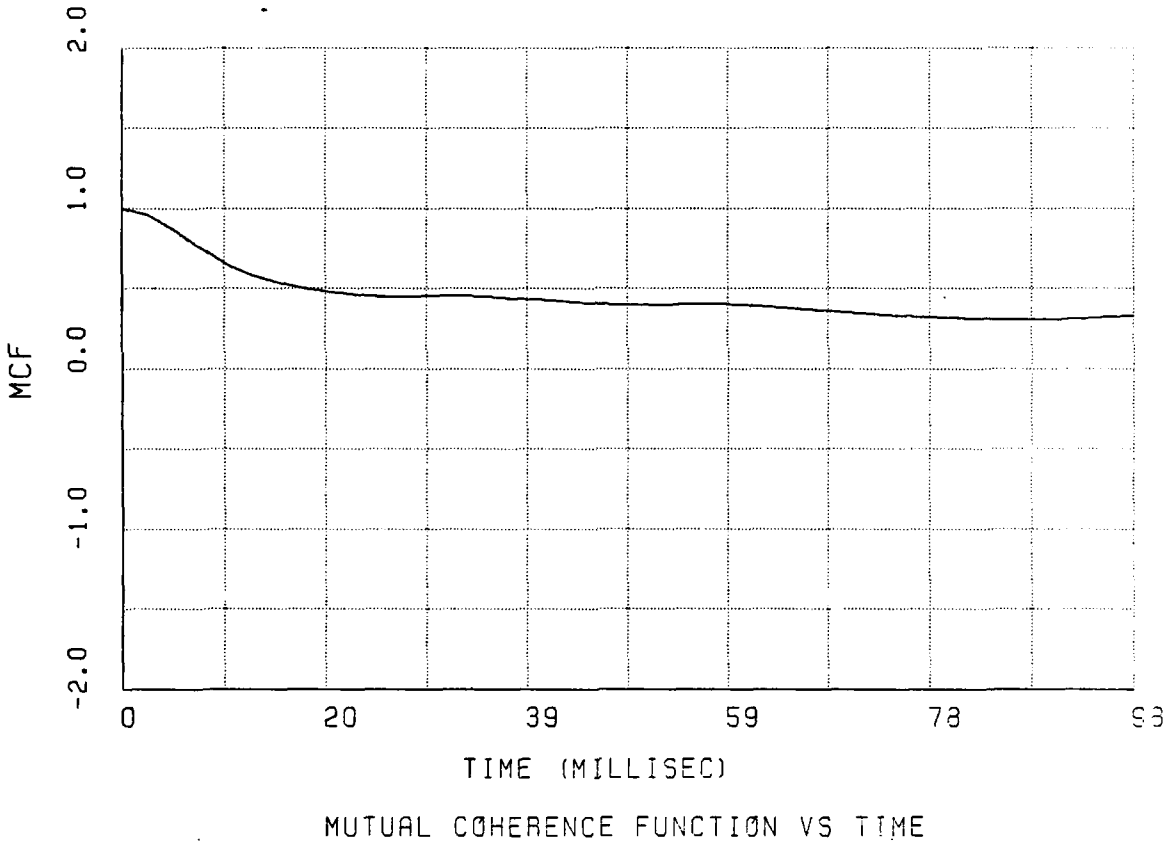

Figure 2-97. Real part of MCF for entire occultation interval.

2.10.3 MCF Data for Symmetric Doppler Spectrum

An examination of the two-sided angular spectrum of the 98-MHz component of the received signal indicates at times a significant asymmetry, showing a preferential angle of arrival of the scattered energy. The magnitude square of the angular spectrum is the power spectrum or the Doppler spectrum, and the transform of the Doppler spectrum is the MCF. Thus, to force a purely real form for the MCF, the Doppler spectrum was artificially constrained to be symmetric about 0 frequency. This was accomplished through averaging of the positive and negative frequencies. For most of the segments, this technique did not substantially alter the data since only approximately 5 to 10 percent of the power in the spectrum was asymmetrically distributed. The two-sided angular spectrum, the MCF, and the structure function are shown in Figures 2-98 through 2-124 for each of the data segments. The structure function is shown as the logarithm of minus the natural log of the MCF.

2.10.4 Comparison With Theory

These data can be compared with the theoretical form, and the in-situ spectral slope and the Rayleigh phase variance can be estimated. Table 2-6 summarizes the results of these calculations. Figure 2-125 shows the theoretical form for the log of the phase structure function corresponding to the forms presented earlier in Section 2.10.1. It is from this function that the slope of the phase PSD roll-off and the best fit to theory can readily be ascertained. In overlaying this figure on the structure function plots, the best fits as summarized in Table 2-6 were derived. Because of the systematic phase trends that distort the MCF, the best fit to theory is expected only over the exponential portion of the MCF at short delay. Accordingly, Figure 2-125 shows the corresponding theoretical form. The best shape is either form C or A when the index is 1.5.

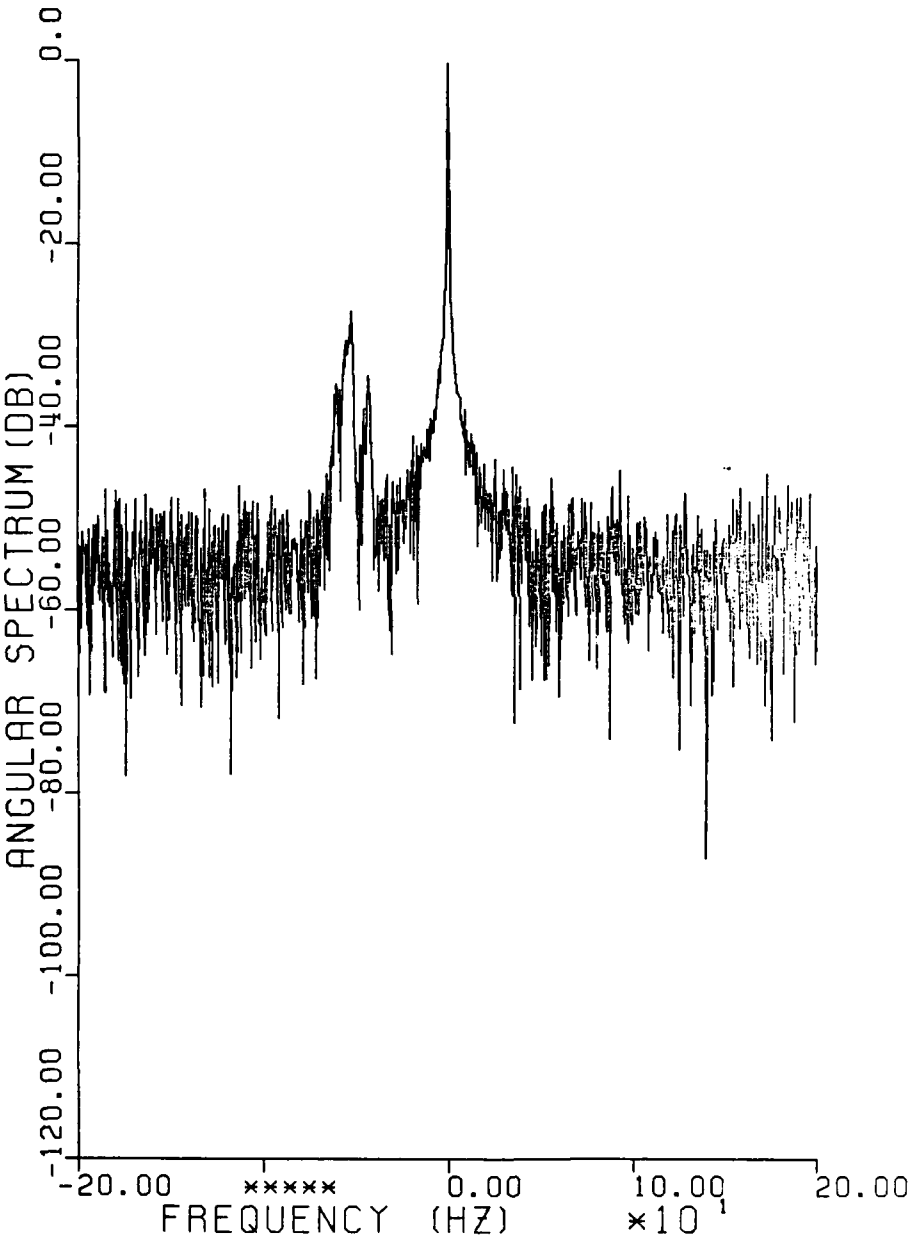

Figure 2-98. Two-sided angular spectrum for Segment 1.

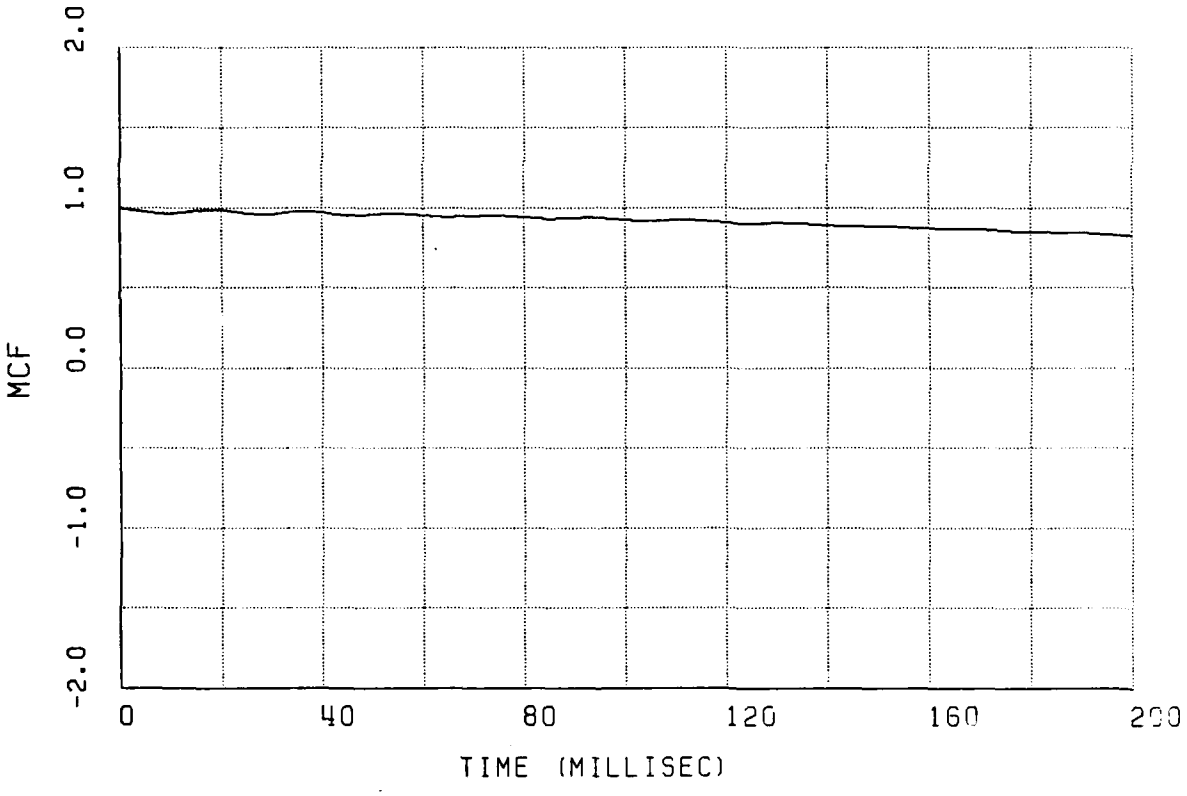

Figure 2-99. Mutual coherence function for Segment 1.

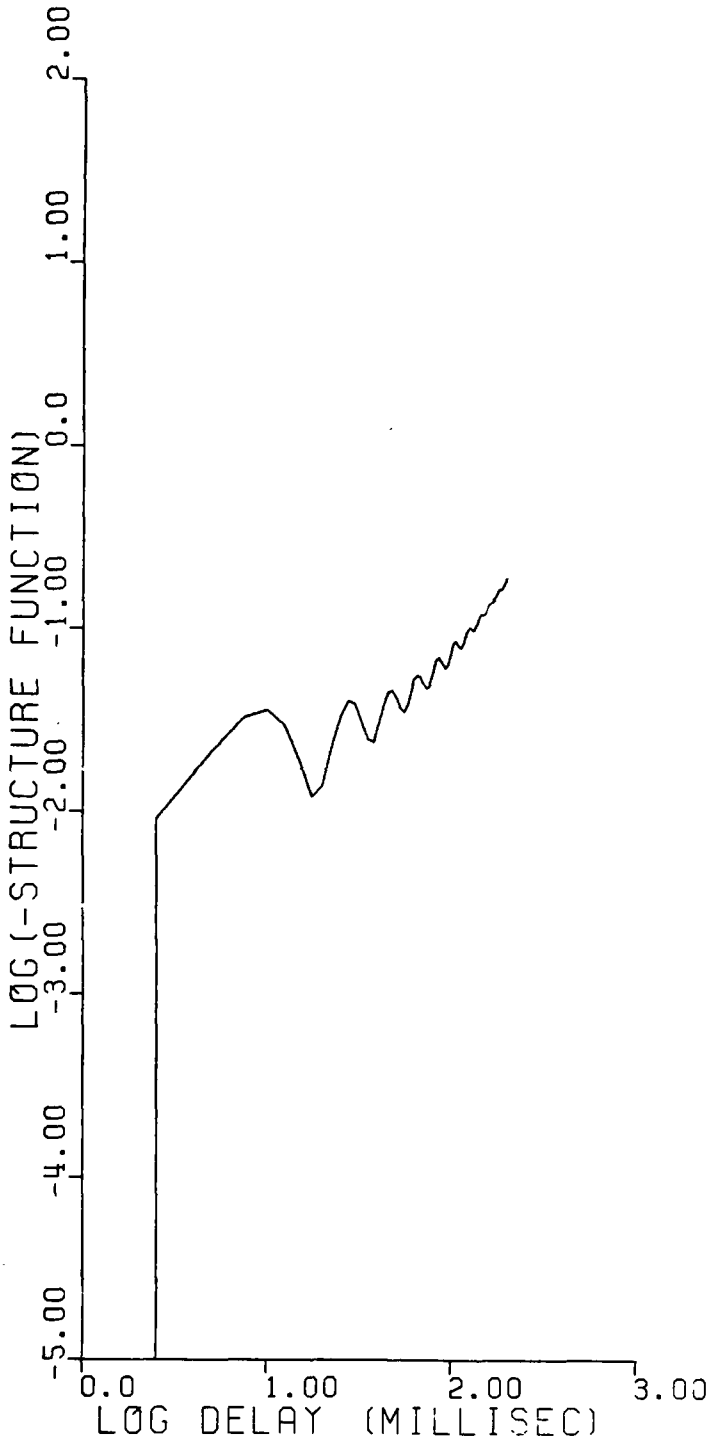

Figure 2-100. Logarithm of phase structure function for Segment 1.

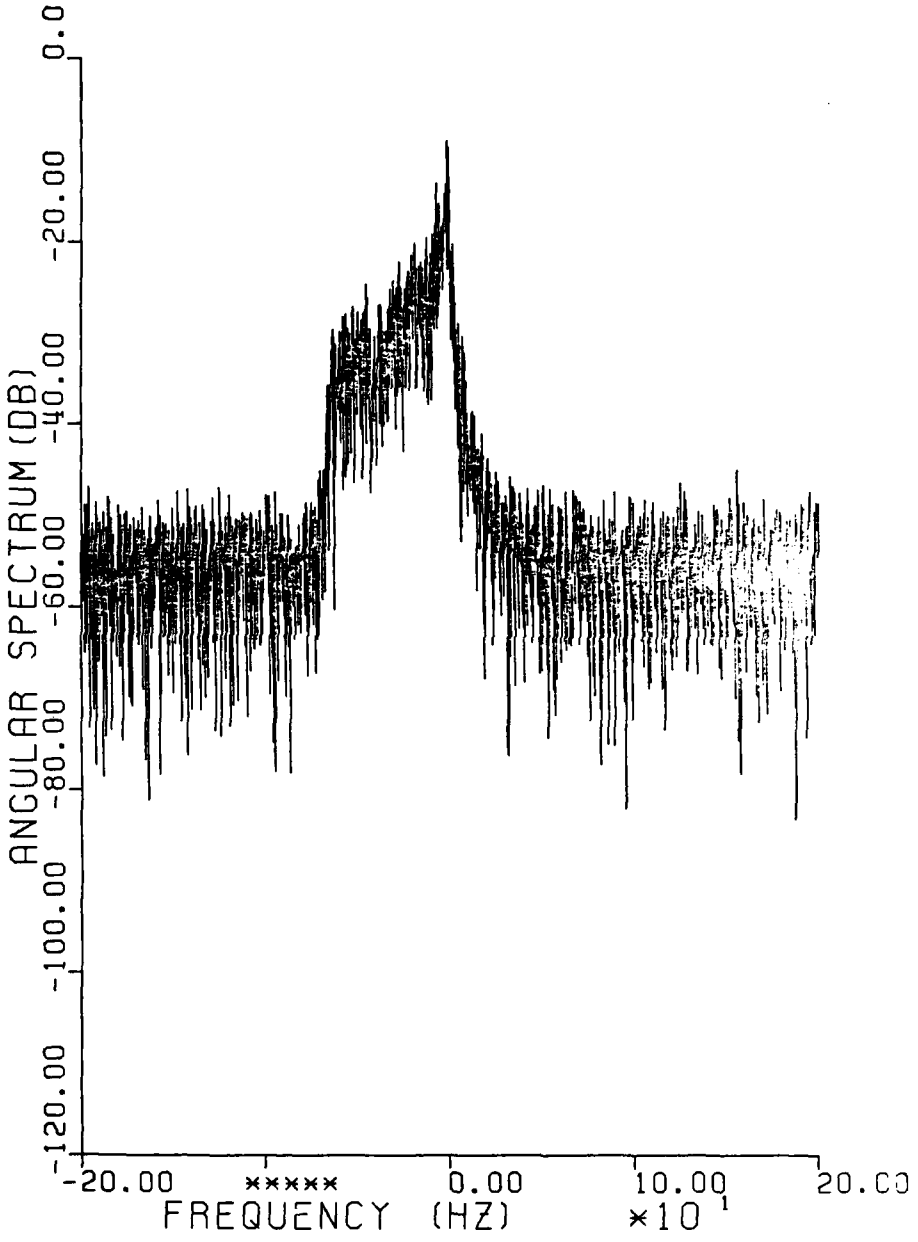

Figure 2-101. Two-sided angular spectrum for Segment 2.

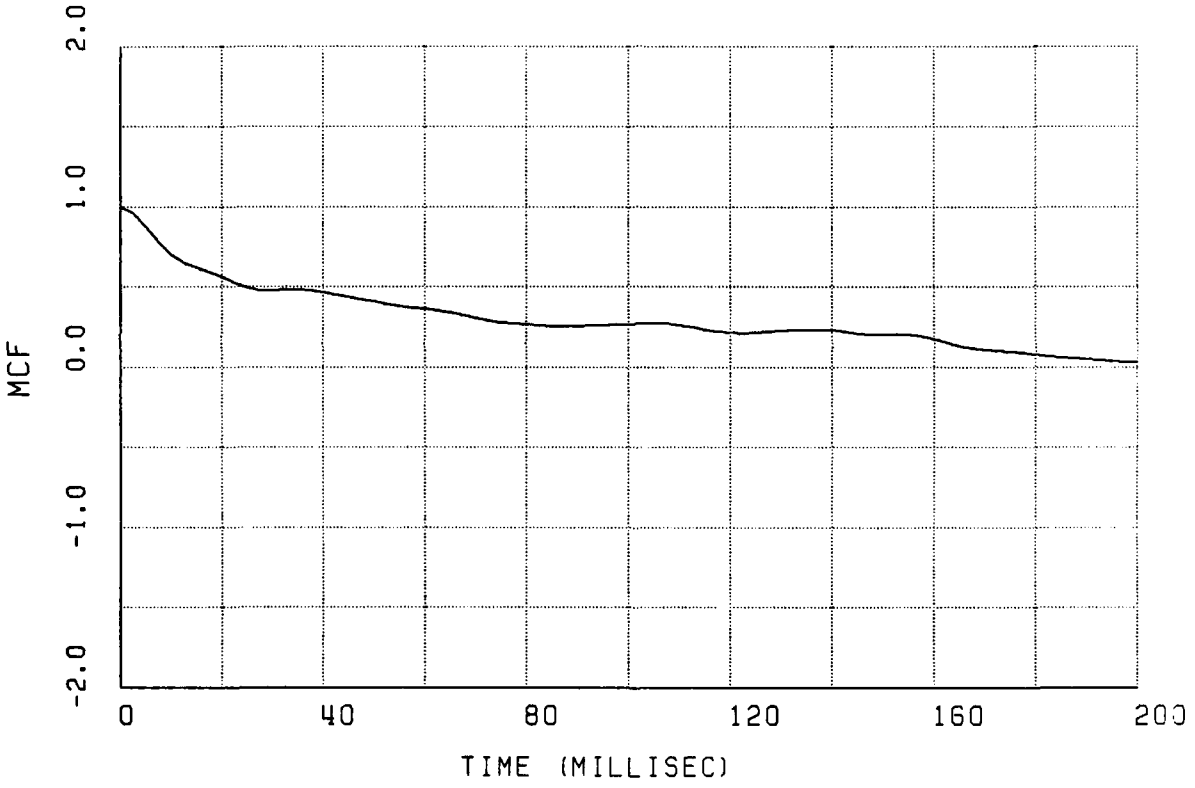

Figure 2-102. Mutual coherence function for Segment 2.

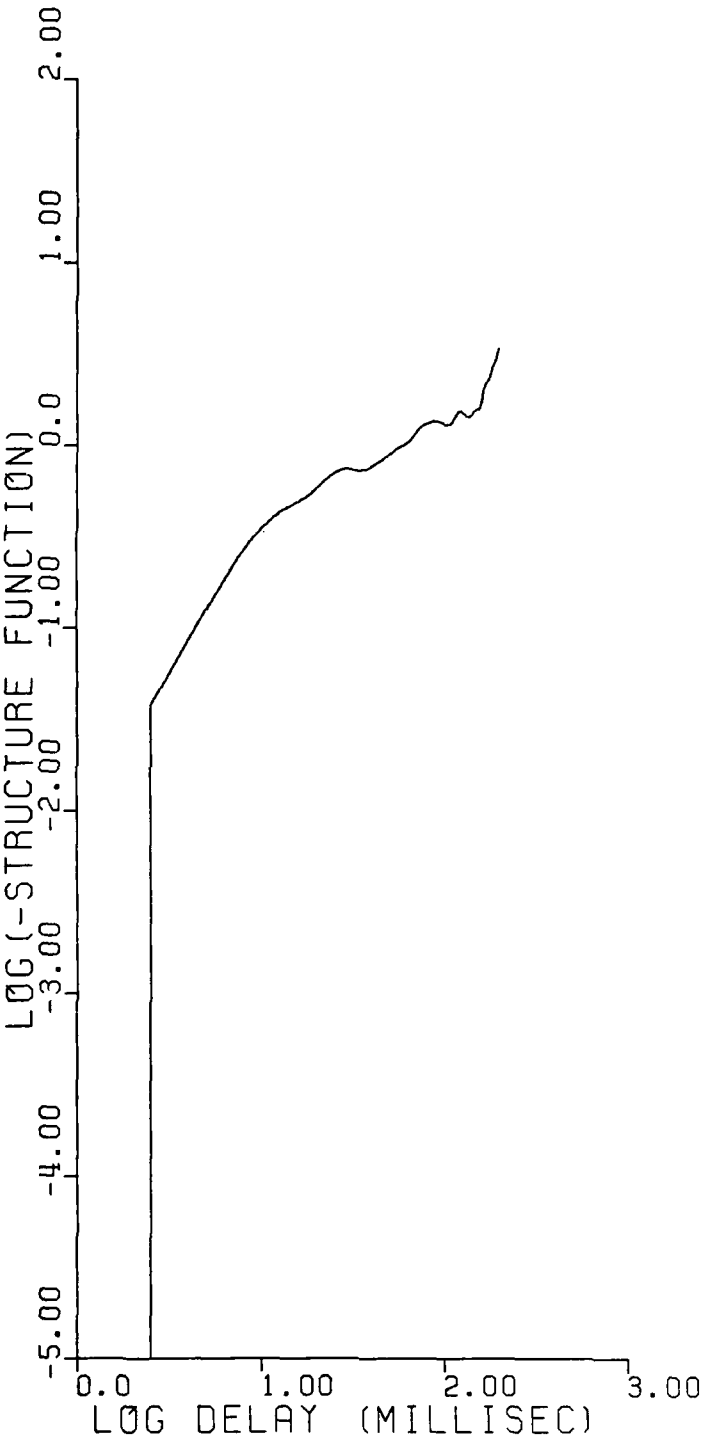

Figure 2-103. Logarithm of phase structure function for Segment 2.

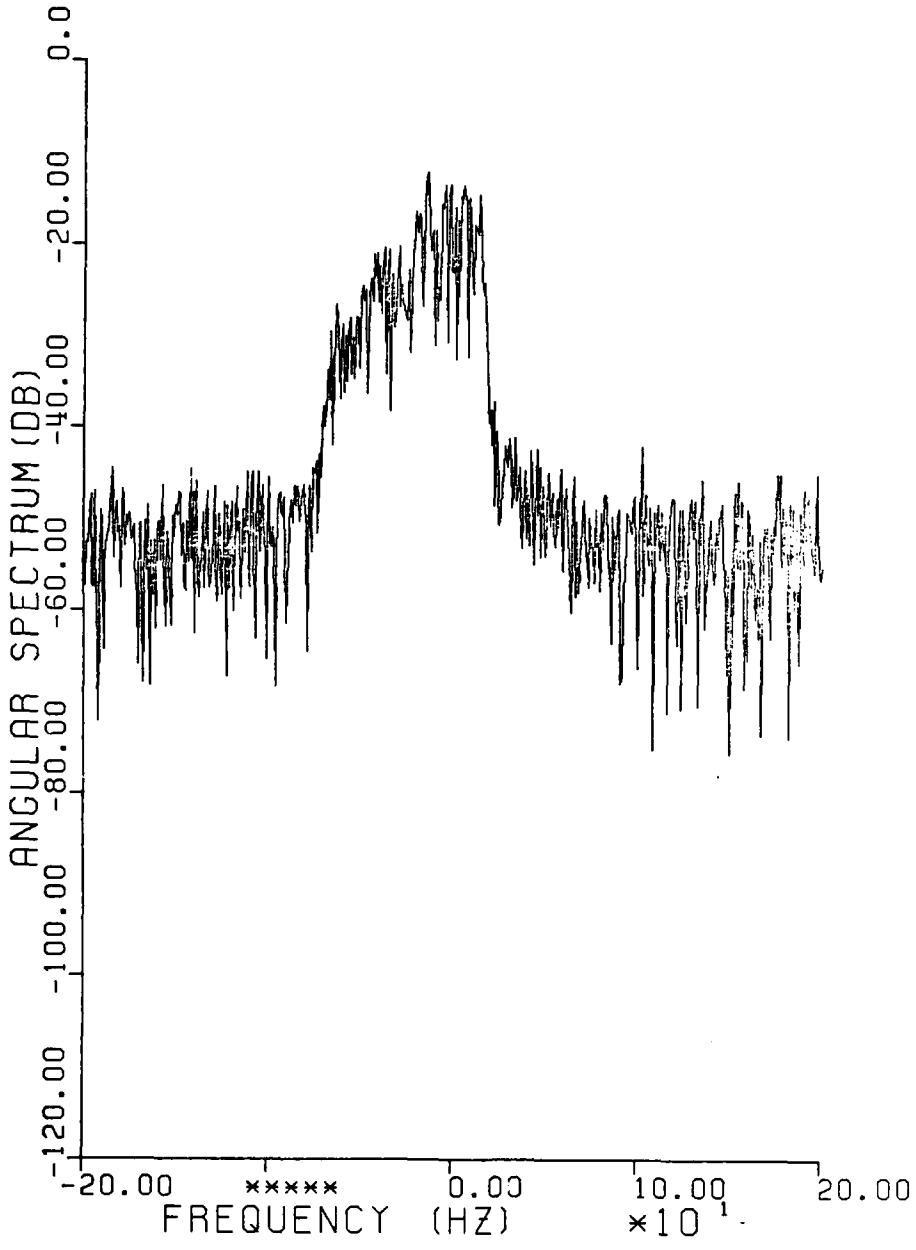

Figure 2-104. Two-sided angular spectrum for Segment 3.

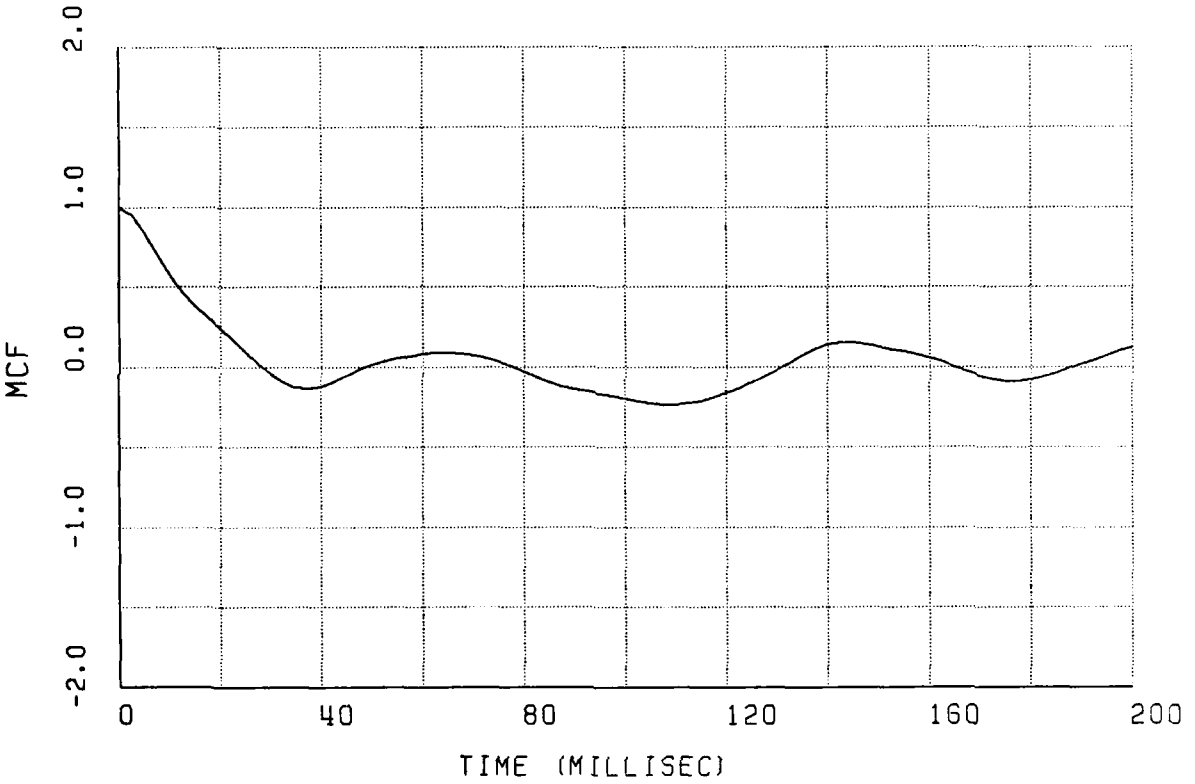

Figure 2-105. Mutual coherence function for Segment 3.

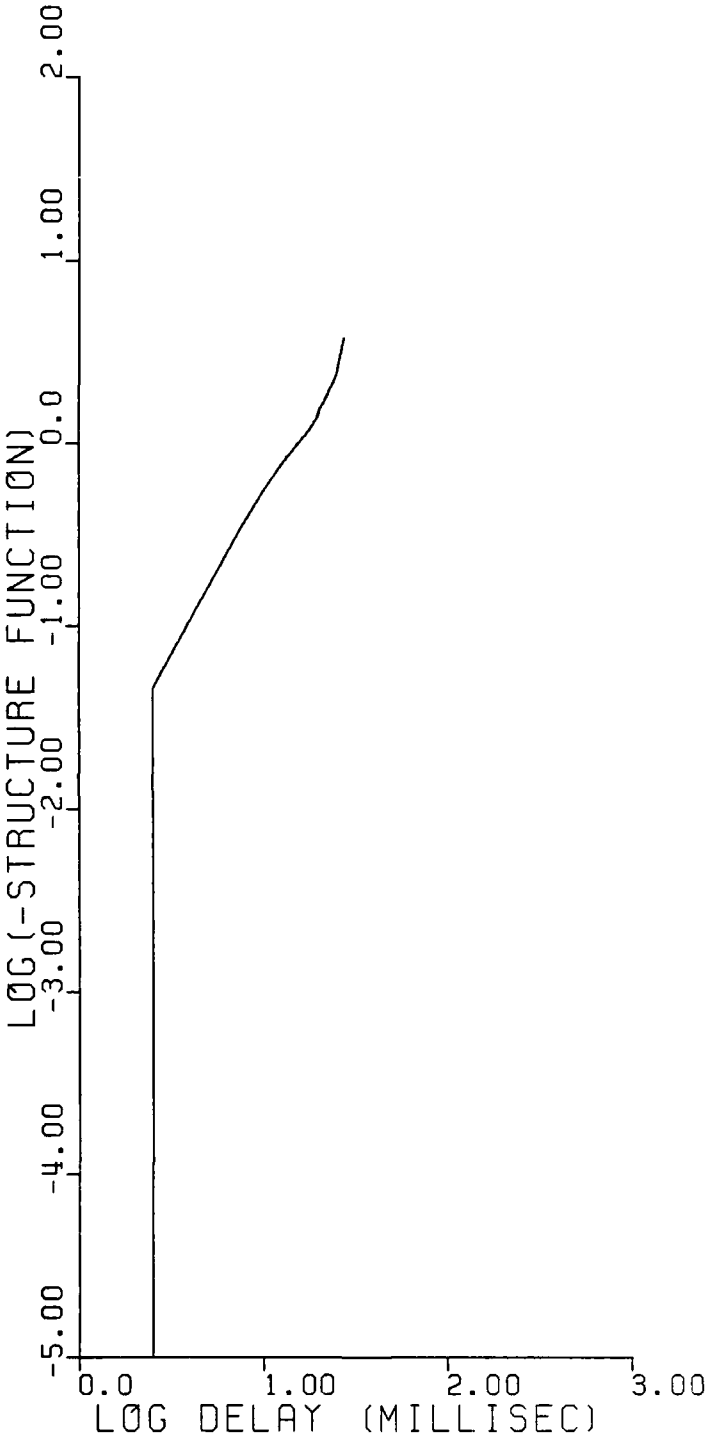

Figure 2-106. Logarithm of phase structure function for Segment 3.

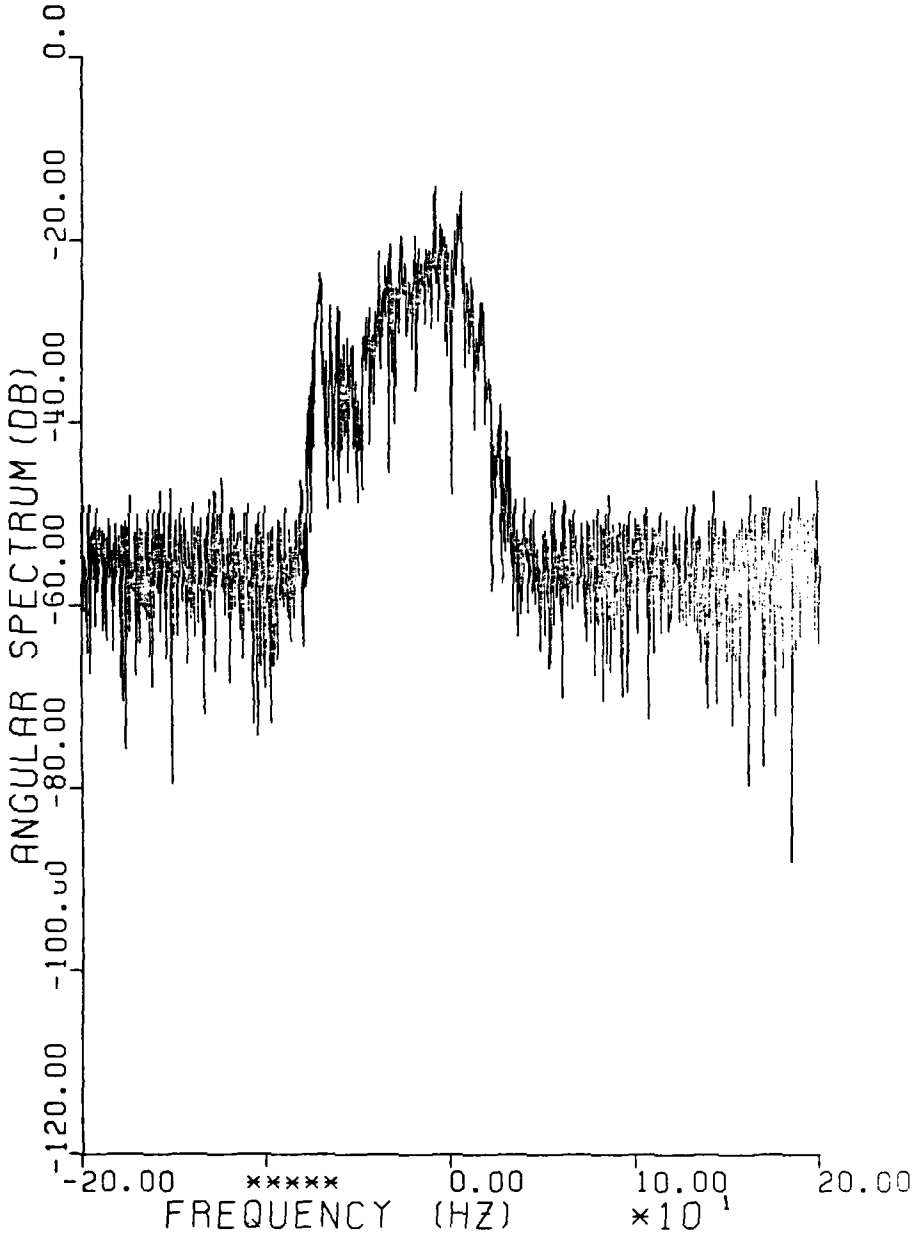

Figure 2-107. Two-sided angular spectrum for Segment 4.

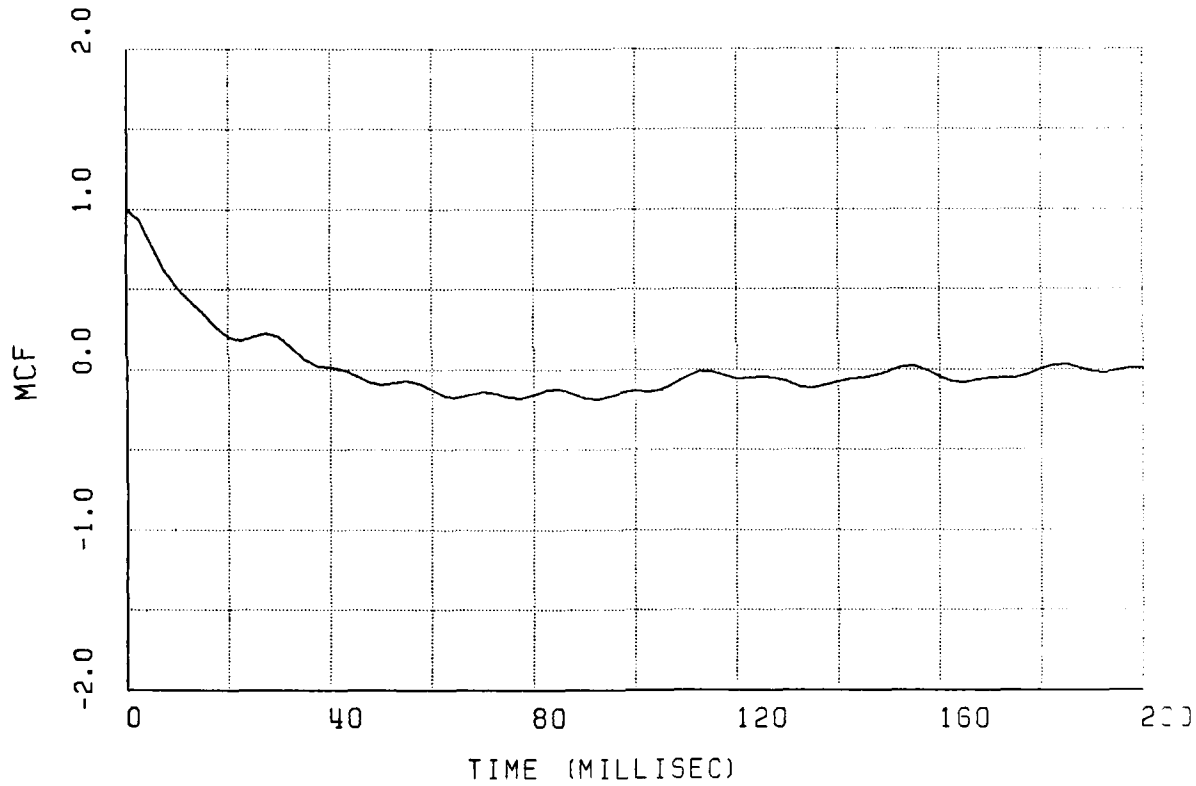

Figure 2-108. Mutual coherence function for Segment 4.

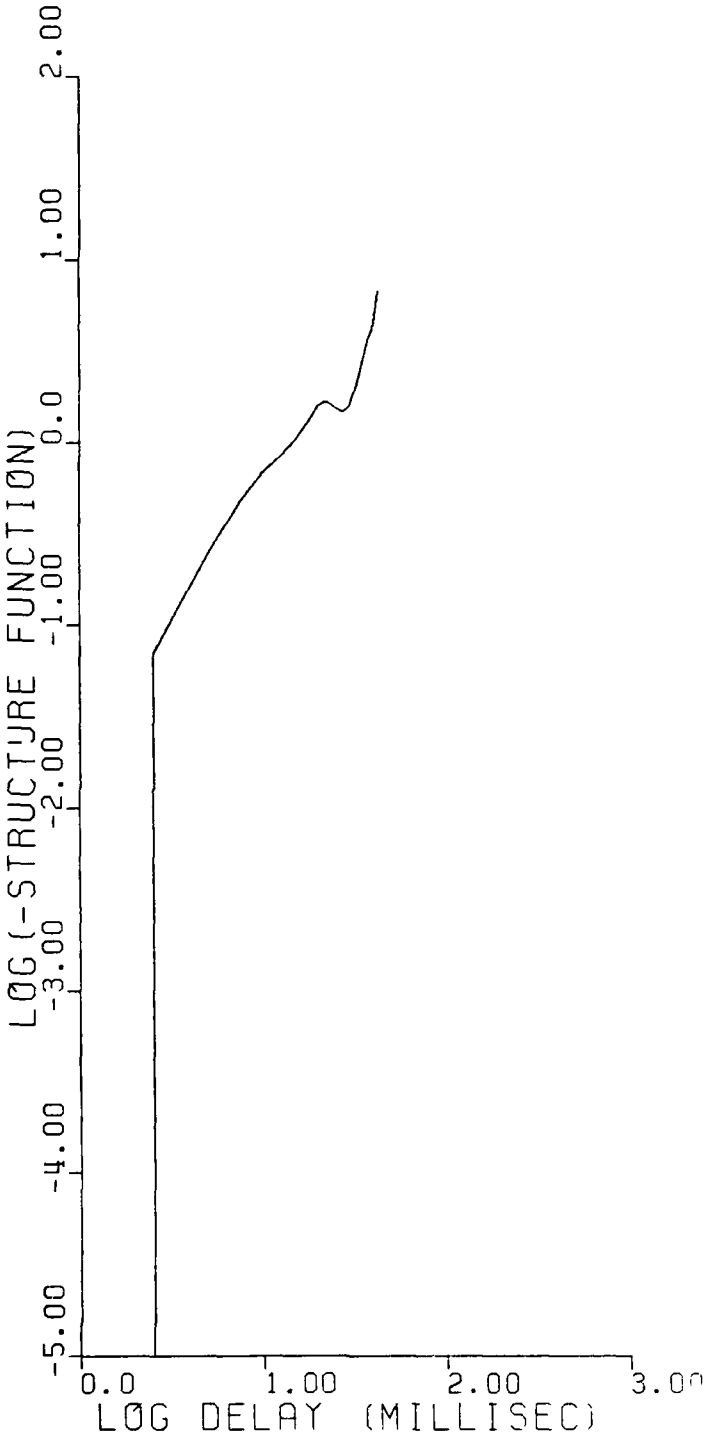

Figure 2-109. Logarithm of phase structure function for Segment 4.

AD-A160 566 PLACES (POSITION LOCATION AND COMMUNICATION EFFECTS SIMULATIONS) BEACON EXPERIMENT TEST RESULTS(U) ESL INC SUNNYVALE CA J MARSHALL ET AL. 01 AUG 84 DNA-TR-84-376 3/5

UNCLASSIFIED DNA001-81-C-0149 F/G 20/14 NL

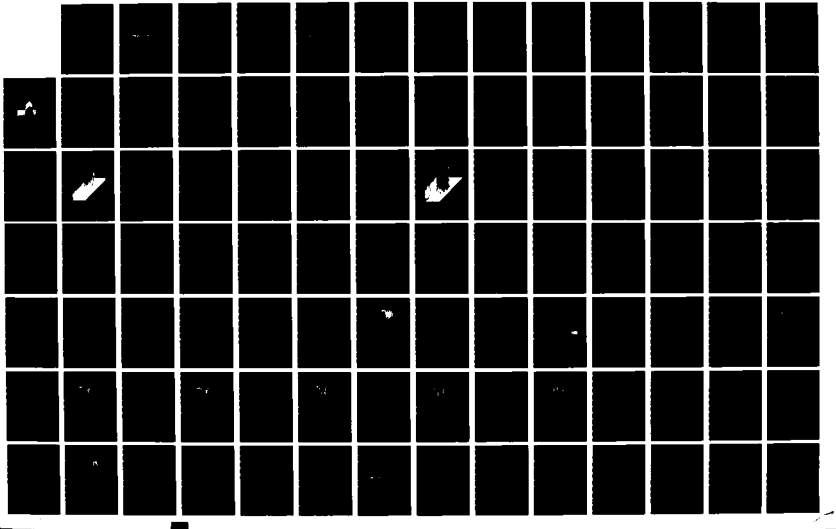

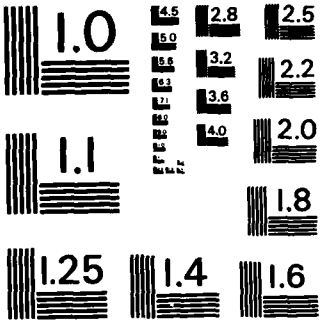

MICROCOPY RESOLUTION TEST CHART
NATIONAL BUREAU OF STANDARDS - 1963 - A

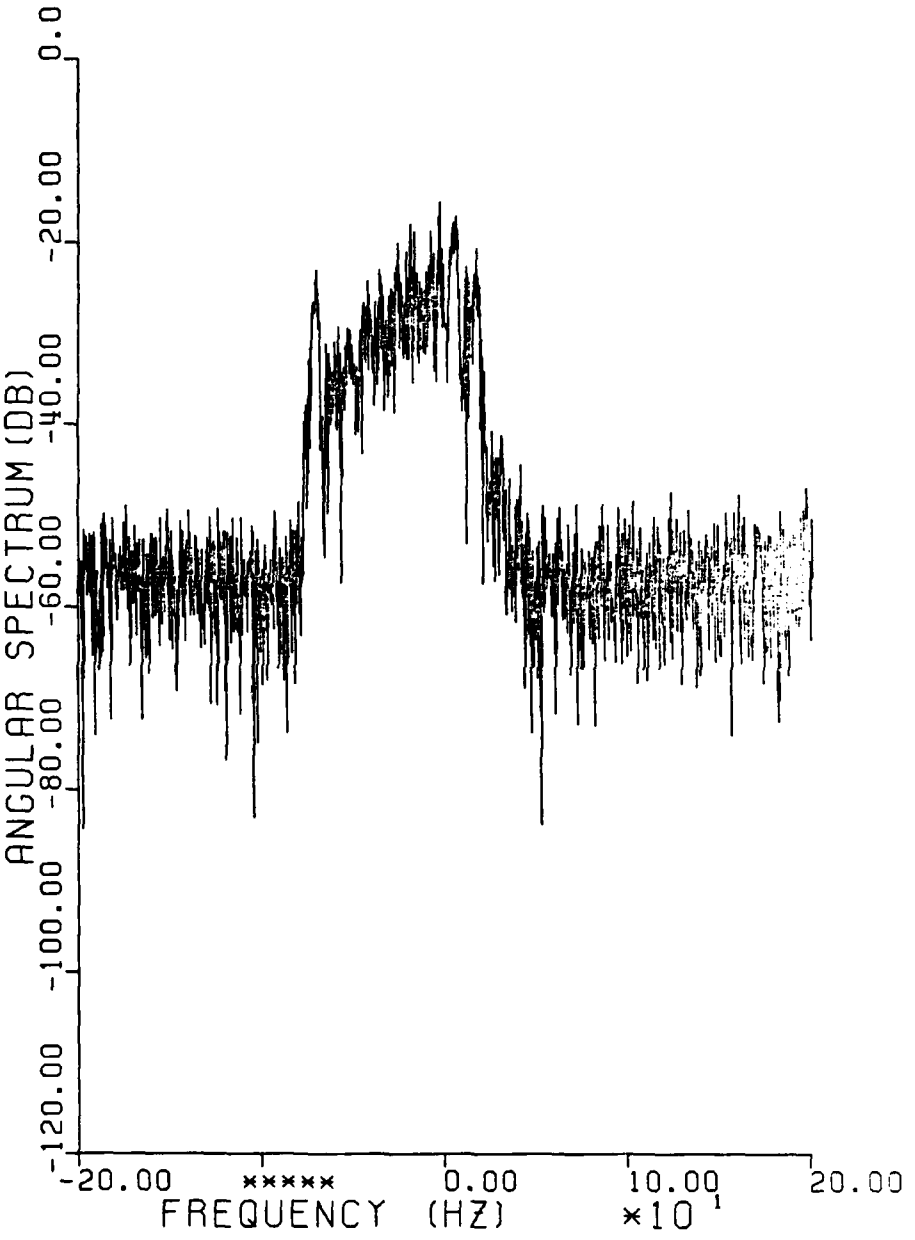

Figure 2-110. Two-sided angular spectrum for Segment 5.

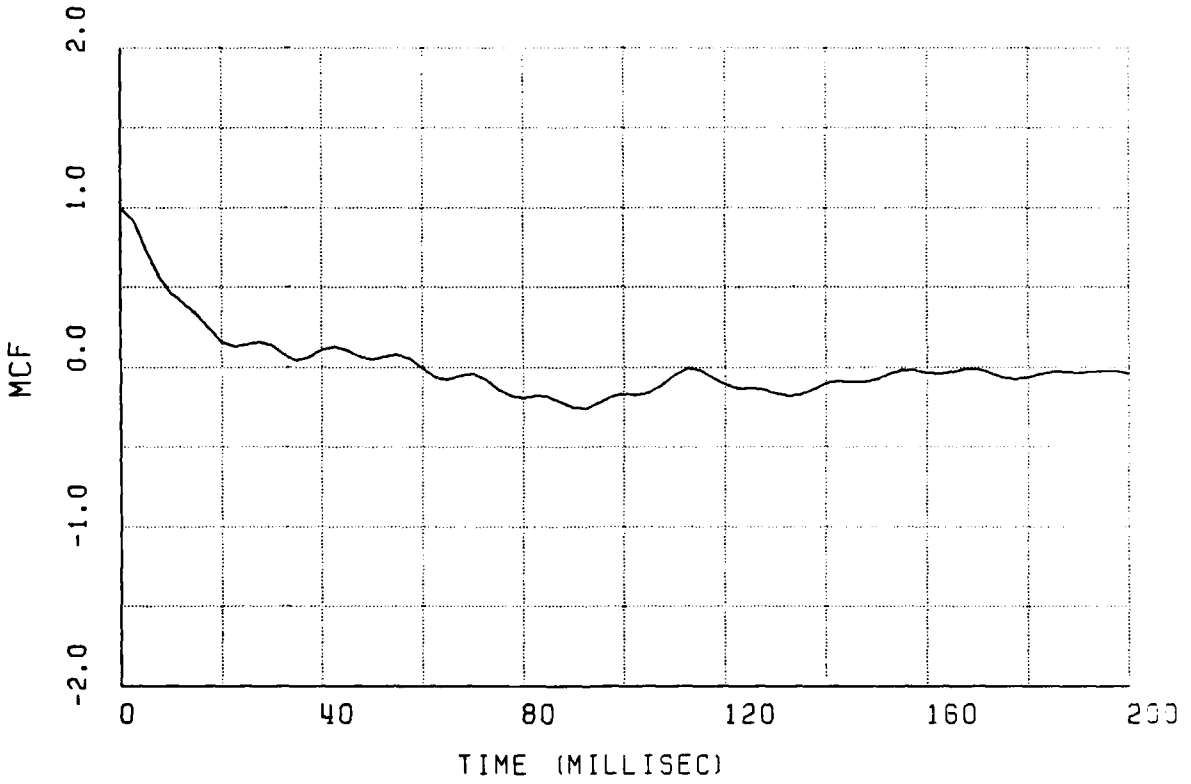

Figure 2-111. Mutual coherence function for Segment 5.

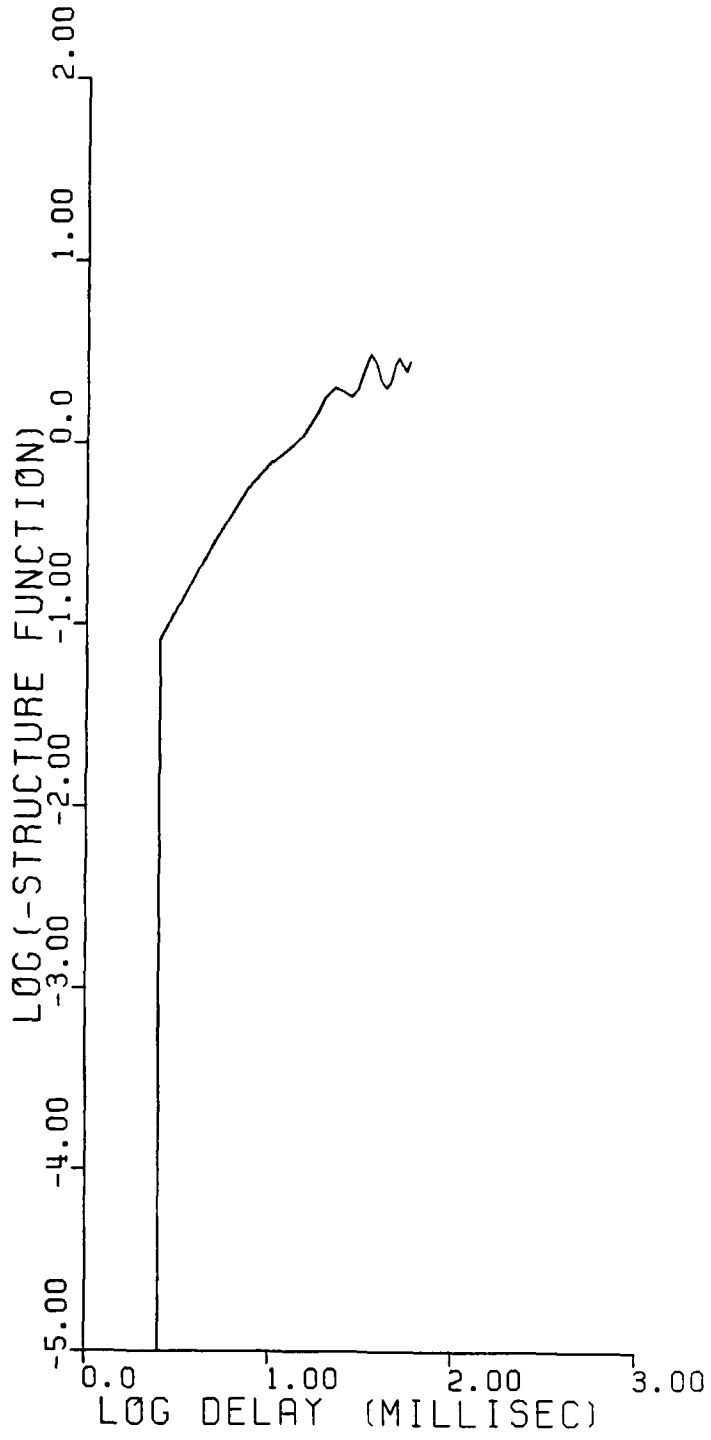

Figure 2-112. Logarithm of phase structure function for Segment 5.

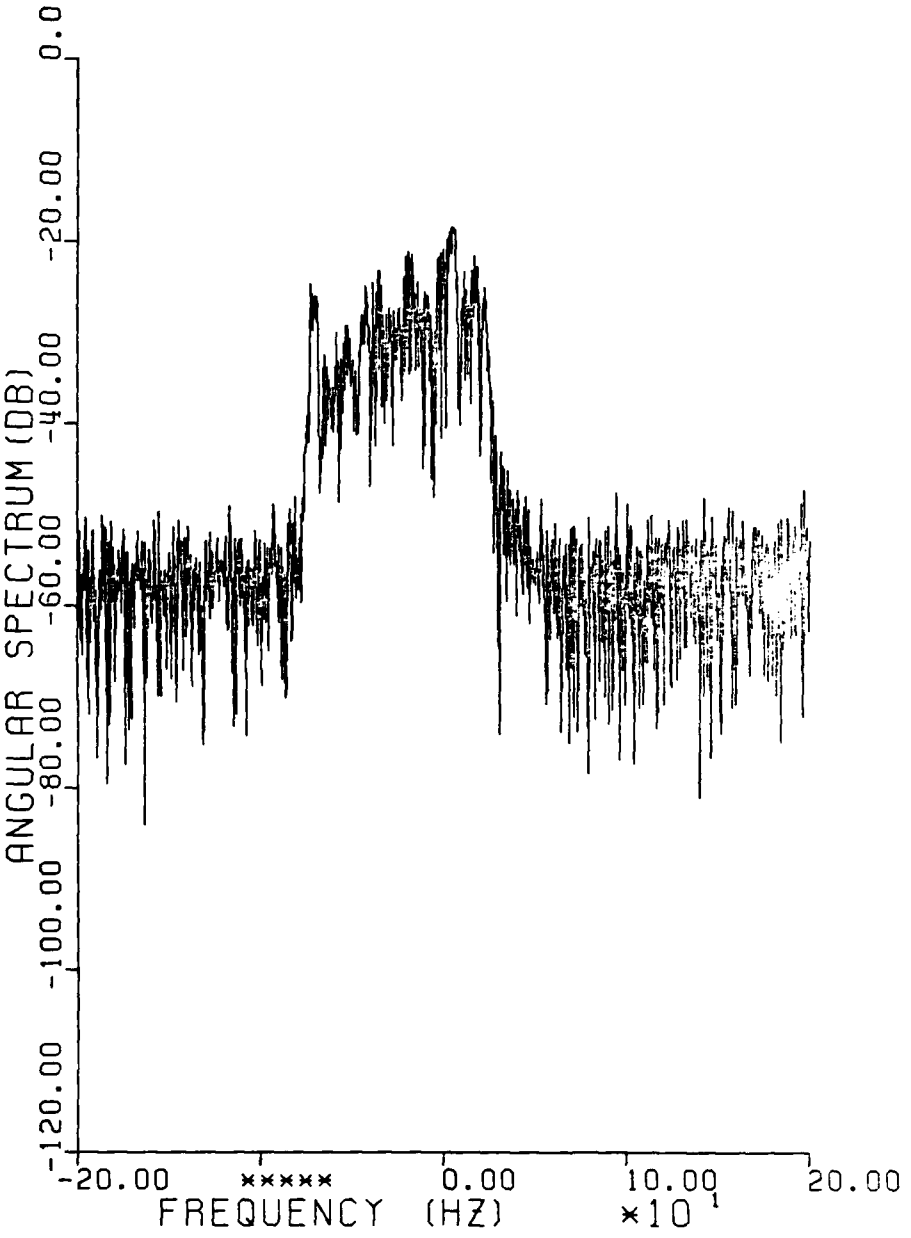

Figure 2-113. Two-sided angular Spectrum for Segment 6.

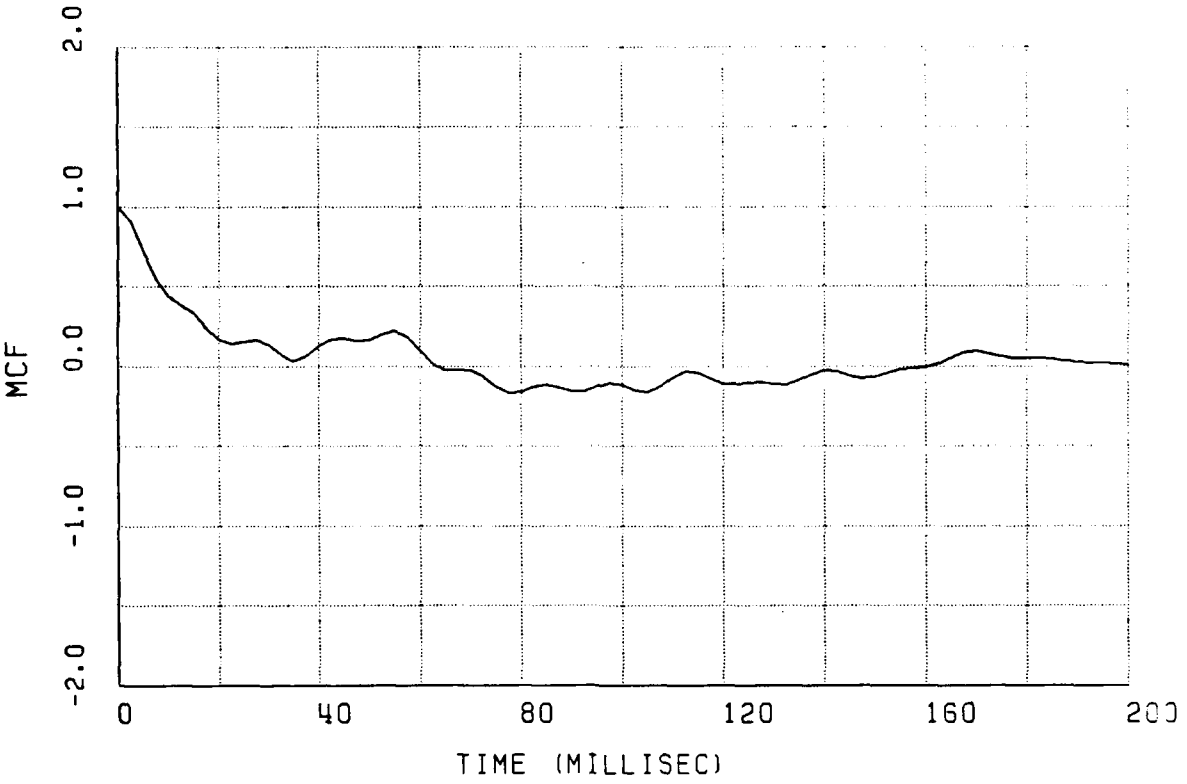

Figure 2-114. Mutual coherence function for Segment 6.

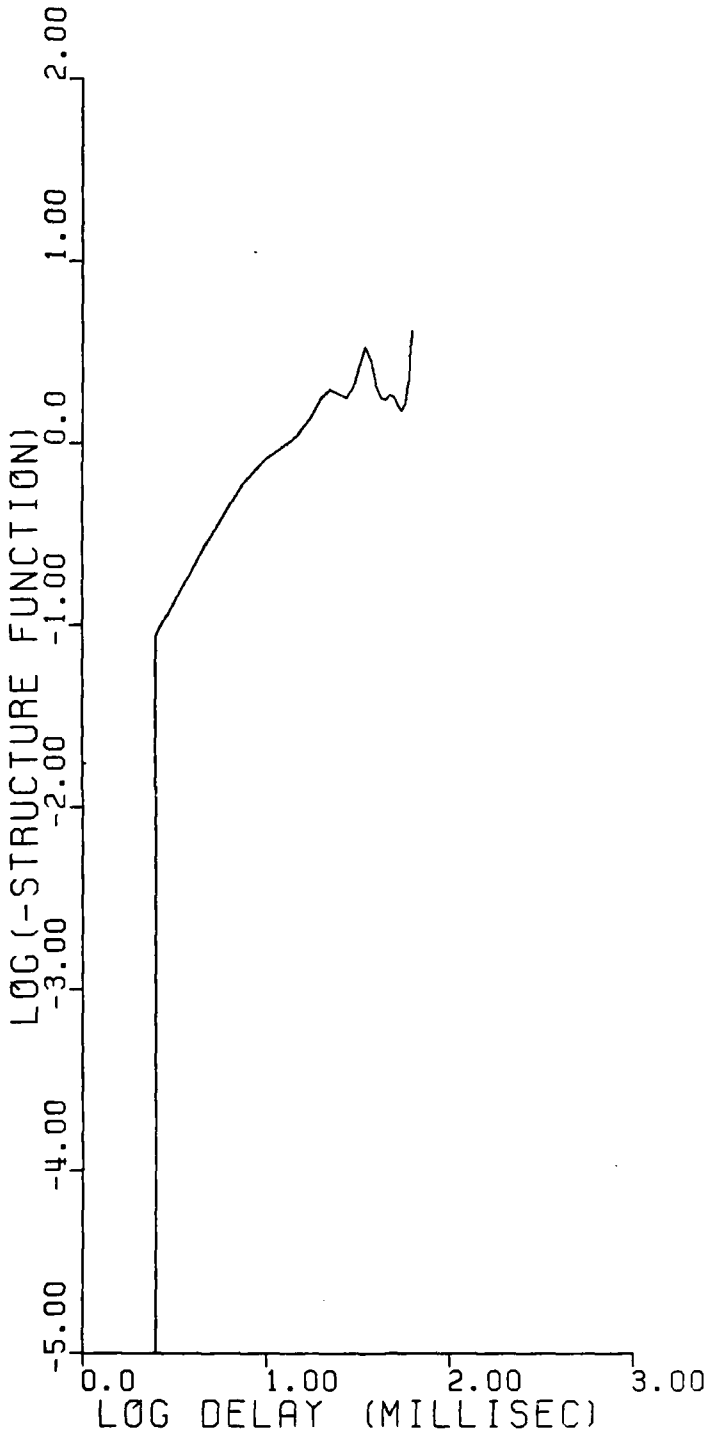

Figure 2-115. Logarithm of phase structure function for Segment 6.

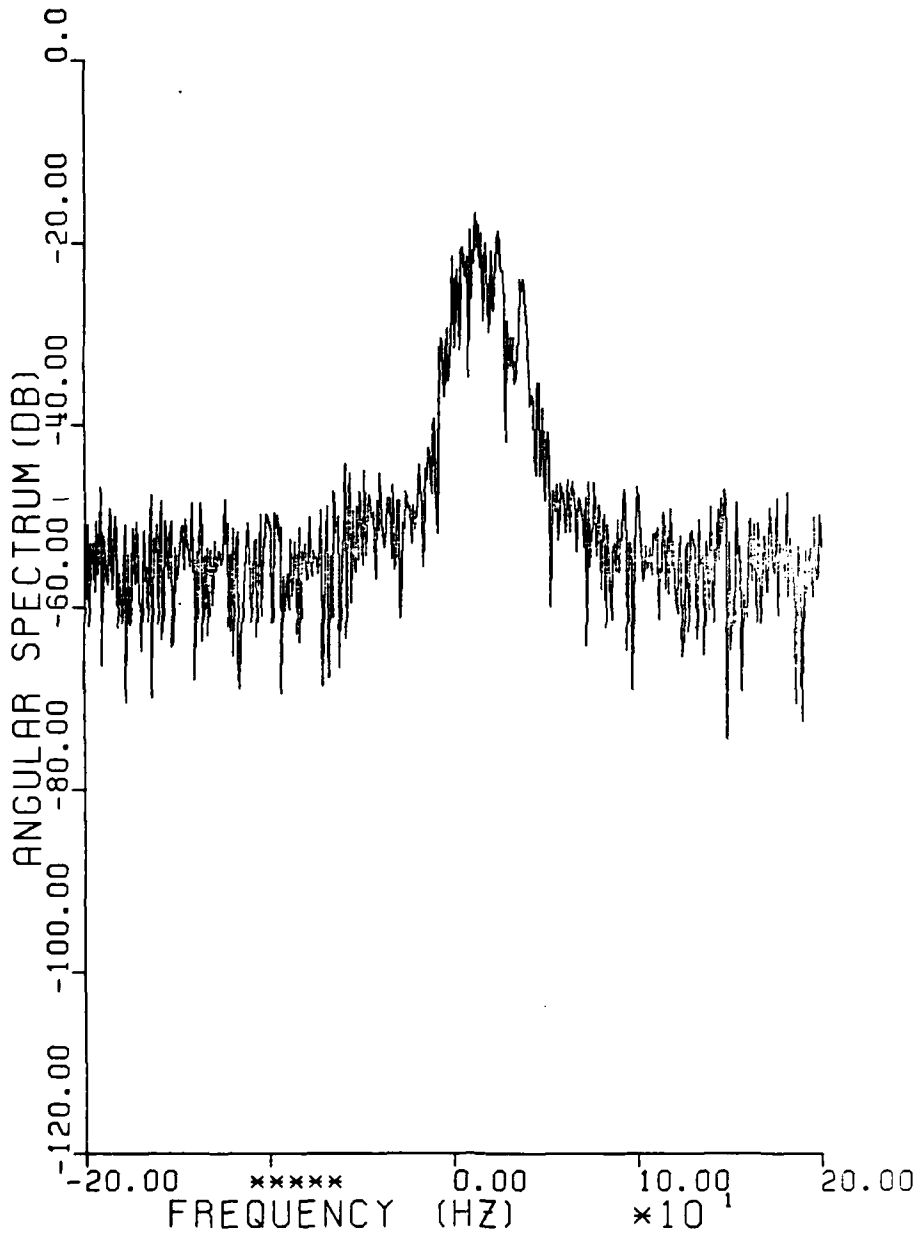

Figure 2-116. Two-sided angular spectrum for Segment 7.

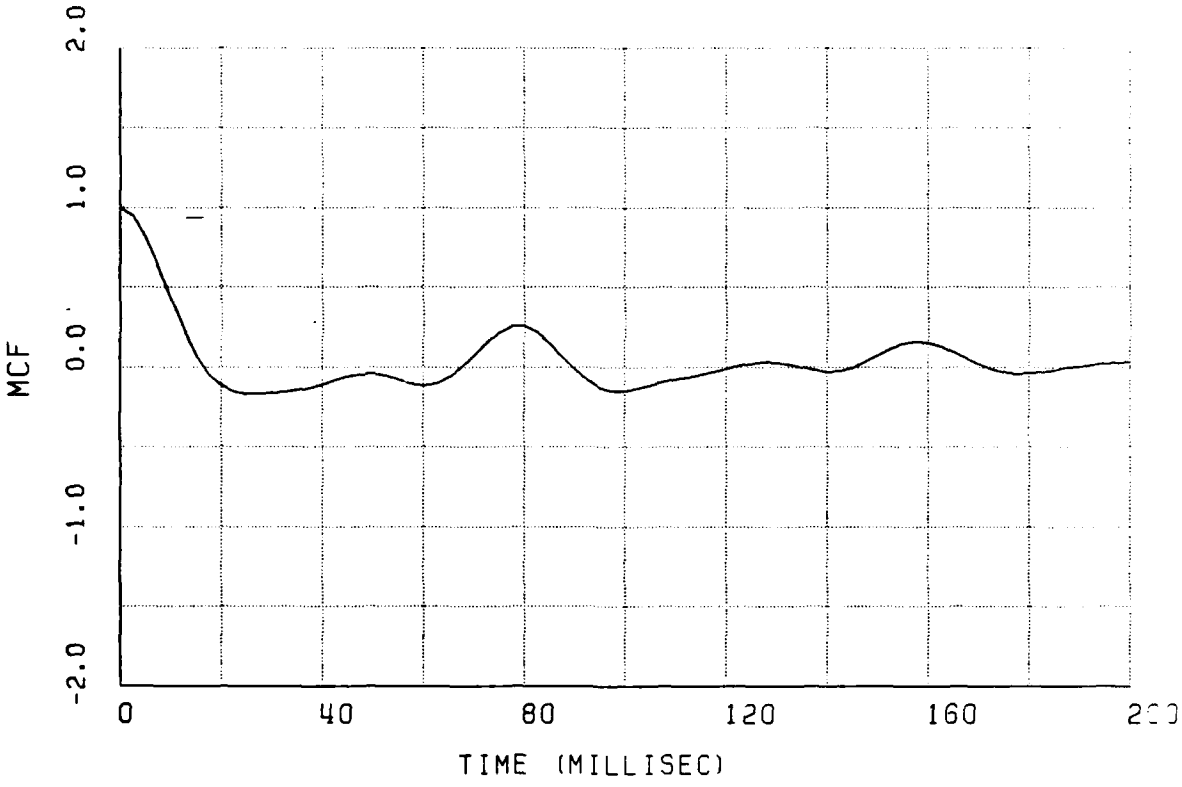

Figure 2-117. Mutual coherence function for Segment 7.

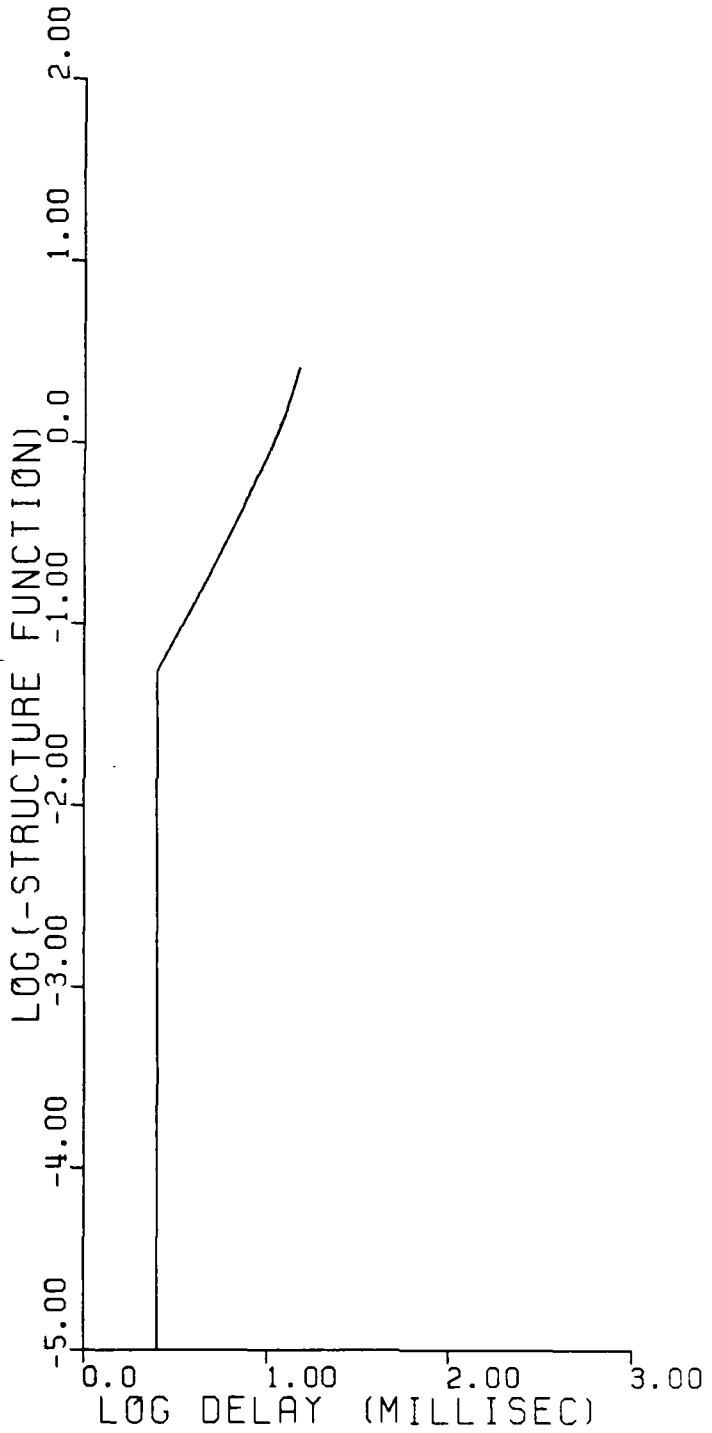

Figure 2-118. Logarithm of phase structure function for Segment 7.

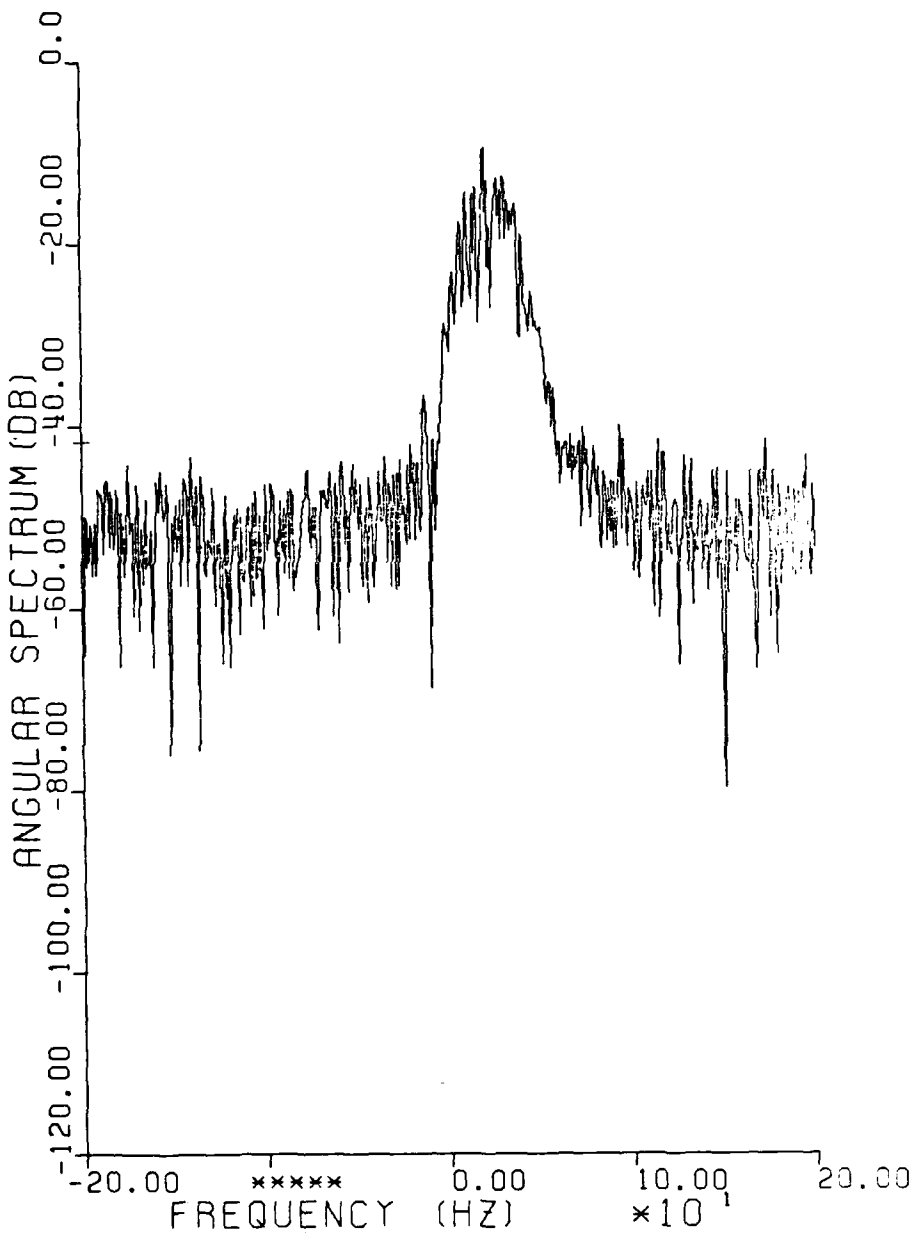

Figure 2-119. Two-sided angular spectrum for Segment 8.

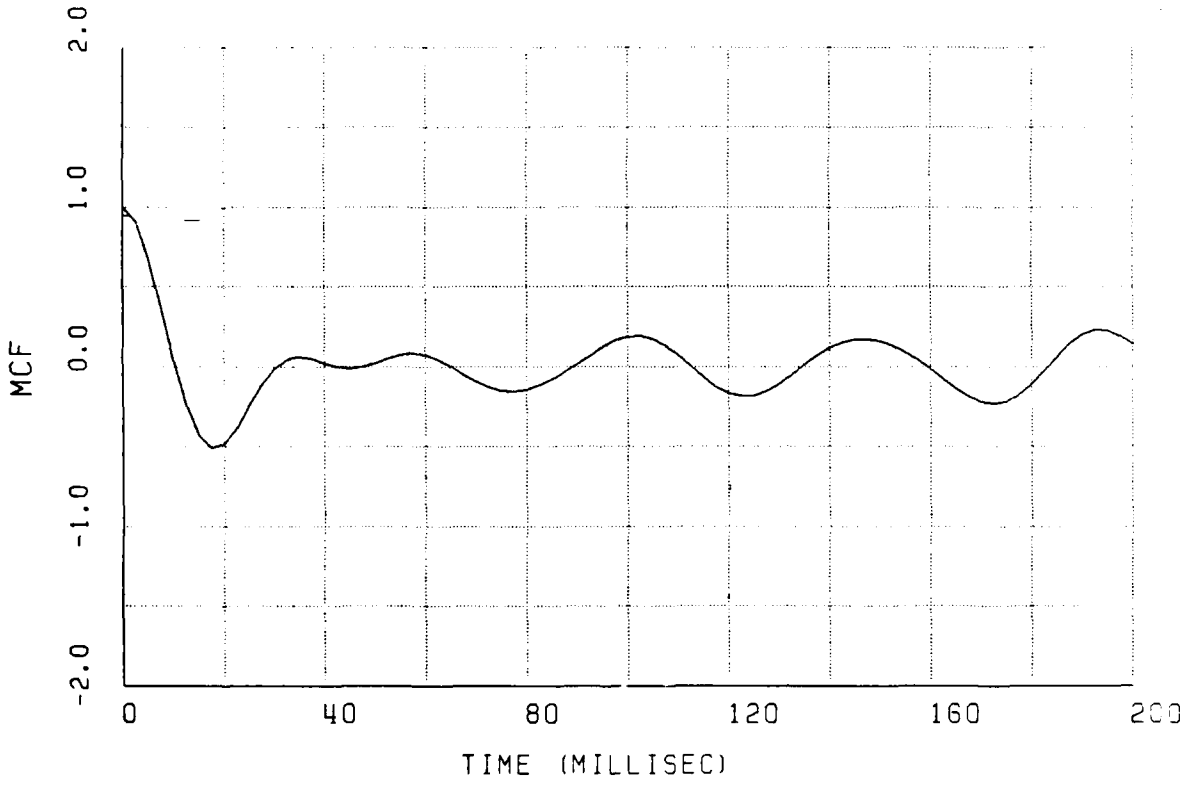

Figure 2-120. Mutual coherence function for Segment 8.

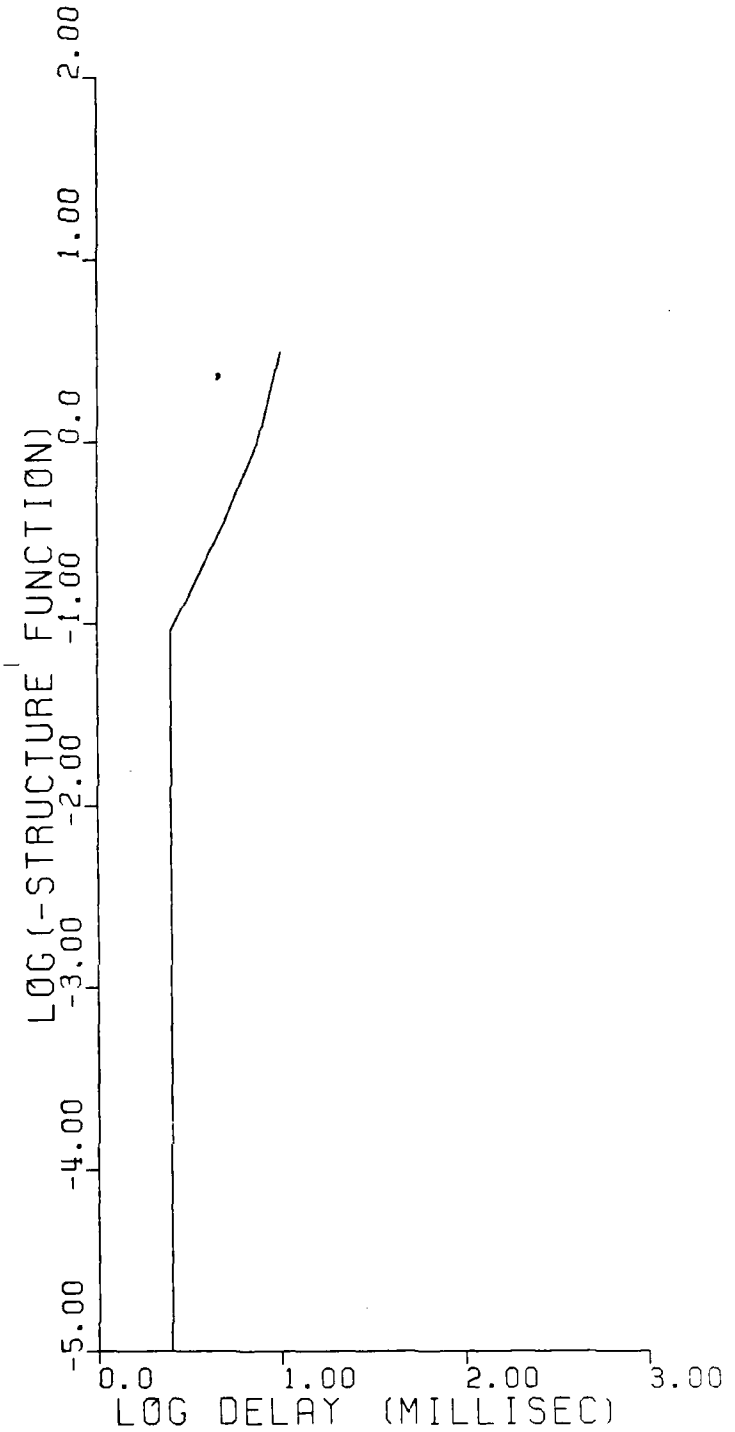

Figure 2-121. Logarithm of phase structure function for Segment 8.

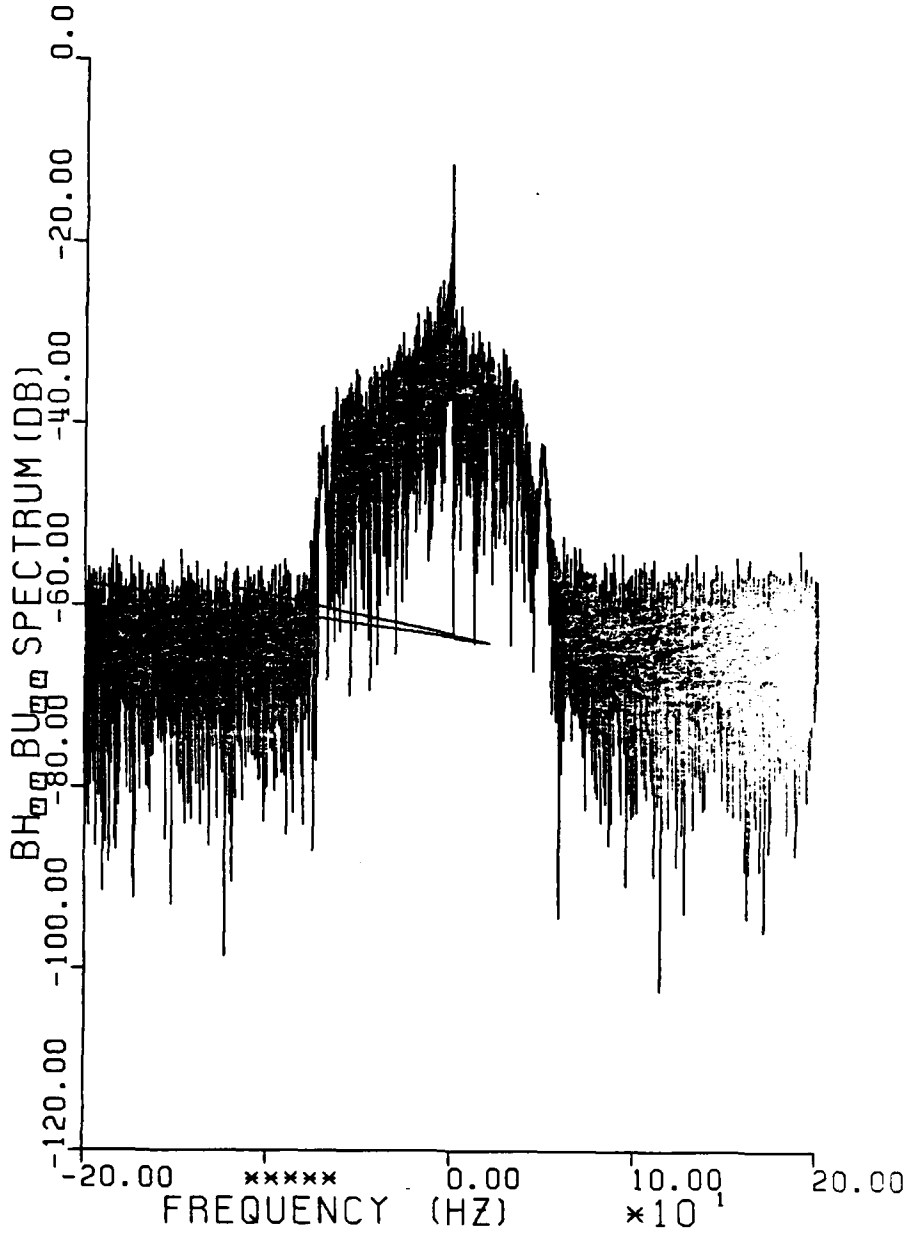

Figure 2-122. Two-sided angular spectrum for entire occultation interval.

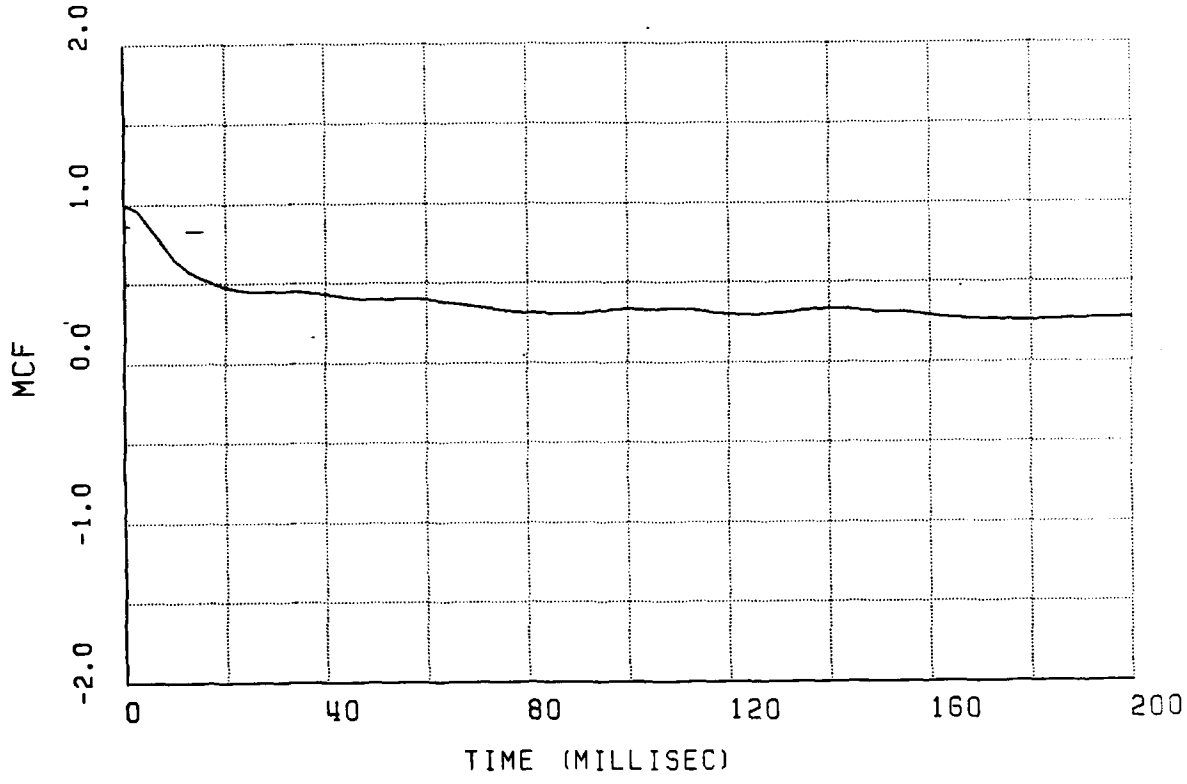

Figure 2-123. Mutual coherence function for entire occultation interval.

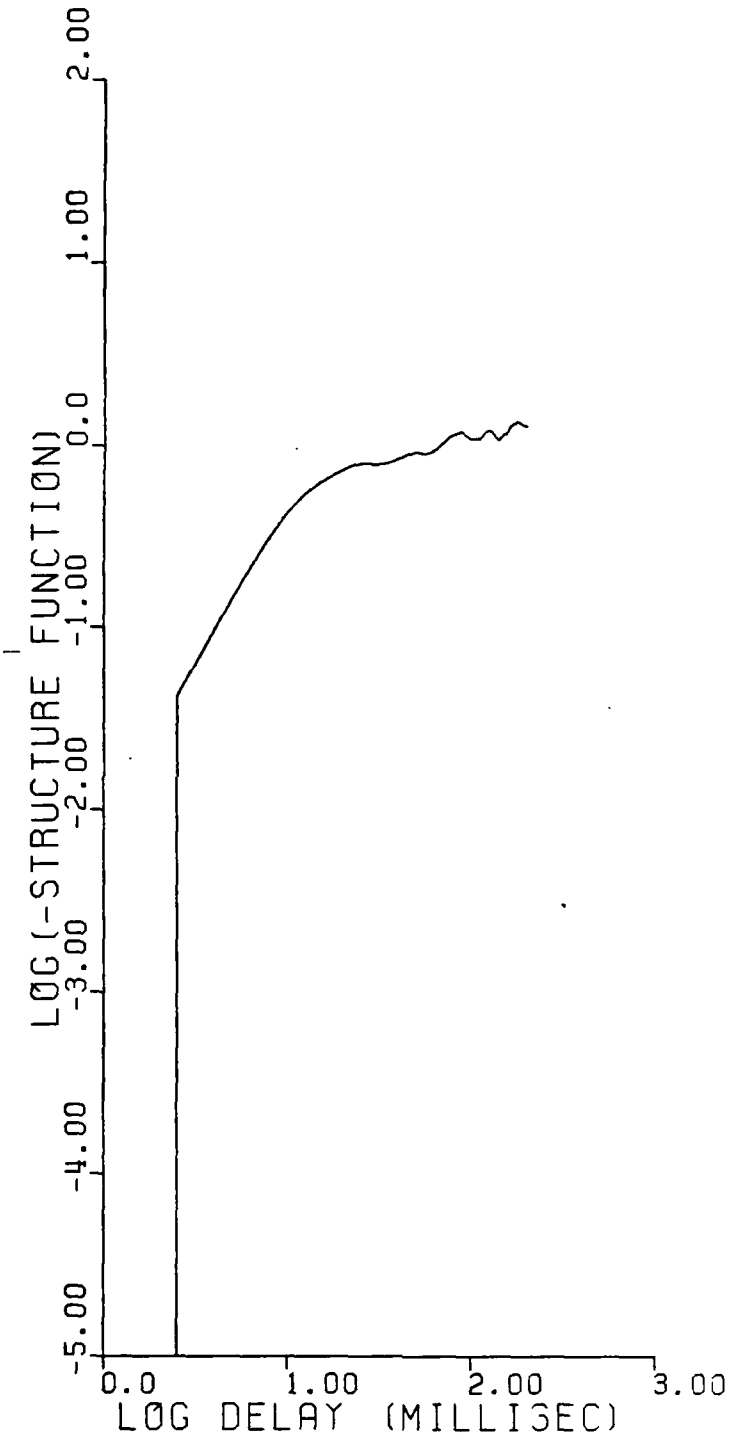

Figure 2-124. Logarithm of phase structure function for entire occultation interval.

Table 2-6. Phase structure function analysis summary.

SEGMENT	BEST SLOPE	$D_C = \tau^{2V-1}$		$D_A = (\tau/\tau_o)^2$	D_B		MCF = e^{-1}
		INDEX V	SLOPE 2V-1	τ_o	τ_o	σ_{ϕ_R}	τ_o
1	–	~ 1.2	~ 1.4	–	–	–	–
2	C	1.3	1.6	15 ms	12	0.9	53 ms
3	C OR A	1.5	2	15	–	–	15
4	C	1.4	1.8	10	10	1.4 RAD	13
5	C OR A OR B	1.5	2.0	10	10	1.6 RAD	13
6	C OR A OR B	1.5	2.0	8	10	1.5 RAD	11
7	C OR A	1.5	2.0	12	–	–	10
8	C OR A	1.5	2.0	8	–	–	7
ENTIRE CLOUD	C OR B	1.45	1.9	14	10	1.0	22

A – $D_A(\tau) = (\tau/\tau_o)^2$

B – $D_B(\tau) = \text{LOG}[1-(\tau/\tau_o)K_1(\tau/\tau_o)]$

C – $D_C(\tau) = \tau^{2V-1}$

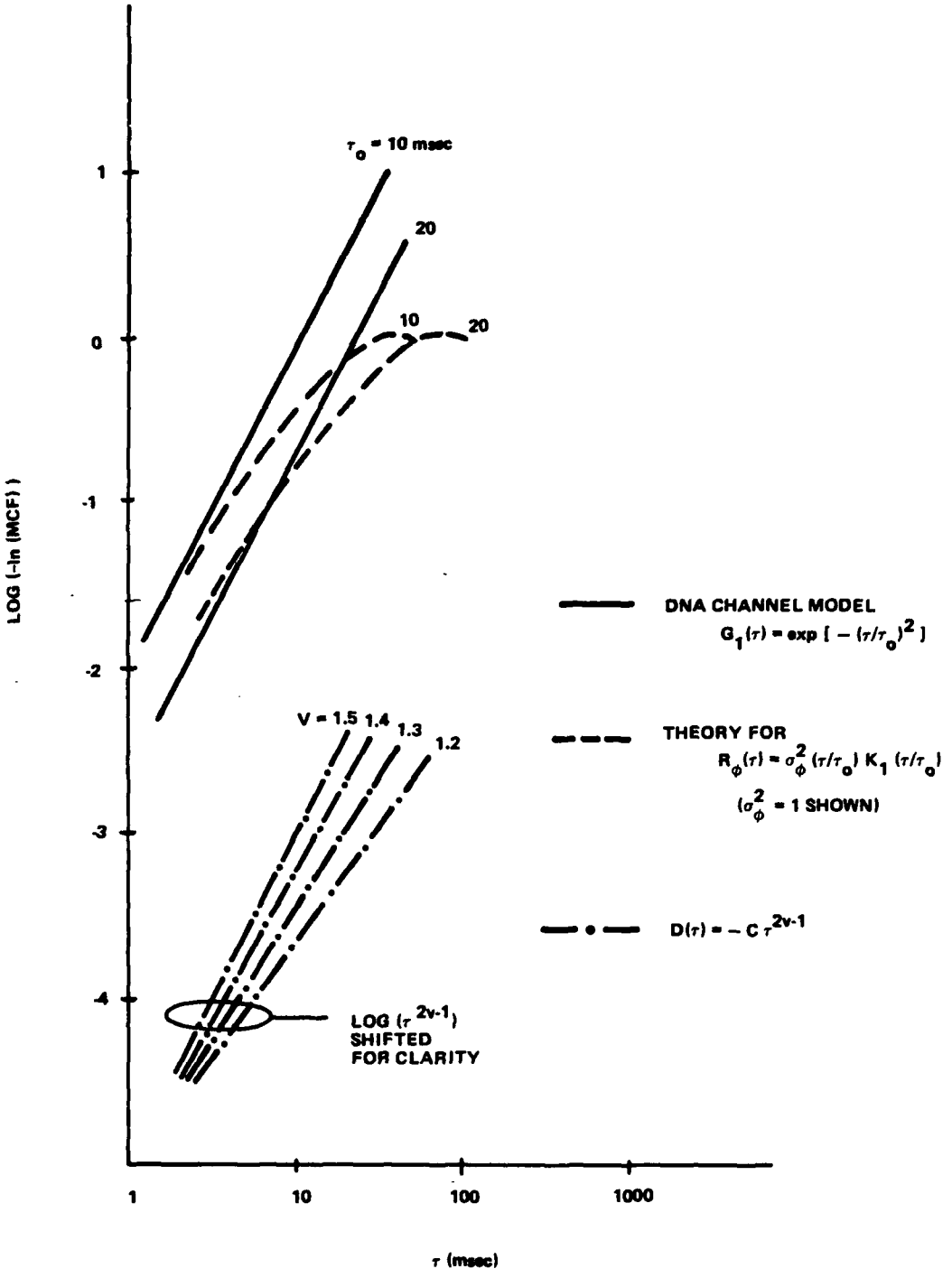

Figure 2-125. Logarithm of phase structure function.

One can obtain an estimate for the Rayleigh phase variance when the functional form is a good fit to the Bessel function form for the phase autocorrelation function out to large values of delay. This was possible only for segments 2,4,5,6 and the cloud average. The height of the structure function in this case determines the phase variance;

$$\log[-\ln(MCF)] = \log \sigma_{\phi R}^2 + \log[1 - \tau/\tau_o \, K_1(\tau/\tau_o)] \quad .$$

The Rayleigh phase variance defines that portion of the phase power spectrum effective in the angular scattering,

$$\sigma_{\phi R}^2 = \int_{f_R}^{\infty} S_\phi(f) \, df$$

From the assumed form for the phase PSD we have

$$S = \frac{\sigma_\phi^2 \, f_a}{[1 + (f/fa)^2]^{3/2}}$$

where

f_a = is the spectrum break frequency corresponding the an outer scale size, l_o.

Evaluating this expression, we obtain

$$\left(\frac{\sigma_{\phi R}}{\sigma_\phi}\right)^2 = 1 - \frac{(f_R/f_a)}{\sqrt{1 + (f_R/f_a)^2}}$$

In Section 2.5, we noted that the dispersive phase effects were determined by spatial structure sizes larger than a Fresnel size of approximately 245 meters. From the aircraft experiment measurements (Reference 2), the outer scale is typically of the order of 2 km for these barium environments. Thus, we expect the ratio of f_R/f_a to be of the order of 7, and, thus,

$$\frac{\sigma_{\phi R}}{\sigma_{\phi}} \simeq 0.086 \quad .$$

Accordingly, for the path integrated rms phase $\sigma_{\phi} = 20$ radians, we expect the Rayleigh phase variance to be approximately 1.7 radians. Thus, the results presented earlier in Table 2-1 for the rms dispersive phase are in good agreement with the values shown here in Table 2-6 for the Rayleigh phase variance.

2.11 COMPARISON WITH AIRCRAFT RESULTS

The results of the Aircraft Experiment were presented in Reference 2. It is of interest to compare the estimates obtained for the path integrated rms phase during the aircraft experiments with those obtained during the Beacon Experiment and summarized in Table 2-1. Unfortunately, a direct comparison is not available because of the failure of the aircraft phase reference during the Beacon Experiment release. Nonetheless, the rms phase appears to follow the systematic trend of the integrated electron content, decreasing with time, that can be used to test the reasonableness of the values obtained.

The data from HOPE Pass 19 at 1 hour 15 minutes after release are especially useful because a good rms phase estimate was obtained from a strong fading pass (Reference 2, Figure 7-58). A value of 4.5 radians was obtained for the aircraft geometry at 250 MHz. Since the rms phase scales directly with frequency, this implies a value of 11.45 radians at 98 MHz. The data from the JAN release showed that the dispersive phase or total electron content scales linearly with the logarithm of time as

$$\phi = 2\pi \, (-34 \log(t) + 78) \quad ,$$

where

t is time in minutes,

ϕ is the phase in radians = $r_e \lambda N_T$.

If we assume the corresponding σ_ϕ is directly related to the total integrated electron content as suggested by Figure 7-58 of Reference 2, the corresponding value of σ_ϕ at R+32 minutes can be estimated to be $\sigma_\phi \sim 21.6$ radians at 98 MHz. The corresponding dispersive jitter should have been approximately 0.035 microseconds. These values are in good agreement with the values given in Table 2-1.

2.12 SUMMARY FOR ST. GEORGE ISLAND, BEACON 1

The intuitive relations derived from geometric optics arguments have been shown to be in good agreement with the data. A geometric optics approach to describing propagation effects supports the DNA channel model as it can be thought of as corresponding to the geometric optics case where the angular spectrum is Gaussian.

Table 2-7 summarizes the results of the measurements derived from the beacon data for the St. George Island receiver, Beacon 1. The occultation interval was divided into a number of segments and estimates of various propagation parameters derived.

The time delay jitter and the total dispersive path integrated rms phase were measured in Section 2.5 and summarized in Table 2-1. These values were shown in Section 2.11 to be in qualitative agreement with that expected from the Aircraft Experiment data.

Table 2-7. Summary for St. George Island, Beacon 1.

			FROM JITTER DATA TABLE 2-1		FROM f_1 DATA TABLE 2-2		FROM JITTER AND f_0 TABLE 2-3		FROM ANGULAR SPECTRUM TABLE 2-5			FROM FREQ CORRELATION TABLE 2-4	FROM MCF DATA TABLE 2-6			INFERRED FROM AIRCRAFT DATA
DATA SEGMENT	DATA INTERVAL START (VT)	DATA INTERVAL END (VT)	σ_j (μsec)	σ_ϕ (RADIANS)	f_0 (MHz)	σ_j/σ_s	σ_s (μsec)	σ_j/σ_s	σ_s (μsec)	σ_θ (deg)	τ_0 (msec)	f_0** (MHz)	IN-SITU PHASE PSD SLOPE	τ_0 (msec)	$\sigma_{\phi m}$ (RAD)	σ_ϕ (RAD)
1	2346:08.9	:11.5	0.0017	1.8	> 4	~ 1	0.0366	4.8				> 4	2.4	–	–	
2	:13.8	:18.7	0.0229	14.1	1.7	0.25	0.0806	0.25				1.2 AVE.	2.6	15	6.9	
3	:18.9	:20.2	0.0316	19.4	1.7	0.25	0.0882	0.36				0.6	3.0	15	–	
4	:20.2	:22.8	0.0335	20.6	1.3	0.25	0.1178	0.28				0.6	2.8	10	1.4	
5	:21.4	:24.0	0.0436	26.8	0.9	0.25	0.1715	0.25				0.8	3.0	10	1.6	
6	:24.0	:26.6	0.0988	60.8	1.25	1.0	0.0804	1.23				–	3.0	8	1.5	
7	:26.6	:27.9	0.0371	22.8	1.7	0.5	0.0860	0.43				0.2	3.0	12	–	
8	:27.9	:29.2	0.0227	14.0	2.0	0.25	0.0763	0.30				–	3.0	8	–	
ENTIRE INTERVAL	:08.9	:29.4	(0.0414)*	–	2.1	0.50	0.0635	0.85	0.086	2.3	12	–	2.9	14	1.0	21.6
ENTIRE INTERVAL						(0.48)*										

* – ESTIMATED FROM TABLE 2–5 DATA
** – DATA FROM 0.1 sec AVE. WITHIN SEGMENTS

The angular scattering is closely given by the angular spectrum of the signal at frequencies near the center of the signal bandwidth. A direct mapping between the angular spectrum and the energy delay profile is demonstrated in Section 2.8. The angular spectrum was shown to be a good fit to a Gaussian functional form as anticipated. The angular spread and decorrelation time were determined from the angular spectrum data and summarized in Table 2-5.

The generalized power spectrum was extracted from the PLACES data and its functional form was shown in Section 2.6 to be in excellent agreement with theory. The differential Doppler data were shown to be in excellent agreement with the generalized power spectrum and the geometric knowns of the experiment. The coherence bandwidth and the rms time delay jitter-to-spread ratio were determined from the best fit to the functional form and summarized in Table 2-2. Using the time delay jitter data from Table 2-1 and the coherence bandwidth from Table 2-2, the rms delay spread was computed along with the ratio of the delay jitter-to-spread ratio for comparison with the values obtained from the functional fit to the generalized power spectrum. As shown in Table 2-3, these were shown to be in excellent agreement with the values derived from the functional fit.

The channel impulse response was measured directly and presented in Section 2.3. These data were transformed to obtain the channel transfer function presented in Section 2.7. The frequency coherence bandwidth, f_o, was determined from the frequency correlation function derived from the channel transfer function data and summarized in Table 2-4. These measurements were shown to be in excellent agreement with the data derived from the generalized power spectrum.

The fading waveform at 98 MHz was synthesized from the channel transfer function data in Section 2.8. In addition to computing the angular spectrum, these data can be used to compute the single frequency mutual coherence function, the two-sided angular spectrum, and the phase structure function as presented in Section 2.10. From the phase structure function, the spectral slope of the in-situ path integrted phase PSD can be derived from the received signal in spite of diffraction effects. The slope of the phase PSD was shown to be in good agreement with the DNA channel model formulation during periods of strong scatter. Furthermore, estimates for the decorrelation time were obtained from the mutual coherence function and structure function. For those data segments for which the mutual coherence function was well behaved to low values, an estimate of the Rayleigh phase variance was obtained. These values were summarized in Table 2-6. In Section 2.11, it was shown that the rms dispersive phase was in good agreement with that of the Aircraft Experiment.

Back-propagation processing of the received signal is another method of obtaining phase PSD data pertinent to striation phenomenology and striation modeling efforts. Back-propagation processing was not successful in that strong diffraction effects could not be removed from the data as discussed in Section 2.9. This was not unexpected, however, because of the unfavorable propagation geometry achieved for both occultations by the beacon rocket. Pertinent characteristics of this geometry are the thickness of the barium cloud and the very close proximity of the transmitting rocket to the cloud.

These data have served as an experimental verification of the DNA channel model for structured plasma and associated propagation theory. As a result of the good agreement obtained, it is believed to be well understood and adequately modeled.

SECTION 3
BEACON EXPERIMENT DATA FOR CAPE SAN BLAS, BEACON 1

3.1 GENERAL

Intense angular scattering effects were also observed on the signal received at Cape San Blas from the first beacon flight. This section discusses these data measurements.

3.1 OCCULTATION GEOMETRY

The first beacon rocket occulted the barium plasma as viewed from Cape San Blas (Site D3A) during the interval 2345:10.1 to 2345:30.7Z. The correlation with the FPS-85 radar data and with the optical data is discussed below.

3.2.1 Correlation to Radar Data

The occultation geometry relative to a radar mapping of the cloud ionization is provided in Figure 3-1. The radar ionization contours are those obtained approximately 2.5 minutes after occultation and translated to the peak electron density track point at 2345:20Z during the center of the occultation interval. These are the same contours presented in Figure 2-1. The contours available during the occultation interval were not as complete and, thus, were not used for presentation purposes.

The direct path to the D3A receiver does not slice the indicated striation region in this maximum density altitude plane. As can be estimated from this figure, the central field line through the maximum density point at 160-km altitude is cut by the propagation path around 145 km in altitude. Accordingly, we note a smaller interval over which strong angular scattering is observed in the data, in general agreement with the radar data.

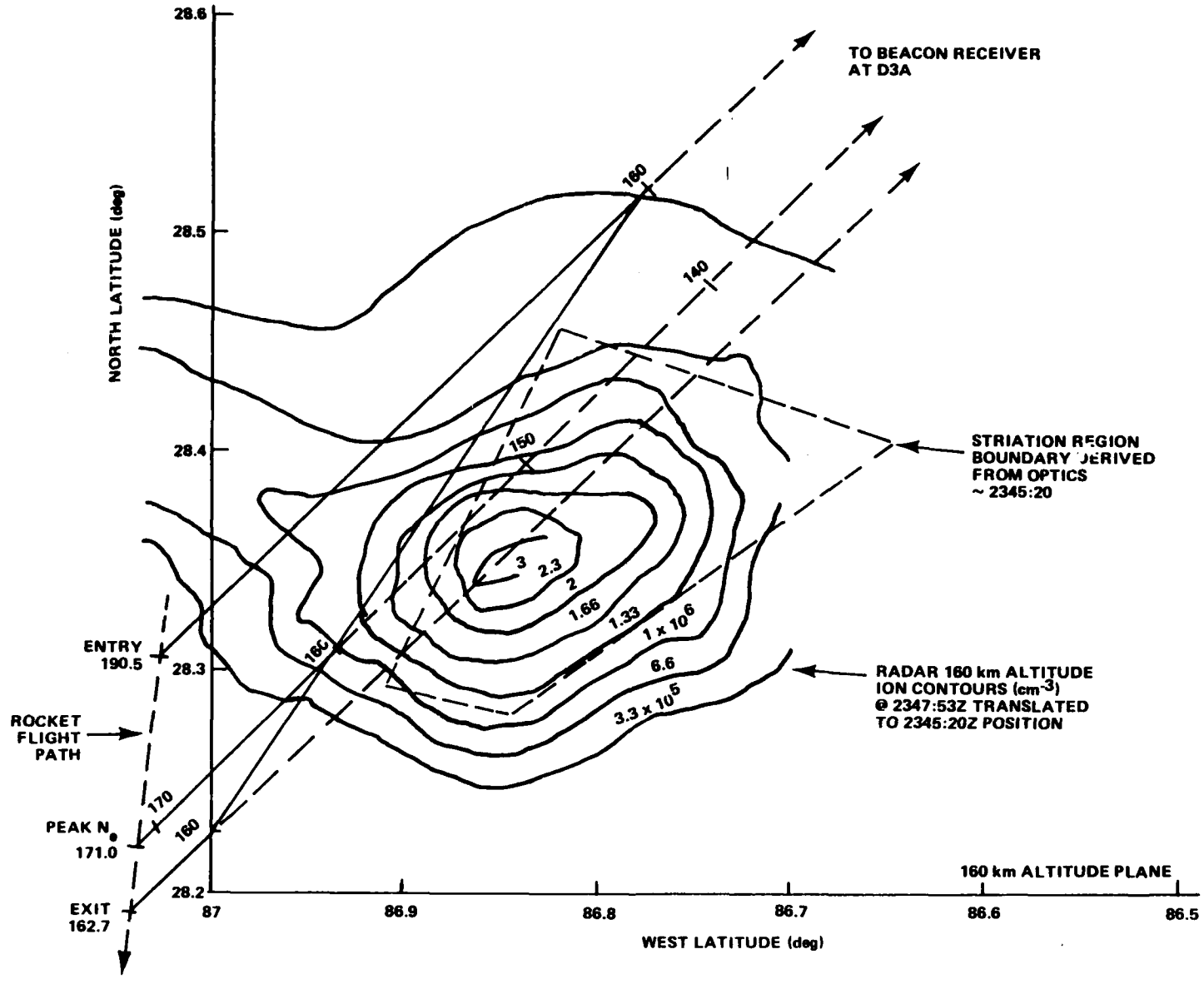

Figure 3-1. Occultation geometry for Cape San Blas (D3A), Beacon 1.

As an aid to interpreting this figure, the intersection of the path with the 160-km altitude plane is indicated by the transition from the solid to dotted line. The three paths show the time at which the first caustic ray is evident in the data, the time at which the maximum electron content (signal delay) is observed, and the time at which the signal ceases to exhibit any angular scattering of time-of-arrival (TOA) delay. The rocket altitude at these times is also indicated. For instance, at the time the path entered the cloud, the rocket was at an altitude of 190.5 km and when the path exited the cloud, its altitude was 162.7 km. Various altitude points are shown along the central ray path as well.

3.2.2 Correlation to Optical Data

Photographic coverage indicates that the bulk of the striations appear to the northeast side of the ion cloud, as described in Section 2.2.2. The optically derived mapping of the striation region boundaries is indicated on Figure 3-1. In the 160-km altitude plane, the line-of-sight path slices just outside the western edge of the optically defined striation region. The path slices the field line through the maximum density point around 145 km in altitude. This view of the striation extent is consistent with the measured signal structure data, which show a smaller extent (duration) of the intense angular scattering.

3.3 MEASURED CHANNEL IMPULSE RESPONSE

This section presents the measured channel impulse response data for Cape San Blas, Beacon 1. The data presented are a good approximation to the channel impulse response when the channel impulse response delay spread is large compared with the signal autocorrelation function. The in-phase and quadrature code cross-correlations performed at the beacon receivers provide a weighted average measurement of the in-phase and quadrature components

of the channel impulse response, averaged over a narrow window (a code chip interval) about the code delay.

3.3.1 Composite Data

The magnitude of the channel impulse response $|h(t,\tau)|$ measured at the Cape San Blas beacon receiver site is shown in Figure 3-2. The time span for this figure is 2345:00.4 to 2345:32.9Z. Well defined caustics are apparent in these data on approach to the cloud, although none appears as the beacon rocket exits from behind the cloud. This is due to the manner in which the path exits the bottom of the striated cloud. As with the St. George Island path, the gross plasma causes the TOA of the direct path energy to be delayed, resulting in the large delay near the center of the occultation. The gross plasma acts like a giant lens causing substantial defocusing to occur, reducing the signal amplitude near the center of the occultation. On this figure, one chip delay is approximately 0.1 microsecond. For plotting purposes, 32 impulse response measurements were averaged to produce each of the approximately 406 horizontal scans presented in the figure.

3.3.2 Energy Delay Profiles

Samples of the energy delay profile (magnitude of the channel impulse response) are shown in Figures 3-3 through 3-6, sampled approximately each 0.5 seconds. Near the time of maximum integrated electron content when the line-of-sight path to Cape San Blas passes through the center of the striations (~2345:26), the signal exhibits a significant defocusing and delay spread. Near this time, a delay spread of approximately 10 chips (~1 microsecond) occurs. A net TOA delay of about 9 chips (~0.9 microseconds) has been added by the gross electron content of the barium cloud. As

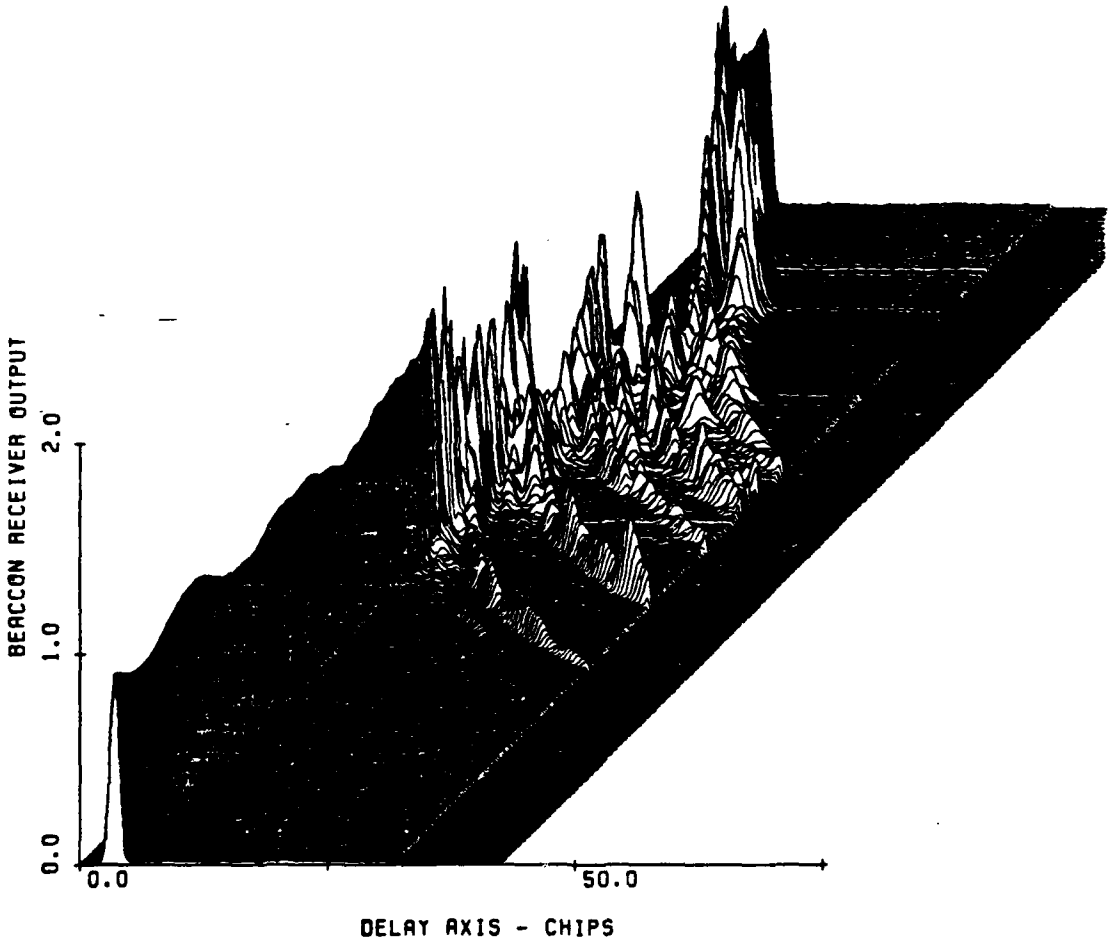

Figure 3-2. Magnitude of channel impulse response, Cape San Blas, first beacon time span from 2345:00.4 to 2345:32.9Z.

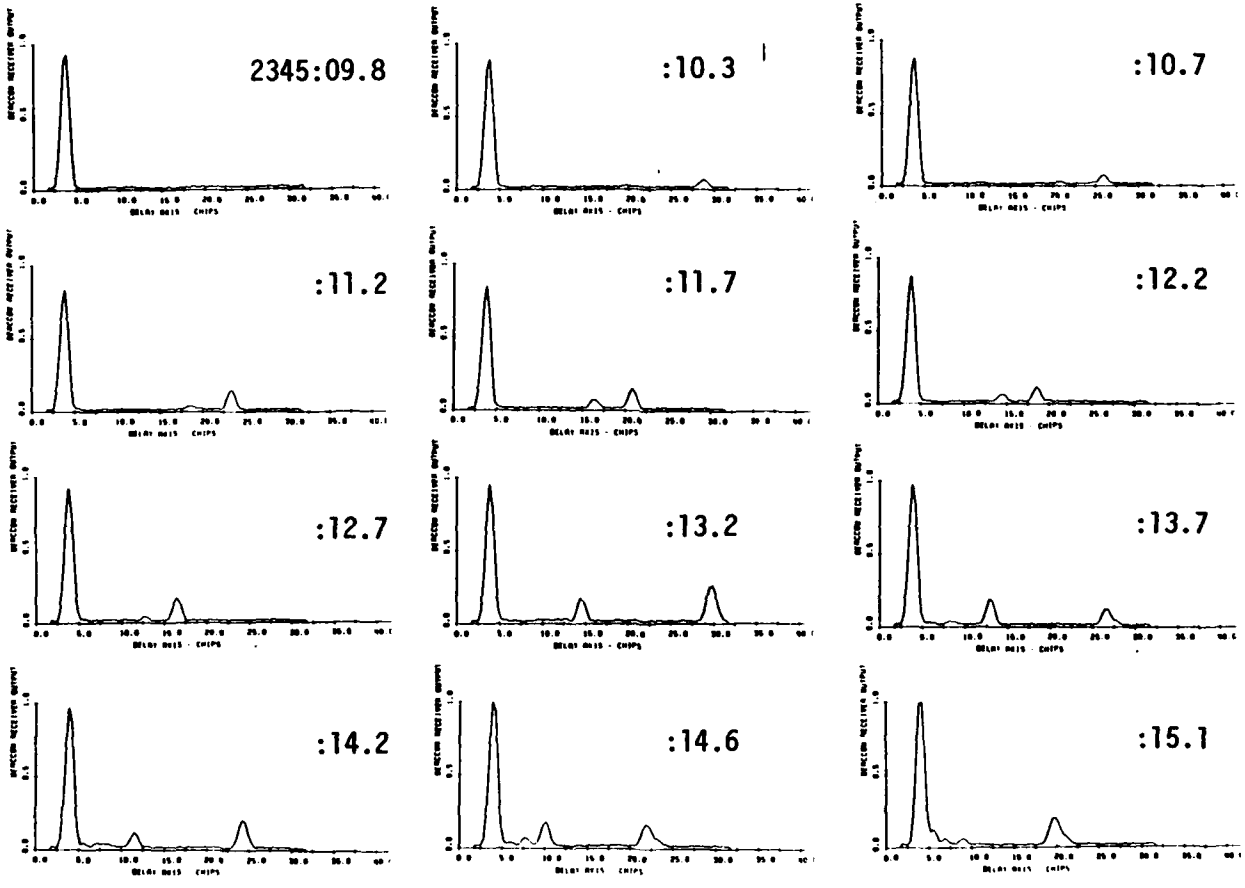

Figure 3-3. Energy delay profile between 2345:09.8 and 2345:15.1Z, Cape San Blas.

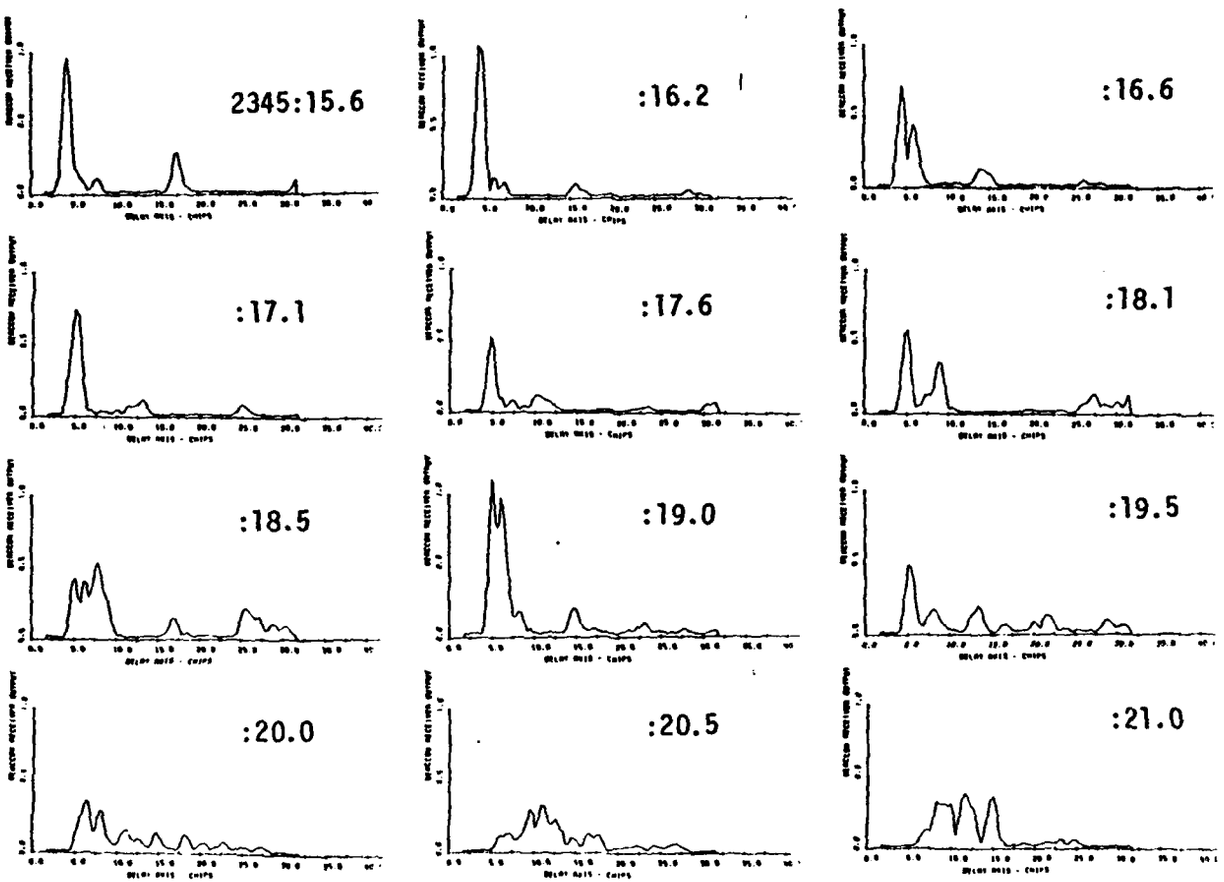

Figure 3-4. Energy delay profile between 2345:15.6 and 2345:21.0, Cape San Blas.

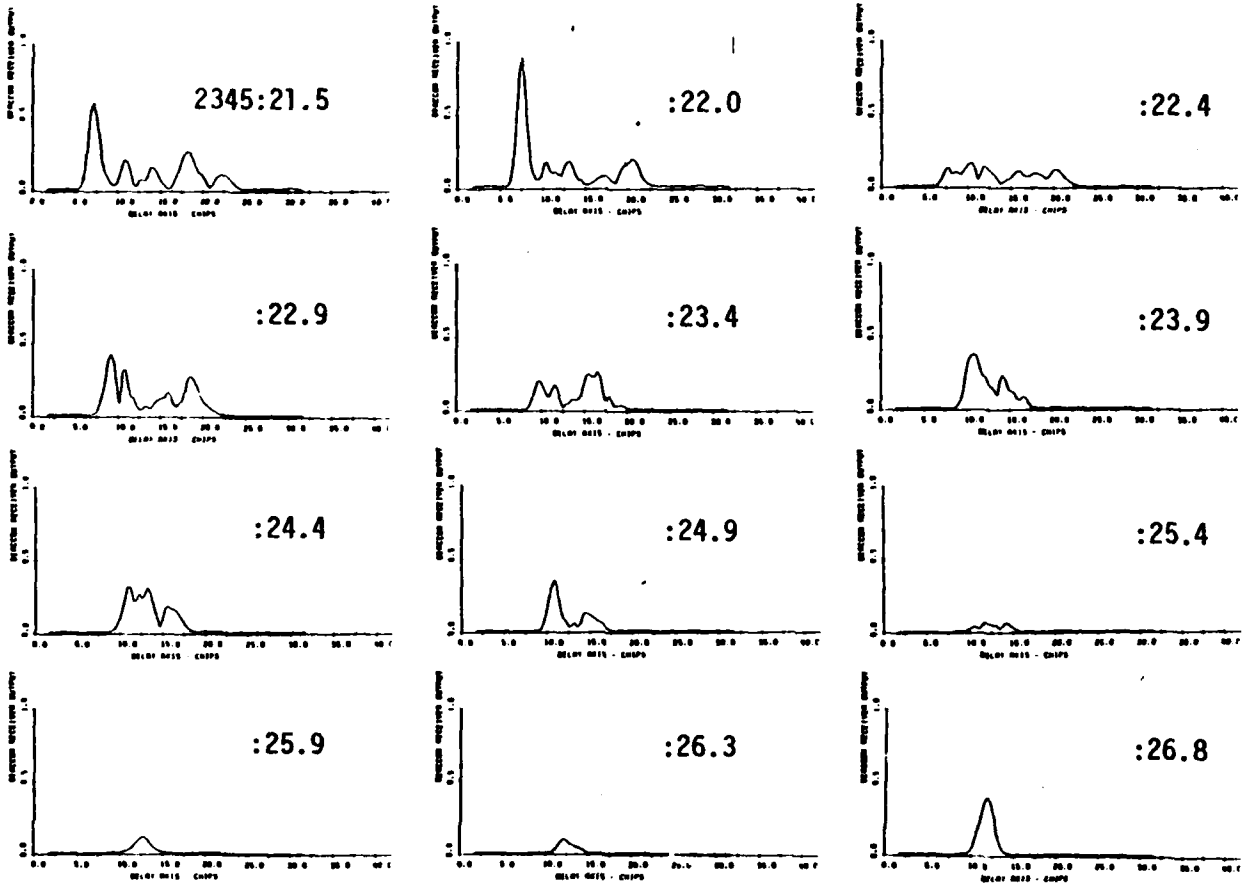

Figure 3-5. Energy delay profile between 2345:21.5 and 2345:26.8, Cape San Blas.

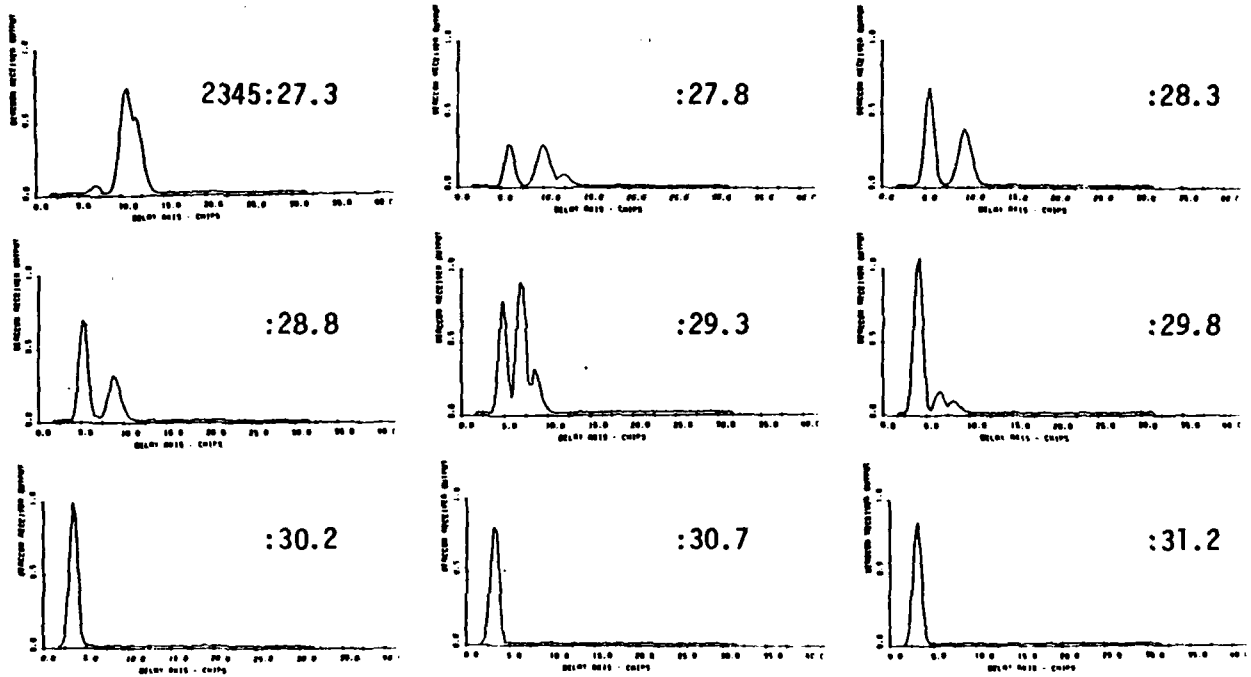

Figure 3-6. Energy delay profile between 2345:27.3 and 2345:31.2, Cape San Blas.

with the data for St. George Island, the significant energy delay spread, especially around 2345:20.5, has significant implications to PNB code tracking system design.

3.4 TOA DELAY

The impulse response data provide a snapshot in time of the energy of arrival profile. In this section we provide a view of the relative delay of the multipath signal components and the integrated electron content associated with the direct path delay.

3.4.1 TOA Composite Data

Figure 3-7 is a plot of the TOA of each energy peak (ray) as a function of the flight time of the rocket behind the barium cloud. As discussed in Section 2.4.1, each point is a plot of the location of the centroid of each peak in signal energy at each sample point in time. The centroiding algorithm is described in Appendix A. Evident in this figure is the TOA jitter of the direct path signal. This figure also clearly shows the caustic rays emerging only from one side of the cloud consistent with the geometry shown in Figure 3-1, which shows the path through the plasma moving away from the striated region before emerging from behind the barium ion cloud.

As with the St. George Island data, the data appear to support a geometric optics approach to the prediction of TOA jitter and delay spread. These geometric relations were tested more extensively for the St. George Island data, as described in Section 2, than time has permitted for the Cape San Blas data.

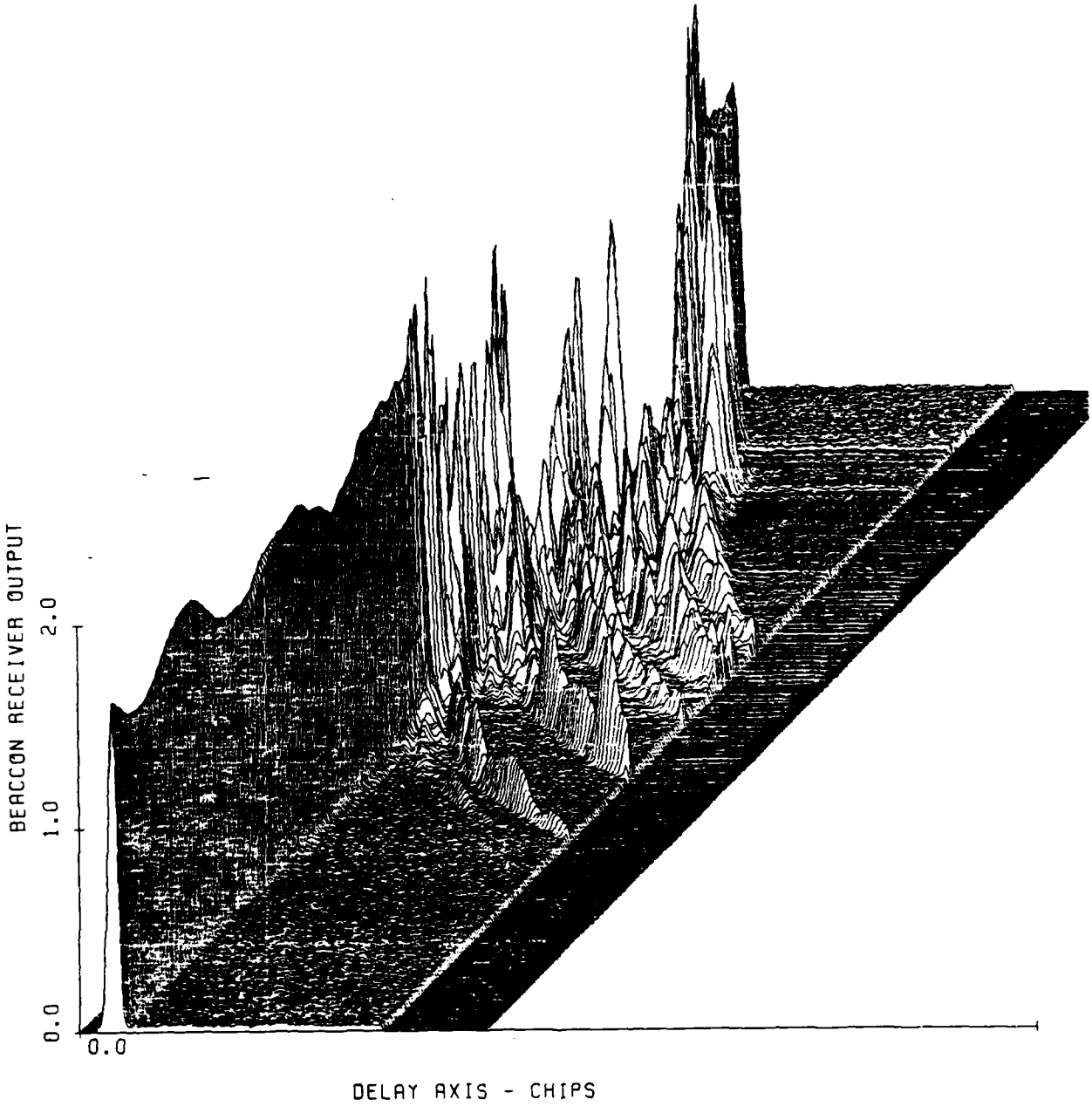

Figure 3-7. Energy delay profile, Cape San Blas, first beacon time span from 2345:00.4 to 2345:32.9.

3.4.2 TOA Direct Path Data and Integrated Electron Content

The TOA of the direct path through the plasma can be extracted from Figure 3-8 and is plotted in Figure 3-9. The algorithm used to distinguish the first peak in signal energy (direct path TOA) from noise is described in Appendix A. The TOA data were extracted by first fitting an approximate curve through the data of Figure 3-8 and then using a tracking algorithm that determined the earliest peak signal arrival in a given window width about that curve. A window width of $\pm$ 2/3 chip was used to construct Figure 3-9. The jitter evident in these data can be associated with the dispersive phase as described in Section 2.5.1.

The integrated electron content can be calculated based on the TOA shift in the received signal at each instant in time. Each microsecond of TOA delay at 98 MHz corresponds to 7.29×10^{12} cm^{-2} of electron content. Thus, for the Cape San Blas path through the barium ion cloud, the peak integrated electron content due to the barium plasma is approximately 6.0×10^{12} cm^{-2}. As discussed in Section 2, the background ionosphere contribution is small, approximately 10 percent of the ion cloud contribution.

3.5 TIME DELAY JITTER, CAPE SAN BLAS, BEACON 1

The jitter associated with the first arrival of signal energy is examined here and is referred to as the direct path TOA delay jitter. Section 2.5.1 provides a discussion of the theoretical relationship of the TOA delay and the dispersive phase.

The occultation interval was divided into several segments as shown in Figure 3-10 to investigate the relationship between the dispersive and angular spread energy components. Each segment

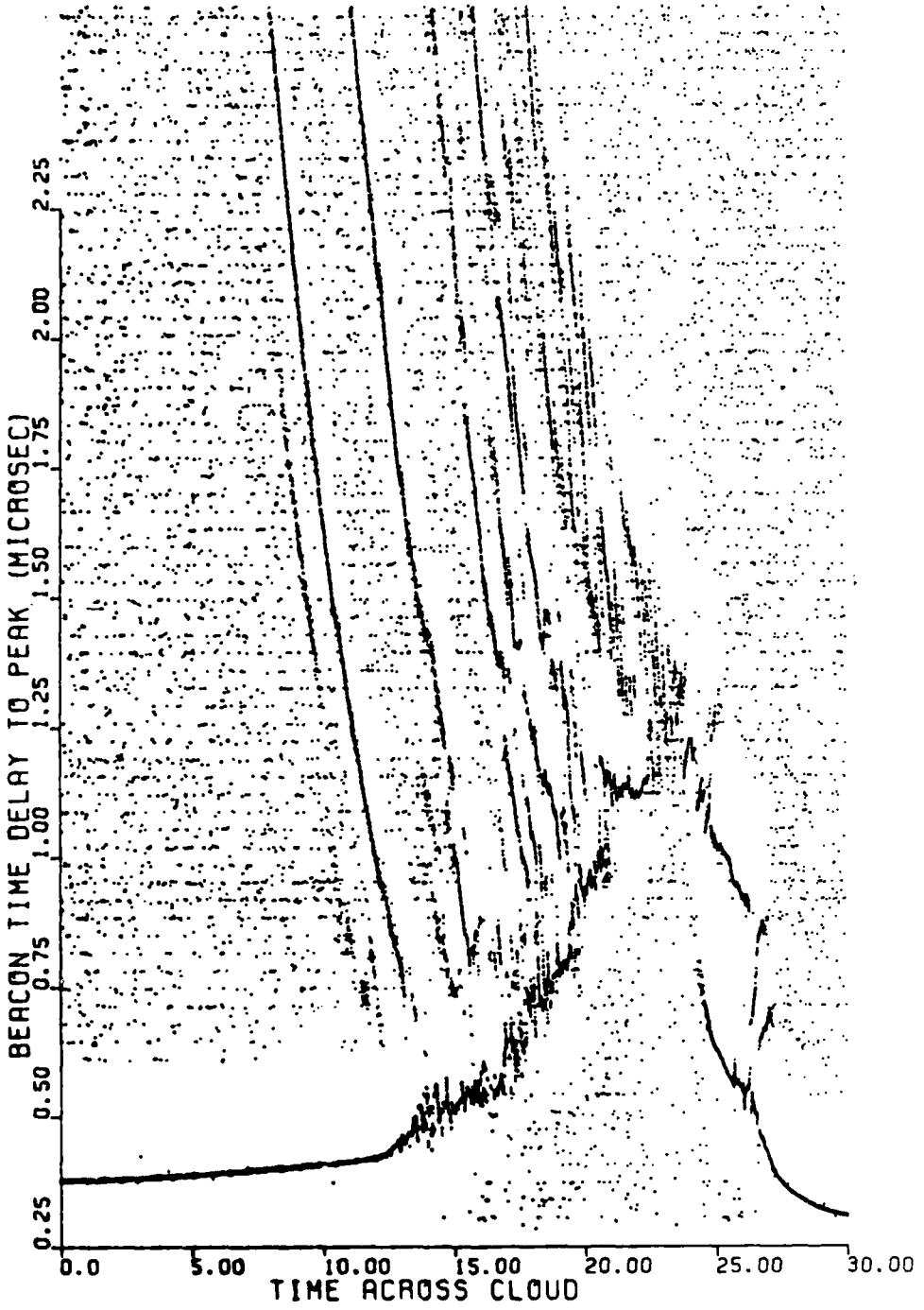

Figure 3-8. Energy peak time-of-arrival delay, all peaks.

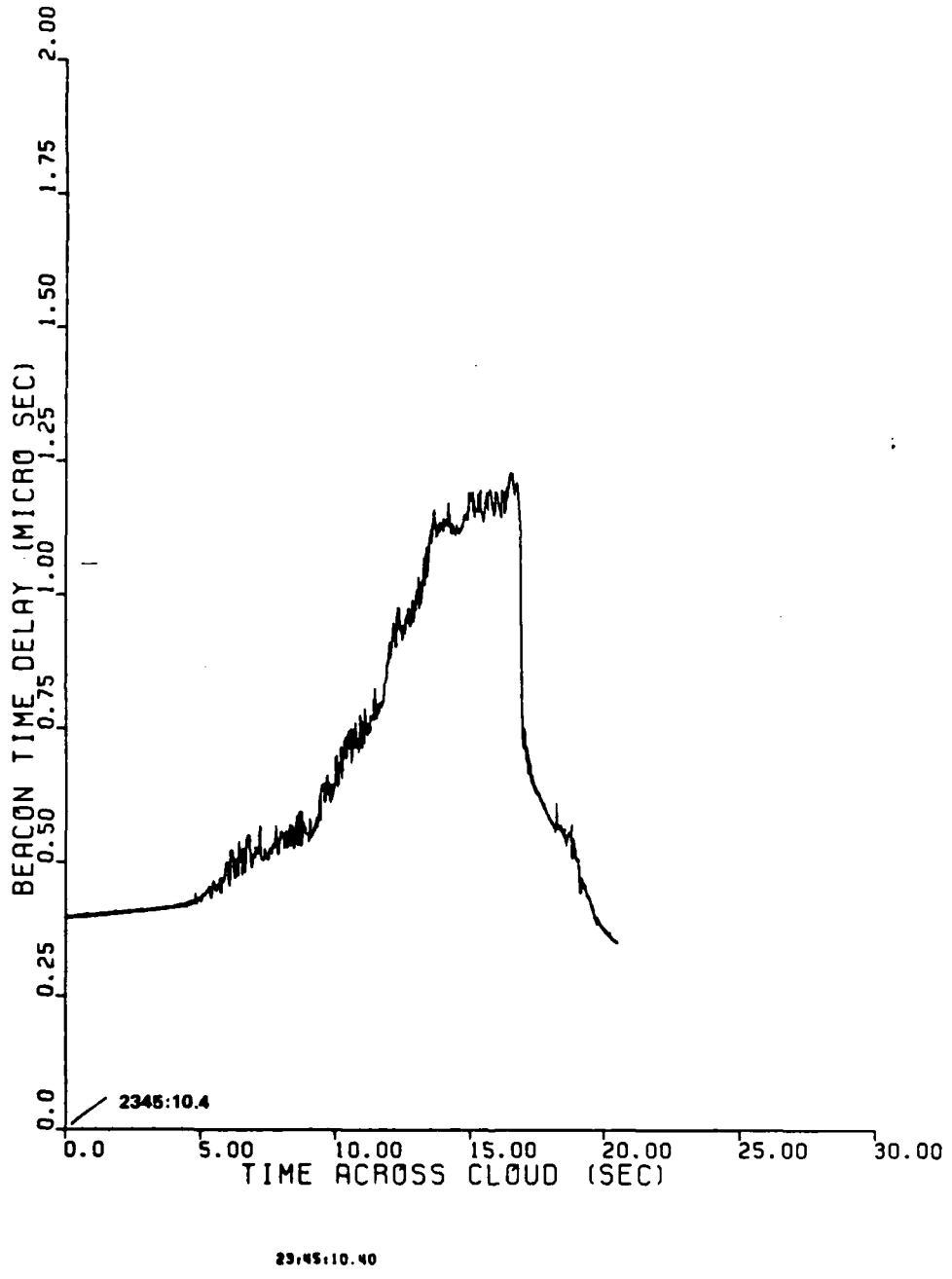

Figure 3-9. Direct path time-of-arrival delay.

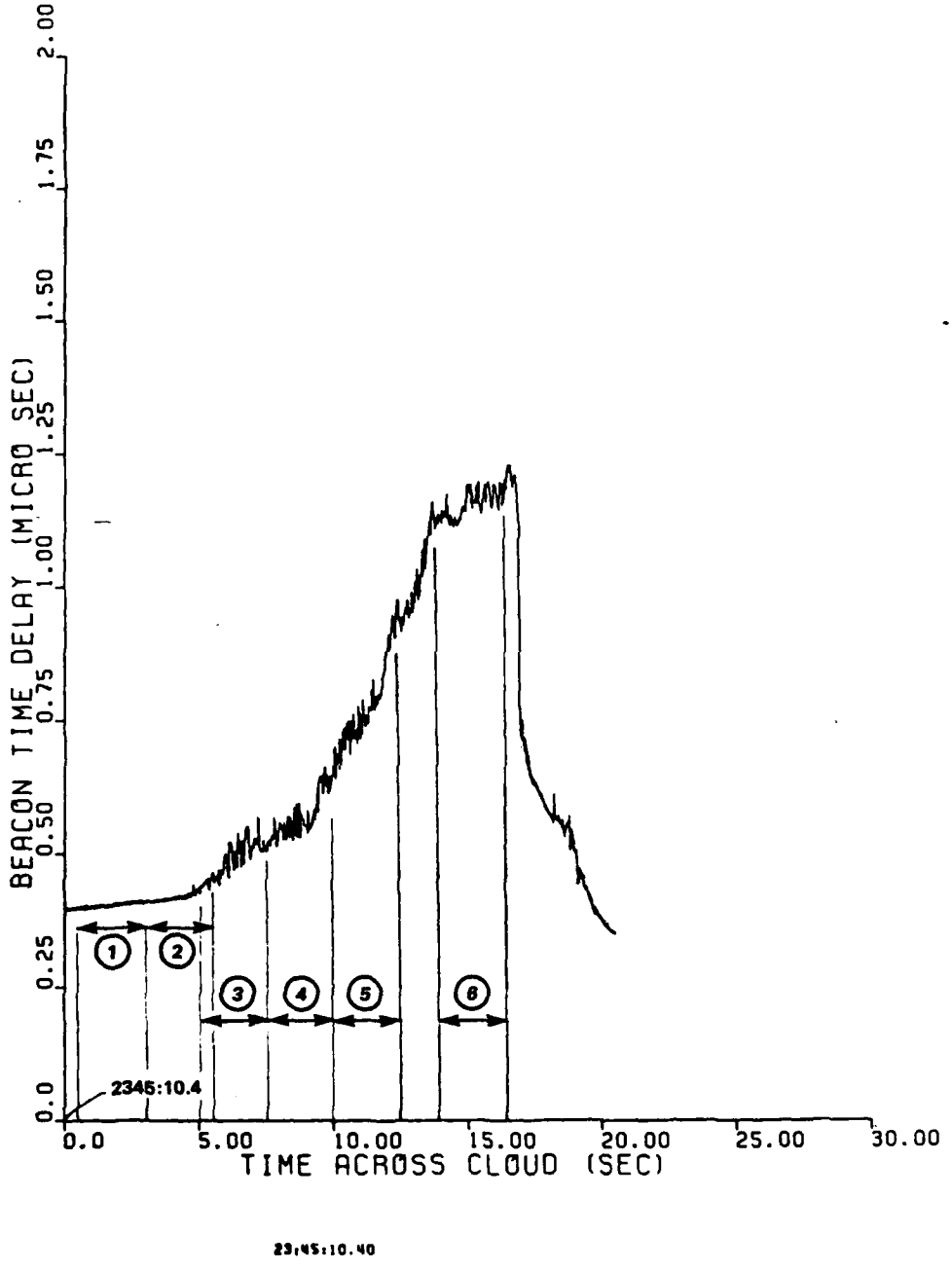

Figure 3-10. Direct path TOA jitter data segments.

was detrended to remove the deterministic TOA delay associated with the background plasma and transformed to determine the rms time delay pause spectrum. Figures 3-11 through 3-16 show the detrended data and the corresponding time-delay jitter spectrum for those intervals noted on Figure 3-10. Table 3-1 provides a summary of the measured rms time-delay jitter and the corresponding path integrated rms dispersive phase.

For these data, the algorithm described in Appendix A used to determine the direct path TOA was set such that the jitter window was ± 1 chip (0.1 microsecond) about the detrended value of TOA.

Generally, the data show a consistent trend toward stronger jitter when the integrated electron content (TOA delay) was at a maximum as the rocket approached the center of the cloud. The data from Segment 1, prior to significant TOA jitter, would indicate a TOA measurement accuracy of approximately 0.5 radian in rms phase. The rms values of rms phase are nearly the same as those derived for the St. George Island path and summarized in Table 2-1. The spectral break frequencies are also generally consistent with those observed on the St. George Island path. Only for Segment 4 were the number of sample points at which a TOA peak could not be found within the ± 1 chip window significant as noted in Table 3-1. This results in an overestimate for the rms delay jitter and the rms dispersive phase. A better estimate is available from the generalized power spectrum described in Section 3.6.

3.6 GENERALIZED POWER SPECTRUM

The analytical expressions for the generalized power spectrum, $\Gamma_1 (f_d,\tau)$, were given in Section 2.6.6. A measure of the goodness to which the measured data conform to this model can be derived from the received beacon signal. Here we examine delay plane of the generalized power spectrum.

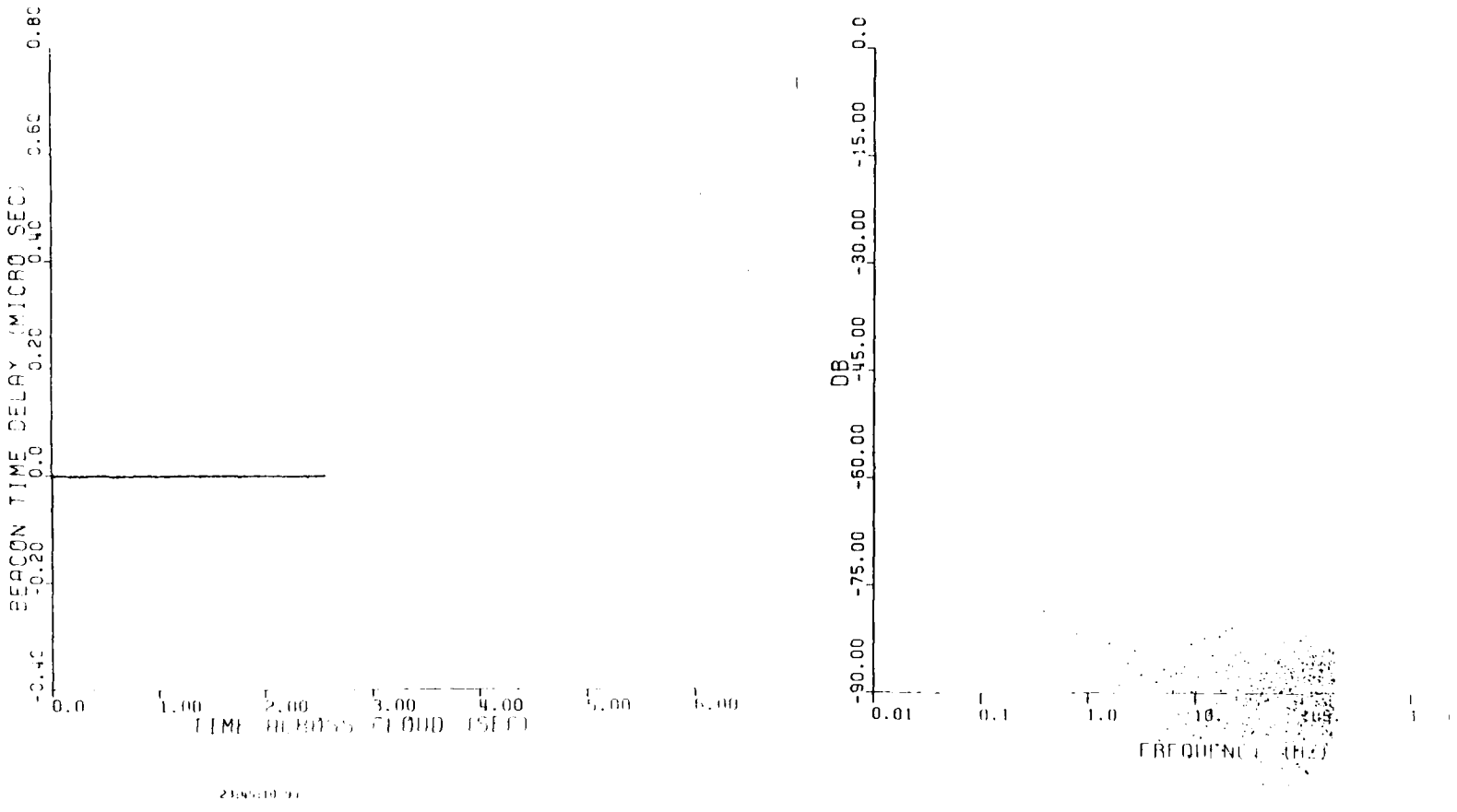

Figure 3-11. Detrended TOA jitter and jitter spectrum for Segment 1, noise only.

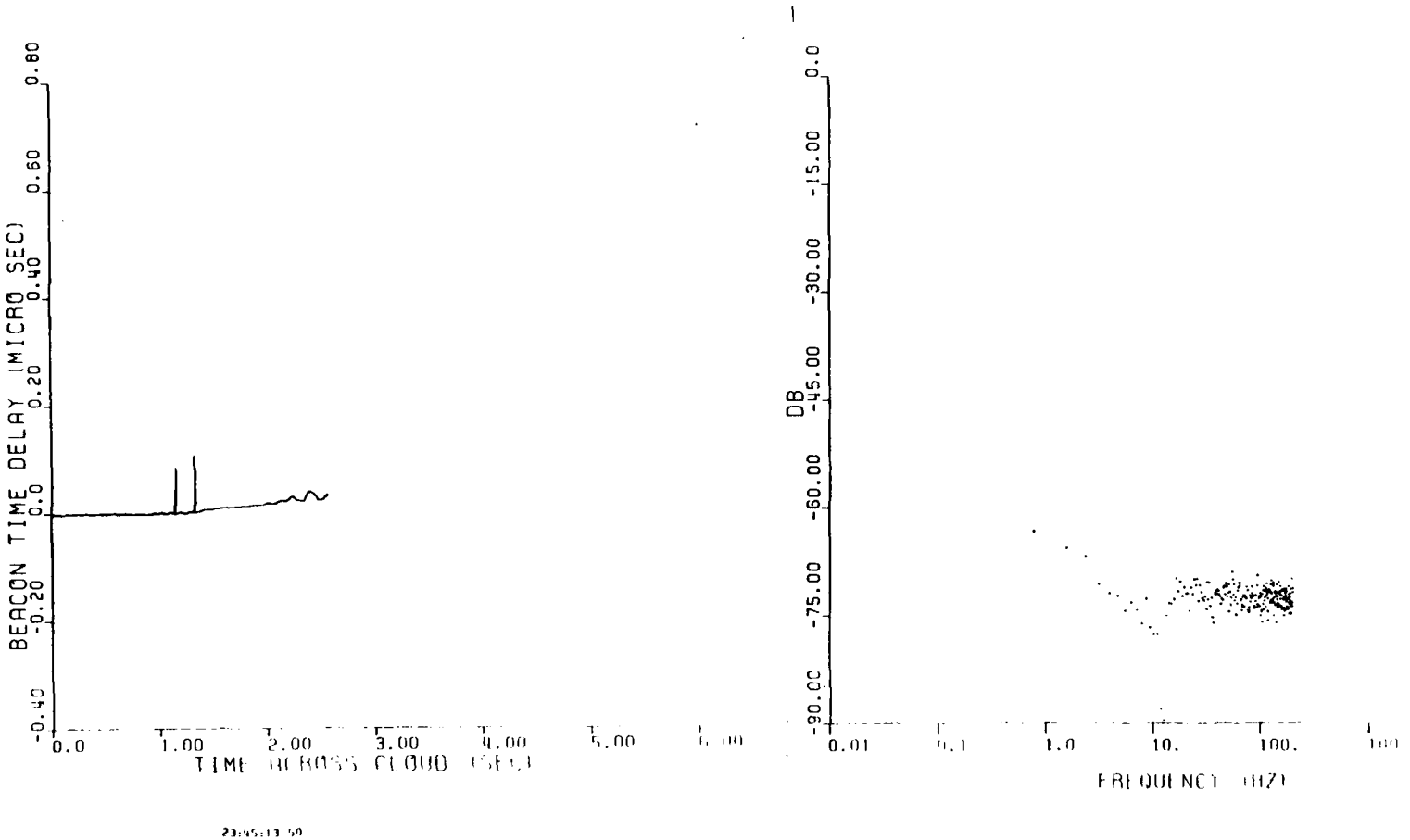

Figure 3-12. Detrended TOA jitter and jitter spectrum for Segment 2.

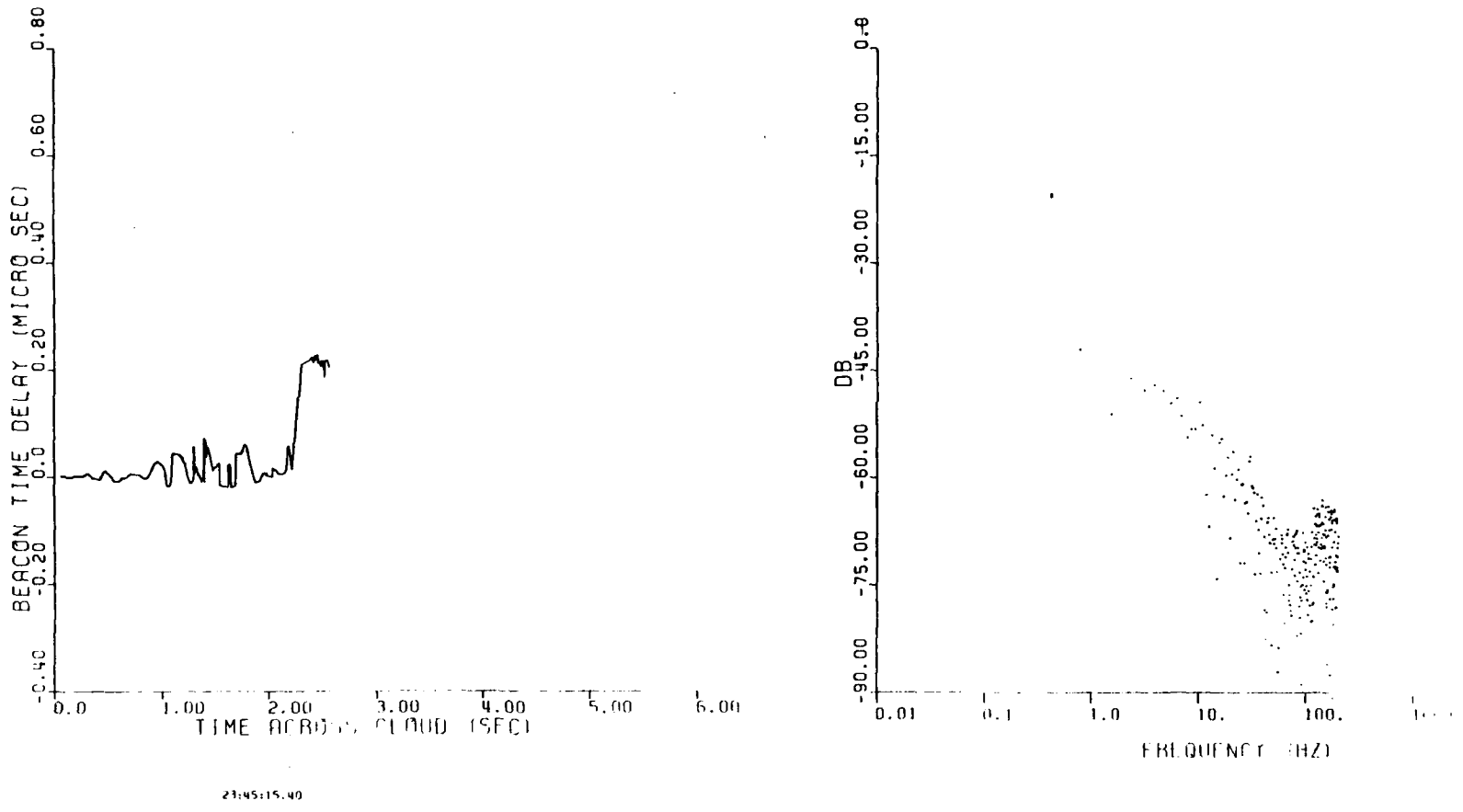

Figure 3-13. Detrended TOA jitter and jitter spectrum for Segment 3.

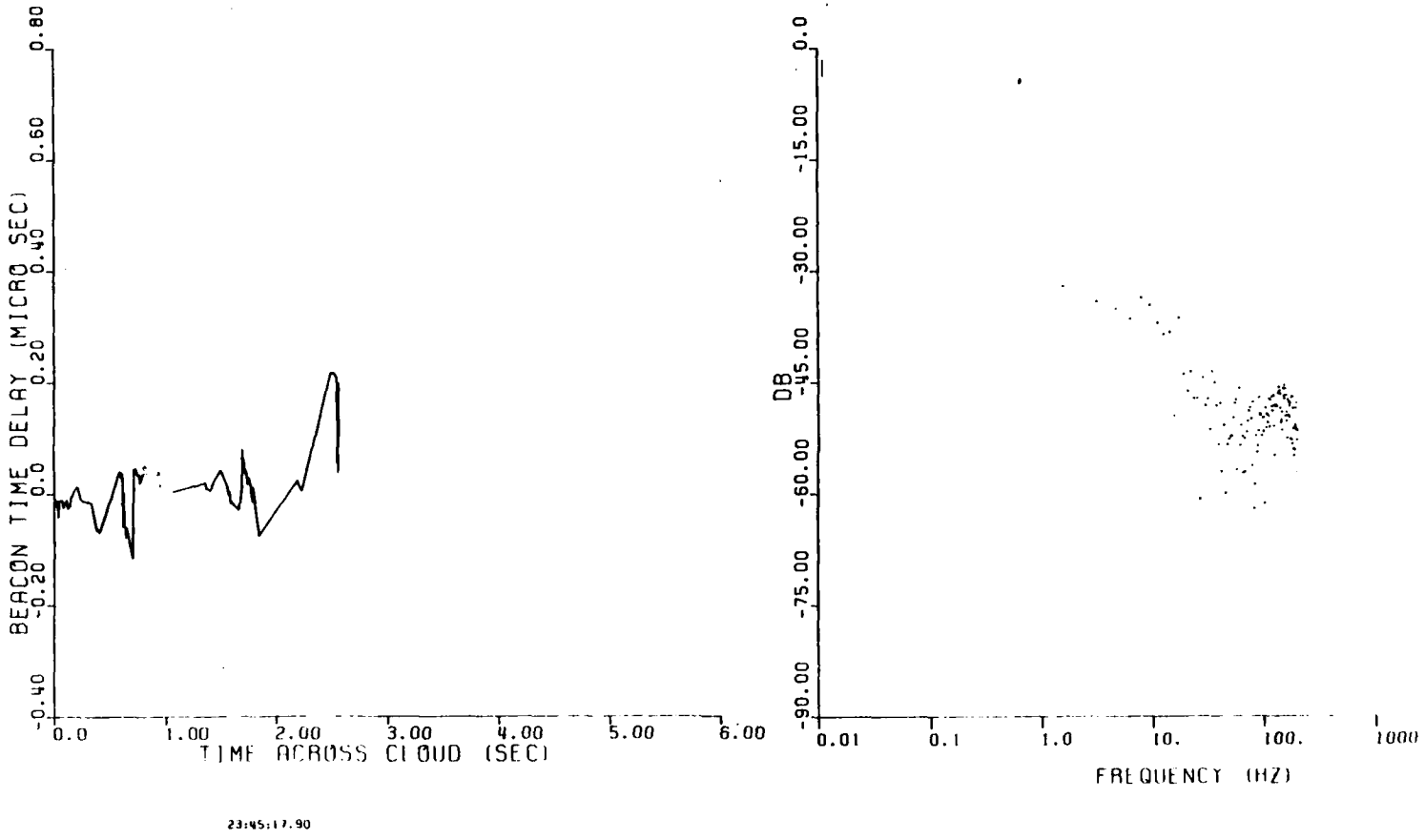

Figure 3-14. Detrended TOA jitter and jitter spectrum for Segment 4.

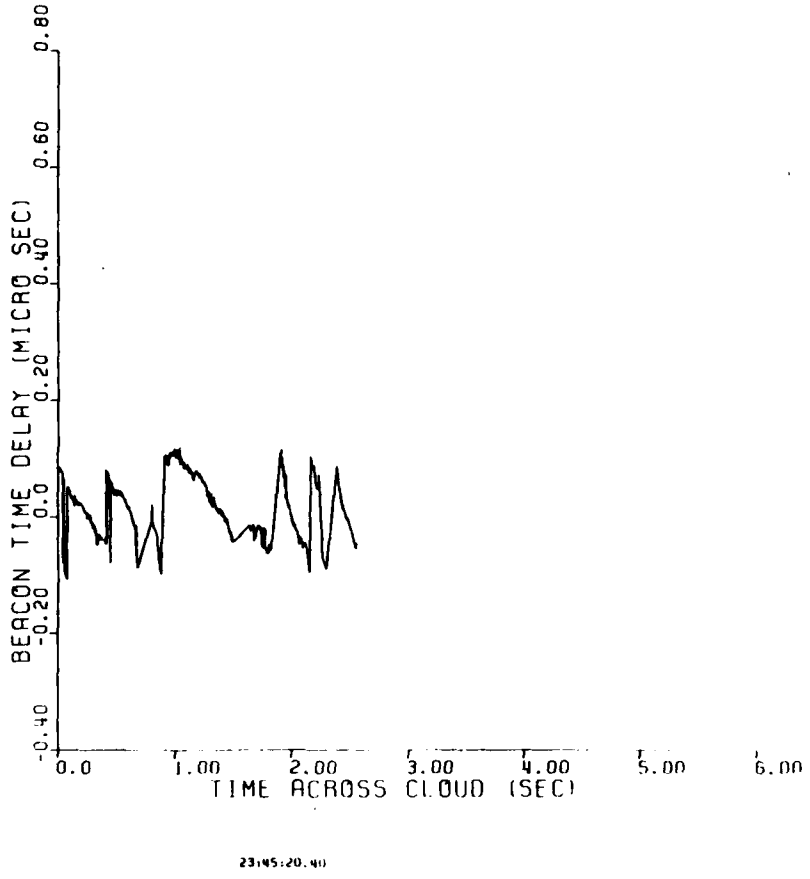

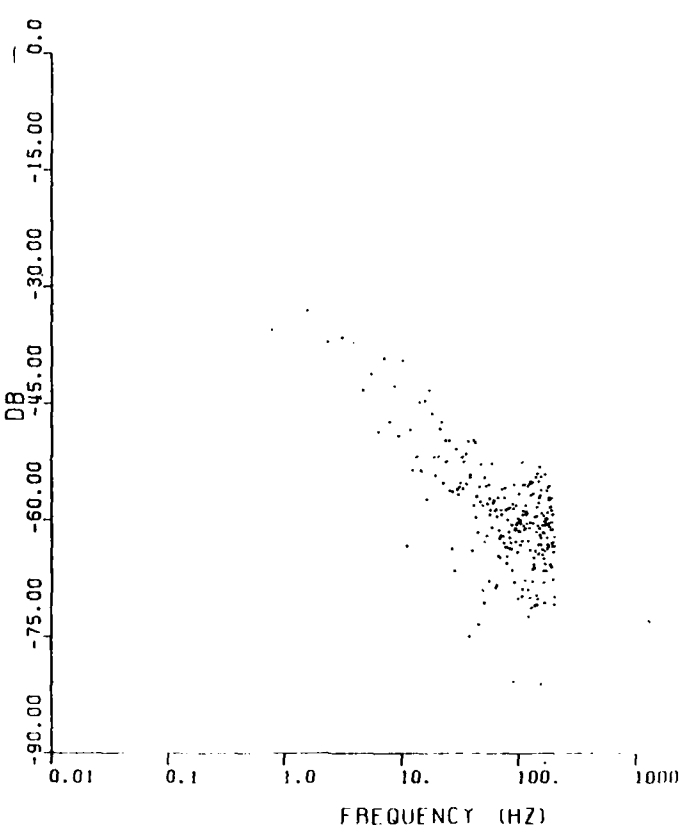

Figure 3-15. Detrended TOA jitter and jitter spectrum for Segment 5.

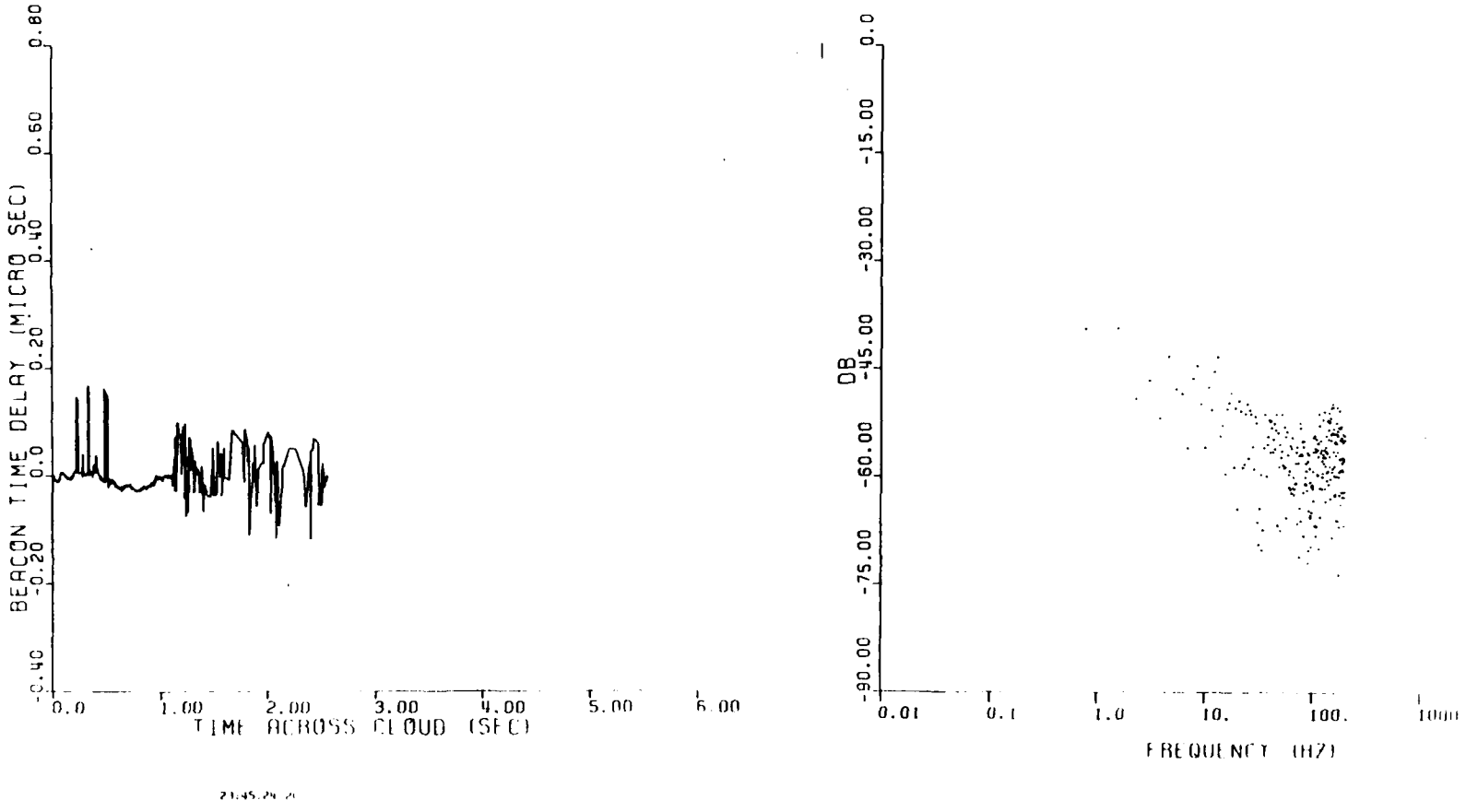

Figure 3-16. Detrended TOA jitter and jitter spectrum for Segment 6.

Table 3-1. RMS time delay jitter data segments summary.

Interval	Data Interval Start (UT)	End (UT)	RMS TOA Jitter (US)	RMS Phase (Radians)	Data Points	Jitter Points	Mean TOA (US)	Comment
1	2345:10.9	:13.5	0.0009	0.5	1024	1023	-.00156	Prior To Noticeable Jitter
2	:13.4	:16.0	0.0129	7.9	1024	739	.00645	Jitter at end of segment
3	:15.4	:18.1	0.0542	33.4	1024	732	.0266	Start of Jitter
4	:17.9	:21.5	0.0671	41.3	1024	209	.0264	Jitter is Then estimated
5	:21.4	:23.1	0.0504	31.0	1024	617	.0199	Rapid increasing TOA
6	:24.2	:26.8	0.0365	22.5	1024	825	.00414	Maximum TOA Jitter Segment

3.6.1 Delay Power Spectrum

The signal delay power spectrum or energy arrival distribution is obtained by integrating out the Doppler frequency variable in the generalized power spectrum,

$$\Gamma_1(\tau) = \int \Gamma_1(f_d,\tau)\, df_d \quad .$$

As described in Section 2.6.7, it is relatively straightforward to compute the delay power spectrum by summing the squares of the channel impulse response magnitudes shown earlier at each tap delay and normalizing the result such that the integral equals unity to correspond with the DNA channel model definition,

$$\int_{-\infty}^{\infty} \Gamma_1(\tau)\, d\tau = 1 \quad .$$

Figures 3-17 through 3-22 show the results of these calculations for the six data segments summarized in Table 3-1. The TOA shown in Figure 3-9 was used to remove the TOA bias. In order not to remove the effects of the dispersive jitter, a mean TOA curve was obtained from Figure 3-9 and the power summed relative to the mean delay at each time sample. Again we anticipate only a first order agreement with theory because of the strong lens-like defocusing effects of the gross plasma. This effect was minimized somewhat by removing the TOA shift and by dividing the data into short 2.56-second segments.

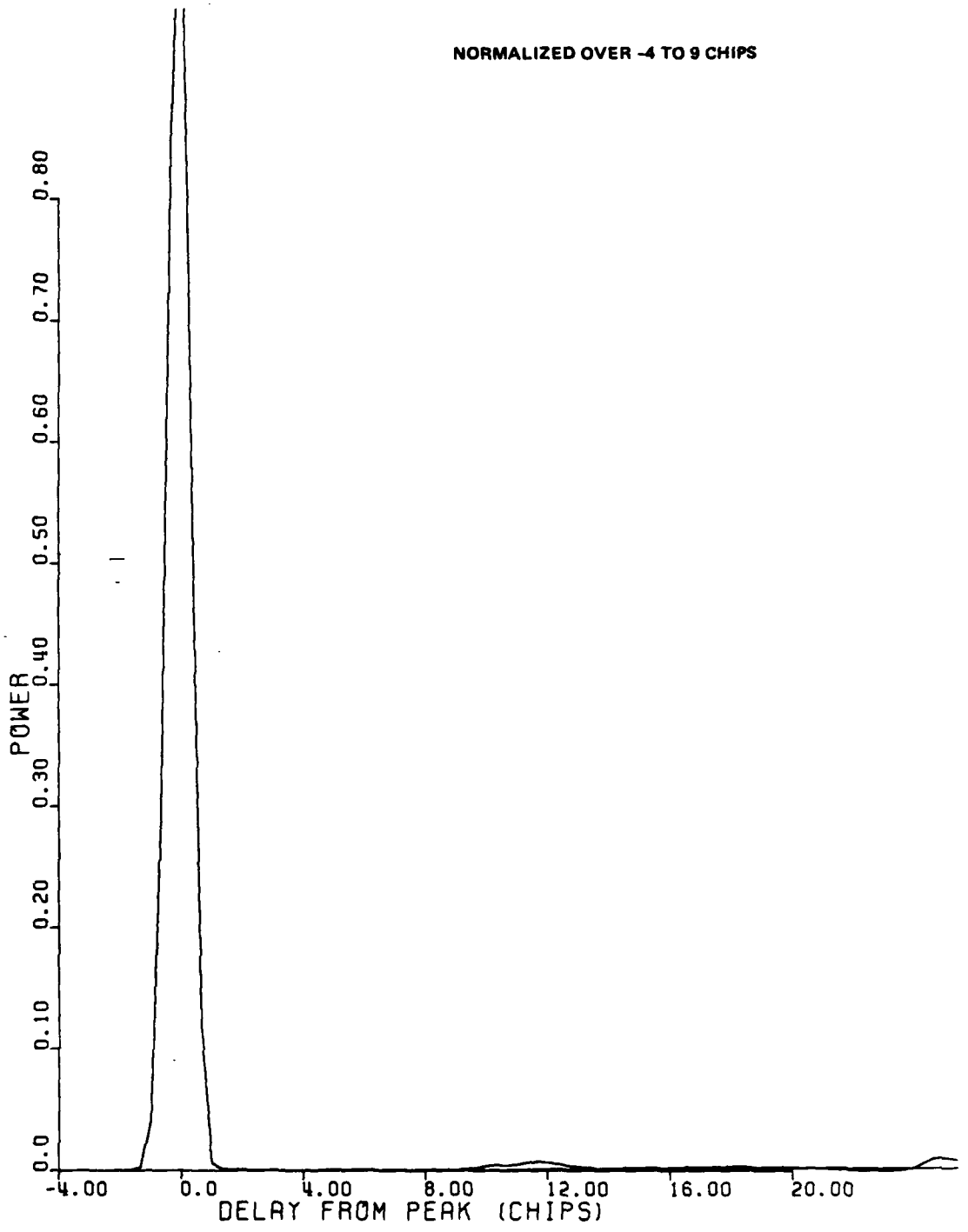

Figure 3-17. Delay power spectrum for Segment 1, Cape San Blas, Beacon 1.

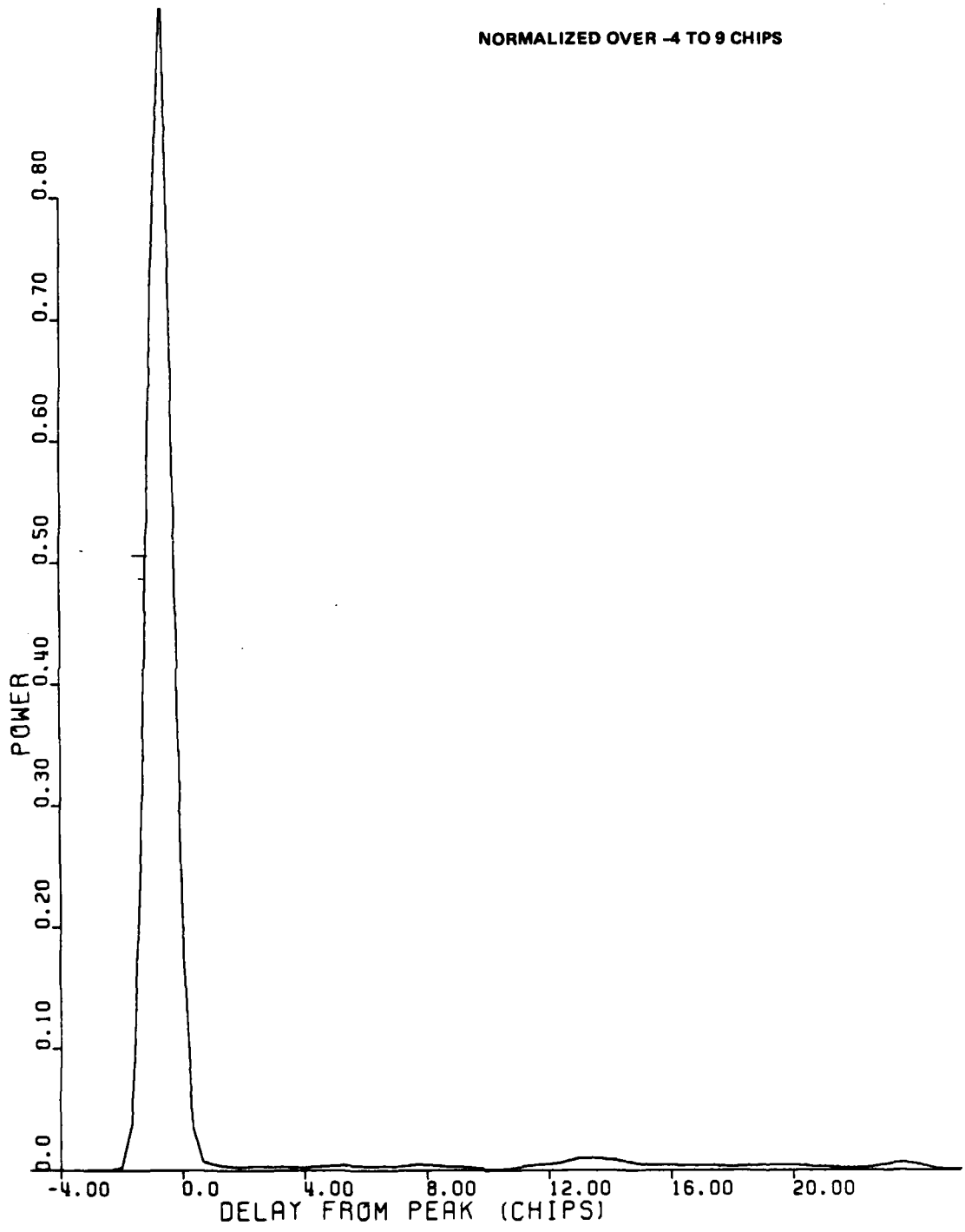

Figure 3-18. Delay power spectrum for Segment 2, Cape San Blas, Beacon 1.

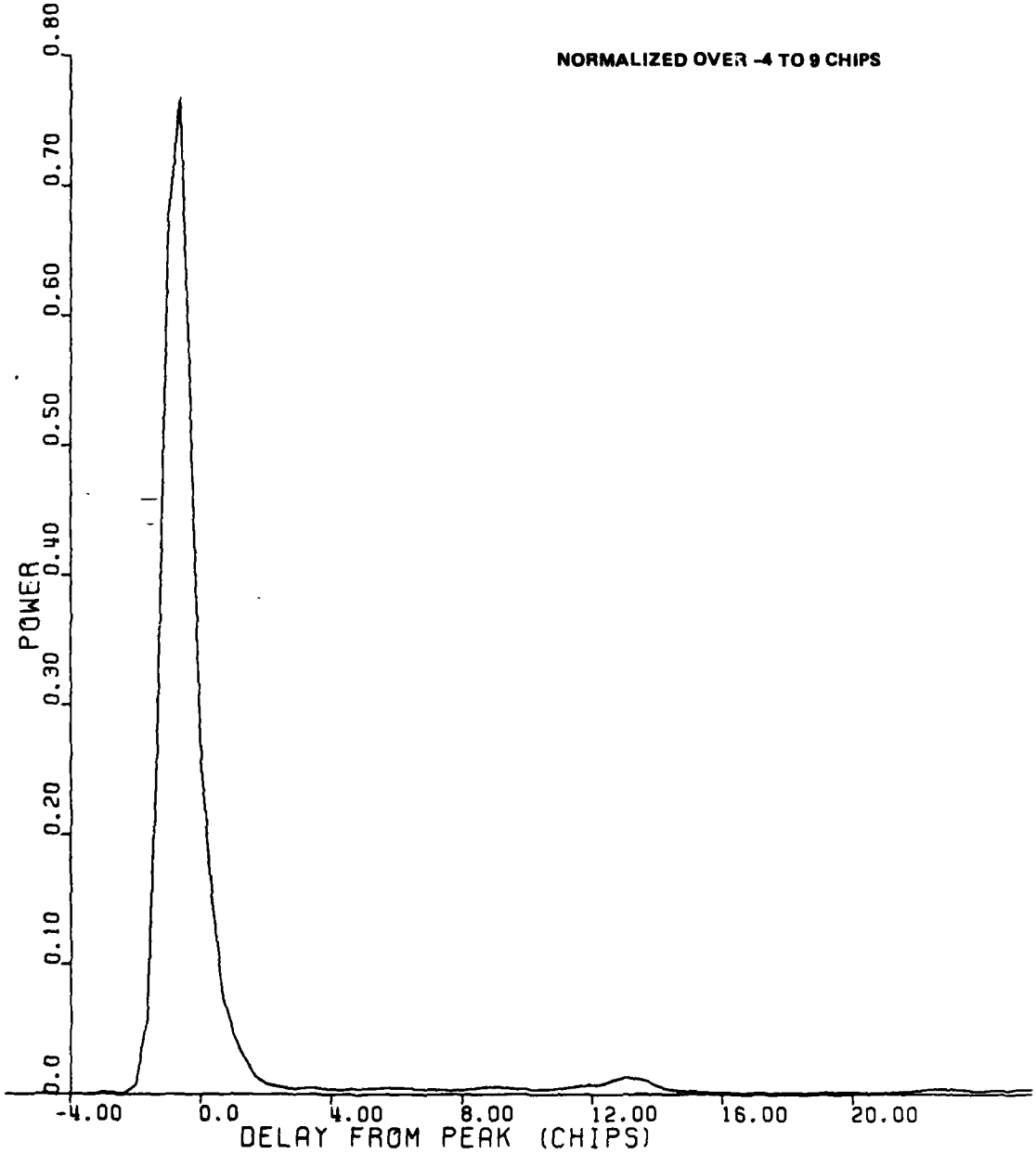

Figure 3-19. Delay power spectrum for Segment 3, Cape San Blas, Beacon 1.

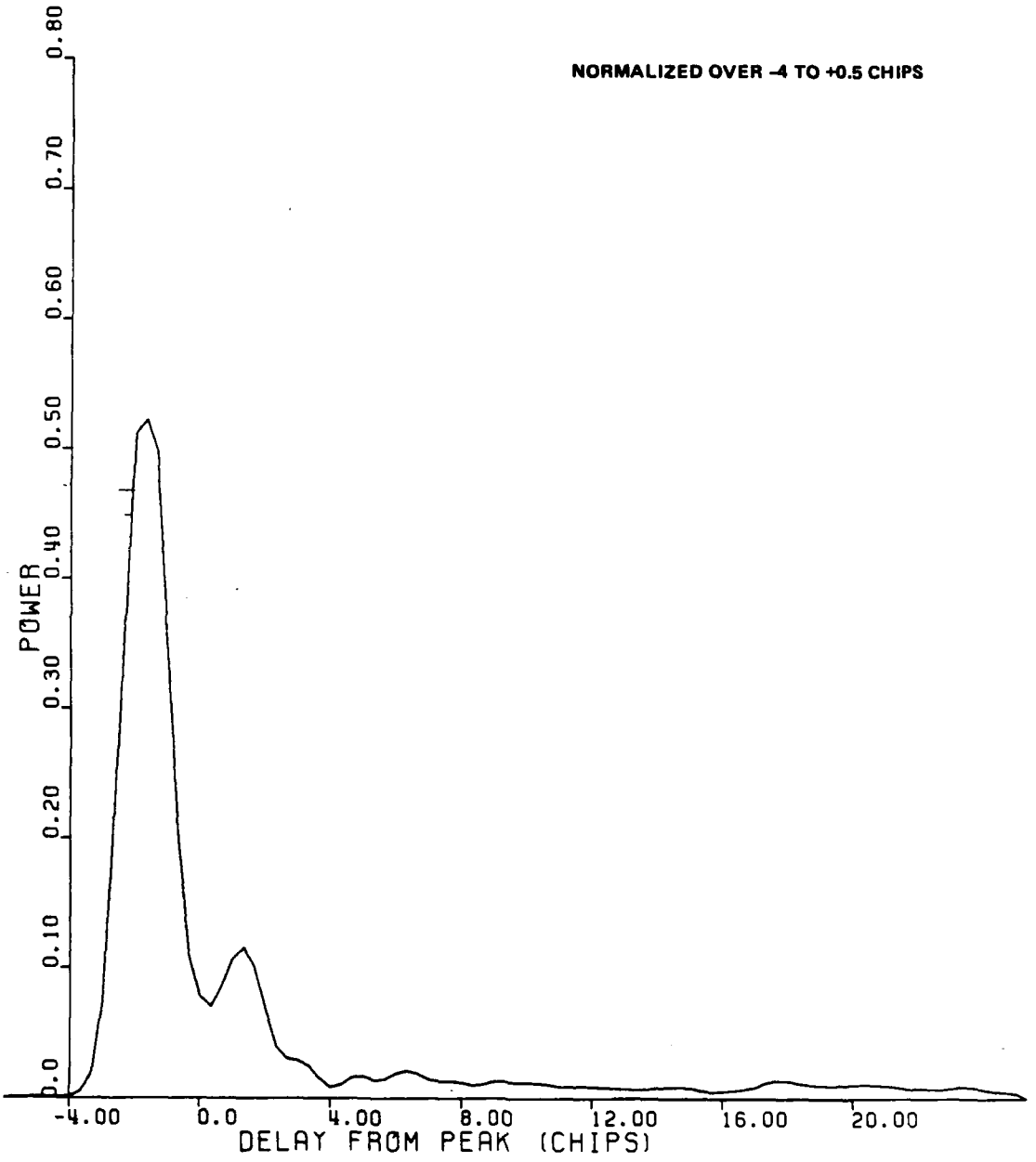

Figure 3-20. Delay power spectrum for Segment 4, Cape San Blas, Beacon 1.

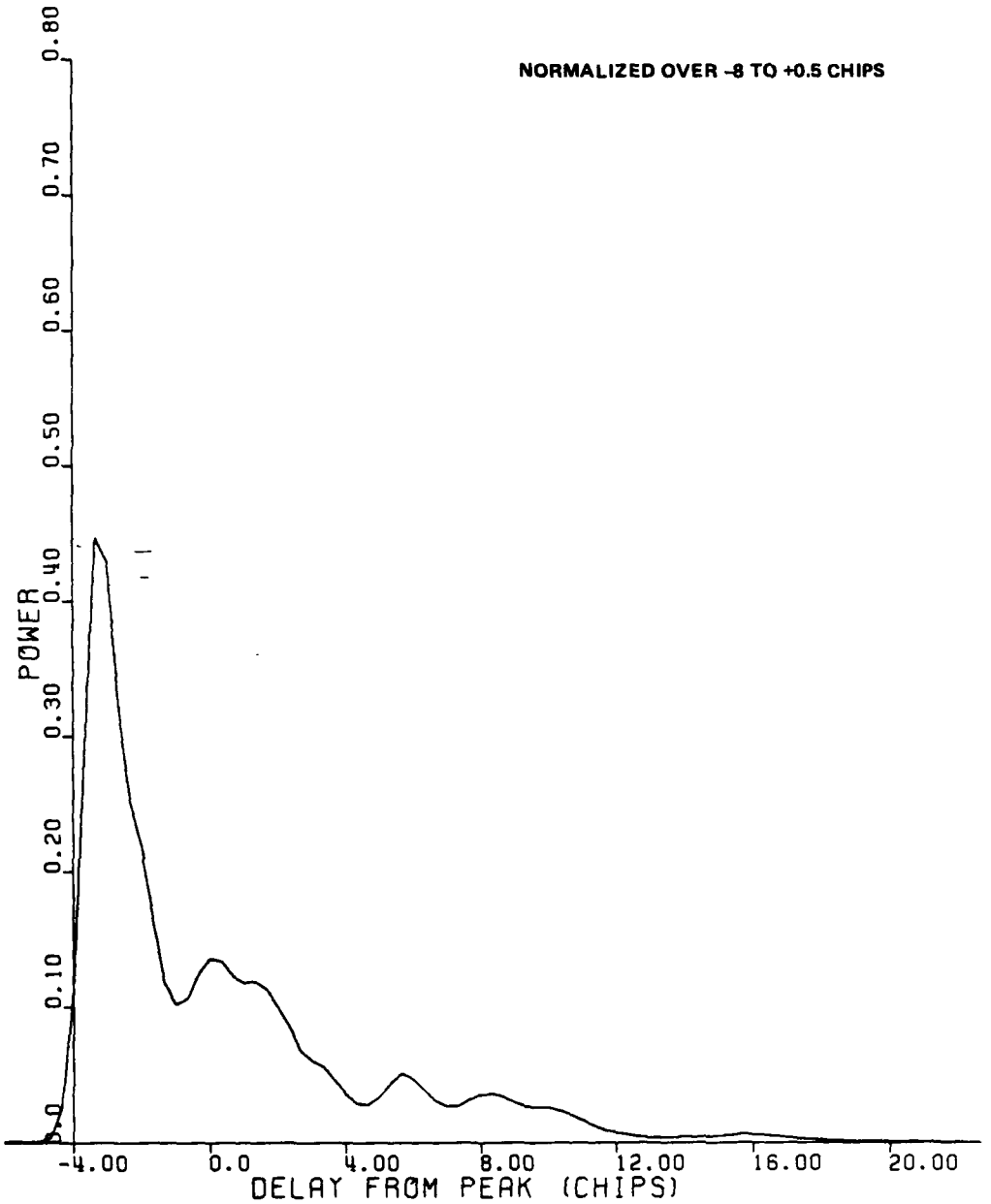

Figure 3-21. Delay power spectrum for Segment 5, Cape San Blas, Beacon 1.

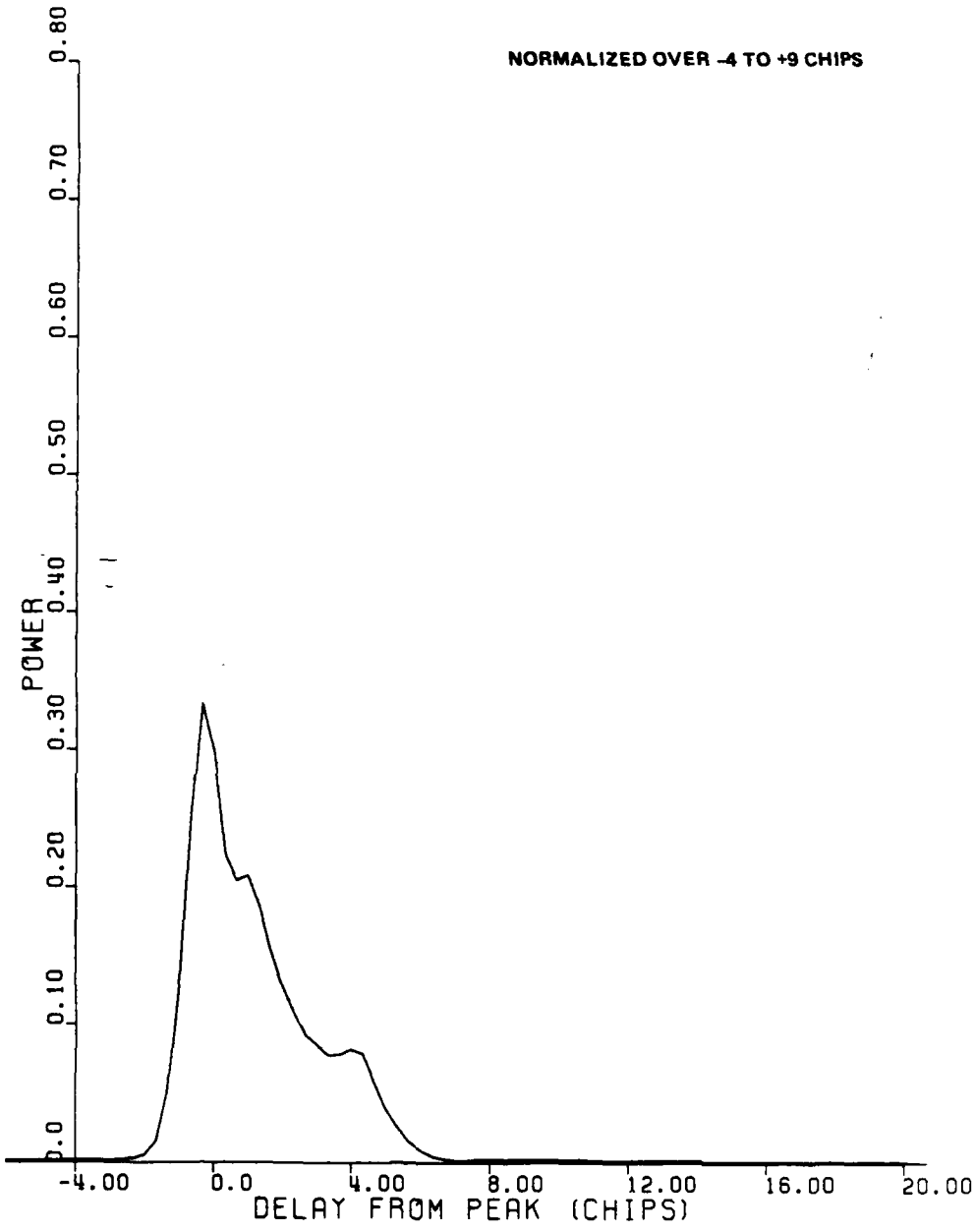

Figure 3-22. Delay power spectrum for Segment 6, Cape San Blas, Beacon 1.

Generally, the individual segments do not conform to the long-term statistical average of the theoretical delay power spectrum because of the discrete rays evident in each segment. To compensate for the energy at large delays, which should average to a much smaller value than the individual rays present during each segment, and to facilitate a comparison with theory, these segments were renormalized over that portion of the profile that appeared to correspond to a smooth power profile. The normalization interval used is indicated on each figure, referenced to the number of chips past zero delay. For Figures 3-20 and 3-21, Segments 4 and 5, the mean delay was incorrectly computed resulting in a bias offset; the zero delay in reality is near the peak of the signal. All other segments are correct as shown.

3.6.2 Comparison With Theory

As discussed in Section 2.6.7.1, theory can be used to estimate the ratio of the rms delay spread to the rms delay jitter parameter and the coherence bandwidth, f_o, by matching theoretical curves against the measured data presented in Figures 3-17 through 3-22. Figures 2-50 through 2-53 provide plots of the theoretical delay power spectrum against which the measured curves may be matched. Again, in fitting the theoretical curves to these data, the lower values at large delays were not emphasized. Rather, the peak amplitude and width of the main lobe were emphasized. Table 3-2 summarizes the results of this comparison.

From the relationship of the frequency correlation bandwidth parameter to the rms delay spread relation described in Section 2.6.7.1, an estimate of the delay spread can be computed using the rms TOA jitter estimate from Table 3-1. The result of this calculation for each data segment is shown in Table 3-3. It was noted that for Segment 4, as anticipated, the rms jitter has been overestimated in Table 3-1. This results in a poor match between the

Table 3-2. Parameter summary for best fit to measured normalized power delay profiles.

SEGMENT	f_o (MHz)	RMS JITTER TO SPREAD RATIO	COMMENTS
1	> 4	~ 0.5	NOISE ONLY
2	> 4	~ 1	PRIMARILY NOISE
3	1.7	0.25	
4	1.8	0.4	
5	1.0	0.25	
6	0.9	0.25	

Table 3-3. Comparison with RMS jitter data.

Segment	From Table 3-2 f_0	From Table 3-2 RMS Jitter to Spread ratio	From Table 3-1 RMS TOA Jitter (us)	COMPUTED RMS Delay Spread (us)	COMPUTED Jitter/ Spread	COMPUTED RMS Delay Jitter (us)	COMPUTED RMS Delay Spread (us)	RMS Phase (Rad)
1	4 MHz	~1.5	0.0008	~0.0533	~0.02			
2	4	~1.5	0.0122	0.1377	~0.04			
3	1.7	1.25	0.0542	0.1764	0.31	0.1227	0.1813	14.1
4	1.3	1.5	0.0670	0.1573	1.13	0.0836	0.1791	14.4
5	1.1	0.25	0.0504	0.1519	0.33			
6	0.9	0.25	0.0365	0.1731	0.21			

computed and estimated value of the jitter-to-spread ratio. As the curve fit to the power spectrum appears to be a sensitive measure, it is possible to compute the jitter and spread implied. This calculation is shown in the last three columns for Segments 3 and 4 where the agreement with the rms jitter calculation was poor. Note that this implies a smaller value for the rms dispersive phase.

3.7 CHANNEL TRANSFER FUNCTION

The channel transfer function, by definition, is the Fourier transform of the channel impulse response. A few samples of the channel transfer function are presented here that correspond to the Mutual Coherence Function Analysis presented in Section 3.10.

The complex channel impulse response measured and presented in Section 3.3.2 can be transformed to obtain a channel transfer function representation. Figure 3-23 and 3-24 show the magnitude of the channel transfer function at two selected times. Figure 3-23 shows the channel transfer function just before the occultation interval at 2345:01.8Z. The central lobe of the sinc squared spectrum is readily apparent. Ninety samples of the impulse response spanning 0.23 second were averaged in making these figures. Figure 3-24 shows the transfer function during occultation at 2345:22.8Z. The prominent nulls appearing in this spectrum are due to strong multipath interference.

Since the signal measured is actually the convolution of the signal autocorrelation function and the channel impulse response, these figures actually represent the product of a sinc squared spectrum and the channel transfer function.

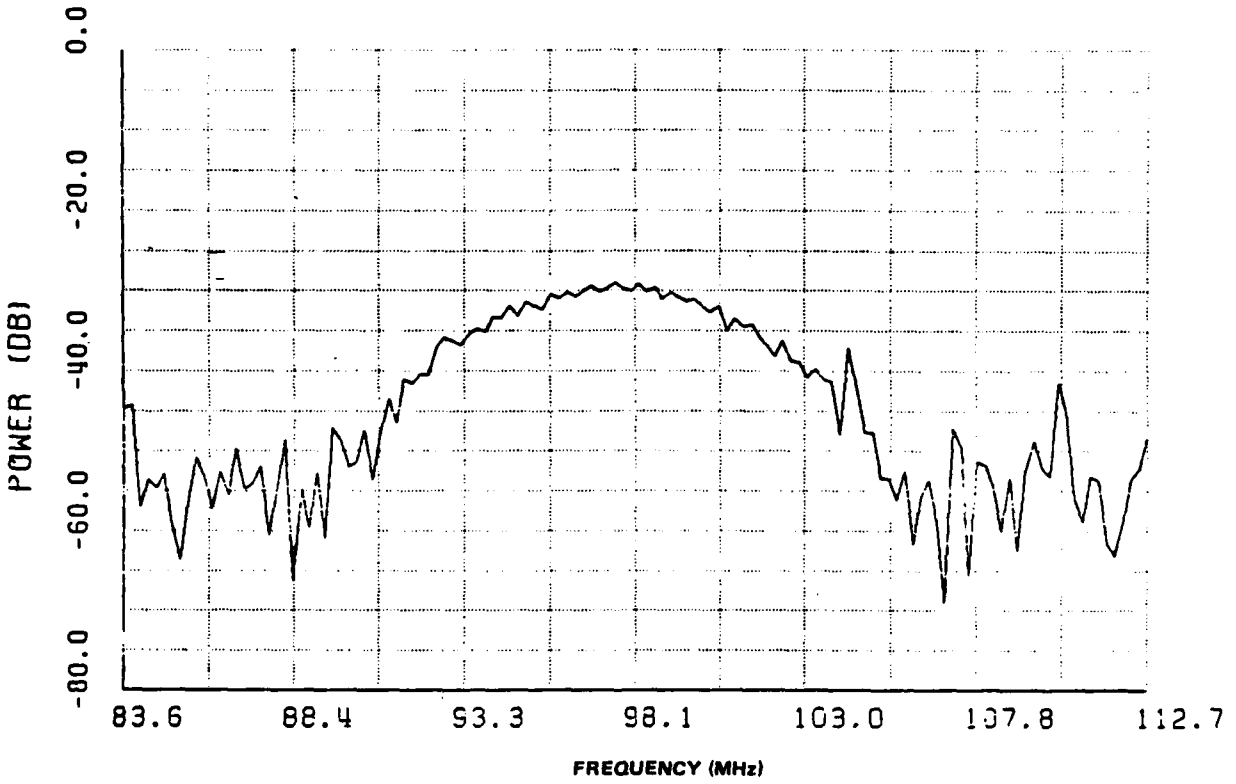

Figure 3-23. Channel transfer function magnitude squared at 2345:01.8Z prior to occultation.

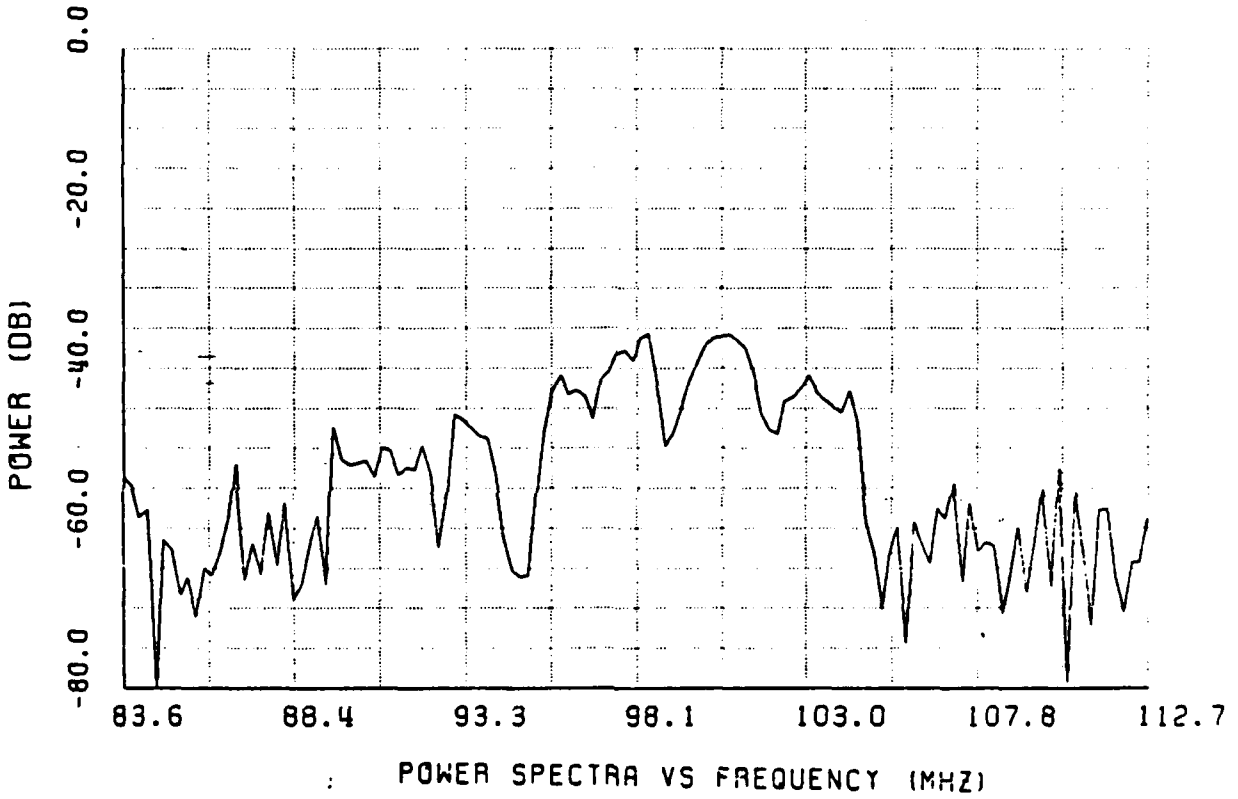

Figure 3-24. Channel transfer function magnitude squared at 2345:22.8Z.

3.8 FADING WAVEFORM AT 98 MHZ

The fading waveform at 98 MHz can be synthesized from the channel transfer function data, as presented earlier. This permits a calculation of the received phase PSD and a calculation of the angular spectrum at 98 MHz. These data are presented here.

3.8.1 Fading Waveform

The fading waveform at 98 MHz can be obtained by transforming the channel impulse response of each data record collected during the occultation to obtain the channel transfer function, samples of which were shown in Section 3.7. From these transformed records, the 98-MHz component can be selected and plotted, as shown in Figure 3-25. The peak phase advance associated with the barium plasma can be estimated to be 91 cycles from these data. As discussed in Section 3.4.2, each cycle of phase shift corresponds to 7.29×10^{10} cm^{-2} of electron content at 98 MHz. This provides an estimate for the peak electron content associated with the barium plasma of approximately 6.6×10^{12} cm^{-2}. This is in excellent agreement with the estimate obtained earlier in Section 3.4.2 from the time-of-arrival shift, which was 6.0×10^{12} cm^{-2}.

3.8.2 Received Phase PSD at 98 MHz

The phase power spectral density (PDS) corresponding to the received signal phase is shown in Figure 3-26. The slope corresponds to approximately 22 dB/decade or $f^{-2.2}$. This is typical of the phase PSD expected in the far field of a diffraction screen[2].

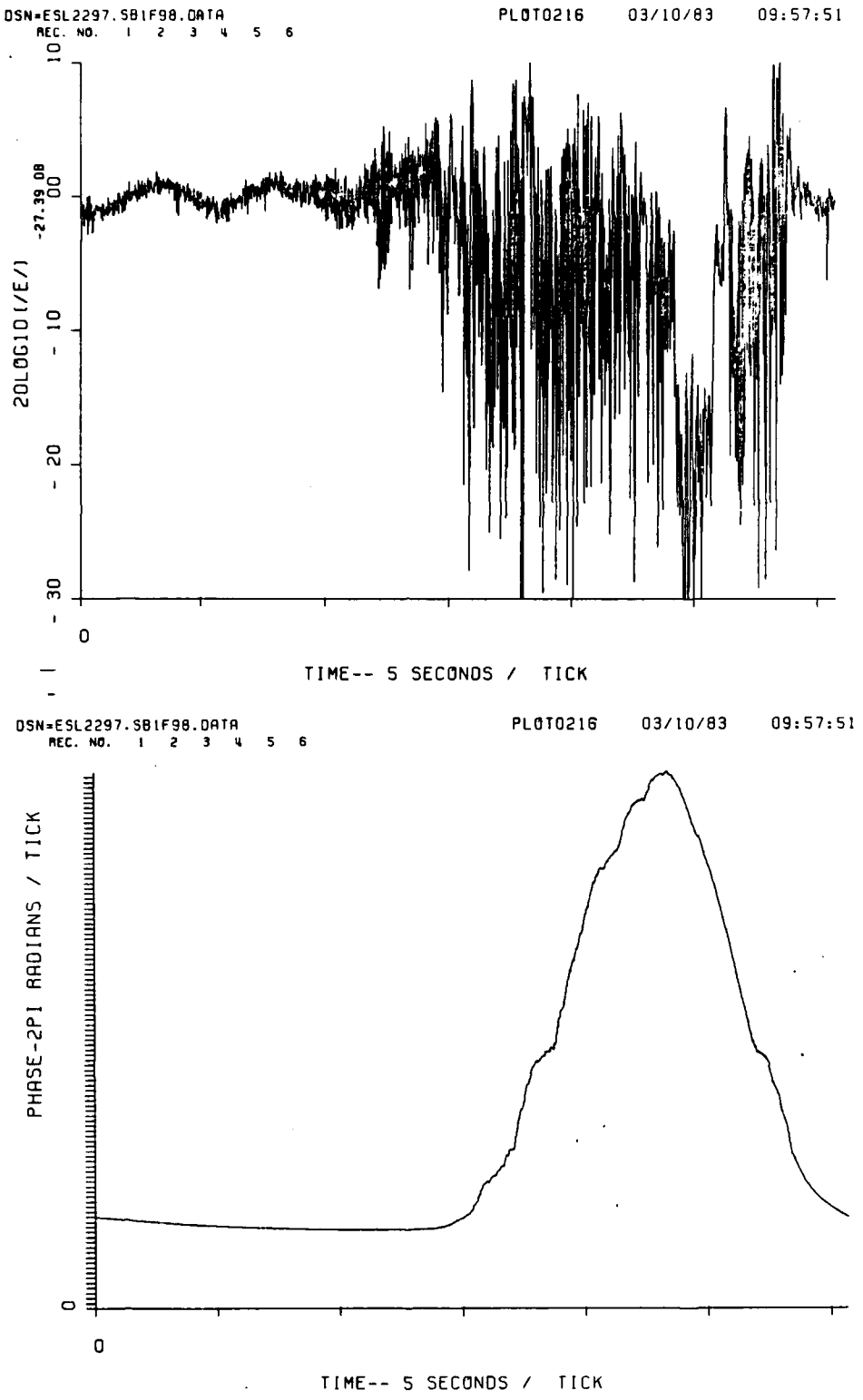

Figure 3-25. Received amplitude and phase at 98 MHz, Cape San Blas, Beacon 1.

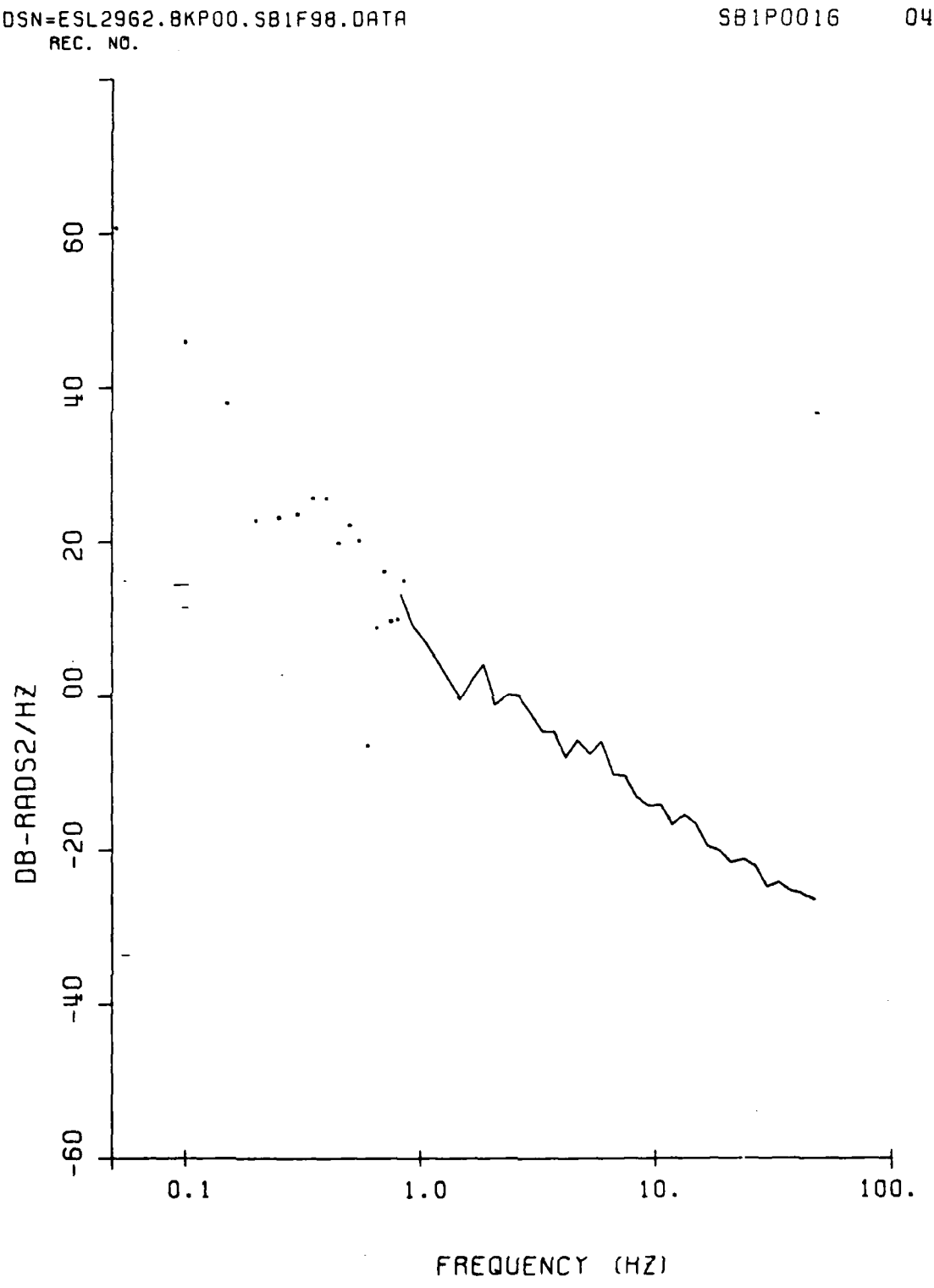

Figure 3-26. Phase power spectral density at 98 MHz.

3.8.3 Angular Spectrum at 98 MHz

The transform of the complex fading waveform at 98 MHz yields the angular spectrum of the received signal. This results since time corresponds to spatial position in the diffraction field. The angular spectrum is shown in Figure 3-27. This spectrum strongly resembles that obtained for the St. George Island beacon receiver path shown in Figure 2-69. The sharp break frequency near 40 Hz is also evident in this figure.

The real frequency axis may be converted to angle through the transform

$$\theta = \sin^{-1} (f\lambda/V) \quad ,$$

where

V is the rocket transverse transit velocity.

Assuming the transverse patter velocity is approximately the same for Cape San Blas as for St. George Island, or approximately 980 m/sec, then 10 Hz corresponds to approximately 1.8 degrees.

3.8.4 RMS Time Delay Spread and Angular Spectrum

As discussed in Section 2.8.4, geometrical arguments indicate that the basic cause of signal TOA spread is the geometric increase in path length produced by the plasma angular scattering. The angular scattering is closely given by the angular spectrum of the signal at frequencies near the center of the signal bandwidth. Thus, a direct mapping between the angular spectrum and the energy delay profile (delay power spectrum) is expected. Since the angular spectrum appears to correspond closely to that for the

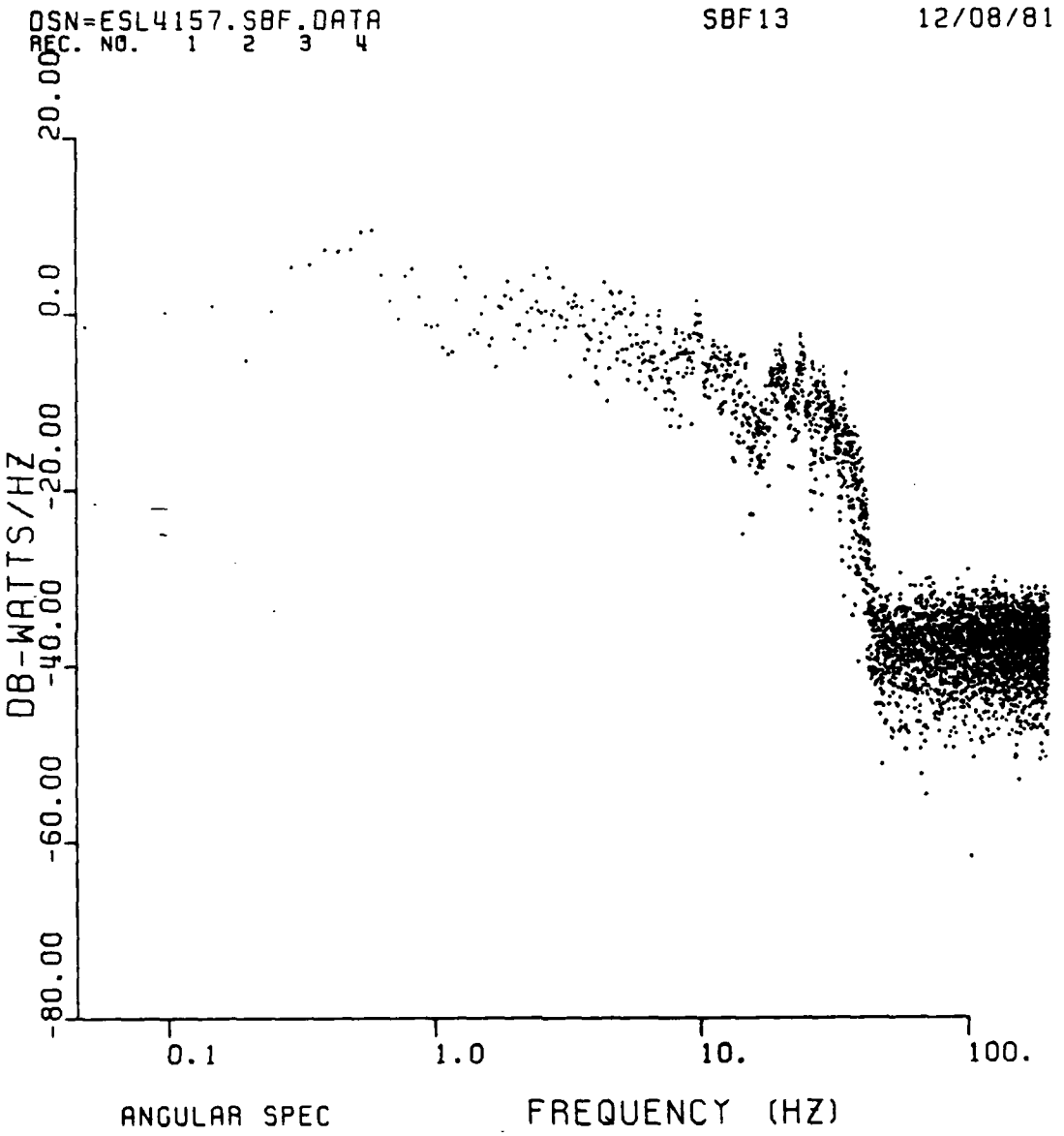

Figure 3-27. Angular spectrum at Cape San Blas, Beacon 1.

St. George Island path, the angular spectrum parameters are approximately as presented previously in Table 2-5.

Likewise, the angular spectrum is again well described by an exponential form as presented in Section 2.8.4.

3.9 BACK-PROPAGATION PROCESSING AT 98 MHZ

Backward propagation of the 98-MHz signal component of the received diffraction pattern swept out by the beacon rocket can be performed as discussed in Section 2.9 using thin phase screen angular spectrum techniques. The extent to which amplitude fluctuations diminish with back-propagation is a function of the extent of the striated plasma along the line-of-sight and the noise received during the measurement. Because the rocket trajectory takes the beacon on a downward path that moves away from the striation mass over the occultation interval, no one back-propagation distance is uniquely correct. For these reasons, it is not possible to determine the in situ phase power spectral density from the beacon data.

The scintillation index and the back-propagation results obtained are described in the following sections for reference. The data are interesting only in that the S^4 index versus back-propagation distance and the 98 MHz signal amplitude behavior provide qualitative agreement with the optical data discussed in Section 3.2.

3.9.1 S^4 Versus Distance

The S^4 scintillation index is used as a measure of the amplitude fluctuation as discussed in Section 2.9.1. The amount the S^4 index decreases with back-propagation and its value after back-propagation gives a good indication as to how well the data back-propagated in a thin phase screen sense. Figure 3-28 is a plot

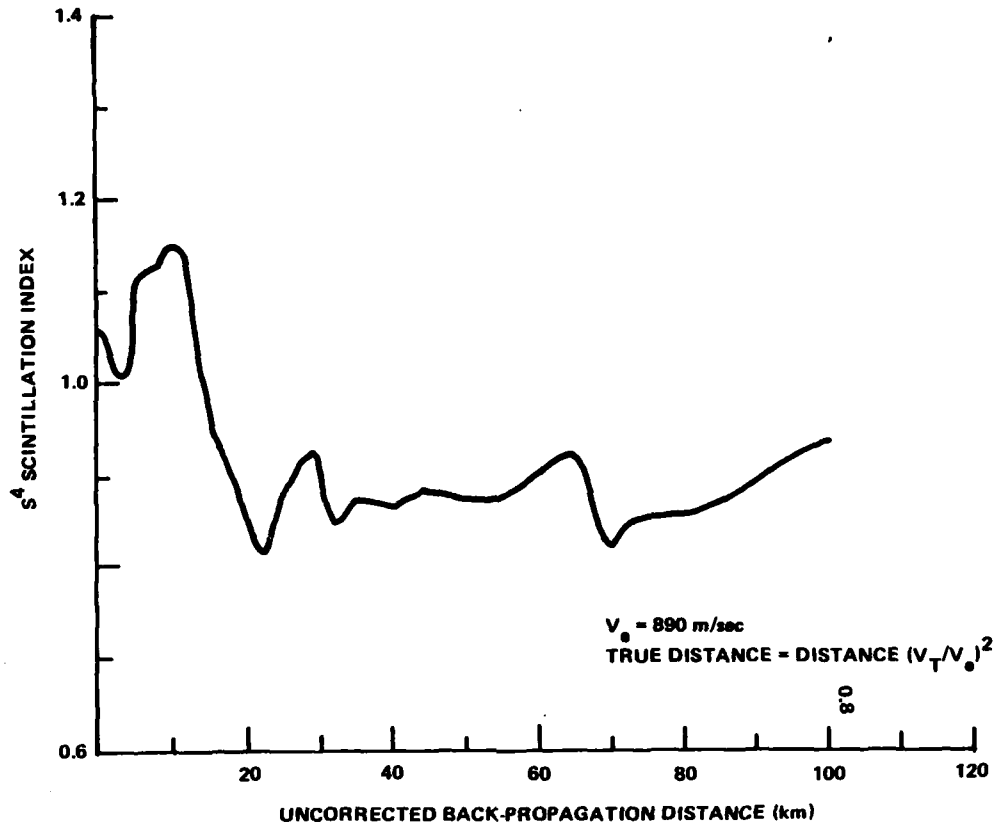

Figure 3-28. S^4 scintillation index versus back-propagation distance for Cape San Blas, Beacon 1.

of the scintillation index versus back-propagation distance for Cape San Blas, Beacon 1. The back-propagation distance was initially computed assuming an effective transverse velocity, V_e, of approximately 890 m/sec. The true velocity is likely to be similar to that of the St. George Island path, approximately 980 m/sec. The distance axis scales by the factor $(V_T/V_e)^2$, where V_T is the true transverse velocity.

The S^4 index exhibits a rapid decrease over the first 23 km and displays a prominent minimum near 23 km (27 km corrected). This is consistent with the optical data that would indicate striations from around 18 to 50 km from the rocket over its occultation interval (see Section 3.2).

3.9.2 Back-Propagation Plots

Plots of the back-propagated signal amplitude, phase and phase power spectrum are presented in Figures 3-29 through 3-46 over the first 40 km. The distances noted are the uncorrected values corresponding to the 890 m/sec velocity.

It can be noted in comparing Figure 3-29 with Figure 3-43 that the scintillation effects near the beginning of the occultation diminish in frequency and intensity near 35 km, consistent with the optical observations of the striation locations presented in Section 3.2.2. It is also noted that near the end of the occultation, the best back propagation distance is near 25 km (see Figure 3-39). As noted, no single back-propagation distance is uniquely correct over the occultation interval. Accordingly, the behavior exhibited versus propagation distance is consistent with expectations.

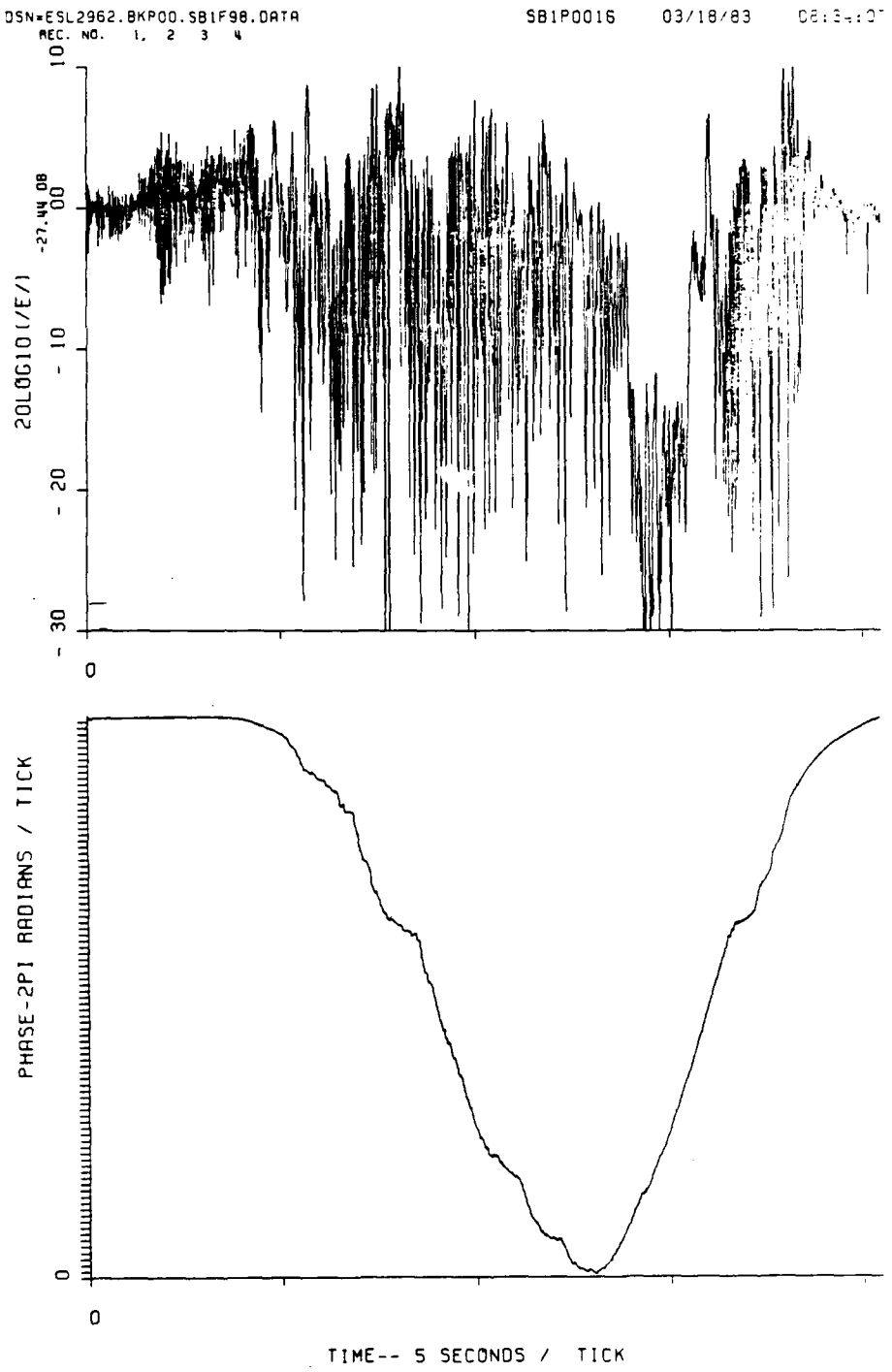

Figure 3-29. Amplitude and phase before back-propagation, Cape San Blas, Beacon 1.

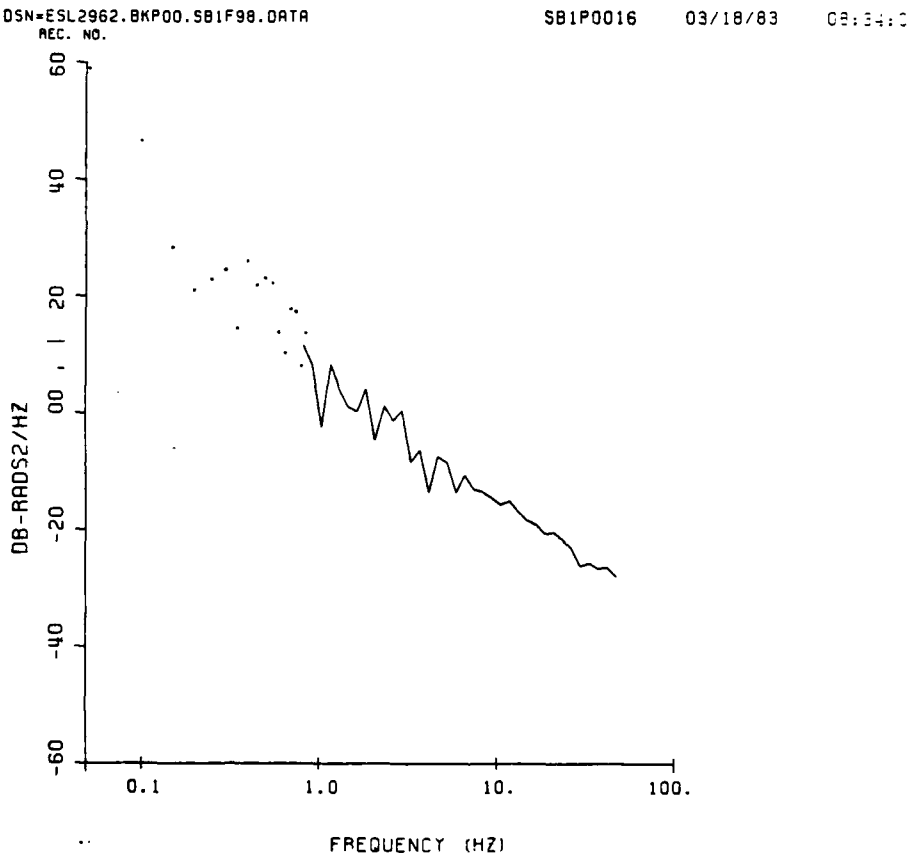

Figure 3-30. Phase power spectrum before back-propagation, Cape San Blas, Beacon 1.

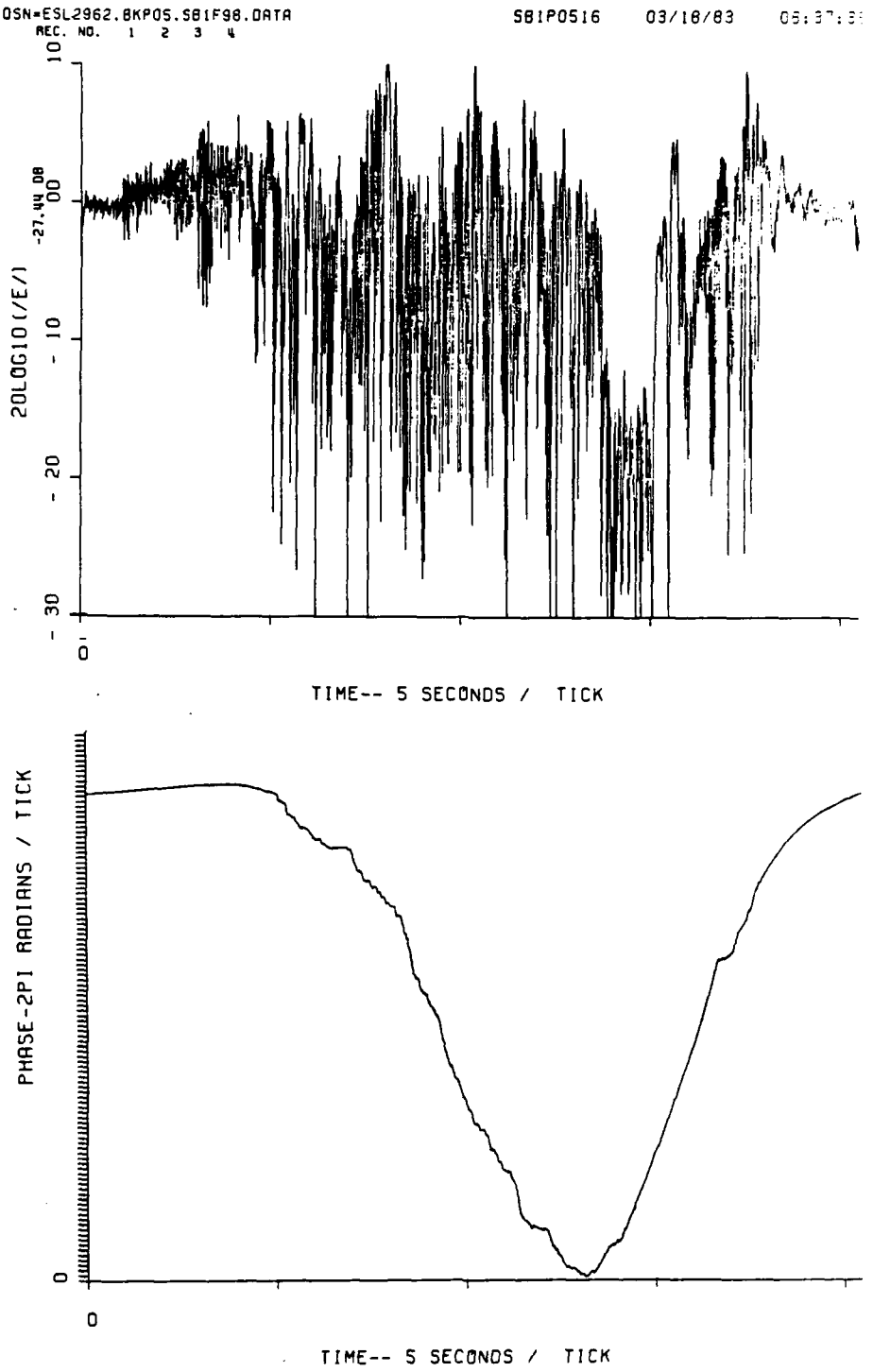

Figure 3-31. Back-propagated amplitude and phase, Cape San Blas, Beacon 1, 5 km.

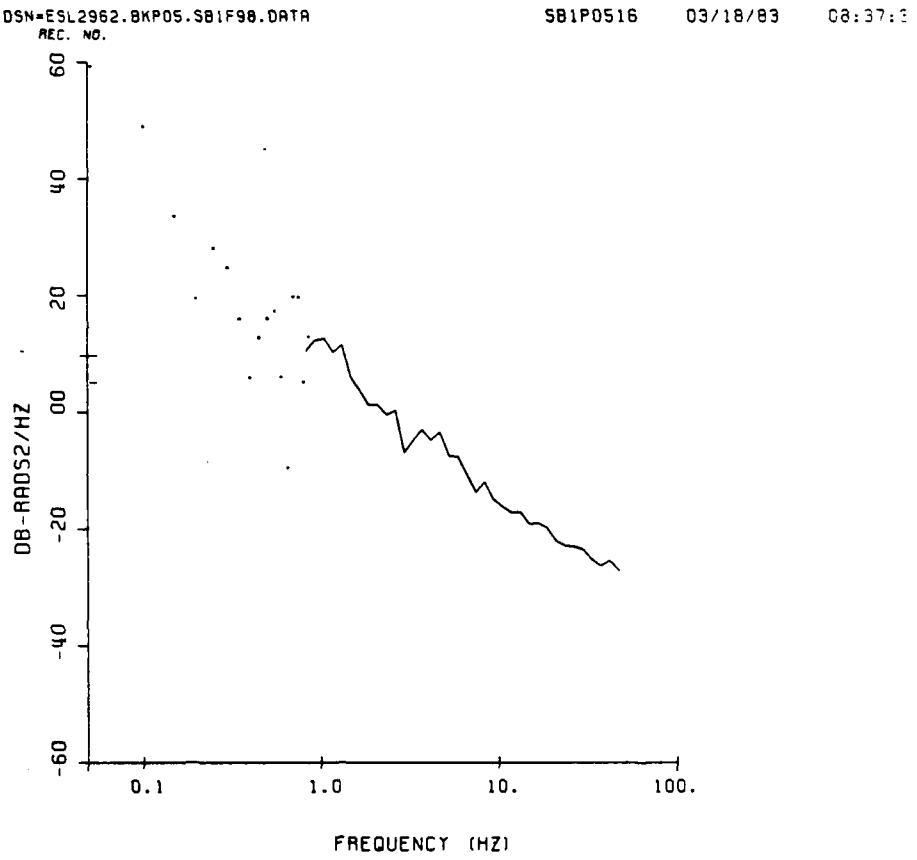

Figure 3-32. Back-propagated phase power spectrum, Cape San Blas, Beacon 1, 5 km.

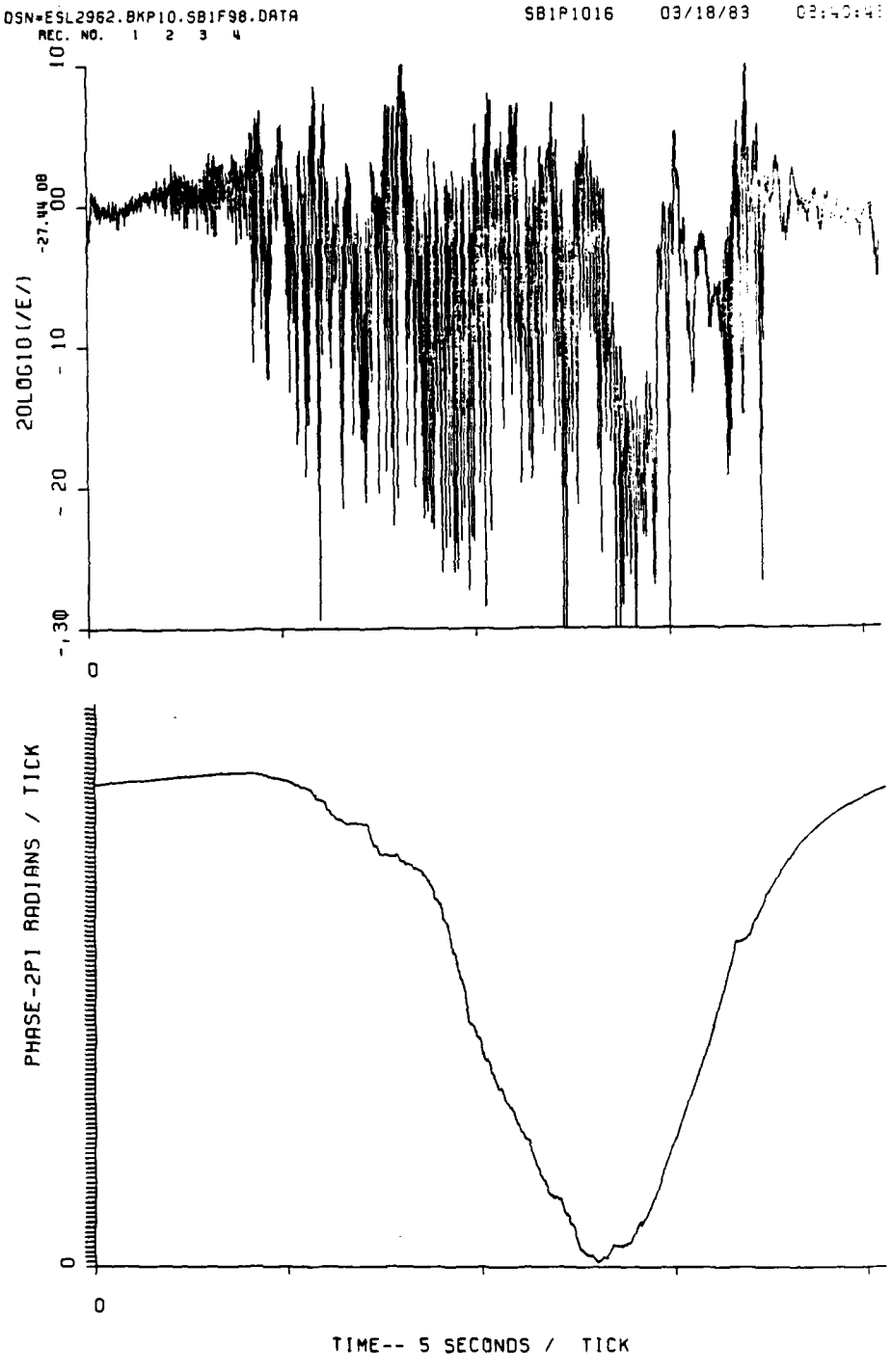

Figure 3-33. Back-propagated amplitude and phase, Cape San Blas, Beacon 1, 10 km.

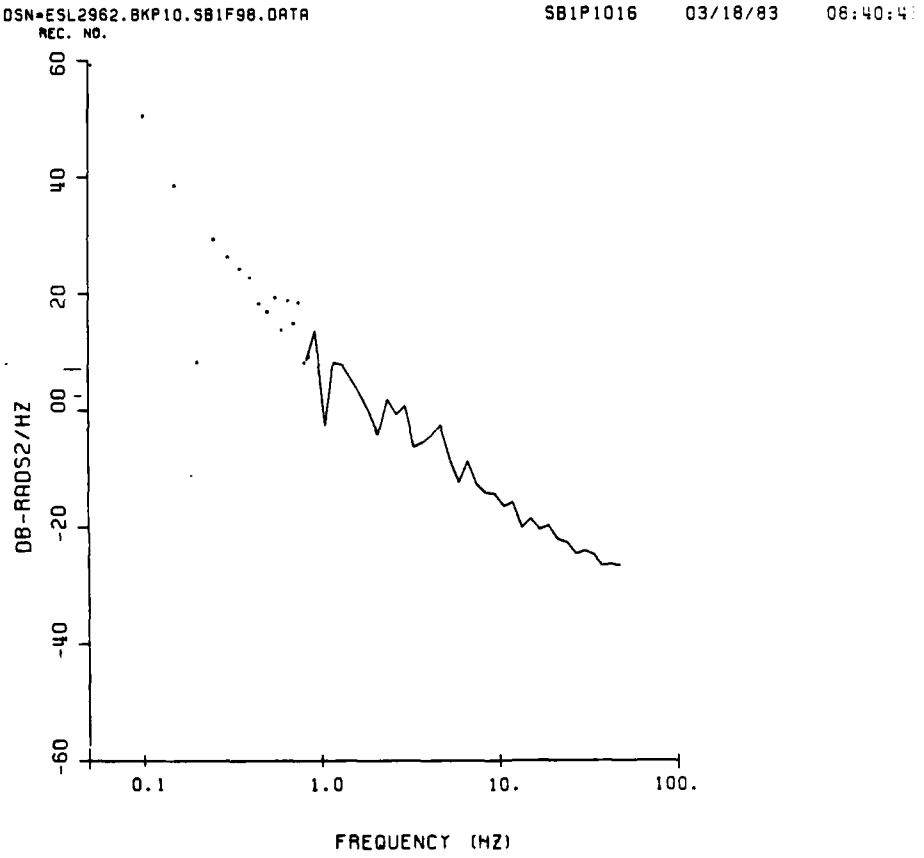

Figure 3-34. Back-propagated phase power spectrum, Cape San Blas, Beacon 1, 10 km.

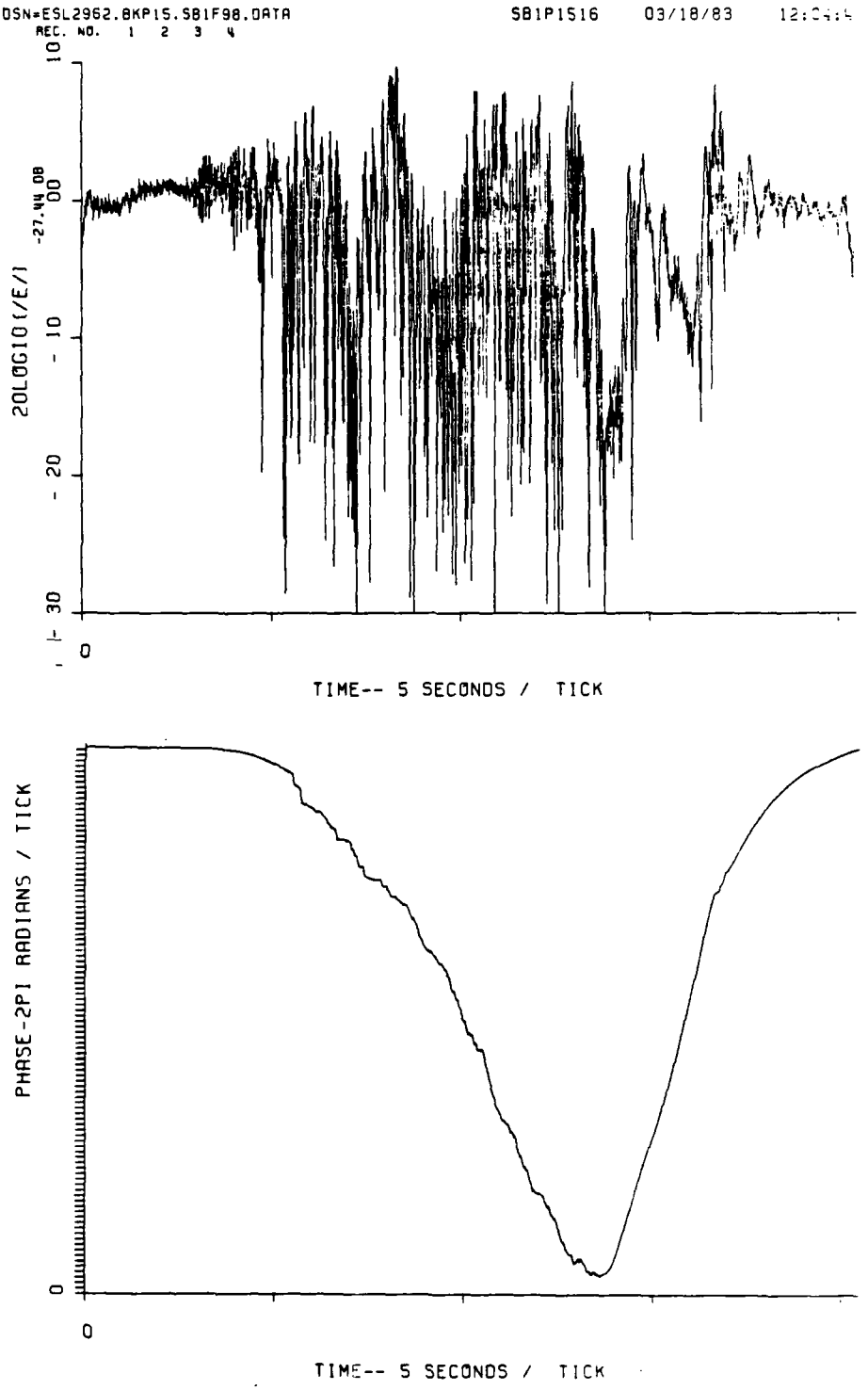

Figure 3-35. Back-propagated amplitude and phase, Cape San Blas, Beacon 1, 15 km.

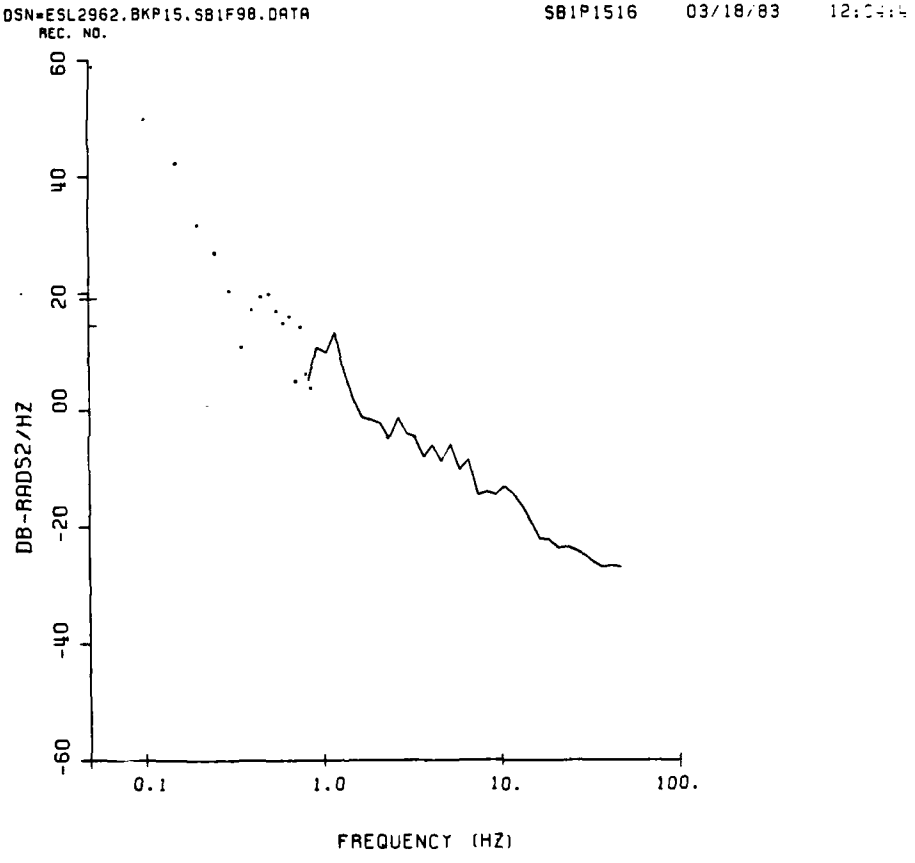

Figure 3-36. Back-propagated phase power spectrum, Cape San Blas, Beacon 1, 15 km.

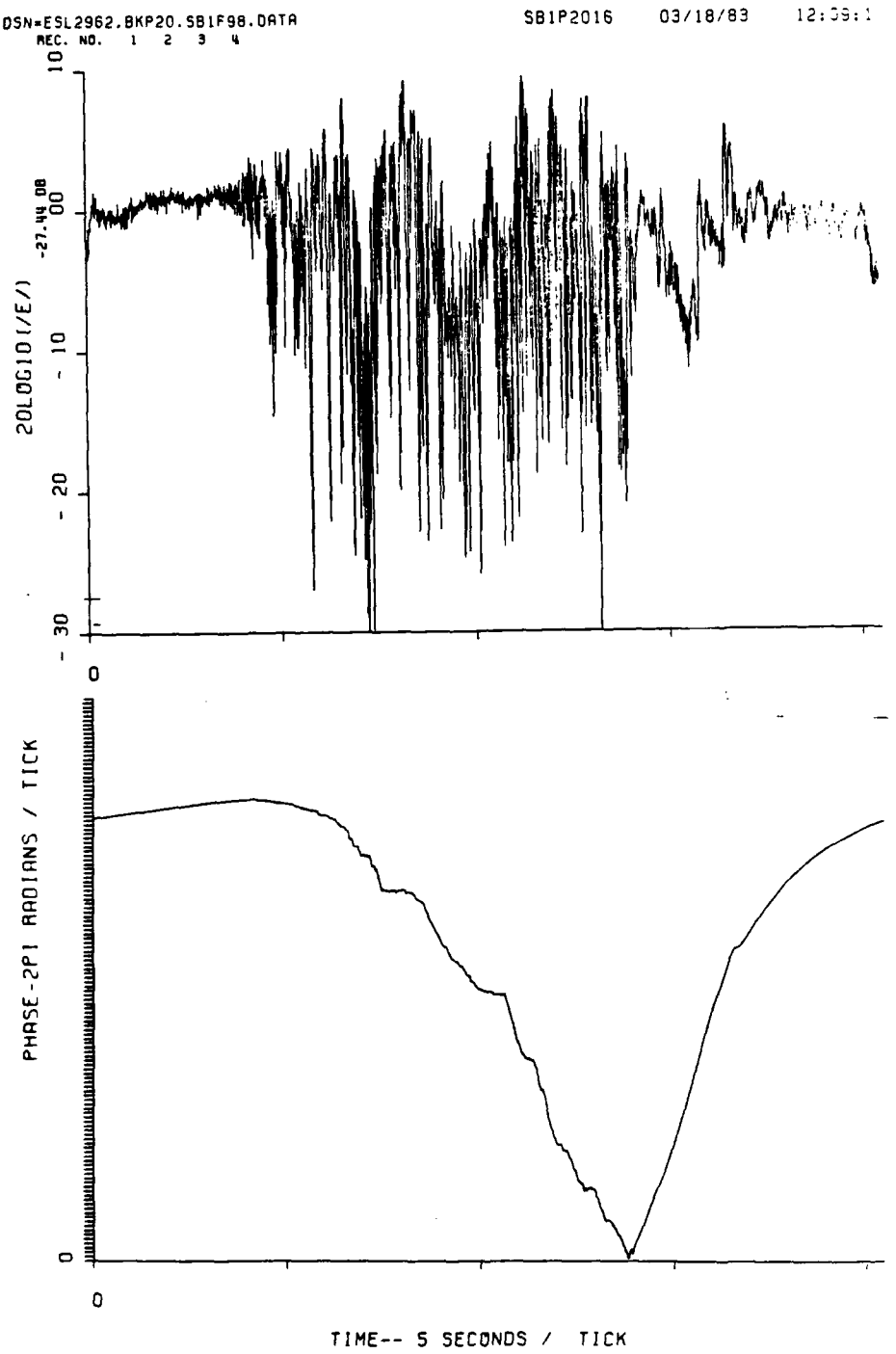

Figure 3-37. Back-propagated amplitude and phase, Cape San Blas, Beacon 1, 20 km.

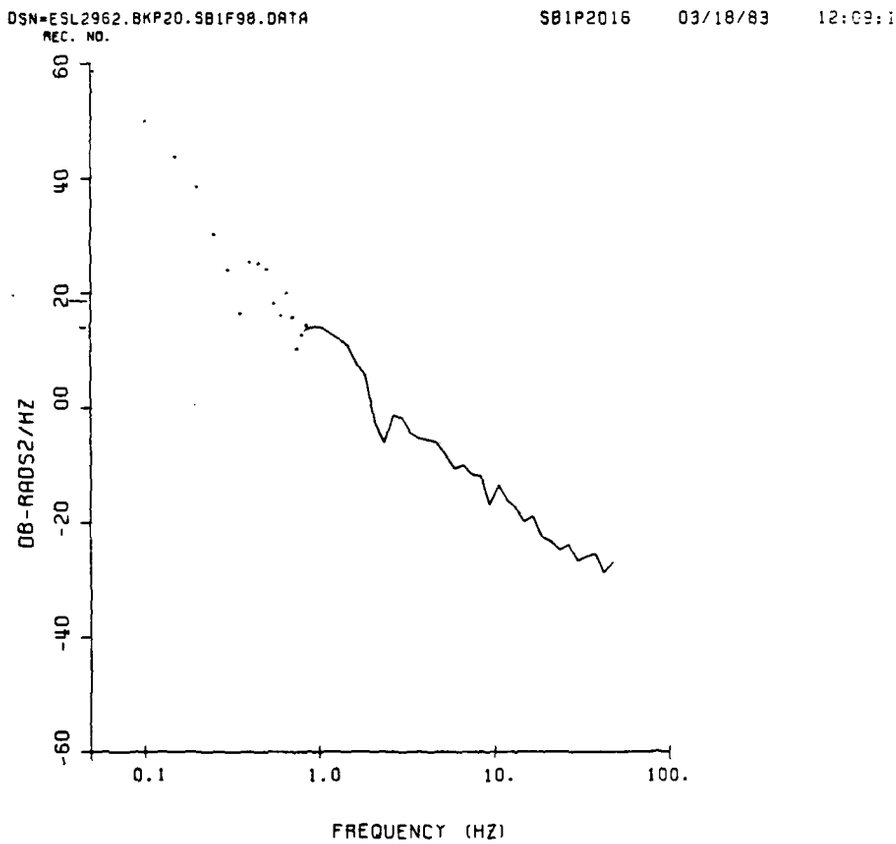

Figure 3-38. Back-propagated phase power Spectrum, Cape San Blas, Beacon 1, 20 km.

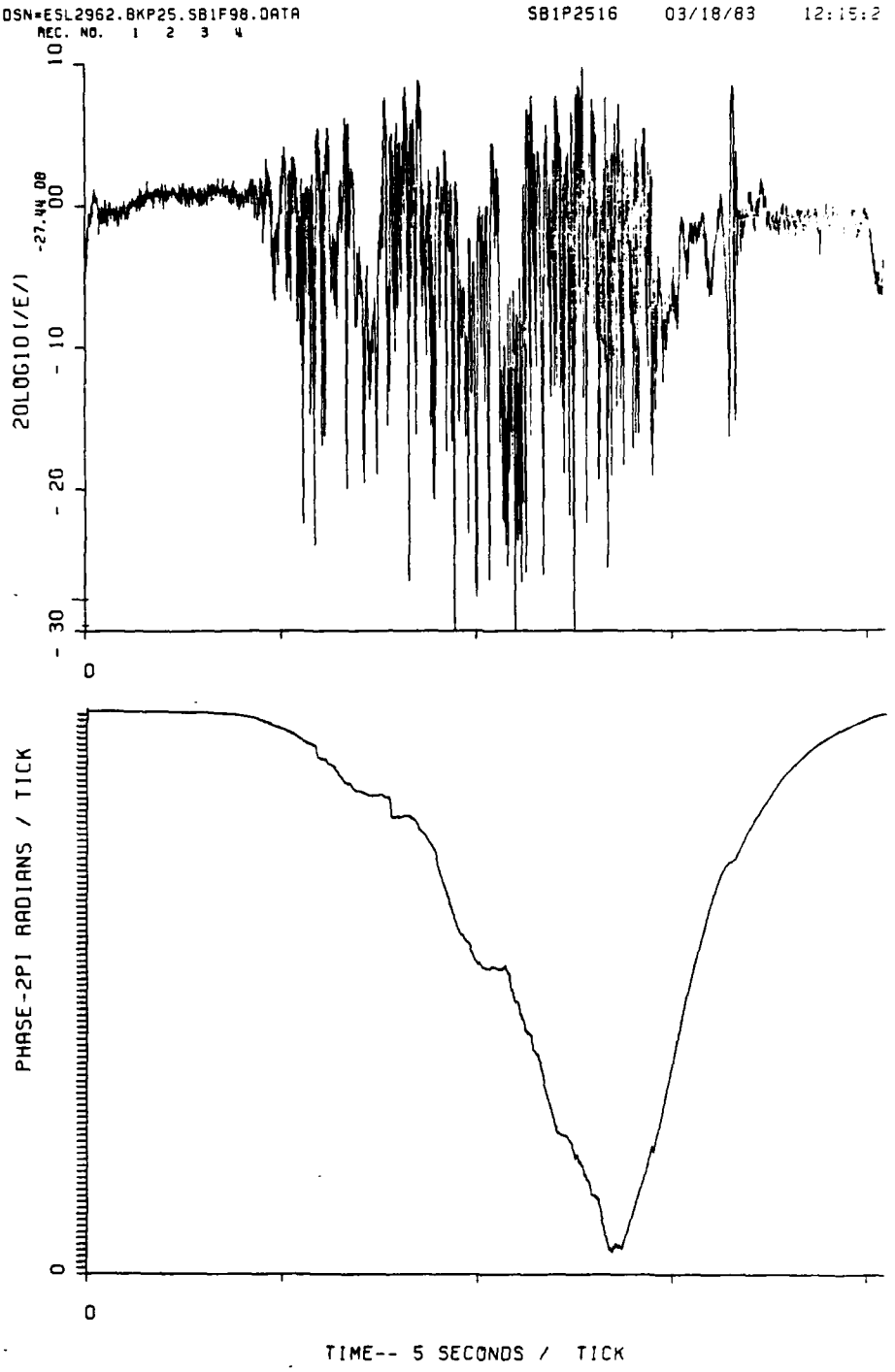

Figure 3-39. Back-propagated amplitude and phase, Cape San Blas, Beacon 1, 25 km.

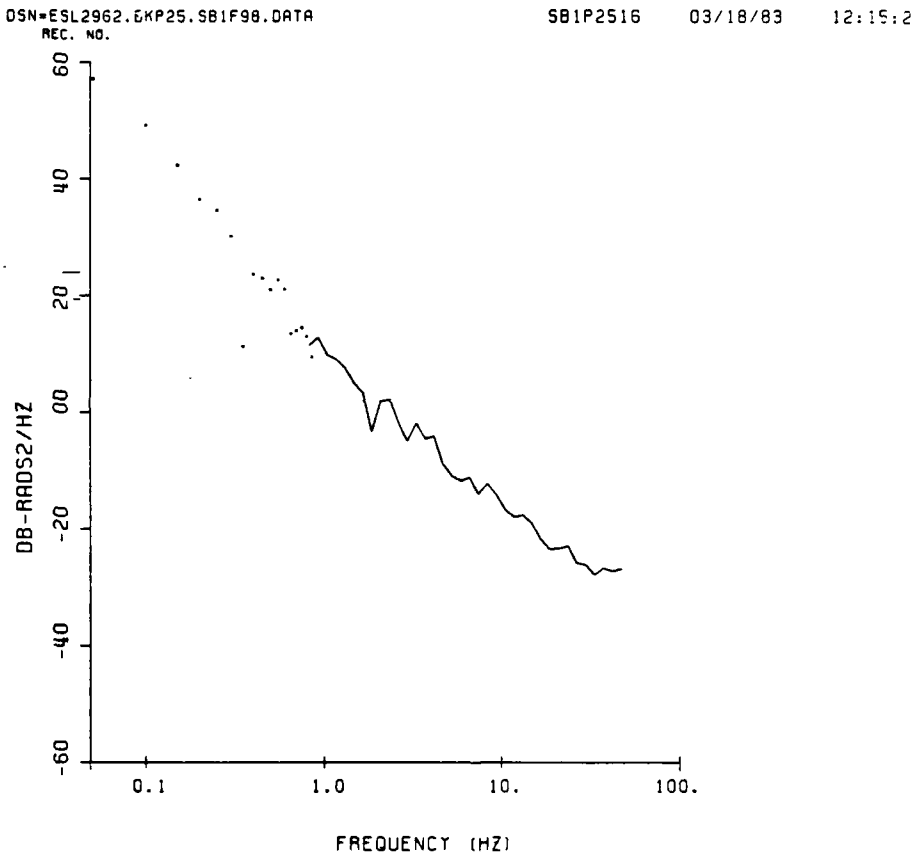

Figure 3-40. Back-propagated phase power spectrum, Cape San Blas, Beacon 1, 25 km.

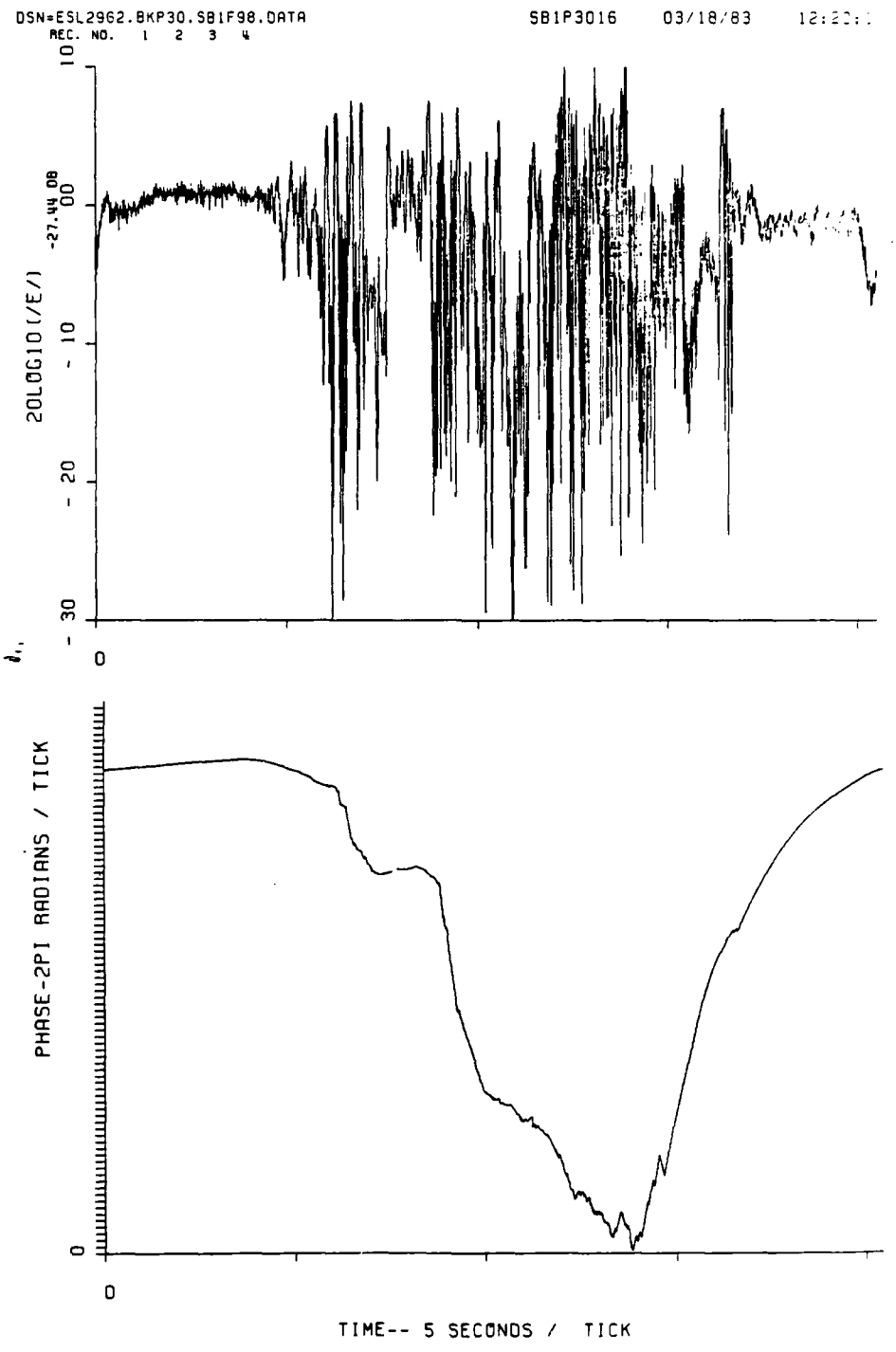

Figure 3-41. Back-propagated amplitude and phase, Cape San Blas, Beacon 1, 30 km

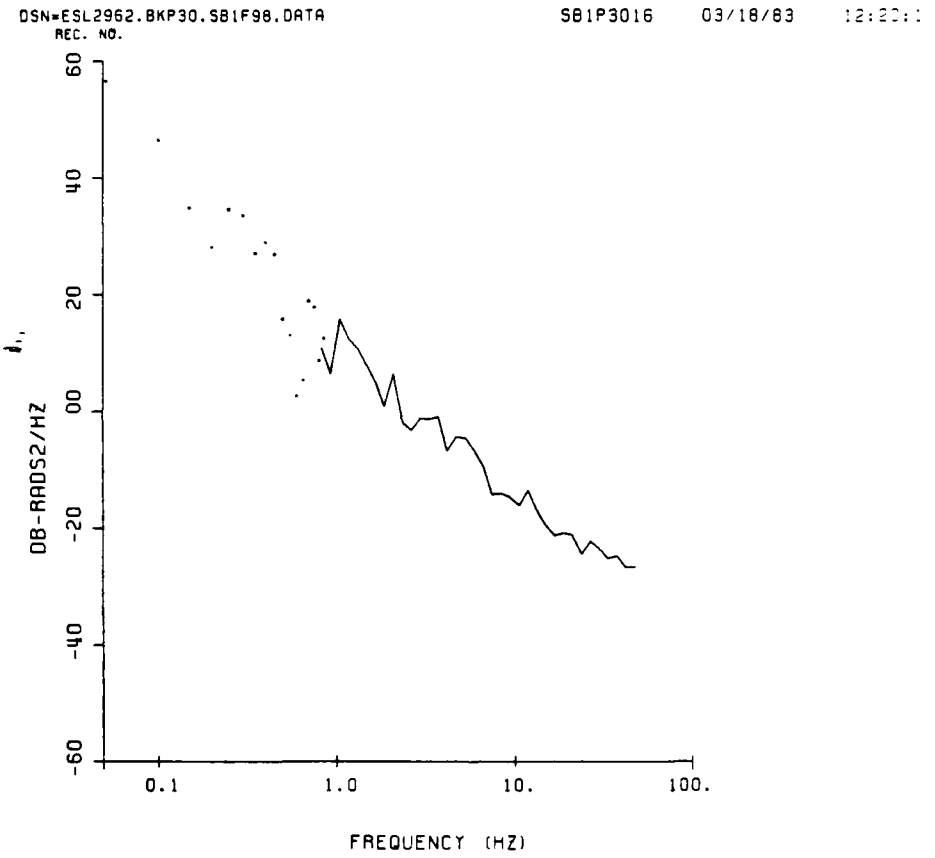

Figure 3-42. Back-propagated phase power spectrum, Cape San Blas, Beacon 1, 30 km.

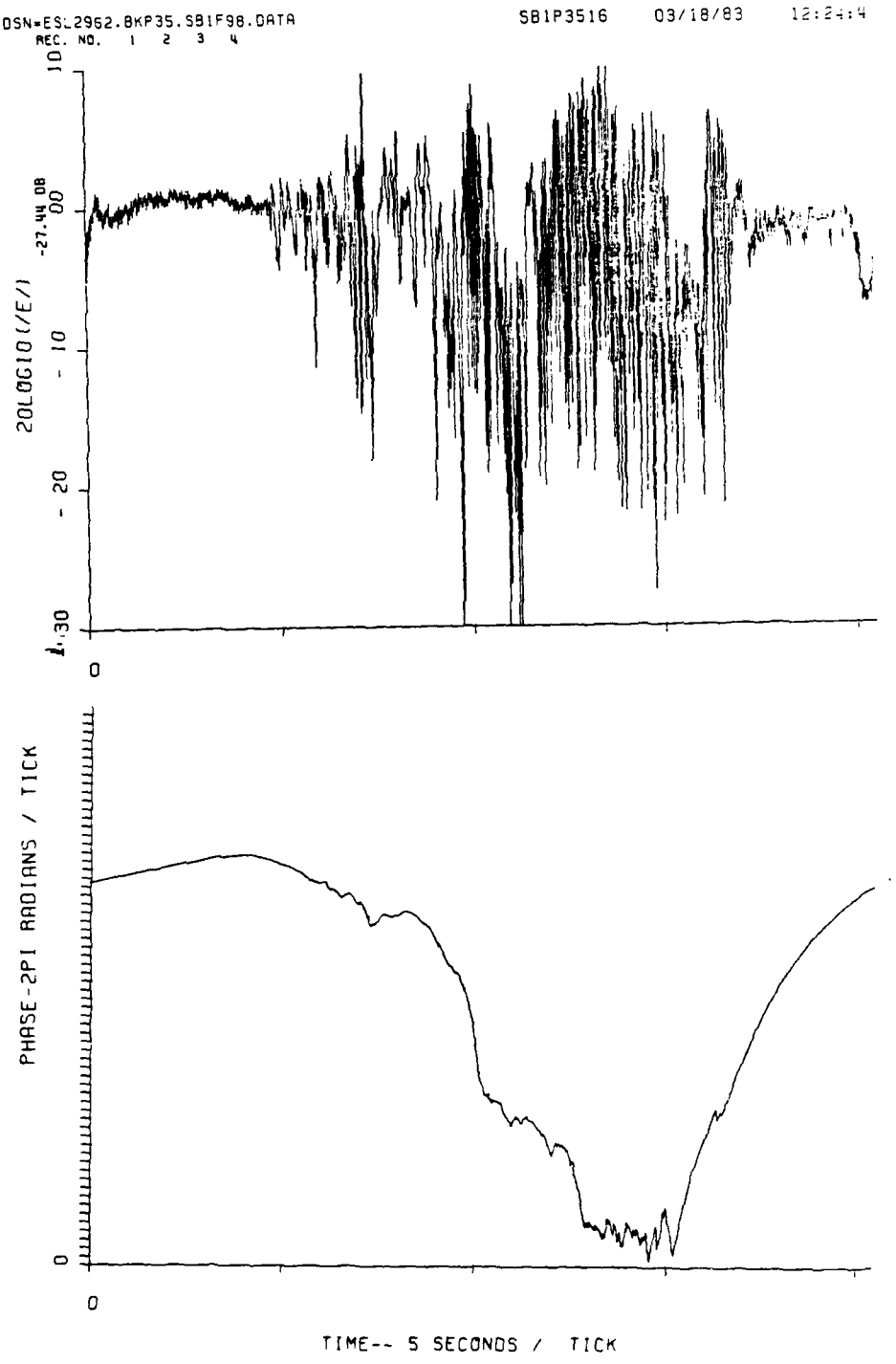

Figure 3-43. Back-propagated amplitude and phase, Cape San Blas, Beacon 1, 35 km.

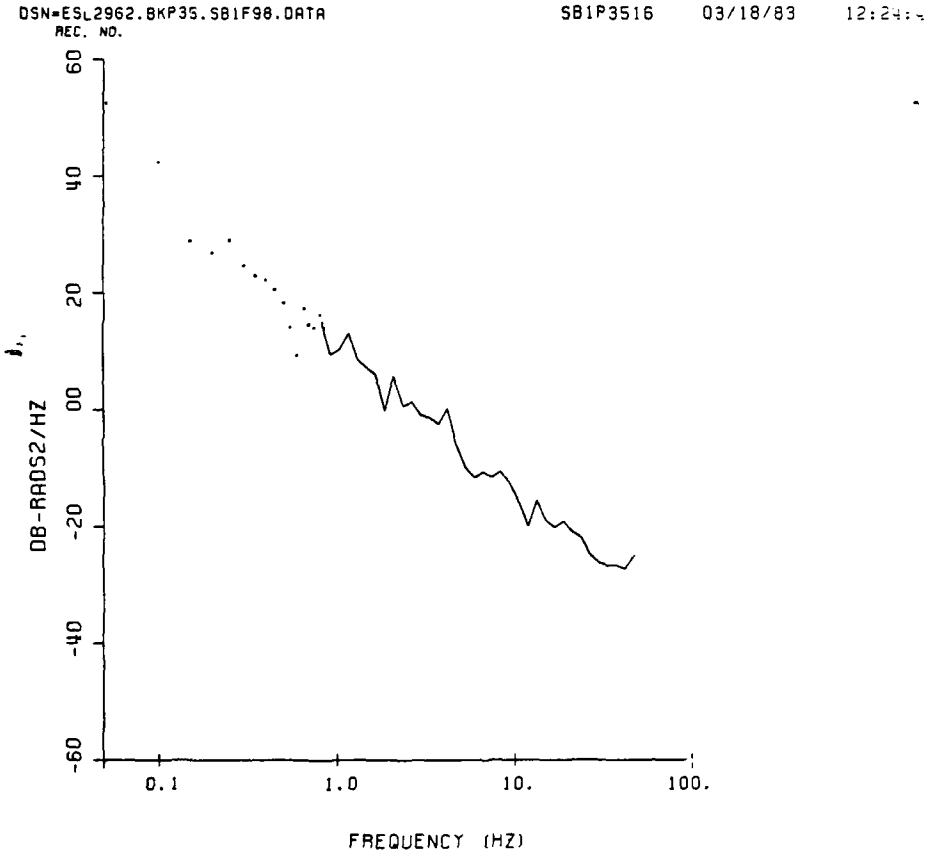

Figure 3-44. Back-propagated phase power spectrum, Cape San Blas, Beacon 1, 35 km.

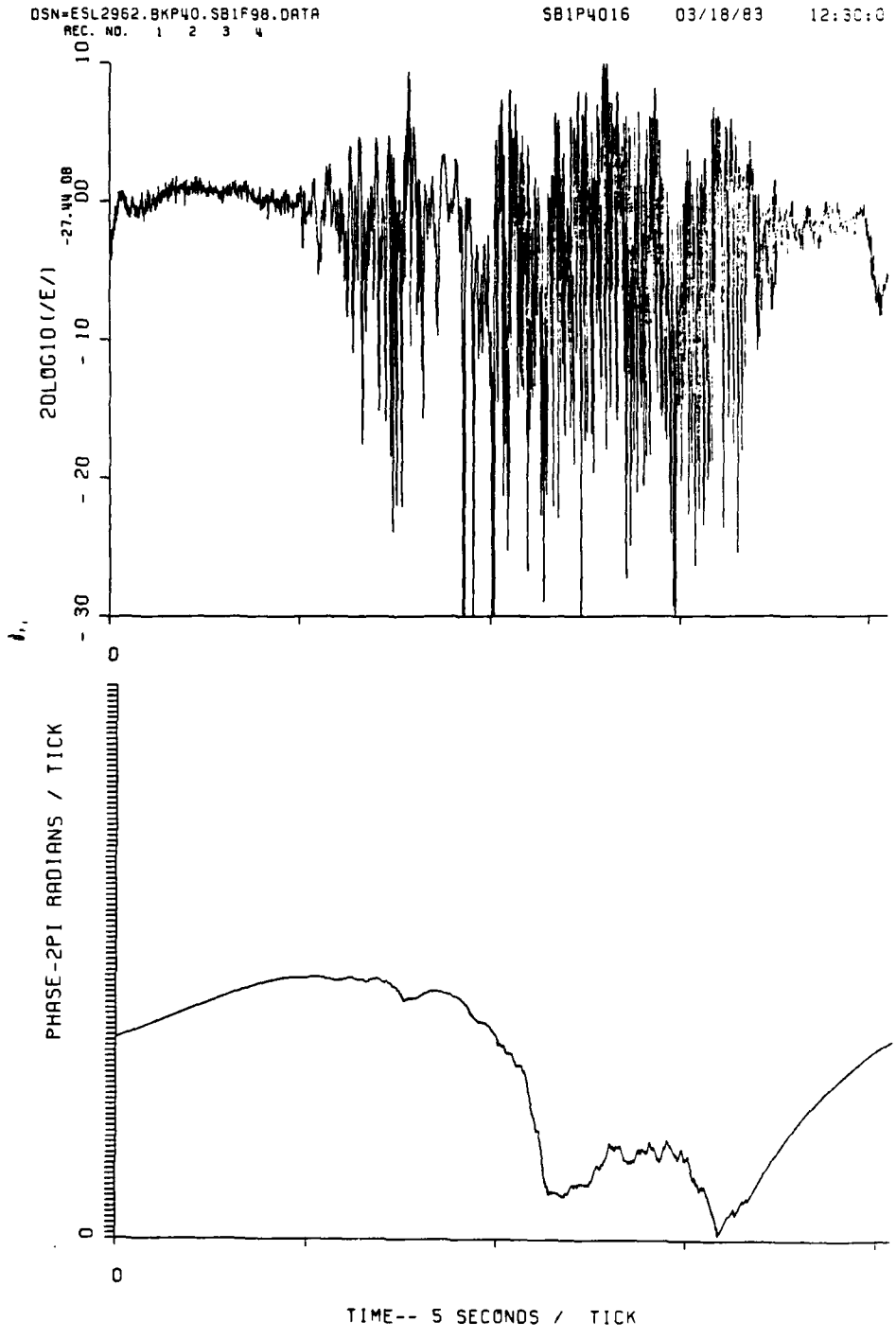

Figure 3-45. Back-propagated amplitude and phase, Cape San Blas, Beacon 1, 40 km.

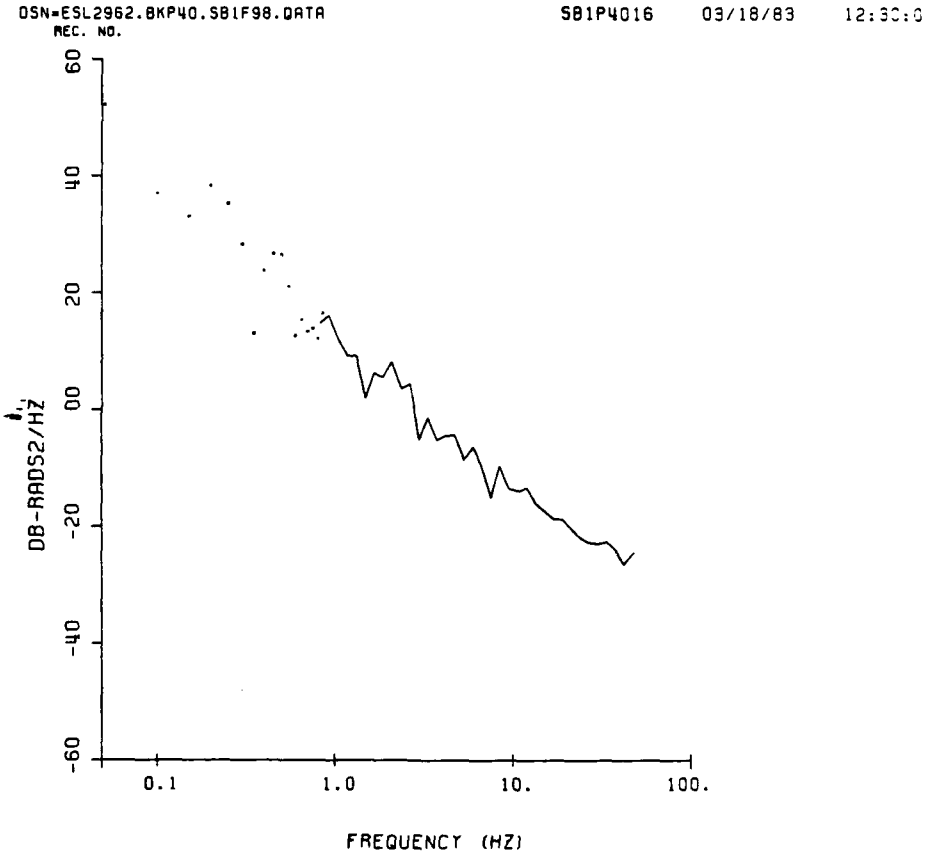

Figure 3-46. Back-propagated phase power spectrum, Cape San Blas, Beacon 1, 40 km.

3.10 MUTUAL COHERENCE FUNCTION AND IN-SITU PHASE SPECTRAL DENSITY

As discussed in Section 2.10, the mutual coherence function (MCF) is not corrupted by diffraction effects and, thus, the in-situ path integrated phase PSD can be derived from the received signal in spite of the diffraction effects that corrupt the back-propagation data. The reader is referred to Section 2.10.1 for a discussion of the MCF and its various forms.

3.10.1 MCF Data for Cape San Blas, Beacon 1, Direct Calculation

The computation of the MCF begins with the extraction of the monochromatic fading data from the complex beacon signal delay measurements as described in Section 2.10.2. This is accomplished through the transformation of the delay measurements to obtain the channel transfer function from which the 98-MHz component is selected. The MCF can then be computed directly from its definition

$$R_u(t) = \langle U(t')\, U^*(t' + t) \rangle \quad .$$

As discussed previously, from a theoretical perspective, in the absence of any systematic or nonstationary component we expect a purely real function to result. As a single example, Figure 3-47 shows the result of this calculation where only the real part of the MCF is plotted. The data interval shown corresponds to the segment 2 presented in Table 3-1. It was noted that over the principal lobe that the imaginary component is significant at times, forcing a negative value to the MCF.

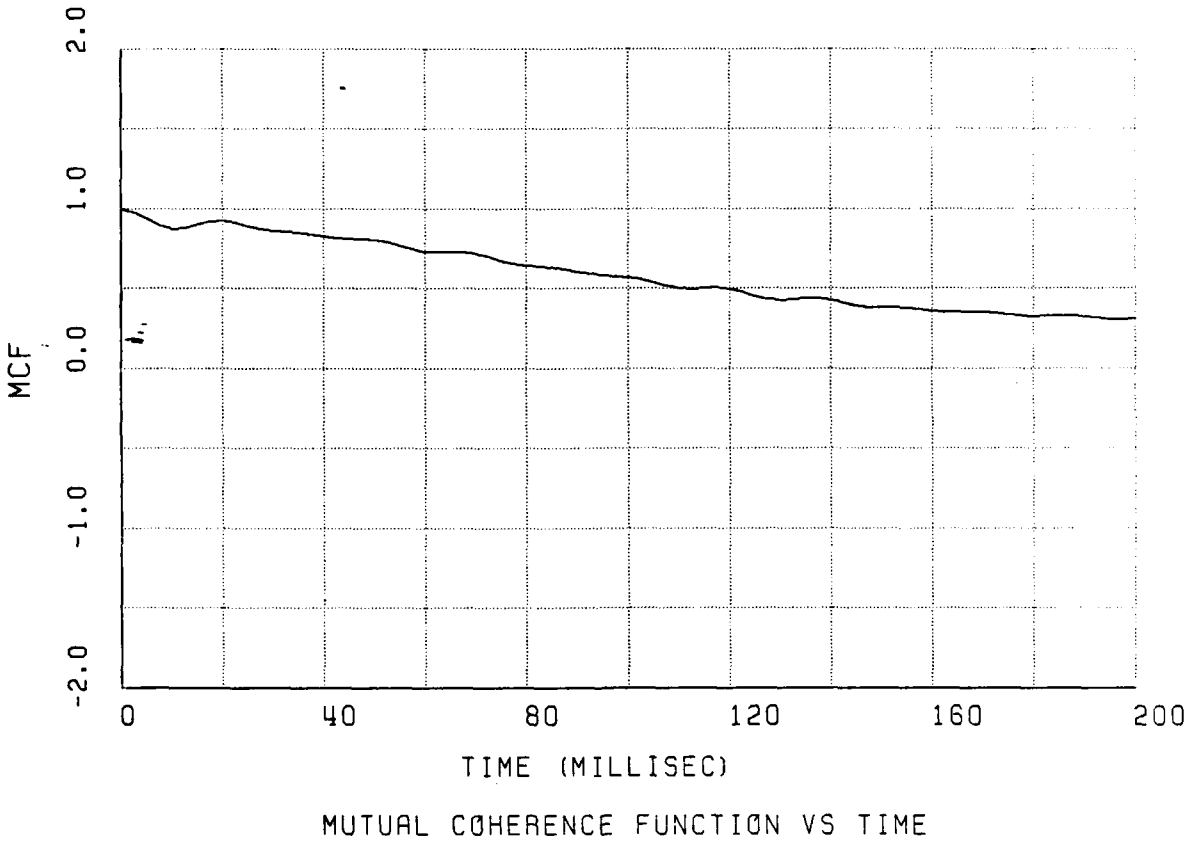

Figure 3-47. Direct calculation of MCF for Segment 2.

3.10.2 MCF Data for Symmetric Doppler Spectrum

An examination of the two-sided angular spectrum of the 98-MHz component of the received signal indicates at times a significant asymmetry, showing a preferential angle of arrival of the scattered energy. The magnitude square of the angular spectrum is the power spectrum or the Doppler spectrum, and the transform of the Doppler spectrum is the MCF. Thus, in order to force a purely real form for the MCF, the Doppler spectrum was artificially constrained to be symmetric about 0 frequency. This was accomplished through averaging of the positive and negative frequencies. For most of the segments, this technique did not substantially alter the data since only approximately 5 to 10 percent of the power in the spectrum was asymmetrically distributed. The two-sided angular spectrum, the MCF, and the structure function are shown in Figures 3-48 through 3-68 for each of the data segments. The structure function is shown as the logarithm of minus the natural log of the MCF.

3.10.3 Comparison With Theory.

These data can be compared with the theoretical form, and the in-situ spectral slope and the Rayleigh phases variance can be estimated. Table 3-4 summarizes the results of these calculations. The theoretical form for the log of the phase structure function was presented in Figure 2-125. In overlaying this figure on the structure function plots, the best fits as summarized in Table 3-4 were derived. Because of the systematic phase trends, which distort the MCF, the best fit to theory is expected only over the exponential portion of the MCF at short delay.

One can obtain an estimate for the Rayleigh phase variance when the functional form is a good fit to the Bessel function form for the phase autocorrelation function out to large values of delay. The height of the structure function in this case determines the phase variance as discussed in Section 2.10.4.

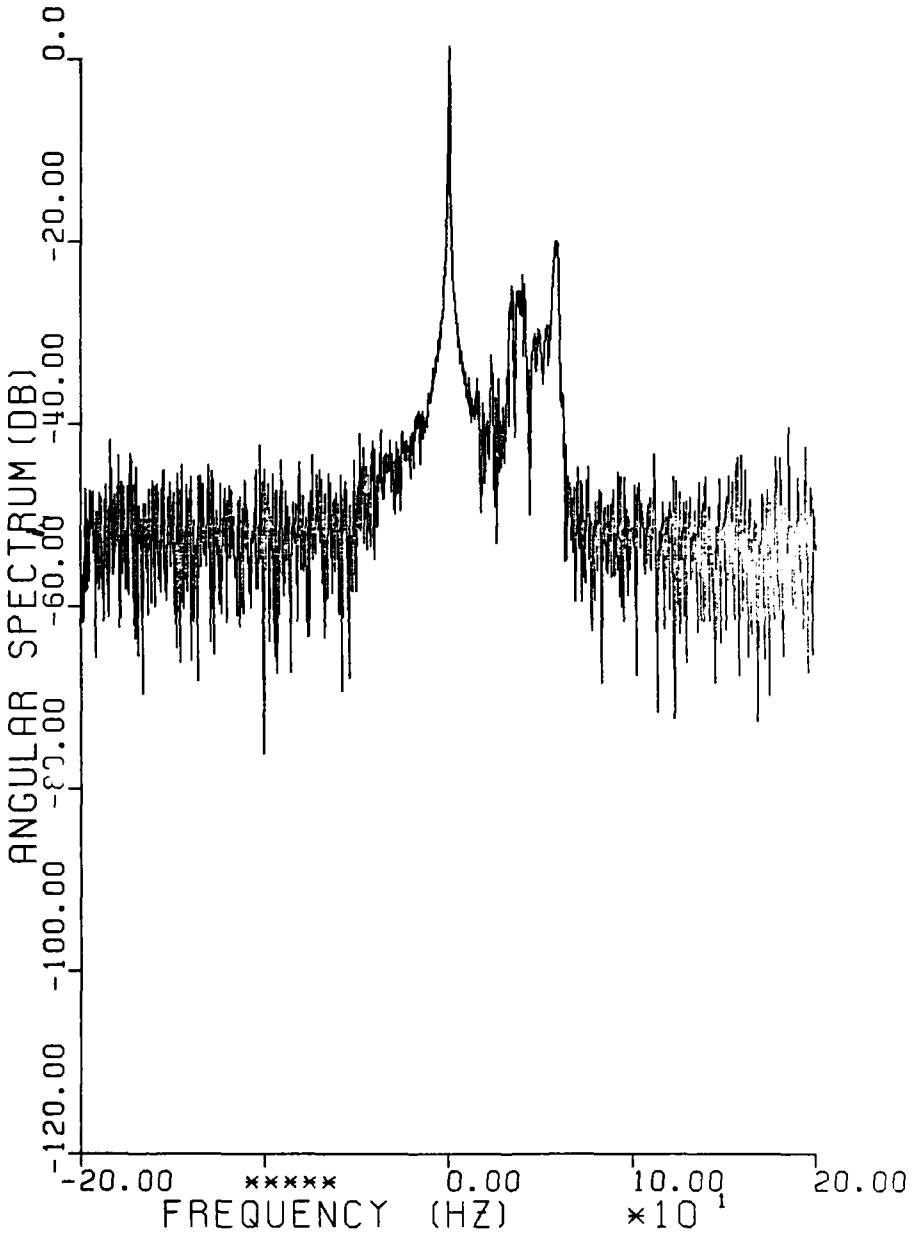

Figure 3-48. Two-sided angular spectrum for Segment 1.

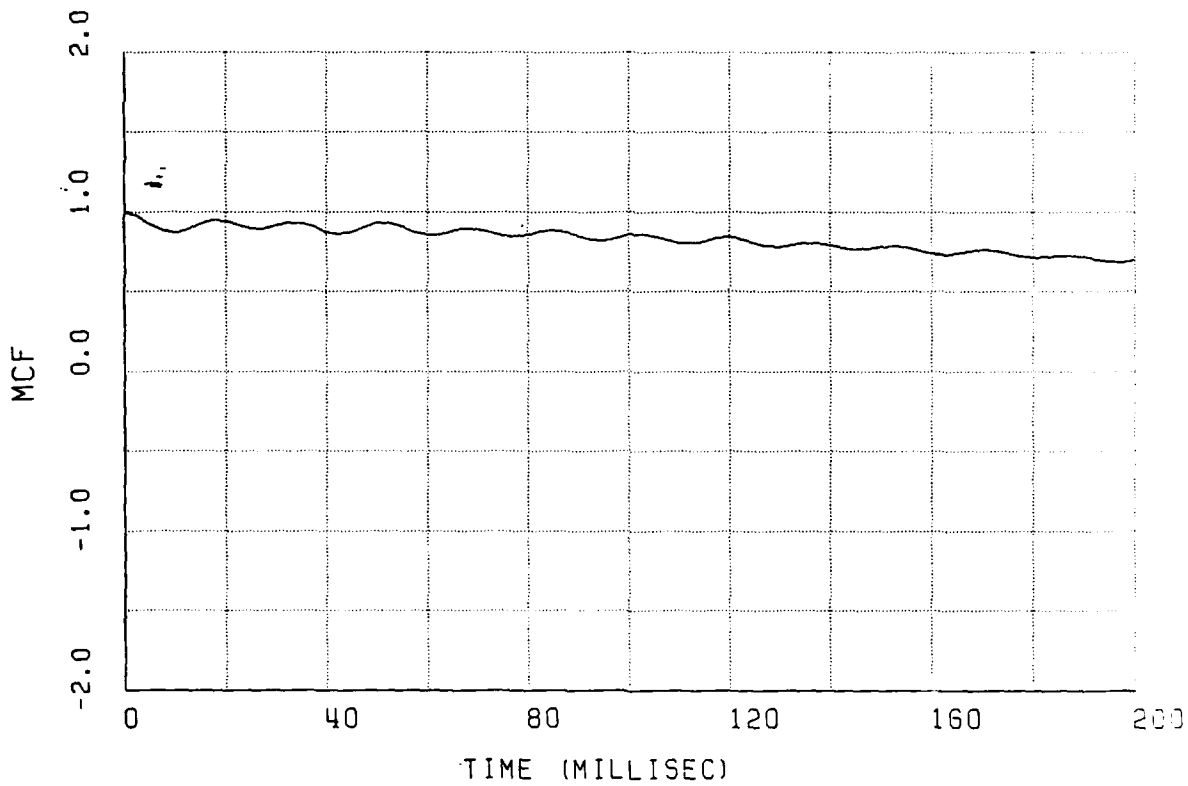

Figure 3-49. Mutual coherence function for Segment 1.

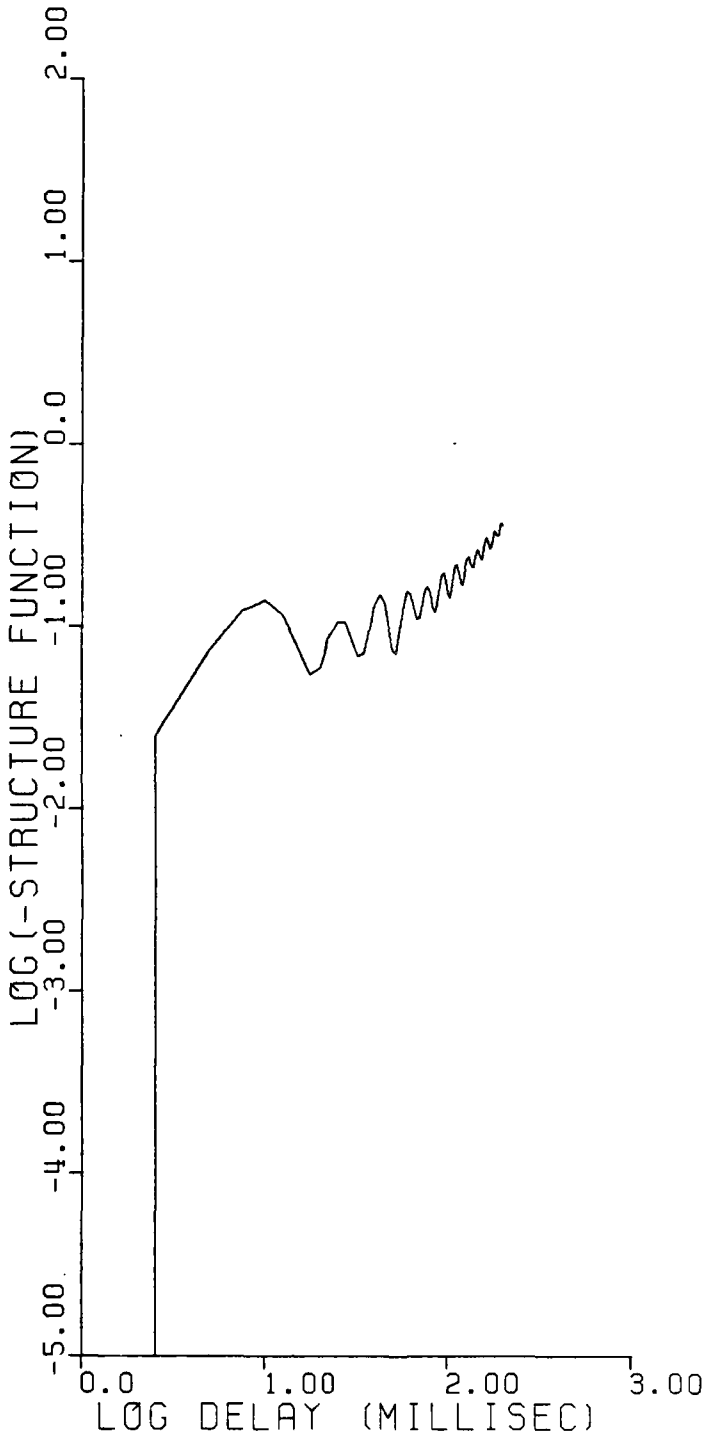

Figure 3-50. Logarithm of phase structure function for Segment 1.

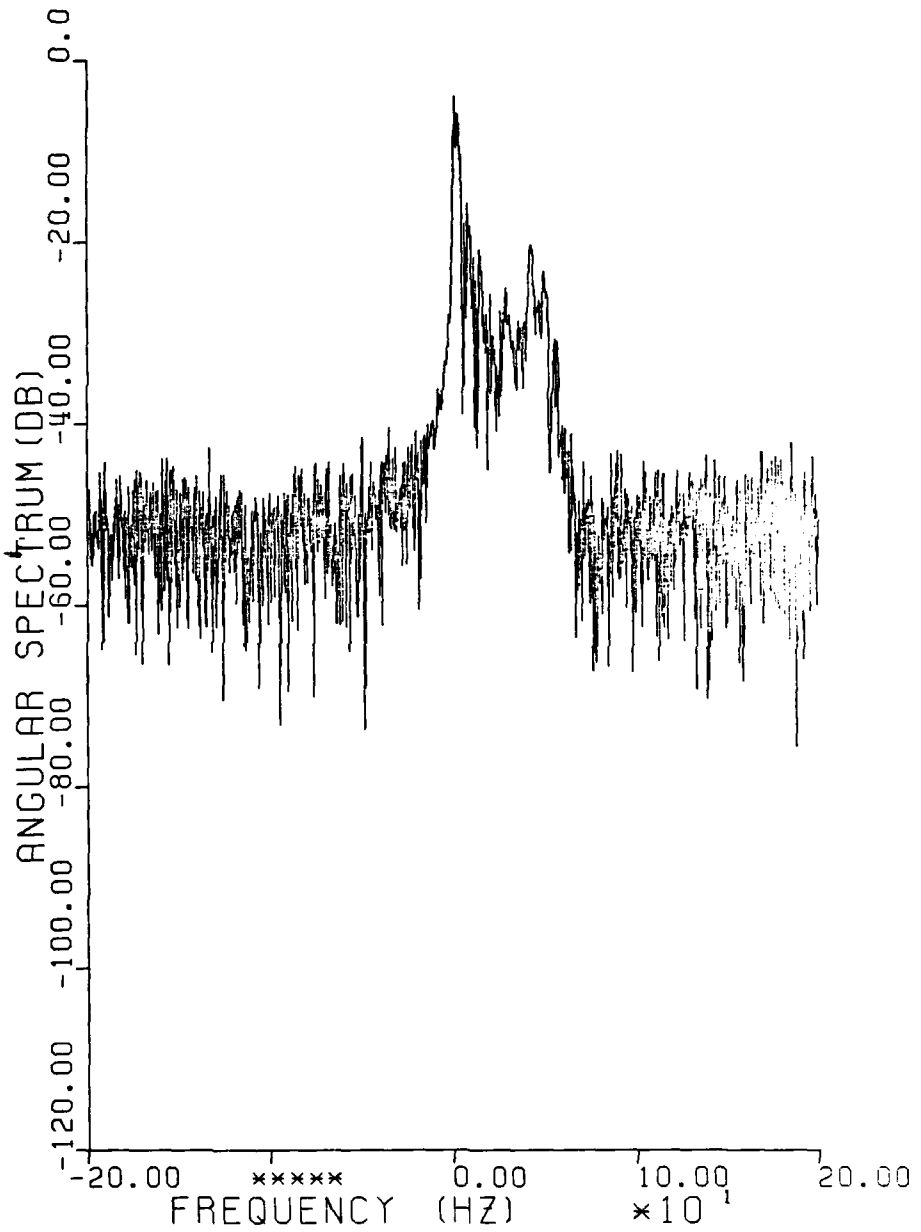

Figure 3-51. Two-sided angular spectrum for Segment 2.

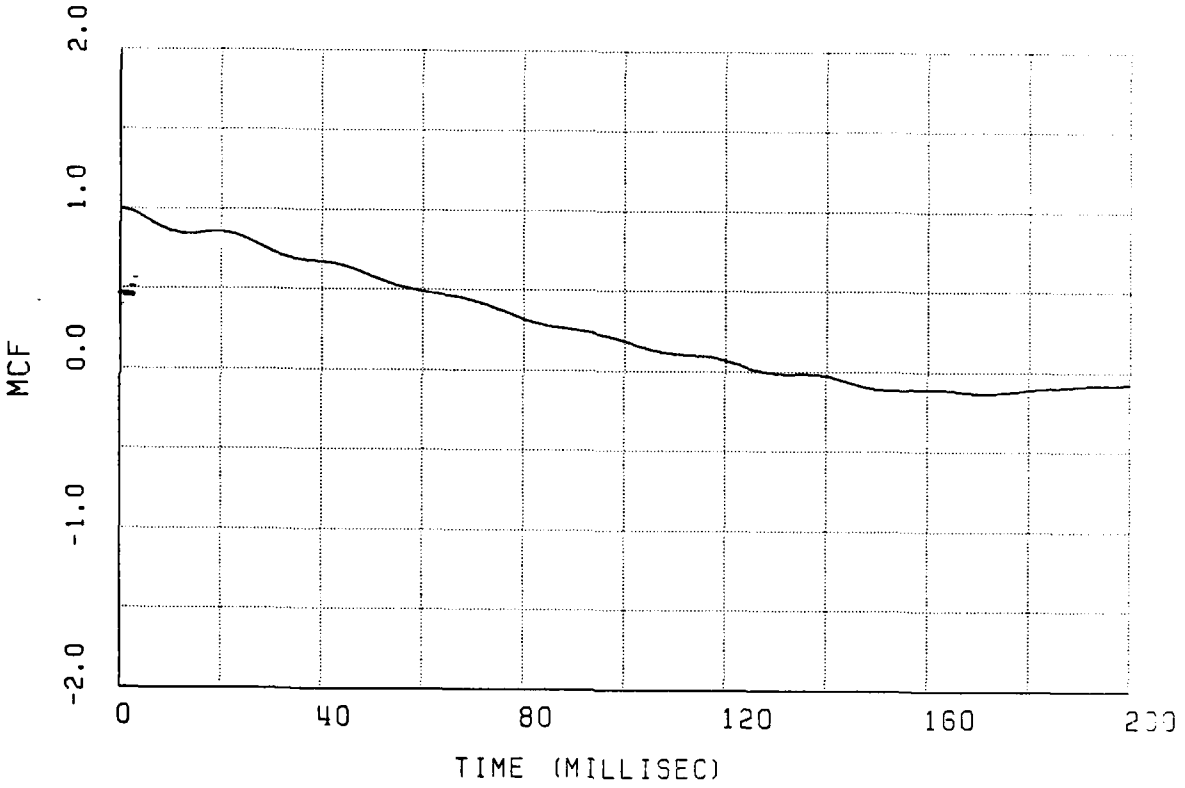

Figure 3-52. Mutual coherence function for Segment 2.

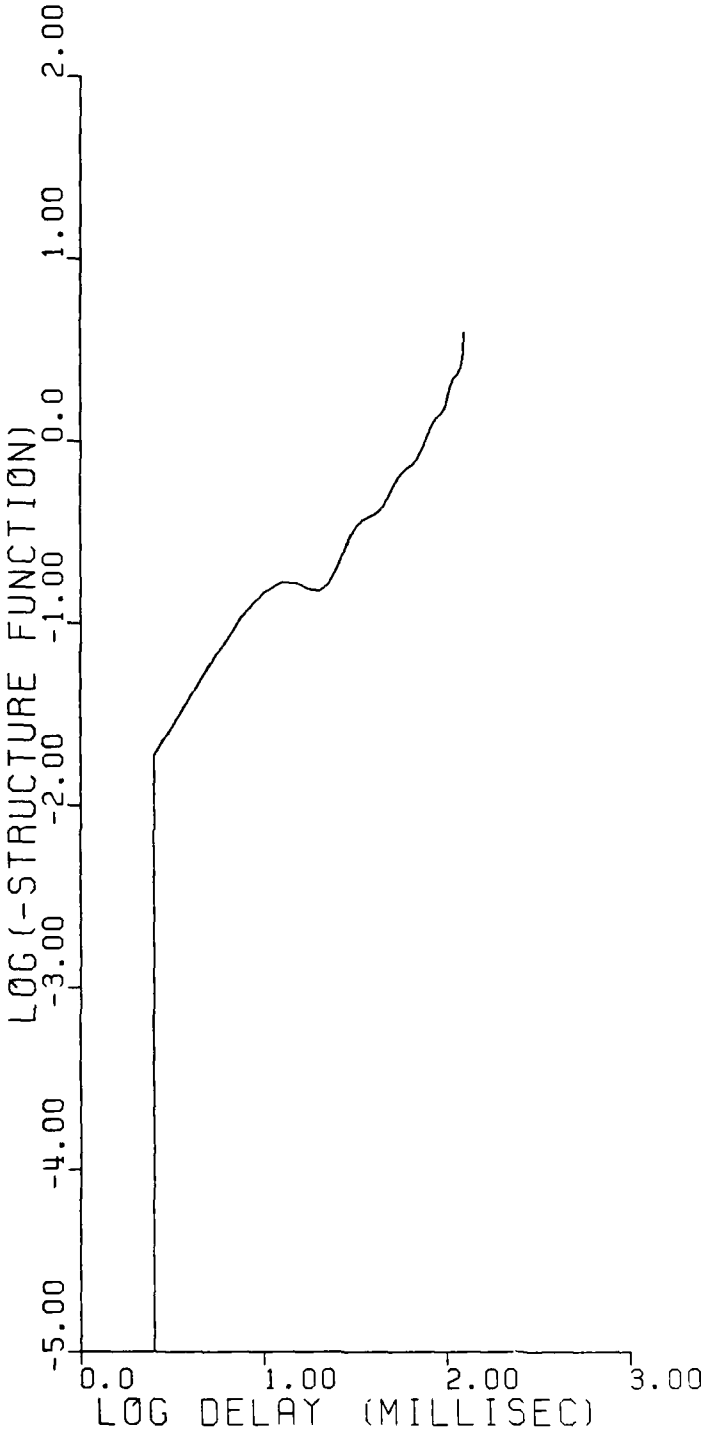

Figure 3-53. Logarithm of phase structure function for Segment 2

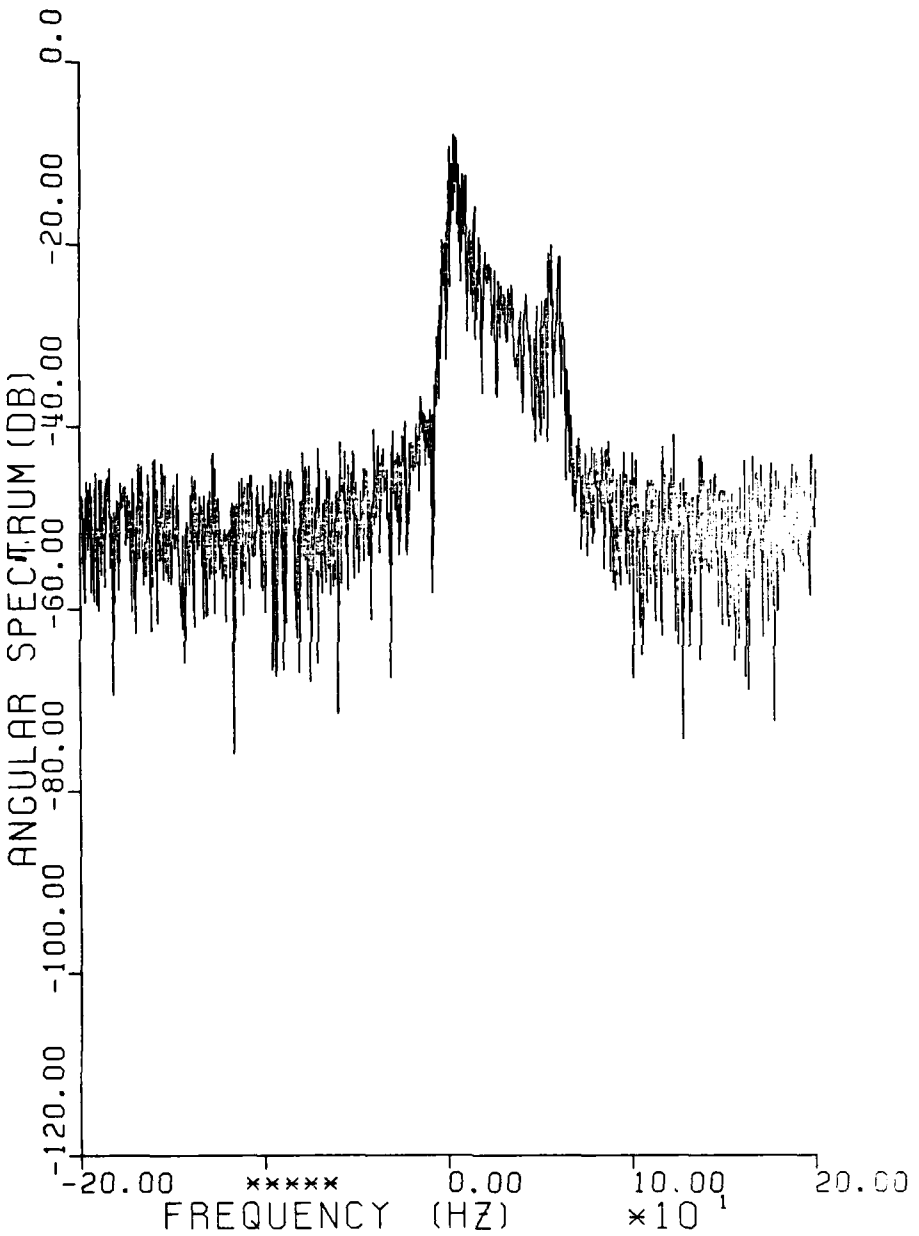

Figure 3-54. Two-sided angular spectrum for Segment 3.

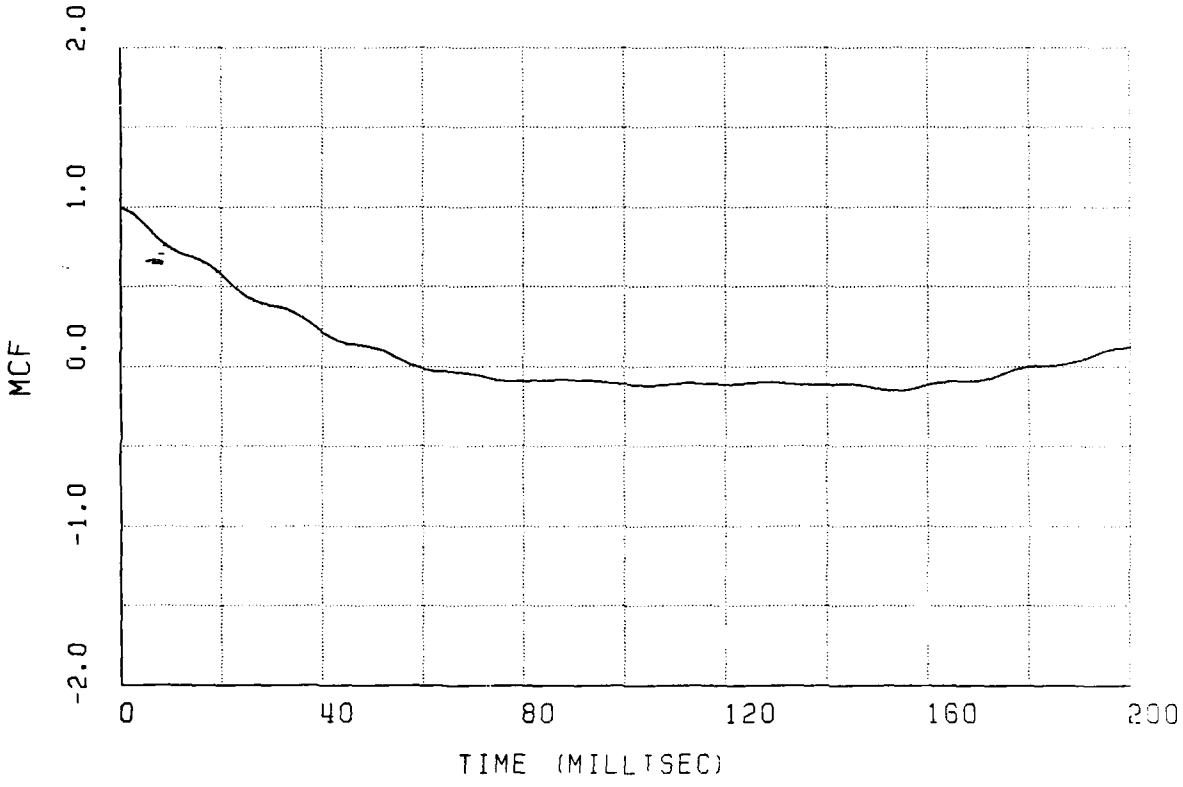

Figure 3-55. Mutual coherence function for Segment 3.

AD-A160 566 PLACES (POSITION LOCATION AND COMMUNICATION EFFECTS SIMULATIONS) BEACON EXPERIMENT TEST RESULTS(U) ESL INC SUNNYVALE CA J MARSHALL ET AL. 01 AUG 84 DNA-TR-84-376 4/5

UNCLASSIFIED DNA001-81-C-0149 F/G 20/14 NL

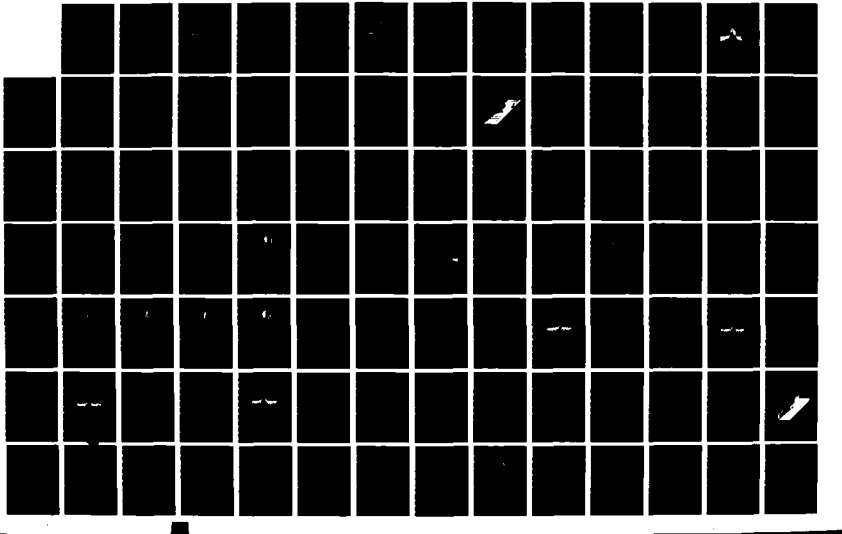

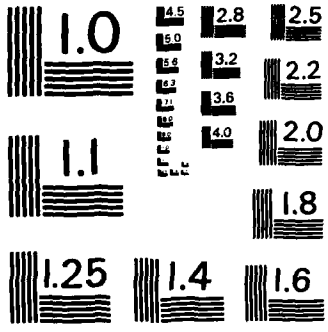

MICROCOPY RESOLUTION TEST CHART
NATIONAL BUREAU OF STANDARDS - 1963 - A

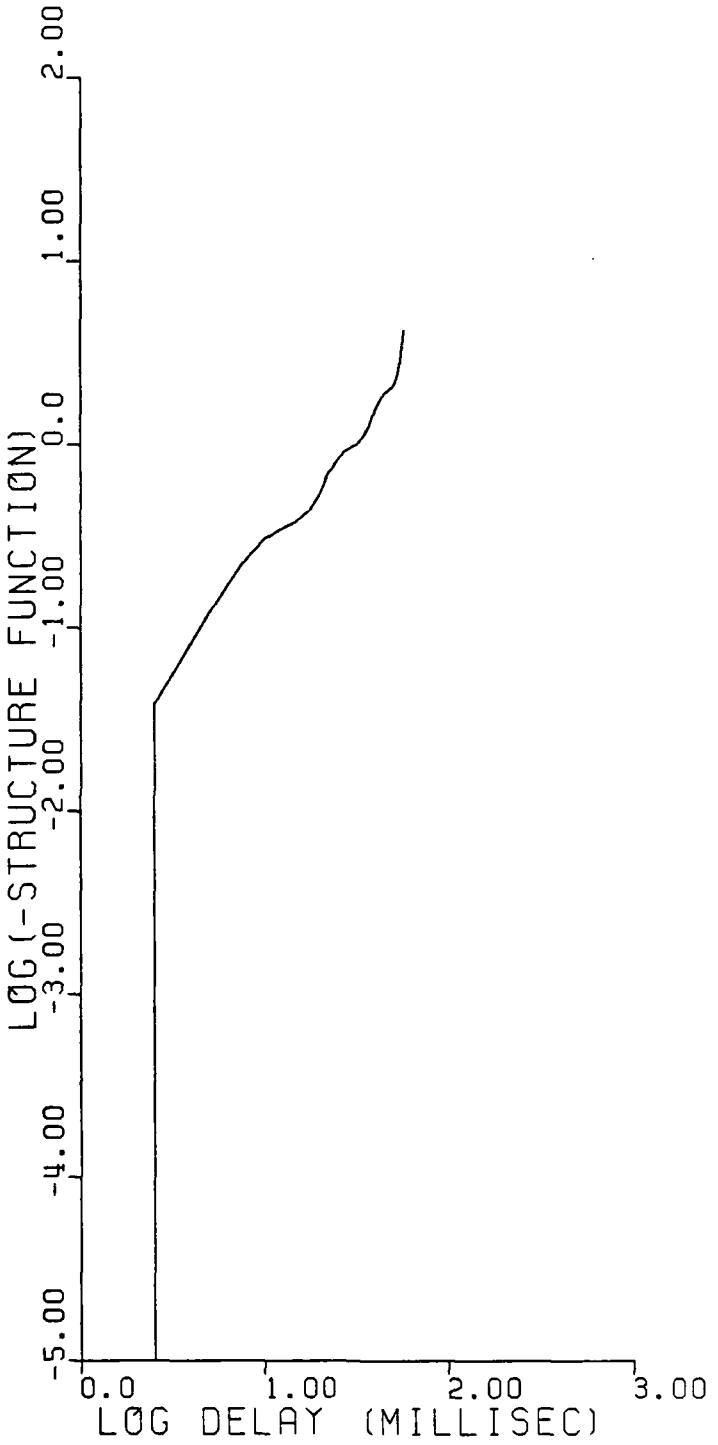

Figure 3-56. Logarithm of phase structure function for Segment 3.

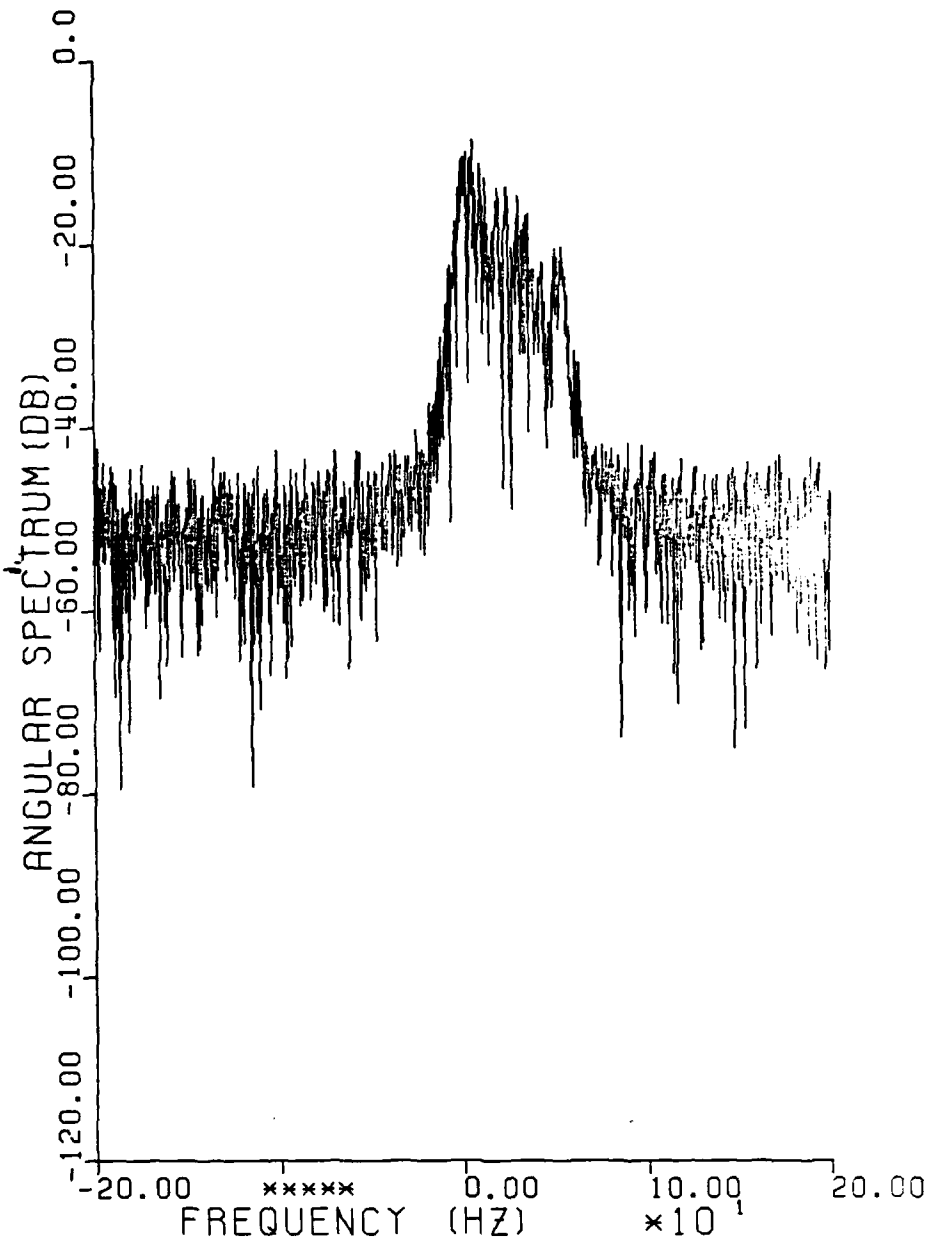

Figure 3-57. Two-sided angular spectrum for Segment 4.

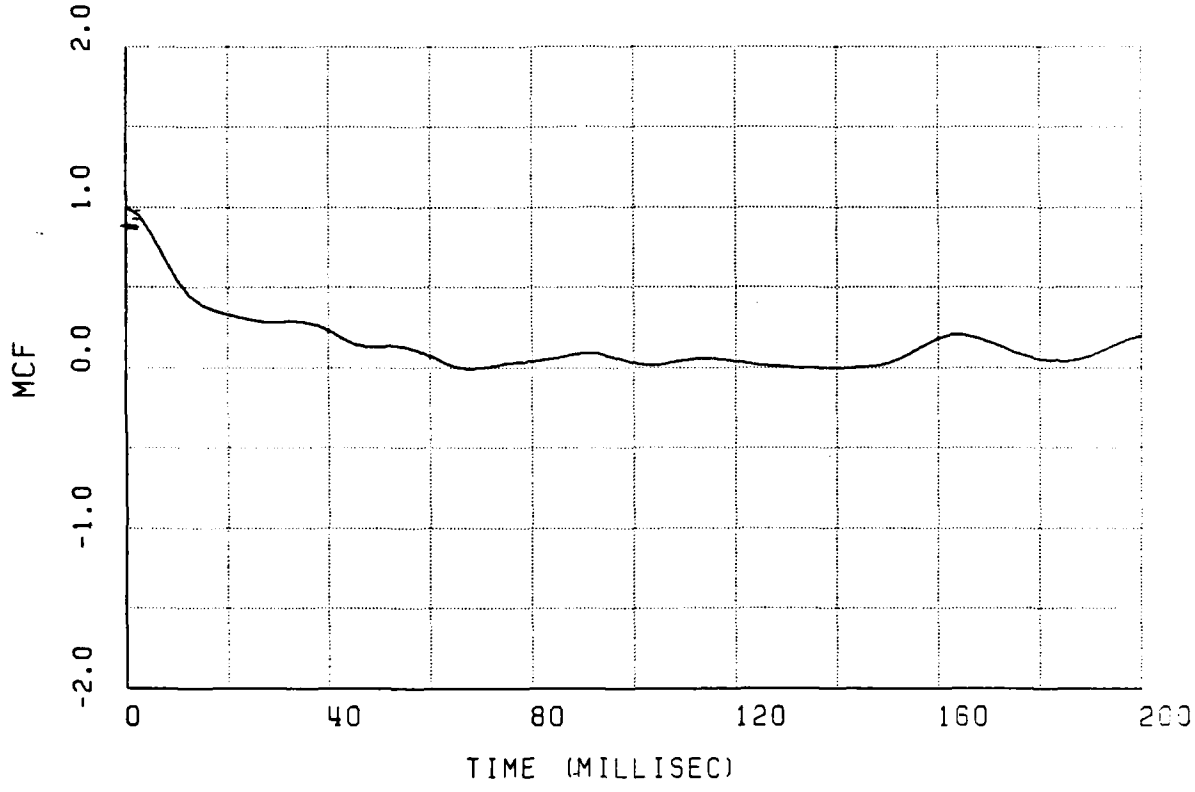

Figure 3-58. Mutual coherence function for Segment 4.

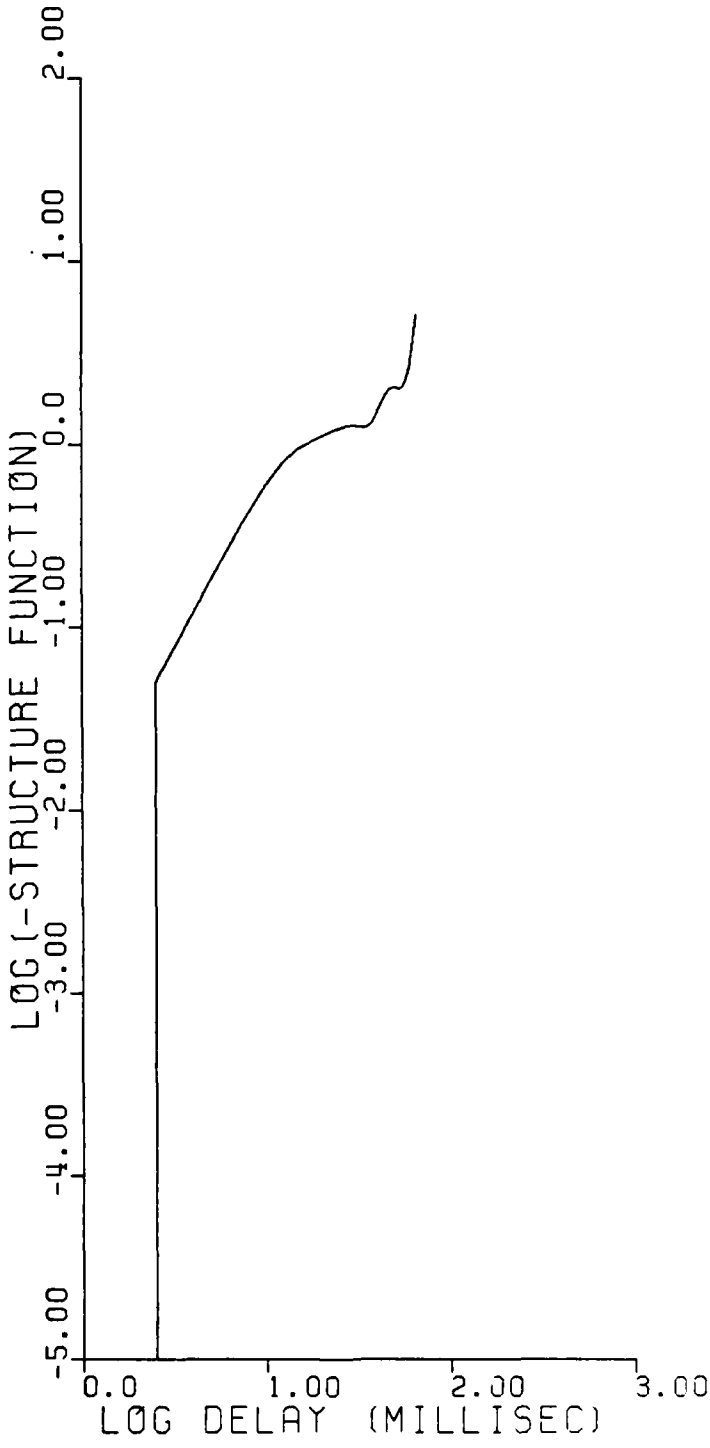

Figure 3-59. Logarithm of phase structure function for Segment 4.

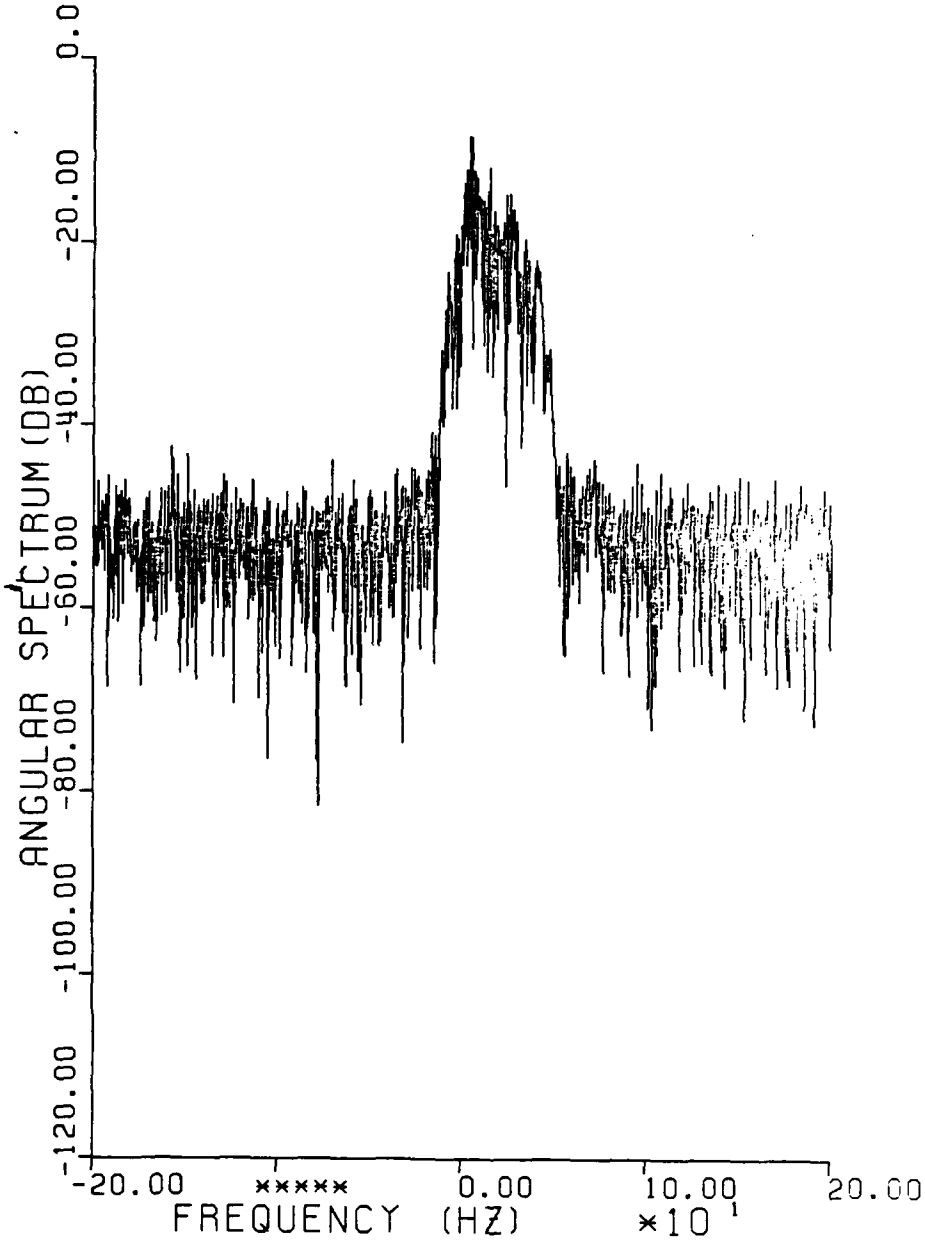

Figure 3-60. Two-sided angular spectrum for Segment 5.

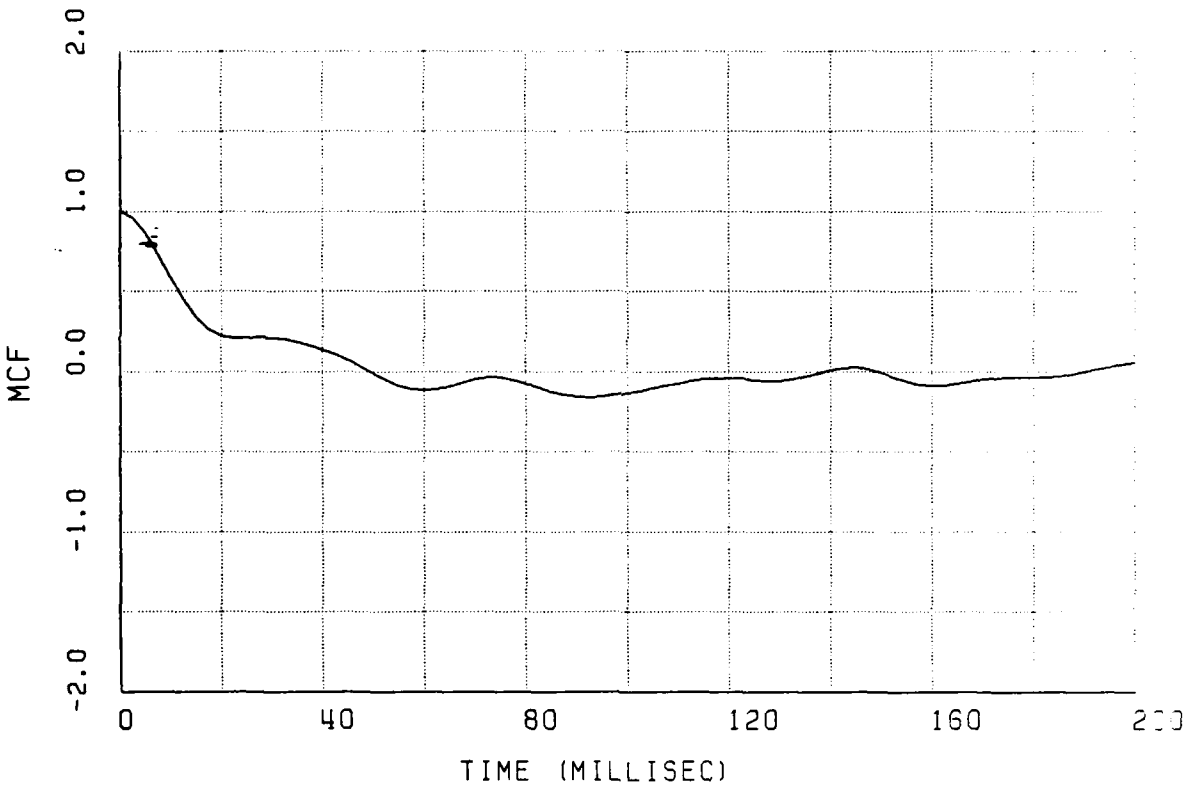

Figure 3-61. Mutual coherence function for Segment 5.

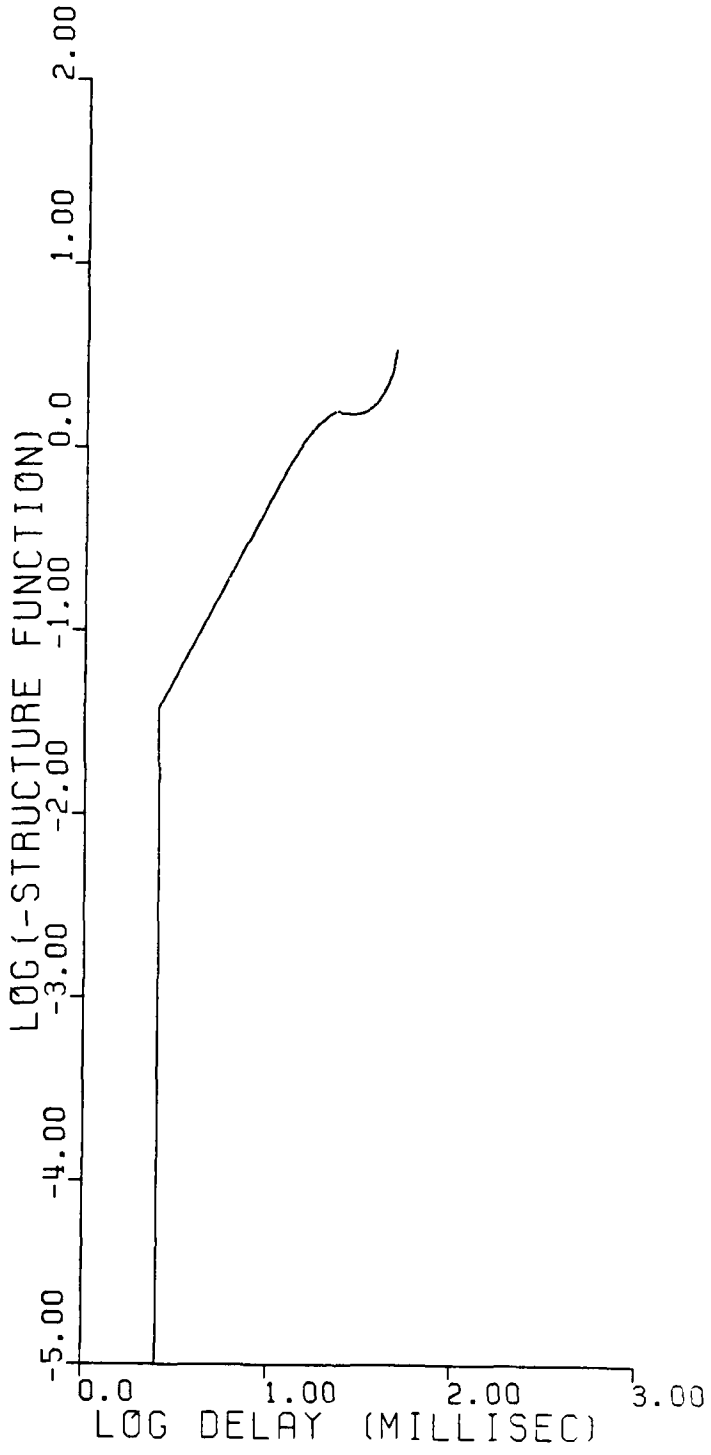

Figure 3-62. Logarithm of phase structure function for Segment 5.

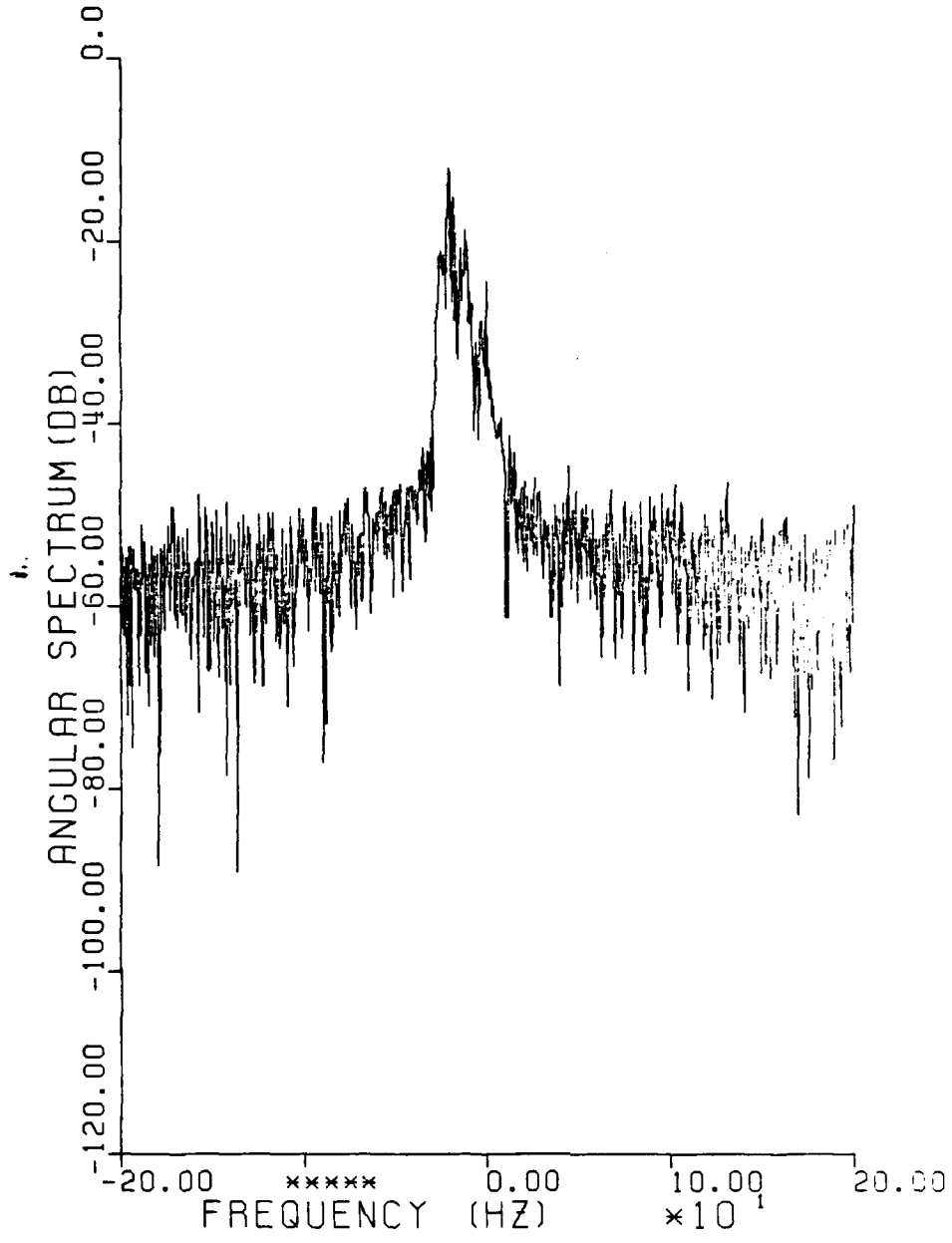

Figure 3-63. Two-sided angular spectrum for Segment 6.

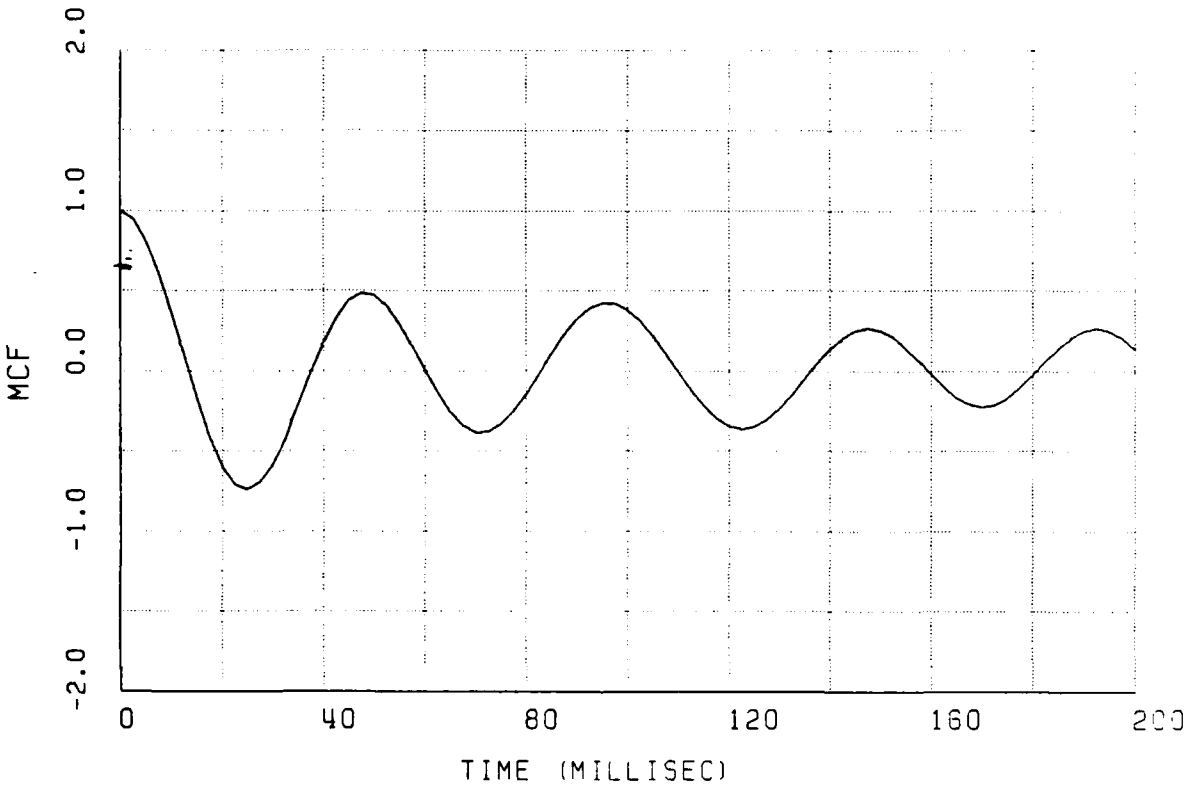

Figure 3-64. Mutual coherence Function for Segment 6.

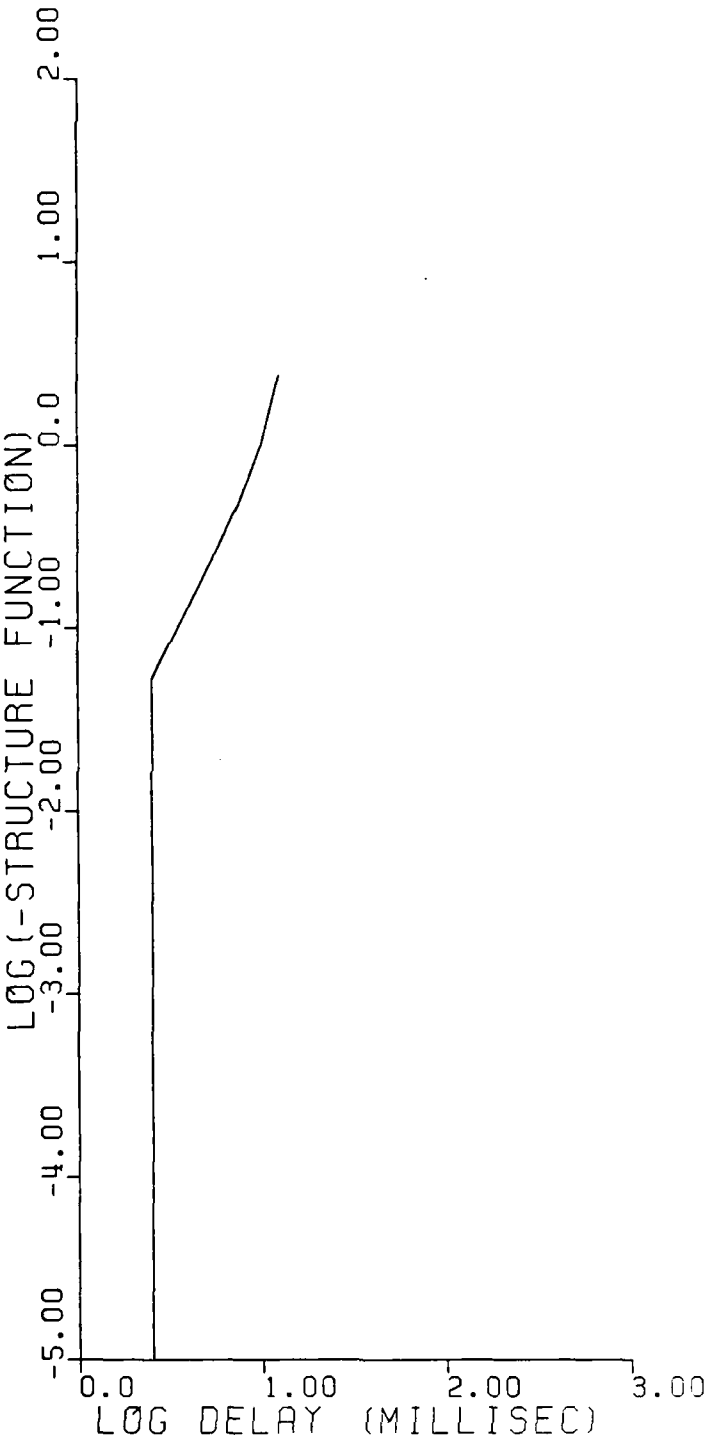

Figure 3-65. Logarithm of phase structure function for Segment 6

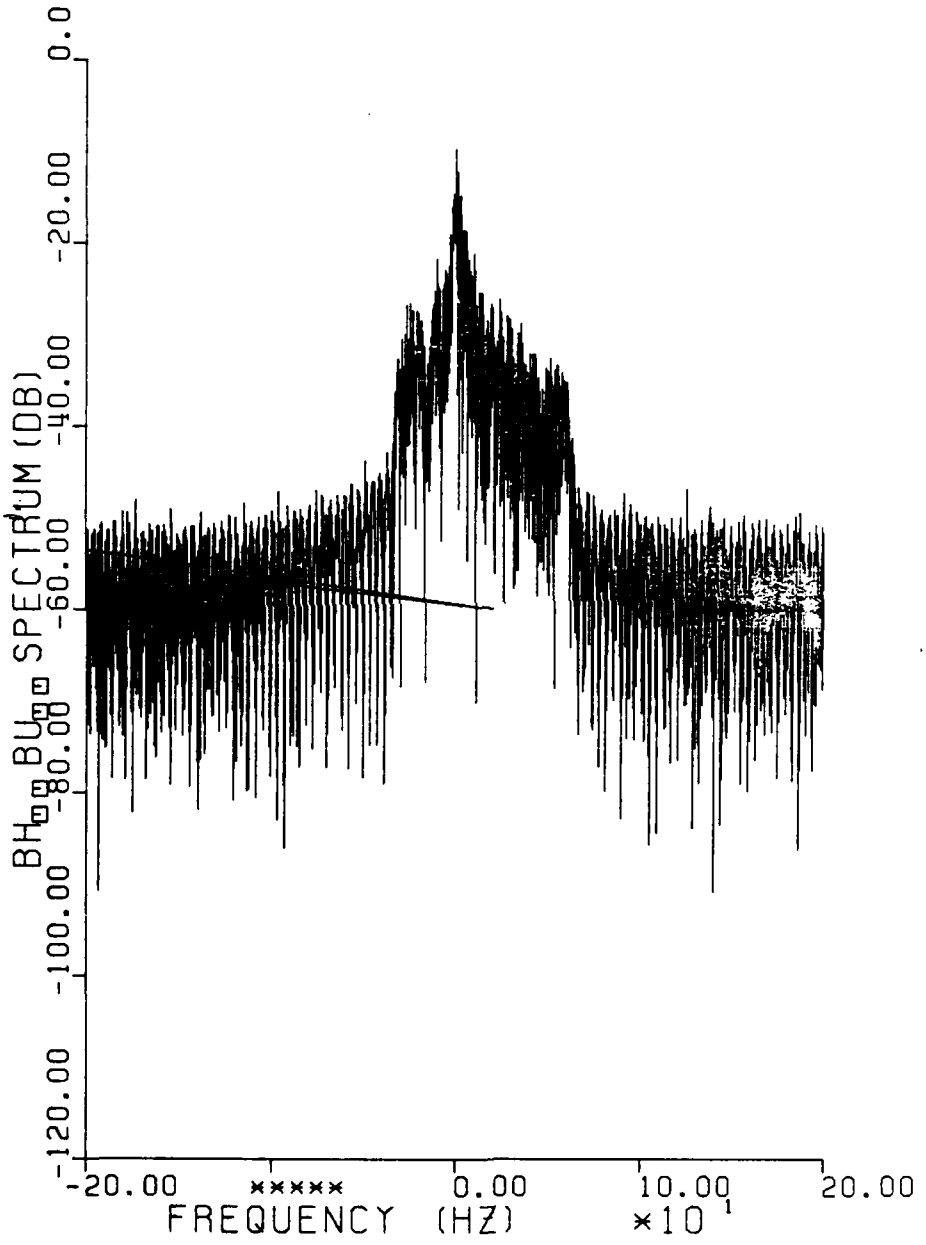

Figure 3-66. Two-sided angular spectrum for entire occultation

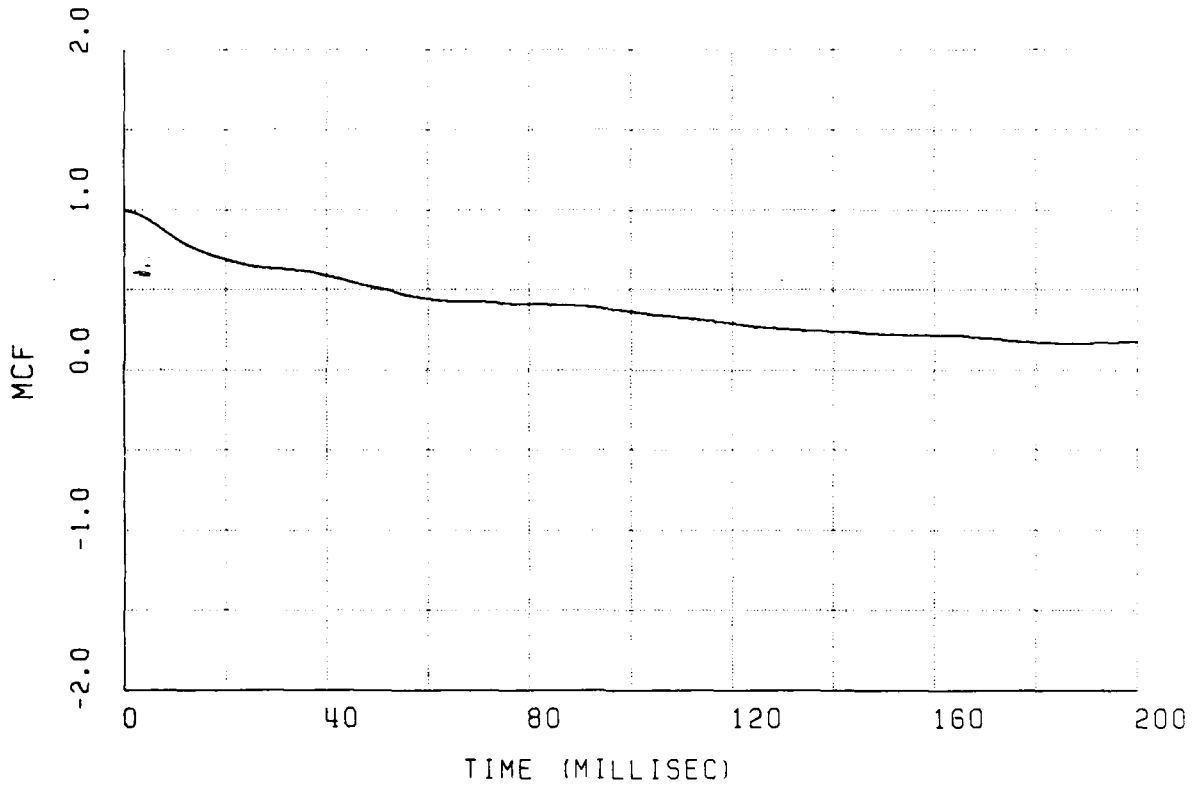

Figure 3-67. Mutual coherence function for entire occultation.

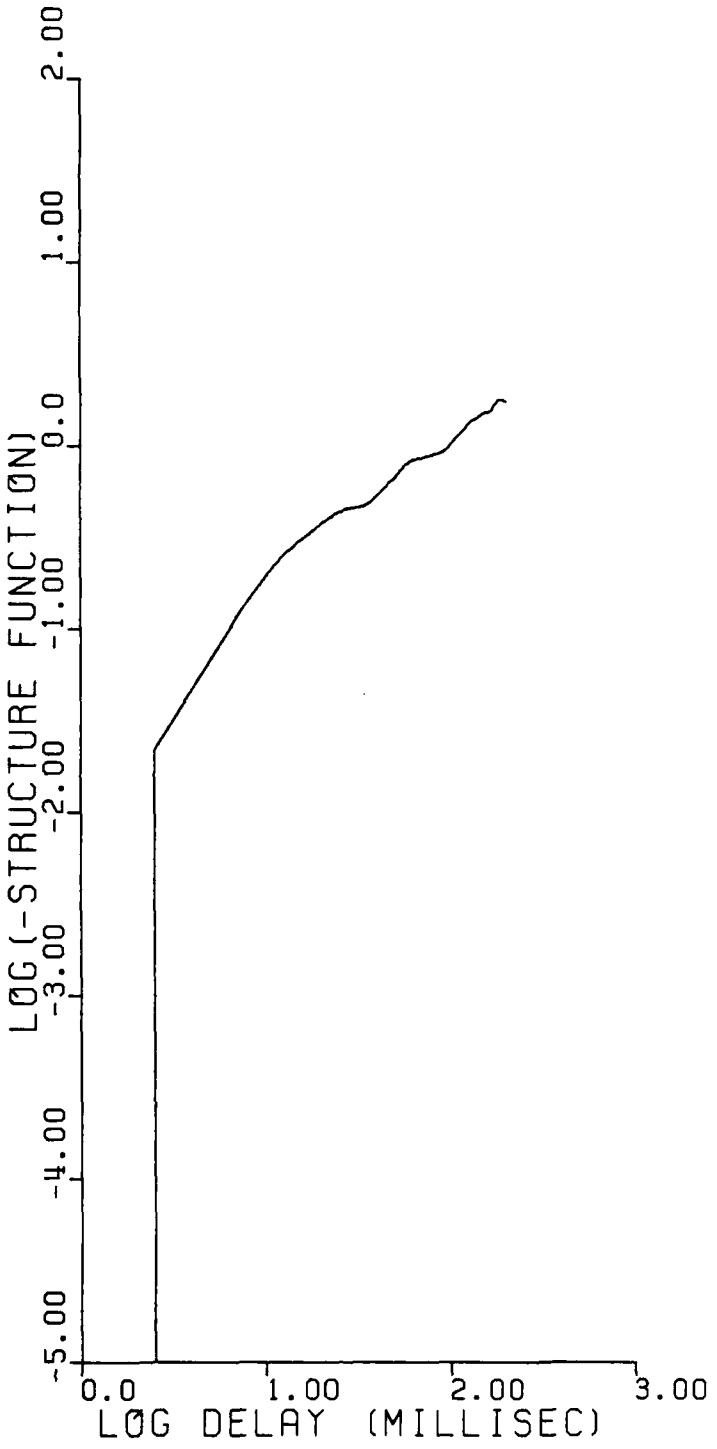

Figure 3-68. Logarithm of phase structure function for entire occultation.

Table 3-4 Phase structure function analysis summary.

SEGMENT	BEST SHAPE	$D_C = \tau^{2v-1}$ INDEX V	$D_C = \tau^{2v-1}$ SLOPE 2v-1	$D_A = (\tau/\tau_o)^2$ τ_o	D_B τ_o	D_B $\sigma_{\phi R}$	MCF = e^{-1} τ_o
1	–	1.4	1.8	–	–	–	–
2	A	1.3	1.6	20 ms	–	–	70 ms
3	C OR A	1.3	1.6	15	–	–	25
4	C, A OR B	1.4	1.8	12	9	1.1 RAD	15
5	C OR A	1.5	2.0	13	–	–	13
6	C OR A	1.5	2.0	11	–	–	10
ENTIRE OCCULTATION	C OR A	1.3	1.6	20	–	–	50

A – $D_A(\tau) = (\tau/\tau_o)^2$

B – $D_B(\tau) = \text{LOG}\,[1 - (\tau/\tau_o)\,K_1\,(\tau/\tau_o)]$

C – $D_C(\tau) = \tau^{2v-1}$

3.11 SUMMARY FOR CAPE SAN BLAS, BEACON 1

The data for Cape San Blas, Beacon 1, have been shown to be consistent with that obtained for the St. George Island path. The intuitive relations derived from geometric optics arguments have been shown to be in good agreement with the data. The generalized power spectrum functional form was shown to be in good agreement with theory. The mutual coherence function approach to estimating the structure function has shown good agreement with the DNA model formulation. In general, the conclusions presented in Section 2.12 for the St. George Island, Beacon 1 data are applicable to this path as well.

SECTION 4
BEACON EXPERIMENT DATA FOR ST. GEORGE ISLAND, BEACON 2

4.1 GENERAL

The angular scattering effects observed on the signal received from the second beacon rocket were much less intense than those observed from the first beacon. An analysis of the occultation geometry indicates the striation region was cut by the propagation path very low in altitude. Presumably, the lower ionization density at the lower altitudes results in less extreme angular scattering. This section discusses the data obtained from the second beacon rocket as received at St. George Island.

4.2 OCCULTATION GEOMETRY

The second beacon rocket occulted the barium plasma as viewed from St. George Island during the interval 2358:10 to 2358:25Z. The correlation with the FPS-85 radar data and with the optical data is discussed in the following subsections.

4.2.1 Correlation to Radar Data

The occultation geometry relative to a radar mapping of the cloud ionization is provided in Figure 4-1. The radar ionization contours are those obtained approximately 2 minutes prior to occultation and translated to the peak electron density track point at 2358:20Z. The ionization contours available during the occultation interval were not as well defined and thus were not used for presentation purposes. The maximum electron density measured by the radar has not changed appreciably from the first occultation ($\sim 3 \times 10^6$ cm^{-3}). The maximum density altitude, however, is somewhat lower, ~153 km in altitude.

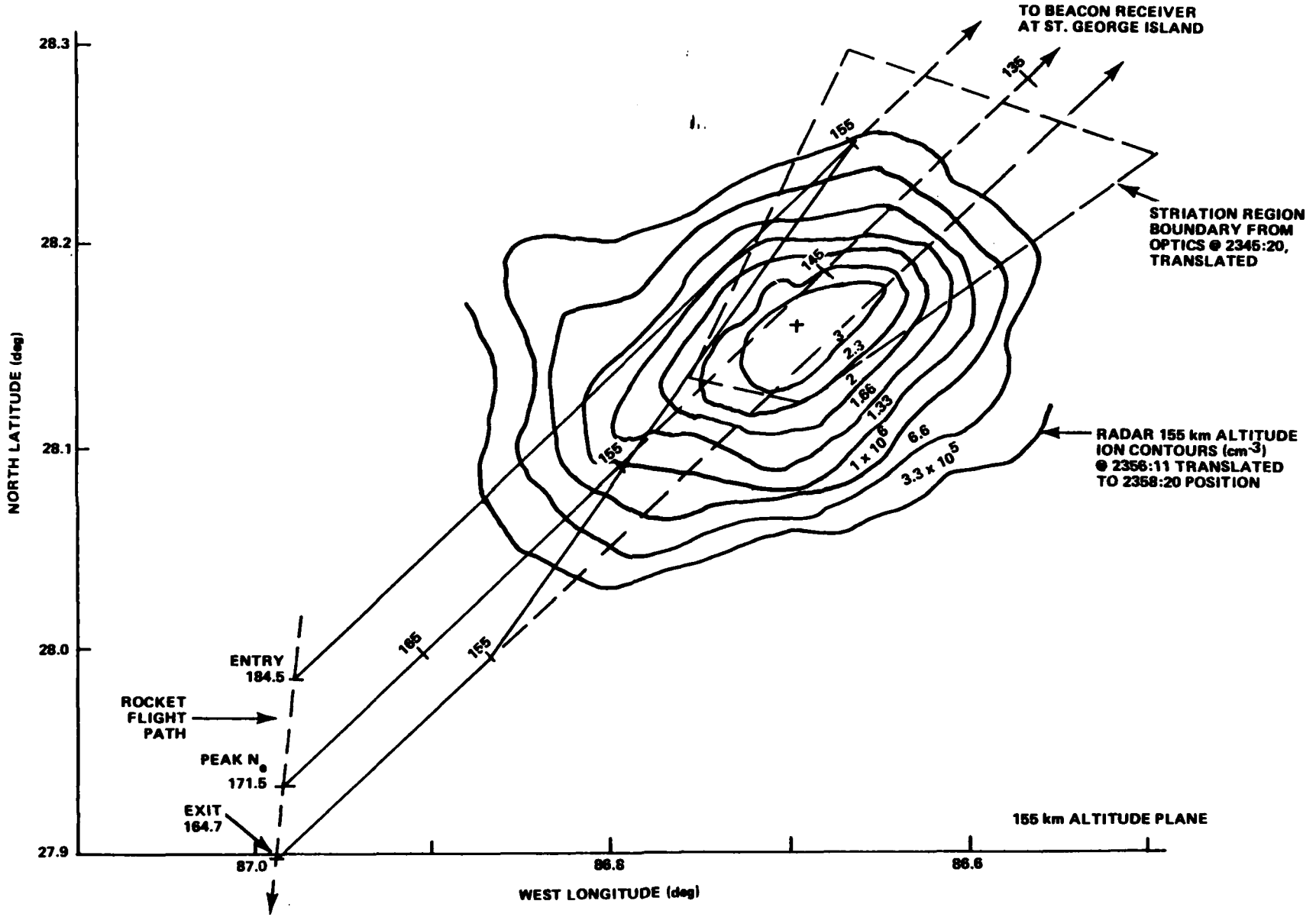

Figure 4-1. Occultation geometry, Beacon 2 to St. George Island.

The line-of-sight path is shown at several times of interest. The intersection of the path with the 155-km altitude plane is indicated by the transition from the solid to dotted line. The three paths show the time at which the first caustic ray is evident in the data, the time at which the maximum electron content (signal delay) is observed, and the time at which the signal ceases to exhibit an excess TOA delay. The rocket altitude at these times is also indicated. For instance, at the time the first caustic ray is observed, the rocket was at an altitude of 184.5 km and when the path exited the cloud, its altitude was 164.7 km. Various altitude points are also shown along the central ray path. The slant range to the maximum electron density point is approximately 42 km from the rocket position at the time the signal TOA delay is greatest.

The direct path to St. George Island slices the 155-km altitude plane several kilometers west of the maximum density region. Like the first beacon rocket path to D3A, the central field line through the maximum electron density region is cut approximately 145 km in altitude. As noted, for each receiver site and each occultation, the time of the maximum signal TOA delay occurs when the path is slightly north of the peak density point, in agreement with the radar data.

4.2.2 Correlation to Optical Data

A determination of the striation region boundary using optical data was not attempted for the second beacon flight. Optical coverage during this second occultation was hampered by the sun setting at the ion cloud altitude. The striation region boundary as determined for the earlier occultation at 2345:20 is shown in Figure 4-1. The striation boundary is positioned the same relative to the maximum density point of the ion cloud. The earlier data were shown for a 160-km altitude plane. The striation boundary has been

translated along the field lines to correspond to the 155-km altitude plane shown here.

Even though the propagation path slices the central field line at approximately the same altitude as the path from Cape San Blas on the first beacon rocket, it can readily be ascertained from Figure 4-1 that the propagation path quickly exits the striated region. The signal data show the angular scattering effects going away prior to the maximum signal delay (maximum integrated electron content) occurring in general agreement with the optical data.

4.3 MEASURED CHANNEL IMPULSE RESPONSE

This section presents the measured channel impulse response data for St. George Island, Beacon 2. The data presented are a good approximation to the channel impulse response when the channel impulse response delay spread is large compared with the signal auto-correlation function. The in-phase and quadrature code cross-correlations performed at the beacon receivers provide a weighted average measurement of the in-phase and quadrature components of the channel impulse response, averaged over a narrow window (a code chip interval) about the code delay.

4.3.1 Composite Data

The magnitude of the channel impulse response $|h(t,\tau)|$ measured at the St. George Island beacon receiver site is shown in Figure 4-2. The time span for this figure is 2358:01.2 to 2358:33.7Z. Well defined caustics are apparent in these data only well after the ion cloud has been occulted and none appear as the beacon rocket exits from behind the cloud. This is due to the manner in which the striated region is cut by the propagation path as shown in Figure 4-1. As with the first St. George Island path, the gross plasma causes the TOA of the direct path energy to be delayed,

resulting in the large delay near the center of the occultation. The gross plasma acts like a giant lens causing substantial defocusing to occur, reducing the signal amplitude near the center of the occultation. On this figure, one chip delay is approximately 0.1 microsecond. For plotting purposes, 32 impulse response measurements were averaged to produce each of the horizontal scans presented in the figure.

The amplitude fluctuation evident on Figure 4-2 prior to occultation is due to rocket coning. The amplitude fluctuation of approximately ± 2 dB occurs at a frequency of approximately 0.2 Hz, which corresponds closely to the coning rate expected of the rocket vehicle. The ± 2 dB amplitude fluctuation is of the correct magnitude for a coning effect of approximately +8 degrees. The line-of-sight to the receiving sites makes an angle of approximately 40 degrees with the rocket axis. As the rocket cones about this angle, the VHF antenna pattern varies by approximately 2 dB as shown in Reference 1.

4.3.2 Energy Delay Profiles

Samples of the energy delay profile (magnitude of the channel impulse response) are shown in Figures 4-3 and 4-4 sampled approximately each 0.5 seconds. Near the time of maximum integrated electron content when the line-of-sight path to St. George Island passes through the center of the striations (~2358:20), the signal exhibits a significant defocusing and delay spread. Near this time, a delay spread of approximately 10 chips (~1 microsecond) occurs. As with the data from the first beacon, the significant energy delay spread and loss in amplitude of the direct path signal, especially around 2358:23, has significant implications to PN code tracking system design.

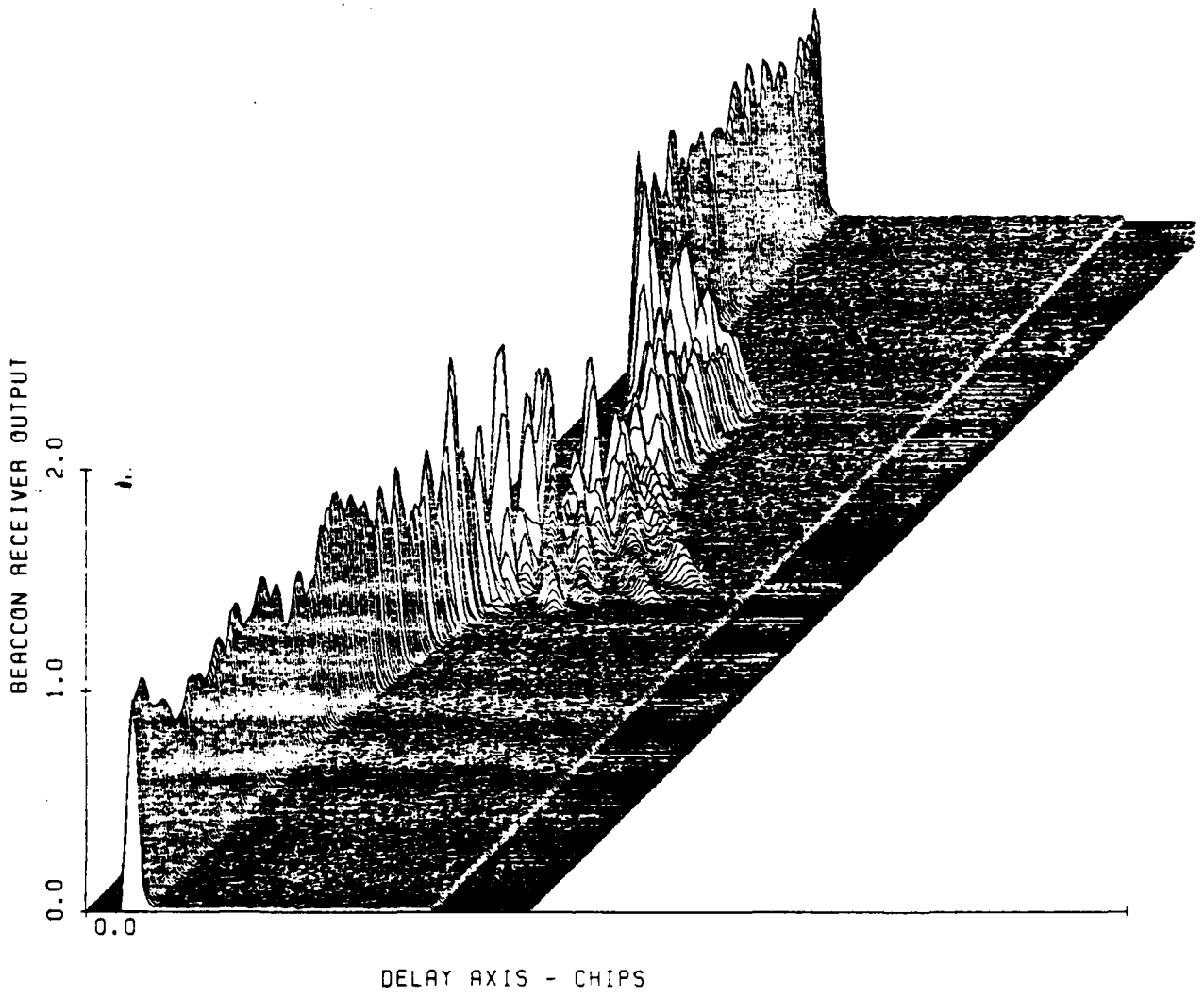

Figure 4-2. Energy delay profile, St. George Island, second beacon time span from 2358:01.2 to 2358:33.7Z.

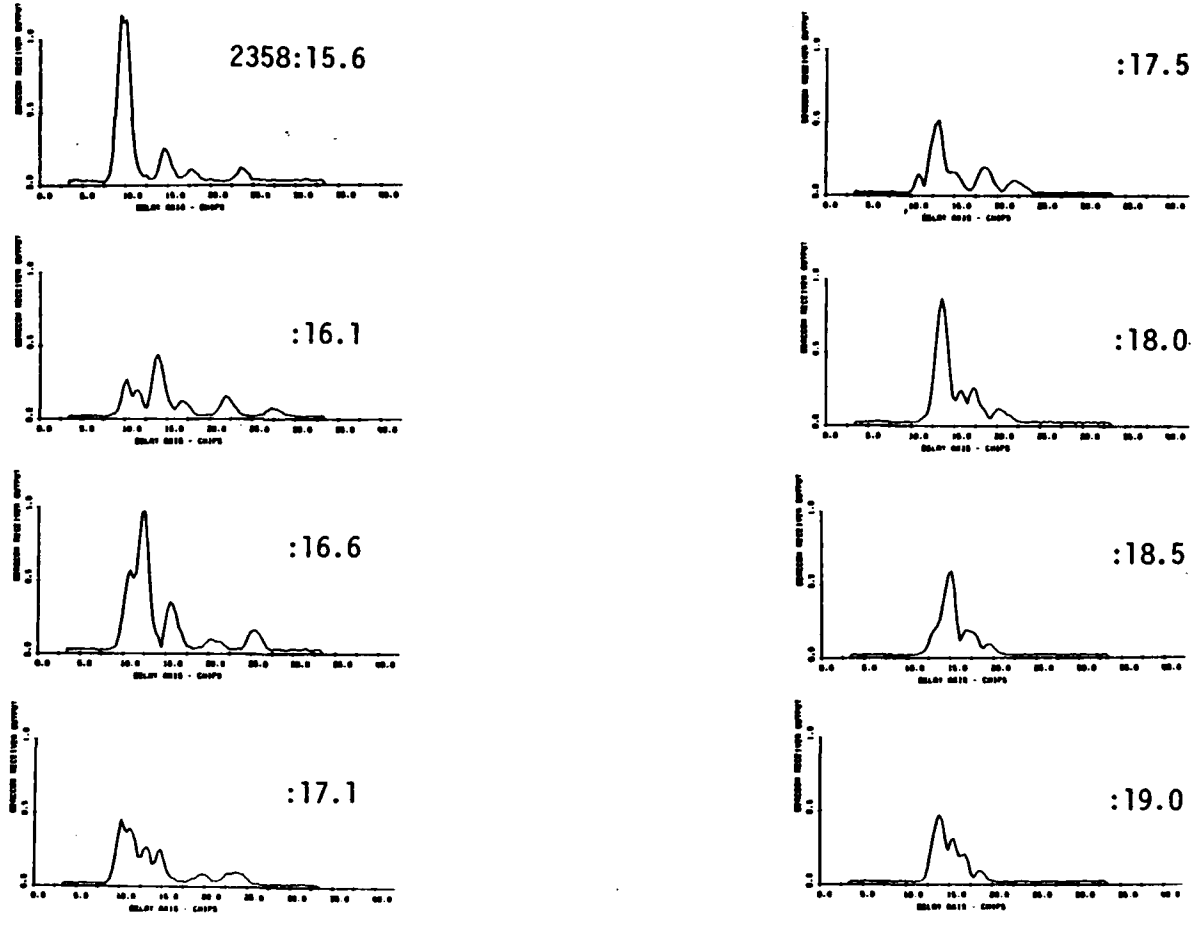

Figure 4-3. Energy delay profile between 2358:15.6 and 2358:19.0Z, St. George Island, second beacon.

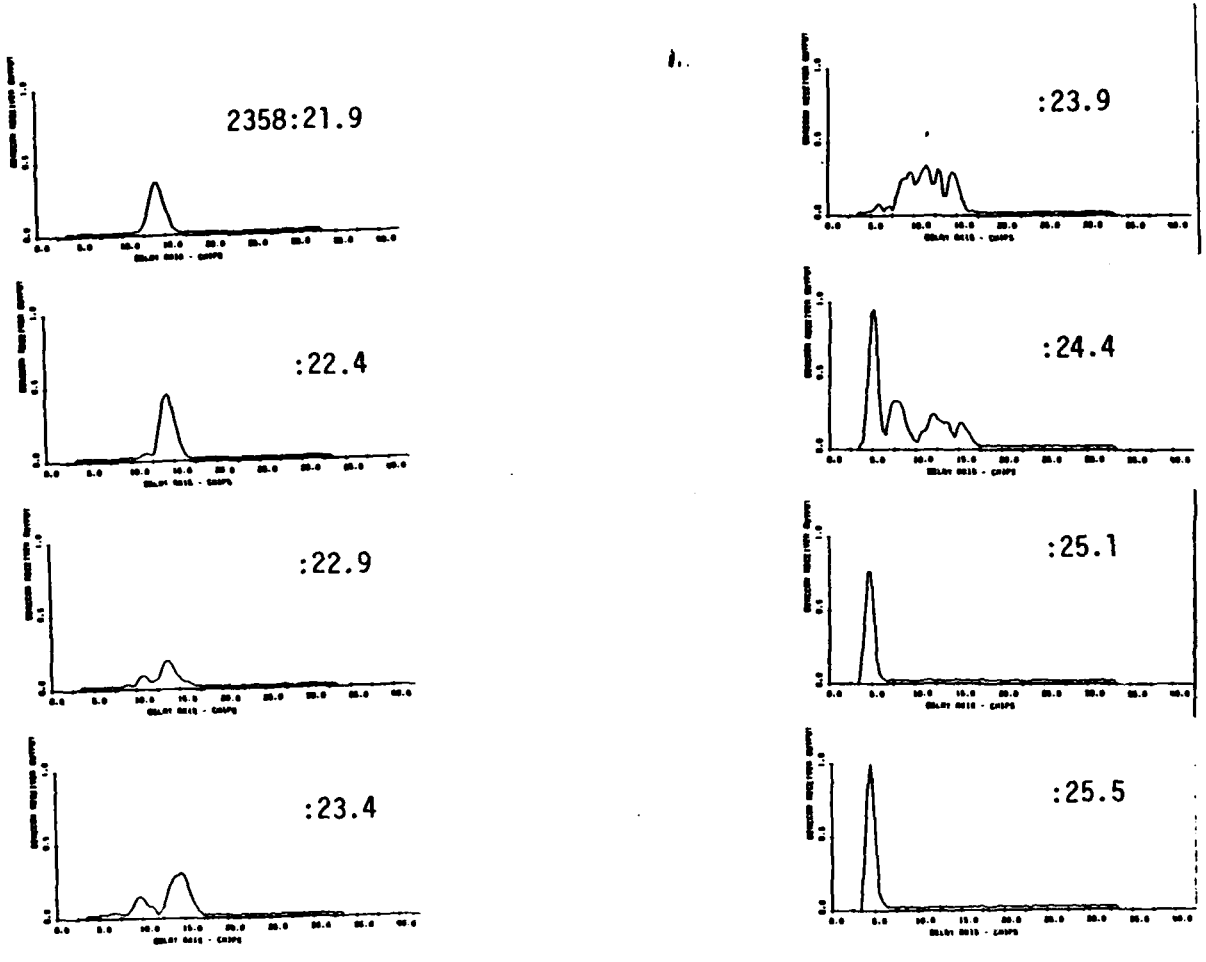

Figure 4-4. Energy delay profile between 2358:21.9 and 2358:25.5Z, St. George Island, second beacon.

4.4 TIME-OF-ARRIVAL DELAY

The impulse response data provide a snapshot in time of the energy-of-arrival profile. In this section we provide a view of the relative delay of the multipath signal components and the integrated electron content associated with the direct path delay.

4.4.1 Time-of-Arrival Composite Data

Figure 4-5 is a plot of the TOA of each energy peak (ray) as a function of the flight time of the rocket behind the barium cloud. As discussed in Section 2.4.1, each point is a plot of the location of the centroid of each peak in signal energy at each sample point in time. The centroiding algorithm is described in Appendix A. Evident in this figure is the TOA jitter of the direct path signal. This figure also clearly shows the caustic rays emerging primarily from one side of the cloud consistent with the geometry shown in Figure 4-1, which shows the path through the plasma largely outside the striated region approximately half way through the occultation. While only a few striations appear to have been occulted, more symmetric scattering appears to have resulted.

As with the St. George Island data from the first beacon, the data appear to support a geometric optics approach to the prediction of TOA jitter and delay spread. These geometric relations were tested more extensively for the first occultation data for St. George Island as described in Section 2 than time has permitted for the second beacon data.

4.4.2 Time-of-Arrival Direct Path Data and Integrated Electron Content

The TOA of the direct path through the plasma can be extracted from Figure 4-5 and is plotted in Figure 4-6. The

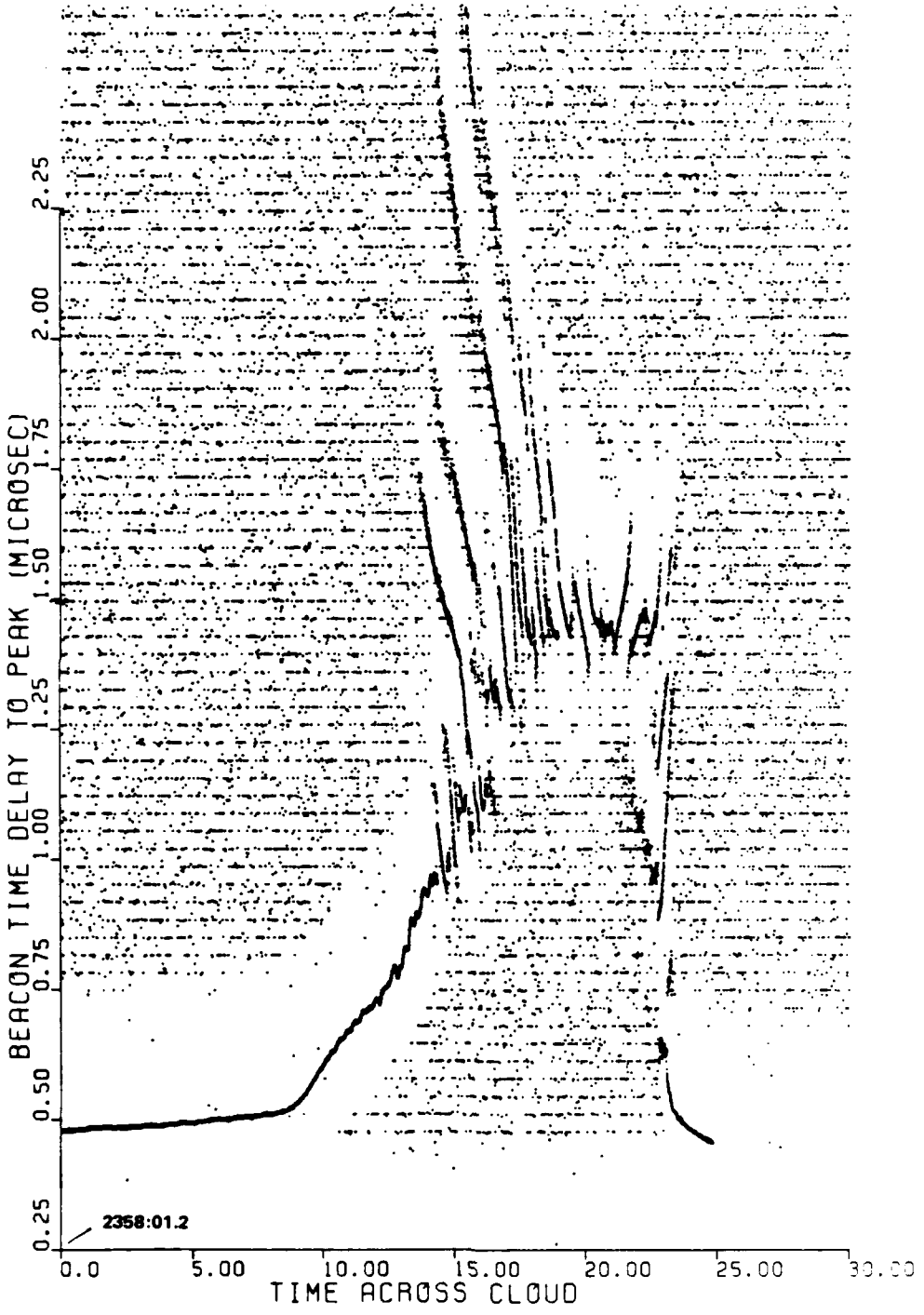

Figure 4-5. Energy peak TOA delay, all peaks.

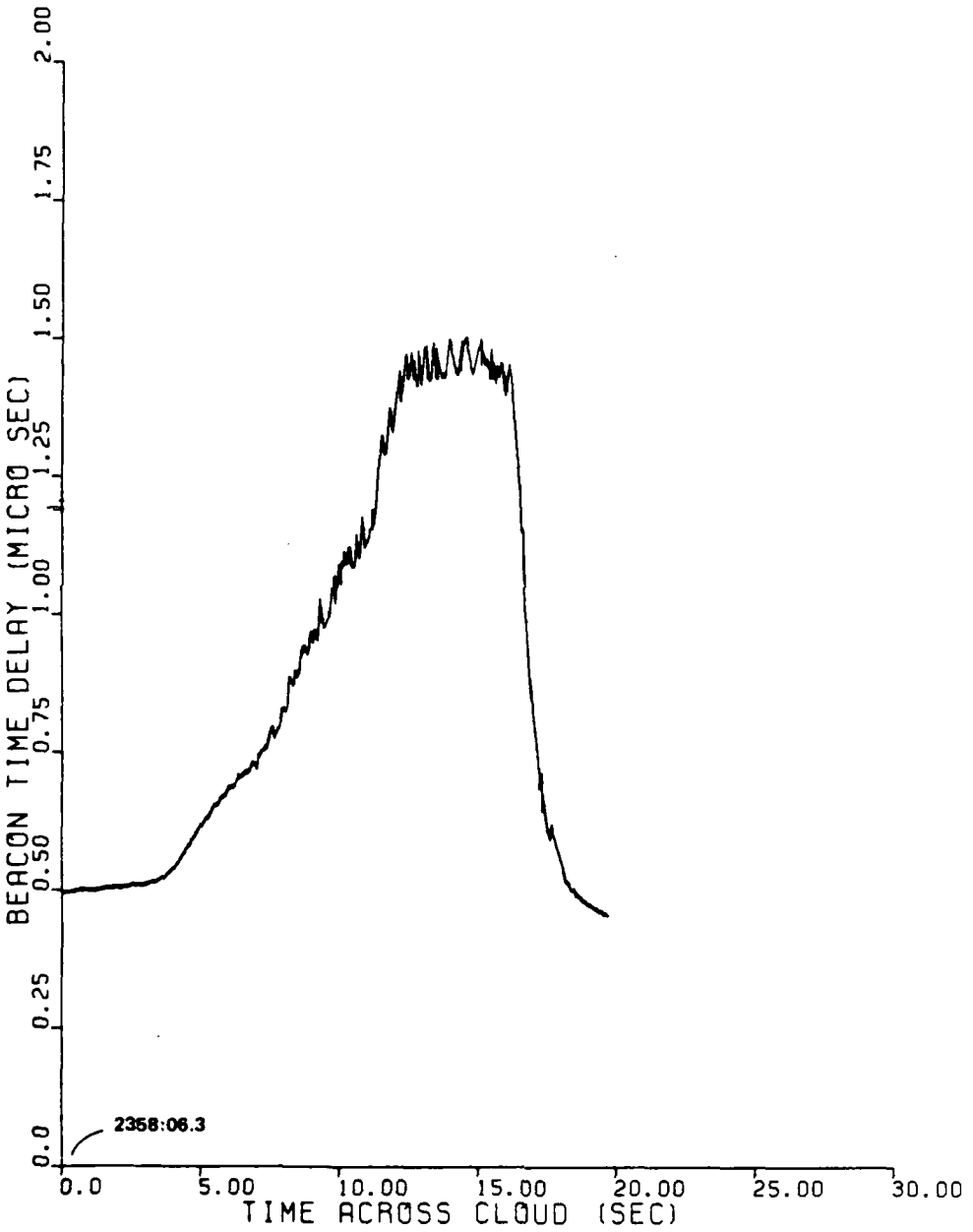

Figure 4-6. Direct path TOA delay.

algorithm used to distinguish the first peak in signal energy (direct path TOA) from noise is described in Appendix A. The TOA data were extracted by first fitting an approximate curve through the data of Figure 4-5 and then using a tracking algorithm that determined the earliest peak signal arrival in a given window width about that curve. A window width of $\pm 2/3$ chip was used to construct Figure 4-6. In retrospect, it appears that the window should have been opened to at least ± 1 chip. The jitter evident in these data can be associated with the dispersive phase as described in Section 2.5.1.

The integrated electron content can be calculated based on the TOA shift in the received signal at each instant in time. Each microsecond of TOA delay at 98 MHz corresponds to 7.29×10^{12} cm^{-2} of electron content. Thus, for the second path through the barium ion cloud to St. George Island, the peak integrated electron content due to the barium plasma is approximately 7.0×10^{12} cm^{-2}. As discussed in Section 2, the background ionosphere contribution is small, approximately 10 percent of the ion cloud contribution.

4.5 TIME DELAY JITTER, ST. GEORGE ISLAND, BEACON 2

The jitter associated with the first arrival of signal energy is examined here and is referred to as the direct path TOA delay jitter. Section 2.5.1 provides a discussion of the theoretical relation of the TOA delay and the dispersive phase.

The occultation interval was divided into several segments as shown on Figure 4-7 to investigate the relationship between the dispersive and angular spread energy components. Each segment was detrended to remove the deterministic TOA delay associated with the background plasma and transformed to determine the rms time delay power spectrum. Figure 4-8 through 4-11 show the detrended data and the corresponding time delay jitter spectrum for those intervals

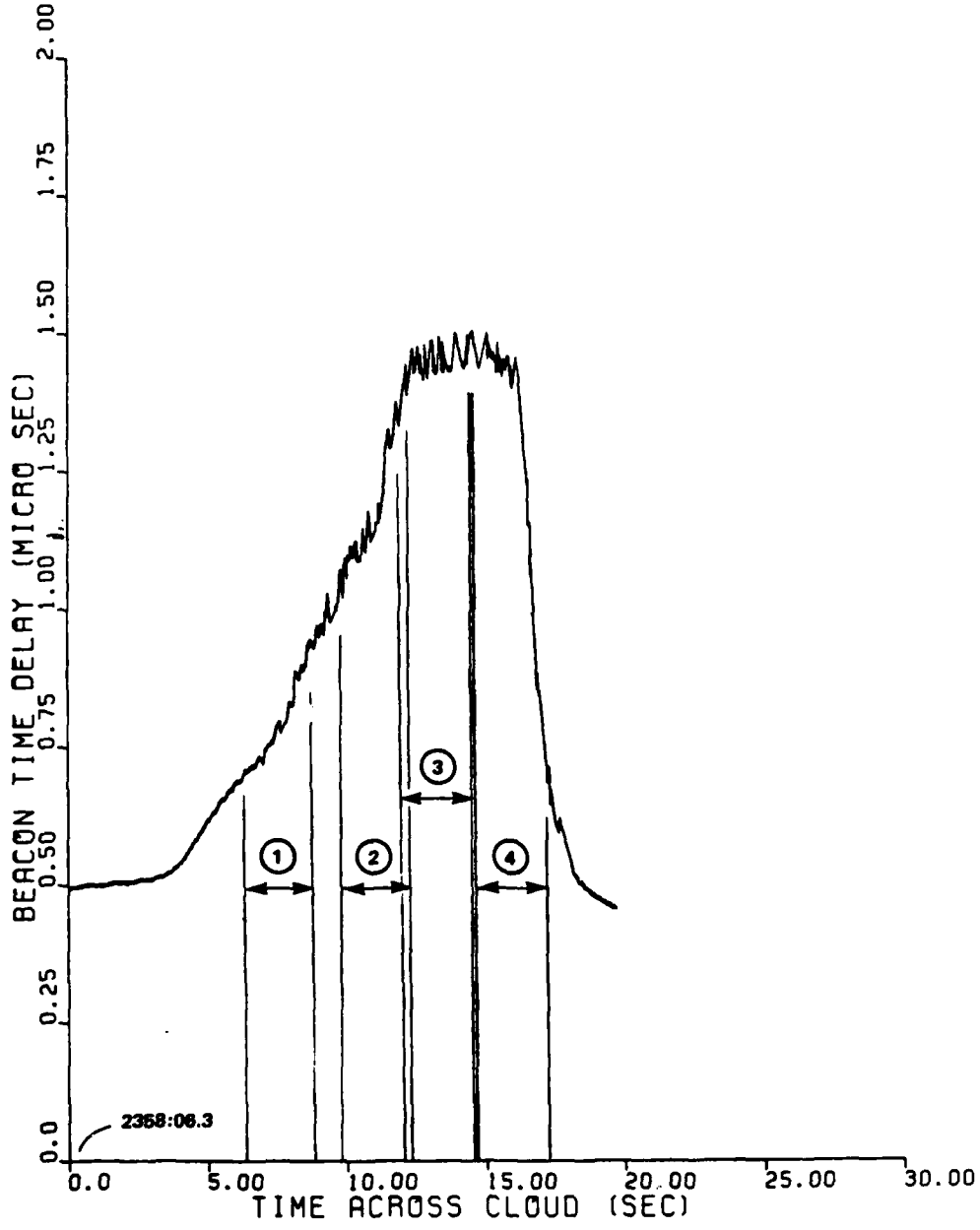

Figure 4-7. Direct path TOA jitter data segments.

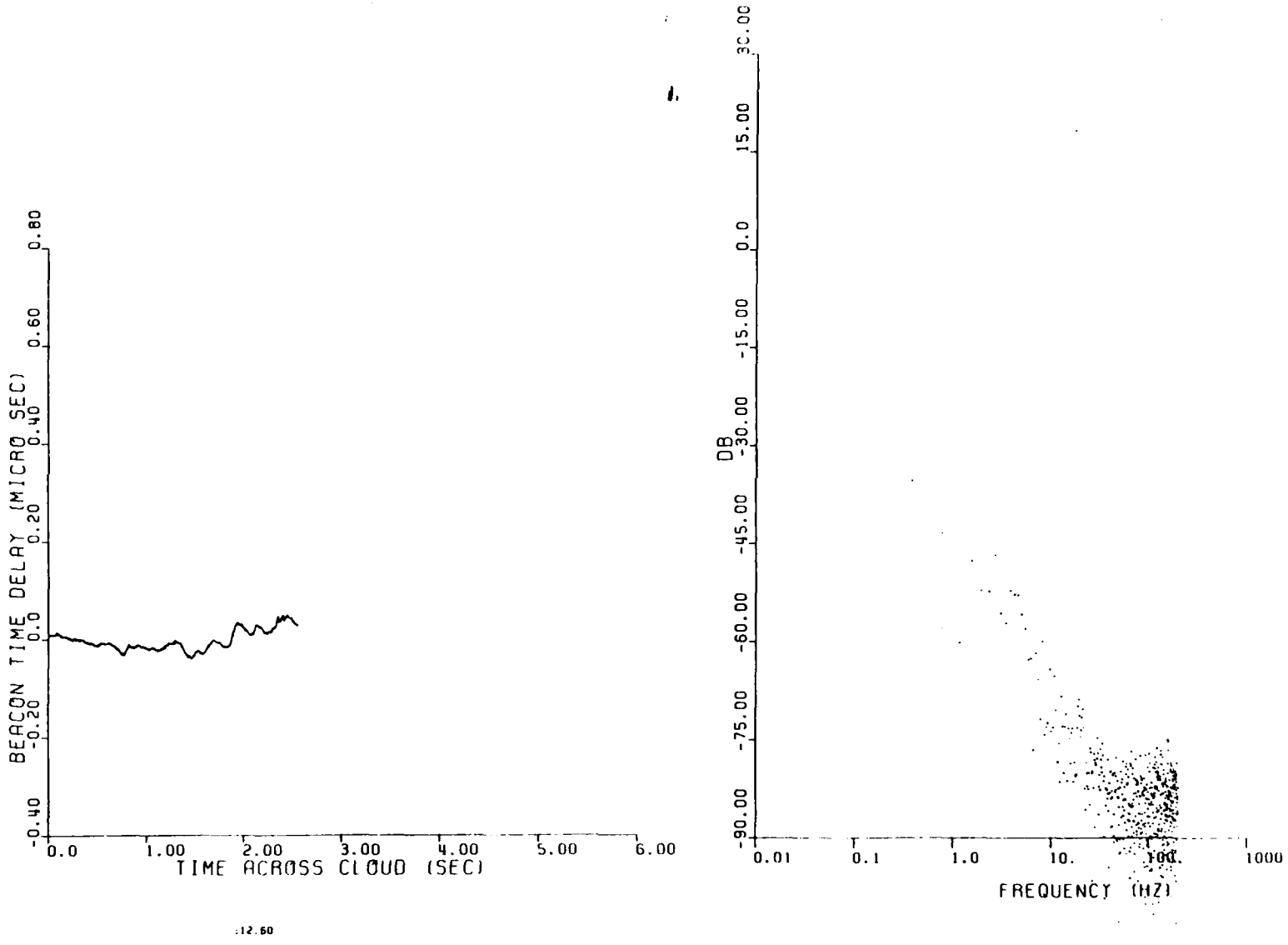

Figure 4-8. Detrended TOA jitter and jitter spectrum for Segment 1.

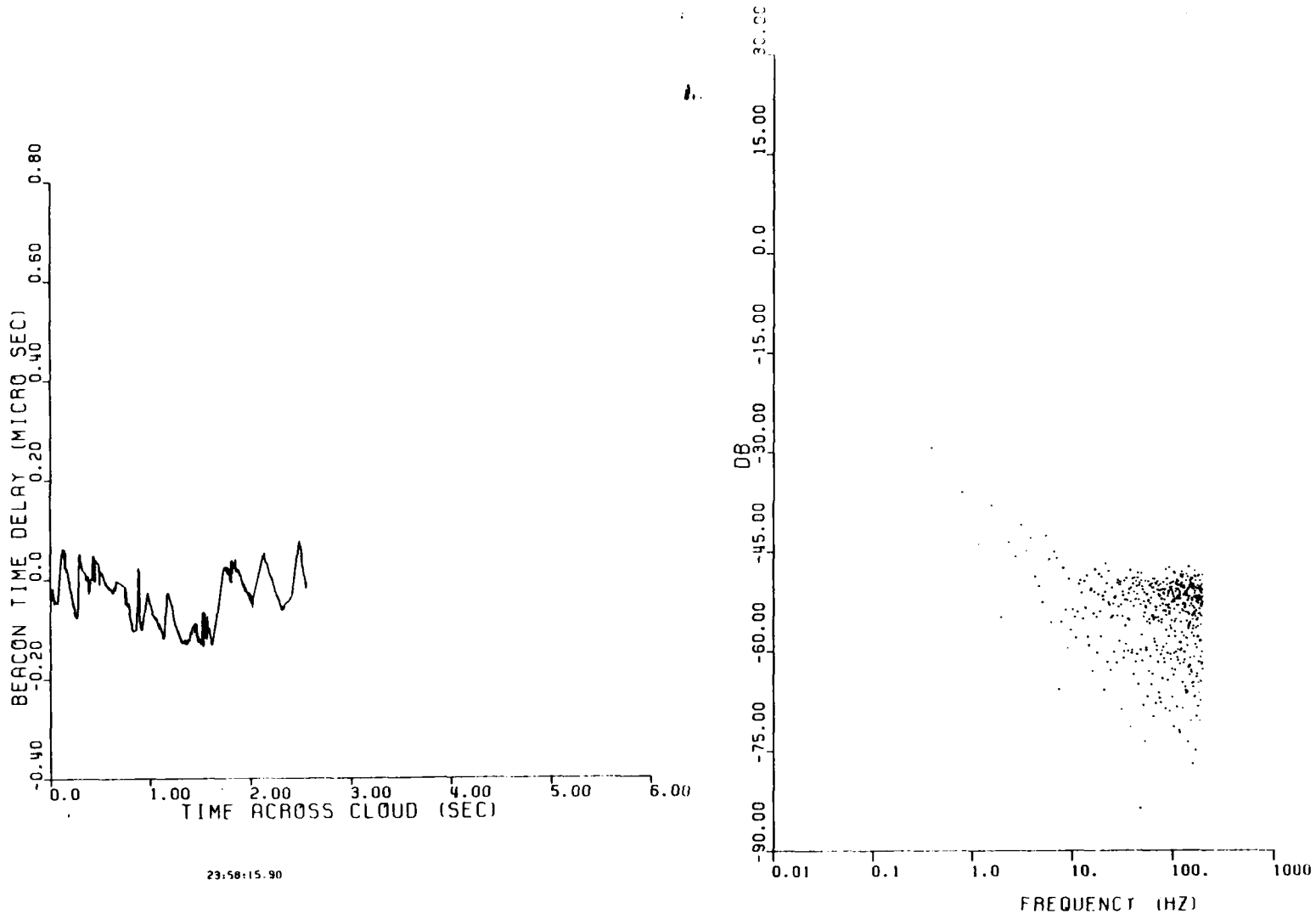

Figure 4-9. Detrended TOA jitter and jitter spectrum for Segment 2.

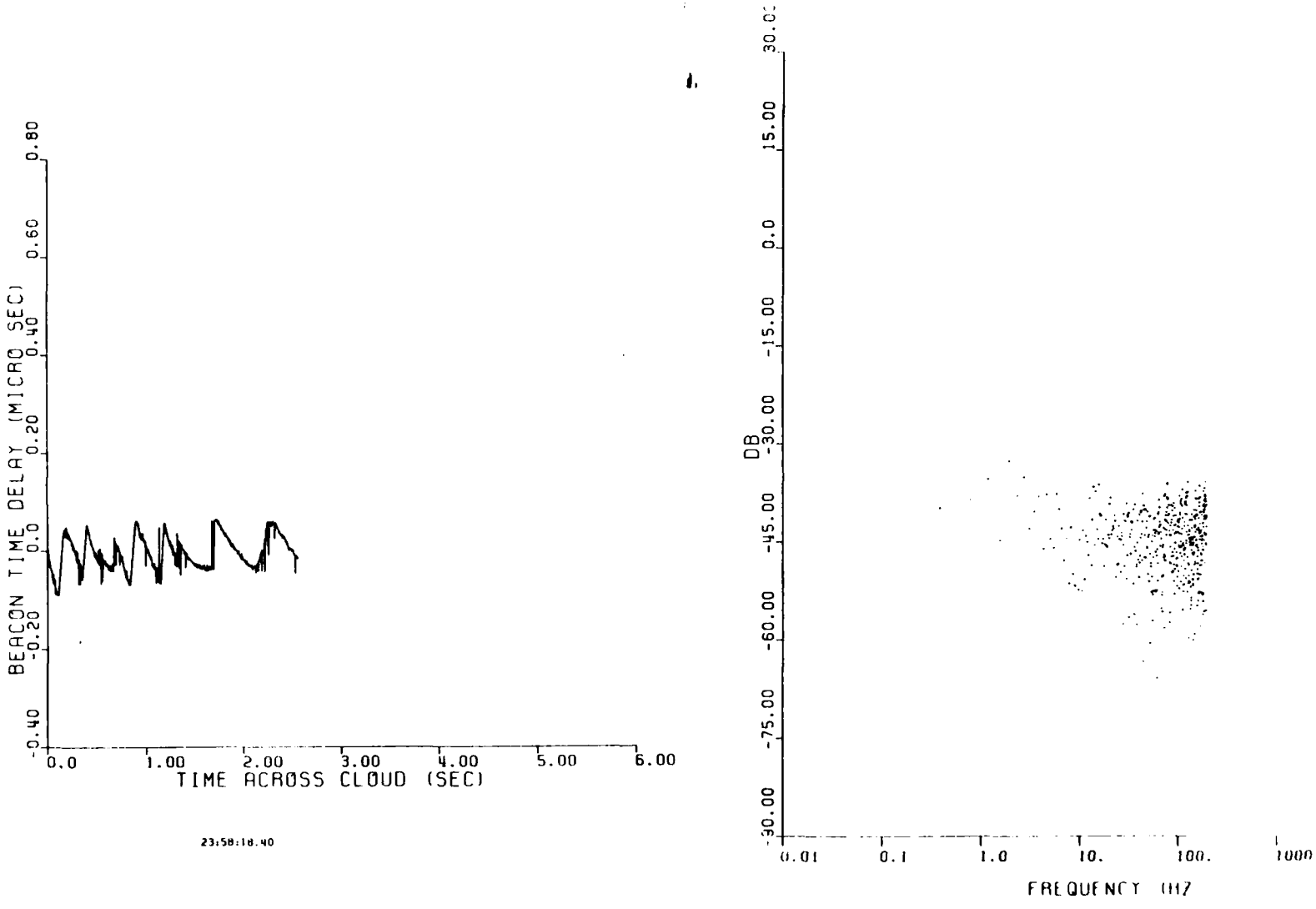

Figure 4-10. Detrended TOA jitter and jitter spectrum for Segment 3.

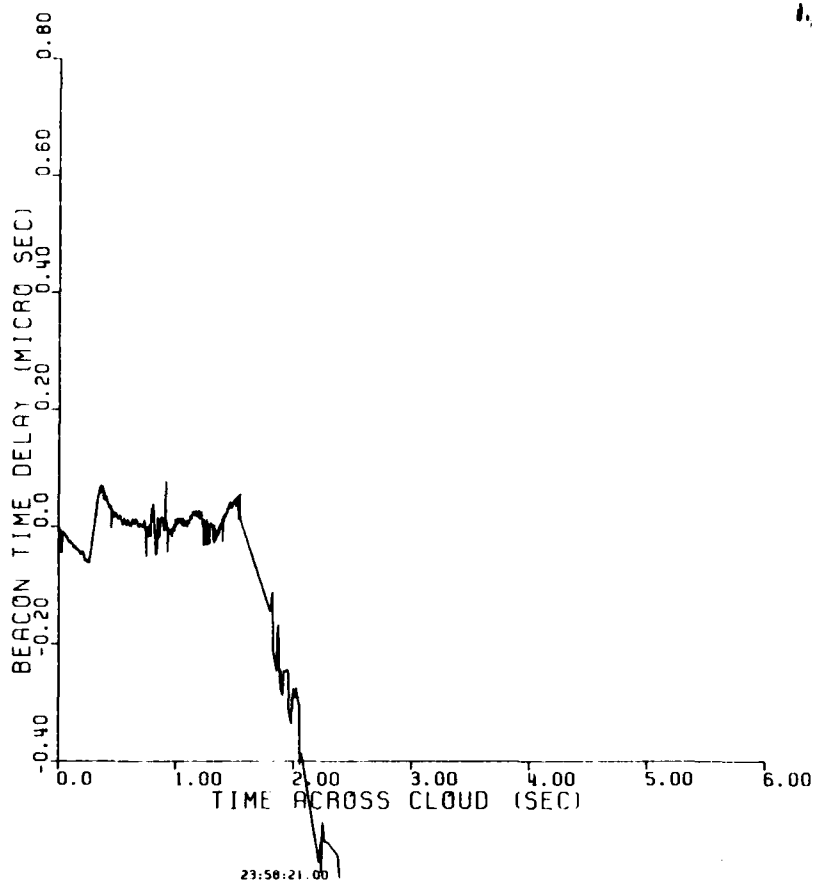

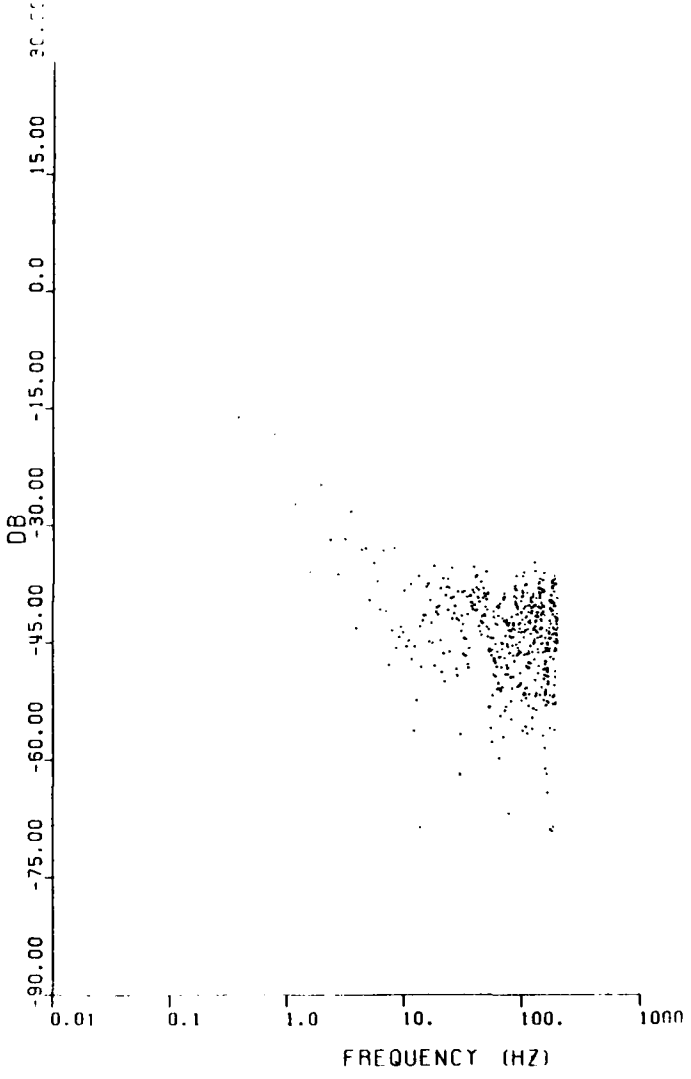

Figure 4-11. Detrended TOA jitter and jitter spectrum for Segment 4.

noted on Figure 4-7. Table 4-1 provides a summary of the measured rms time delay jitter and the corresponding path integrated rms dispersive phase.

For these data, the algorithm described in Appendix A used to determine the direct path TOA was set such that the jitter window was ± 1 chip (0.1 microsecond) about the detrended value of TOA.

Generally, the data show a consistent trend toward stronger jitter when the integrated electron content (TOA delay) is its maximum as the rocket approaches the center of the cloud. The rms values of rms phase are nearly the same as those derived for the first beacon measurements on the St. George Island path and summarized in Table 2-1. The spectral break frequencies are difficult to estimate. The TOA fluctuations appear to take on a repetitive saw-tooth pattern near the maximum delay as shown in Figure 4-10. This is much different than noted previously.

4.6 GENERALIZED POWER SPECTRUM

The analytical expressions for the generalized power spectrum, $\Gamma_l(f_d, \tau)$, were given in Section 2.6.6. A measure of the goodness to which the measured data conform to this model can be derived from the received beacon signal. Here we examine delay plane of the generalized power spectrum.

4.6.1 Delay Power Spectrum

The signal delay power spectrum or energy arrival distribution is obtained by integrating out the Doppler frequency variable in the generalized power spectrum,

$$\Gamma_l(\tau) = \int \Gamma_l(f_d, \tau)\, df_d \quad .$$

Table 4-1. RMS line delay jitter data segment summary.

Interval	Data Interval Start (UT)	End (UT)	RMS TOA Jitter (uS)	RMS Phase (Radians)	Data Points	Jitter Points	Mean TOA (uS)	Comments
1	2353:12.6	:15.2	0.0206	12.7	1024		-.0018	
2	:16.0	:18.6	0.0513	31.9	1024		-.0352	
3	:19.4	:22.0	0.1324	81.1	1024		-.0027	+/- TOA Pea
+*	:21.3	:33.8	0.1170*	- -	1124		-.1257	+/- TOA Pea

* = rms jitter data not properly corrected

As described in Section 2.6.7, it is relatively straightforward to compute the delay power spectrum by summing the squares of the channel impulse response magnitudes shown earlier at each tap delay and normalizing the result such that the integral equals unity to correspond with the DNA channel model definition,

$$\int_{-\infty}^{\infty} \Gamma_1(\tau)\, d\tau = 1 \quad .$$

Figures 4-12 through 4-15 show the results of these calculations for the four data segments summarized in Table 4-1. The TOA shown in Figure 4-7 was used to remove the TOA bias. In order not to remove the effects of the dispersive jitter, a mean TOA curve was obtained from Figure 4-7 and the power summed relative to the mean delay at each time sample. Any defocusing effect is minimized by removal of the TOA shift and dividing the data into short 2.56-second segments.

Unlike the first beacon rocket occultation data, defocusing effects appear rather small. Thus, the individual segments appear to conform better to the long-term statistical average of the theoretical delay power spectrum. The normalization interval for each plot spans the entire delay profile shown.

4.6.2 Comparison With Theory

As discussed in Section 2.6.7.1, theory can be used to estimate the ratio of the rms delay spread to the rms delay jitter parameter and the coherence bandwidth, f_o, by matching theoretical curves against the measured data presented in Figures 4-12 through 4-15. Figures 2-50 through 2-53 provide plots of the theoretical delay power spectrum against which the measured curves may be matched. Again, in fitting the theoretical curves to these data, the lower values at large delays were not emphasized. Figure 4-16 shows

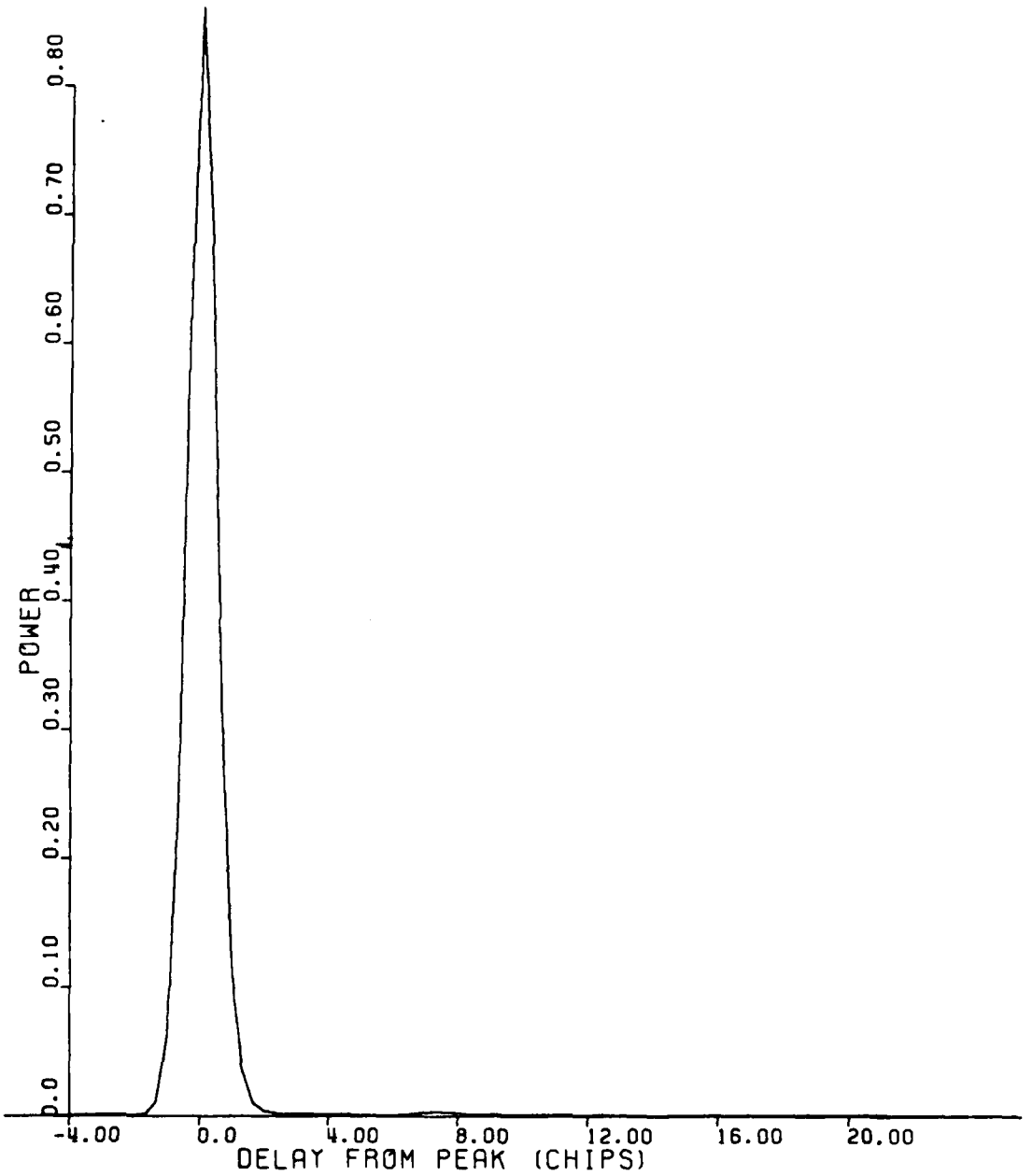

Figure 4-12. Delay power spectrum for Segment 1, St. George Island, Beacon 2.

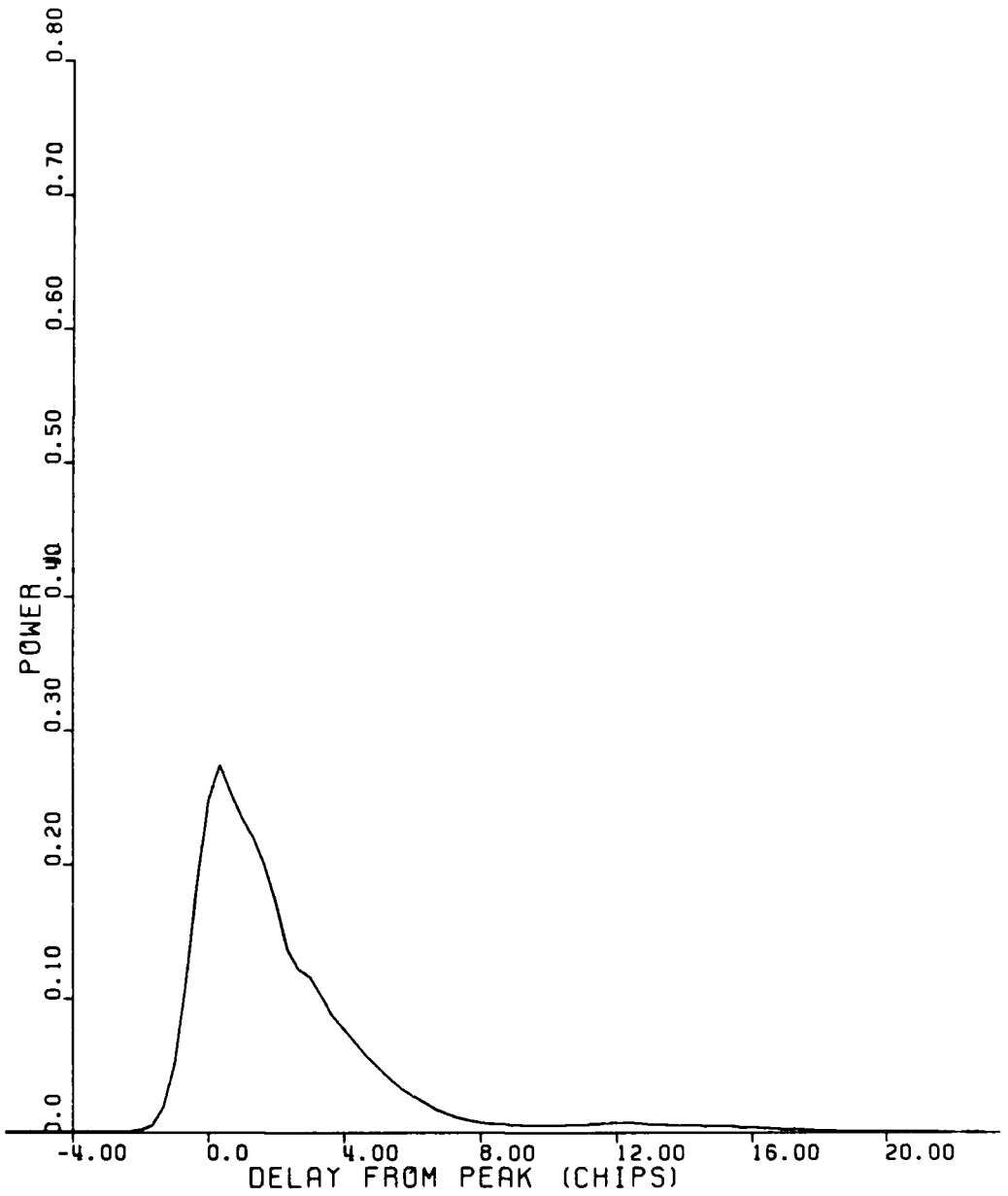

Figure 4-13. Delay power spectrum for Segment 2, St. George Island, Beacon 2.

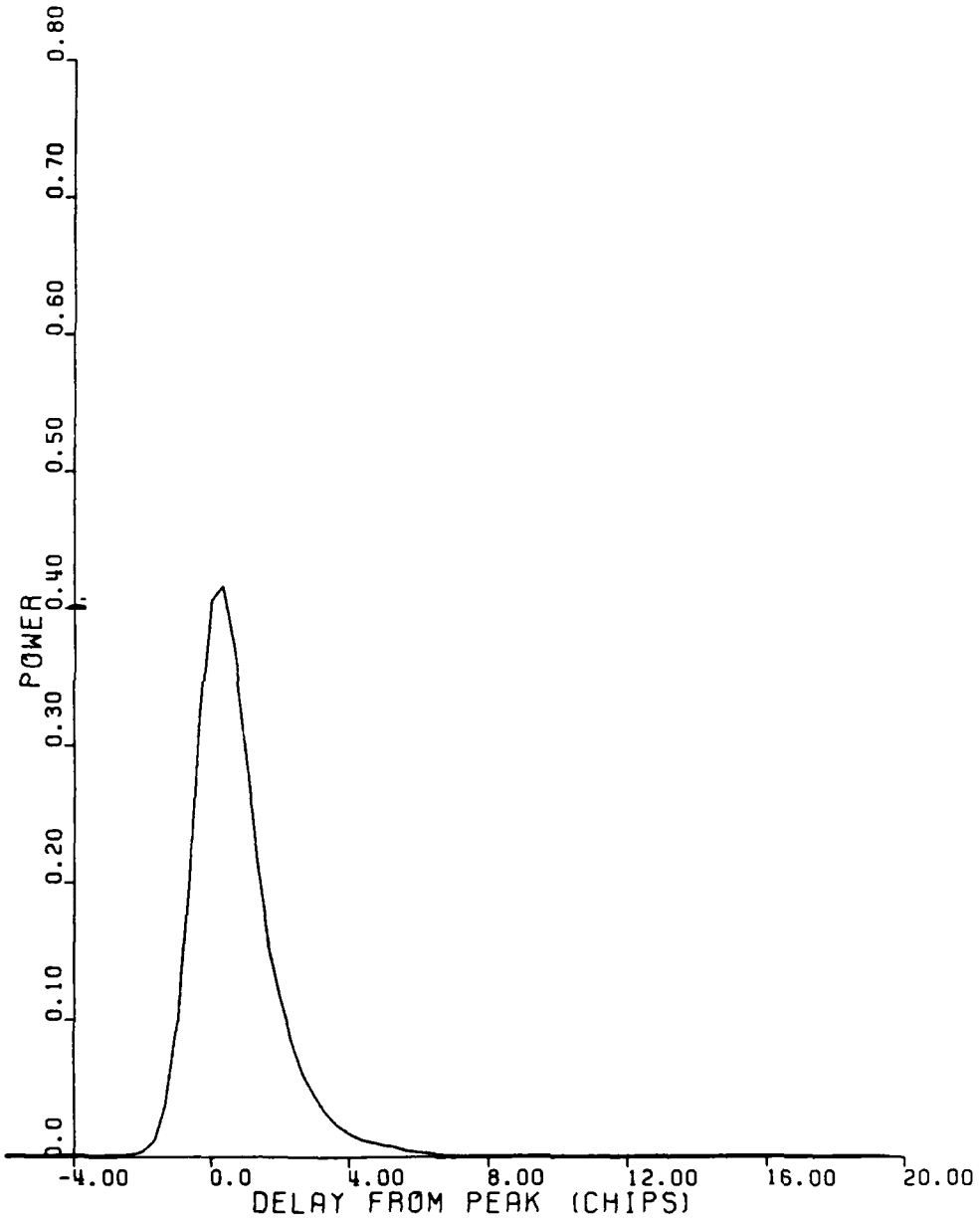

Figure 4-14. Delay power spectrum for Segment 3, St. George Island, Beacon 2.

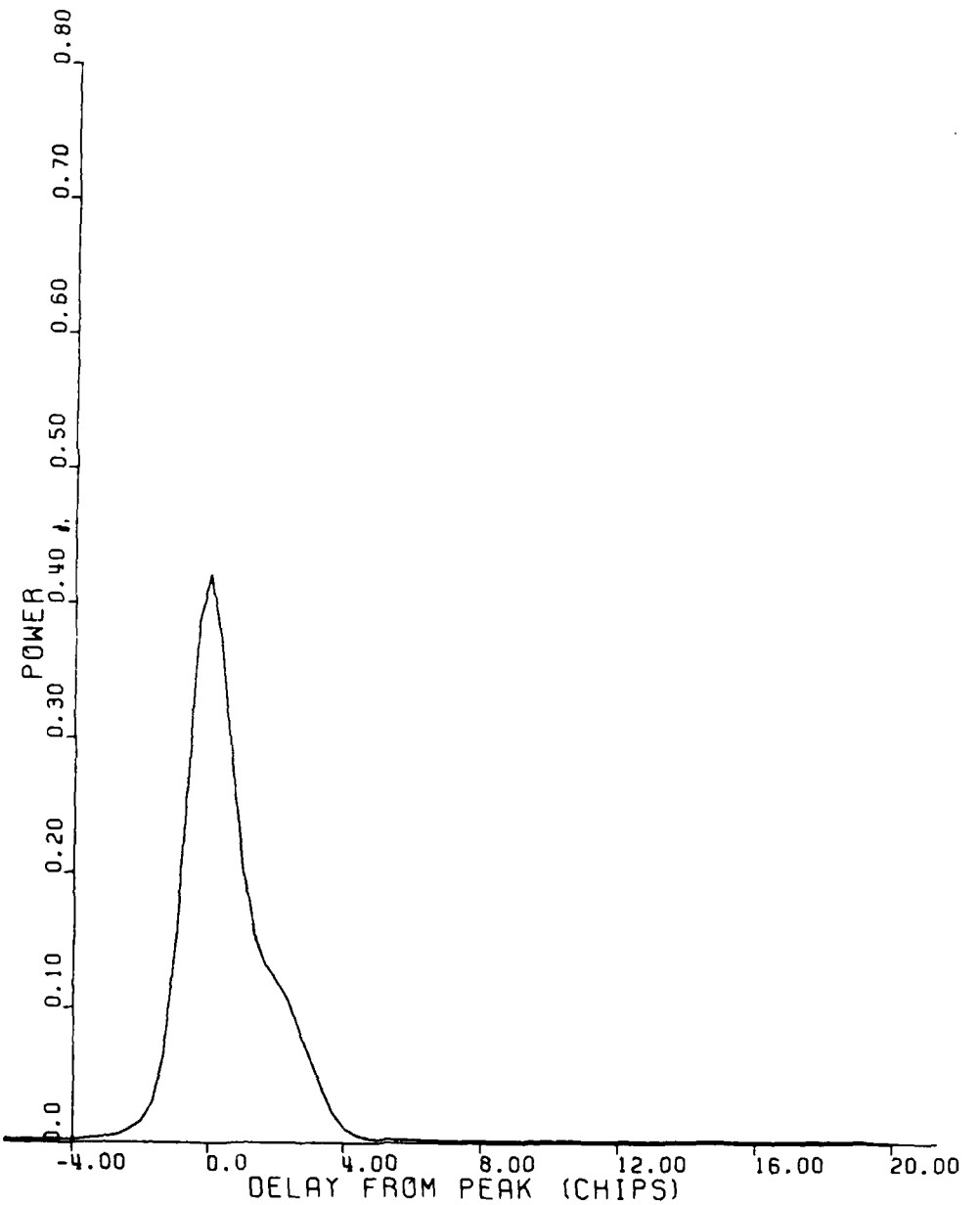

Figure 4-15. Delay power spectrum for Segment 4, St. George Island, Beacon 2.

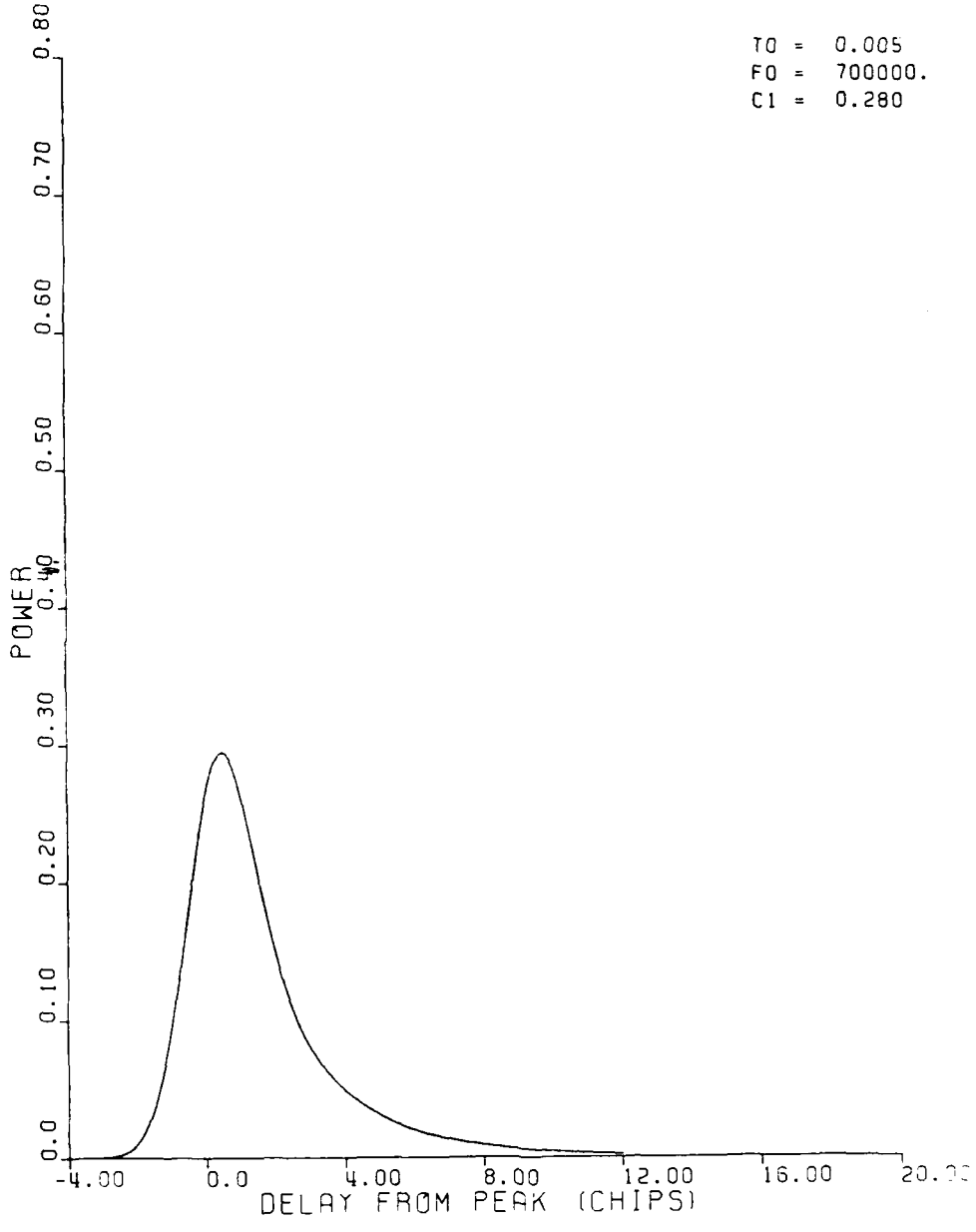

Figure 4-16. Theoretical delay power spectrum for f_o = 0.7 MHz and a jitter-to-spread ratio of 0.28, corresponding to Segment 2.

the best fit for Segment 2, while Figure 4-17 shows the best fit for Segments 3 and 4; these figures serve to illustrate the excellent fit obtained. Table 4-2 summarizes the results of this comparison.

From the relationship of the frequency correlation bandwidth parameter to the rms delay spread relation described in Section 2.6.7.1, an estimate of the delay spread can be computed using the rms TOA jitter estimate from Table 4-1. The result of this calculation for each data segment is shown in Table 4-3. For Segment 4, a good estimate of the rms jitter was not available. Using the result of the curve fit, the jitter and spread have been calculated as shown in the last three columns. Note that this implies the rms dispersive phase is approximately 30 radians over Segments 2, 3, and 4.

4.7 FADING WAVEFORM AT 98 MHZ

The fading waveform at 98 MHz can be synthesized from the channel transfer function data. This permits a calculation of the received phase PSD and a calculation of the angular spectrum at 98 MHz. These data are presented here.

4.7.1 Fading Waveform

The fading waveform at 98 MHz can be obtained by transforming the channel impulse response of each data record collected during the occultation to obtain the channel transfer function. From these transformed records, the 98-MHz component can be selected and plotted as shown in Figure 4-18. The peak phase advance associated with the barium plasma can be estimated to be 91.5 cycles from these data. As discussed in Section 4.4.2, each cycle of phase shift corresponds to 7.29×10^{10} cm^{-21} of electron content at 98 MHz. This provides an estimate for the peak electron content associated with the barium plasma of approximately 6.7×10^{12} cm^{-2}. This is in good

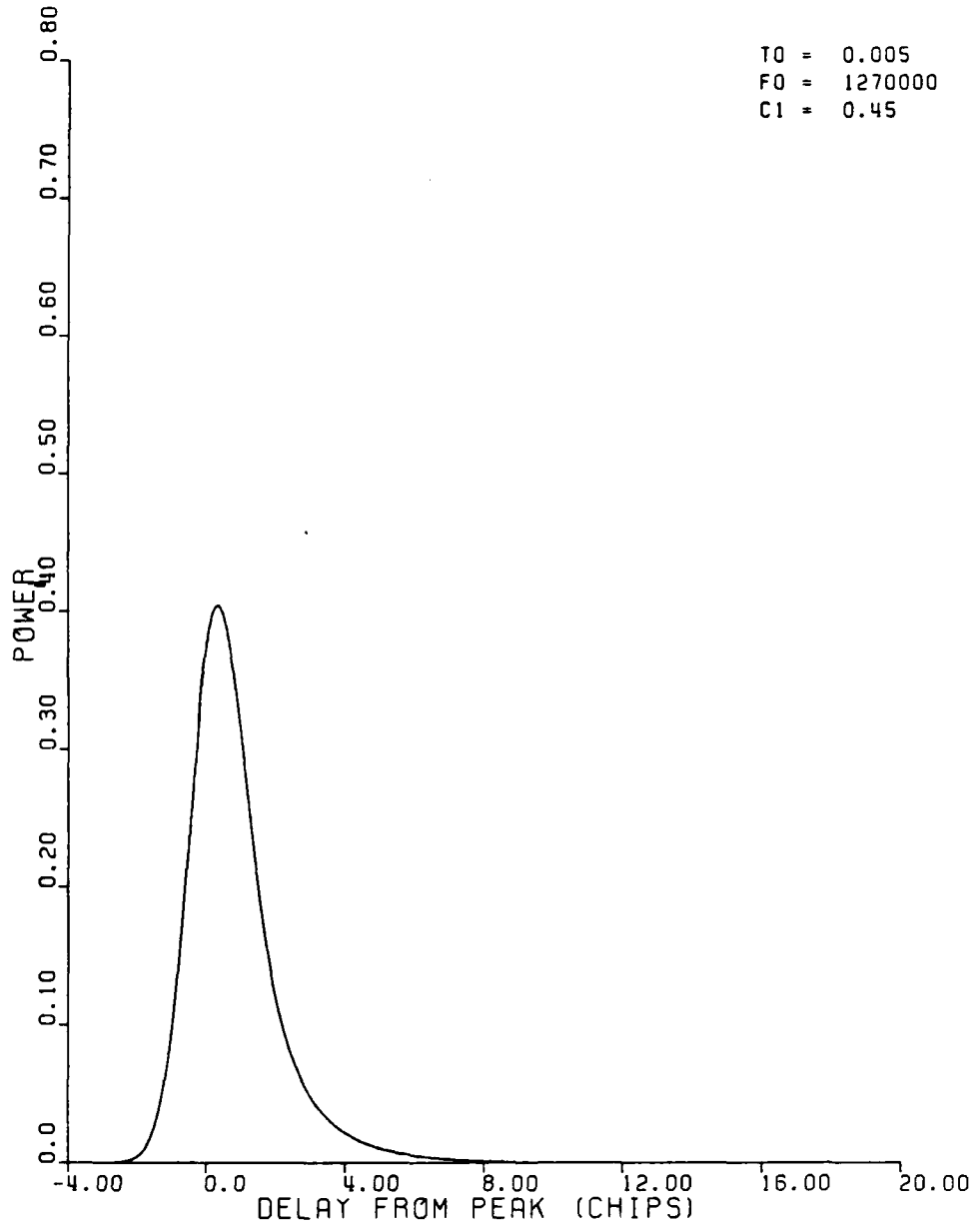

Figure 4-17. Theoretical delay spectrum for f_o = 1.27 MHz and a jitter-to-spread ratio of 0.45, corresponding to Segments 3 and 4.

Table 4-2. Parameter summary for best fit to measured normalized power delay profiles.

SEGMENT	f_o (MHz)	RMS JITTER TO SPREAD RATIO	COMMENTS
1	3.2	~ 0.5	WEAK TOA JITTER
2	0.7	0.28	EXCELLENT FIT
3	1.27	0.45	EXCELLENT FIT
4	1.27	0.45	GOOD FIT

Table 4-3. Comparison with RMS jitter data.

Segment	From Table 4-2 f_c	From Table 4-2 RMS Jitter to Spread ratio	From Table 4-1 RMS TOA Jitter (us)	COMPUTED RMS Delay Spread (us)	COMPUTED Jitter/ Spread	COMPUTED RMS Delay Jitter (us)	COMPUTED RMS Delay Spread (us)	RMS Phase (Rad)
1	3.2 MHz	~0.5	0.0206	0.0453	~0.45			
2	1.7	~0.25	0.0519	0.2215	~0.23			
3	1.27	0.45	0.0324	0.1211	0.27	0.0326	0.1143	0.17
4	1.27	0.45	- -	- -	- -	0.0326	0.1143	0.17

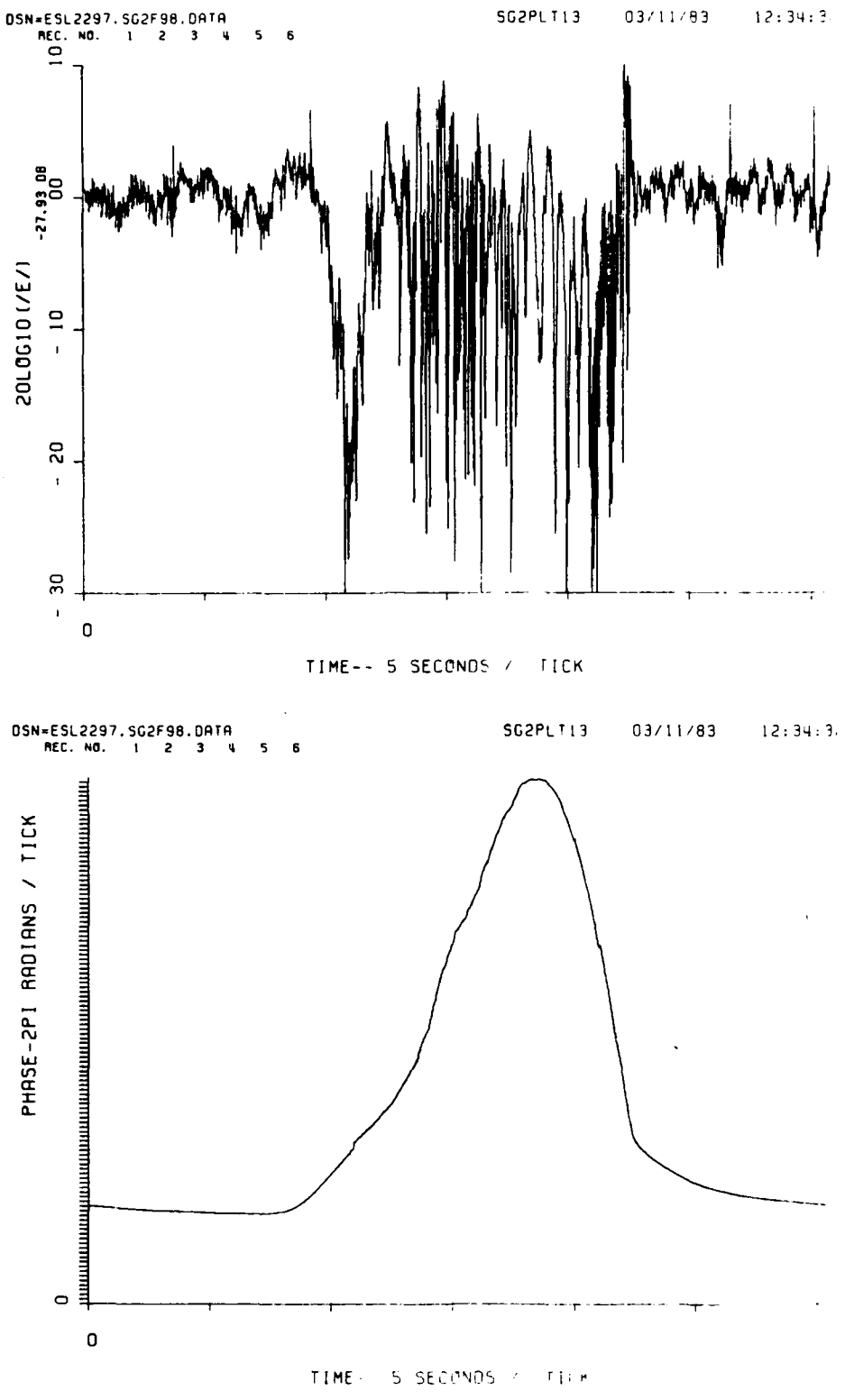

Figure 4-18. Received amplitude and phase at 98 MHz, St. George Island, Beacon 2.

agreement with the estimate obtained earlier in Section 4.4.2 from the TOA shift, which was 7.0×10^{12} cm^{-2}.

4.7.2 Received Phase PSD at 98 MHz

The phase PSD corresponding to the received signal phase is shown in Figure 4-19. The slope corresponds to approximately 20 dB/decade or f^{-2} at the higher frequencies. This is typical of the phase PSD expected in the far field of a diffraction screen[2].

4.7.3 Angular Spectrum at 98 MHz

The transform of the complex fading waveform at 98 MHz yields the angular spectrum of the received signal. This results since time corresponds to spatial position in the diffraction field. The angular spectrum is shown in Figure 4-20. This spectrum resembles the earlier spectrum obtained for Beacon 1. A sharp break frequency near 40 Hz is also evident in this figure.

4.8 BACK-PROPAGATION PROCESSING AT 98 MHZ

Backward propagation of the 98-MHz signal component of the received diffraction pattern swept out by the beacon rocket can be performed as discussed in Section 2.9 using thin phase screen angular spectrum techniques. The extent to which amplitude fluctuations diminish with back-propagation is a function of the extent of the striated plasma along the line-of-sight and the noise received during the measurement. Because the rocket trajectory takes the beacon on a downward path that moves away from the striation mass over the occultation interval, no one back-propagation distance is uniquely correct. For these reasons, it is not possible to determine the in-situ phase power spectral density from the beacon data.

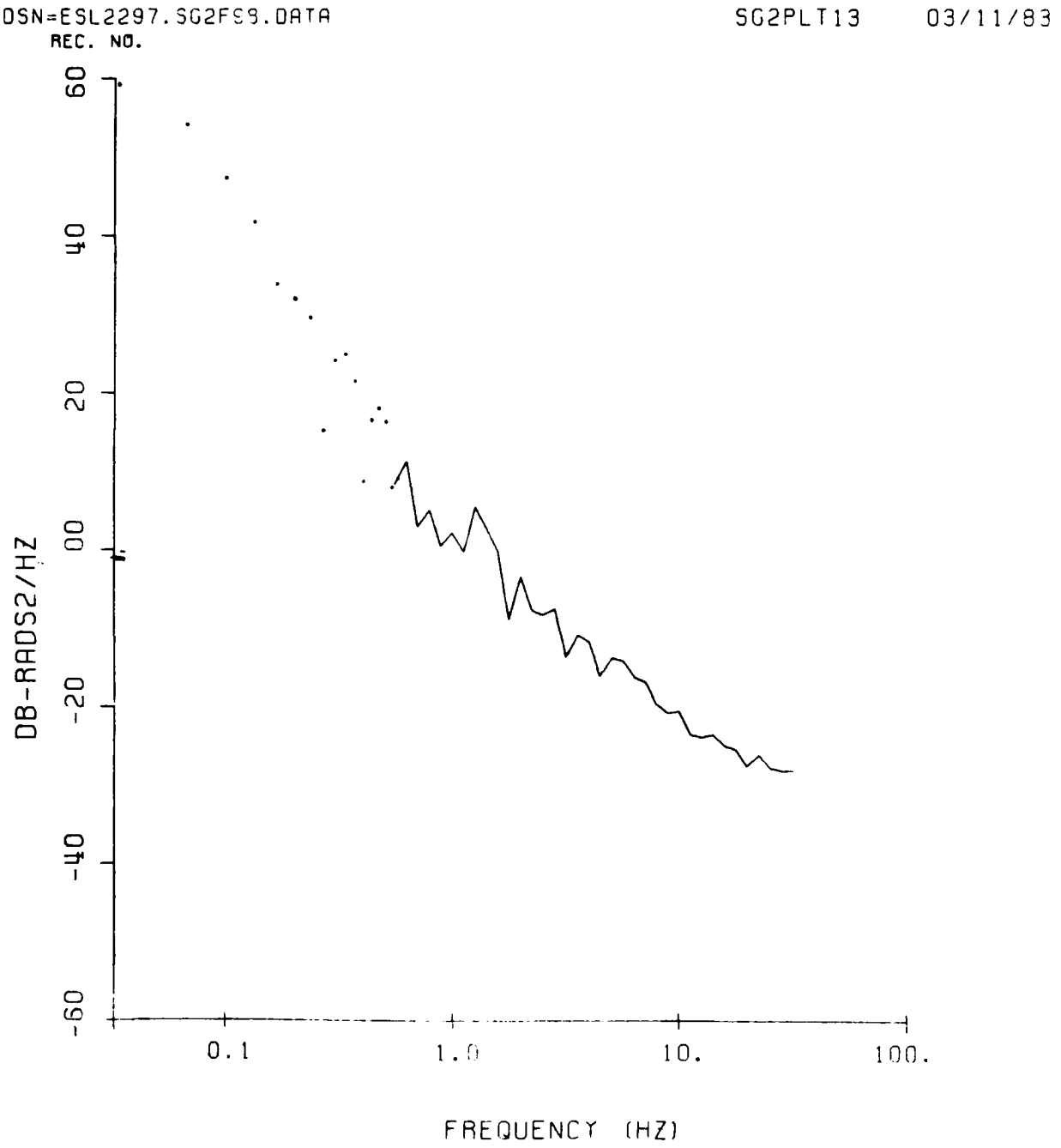

Figure 4-19. Phase power spectral density at 98 MHz.

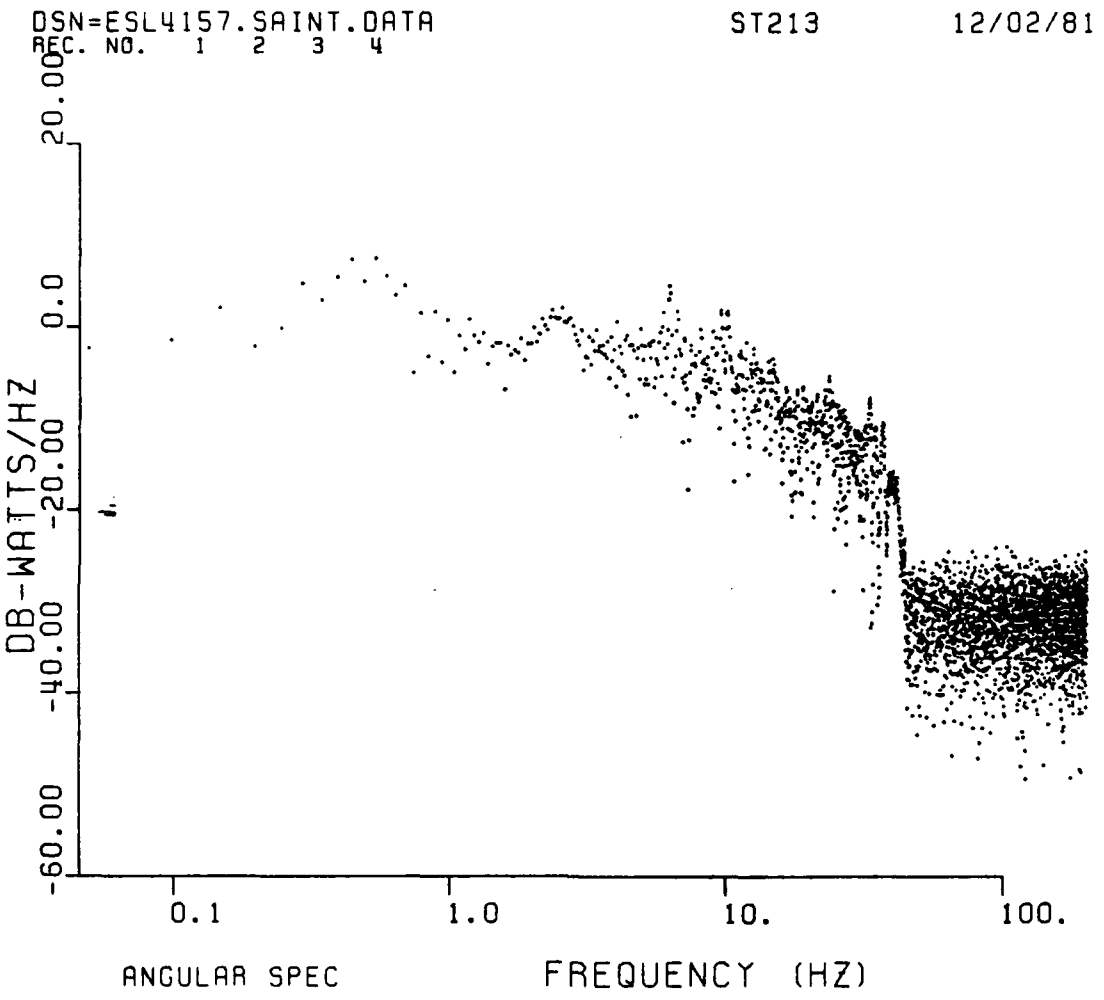

Figure 4-20. Angular spectrum at St. George Island, Beacon 2.

The scintillation index and the back-propagation results obtained are described in the following sections for reference. The data are interesting only in that the S^4 index versus back-propagation distance and the 98-MHz signal amplitude behavior provide qualitative agreement with the optical data discussed in Section 4.2.

4.8.1 S^4 Versus Distance

The S^4 scintillation index is used as a measure of the amplitude fluctuation as discussed in Section 2.9.1. The amount the S^4 index decreases with back-propagation and its value after back-propagation gives a good indication as to how well the data back-propagated in a thin phase screen sense. Figure 4-21 is a plot of the scintillation index versus back-propagation distance for St. George Island, Beacon 2. The back-propagation distance was initially computed assuming an effective transverse velocity, V_e, of approximately 890 m/sec. The true velocity is likely to be similar to that of the first beacon, approximately 980 m/sec. The distance axis scales by the factor $(V_T/V_e)^2$, where V_T is the true transverse velocity.

The S^4 index exhibits a rapid decrease over the first 10 km. This is in reasonable agreement with the optical data (see Section 4.2).

4.8.2 Back-Propagation Plots

Plots of the back-propagated signal amplitude and phase are presented in Figures 4-22 through 4-30 over the first 40 km. The distances noted are the uncorrected values corresponding to the 890 m/sec velocity.

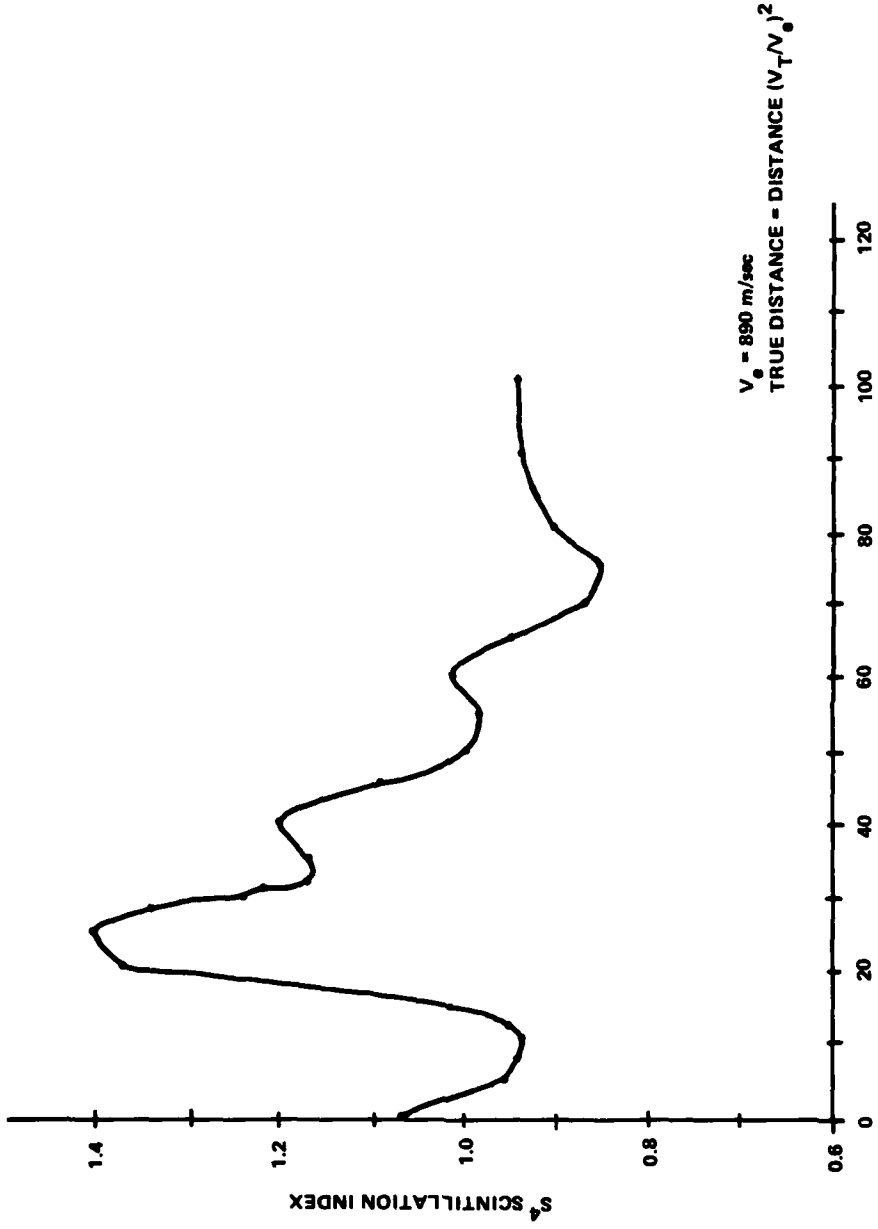

Figure 4-21. S^4 scintillation index versus back-propagation distance for St. George Island, Beacon 2.

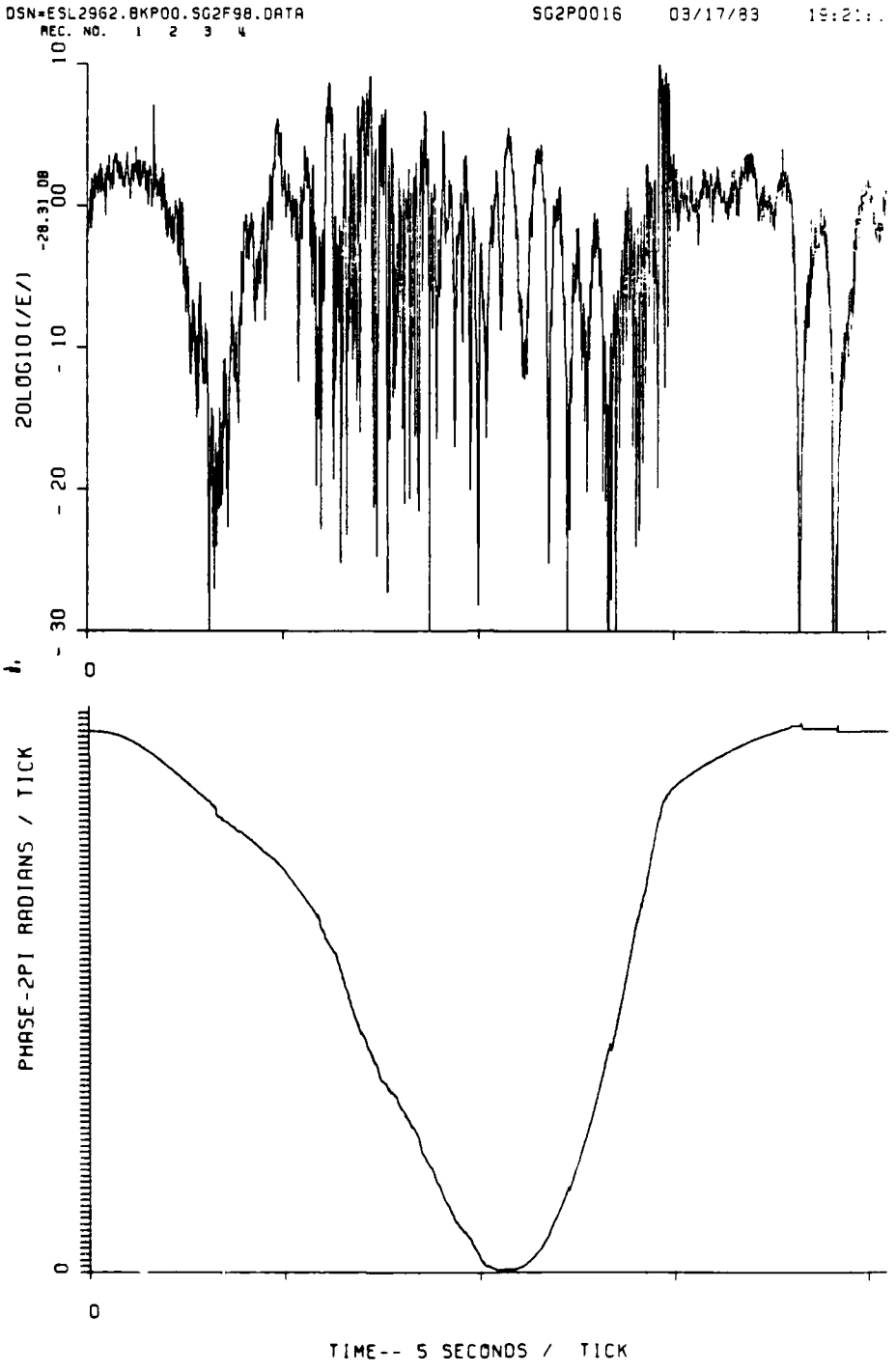

Figure 4-22. Amplitude and phase before back-propagation, St. George Island, Beacon 2.

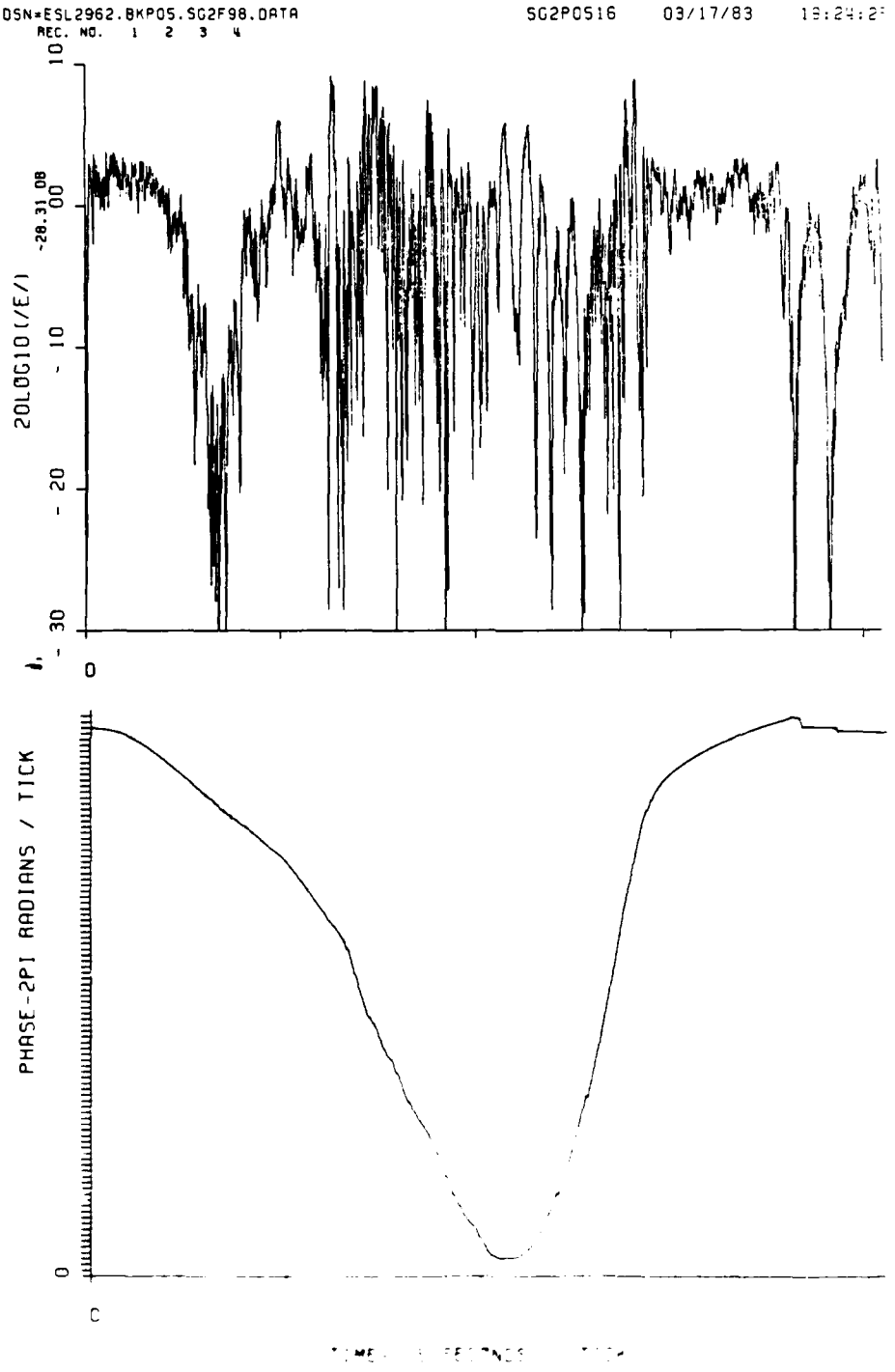

Figure 4-23. Back-propagated amplitude and phase, St. George Island, Beacon 2, 5 km.

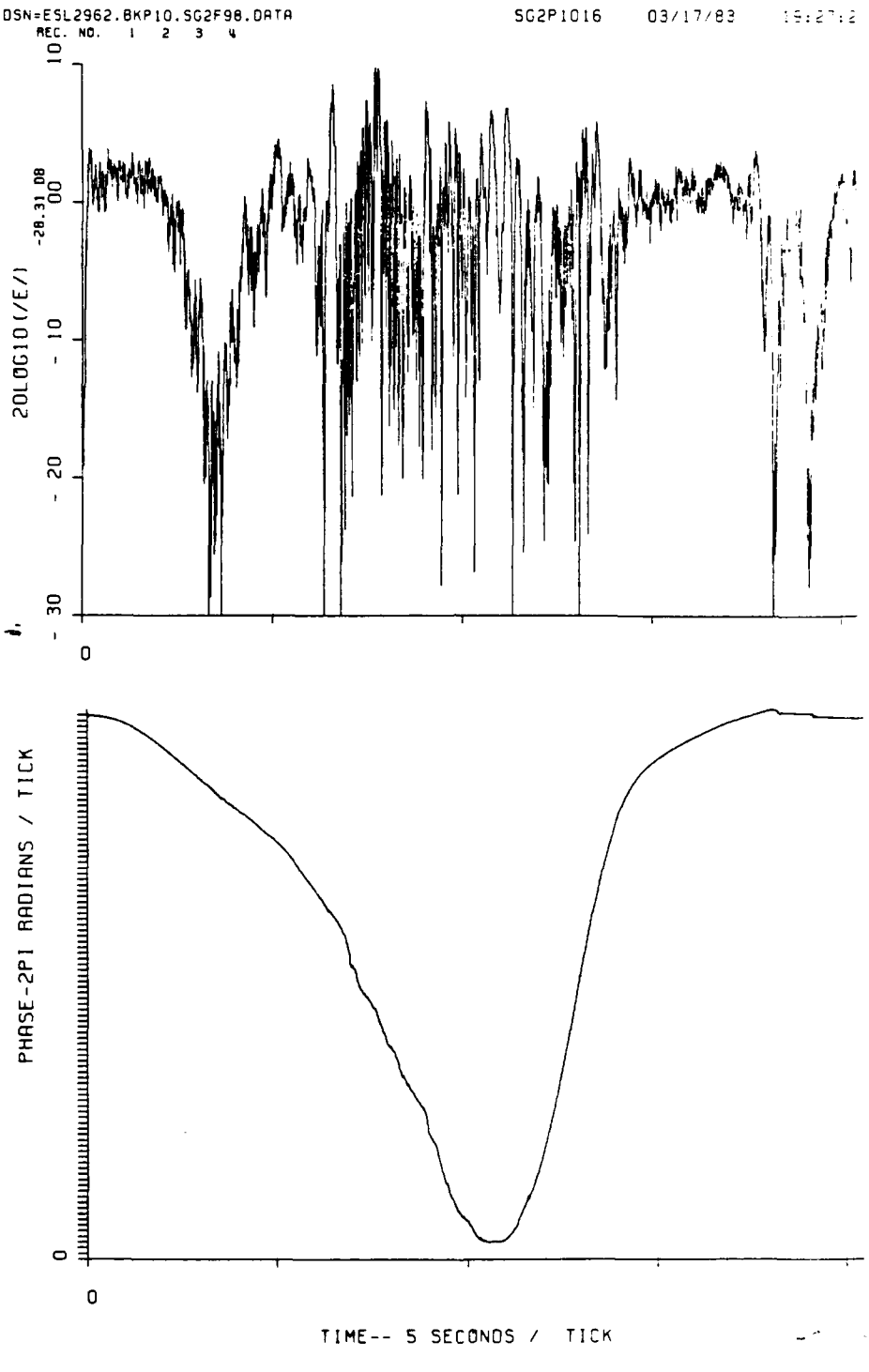

Figure 4-24. Back-propagated amplitude and phase, St. George Island, Beacon 2, 10 km.

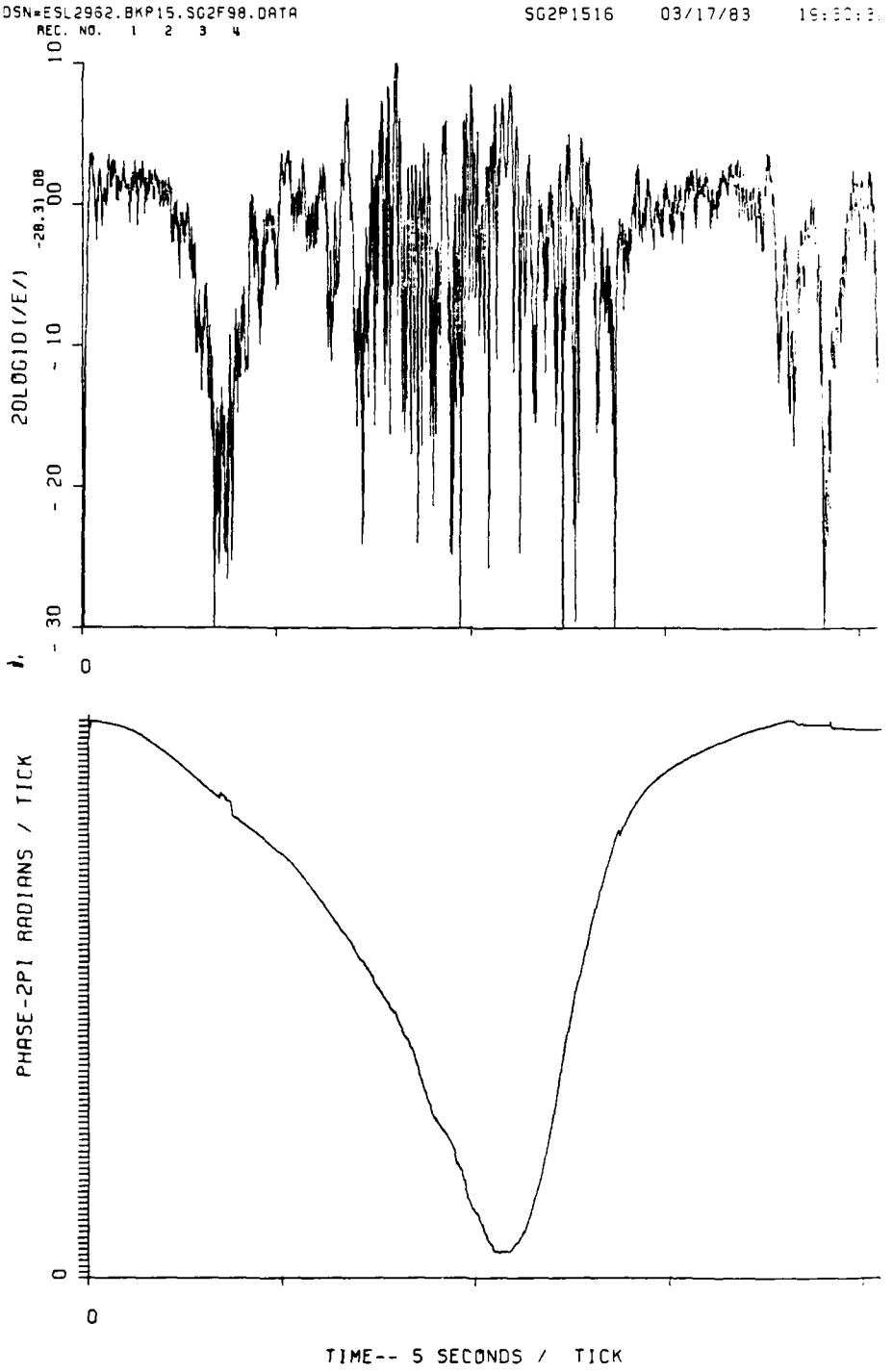

Figure 4-25. Back-propagated amplitude and phase, St. George Island, Beacon 2, 15 km.

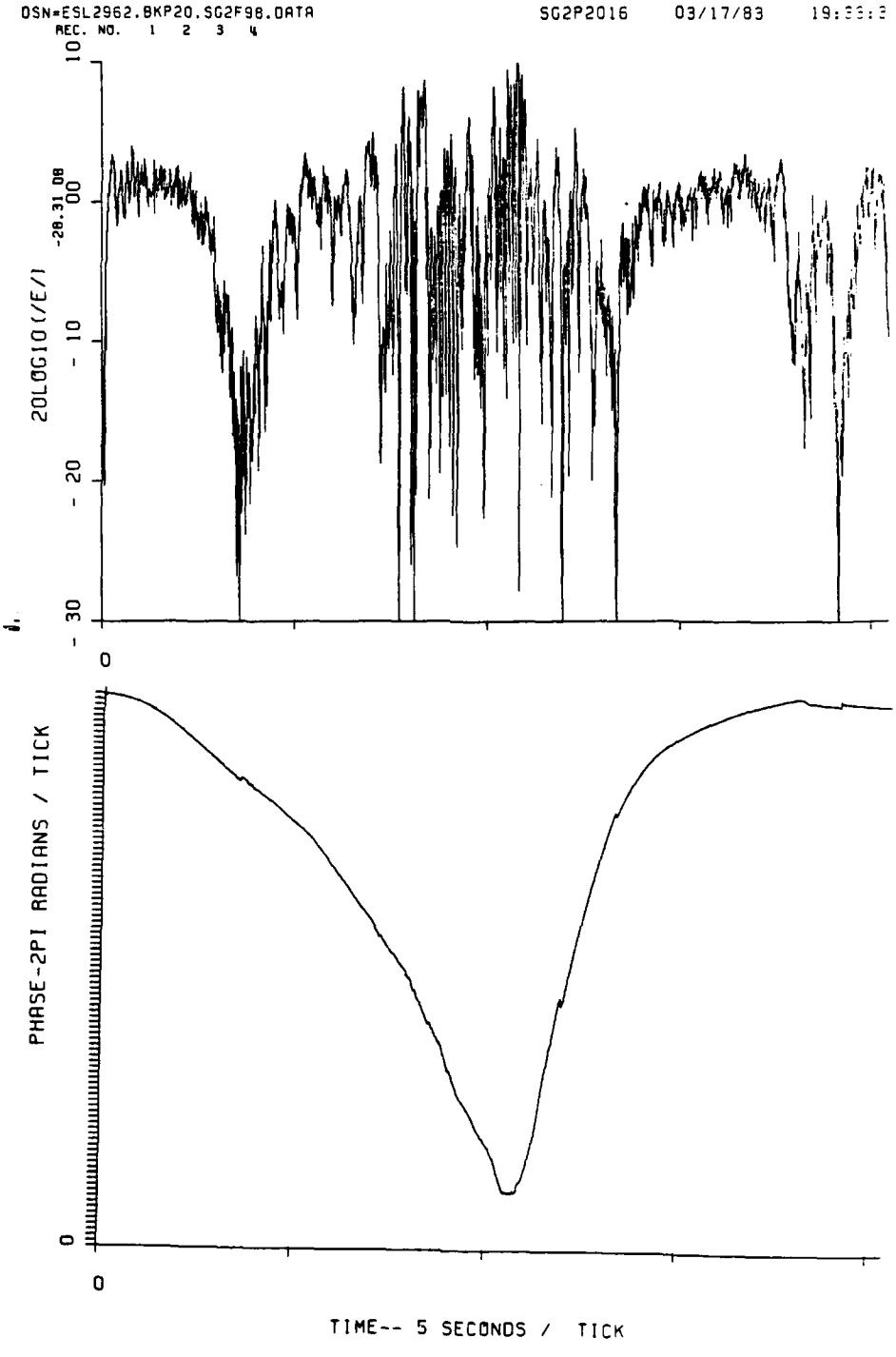

Figure 4-26. Back-propagated amplitude and phase, St. George Island, Beacon 2, 20 km.

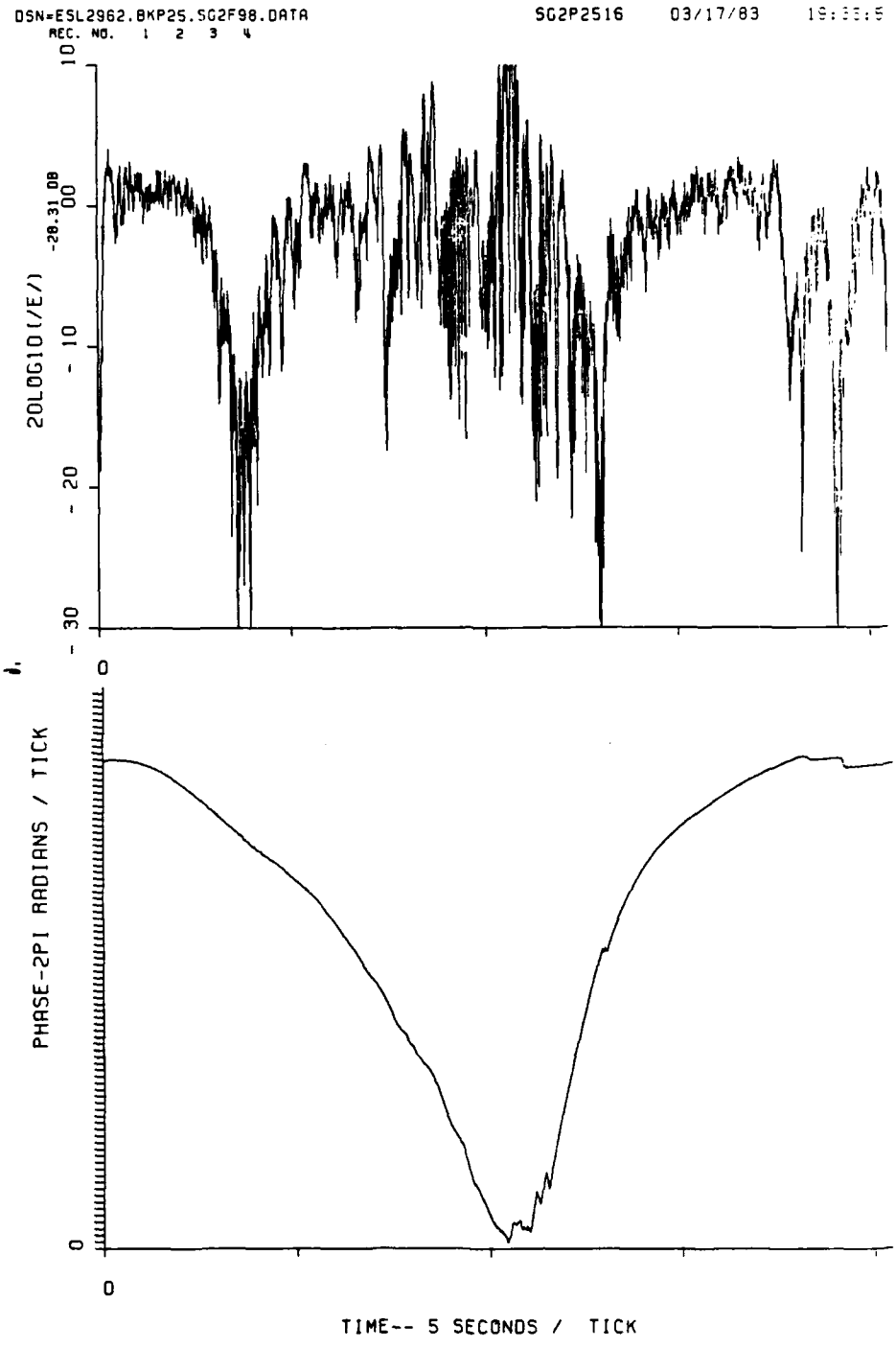

Figure 4-27. Back-propagated amplitude and phase, St. George Island, Beacon 2, 25 km.

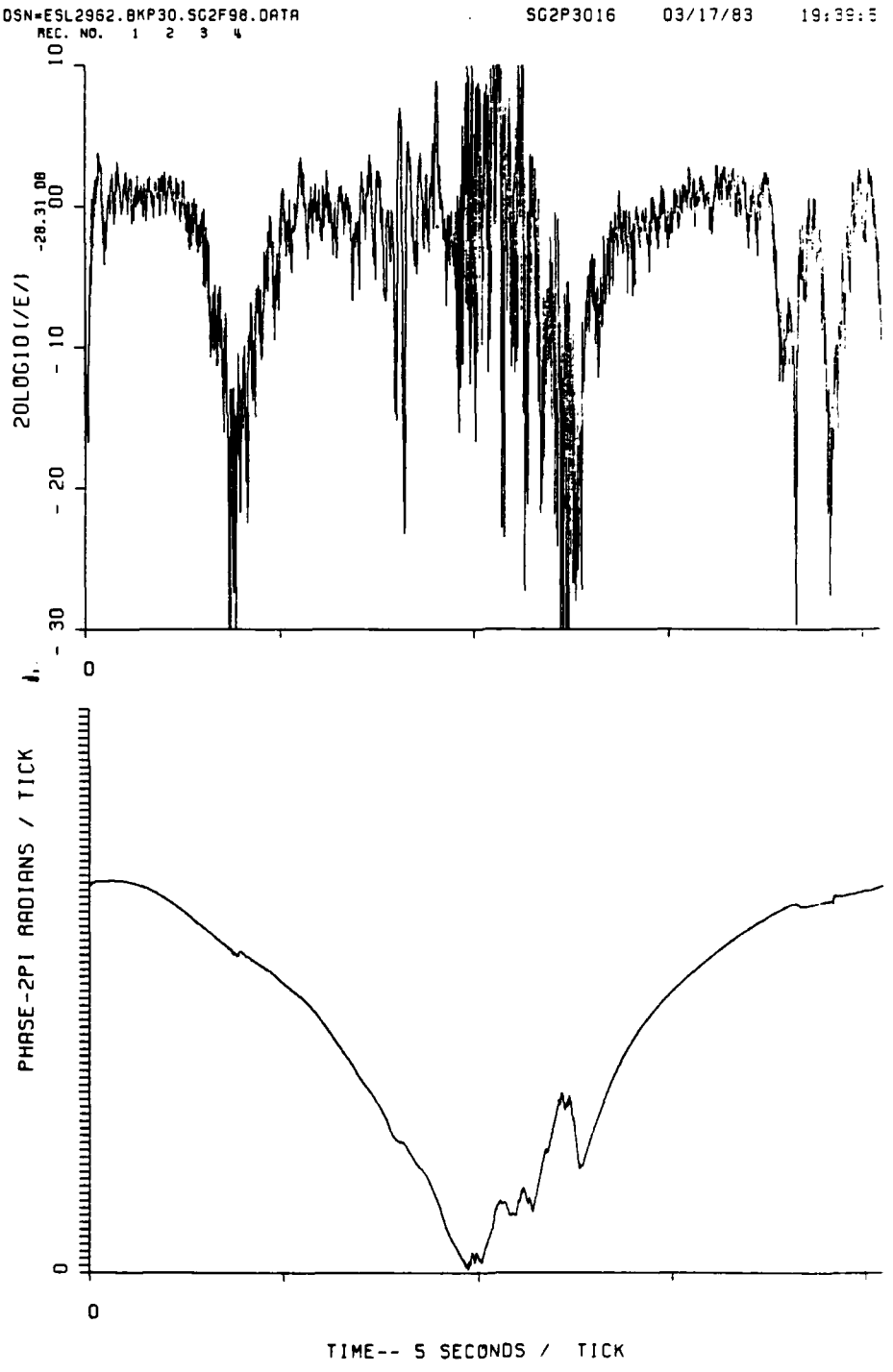

Figure 4-28. Back-propagated amplitude and phase, St. George Island, Beacon 2, 30 km.

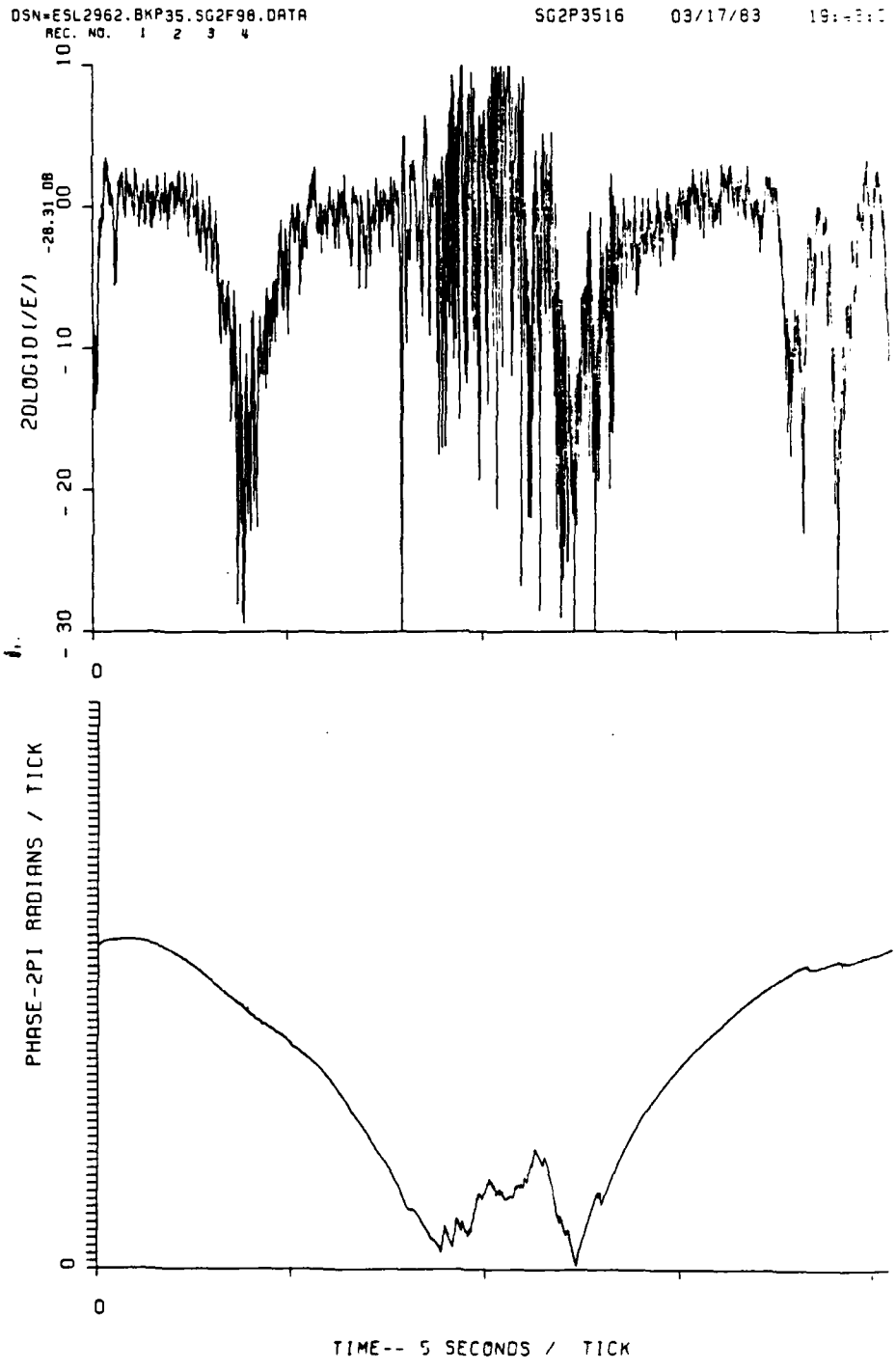

Figure 4-29. Back-propagated amplitude and phase, St. George Island, Beacon 2, 35 km.

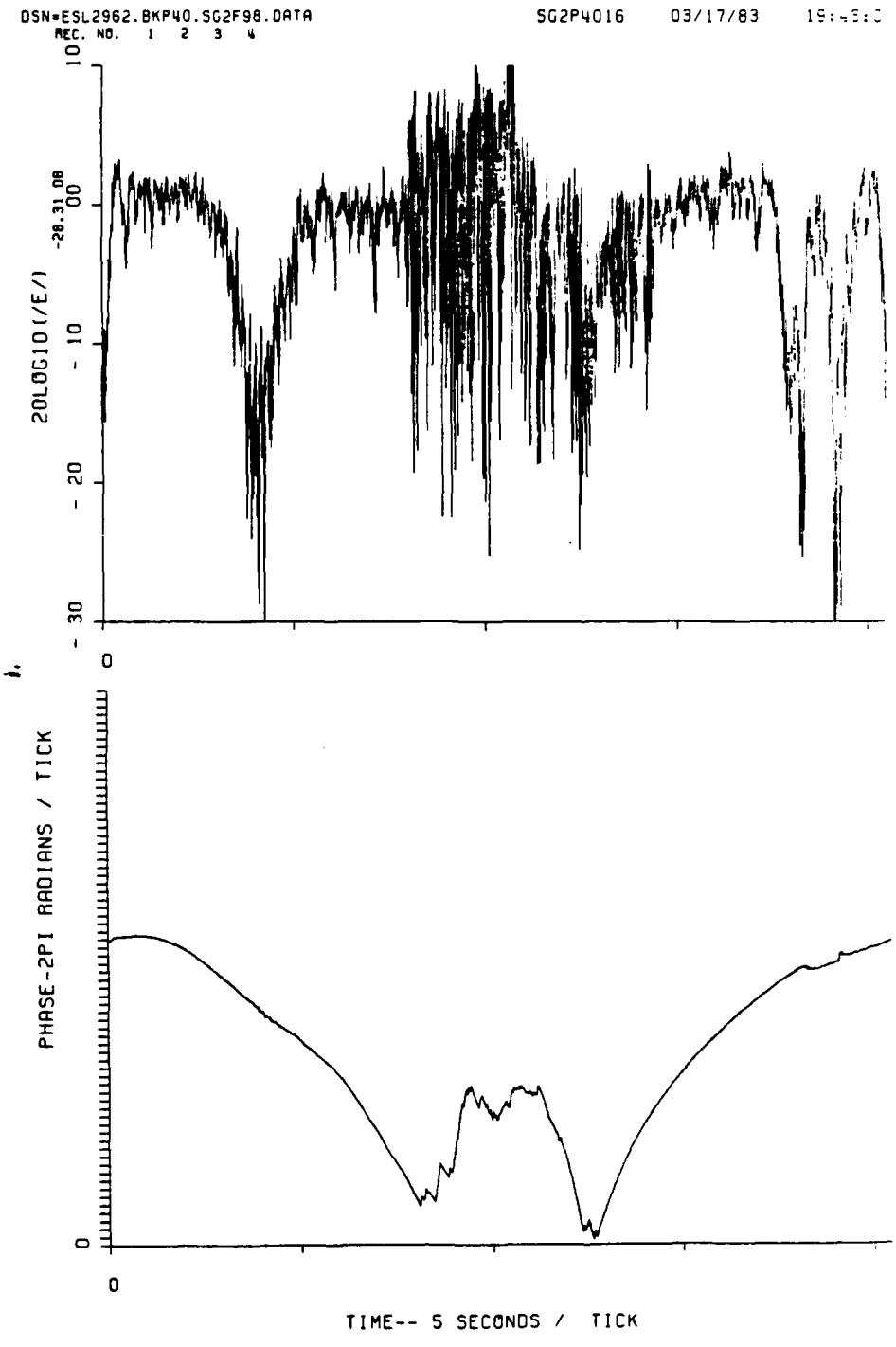

Figure 4-30. Back-propagated amplitude and phase, St. George Island, Beacon 2, 40 km.

It can be noted in comparing Figure 4-22 with Figure 4-30 that the scintillation effects appear to be the least intense between 35 and 40 km in distance. This appears to be consistent with the optical data presented in Section 4.2.2, which indicates the striations are further away from the beacon rocket during the second occultation. As noted, no single back-propagation distance is uniquely correct over the occultation interval. Accordingly, the behavior exhibited versus propagation distance is consistent with expectations.

4.9 MUTUAL COHERENCE FUNCTION AND IN-SITU PHASE SPECTRAL DENSITY

As discussed in Section 2.10, the Mutual Coherence Function (MCF) is not corrupted by diffraction effects and, thus, the in-situ path integrated phase PSD can be derived from the received signal in spite of the diffraction effects that corrupt the back-propagation data. The reader is referred to Section 2.10.1 for a discussion of the MCF and its various forms.

4.9.1 MCF Data for Cape San Blas, Beacon 1, Direct Calculation

The computation of the MCF begins with the extraction of the monochromatic fading data from the complex beacon signal delay measurements as described in Section 2.10.2. This is accomplished through the transformation of the delay measurements to obtain the channel transfer function from which the 98-MHz component is selected. The MCF can then be computed directly from its definition

$$R_u(t) = \langle U(t')\, U^*(t' + t) \rangle \quad .$$

As discussed previously, from a theoretical perspective, in the absence of any systematic or nonstationary component, we expect a purely real function to result. As an example, Figures 4-31 and 4-32 show the result of this calculation where only the real part of the MCF is plotted. The data interval shown spans 5.1 seconds covering Segments 1, 2, and 3 as presented in Table 4-1. It was noted that over the principal lobe that the imaginary component is significant at times, forcing a negative value to the MCF.

4.9.2 MCF Data for Symmetric Doppler Spectrum

An examination of the two sided angular spectrum of the 98-MHz component of the received signal indicates at times a significant asymmetry, showing a preferential angle of arrival of the scattered energy. The magnitude square of the angular spectrum is the power spectrum or the Doppler spectrum, and the transform of the Doppler spectrum is the MCF. Thus, to force a purely real form for the MCF, the Doppler spectrum was artificially constrained to be symmetric about 0 frequency. This was accomplished through averaging of the positive and negative frequencies. For most of the segments, this technique did not substantially alter the data since only approximately 5 to 10 percent of the power in the spectrum was asymmetrically distributed. The two-sided angular spectrum, the MCF, and the structure function are shown in Figures 4-33 through 4-44 for each of the data segments. The structure function is shown as the logarithm of minus the natural log of the MCF.

4.9.3 Comparison With Theory

These data can be compared with the theoretical form, and the in-situ spectral slope and the Rayleigh phase variance can be estimated. Table 4-4 summarizes the results of these calculations. The theoretical form for the log of the phase structure function was presented in Figure 2-125. In overlaying this figure on the

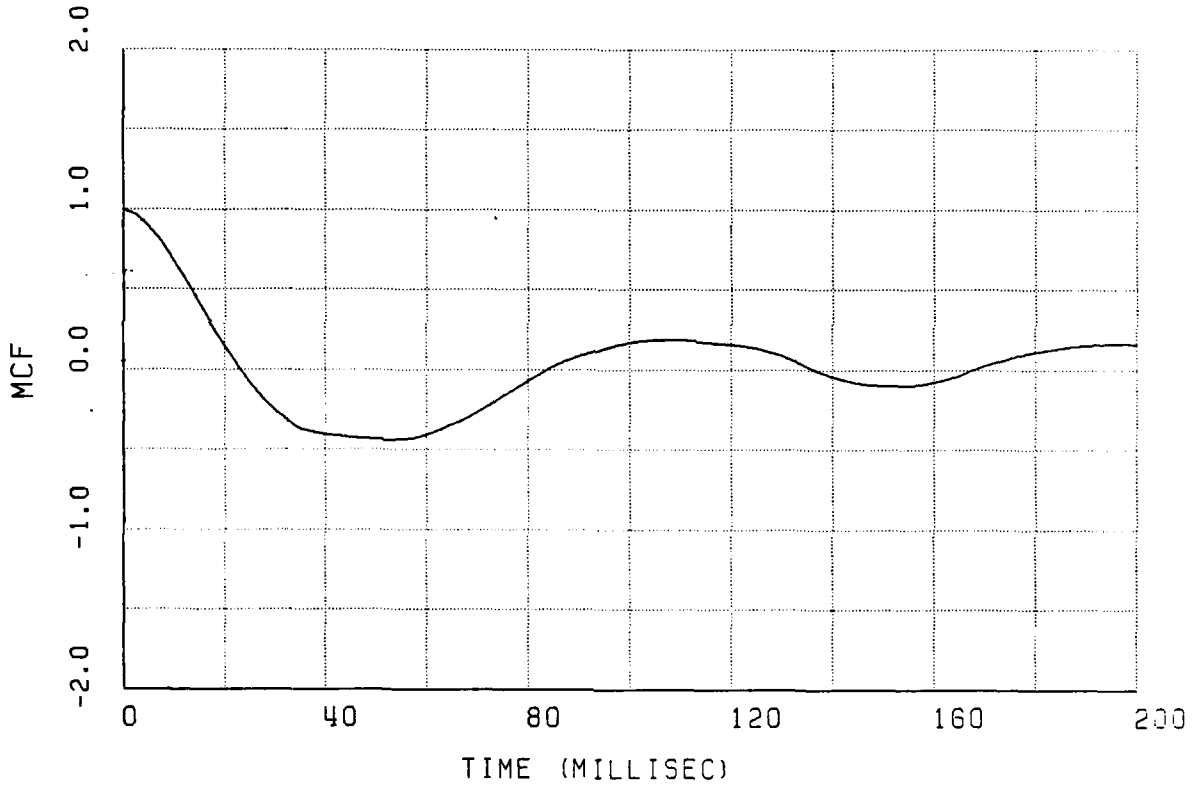

Figure 4-31. Direct calculation of MCF for 2358:11.4 to 2358:16.52.

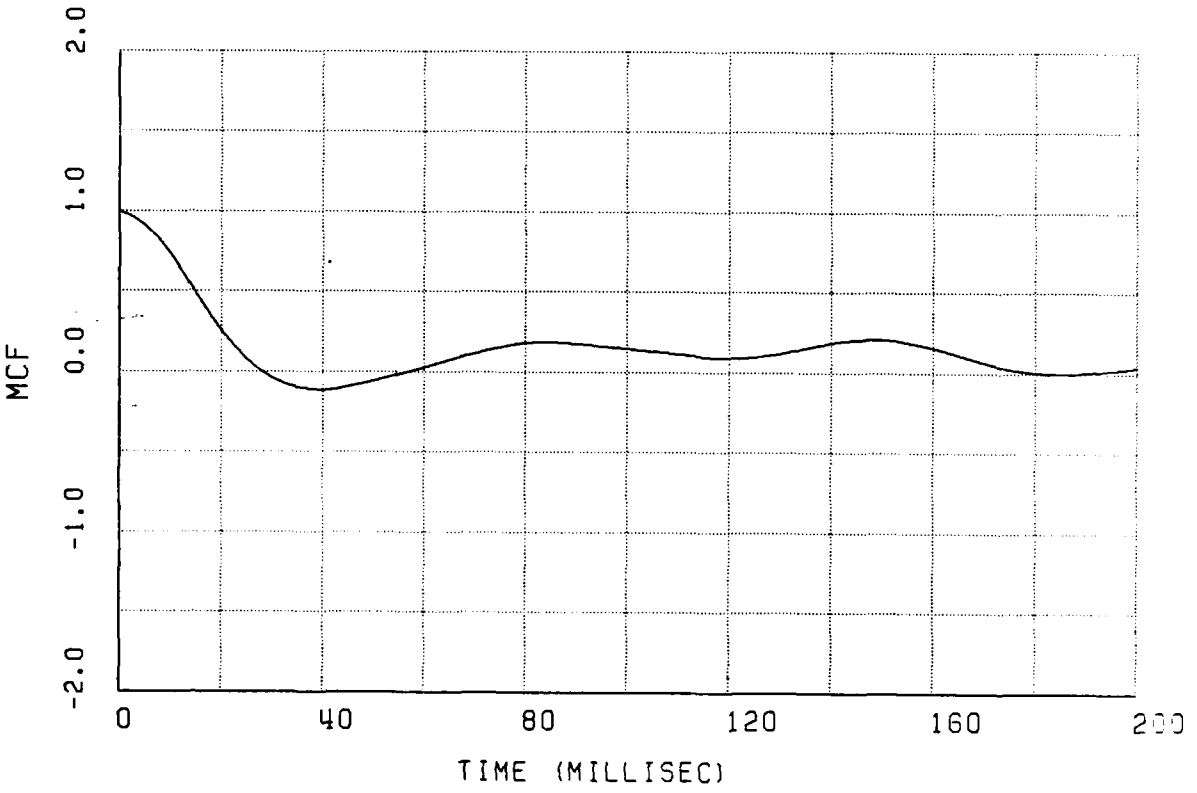

Figure 4-32. Direct calculation of MCF for 2358:16.6 to 2358:21.7Z.

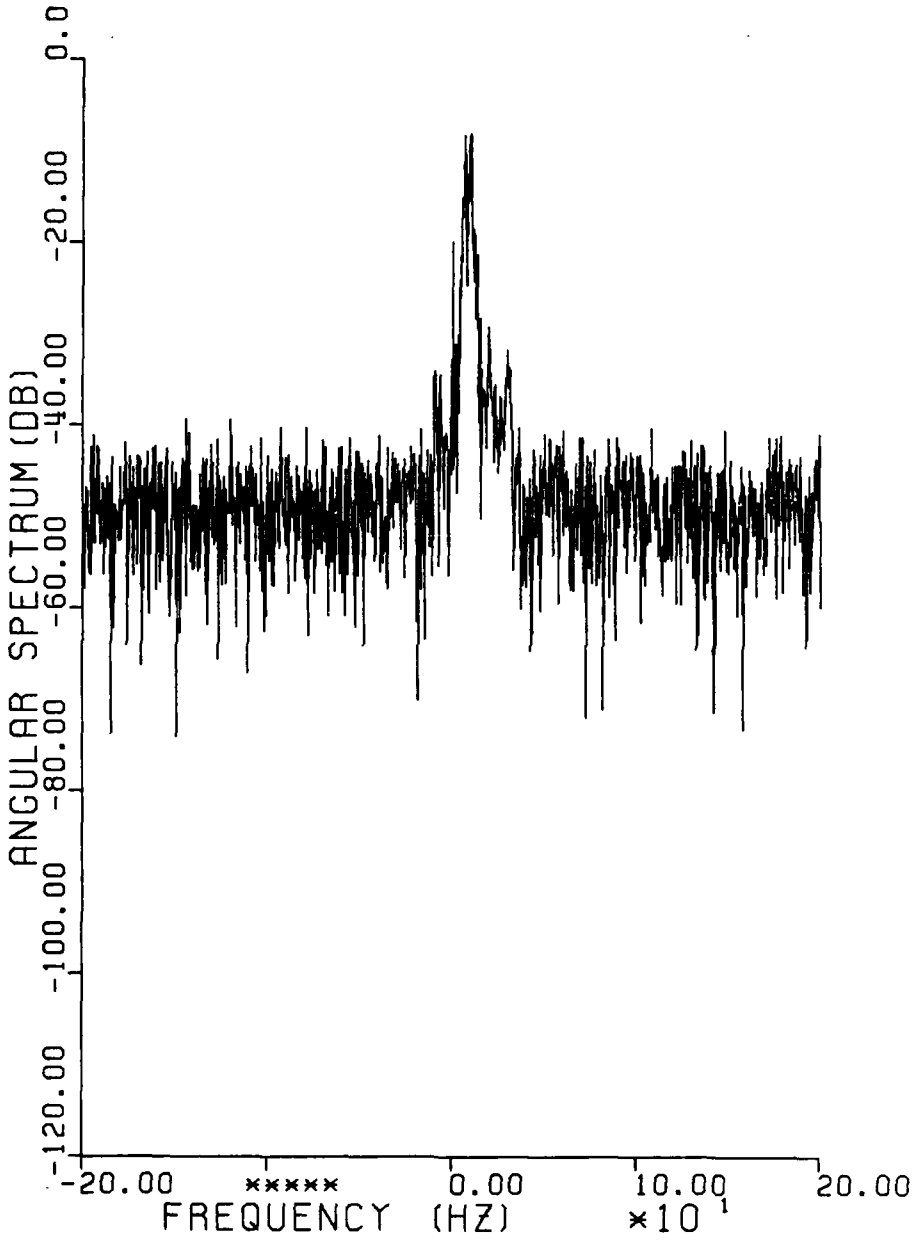

Figure 4-33. Two-sided angular spectrum for Segment 1.

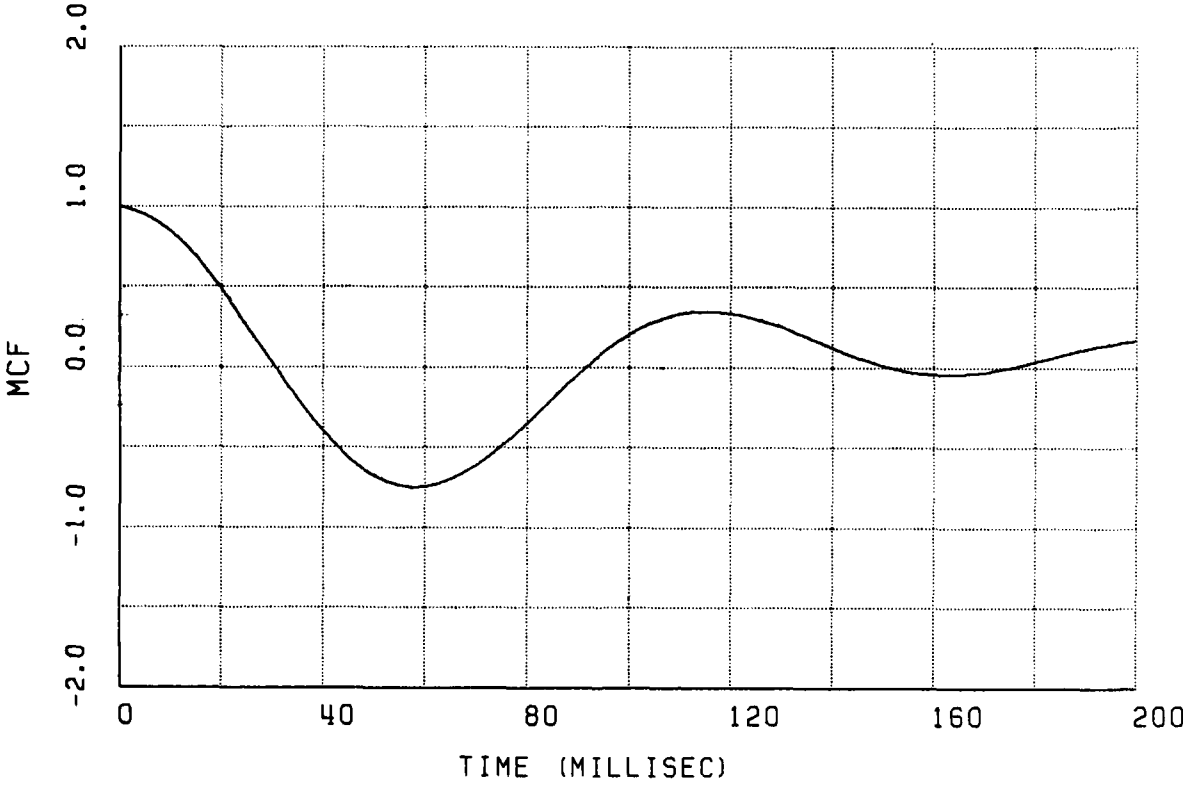

Figure 4-34. Mutual coherence function for Segment 1.

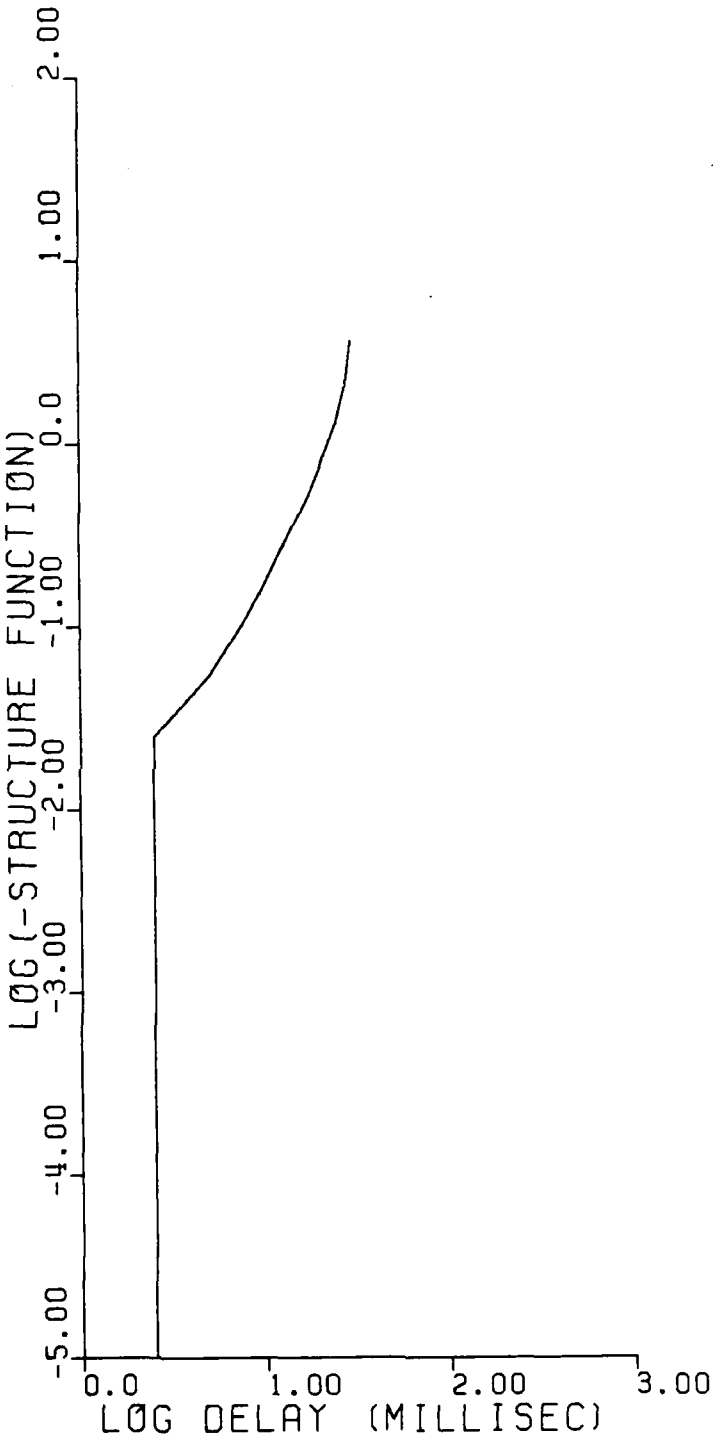

Figure 4-35. Logarithm of phase structure function for Segment 1.

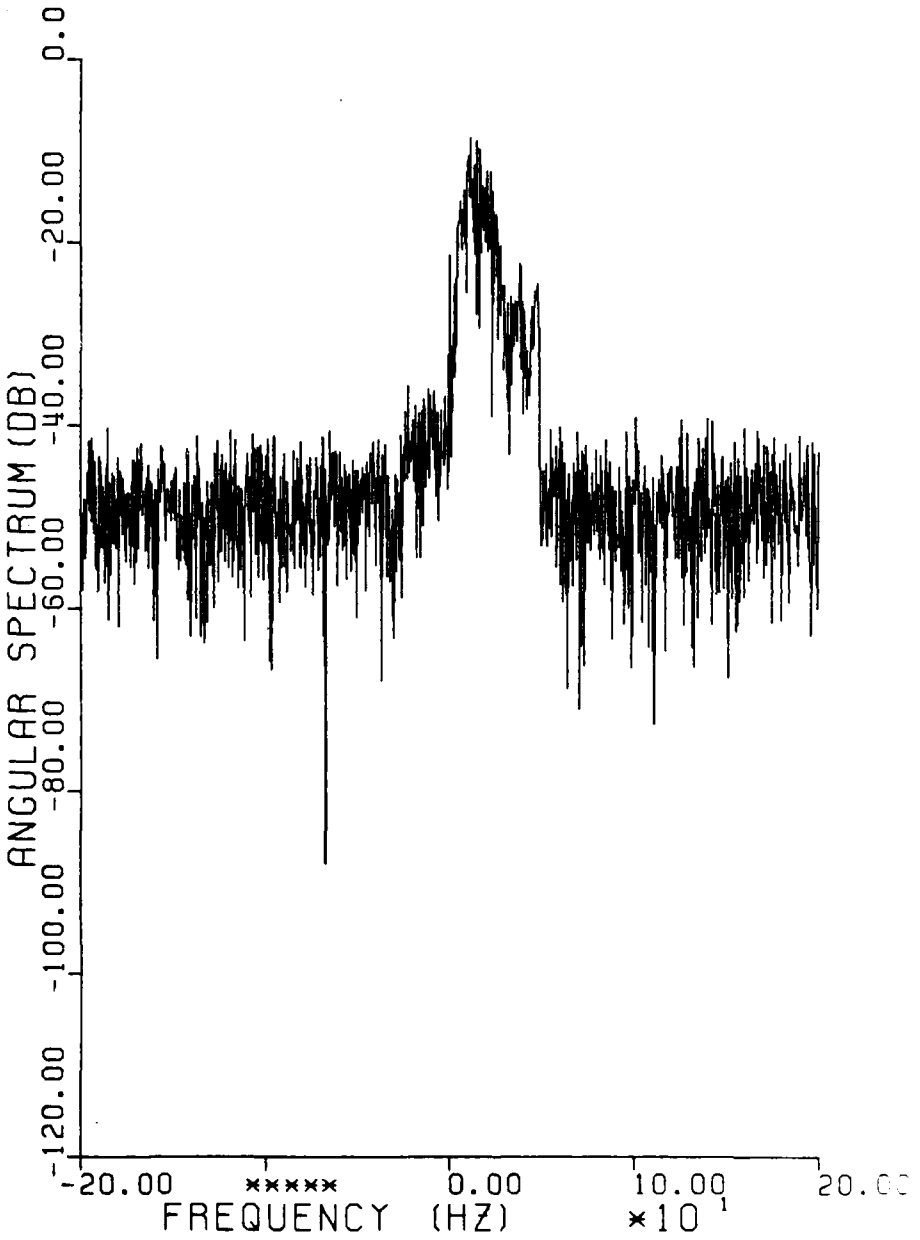

Figure 4-36. Two-sided angular spectrum for Segment 2.

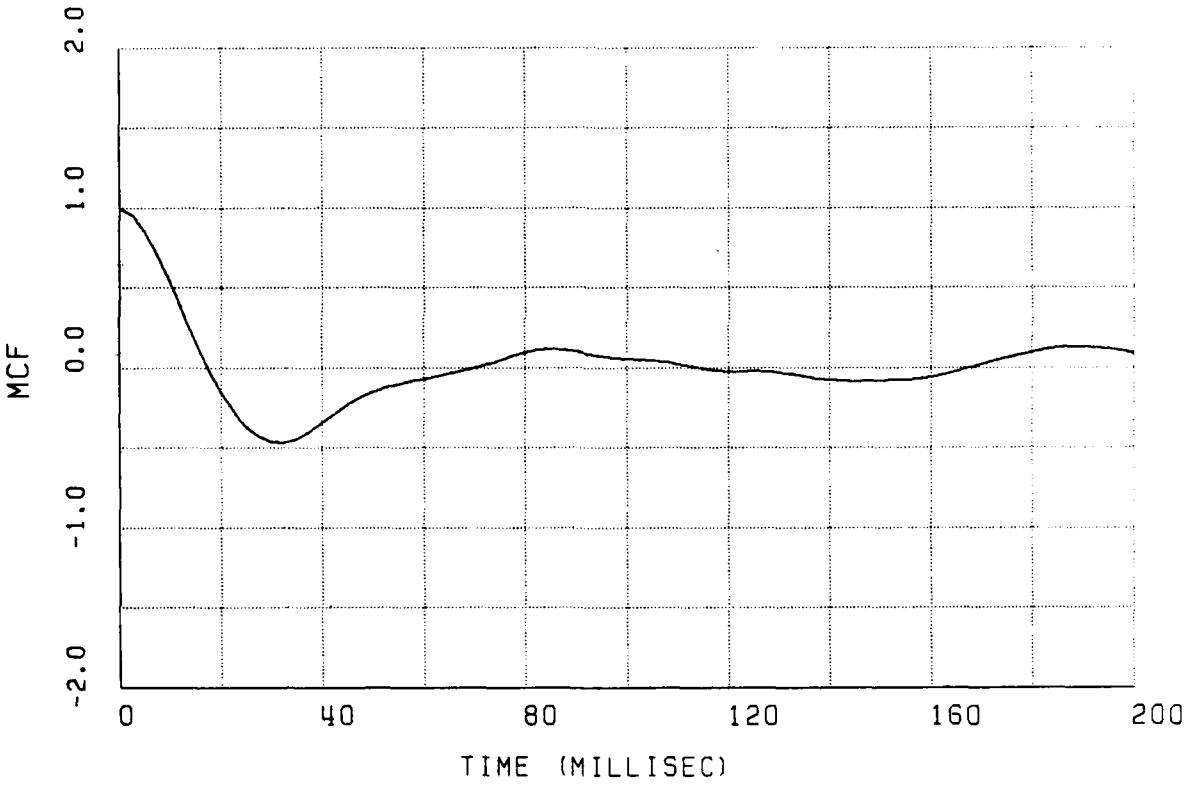

Figure 4-37. Mutual coherence function for Segment 2.

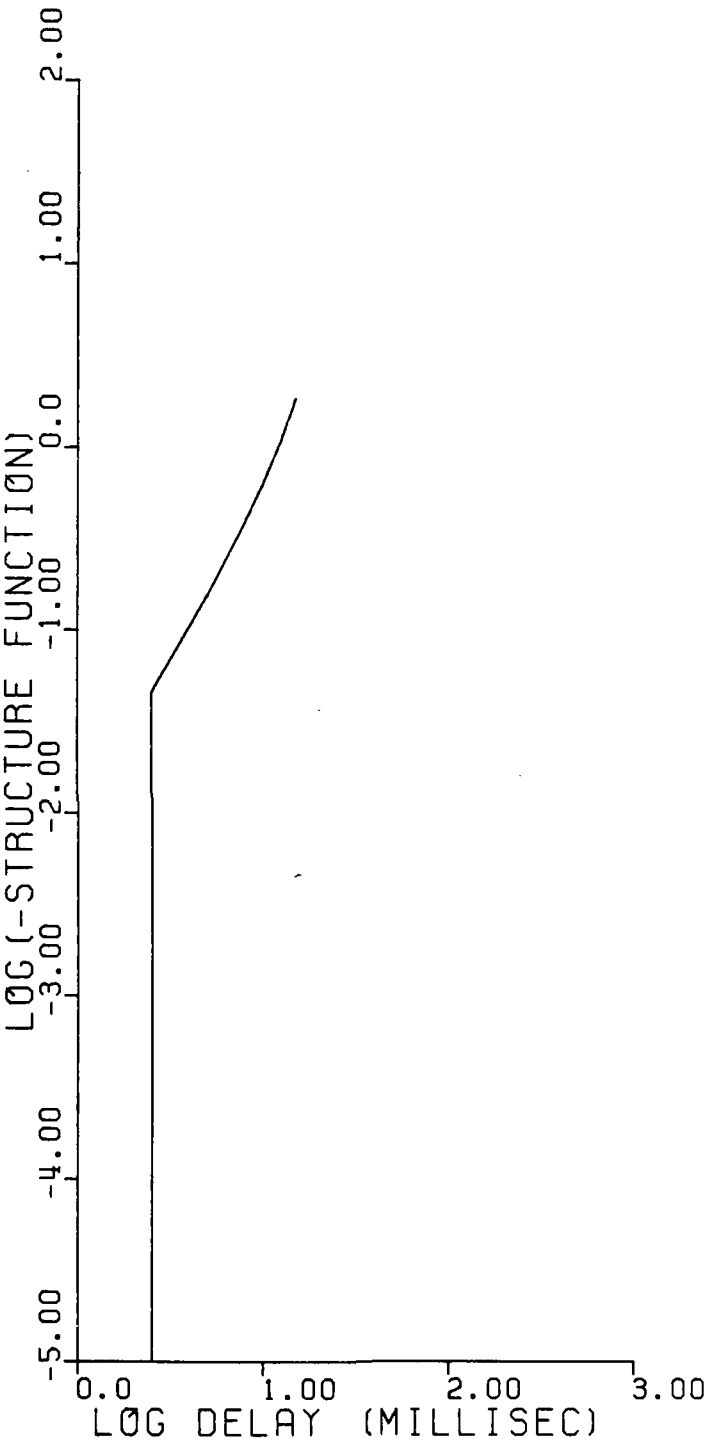

Figure 4-38. Logarithm of phase structure function for Segment 2.

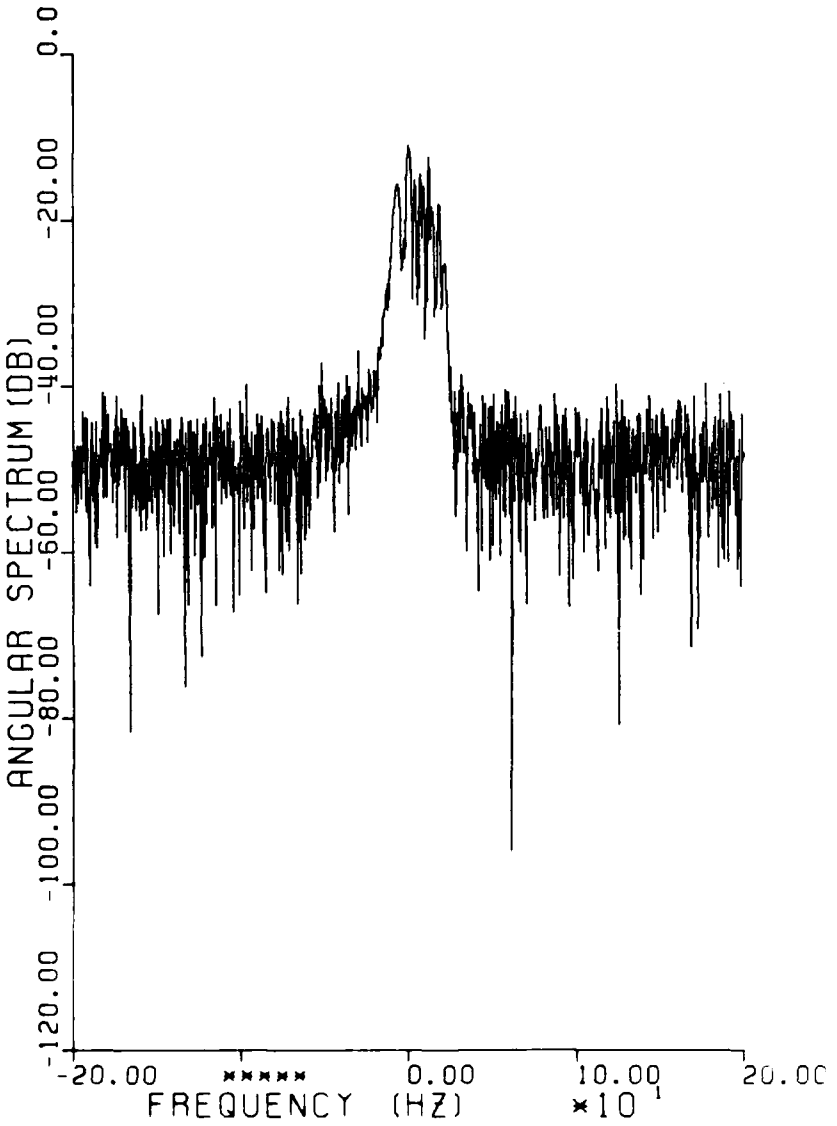

Figure 4-39. Two-sided angular spectrum for Segment 3.

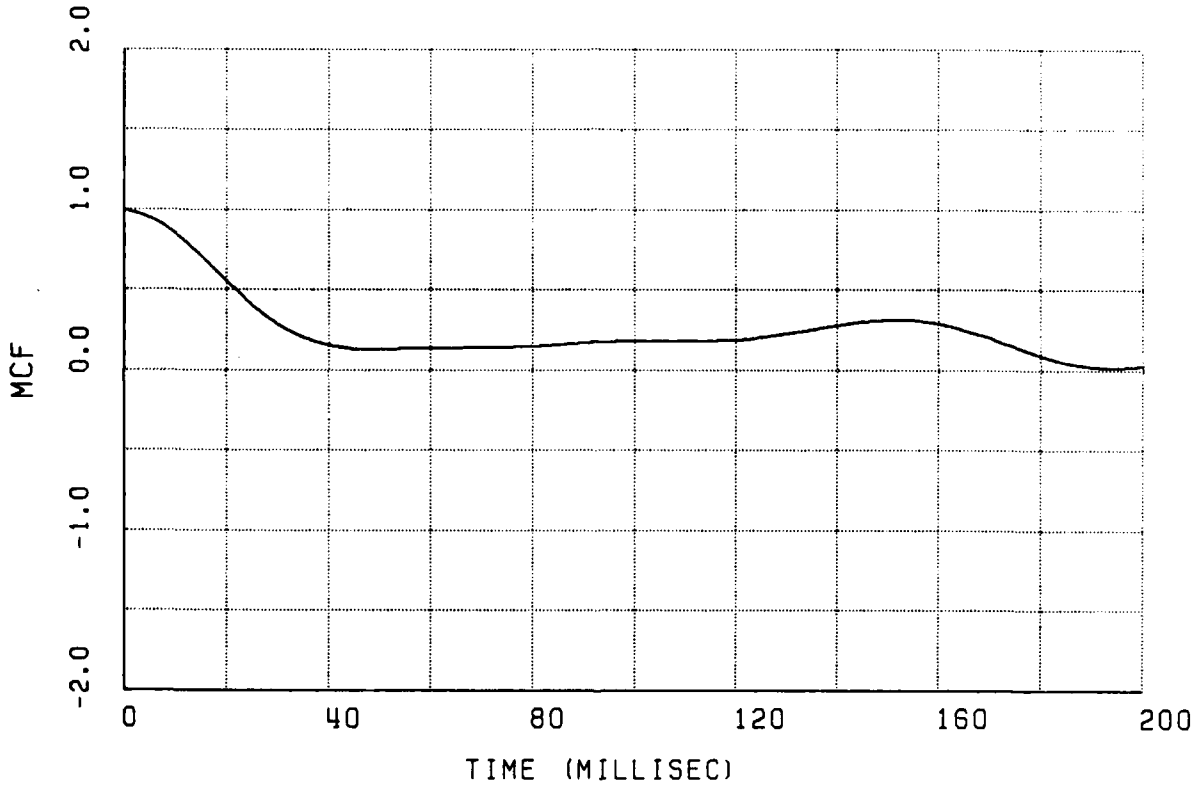

Figure 4-40. Mutual coherence function for Segment 3.

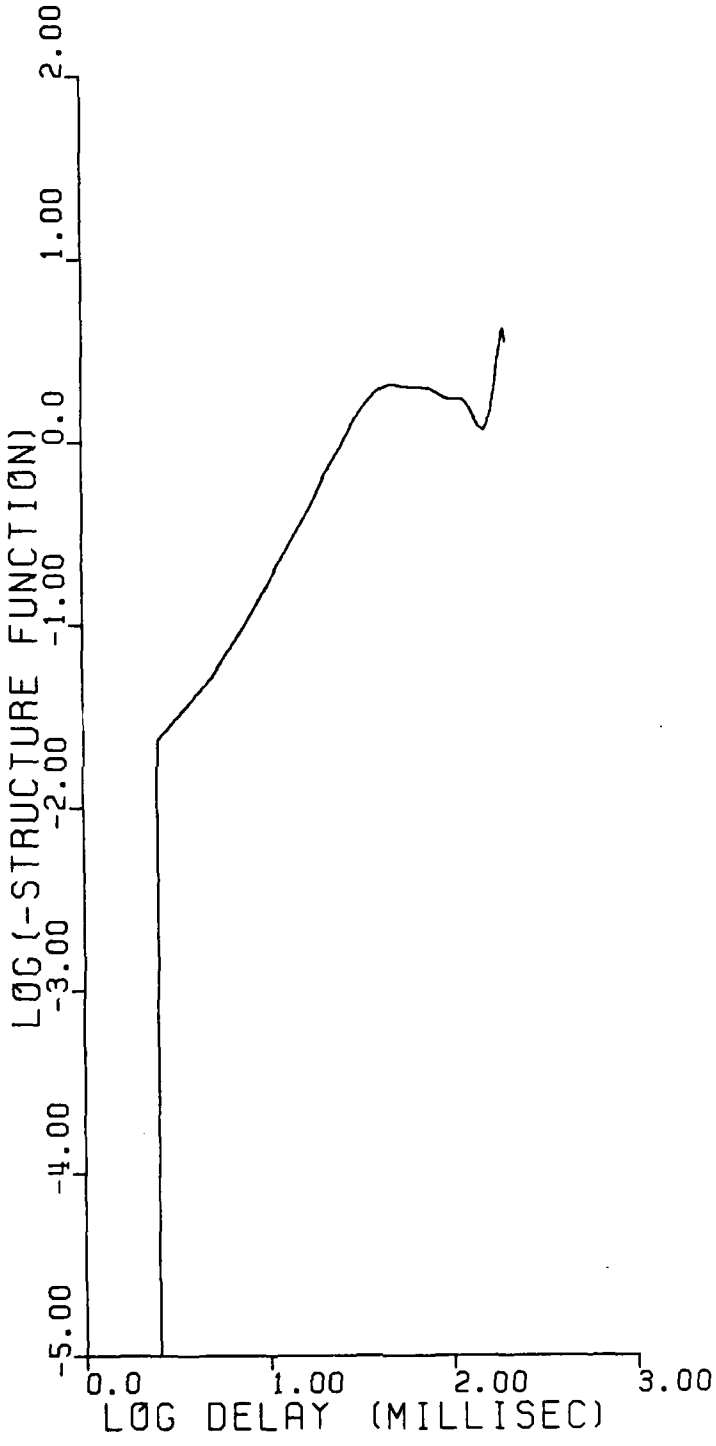

Figure 4-41. Logarithm of phase structure function for Segment 3.

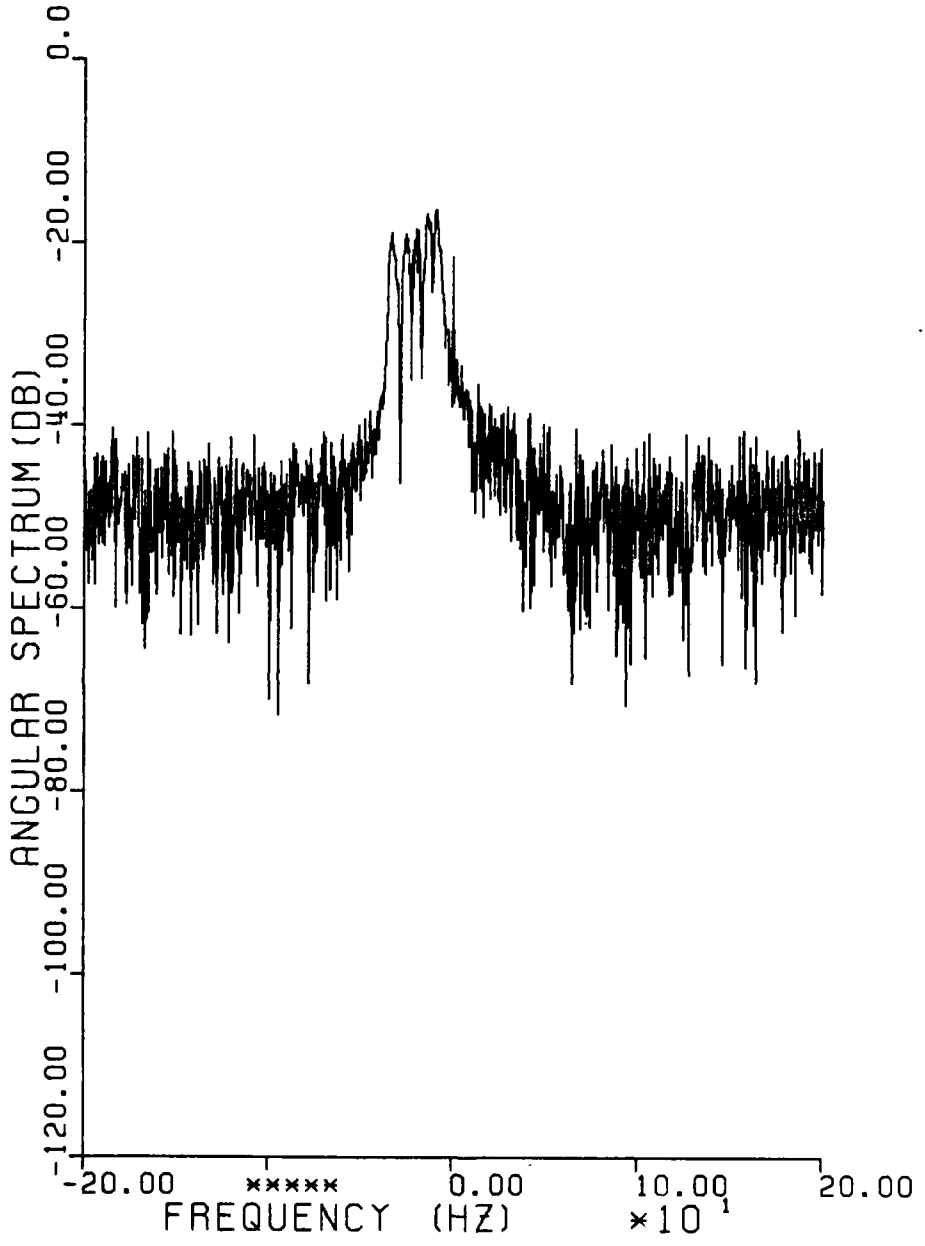

Figure 4-42. Two-sided angular spectrum for Segment 4.

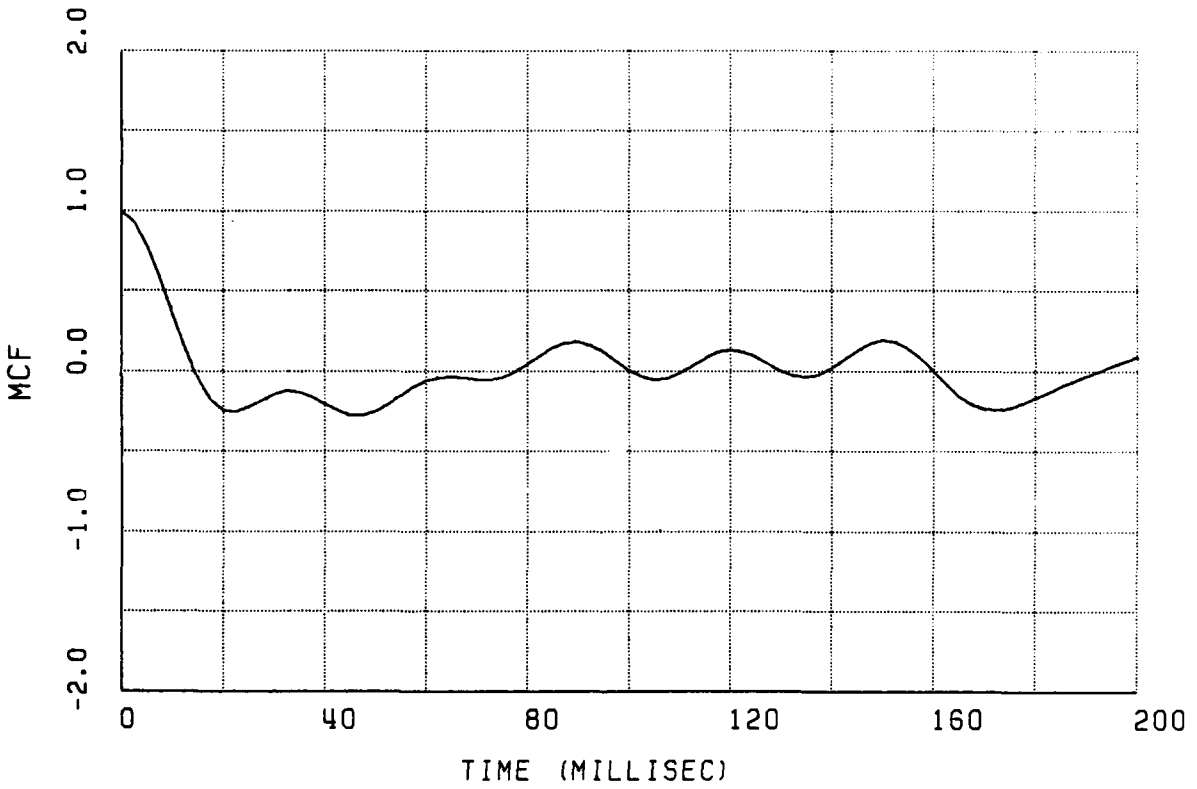

Figure 4-43. Mutual coherence function for Segment 4.

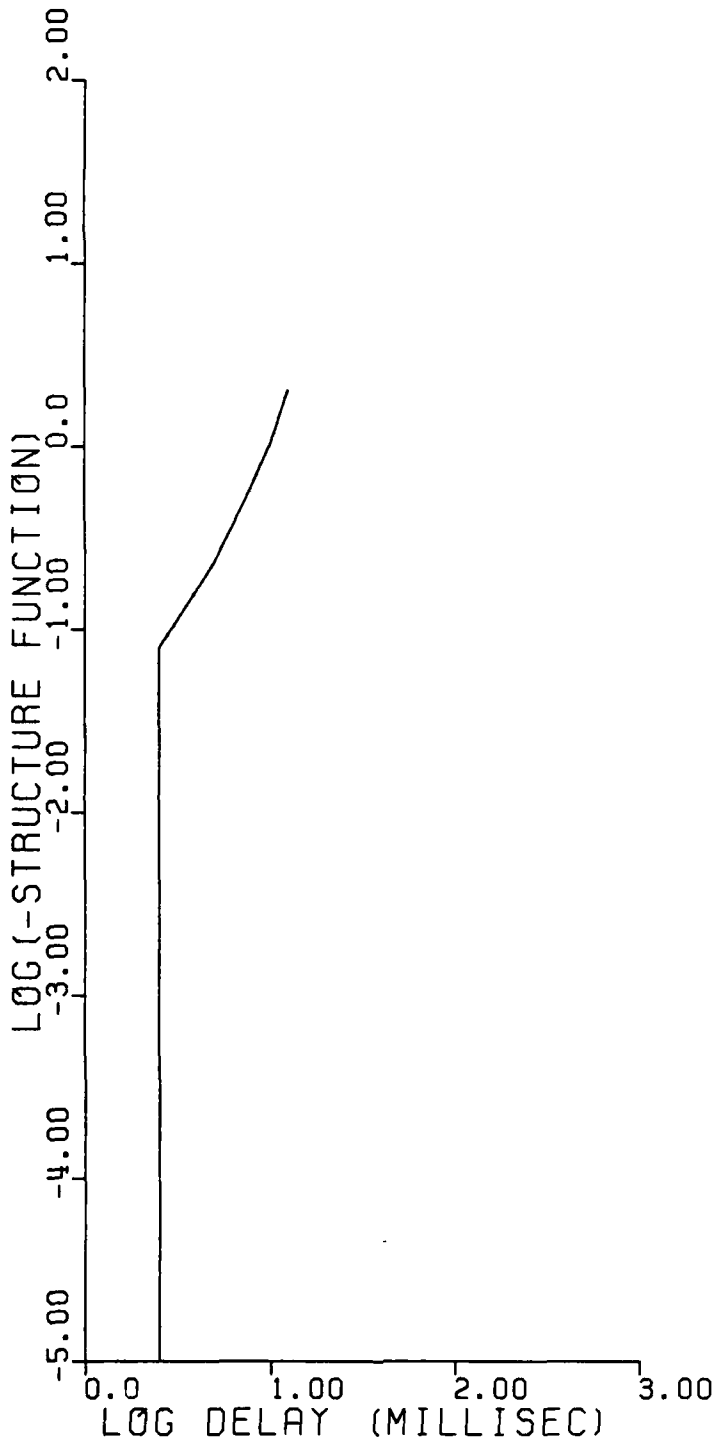

Figure 4-44. Logarithm of phase structure function for Segment 4.

Table 4-4. Phase structure function analysis summary.

SEGMENT	BEST SHAPE	$D_C = \tau^{2v-1}$		$D_A = (\tau/\tau_o)^2$	D_B		MCF = e^{-1}
		INDEX V	SLOPE 2v-1	τ_o	τ_o	$\sigma_{\phi R}$	τ_o
1	C OR A	1.3	1.6	20 ms	–	–	22 ms
2	A OR C	1.5	2.0	13 ms	–	–	12 ms
3	A, B OR C	1.4	1.8	22 ms	20 ms	1.4	22 ms
4	A	1.5	2.0	10 ms	–	–	10 ms

A – $D_A(\tau) = (\tau/\tau_o)^2$

B – $D_B(\tau) = \text{LOG}\,[1 - (\tau/\tau_o)\,K_1\,(\tau/\tau_o)]$

C – $D_C(\tau) = \tau^{2v-1}$

structure function plots, the best fits as summarized in Table 4-4 were derived. Because of the systematic phase trends that distort the MCF, the best fit to theory is expected only over the exponential portion of the MCF at short delay.

One can obtain an estimate for the Rayleigh phase variance when the functional form is a good fit to the Bessel function form for the phase autocorrelation function out to large values of delay. The height of the structure function in this case determines the phase variance as discussed in Section 2.10.4.

In general, these data for St. George Island, Beacon 2 provide the best agreement with theory. The angular spectra are the most nearly symmetric of the data obtained and yield well behaved MCF and structure function data. The structure function data are well fit by theory.

4.10 SUMMARY FOR ST. GEORGE ISLAND, BEACON 2

The data for St. George Island, Beacon 2, have proven to be perhaps the most consistent with theory of that obtained. Even though the angular scattering was less intense, the angular spectrum data were more nearly symmetric giving rise to excellent agreement with theory for the generalized power spectrum data as well as the MCF and structure function data. The intuitive relations derived from geometric optics arguments are in good agreement with these data. The conclusions presented in Section 2.12 for the first beacon occultation data are also applicable here.

SECTION 5
BEACON EXPERIMENT DATA FOR CAPE SAN BLAS, BEACON 2

5.1 GENERAL

No angular scattering effects were observed on the signal received at Cape San Blas during the second beacon rocket occultation. This is consistent with the occultation geometry described herein. As a consequence, the data from this receiver site have not been analyzed in detail.

5.2 OCCULTATION GEOMETRY

The second beacon rocket occulted the barium plasma as viewed from Cape San Blas during the interval 2358:17 to 2358:27. The correlation with the FPS-85 radar data and with the opticl data is discussed in the following subsections.

5.2.1 Correlation to Radar Data

The occultation geometry relative to a radar mapping of the cloud ionization is provided in Figure 5-1. The radar ionization contours are those obtained approximately 2 minutes before occultation and translated to the peak electron density track point at 2358:20Z. These are the same contours as presented in Figure 4-1.

The line-of-sight path is shown at several times of interest. The intersection of the path with the 155-km altitude plane is indicated by the transition from the solid to dotted line. The two paths show the time at which the TOA first shifts in excess of that due to the background ionosphere, and when it returns to that due to the background ionosphere. The rocket altitude at these times is also indicated. For instance, at the time of entry, the rocket

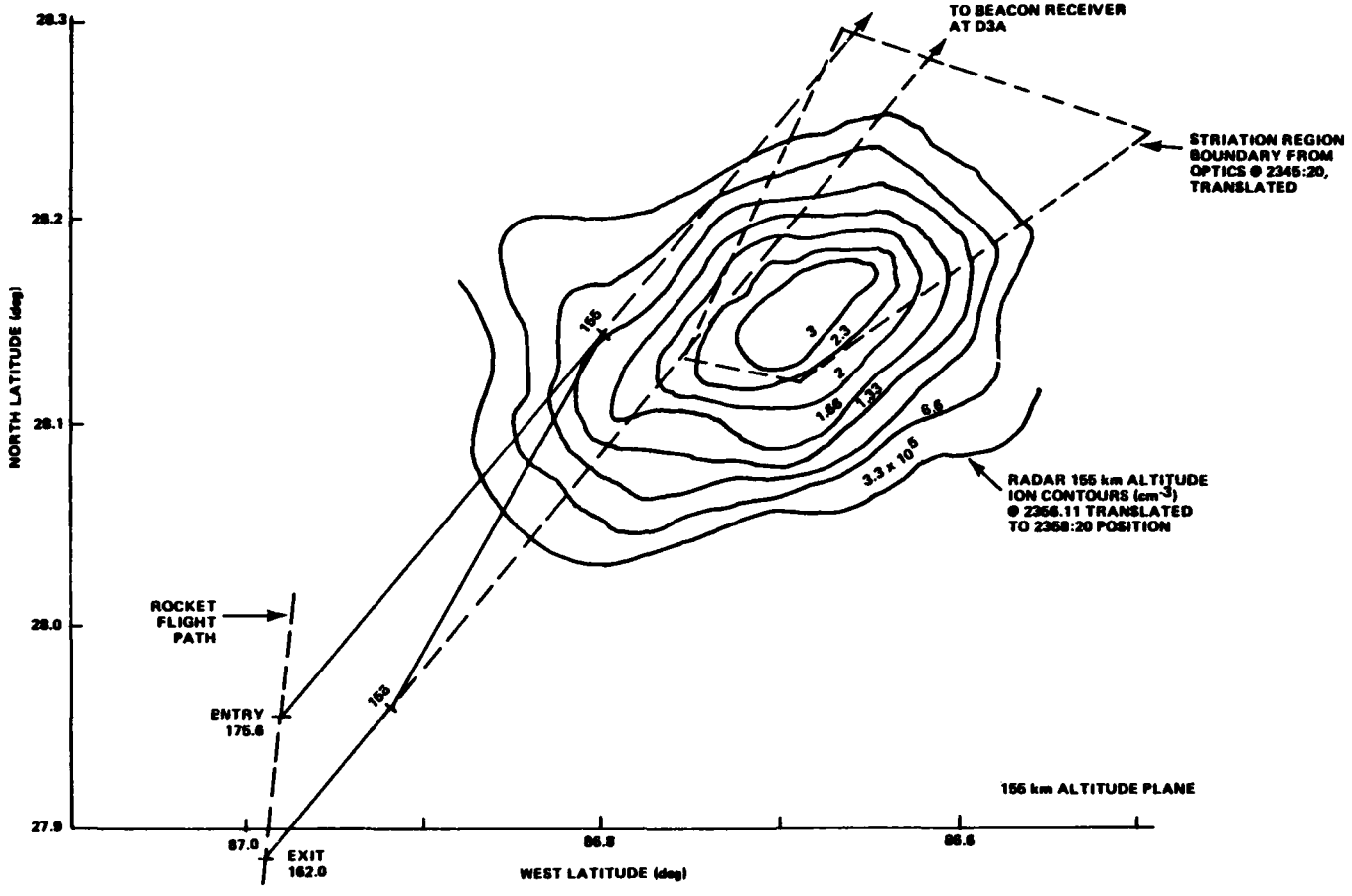

Figure 5-1. Occultation geometry, Beacon 2 to D3A.

altitude was approximately 175.6 km, and when the path exited the cloud its altitude was 162 km.

The direct path to St. George Island slices the 155-km altitude plane substantially to the west of the maximum electron density point as determined by the radar. The central field line through the maximum electron density region is cut approximately 125 km in altitude. Significant barium plasma presumably does not extend down to the altitudes at which the striations are cut.

5.2.2 Correlation to Optical Data

A determination of the striation region boundary using optical data was not attempted for the second beacon flight. At the time of the second occultation the sun was setting at the barium cloud altitude resulting in lack of photographic definition. As discussed, the striation region boundary as determined for the earlier occultation at 2345:20 is shown on Figure 5-1 translated to the corresponding position relative to the peak ion cloud density at 2358:20Z.

The propagation path slices the 155-km altitude plane well to the southwest of the striation boundary region. Based on these data, angular scattering effects would not be anticipated and none were observed.

5.3 MEASURED CHANNEL IMPULSE RESPONSE

This section presents the measured channel impulse response data for Cape San Blas, Beacon 2. The data presented are only a good approximation to the channel impulse response convolved with the signal autocorrelation function. As little angular scattering was observed, the data should more properly be viewed as the received cross-correlation. The in-phase and quadrature code cross-correlations performed at the beacon receivers provide the

appropriate measurement of the in-phase and quadrature components of the channel impulse response convolved with the signal autocorrelation function.

5.3.1 Composite Data

The magnitude of the channel impulse response $|h(t,\tau)|$ measured at the Cape San Blas beacon receiver site is shown in Figure 5-2. The time span for this figure is 2358:05.4 to 2358:37.9Z. Notably absent during this occultation are refracted ray caustics. This is due to the ion cloud being cut well behind the striated region by the propagation path as shown in Figure 5-1. The gross plasma causes the TOA of the direct path energy to be delayed, resulting in the large delay near the center of the occultation. On this figure, one chip delay is approximately 0.1 microsecond. For plotting purposes, 32 impulse response measurements were averaged to produce each of the horizontal scans presented in the figure.

The signal drop out evident at the end of the occultation interval is due to the adjustment made by the beacon receiver operator during the measurement. A time delay tracking adjustment was made that caused the signal to be shifted largely out of the measurement window at 2358:25. A few seconds later (at 2358:30), the measurement window was shifted to again encompass the signal.

5.3.2 Energy Delay Profiles

Figure 5-3 shows a sample of the weakly fading signal. This figure is a 50 millisecond average taken at 2358:23.3Z.

5.4 TIME-OF-ARRIVAL DELAY

In this section, we provide a view of the relative delay of the multipath signal components and the integrated electron content associated with the direct path delay.

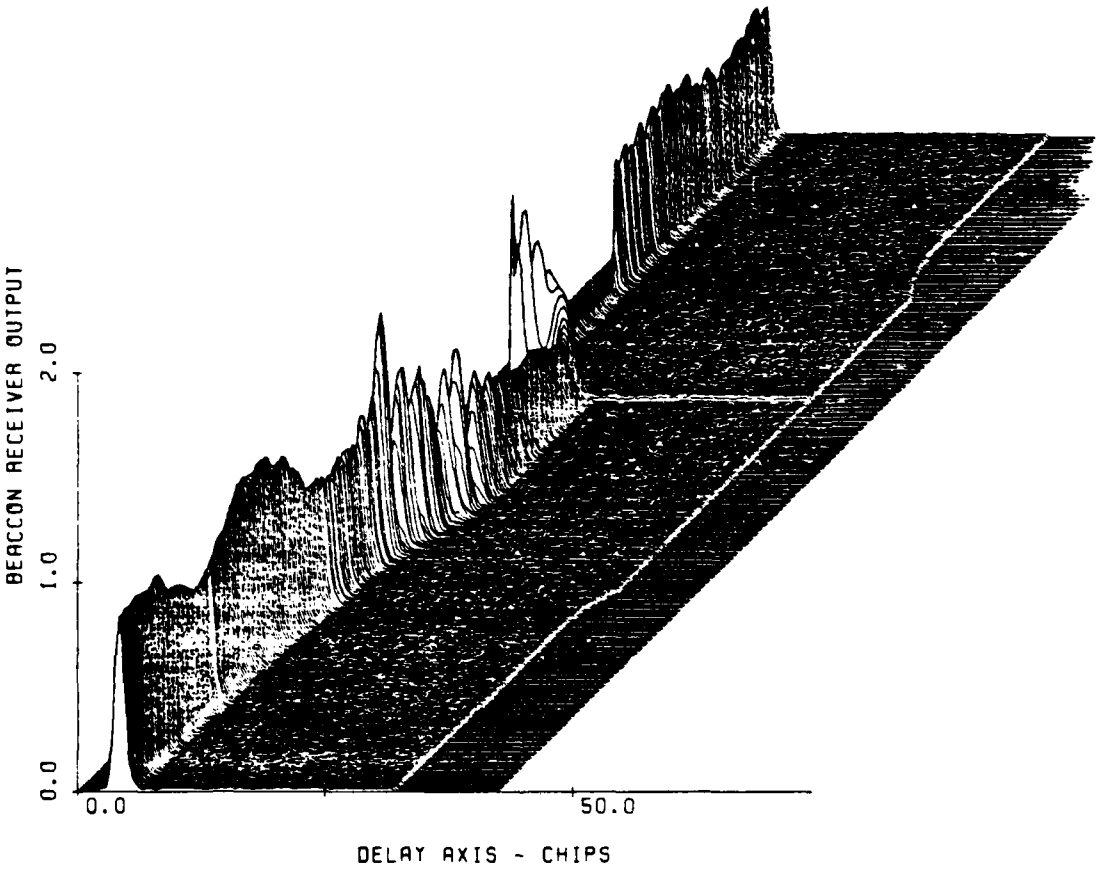

Figure 5-2. Pulse delay profile, Cape San Blas, second beacon time span from 2358:05.4 to 2358:37.9.

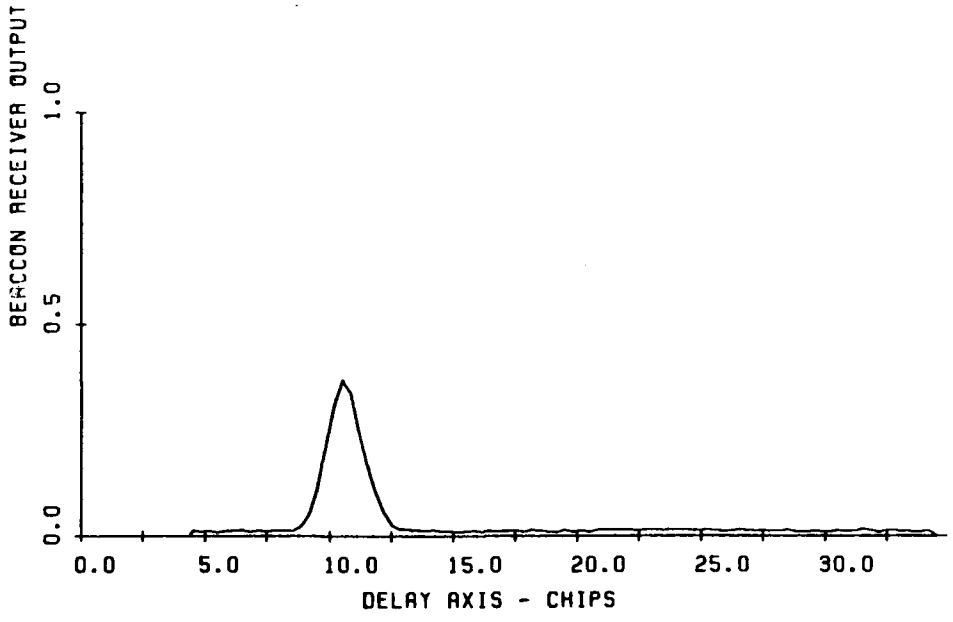

Figure 5-3. Detail of the impulse response for Cape San Blas during occultation. Second Beacon, time of 2358:23.3.

5.4.1 TOA Composite Data

Figure 5-4 is a plot of the TOA of each energy peak (ray) as a function of the flight time of the rocket behind the barium cloud. As discussed in Section 2.4.1, each point is a plot of the location of the centroid of each peak in signal energy at each sample point in time. The centroiding algorithm is described in Appendix A. Evident in this figure is a small amount of TOA jitter of the direct path signal. This figure also clearly shows the absence of caustic rays consistent with the geometry shown in Figure 5-1, which shows the path well outside the striated plasma region.

5.4.2 TOA Direct Path Data and Integrated Electron Content

The TOA of the direct path through the plasma can be extracted from Figure 5-4 and is plotted in Figure 5-5. This serves as an illustration of the performance of the TOA estimation algorithm. The algorithm used to distinguish the first peak in signal energy (direct path TOA) from noise is described in Appendix A. The TOA data were extracted by first fitting an appropriate curve through the data of Figure 5-4 and then using a tracking algorithm that determined the earliest peak signal arrival in a given window width about that curve. A window width of $\pm 2/3$ chip was used to construct Figure 5-5. The small amount of jitter evident in these data can be associated with the dispersive phase as described in Section 2.5.1.

The integrated electron content can be calculated based on the TOA shift in the received signal at each instant in time. Each microsecond of TOA delay at 98 MHz corresponds to 7.29×10^{12} cm^{-2} of electron content. Thus, for the Cape San Blas path through the barium ion cloud, the peak integrated electron content due to the barium plasma is approximately 4.9×10^{12} cm^{-2}. As discussed in Section 2, the background ionosphere contribution is small, approximately 10 percent of the ion cloud contribution.

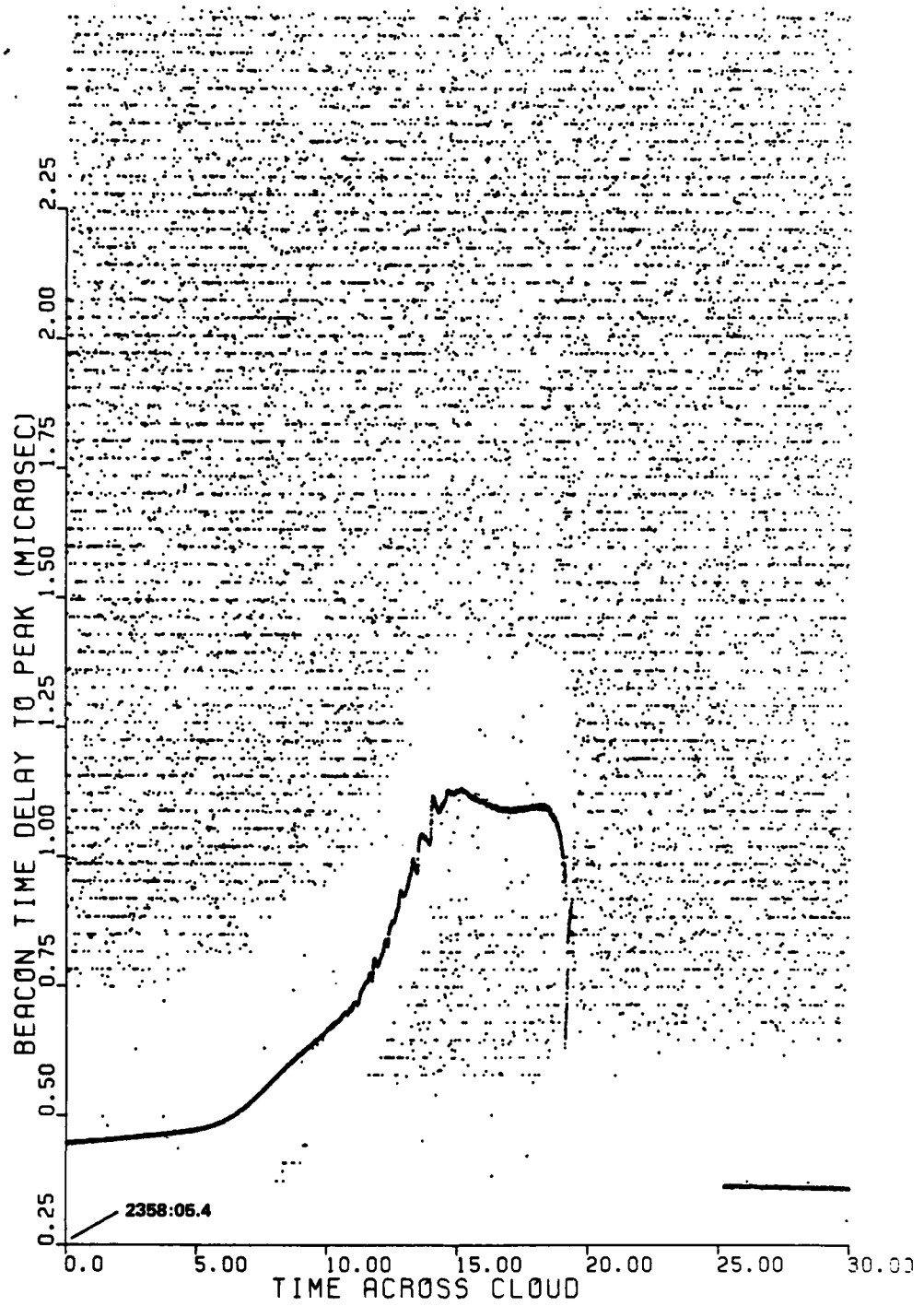

Figure 5-4. Energy peak TOA delay, all peaks.

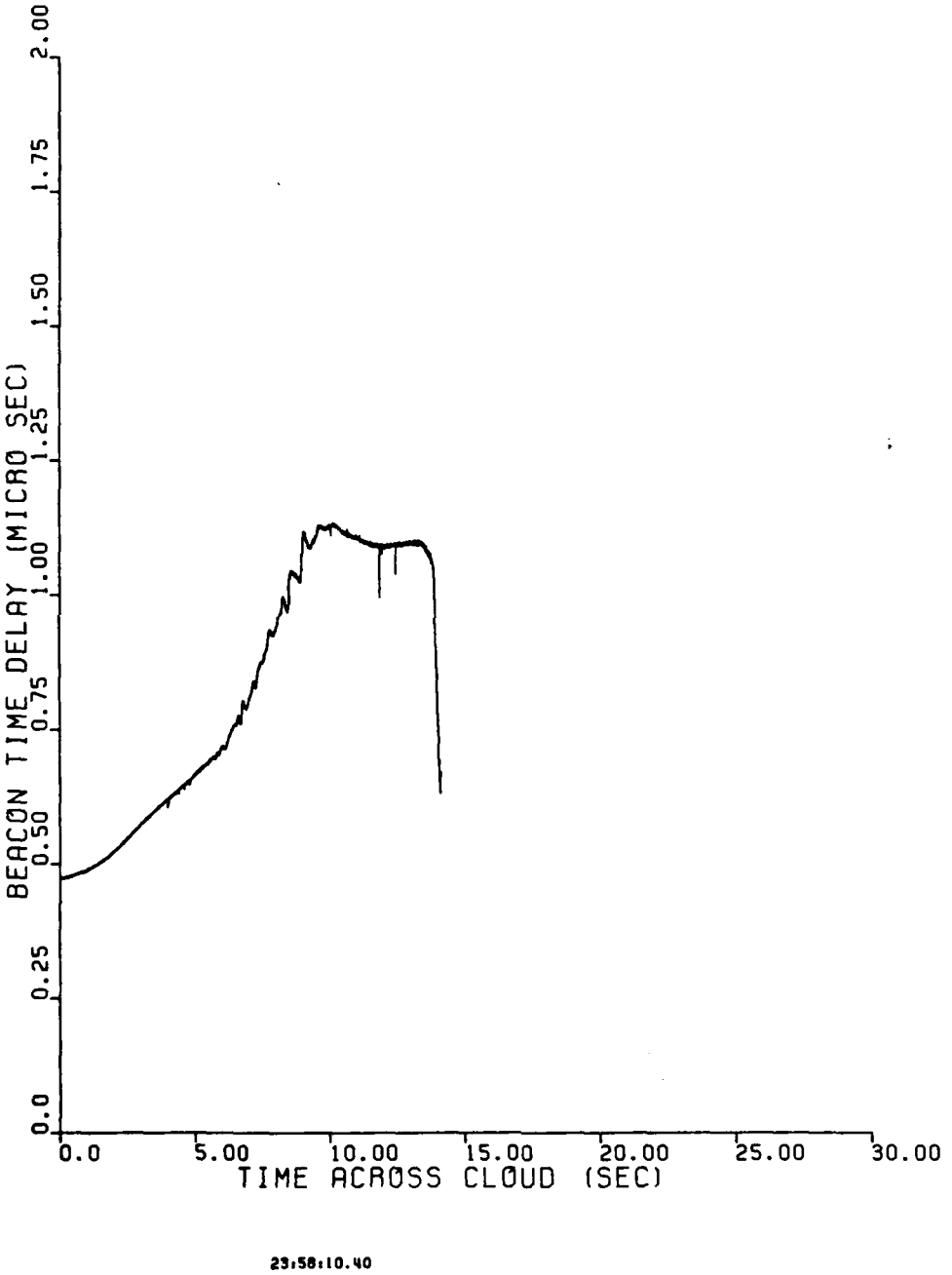

Figure 5-5. Direct path TOA delay.

5.5 BACK-PROPAGATION PROCESSING AT 98 MHZ

Even though there is no significant delay spread of energy, the received signal exhibits some minor amplitude and phase scintillation typical of a flat fading channel. Backward propagation of the 98-MHz signal component of the received diffraction pattern swept out by the beacon rocket can be performed as discussed in Section 2.9 using thin phase screen angular spectrum techniques.

The scintillation index and the back-propagation results obtained are described in the following sections for reference.

5.5.1 S^4 Versus Distance

The S^4 scintillation index is used as a measure of the amplitude fluctuation as discussed in Section 2.9.1. The amount the S^4 index decreases with back-propagation and its value after back-propagation gives a good indication as to how well the data back-propagated in a thin phase screen sense. In this case, however, the data drop out interval at the end of the interval obscures the behavior of the scintillation data. Figure 5-6 is a plot of the scintillation index versus back-propagation distance for Cape San Blas, Beacon 2. The back-propagation distance was initially computed assuming an effective transverse velocity, V_e, of approximately 890 m/sec. The true velocity is likely to be similar to that of the first beacon, approximately 980 m/sec. The distance axis scales by the factor $(V_T/V_e)^2$, where V_T is the true transverse velocity.

The S^4 index exhibits a rapid decrease over the first 20 km. This is in reasonable agreement with the optical data (see Section 5.2).

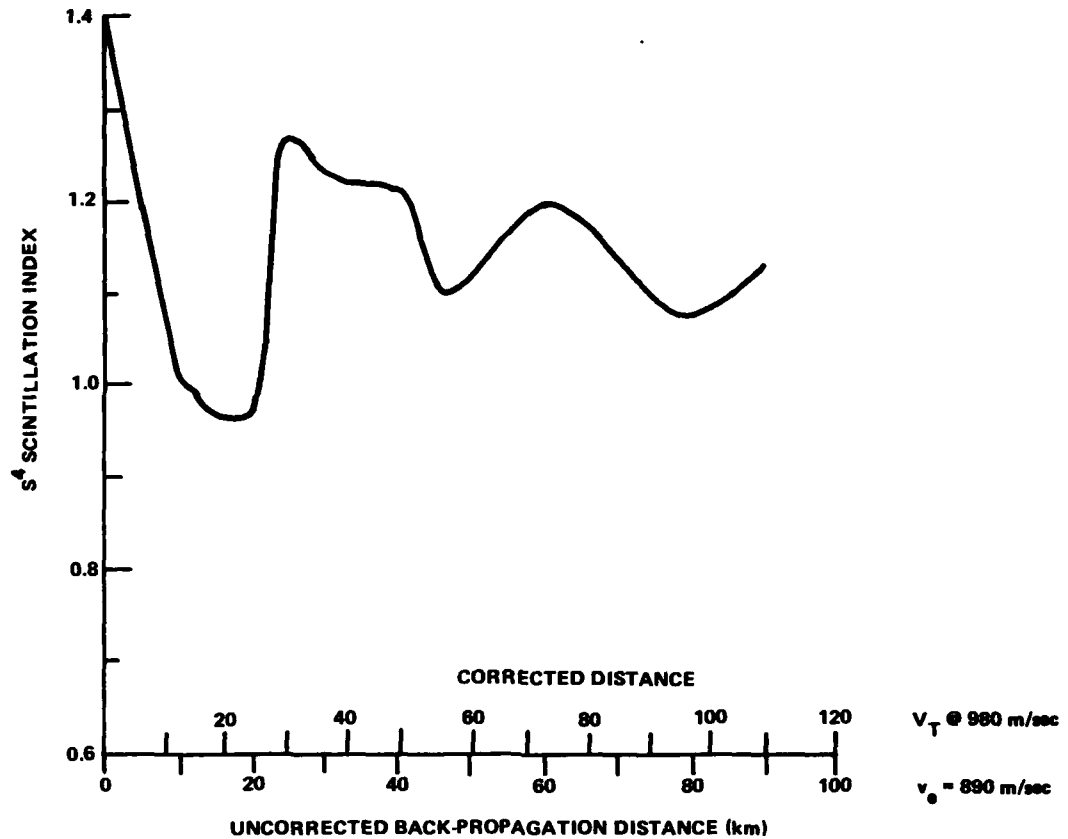

Figure 5-6. S^4 scintillation index versus back-propagtion distance for Cape San Blas, Beacon 2.

5.5.2 Back-Propagation Plots

Plots of the back-propagated signal amplitude and phase are presented in Figures 5-7 through 5-14 over the first 40 km. The distances noted are the uncorrected values corresponding to the 890 m/sec velocity. The data drop out interval at the end of the occultation is due to receiver mistuning and is not associated with fading effects. It is this data interval that results in a misleading S^4 versus distance. There does not appear to be a satisfactory back-propagation distance for which the scintillation effects truly diminish in amplitude.

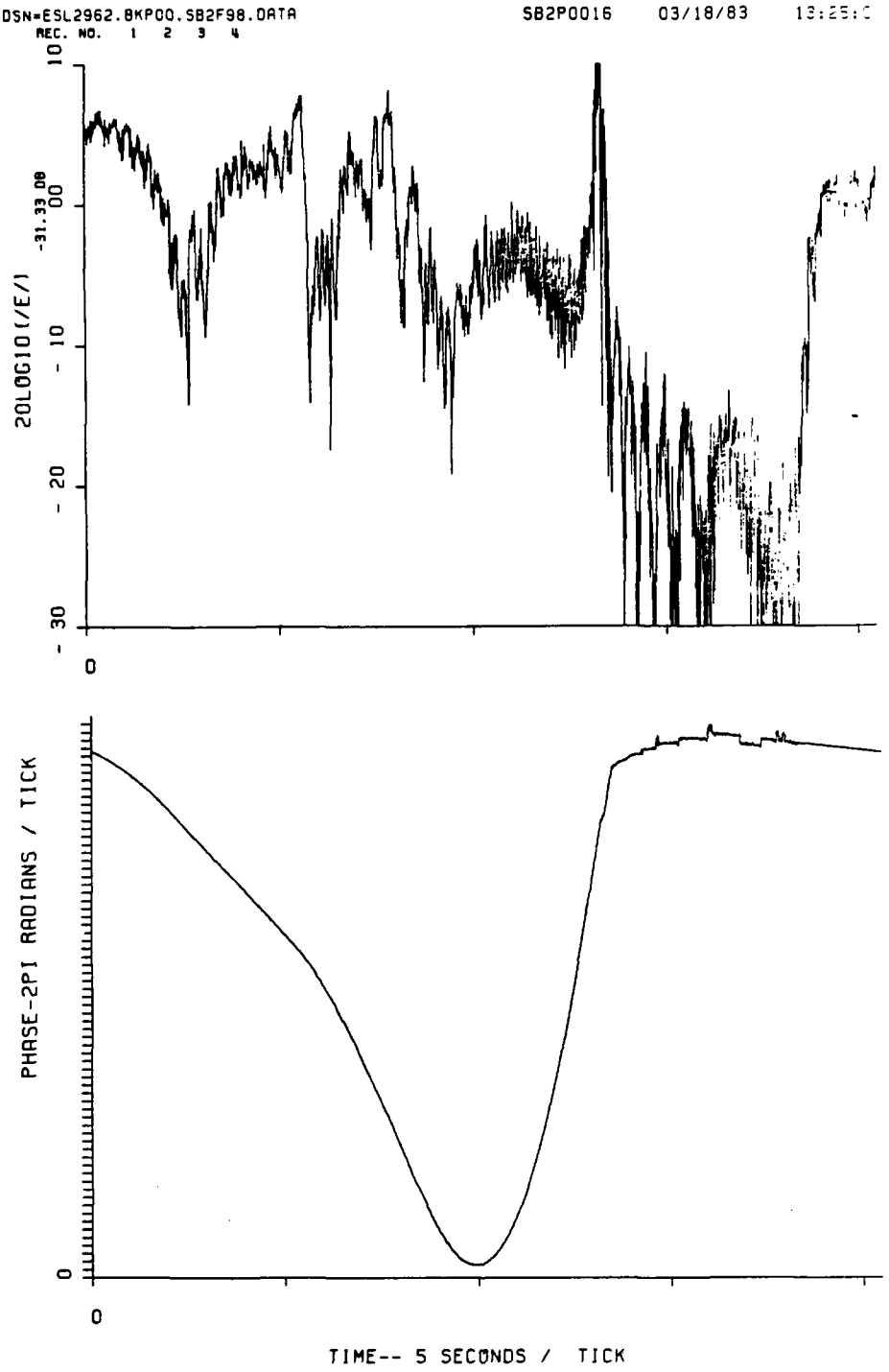

Figure 5-7. Amplitude and phase before back-propagation, Cape San Blas, Beacon 2.

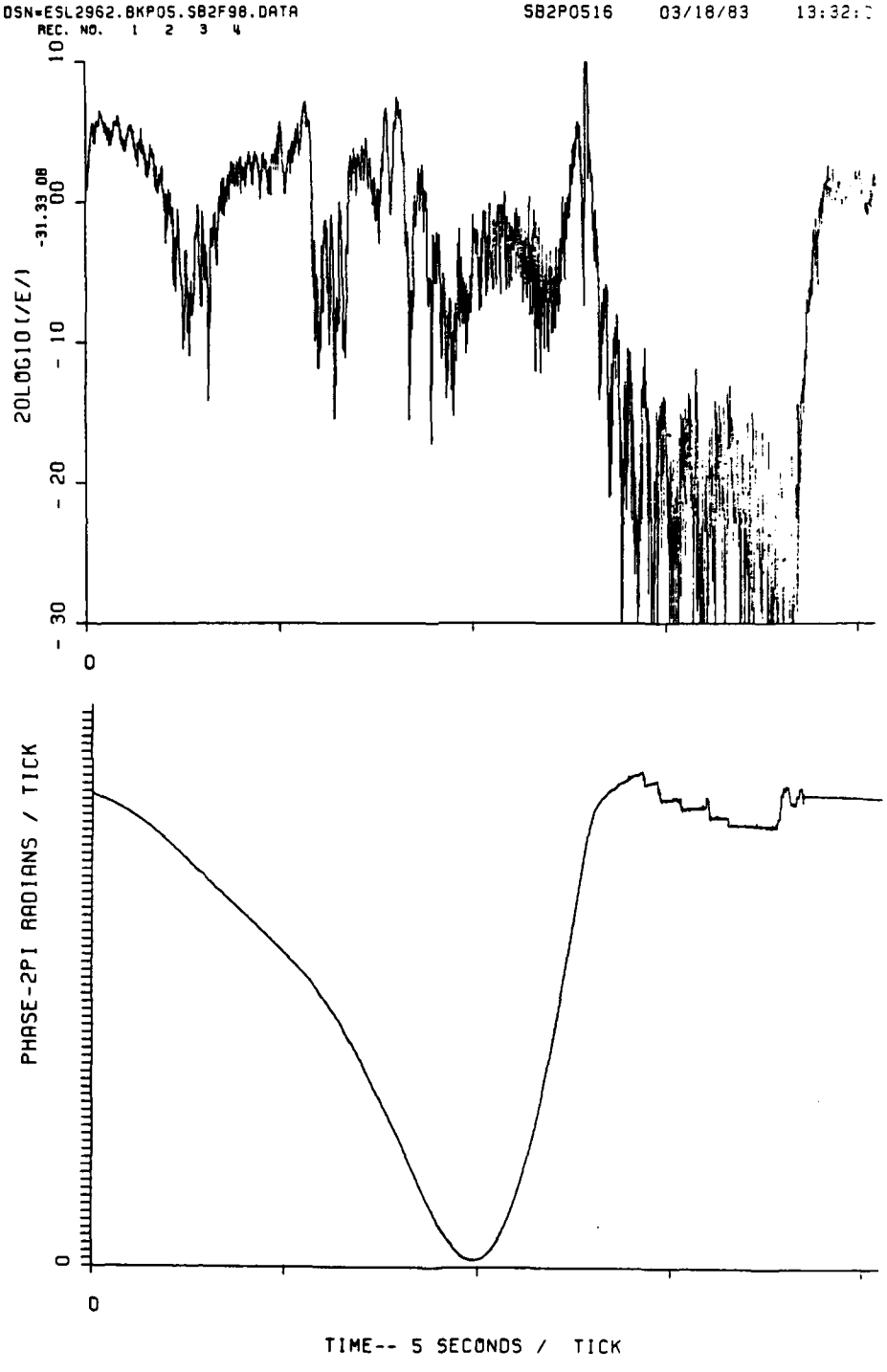

Figure 5-8. Back-propagated amplitude and phase, Cape San Blas, Beacon 2, 5 km.

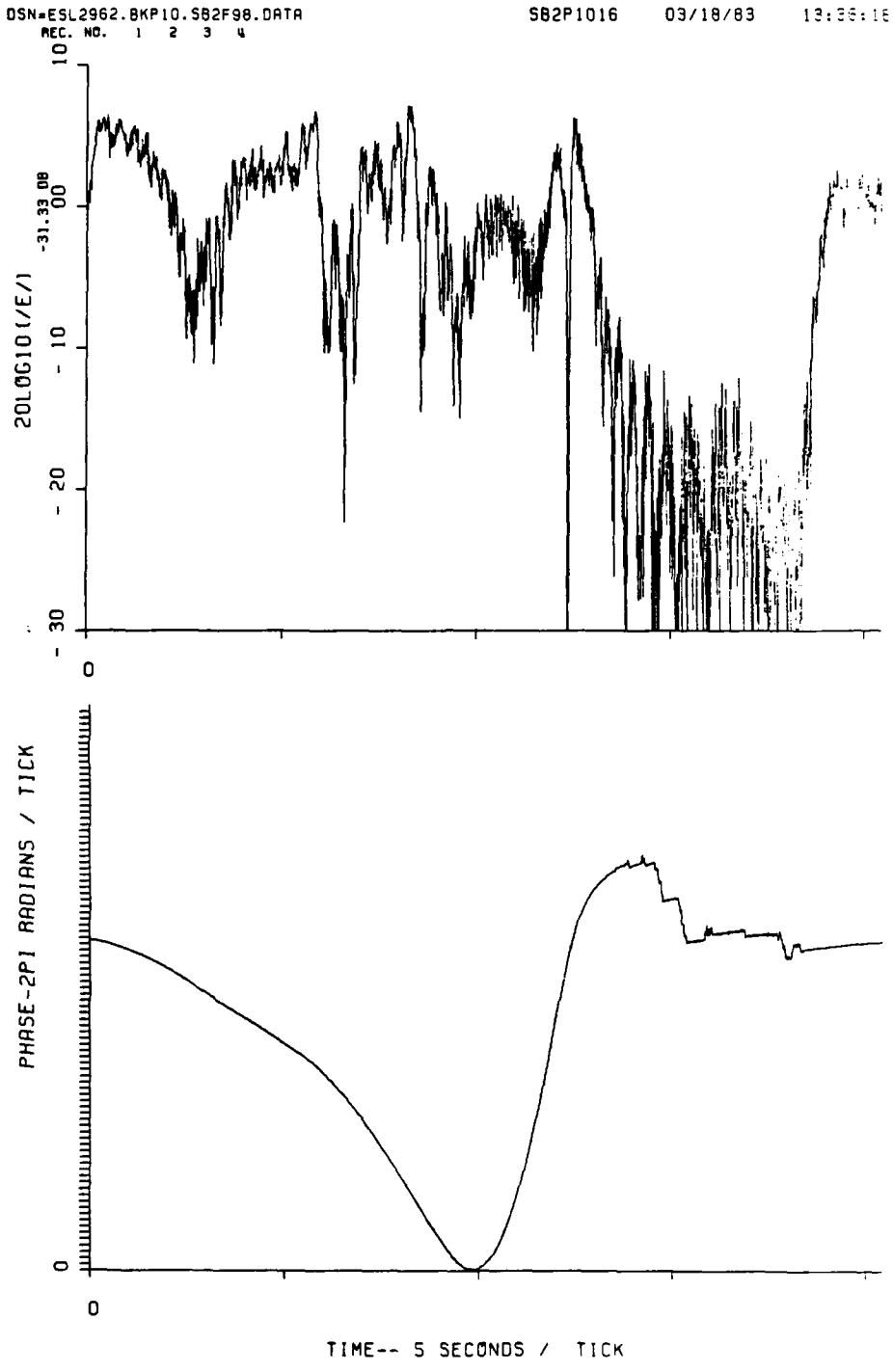

Figure 5-9. Back-propagated amplitude and phase, Cape San Blas, Beacon 2, 10 km.

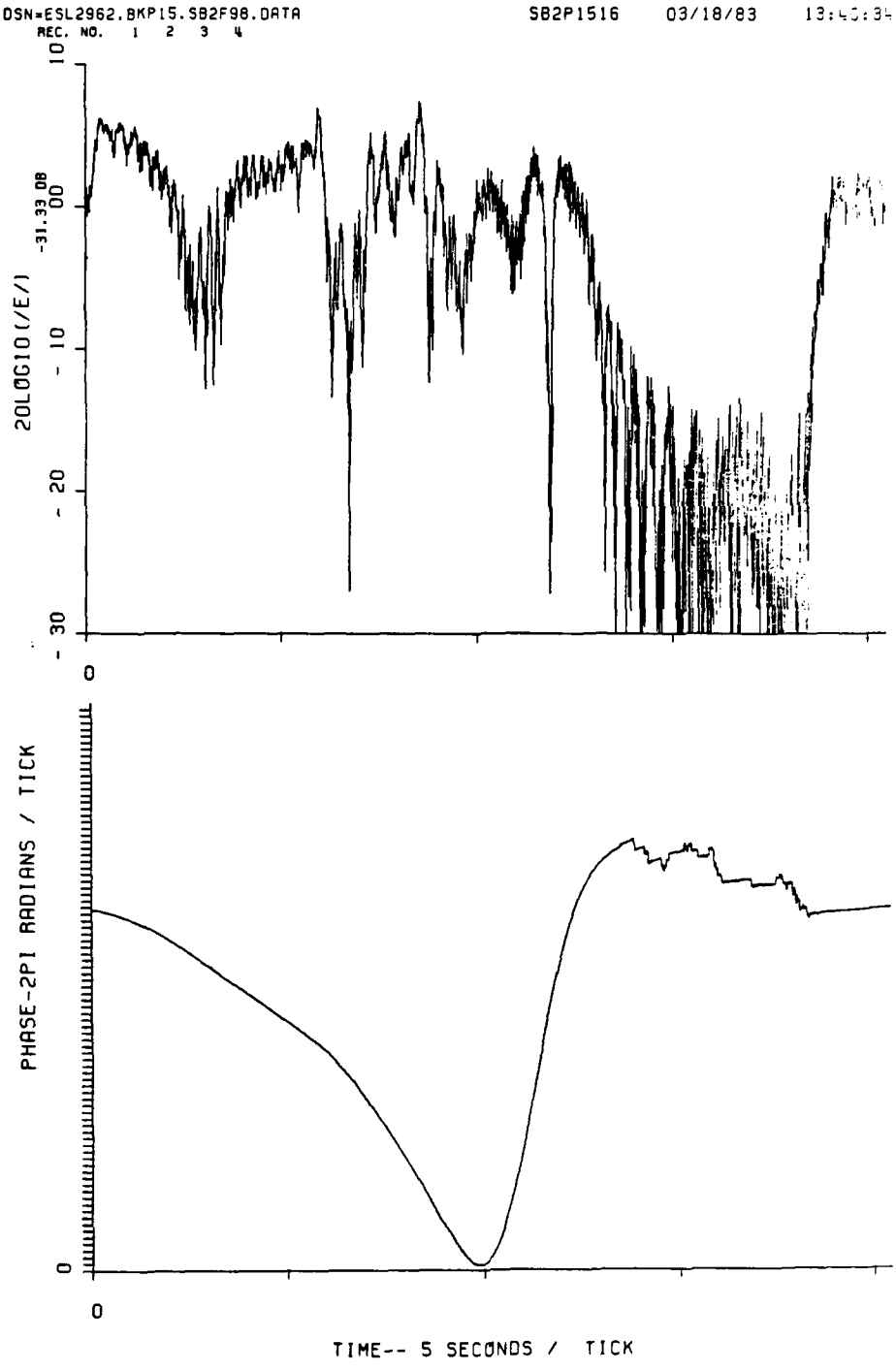

Figure 5-10. Back-propagated amplitude and phase, Cape San Blas, Beacon 2, 15 km.

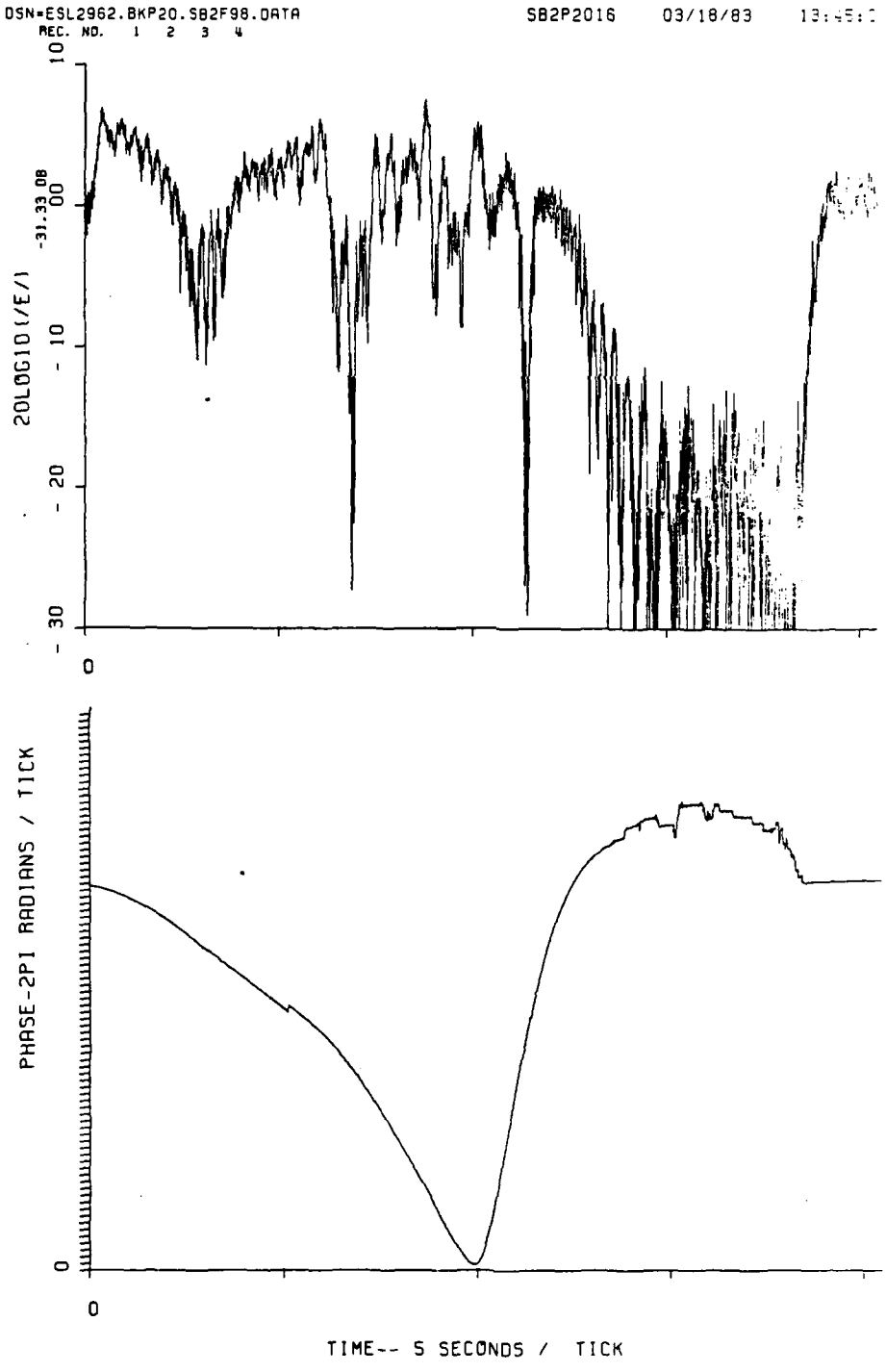

Figure 5-11. Back-propagated amplitude and phase, Cape San Blas, Beacon 2, 20 km.

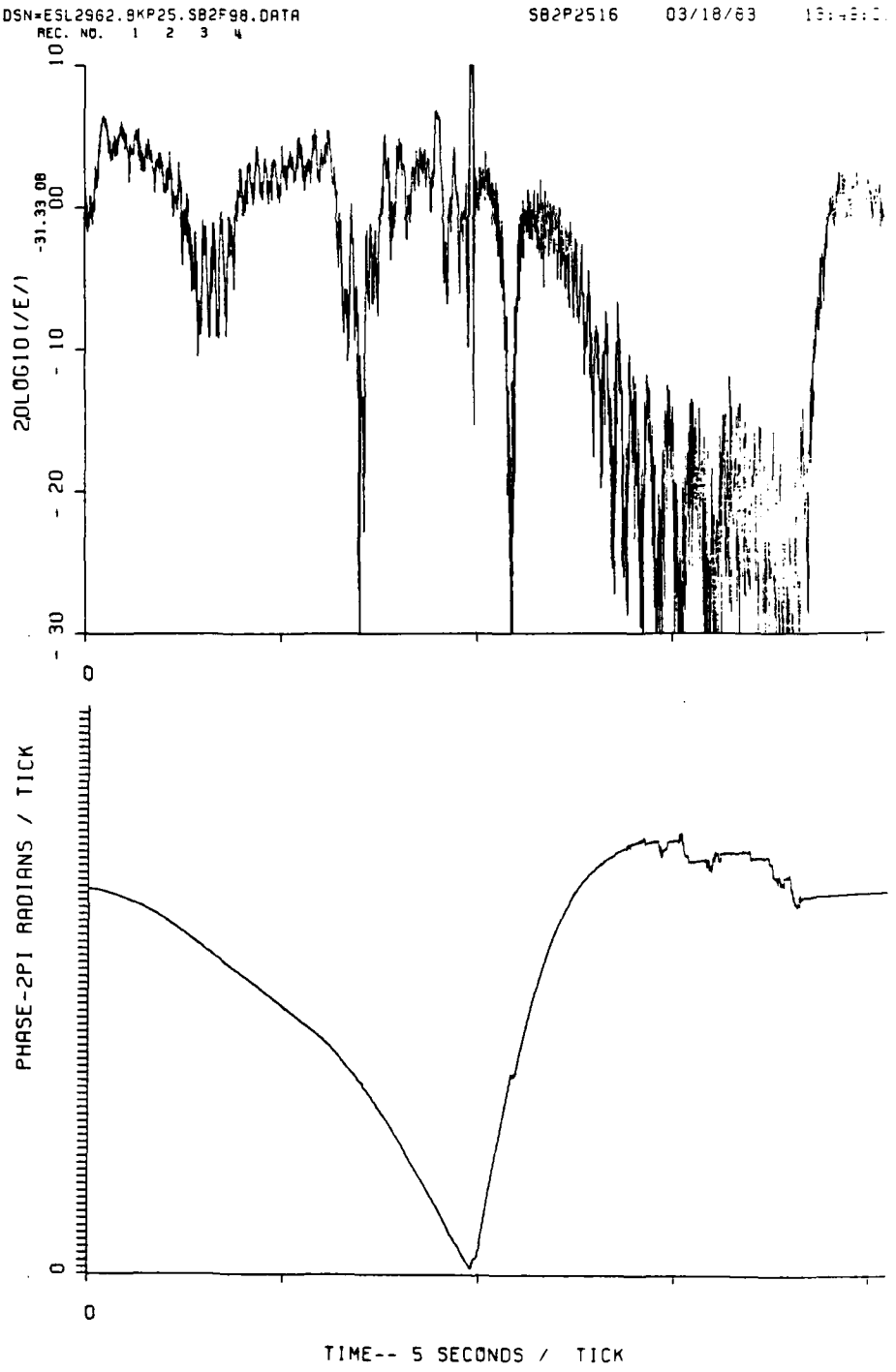

Figure 5-12. Back-propagated amplitude and phase, Cape San Blas, Beacon 2, 25 km.

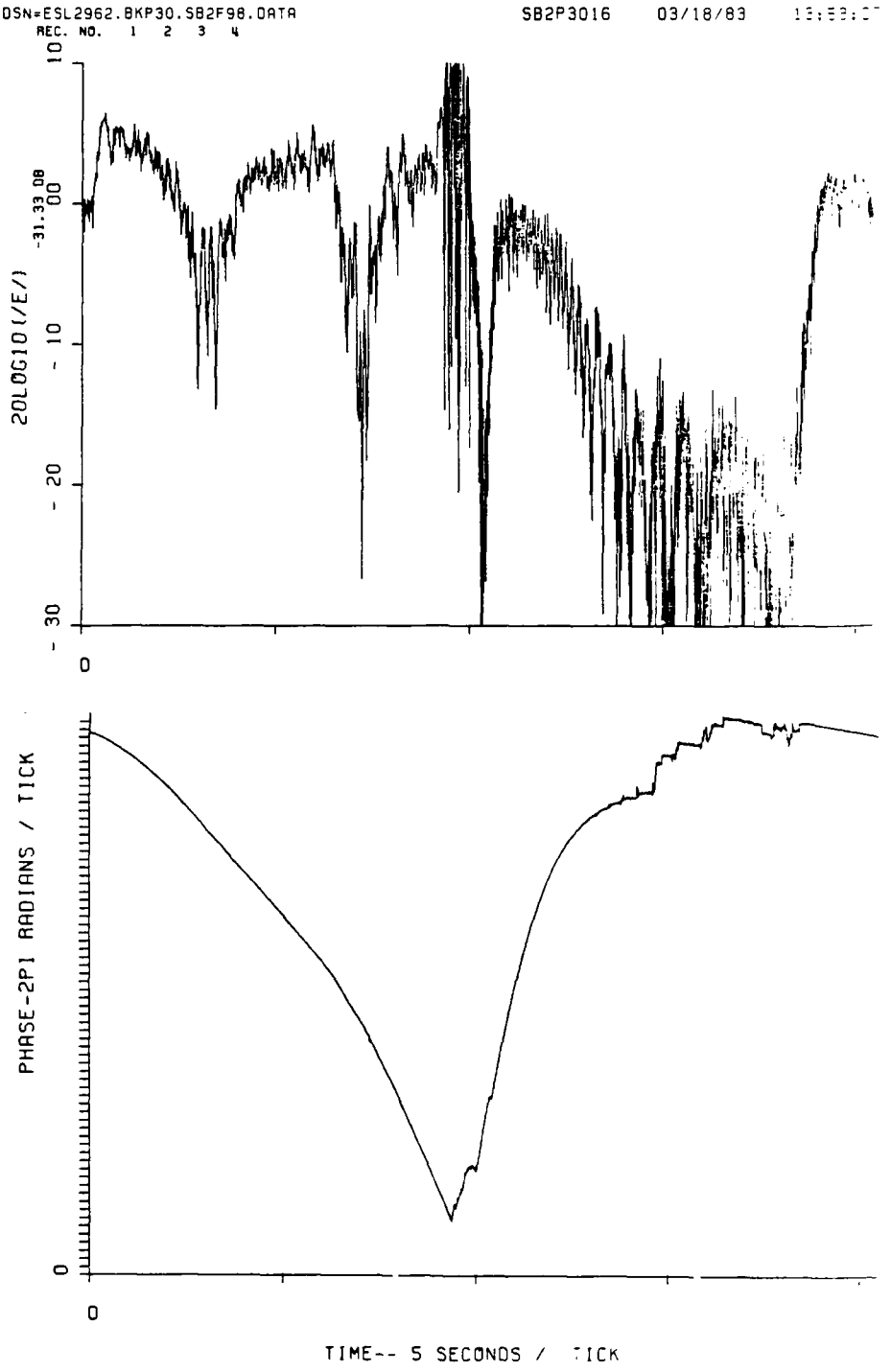

Figure 5-13. Back-propagated amplitude and phase, Cape San Blas, Beacon 2, 30 km.

AD-A160 566 PLACES (POSITION LOCATION AND COMMUNICATION EFFECTS SIMULATIONS) BEACON EXPERIMENT TEST RESULTS(U) ESL INC SUNNYVALE CA J MARSHALL ET AL. 01 AUG 84 DNA-TR-84-376 5/5

UNCLASSIFIED DNA001-81-C-0149 F/G 20/14 NL

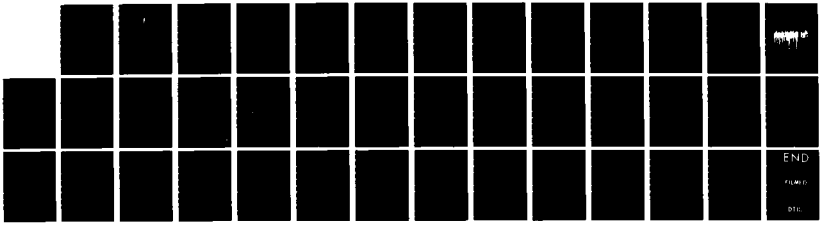

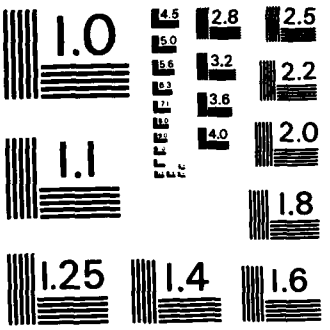

MICROCOPY RESOLUTION TEST CHART
NATIONAL BUREAU OF STANDARDS - 1963 - A

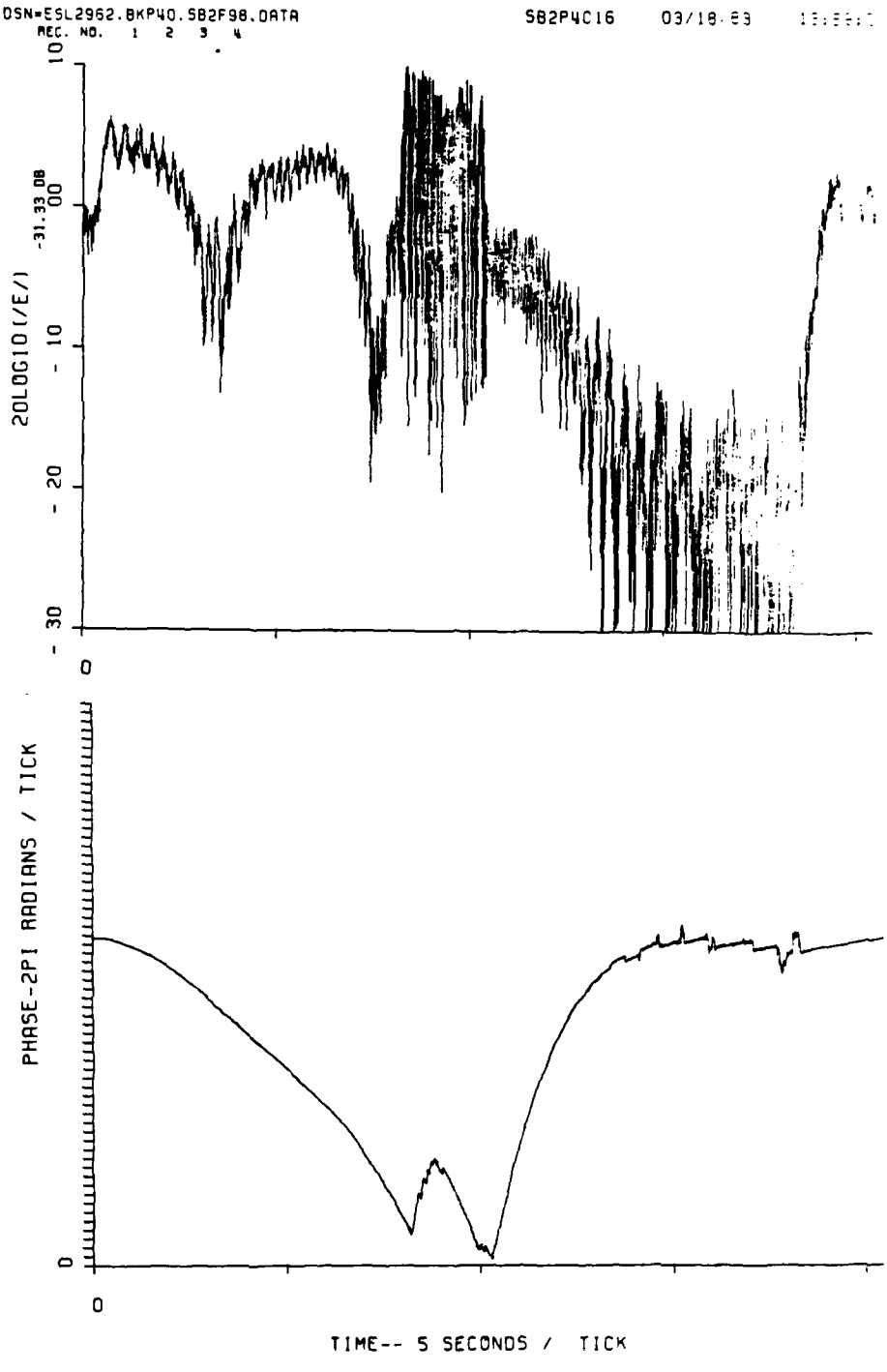

Figure 5-14. Back-propagated amplitude and phase, Cape San Blas, Beacon 1, 40 km.

SECTION 6
REFERENCES

1 Dr. James Marshall, Jeff Lehman, Gary Elston, and Wayne Solbrig, "PLACES Quick-Look Report for Beacon and Aircraft Experiments," DNA 5737F, ESL Inc., March 1981.

2 Dr. James Marshall, Wayne Solbrig, Jeff Lehman, "PLACES Aircraft Experiment Test Results," ESL-TM1466, ESL Inc., May 1982.

3 Dr. Clifford Prettie, "Results of PLACES Data Analysis," PD-BRA-82-278R, Berkeley Research Associates, September 1982.

4 Dr. Dan McDaniel, Compiler, "Proceedings of the PLACES Preliminary Data Review Meeting, 20 and 21 May 1981," DNA 5848P, SRI International, July 1981.

5 Roger Swanson, Dr. James Marshall, Allen Johnson, "PLACES Airborne Experiment," AFWAL-TR-81-1250, Air Force Wright Aeronautical Laboratories, May 1982.

6 Norman Chang, "PLACES TV-Track, Ionosonde, and Magnetometer Operations," DNA 5806F, SRI International, 1 June 1981.

7 W. Walker, L. Rollstin, "Final Report on Sandia National Laboratories Participation for Project PLACES," SAND 81-1923, Sandia National Laboratories, May 1982.

8 Larry Rollstin, Fred Wyatt, "Real-Time Tracking and Targeting Computations and Rocket Vehicle Aeroballistics for the PLACES Ionospheric Plasma Test Series," SAND 81-2091, Sandia National Laboratories, February 1982.

REFERENCES (Continued)

9 R. Narcisi, et al., "Composition and Structure Measurements in an Ionospheric Barium Cloud," ERP No. 760, AFGL-TR-82-0003, Air Force Geophysics Laboratory (LKD), Hanscom AFB, Mass., 23 December 1981.

10 Victor Gonzalez, "Radar Tracking of Barium Ion Clouds: Results of the PLACES Experiment," DNA 5851F, SRI International, 1 August 1981.

11 Charles Rino, Jacqueline Owen, R. Livingston, "Analysis of Nuclear Propagation Effects Utilizing Wideband Satellite Data," DNA 5807F, SRI International, 1 April 1981.

12 Phillip Bello, "A Study of the Relationship Between Multipath Distortion and Wave-Number Spectrum of Refractive Index in Radio Links," Proc. IEEE, Vol. 59, No. 1, January 1971, p. 47.

13 Capt. Leon Wittwer, "Radio Wave Propagation in Structured Ionization for Satellite Applications," DNA 5304D, Defense Nuclear Agency, 31 December 1979.

14 E. Szuszczewicz, J. Holmes, M. Swinney, and C. Lin, "DNA/PLACES Barium Event JAN: Quick-Look Field Report of 'In Situ' Probe Measurements," NRL Memorandum Report 4476, Naval Research Laboratory, 26 March 1981.

15 W.E. Walker, L.R. Rollstin, "Final Report on Sandia National Laboratories Participation in Project PLACES, SAND81-1923, Sandia National Laboratories, May 1982.

REFERENCES (Concluded)

16 Dr. Victor Gonzales, SRI International, Private Communication, July 1981.

17 David J. Simons, et.al., "Evolution of Structure in the PLACES Barium Clouds, LA-9648-MS, Los Alamos National Laboratories, February 1984.

18 Clifford Prettie, Private Communiction, 21 April 1982.

19 David Middleton, "An Introduction to Statistical Communication Theory," McGraw Hill Book Co., 1960.

APPENDIX A
TOA ESTIMATION ALGORITHM

A.1 PEAK DETECTION ALGORITHM

The task of identifying the signal time of arrival (TOA) delay profile of the beacon rocket data necessitated the development of an algorithm that could locate all the peaks and plateaus in the data records and then select the peak corresponding to the earliest detection of signal energy. Each beacon record consisted of 90 data points spaced apart in time by one third of a chip. The algorithm to locate peaks searched and found all those data points that were preceded in the record by two data points of descending amplitude and followed by a data point of equal or lesser magnitude. Each point satisfying this criteria was then tested to see whether it was in fact a real peak, a plateau, or part of an increasing rising edge to a different peak. This was accomplished by checking the value of the data point two points after the data point in question. If this point had a smaller amplitude than the preceding data point, the point being studied was classified as a peak. If this point had a larger amplitude than the preceding point, but both points were within 10 percent of the value of the point in question, then a plateau was determined.

To make the location of peaks less subject to random noise variations, it was determined that the centroid of each peak would be a more accurate measurement of the true TOA. For all peaks detected via the process described above, the minimum points on each side of the peak were next determined. The centroiding operation was then done over the region between the two locations that lie half way down from the peak to the largest minimum point. This process smoothed out much of the small scale jitter in the delay profile. For signal plateaus, the first point on the plateau was selected as this represented the earliest time when signal energy had reached a peak.

A.2 DIRECT PATH TOA ALGORITHM

The process of distinguishing the peaks corresponding to the first arrival of signal energy from those resulting from random noise and multipath components required initial plots showing all of the selected peaks and plateaus. The general shape of the signal TOA delay profile can be estimated from this graph and is used to provide an estimate of the signal TOA for subsequent processing. At each position throughout the cloud, a test is then made to determine whether any of the peaks found at that position fall within a window of±1 chip from the value of the estimated TOA curve drawn above. If no peak occurs within the window, it is assumed that no signal peak was detected and the next position in the cloud is searched. By this procedure, only real data points corresponding to the first arrival of signal energy are shown on the final curves of the TOA delay profiles.

A.3 SIGNAL POWER RELATIVE TO DIRECT PATH DELAY COMPONENT ALGORITHM

The algorithm used to calculate the average power as a function of delay over various data segments was also developed. This algorithm involved the scanning of each data record to find the direct path signal peak. The data points on each side of this peak were then kept in storage registers specifically assigned for the data points one point after the peak, two points after the peak, etc. After all the data records spanning the period of the occultation were scanned and stored, a summation of the square of all the data in each storage register was made and divided by the number of records to give the power at each data position relative to the position of the direct path signal. The direct path signal peak was found by selecting the data point of highest value and could be in error by an amount approaching 1/3 of a chip, limiting the accuracy of this curve to a time value of that magnitude.

APPENDIX B
BEACON ROCKET TRAJECTORY DATA

B.1 INTRODUCTION

A summary of the beacon trajectory data over the occultation interval for each flight is provided for reference in this appendix. The beacon rockets were traced by three FPS-16 radars. Two of these agree within 50 meters while the third differs by no more than 500 meters over the occultation period. The data presented are from one of the two radars that were in close agreement.

The beacon receiving site locations were estimated from topographicl maps with reasonbly high accuracy ($\pm$100 meters, est.). Table B-1 summarizes the location of the beacon receiver sites.

B.2 BEACON 1

Table B-2 summarizes the trajectory data for Beacon 1 over the first occultation interval.

B.3 BEACON 2

Table B-3 summarizes the trajectory data for Beacon 2 over the second occultation interval.

Table B-1. Location of receiver sites.

Site	Altitude (m)	Latitude (deg)	Longitude (deg)
St. George Island	~15	29.6433	84.9117
Cape San Blas (D3A)	~15	29.6667	85.3550

Table B-2. Trajectory data for Beacon No. 1 during occultation interval.

Time	Altitude (km)	Latitude (deg)	Longitude (deg)
2345:07.1	194.25	28.3232	87.0239
2345:08.1	193.04	28.3174	87.0243
2345:09.2	191.71	28.3112	87.0252
2345:10.2	190.52	28.3058	87.0260
2345:11.2	189.34	28.3005	87.0269
2345:12.2	188.12	28.2949	87.0274
2345:13.2	186.87	28.2892	87.0277
2345:14.3	185.47	28.2828	87.0285
2345:15.3	184.84	28.2800	87.0288
2345:16.3	183.01	28.2721	87.0300
2345:17.3	181.77	28.2667	87.0305
2345:18.3	180.46	28.2609	87.0311
2345:19.4	179.01	28.2546	87.0318
2345:20.4	177.76	28.2494	87.0324
2345:22.4	175.14	28.2382	87.0339
2345:23.4	173.80	28.2326	87.0348
2345:24.5	172.34	28.2265	87.0354
2345:25.5	171.00	28.2210	87.0358
2345:26.5	169.65	28.2154	87.0364
2345:27.5	168.30	28.2098	87.0372
2345:28.5	166.88	28.2040	87.0378
2345:29.6	165.32	28.1976	87.0383
2345:30.6	163.99	28.1924	87.0391
2345:31.6	162.66	28.1872	87.0403

Table B-3. Trajectory data for Beacon No. 2 during occultation interval.

Time	Altitude (km)	Latitude (deg)	Longitude (deg)
2358:10.0	184.47	27.9952	86.9738
2358:11.0	183.23	27.9887	86.9741
2358:12.0	182.02	27.9825	86.9748
2358:13.0	180.78	27.9762	86.9754
2358:14.0	179.53	27.9698	86.9758
2358:15.1	178.16	27.9630	86.9768
2358:16.1	176.85	27.9564	86.9771
2358:17.1	175.55	27.9499	86.9773
2358:18.1	174.26	27.9436	86.9782
2358:19.1	172.98	27.9373	86.9787
2358:20.2	171.50	27.9301	86.9787
2358:21.2	170.21	27.9238	86.9796
2358:22.2	168.89	27.9175	86.9805
2358:23.2	167.53	27.9110	86.9809
2358:24.2	166.18	27.9046	86.9811
2358:25.3	164.70	27.8977	86.9817
2358:26.3	163.31	27.8912	86.9822
2358:27.3	161.96	27.8849	86.9827

APPENDIX C
MEASUREMENT OF DIFFERENTIAL DOPPLER

The differential Doppler of each refracted ray (or at each tap delay position) can be measured in two straightforward ways. Since the C-band reference on the beacon rocket removes the effects of rocket motion relative to the direct path, it is only necessary to measure the Doppler at each tap delay position. This can be done by measuring the phase or Doppler at any given tap as the refracted ray moves through that tap delay position. The output of each complex tap is the cross-correlation of the in-phase and quadrature received signal with a locally generated reference signal replica of the transmitted signal at a fixed delay offset in time.

Figures C-1, C-2, and C-3 provide an example of this process. Figure C-1 shows the magnitude of a weak refracted ray as it passes through the 70th tap position. In this particular case, the direct path is centered in the 11th tap position. Each tap corresponds to 0.0346 μsec of delay. The code cross-correlation self noise floor is dependent on the direct path signal strength. Additionally, interference from other signals is present randomizing the self noise. The dominant self noise, however, results in the quantized appearance of the noise.

Figure C-2 shows the corresponding phase at this tap position. The phase as the ray moves through the tap follows a distinctive linear ramp or constant Doppler. The Doppler can be measured directly to be approximately 54 Hz. Alternatively, since the Doppler corresponds to a given angle of scatter, the Doppler can be obtained directly from the angular spectrum as shown in Figure C-3. In this case, there is only one ray so the corresponding Doppler spectrum can be determined unambiguously. The spectral width can also be measured at the -10 dB points giving approximately $\pm$3.4 Hz about the peak at 54.4 Hz. In other situations where many

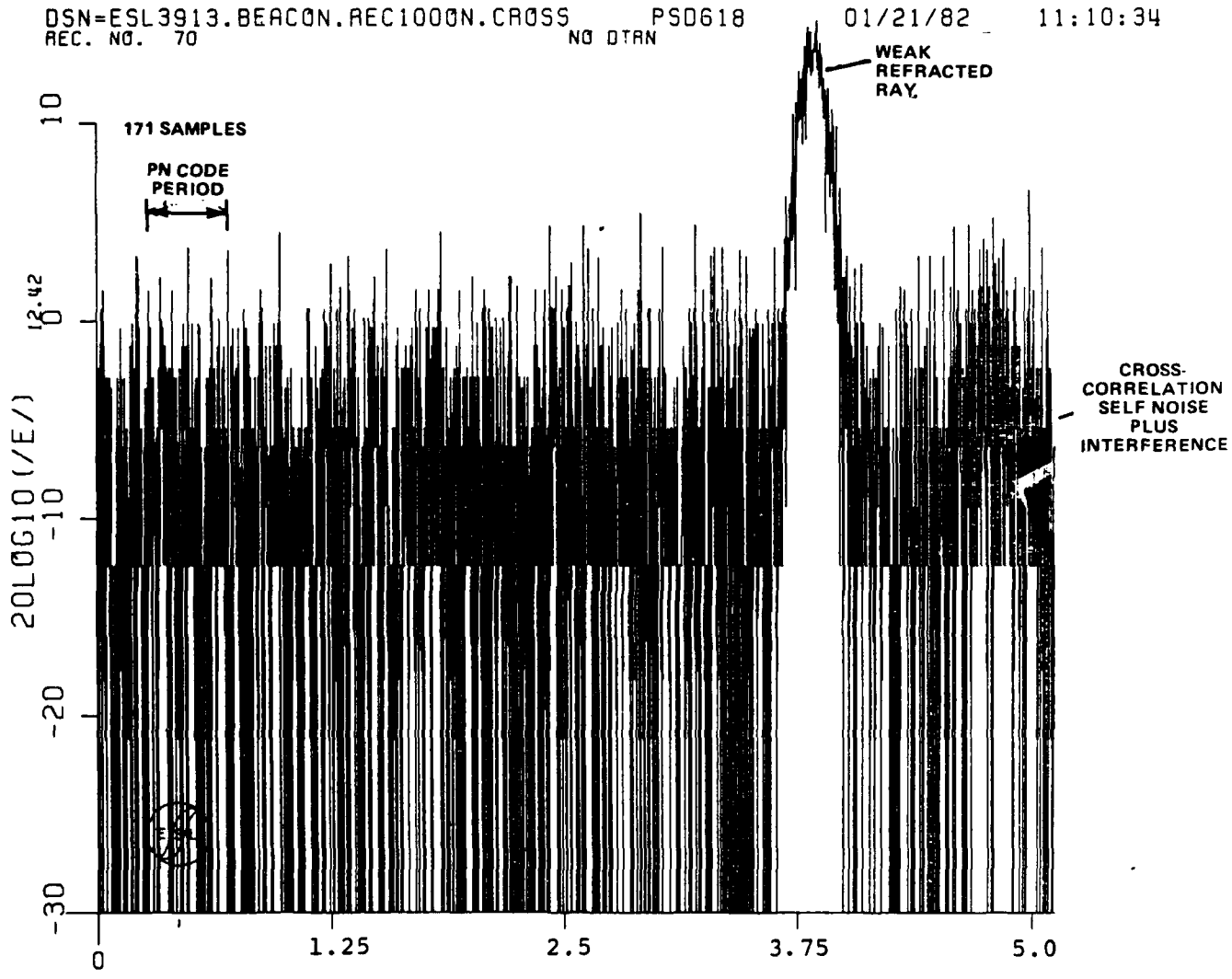

Figure C-1. Amplitude of Tap 70 (2.43 μsec).

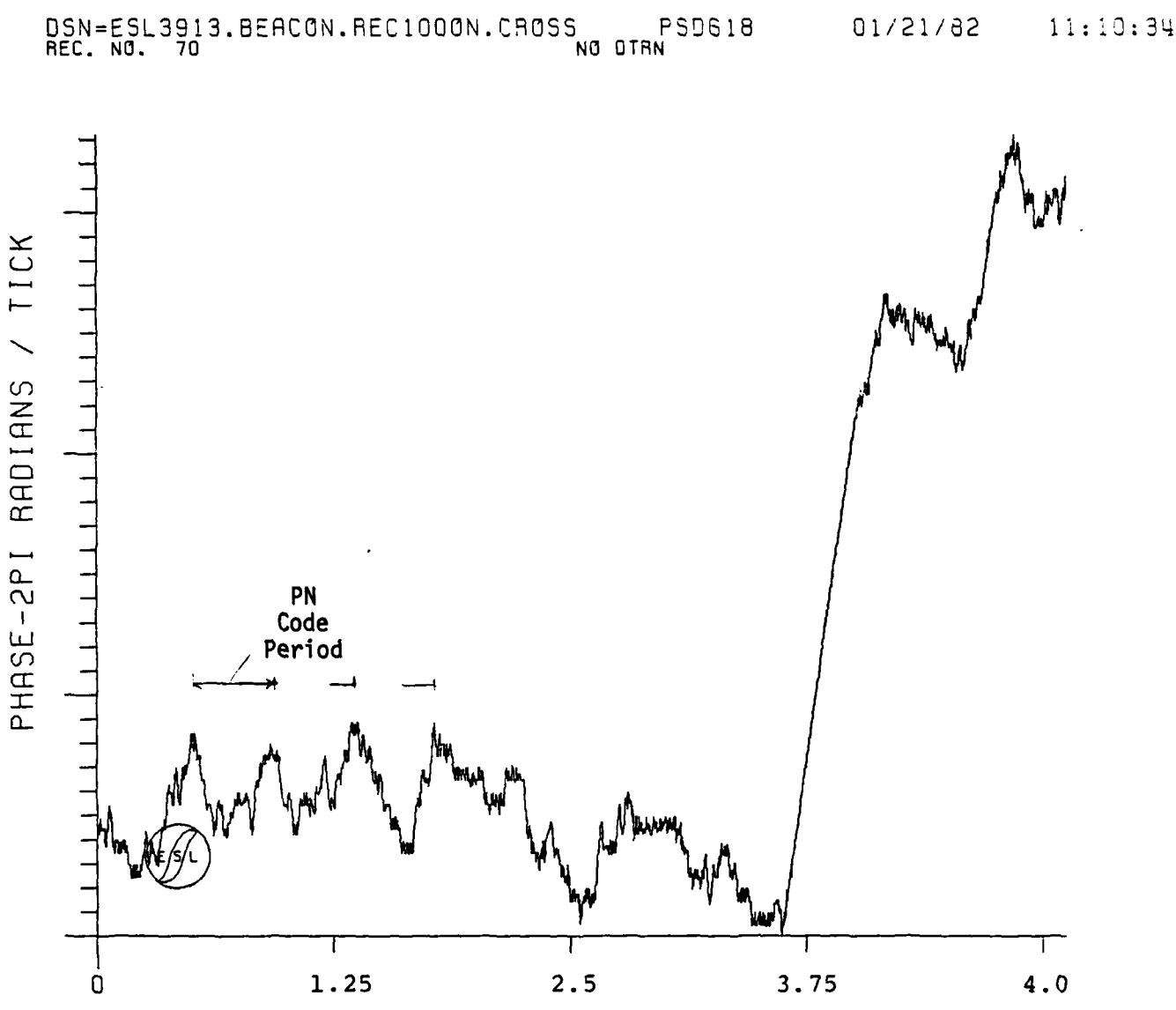

Figure C-2. Phase of Tap 70.

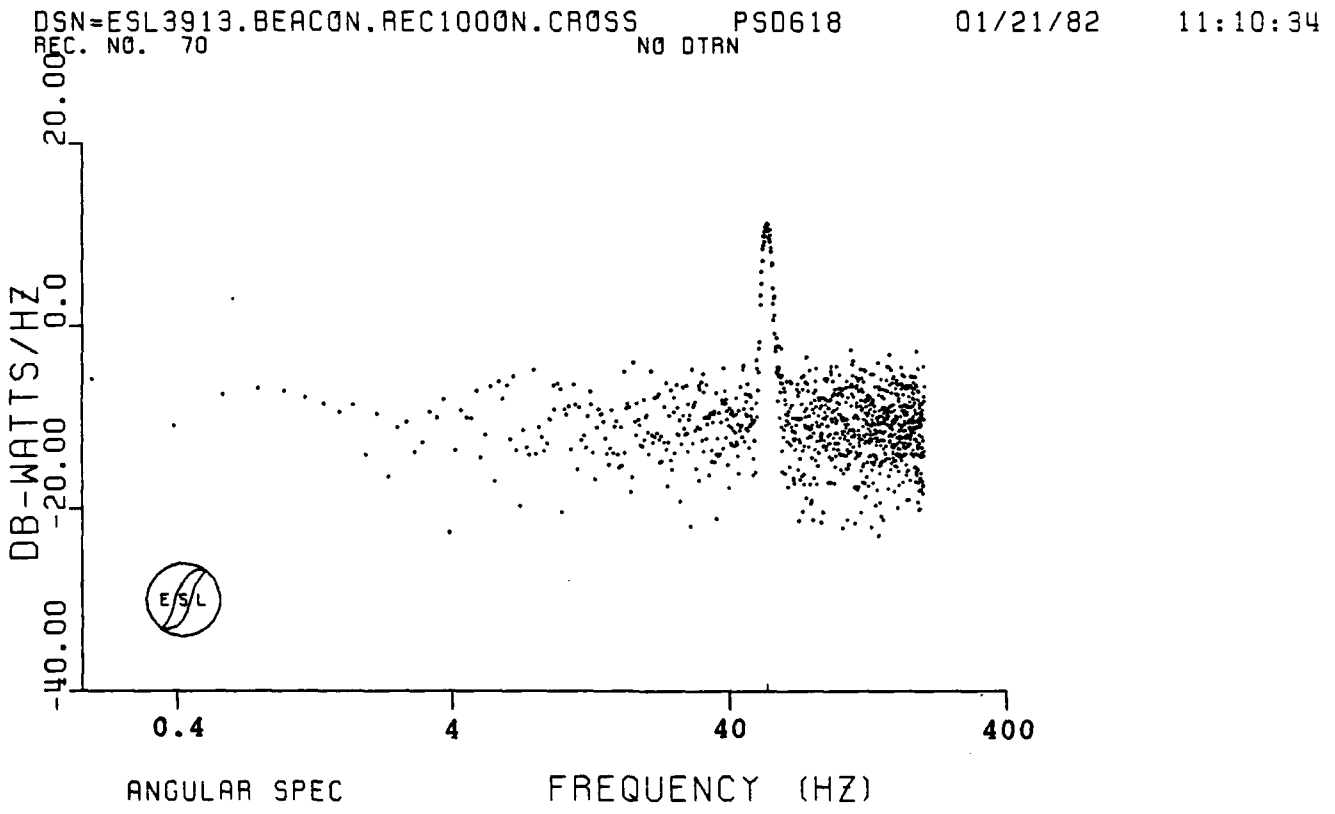

Figure C-3. Angular spectrum.

rays pass through the tap during the observation interval, either a smaller interval must be processed, or the Doppler determined from the phase slope for each ray.

No averaging or filtering of the output of each tap was performed, nor were any weighting functions used in the FFT spectrum calculations. Each tap is sampled at a 400-Hz rate. The cross-correlation is performed over 2450 code chips or approximately 1/1712th of the PN code period (or 0.25 msec).

APPENDIX D
TRANSVERSE PATTERN VELOCITY CALCULATION

D.1 DEFINING RELATIONS

The effective transverse field pattern velocity is determined primarily by the beacon rocket velocity. The cloud drift velocity is of the order of 32 m/sec and is neglected here in comparison to the rocket velocity of 1440 m/sec. The diffraction pattern created by the striations will vary in a direction orthogonal to the striations in the viewing plane. Visualize for the moment a plane wave incident at the striations from a transmitter at the beacon receiver location. The beacon rocket occults the striations in such a way that the diffraction pattern is measured transiting partially down the diffraction pattern in the largely nonvarying diffraction field direction and partially across the diffraction pattern in the rapidly varying field direction. Additionally, the rocket moves away from the striation mass and away from the beacon receiver site. The true or effective pattern velocity can be determined by computing the distance traveled across the diffraction pattern in the maximum rate of change direction in a given time increment.

The transverse velocity of the rocket transmitter signal can be determined by knowing two rocket locations, the elapsed time between the two rocket locations, the magnetic field line vector, and the ground receiver location as shown in Figure D-1.

$\vec{B}$ - Magnetic field line vector through point T_1 (unit vector)

T_1 - Rocket location at time #1

T_2 - Rocket location at time #2

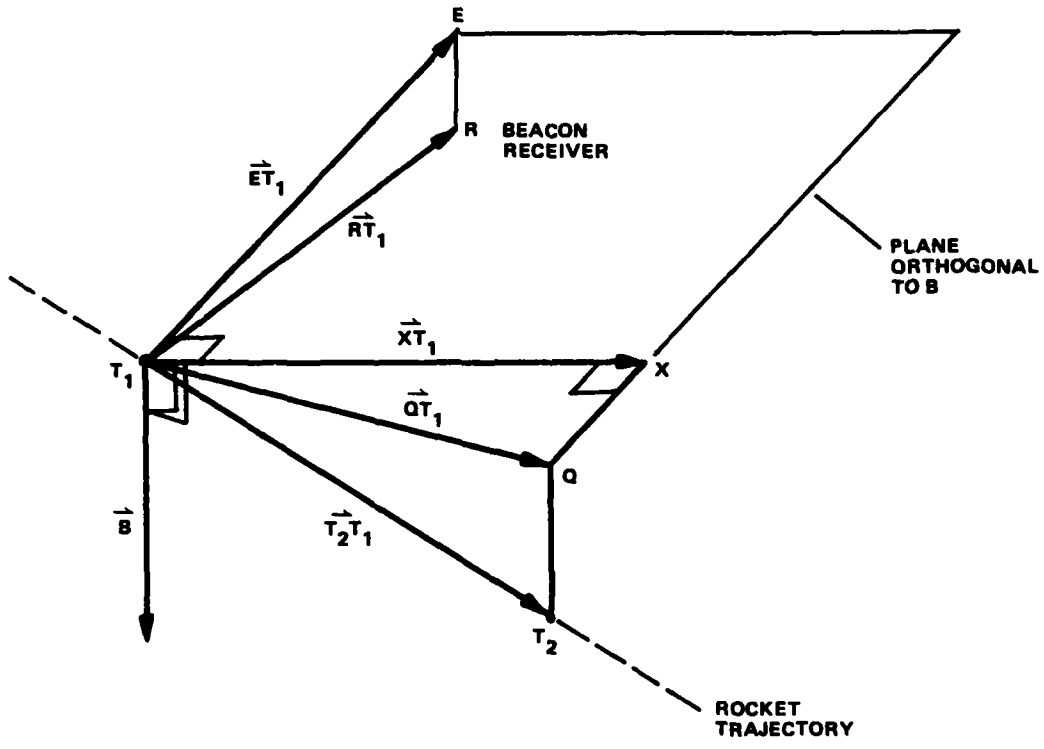

Figure D-1. Transverse pattern velocity calculation geometry.

R - Ground receiver location

Q - Projection of point T_2 into plane orthogonal to $\vec{B}$

E - Projection of point R into plane orthogonal to $\vec{B}$

X - Projection of point Q to vector orthogonal to line-of-sight projection $\vec{ET}_1$.

The transverse velocity is determined by the velocity along the XT_1 vector in the plane perpendicular to the magnetic field vector through T_1. This vector is also orthogonal to the line-of-sight projection onto this plane. The effective pattern velocity must be corrected to the actual velocity at the striations, which are some distance from T_1 as described later.

The first step in the calculation is to compute the vector $\vec{QT}_1$. $\vec{QT}_1$ is orthogonal to B, thus:

$$\vec{QT}_1 \cdot \vec{B} = 0 \quad . \tag{D-1}$$

Furthermore, $\vec{QT}_1$ lies along the vector $\vec{A}$ where:

$$\vec{A} = \overrightarrow{T_2T_1} + a\,\vec{B} \quad . \tag{D-2}$$

By choosing the scalar a so that Equation (D-1) is satisfied defines $\vec{QT}_1 = \vec{A}$ with:

$$a = -\frac{\vec{B} \cdot \overrightarrow{T_2T_1}}{|\vec{B}|^2} \quad . \tag{D-3}$$

The vector $\vec{ET}_1$ is determined similarly. $\vec{ET}_1$ is orthogonal to $\vec{B}$, thus:

$$\vec{ET}_1 \cdot \vec{B} = 0 \quad . \tag{D-4}$$

Furthermore, $\vec{ET}_1$ lies along the vector $\vec{C}$ where:

$$\vec{C} = \vec{RT}_1 + b\vec{B} \quad . \tag{D-5}$$

By choosing the scalar b so that Equation (D-4) is satisfied gives $\vec{ET}_1 = \vec{C}$ with:

$$b = - \frac{\vec{B} \cdot \vec{RT}_1}{|\vec{B}|^2} \quad . \tag{D-6}$$

We note the projected distance Z_T is given by the magnitude of $\vec{ET}_1$

$$Z_T = |\vec{ET}_1| \quad . \tag{D-7}$$

Next a vector $\vec{D}$ is formed along which $\vec{XT}_1$ is located.

$$\vec{D} = \vec{QT}_1 + d\,\vec{ET}_1 \quad . \tag{D-8}$$

This vector is equal to $\vec{XT}_1$ when the scalar d is chosen to satisfy the orthogonality relation:

$$\vec{XT}_1 \cdot \vec{ET}_1 = 0 = \vec{D} \cdot \vec{ET}_1 \quad . \tag{D-9}$$

and

$$d = - \frac{\vec{QT}_1 \cdot \vec{ET}_1}{|\vec{ET}_1|^2} \tag{D-10}$$

The desired velocity is that along the $\vec{XT}_1$ direction. The rocket velocity is easily determined from the trajectory data (Appendix B),

$$V = \frac{\overrightarrow{T_2T_1}}{(\tau_2 - \tau_1)} \qquad \text{(D-11)}$$

where τ_1, τ_2 are the times corresponding to points T_1 and T_2.

The velocity along the $\vec{XT}_1$ direction is therefore given by

$$\vec{V}_x = \vec{V} \cdot \vec{XT}_1 \qquad \text{(D-12)}$$

and

$$V_x = |\vec{V}_x| \quad . \qquad \text{(D-13)}$$

It remains to correct the V_x to that at the striations that are some distance Z_1 from T_1. Figure D-2 illustrates the smaller velocity of the propagation path across the striations as a result of their being closer to the receiver. In a time interval T the distance transversed along $\vec{XT}_1$ is given by $V_x\Delta T$; at the striations this corresponds to $V_e\Delta T$. By the geometry involved,

$$\frac{V_e\Delta T}{Z_T - Z_1} = \frac{V_x\Delta T}{Z_T} \quad . \qquad \text{(D-14)}$$

so the effective transverse pattern velocity is given by:

$$V_e = \frac{Z_T - Z_1}{Z_T} \quad V_x \quad . \qquad \text{(D-15)}$$

As a final note, the magnetic Aspect angle, α, is given by:

$$\vec{B} \cdot \vec{RT}_1 = \cos\alpha \quad . \qquad \text{(D-16)}$$

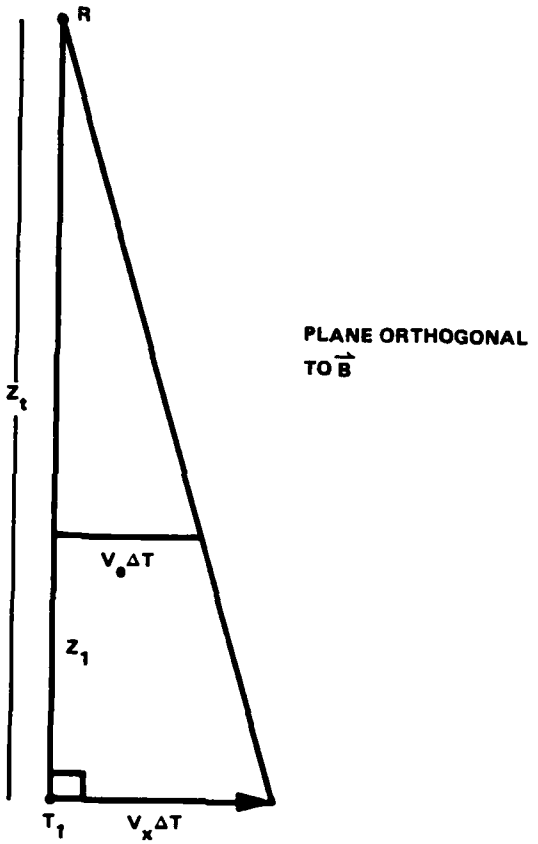

Figure D-2. Moment arm weighting of transverse pattern velocity.

D.2 ST. GEORGE ISLAND, BEACON 1

The result of carrying out these calculations for the St. George Island geometry for Beacon No. 1, yields V_x = 1120 m/sec and V_e = 980 m/sec at 40 km distance or V_e = 890 m/sec at 65 km distance.

APPENDIX E
DERIVATION OF TWO DOG-LEG DIFFERENTIAL DOPPLER RELATION

E.1 TWO-DIMENSIONAL SCATTER GEOMETRY

If both the transmitter and receiver are relatively close to the plasma, the TOA delay of the refracted ray is dependent on two dog-leg paths as illustrated in Figure E-1. The differential Doppler, F_d, of a refracted ray relative to the direct path can be expressed in terms of the TOA delay, , the distance from the receiver to the viewing plane, Z_2, the refraction offset distance, d, and the distance from the rocket to the viewing plane through the refracting object, Z_1. The functional relationship can be derived from the expression for the excess phase,

$$\phi = k(\Delta Z_1 + \Delta Z_2) \quad . \tag{E-1}$$

Differentiating the differential Doppler is obtained as

$$\omega_d = \dot{\phi} = k(\Delta \dot{Z}_1 + \Delta \dot{Z}_2) \quad . \tag{E-2}$$

The differential distances can be expressed in tems of the pattern velocity V through the relation

$$V = \dot{d} \tag{E-3}$$

and

$$d^2 = \ell_2^2 - z_2^2 = \ell_1^2 - z_1^2 \tag{E-4}$$

$$2d\dot{d} = 2\ell_2\dot{\ell}_2 = 2\ell_1\dot{\ell}_1 \tag{E-5}$$

$$= 2\ell_2\Delta\dot{Z}_2 = 2\ell_1\Delta\dot{Z}_1 \tag{E-6}$$

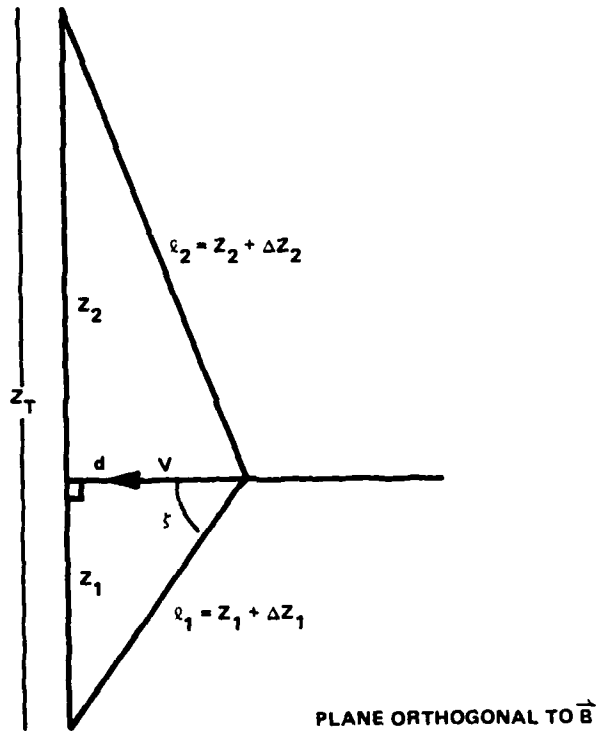

Figure E-1. Two dog-leg geometry.

or

$$V = \dot{d} = \frac{\ell_2 \dot{\Delta z}_2}{d} = \frac{\ell_1 \dot{\Delta z}_1}{d} \quad . \tag{E-7}$$

Substituting into the differential Doppler expression, we obtain

$$f_d = \frac{V}{\lambda} d \left(\frac{\ell_1 + \ell_2}{\ell_1 \ell_2} \right) . \tag{E-8}$$

Expression ℓ_1 and ℓ_2 in terms of z_1 and z_2

$$f_d = \frac{V}{\lambda} d \left(\frac{z_1 + z_2 + \Delta z_2 + \Delta z_1}{z_1 z_2 + \Delta z_2 z_1 + \Delta z_1 z_2 \Delta z_1 \Delta z_2} \right) . \tag{E-9}$$

Now the measured delay τ is given by

$$\tau = 1/c(\Delta z_1 + \Delta z_2) \quad . \tag{E-10}$$

Additionally, the denominator terms are small compared to $z_1 z_2$ for the geometries of interest, thus we obtain

$$f_d \cong \frac{V}{\lambda} d \left(\frac{z_1 + z_2 + C\tau}{z_1 z_2} \right) . \tag{E-11}$$

It remains to express d in terms of z_1, z_2, and τ as follows. The total time delay can be related to d as

$$T_T = \frac{1}{c}(z_1 + z_2) + \tau = \frac{1}{c}(\ell_1 + \ell_2)$$

$$= \frac{1}{c} \left(\sqrt{d^2 + z_2^2} + \sqrt{d^2 + z_1^2} \right) . \tag{E-12}$$

Taking the square of both sides and rearranging terms we obtain

$$\sqrt{d^2 + z_2^2} \sqrt{d^2 + z_1^2} = \left[\frac{(z_1 + z_2 + C\tau)^2 - (z_2^2 + z_1^2)}{2} \right] - d^2 \quad . \tag{E-13}$$

Squaring both sides once again

$$d^4+d^2(z_1^2+z_2^2)+z_1^2z_2^2 = \left[\quad .\quad\right]^2 - 2d^2\left[\quad .\quad\right] + d^4 \quad . \qquad \text{(E-14)}$$

From which we solve for d as

$$d = \sqrt{\frac{\left[\quad .\quad\right]^2 - z_1^2z_2^2}{2\left[\quad .\quad\right] + (z_1^2+z_2^2)}} \quad . \qquad \text{(E-15)}$$

Simplifying,

$$d = \sqrt{\frac{\left[\dfrac{(z_1+z_2+c\tau)^2 - (z_2^2+z_1^2)}{2}\right]^2 - z_1^2z_2^2}{(z_1+z_2+c\tau)^2}} \qquad \text{(E-16)}$$

to

$$f_d \cong \frac{V}{\lambda}\sqrt{\frac{1}{z_1^2z_2^2}\left[\frac{(z_1+z_2+c\tau)^2 - (z_2^2+z_1^2)}{2}\right]^2 - 1} \qquad \text{(E-17)}$$

$$\cong \frac{V}{\lambda}\sqrt{\left[1 + c\tau\left(\frac{z_1+z_2}{z_1z_2}\right) + \frac{c^2\tau^2}{2z_1z_2}\right]^2 - 1} \qquad \text{(E-18)}$$

dropping $c^2\tau^2$ term and completing square we obtain the relation

$$f_d \cong \frac{V}{\lambda}\sqrt{\frac{2c\tau}{z_1}\cdot\left(1 + \frac{z_1}{z_2}\right)} \quad . \quad = \frac{V}{\lambda}\sqrt{\frac{2c\tau}{z_1}\left(\frac{z_T}{z_T - z_1}\right)} \qquad \text{(E-19)}$$

This relationship, when compared with the expression obtained for an incident plane wave, would imply approximately a 5 percent larger f_d for the same delay τ. The Doppler is increased over that obtained from an incident plane wave situation by the term $\sqrt{\frac{z_T}{z_T - z_1}}$.

E.2 EXTENSION TO 3-DIMENSIONAL SCATTER GEOMETRY

Equation (E-19) is appropriate for the 2-D situation where the transmitter and receiver are in the plane orthogonal to the magnetic field. To apply these geometric relations to the PLACES data, it is necessary to modify the dog-leg delay term to account for the 3-dimensional nature of the problem. The direct and scattered ray path both extend a distance y out of the plane of Figure E-1 as shown in Figure E-2. The distance y is related to Z_1 through the Magnetic Aspect Angle α as;

$$y = Z_1 \operatorname{ctn}\alpha \quad . \tag{E-20}$$

A magnetic aspect angle of 90° denotes wave incidence broadside to the geomagnetic field.

Thus, for an incident plane wave, the dog-leg delay becomes

$$\Delta Z = \sqrt{x^2+y^2+z_1^2} - \sqrt{y^2+z_1^2} \tag{E-21}$$

which for small angle scatter reduces to

$$\Delta Z = \frac{x^2}{2\sqrt{y^2+z_1^2}} = \frac{x^2 \sin\alpha}{2Z_1} \quad . \tag{E-22}$$

The differential delay is given by

$$\tau = \frac{\Delta Z}{C} = \frac{x^2 \sin\alpha}{2Z_1 C} \quad . \tag{E-23}$$

The differential Doppler is given by

$$f_d = \frac{1}{\lambda} \dot{\Delta} Z = \frac{1}{\lambda} \frac{x\dot{x} \sin\alpha}{Z_1} \quad . \tag{E-24}$$

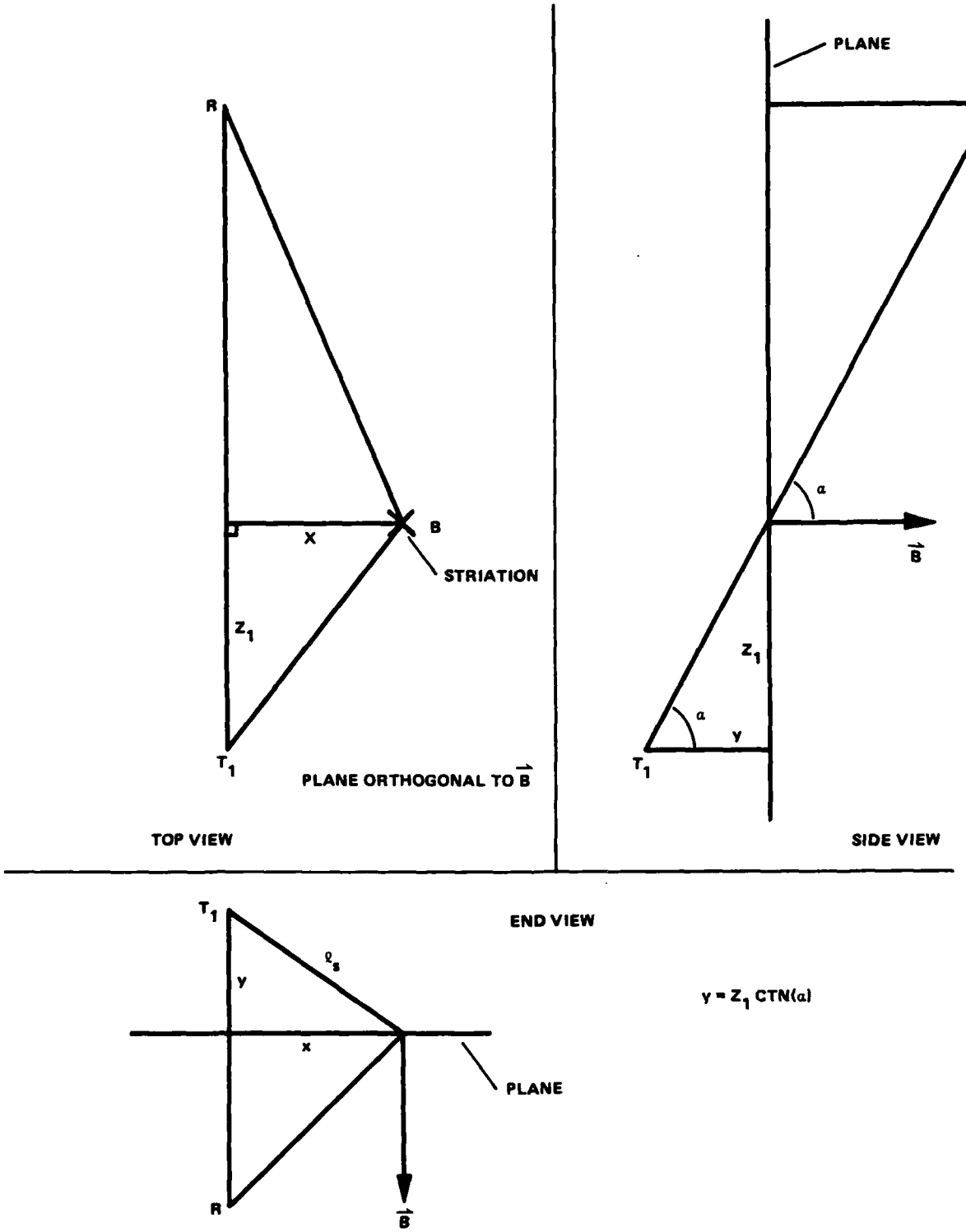

Figure E-2. Three-dimensional nature of dog-leg delay.

and from the above expression for τ we obtain

$$f_d = \frac{\dot{x}}{\lambda} \sqrt{\frac{2C\tau}{Z_1} \sin \alpha} \quad . \tag{E-25}$$

Thus, the delay Doppler relationship must be modified for the PLACES 3-Dimensional Scattering Geometry to include the effective Fresnel distance term $Z_1 \, CSC\alpha$.

If the transverse beacon rocket velocity, V_x, is related to the effective transverse striation velocity through the relation (see Appendix D)

$$V_e = \frac{Z_T - Z_1}{Z_1} V_x \tag{E-26}$$

where $\dot{x}$ in the above expression is equal to V_e, then the final generalized form of the delay Doppler expression is obtained;

$$f_d = \frac{V_x}{\lambda} \sqrt{\frac{2C\tau}{Z_1 \, CSC\alpha}} \left(\frac{Z_T - Z_1}{Z_T}\right) \quad . \tag{E-27}$$

APPENDIX F
CORRESPONDENCE OF MCF APPROACH AND COMMUNICATIONS CHANNEL INTERPRETATION

F.1 COMMUNICATIONS APPROACH

The received phase PSD does not correspond to the phase PSD of the in situ striation structure because of diffraction effects. At a high enough frequency where diffraction effects can be neglected, the received phase is an integral measure of the in-situ path integrated structure along the propagation path. The in-situ path integrated phase PSD can be derived from the received signal. The signal exiting the phase shifting plasma screen can be represented as

$$y(t) = A \cos[w_o t + \phi(t)] \quad ,$$

where $\phi(t)$ is the random phase modulation imparted to the signal by the plasma striations. Under the assumption that the phase modulation is a wide sense stationary narrow-band random process with finite variance, the autocorrelation of $y(t)$ is given by

$$R_y(\tau) = A^2/2 \, \mathrm{Re}[\exp(jw_o\tau) \, R_z(\tau)] \quad ,$$

where $z(t)$ is the complex envelope of $y(t)$, and

$$Z(t) = \exp[j\phi(t)] \quad .$$

For ϕ a Gaussian random variable with zero mean and finite variance (see Appendix G),

$$R_z(\tau) = \exp[-\{R_\phi(0) - R_\phi(\tau)\}] \quad .$$

After propagation to the ground, the received signal can be represented as

$$g(t) = b(t) A \cos w_o t + \xi(t)] \quad .$$

The complex envelope, q(t), of the received signal is given by

$$q(t) = b(t) \exp[j\xi(t)] \quad .$$

Since signal propagation does not affect the signal power spectrum (angular spectrum), it follows that

$$R_q(\tau) = R_z(\tau) = \exp[-\{R_\phi(0) - R_\phi(\tau)\}] \quad .$$

And thus, the phase power spectrum can be obtained from the transform relation

$$\mathcal{F}\{\ln R_q(\tau)\} = -\sigma_\phi^2 \delta(0) + S_\phi(f) \quad .$$

F.2 CORRESDONDENCE TO MCF APPROACH

The mutual coherence function is generally defined as

$$R_q(\vec{\Delta\rho}, z) = \langle q(\vec{\rho}, z)\, q^*(\vec{\rho}, z) \rangle$$

where $q(\rho, z)$ is the complex envelope of the diffraction field and satisfies the parabolic wave equation. z is in the propagation direction. Under a narrow angle scatter approximation,

$$R_q(\vec{\Delta\rho}, z) = \exp[D(\vec{\Delta\rho})/2] \quad ,$$

where

$D(\vec{\rho}, \vec{\rho})$ is the phase structure function. And

$$D(\vec{\rho}, \vec{\rho}') = \langle [\phi(\vec{\rho}) - \phi(\vec{\rho}')]^2 \rangle \quad ,$$

where

$$\phi(\vec{\rho}) = - r_e \lambda \int_o^z N_e(\vec{\rho}, \eta) d\eta \quad .$$

This assumes D is a function only of $\Delta\vec{\rho}$, independent of location in the transverse plane. The 1-D Fourier transform of R_q gives the Doppler spectrum with $\Delta\vec{\rho} = \vec{V}\ \Delta t$.

Now

$$D(\vec{\rho}, \vec{\rho}') = \langle \phi^2(\vec{\rho}) \rangle + \langle \phi^2(\vec{\rho}') \rangle - 2\langle \phi(\vec{\rho}) \phi(\vec{\rho}') \rangle$$

which gives for ϕ a zero mean random variable,

$$D(\Delta\vec{\rho}) = 2[R_\phi(0) - R_\phi(\Delta\vec{\rho})] \quad ,$$

So

$$R_q(\Delta\vec{\rho}, z) = \exp[-\{R_\phi(0) - R_\phi(\Delta\vec{\rho})\}] \quad .$$

and a Gaussian assumption for the phase does not appear necessary.

APPENDIX G
DERIVATION OF AUTOCORRELATION OF PHASE MODULATED SIGNAL

Given a phase modulated signal of the form

$$y(t) = A \cos[w_o t + \phi(t)] ,$$

the autocorrelation is given by

$$R_y(\tau) = E[y(t+\tau)y^*(t)] = 1/2\ R_e[e^{-jw_o\tau} R_z(\tau)]$$

and from Reference 19, Equation 3.82,

$$R_z(\tau) = E[z(t)\ Z^*\ (t+\tau)]$$

$$= E[A(t)A(t+\tau)\ e^{-j\ \phi(t)\ +\ j\phi\ (t+\tau)}]$$

where

$$z(t) = A(t)\ \exp[j\phi(t)] \quad .$$

For A constant,

$$R_z(\tau) = A^2\ E\left[e^{\ -j\ \phi(t)\ +j\phi\ (t+\tau)}\right]$$

If ϕ are Gaussian, then from the characteristic function

$$E\left[e^{j(w_1 x + w_2 Y)}\right] = e^{j(w_1\eta_1 + w_2\eta_2)} \cdot e^{-1/2(\sigma_1{}^2 w_1{}^2 + 2r\sigma_1\sigma_2 w_1 w_2 + \sigma_2{}^2 w_2{}^2)}$$

where $r = E(x,y)/\sigma_1\sigma_2$, and
x and y are Gaussian random variables.

With $w_1 = 1, w_2 = -1, \sigma_1 = \sigma_2 = \sigma_\phi , \eta_1 = \eta_2 ,$

and assuming wide sense stationarity,

$$R_z(\tau) = A^2 \exp[-\{\sigma_\phi^2 - R(\tau)\}] ,$$

which does not require zero mean. Since $R_z(\tau)$ is real,

$$R_y(\tau) = A^2/2 \exp[-\{\sigma_\phi^2 - R(\tau)\}] \cos(w_o\tau) .$$

DISTRIBUTION LIST

DEPARTMENT OF DEFENSE

Defense Intell Agency
ATTN: RTS-2B

Defense Nuclear Agency
ATTN: NATF
ATTN: NAWE
ATTN: RAAE
ATTN: RAAE, P. Lunn
ATTN: RAAE, K. Schwartz
ATTN: RAEE
ATTN: STNA
4 cys ATTN: STTI-CA

Defense Tech Info Ctr
12 cys ATTN: DD

DEPARTMENT OF THE ARMY

US Army Nuclear & Chemical Agency
ATTN: Library

DEPARTMENT OF THE NAVY

Naval Ocean Systems Ctr
ATTN: Code 532
ATTN: Code 5322, M. Paulson
ATTN: Code 5323, J. Ferguson

Naval Rsch Laboratory
ATTN: Code 4108, P. Rodriguez
ATTN: Code 4187
ATTN: Code 4700
ATTN: Code 4700, S. Ossakow
ATTN: Code 4780
ATTN: Code 6700
ATTN: Code 7500, B. Wald
ATTN: Code 7950, J. Goodman

DEPARTMENT OF THE AIR FORCE

Air Force Weapons Laboratory
ATTN: NTN
ATTN: SUL

Air University Library
ATTN: AUL-LSE

Foreign Tech Div
ATTN: NIIS, Library
ATTN: TQTD, B. Ballard

Space Command
ATTN: DC, T. Long

Strategic Air Command
ATTN: SAC/SIJ
ATTN: NRI/STINFO
ATTN: SAC/SIZ
ATTN: XPFC
ATTN: XPFS
ATTN: XPQ

DEPARTMENT OF ENERGY CONTRACTORS

Los Alamos National Laboratory
ATTN: D. Simons

DEPARTMENT OF ENERGY CONTRACTORS (Continued)

EG&G, Inc
ATTN: D. Wright
ATTN: J. Colvin

DEPARTMENT OF DEFENSE CONTRACTORS

Autometric, Inc
ATTN: C. Lucas

Berkeley Rsch Associates, Inc
ATTN: C. Prettie
ATTN: J. Workman
ATTN: S. Brecht

ESL, Inc
2 cys ATTN: Dr. J. Marshall
2 cys ATTN: G. Elston
2 cys ATTN: J. Lehman

JAYCOR
ATTN: J. Sperling

Johns Hopkins University
ATTN: C. Meng
ATTN: J. Phillips
ATTN: J. Newland
ATTN: K. Potocki
ATTN: R. Stokes
ATTN: T. Evans

Kaman Tempo
ATTN: B. Gambill
ATTN: DASIAC
ATTN: W. McNamara

Kaman Tempo
ATTN: DASIAC

MAXIM Technologies, Inc
ATTN: E. Tsui
ATTN: J. Marshall
ATTN: R. Morganstern

Mission Rsch Corp
ATTN: Tech Library

Pacific-Sierra Rsch Corp
ATTN: H. Brode, Chairman SAGE

Pacifica Technology
ATTN: E. Giller

Physical Dynamics, Inc
ATTN: E. Fremouw

R&D Associates
ATTN: P. Haas

SRI International
ATTN: C. Rino
ATTN: D. McDaniel
ATTN: J. Vickrey
ATTN: R. Livingston
ATTN: V. Gonzalez

END

FILMED

12-85

DTIC